Spectrum and Energy Efficient Digital Modulation Techniques for Practical Visible Light Communication Systems

Mohamed Sufyan Islim

A thesis submitted for the degree of Doctor of Philosophy.
The University of Edinburgh.
October 2018

Abstract

The growth in mobile data traffic is rapidly increasing in an unsustainable direction given the radio frequency (RF) spectrum limits. Visible light communication (VLC) offers a lucrative solution based on an alternative license-free frequency band that is safe to use and inexpensive to utilize. Improving the spectral and energy efficiency of intensity modulation and direct detection (IM/DD) systems is still an on-going challenge in VLC. The energy efficiency of inherently unipolar modulation techniques such as pulse-amplitude modulation discrete multitone modulation (PAM-DMT) and asymmetrically clipped optical orthogonal frequency division multiplexing (ACO-OFDM) degrades at high spectral efficiency. Two novel superposition modulation techniques are proposed in this thesis based on PAM-DMT and ACO-OFDM. In addition, a practical solution based on the computationally efficient augmented spectral efficiency discrete multitone (ASE-DMT) is proposed. The system performance of the proposed superposition modulation techniques offers significant electrical and optical power savings with up to 8 dB in the electrical signal-to-noise ratio (SNR) when compared with DC-biased optical orthogonal frequency division multiplexing (DCO-OFDM). The theoretical bit error ratio (BER) performance bounds for all of the proposed modulation techniques are in agreement with the Monte-Carlo simulation results. The proposed superposition modulation techniques are promising candidates for spectrum and energy efficient IM/DD systems.

Two experimental studies are presented for a VLC system based on DCO-OFDM with adaptive bit and energy loading. Micrometer-sized Gallium Nitride light emitting diode (m-LED) and light amplification by stimulated emission of radiation diode (LD) are used in these studies due to their high modulation bandwidth. Record data rates are achieved with a BER below the forward error correction (FEC) threshold at 7.91 Gb/s using the violet m-LED and at 15 Gb/s using the blue LD. These results highlight the potential of VLC systems in practical high speed communication solutions. An additional experimental study is demonstrated for the proposed superposition modulation techniques based on ASE-DMT. The experimentally achieved results confirm the theoretical and simulation based performance predictions of ASE-DMT. A significant gain of up to 17.33 dB in SNR is demonstrated at a low direct current (DC) bias.

Finally, the perception that VLC systems cannot work under the presence of sunlight is addressed in this thesis. A complete framework is presented to evaluate the performance of VLC systems in the presence of solar irradiance at any given location and time. The effect of sunlight is investigated in terms of the degradations in SNR, data rate and BER. A reliable high speed communication system is achieved under the sunlight effect. An optical bandpass blue filter is shown to compensate for half of the reduced data rate in the presence of sunlight. This thesis demonstrates data rates above 1 Gb/s for a practical VLC link under strong solar illuminance measured at 50350 lux in clear weather conditions.

Lay summary

There is an increasing demand for wireless data access which is partially due to the rapid adoption of recent information and communications technologies. The radio frequency (RF) is a limited resource that cannot accommodate the bandwidth requirements endlessly. The visible light spectrum domain offers an alternative medium that is free, safe and inexpensive to be used. Visible light communication (VLC) is envisaged to use mainly low-cost light sources such as light emitting diodes (LEDs). Therefore, data can only be encoded through the rapid changes of light intensity. The adoption of state-of-the-art high speed digital modulation techniques in the optical domain is not straightforward and results in efficiency losses. A number of spectrum and energy efficient digital modulation techniques are proposed in this thesis. In addition, a novel solution is proposed to reduce the computational complexity of these modulation techniques. The proposed techniques offer significant energy savings in comparison with the other state-of-the-art techniques.

A number of experimental studies on high speed and energy efficient VLC systems are demonstrated in this thesis. The results demonstrate the suitability of VLC systems in high speed communications solutions. An implementation of a computationally and energy efficient modulation technique is additionally presented in this thesis. The presented results demonstrate that substantial power efficiency gains can be achieved using the proposed modulation technique.

There is a misconception that VLC cannot work under the sunlight effect. Theoretical and experimental studies are provided in this thesis to refute this mistaken belief. The results of these studies show that sunlight degrades the performance of VLC but does not hinder the operation of the system. A blue optical filter was found to limit the impact of sunlight on the performance of VLC. A practical VLC system is demonstrated at 1 Gb/s under the effect of sunlight.

Declaration of originality

I hereby declare that the research recorded in this thesis and the thesis itself was composed and originated entirely by myself in the LiFi Research and Development Centre, Institute of Digital Communications, School of Engineering, The university of Edinburgh.

The exceptions to the above are listed below:

- The MATLAB$^®$ code used for the implementation of the DC-biased optical orthogonal frequency division multiplexing (DCO-OFDM) in the experimental Study I and Study II in Chapter 4 is written by Dr. Dobroslav Tsonev within the LiFi R&D Centre at the University of Edinburgh.

- The experimental Study II in Chapter 4 is performed in collaboration with Shaun Viola from the School of Engineering, University of Glasgow. S. Viola assisted in assembling the experimental setup, thermoelectric cooler (TEC) and the measurement of the frequency response.

Mohamed Sufyan Islim

Acknowledgments

Contents

List of figures

List of tables

Acronyms and abbreviations

ACO-OFDM	asymmetrically clipped optical orthogonal frequency division multiplexing
ADC	analog-to-digital converter
ADO-OFDM	asymmetrically DC-biased optical orthogonal frequency division multiplexing
AGC	automatic gain control
AM	air mass
APD	avalanche photodiode
ASCO-OFDM	asymmetrically and symmetrically clipping optical orthogonal frequency division multiplexing
ASE-DMT	augmented spectral efficiency discrete multitone
ASIC	application-specific integrated circuit
ASTM	American society for testing and materials
AR/VR	augmented and virtual reality
AWG	arbitrary waveform generator
AWGN	additive white Gaussian noise
BER	bit error ratio
BPSK	binary phase-shift keying
CCD	charge coupled device
CCDF	complementary cumulative distribution function
CCT	correlated color temperature
CDF	cumulative distribution function
CIE 1930	Commission Internationale de l'Eclairage
CLT	central limit theorem
CMOS	complementary metal oxide semiconductor
CP	cyclic prefix

CPC	compound parabolic condenser
CRI	color rendering index
CSK	color shift keying
CW Laser	continuous wave laser
DAC	digital-to-analog converter
DC	direct current
DCO-OFDM	DC-biased optical orthogonal frequency division multiplexing
DFT	discrete Fourier transform
DHT	discrete Hartley transformation
DMT	discrete multi-tone
DoF	degrees of freedom
DSB	double sided bandwidth
eACO-OFDM	enhanced asymmetrically clipped optical orthogonal frequency division multiplexing
E-O	electrical to optical
ePAM-DMT	enhanced pulse-amplitude modulation discrete multitone modulation
eU-OFDM	enhanced unipolar orthogonal frequency division multiplexing
FCC	federal communications commission
FEC	forward error correction
FFT	fast Fourier transform
FIR	finite impulse response
FLIP-OFDM	flip orthogonal frequency division multiplexing
FOV	field of view
FSO	free space optical
FWHM	full width at half maximum
FWHT	fast Walsh-Hadamard transformation
GMST	Greenwich mean sidereal time

GREENER-OFDM	generalized enhanced unipolar orthogonal frequency division multiplexing
HACO-OFDM	hybrid asymmetrical clipped orthogonal frequency division multiplexing
HCM	Hadamard coded modulation
IDI	inter-depth interference
IEEE	Institute of Electrical and Electronics Engineers
IFFT	inverse fast Fourier transform
i.i.d.	independent identically distributed
IM/DD	intensity modulation and direct detection
IoT	internet of things
IR	infra-red
ISI	inter-symbol interference
ITU	International Telecommunication Union
I-V	current-voltage
LaaS	light as a service
LACO-OFDM	layered asymmetrically clipped optical orthogonal frequency division multiplexing
LD	light amplification by stimulated emission of radiation diode
LED	light emitting diode
L-I	luminance-current
LiFi	light fidelity
LMST	local mean sidereal time
LoS	line-of-sight
LSB	lower side band
LPF	low pass filter
L-V	luminance-voltage
M2M	machine to machine
MCM	multi-carrier modulation
MIMO	multiple-inputs multiple-outputs

M-PAM	*M*-ary pulse-amplitude modulation
MPPM	multiple pulse position modulation
M-QAM	*M*-ary quadrature amplitude modulation
ND	neutral density
NLoS	non line-of-sight
OCC	optical camera communication
OFDM	orthogonal frequency division multiplexing
OFDMA	orthogonal frequency division multiple access
OLED	organic light emitting diode
OOK	on-off keying
OWC	optical wireless communication
PAM	pulse-amplitude modulation
PAM-DMT	pulse-amplitude modulation discrete multitone modulation
PAPR	peak-to-average power ratio
PC-LED	phosphor coated light emitting diode
PD	photodiode
PDF	probability density function
PIN-PD	P-type intrinsic N-type photodiode
PM-OFDM	position modulation orthogonal frequency division multiplexing
PMT	photo-multiplier tube
P-OFDM	polar orthogonal frequency division multiplexing
PPM	pulse position modulation
PRBS	pseudo random binary sequence
PSD	power spectral density
M-PSK	*M*-ary phase shift keying
PV	photo-voltaic
PWM	pulse width modulation
QAM	quadrature amplitude modulation

RC-LED	resonant cavity light emitting diode
RF	radio frequency
RGB-LD	red, green and blue light amplification by stimulated emission of radiation diode
RGB-LED	red, green and blue light emitting diode
RPO-OFDM	reverse polarity optical orthogonal frequency division multiplexing
RRC	root raised cosine
SCM	single-carrier modulation
SCO-OFDM	symmetrical clipping optical orthogonal frequency division multiplexing
SEE-OFDM	spectrally and energy efficient orthogonal frequency division multiplexing
SFO-OFDM	spectrally factorized optical orthogonal frequency division multiplexing
SNR	signal-to-noise ratio
SPAD	single photon avalanche photodiode
SSB	single sided bandwidth
SSL	solid-state lighting
SWIPT	simultaneous wireless information and power transfer
m-LED	micrometer-sized Gallium Nitride light emitting diode
U-OFDM	unipolar orthogonal frequency division multiplexing
USB	upper side band
UV	ultra-violet
VCSEL	vertical-cavity surface-emitting laser
VLC	visible light communication
VLCC	visible light communication consortium
VPPM	variable pulse position modulation
WDM	wavelength division multiplexing
WiFi	wireless fidelity
WPDM	wavelet packet division multiplexing

Nomenclature

$*$	convolution operation
$\lvert \cdot \rvert$	absolute value
$\Im[\cdot]$	operator to obtain the imaginary part of a complex number
$\Re[\cdot]$	operator to obtain the real part of a complex number
$\mathrm{E}[\cdot]$	statistical expectation
$\mathrm{f_{clip}}\{\cdot\}$	clipping function of an OFDM waveform at the zero-level
$\lfloor \cdot \rfloor$	greatest integer less than or equal to an input real number
$\overline{F}$	time-flipping operation on the subframe F that has a length L_F; $\overline{F}[n] = F[L_F - 1 - n]$
$\mathrm{IFFT}[\cdot]$	inverse fast Fourier transformation
$z(\cdot)$	nonlinear transformation of the light source
$\mathrm{ABER_{SM}^{opt}}$	average BER performance of a superposition modulation technique as a function of the optical SNR
$\mathrm{ABER_{SM}^{opt}}$	average BER performance of a superposition modulation technique as a function of the electrical SNR
AM	optical air mass
α^{ra}	right ascension
α	attenuation factor of the nonlinear transformation
$\alpha_{\mathrm{elec}}^{P}(D, \underline{\gamma})$	ratio of the average electrical power of superposition modulation waveform to the average electrical power of an inherently unipolar waveform
$\alpha_{\mathrm{elec}}^{\mathrm{ASE}}(D, d, \underline{\gamma})$	the increase in the dissipated electrical energy per bit in ASE-DMT compared with the electrical energy dissipation per bit of PAM-DMT stream at depth d
$\alpha_{\eta}^{\mathrm{ASE}}(D, d)$	spectral efficiency ratio of ASE-DMT to a PAM-DMT scheme with a similar constellation size
$\alpha_{\mathrm{elec}}^{\mathrm{eACO}}(D, d, \underline{\gamma})$	the increase in the dissipated electrical energy per bit in eACO-OFDM compared with the electrical energy dissipation per bit of ACO-OFDM stream at depth d
$\alpha_{\eta}^{\mathrm{eACO}}(D, d)$	spectral efficiency ratio of the eACO-OFDM to an ACO-OFDM scheme with a similar constellation size

α^{EO}	the ratio of the electrical to optical average power of a superposition modulation technique
$\alpha_{\mathrm{elec}}^{\mathrm{ePAM}}(D, d, \underline{\gamma})$	the increase in the dissipated electrical energy per bit in ePAM-DMT compared with the electrical energy dissipation per bit of PAM-DMT stream at depth d
$\alpha_{\eta}^{\mathrm{ePAM}}(D, d)$	spectral efficiency ratio of the ePAM-DMT to a PAM-DMT scheme with a similar constellation size
A_{d}	active detection area of the photodetector
$A_{d,l}$	time domain subframe at depth d with samples between 0 and $N_{\mathrm{FFT}}/2$ of the l-th PAM-DMT/ACO-OFDM frame
$\widetilde{A_{d,l}}$	modified subframe that consists of the first half of the l-th PAM-DMT frame $A_{d,l}$ and the cyclic prefix $\mathrm{CP}_{B_{d,l}}$ at the modulation depth d
$\overline{A_{d,l}}$	time-flipped version of the first half of the l-th PAM-DMT frame $A_{d,l}$ at a modulation depth d
$\overline{\widetilde{A_{d,l}}}$	time-flipped version of the modified subframe that consists of the time-flipped version of the first half of the l-th PAM-DMT frame, $\overline{A_{d,l}}$, and the time-flipped cyclic prefix $\overline{\mathrm{CP}_{B_{d,l}}}$ at a modulation depth d
$A_d^{\mathrm{PAM}}[k]$	PAM modulated symbol loaded at the real component of a subcarrier k from the superimposed stream of the modulation depth d in an ASE-DMT modulation technique
Al	solar altitude in the horizontal coordinate
Az	solar azimuth in the horizontal coordinate
$\mathrm{BER}_{\mathrm{ASE}}$	analytical BER performance of a single stream in the ASE-DMT modulation technique
$\mathrm{BER}_{\mathrm{eACO}}$	analytical BER performance of a single stream in the eACO-OFDM modulation technique
$\mathrm{BER}_{\mathrm{ePAM}}$	analytical BER performance of a single stream in the ePAM-DMT modulation technique
$\mathrm{BER}_{\mathrm{QAM}}$	analytical BER performance of the M-QAM in a real-valued bipolar OFDM modulation technique
$\mathrm{BER}_{\mathrm{SM}}$	analytical BER of a single stream in a superposition modulation technique

$\mathrm{BER}(M_k, \nu_k)$	analytical BER at a subcarrier k with a modulation order M_k and a SNR ν_k
β	ecliptic latitude
b	number of bits encoded in a symbol
B	single sided bandwidth
$B_{\mathrm{DC}}^{\mathrm{dB}}$	electrical power penalty due to the addition of a DC bias in DCO-OFDM
$B_{d,l}$	time domain subframe at depth d with samples between $N_{\mathrm{FFT}}/2 + 1$ and $N_{\mathrm{FFT}} - 1$ of the l-th PAM-DMT/ACO-OFDM frame
$\widetilde{B_{d,l}}$	modified subframe that consists of the second half of the l-th PAM-DMT frame $B_{d,l}$ and the cyclic prefix $\mathrm{CP}_{A_{d,l}}$ at the modulation depth d
$\overline{B_{d,l}}$	time-flipped version of the second half of the l-th PAM-DMT frame $B_{d,l}$ at a modulation depth d
$\overline{\widetilde{B_{d,l}}}$	time-flipped version of the modified subframe that consists of the time-flipped version of the second half of the l-th PAM-DMT frame, $\overline{B_{d,l}}$, and the time-flipped cyclic prefix $\overline{\mathrm{CP}_{A_{d,l}}}$ at a modulation depth d
b_k	number of bits conveyed at a subcarrier k
$B_d^{\mathrm{PAM}}[k]$	PAM modulated symbol loaded at the imaginary component of a subcarrier k from the superimposed stream at the modulation depth d in ASE-DMT modulation technique
$B^{\mathrm{PAM}}[k]$	PAM modulated symbol loaded at the imaginary component of a subcarrier k in PAM-DMT
$\hat{B}_1^{\mathrm{PAM}}[k]$	the imaginary part of the recovered PAM symbol at a subcarrier k of the first modulation depth in an ASE-DMT modulation technique
CP	cyclic prefix of an OFDM frame
$\mathrm{CP}_{A_{d,l}}$	cyclic prefix of the l-th PAM-DMT subframe $A_{d,l}$ at the modulation depth d
$\overline{\mathrm{CP}_{A_{d,l}}}$	time-flipped version of the cyclic prefix of the l-th PAM-DMT subframe $A_{d,l}$ at a modulation depth d
$\mathrm{CP}_{B_{d,l}}$	cyclic prefix of the l-th PAM-DMT subframe $B_{d,l}$ at the modulation depth d
$\overline{\mathrm{CP}_{B_{d,l}}}$	time-flipped version of the cyclic prefix of the l-th PAM-DMT subframe $B_{d,l}$ at a modulation depth d
$C_{\mathrm{ASE}}(D)$	computation complexity per bit of ASE-DMT

$C_{\text{ASE}}^{\text{Rx}}$	asymptotic computation complexity of the ASE-DMT receiver with an infinite number of modulation depths
$C_{\text{ASE}}^{\text{Rx}}(D)$	computation complexity of the ASE-DMT receiver with a maximum number of modulation depths D
$C_{\text{ASE}}^{\text{Tx}}$	asymptotic computation complexity of the ASE-DMT transmitter with an infinite number of modulation depths
$C_{\text{ASE}}^{\text{Tx}}(D)$	computation complexity of the ASE-DMT transmitter with a maximum number of modulation depths D
C_{DCO}	computation complexity per bit of DCO-OFDM
$C_{\text{eACO}}(D)$	computation complexity per bit of eACO-OFDM
$C_{\text{eACO}}^{\text{Rx}}$	asymptotic computation complexity of the eACO-OFDM receiver with an infinite number of modulation depths
$C_{\text{eACO}}^{\text{Rx}}(D)$	computation complexity of the eACO-OFDM receiver with a maximum number of modulation depths D
$C_{\text{eACO}}^{\text{Tx}}$	asymptotic computation complexity of the eACO-OFDM transmitter with an infinite number of modulation depths
$C_{\text{eACO}}^{\text{Tx}}(D)$	computation complexity of the eACO-OFDM transmitter with a maximum number of modulation depths D
$C_{\text{ePAM}}(D)$	computation complexity per bit of ePAM-DMT
$C_{\text{ePAM}}^{\text{Rx}}$	asymptotic computation complexity of the ePAM-DMT receiver with an infinite number of modulation depths
$C_{\text{ePAM}}^{\text{Rx}}(D)$	computation complexity of the ePAM-DMT receiver with a maximum number of modulation depths D
$C_{\text{ePAM}}^{\text{Tx}}$	asymptotic computation complexity of the ePAM-DMT transmitter with an infinite number of modulation depths
$C_{\text{ePAM}}^{\text{Tx}}(D)$	computation complexity of the ePAM-DMT transmitter with a maximum number of modulation depths D
$C_{\text{PAM}}^{\text{Tx/Rx}}$	computation complexity of a PAM-DMT transmitter or receiver
δ	declination of the Sun
Δf	sub-carrier spacing
d	modulation depth index in multistream superimposition OFDM techniques

D	total number of depths in multistream superimposition OFDM techniques
D_s	diameter of the m-LED
D_lens	diameter of a lens
d_E	Euclidean distance between the transmitter and the receiver
D_o	time elapsed since the Greenwich noon of the 1st of January 2000
d'	distance between the m-LED and the transmitter lens
ϵ	axial tilt between the equatorial plane and the ecliptic plane
η	spectral efficiency of bipolar OFDM
η_ACO	spectral efficiency of the ACO-OFDM modulation technique
$\eta_\mathrm{ACO}(d)$	spectral efficiency of the ACO-OFDM stream at the modulation depth d in an eACO-OFDM modulation technique
$\eta_\mathrm{ASE,T}(D)$	spectral efficiency of the ASE-DMT waveform with a total number of superimposed streams D
$\eta_\mathrm{ASE}(d)$	spectral efficiency of the PAM-DMT stream at the modulation depth d in an ASE-DMT modulation technique
η_DCO	spectral efficiency of the DCO-OFDM modulation technique
$\eta_\mathrm{eACO}(D)$	spectral efficiency of the eACO-OFDM waveform with a total number of superimposed streams D
$\eta_\mathrm{ePAM}(D)$	spectral efficiency of the ePAM-DMT waveform with a total number of superimposed streams D
η_eU	spectral efficiency of the eU-OFDM modulation technique
η_PAM	spectral efficiency of the PAM-DMT modulation technique
$\eta_\mathrm{PAM}(d)$	spectral efficiency of the PAM-DMT stream at the modulation depth d in an ePAM-DMT modulation technique
η_SM	spectral efficiency of a superposition modulation technique
η_U	spectral efficiency of the U-OFDM modulation technique
η_k^Sh	the theoretical limit on the spectral efficiency at a subcarrier k
$E_{\mathrm{b}k}$	energy per bit at a subcarrier k
$E_\mathrm{b,elec}^\mathrm{SM}$	electrical energy per bit of a superposition modulation
$E_\mathrm{b,elec}^\mathrm{SM}/N_o$	electrical SNR of a superposition modulation
$E_\mathrm{b,opt}^\mathrm{SM}$	optical energy per bit of a superposition modulation
$E_\mathrm{b,opt}^\mathrm{SM}/N_o$	optical SNR of a superposition modulation

$\phi(x)$	probability density function of the standard Gaussian distribution
ϕ	radiant intensity angle
$\Phi_{1/2}$	semi-angle of a LED
ϕ_0	latitude angle of the observer
$\Phi_{1/2}^{\text{lens}}$	semi-angle at half power after the lens at the transmitter
ψ	angle of incidence
Ψ_{c}	field of view of a detector
$\mathbf{F}$	DFT matrix
F'	excess noise
f_{lens}	focal length of a lens
F_n	photodiode noise figure
$F[n]$	reference subframe
$FFT[\cdot]$	fast Fourier transformation
GMST	the Greenwich mean sidereal time
$\gamma_{\text{SM},d}^{\text{can.}}$	a scaling factor at depth d of a superposition modulation which has D superimposed streams
γ_d	amplitude scaling factor of the unipolar time-domain stream at modulation depth d in a superposition modulation technique
$\gamma_{\max,d}^{\text{dB}}$	the upper bound of the scaling factor at depth d of a superposition modulation which has D superimposed streams
$\gamma_{\min,d}^{\text{dB}}$	the lower bound of the scaling factor at depth d of a superposition modulation which has D superimposed streams
Γ_k	signal to noise ratio per symbol at a subcarrier k
$\mathcal{G}_{(\varsigma,D)}^{\text{can.}}$	the set of optimal power scaling factors for all of the possible candidates of constellation sizes in the set $\mathcal{M}_{(\varsigma,D)}^{\text{can.}}$
$\mathcal{G}_D^{\text{SM}}$	the optimal scaling factors for each of the optimal constellation sizes that achieve a target spectral efficiency with a maximum total number of superimposed depths D
$\underline{\gamma}_{(\eta,\varsigma,D)}^{\text{can.}}$	optimal scaling factor for the possible candidates of constellation sizes given in $\mathcal{M}_{(\varsigma,D)}^{\text{can.}}$
$\underline{\gamma}_{(\eta,D)}^{\text{SM}}$	the scaling factors associated with the optimal constellation sizes at a spectral efficiency η for a superposition modulation with a total number of superimposed depths D

$\underline{\gamma}_{(\eta,\varsigma,D)}^{\mathrm{max,dB}}$	the upper bound of the scaling factors ranges given in decibel at spectral efficiency η of a superposition modulation with a total number of superimposed depths D and a modulation technique specified by a variable ς
$\underline{\gamma}_{(\eta,\varsigma,D)}^{\mathrm{min,dB}}$	the lower bound of the scaling factors ranges given in decibel at spectral efficiency η of a superposition modulation with a total number of superimposed depths D and a modulation technique specified by a variable ς
g_{o}	mean anomaly of the Sun
$g(\psi)$	gain of an optical concentrator
G^{APD}	conversion gain of an APD given in V/W
G^{PIN}	conversion gain of a PIN-PD given in V/W
$\mathbf{H}$	circulant convolution channel matrix with the first column representing the channel impulse response
$|H(k)|^2$	channel gain at a subcarrier k
$h_{\mathrm{fe}}[n]$	discrete time channel impulse response function of the front-ends frequency response
$h_{\mathrm{mp}}[n]$	discrete time channel impulse response function of the multipath propagations of OWC
h_{o}	hour angle
h_k	channel impulse response at a subcarrier k
$h(t)$	continuous time impulse response of the channel
$h[n]$	discrete time impulse response of the channel
i	imaginary unit, i.e. $\sqrt{i} = -1$
I_{b}	average photocurrent generated due to the background light
I_{d}	total dark current
I_{DC}	DC bias current
I_{dg}	bulk dark current
I_{ds}	surface dark current
I_N	identity matrix
I_x	average photocurrent generated due to the LED source
κ	holes/electrons ionization rate
k	subcarrier index

k_{DC}	DC bias level
k^{B}	Boltzmann constant
λ	wavelength
λ_{el}	ecliptic longitude
λ_0	longitude of the observer
Λ^{APD}	conversion gain factor
$\boldsymbol{\Lambda}$	diagonal matrix with the eigenvalues of the channel Λ_k
l	index of the inherently unipolar subframe in a superposition modulation technique
L	number of channel taps
L_F	length of a subframe F
$\mathcal{M}_{(\varsigma,D)}^{\mathrm{can.}}$	the set of of all possible candidates of constellation sizes that achieve a target spectral efficiency with a maximum total number of superimposed depths D and a modulation technique specified by a variable ς
$\mathcal{M}_D^{\mathrm{SM}}$	the optimal set of all possible candidates of constellation sizes that achieve a target spectral efficiency with a maximum total number of superimposed depths D
$\underline{M}_{(\eta,\varsigma,D)}^{\mathrm{can.}}$	possible candidates of constellation sizes that can achieve a spectral efficiency target η with a total number of superimposed depths D and a modulation technique specified by a variable ς
$\underline{M}_{(\eta,D)}^{\mathrm{SM}}$	the optimal constellation sizes at a spectral efficiency η for a superposition modulation with a total number of superimposed depths D
m	Lambertian order
M	modulation order (constellation size)
$M_{\mathrm{ASE},d}$	constellation size of the PAM symbols used at the modulation depth d in an ASE-DMT modulation technique
$M_{\mathrm{eACO},d}$	constellation size of the QAM symbols used at the modulation depth d in an eACO-OFDM modulation technique
$M_{\mathrm{ePAM},d}$	constellation size of the PAM symbols used at the modulation depth d in an ePAM-DMT modulation technique
$M_{\mathrm{SM},D}^{\mathrm{can.}}$	the constellation size at depth d of a superposition modulation which has D superimposed streams
m_{mLED}	Lambertian order of a m-LED

M_{APD}	the average gain of the APD
M_{DCO}	constellation size of the QAM symbols used in DCO-OFDM
m_{lens}	Lambertian order of the lens
M_k	constellation size at a subcarrier k
$M_{\text{SM},\eta}^{\text{Max}}$	the maximum permitted constellation size at a spectral efficiency target η for the considered superposition modulation technique
ν_k	signal to noise ratio per symbol at a subcarrier k
n	discrete time index
n_{c}	refractive index of a concentrator
N_{CP}	cyclic prefix length
$N_{\text{CP}}^{\text{ePAM,max}}$	maximum cyclic prefix length for ePAM-DMT with a total number of depths D
N_{FFT}	OFDM frame length
$N_{d,l}$	negative inherently unipolar OFDM frame, where the subscripts denote that the frame at depth-d belongs to the l-th original bipolar OFDM frame
N_d^{ePAM}	OFDM frame length at depth d of ePAM-DMT
N_o	single sided power spectral density of the noise at the receiver
N_o^{sh}	power spectral density of the shot noise
N_o^{th}	power spectral density of the thermal noise
N^{Avg}	the total number of averaged waveforms at the oscilloscope
N_d^{eACO}	OFDM frame length at depth d of eACO-OFDM
$\mathcal{O}(\cdot)$	computation complexity given as the number of complex multiplications
$P_{\text{elec},d}^{\text{avg}}$	average electrical power of an inherently unipolar waveform at depth d
$P_{\text{opt}}^{\text{R,APD}}$	received optical power at an APD
$P_{\text{opt}}^{\text{R,lens}}$	optical power after the transmitter lens
$P_{\text{opt}}^{\text{T,mLED}}$	transmitted power by a m-LED
P_{SC}	solar constant flux density
$P_{d,l}$	positive inherently unipolar OFDM frame, where the subscripts denote that the frame at depth-d belongs to the l-th original bipolar OFDM frame
P_e^{T}	probability of error target
P_n	average optical power of the background illumination

$P_{\text{elec}}^{\text{avg,min}}$	minimum required electrical power to achieve the forward error correction threshold
$P_{\text{opt}}^{\text{avg,min}}$	minimum required optical power to achieve the forward error correction threshold
$P_{\text{elec}}^{\text{avg}}(D, \underline{\gamma})$	average electrical power of a superpositon modulation waveform with a total number of depths D, and scaling factor vector $\underline{\gamma}$
$P_{\text{opt}}^{\text{avg}}(D, \underline{\gamma})$	average optical power of a superpositon modulation waveform with a total number of depths D, and scaling factor vector $\underline{\gamma}$
$P_{\text{elec}}^{\text{avg}}$	average electrical power
$P_{\text{opt}}^{\text{avg}}$	average optical power
$P_{\text{Max}}^{\text{L}}$	maximum transmitted optical power
$P_{\text{Measured}}^{\text{L}}$	measured optical irradiance of the LED
P_{T}^{L}	transmitted optical irradiance from the LED source
P^{opt}	received optical power
P_{D}^{S}	direct solar irradiance
q	electron charge
q_{ml}	mean longitude
$Q(\cdot)$	complementary cumulative distribution function for the standard normal distribution
ρ_{c}	ceiling reflectivity
ρ_{f}	floor reflectivity
ρ_{w}	walls reflectivity
R	intrinsic responsivity of the photodetector
R_{L}	feedback resistor of the transimpedance amplifier of the photodetector
R_{Max}	maximum theoretical limit on the data rate
$R^{\text{LED}}(\phi)$	radiant intensity at angle ϕ
σ_{d}	standard deviation of the dark current noise
σ_{sh}	standard deviation of the shot noise
σ_{th}	standard deviation of the thermal noise
$\sigma_{w_{\text{c}}}$	standard deviation of the nonlinear distortion noise w_{c}
σ_n	standard deviation of the AWGN noise
σ_x	standard deviation of the time-domain OFDM signal

ς	a variable that specifies the choice of the modulation technique; $\varsigma = 1$ for eACO-OFDM and $\varsigma = 2$ for ePAM-DMT and ASE-DMT
Ξ	angle between the Sun and the fundamental plane in the arbitrary co-ordinates
Θ	angle between the principle and the projection of the Sun at the fundamental plane in the arbitrary coordinates
θ_L	angle between the meridian and the March equinox
θ_Z	solar angle relative to zenith in the horizontal coordinate
T_{lens}	transmittance of a lens
T_{bf}	transmittance of the bandpass optical blue filter
T_{s}	sampling time
T_{Sym}	symbol duration
T_d	delay spread of the channel
$T(\psi)$	transmittance of the filter at the photodetector
T^{K}	temperature given in kelvin
V_{DC}	DC bias voltage
V_{PP}	peak-to-peak voltage
$\mathbf{w}$	discrete AWGN
w_{c}	nonlinear distortion noise
$W_{\text{c}}(f)$	frequency representation of the nonlinear distortion noise w_{c}
$w_j[n]$	the j–th sample of the additive white Gaussian noise at discrete time index n
$w(t)$	continuous time additive white Gaussian noise at the receiver
$W[k]$	frequency domain realization of the additive white Gaussian noise at the receiver
$w[n]$	discrete time additive white Gaussian noise at the receiver
$\mathbf{x}$	transmitted waveform
$X_{\text{eACO},d}[k]$	modulated symbol loaded at a subcarrier k from the superimposed stream of the modulation depth d in an eACO-OFDM modulation technique
$x_{\text{ePAM},d}[n]$	transmitted ePAM-DMT signal at the modulation depth d and the discrete time sample n
$x_{\text{ACO}}[n]$	transmitted ACO-OFDM signal at the discrete time sample n

X_{C}	x axis of the Cartesian coordinates
X_{Ecl}	x axis of the ecliptic coordinates
X_{Equ}	x axis of the equatorial coordinates
X_{Hor}	x axis of the horizontal coordinates
$x_{\mathrm{PAM}}[n]$	transmitted PAM-DMT signal at the discrete time sample n
$x_{\mathrm{SM}}(t)$	transmitted superposition modulation signal at the continuous time sample t
$x_{\mathrm{T}}(t)$	transmitted ASE-DMT signal at the continuous time sample t
$x_{\mathrm{T}}[n]$	transmitted ASE-DMT signal at the discrete time sample n
$X_d[k]$	modulated symbol loaded at a subcarrier k from the superimposed stream of the modulation depth d in an ASE-DMT modulation technique
$x_d[n]$	bipolar ASE-DMT stream at the modulation depth d and discrete time sample n before zero-level clipping
$\hat{x}_d[n]$	the remodulated stream at depth d of an ASE-DMT modulation technique
$x_j[n]$	the j–th sample of the transmitted waveform at the discrete time index n
$x(t)$	continuous time transmitted waveform
$X[k]$	subcarrier at the discrete frequency k
$x[n]$	discrete time transmitted waveform
$X_{\mathrm{eACO},d}^{\mathrm{c}}[k]$	frequency representation at a subcarrier k of the clipped superimposed stream of the modulation depth d in an eACO-OFDM modulation technique
$X_d^{\mathrm{c}}[k]$	frequency representation at a subcarrier k of the clipped superimposed stream of the modulation depth d in an ASE-DMT modulation technique
$x_d^{\mathrm{c}}[n]$	ASE-DMT stream at the modulation depth d and discrete time sample n after zero-level clipping
$x^{\mathrm{c}}[n]$	clipped OFDM waveform at the zero-level
$X^{\mathrm{c}}[n]$	frequency representation of the clipped OFDM waveform at zero-level
$x_d^{\mathrm{SM}}(t)$	superimposed stream at the modulation depth d and continuous time sample t after zero-level clipping
$X_{\mathrm{T}}[k]$	The symbol at a subcarrier k of the transmitted ASE-DMT waveform

y	received waveform
Y_{C}	y axis of the Cartesian coordinates
Y_{Ecl}	y axis of the ecliptic coordinates
Y_{Equ}	y axis of the equatorial coordinates
Y_{Hor}	y axis of the horizontal coordinates
$y_j[n]$	the j–th sample of the received waveform at the discrete time index n
$y(t)$	continuous time received signal
$y[n]$	discrete time received signal
$y^{\mathrm{Avg}}[n]$	received averaged waveform at the discrete time index n
Z_{C}	z axis of the Cartesian coordinates
Z_{Ecl}	z axis of the ecliptic coordinates
Z_{Equ}	z axis of the equatorial coordinates
Z_{Hor}	z axis of the horizontal coordinates

Chapter 1
Introduction

1.1 Motivations

The demand for wireless access is predicted to surge significantly. This is partially due to disruptive and increasingly adopted technologies such as internet of things (IoT), machine to machine (M2M), augmented and virtual reality (AR/VR), smart televisions and cloud-based services. It is estimated that 75% of the generated traffic in 2021 will originate from non-PC devices [1]. The traffic generated by AR/VR is expected to increase 20 folds between 2016 and 2021 [1]. The overall number of networked devices is expected to reach 27.1 billion in 2021. These devices are predicted to generate an annual global internet traffic at 3.3 Zettabyte (3.3×10^{21} bytes) by 2021 [1]. Specifically, the traffic from wireless and mobile devices will account for 73% of the total internet traffic by 2021 [2]. The global mobile traffic is predicted to increase exponentially to reach 49 Exabytes per month in 2021 as shown in Fig. 1.1.

The electromagnetic spectrum is a scarce resource with frequency bands ranging from extremely low frequencies at 3 Hz to Gamma rays at 300 EHz. Each wireless transmission occupies a certain frequency band within the electromagnetic spectrum for a defined time. The spectrum is licensed globally through the International Telecommunication Union (ITU) and locally through auctions by regulatory bodies such as the federal communications commission (FCC) in the United States and Ofcom in the United Kingdom. The limited availability of the radio frequency (RF) spectrum[1] is becoming an ever more important challenge as the demand for higher data rates in wireless broadband access increases. A recent auction by Ofcom has resulted in a license award at an average cost of $7.8 million per single MHz in the 3.4 GHz spectrum band [3].

Martin Cooper, considered by many as the father of mobile telephony, has predicted

---

[1]The term RF is used for the radio, microwave and millimeter frequency bands between 3 KHz and 300 GHz throughout this thesis.
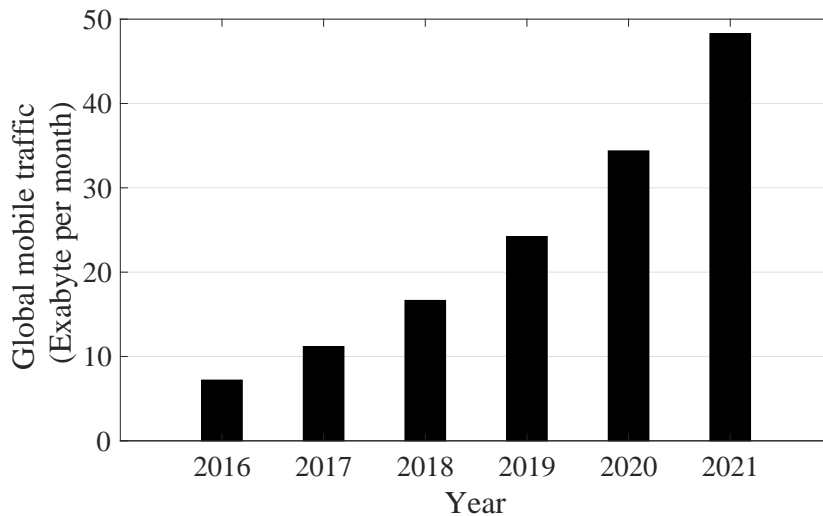
Figure 1.1: *Cisco prediction for the global mobile traffic between 2016 and 2021 given in Exabyte [1].*

that wireless capacity has almost doubled every 30 months since Guglielmo Marconi's first wireless transmissions in 1895. This is almost a 2 million fold improvement since 1957. Breaking down the growth of wireless capacity between 1957 and 2008 [4], it was estimated that 25-folds of the increases were achieved by releasing additional spectrum. Additional 5-folds of the increases arise from refarming the spectrum and another 5-folds increases are achieved by the improved design of physical layer techniques. A significant 1600-folds contribution of this growth was attributed to the reduction in the sizes of the cells and the transmition distances. This was also accompanied by an expected increase in the number of cells. In fact, the increase in the density of the cells is required to increase the capacity per unit area by decreasing the cells sizes [5]. However, impairments such as co-channel interference limit the benefits of reducing the sizes of the cells in the RF domain. Strikingly, wireless access points for wireless fidelity (WiFi) were mounted below the seats in stadiums in order to minimize the interference by using the human body for attenuation [6].

There has been an increasing interest in using the millimeter frequency bands between 28 and 250 GHz for communications purposes. Massive multiple-inputs multiple-outputs (MIMO) antennas are promising candidates to enable beamforming in millimeter waves communication as the small wavelengths in the millimeter frequency band enable dozens of antennas elements to be mounted on a relatively compact physical area. This allows millimeter waves communications to minimize the interference within

the small cells concept. However, the wave propagation at high frequencies suffers from high pathloss and reduced diffraction which makes millimeter wave communication more vulnerable to blocking [7].

The overall RF spectrum is predicted to be fully utilized by 2035 [6]. This highlights the necessity of unlocking new access technologies based on different frequency bands that could meet the increasing demand for wireless access. The interest in optical wireless communication (OWC) started with the pioneering work of Gfeller and Bapst in 1979 in-which they proposed and investigated an infrared-based OWC system for a wireless in-home network [8].

The advances of solid-state lighting (SSL) has enabled the emergence of OWC based on the visible spectrum between wavelength $\lambda = 400$ nm and $\lambda = 700$ nm, which is known as visible light communication (VLC) [9,10]. VLC offers an abundant frequency bandwidth that is unlicensed and generally safe to use as long as the eye safety regulations are considered. It was predicted that data rates in the excess of 100 Gb/s are achievable if the complete visible spectrum is utilized [11]. However, it is technically difficult to fully utilize the overall visible spectrum. The bandwidth of a VLC system is generally defined by the frequency response of the front-end devices which can be as high as 6.8 GHz [12].

SSL provides a higher degree of spectral and intensity control over conventional light sources. Combinations of SSL sources and color converters can be used to achieve the desired spectra. In addition, the optical spatial distribution of SSL light sources can be controlled using small sized low-cost optics [13]. The adoption of SSL has resulted in significant energy savings for consumers and additional considerable savings are expected due to the emergence of light as a service (LaaS). Lights can now be connected with IoT sensors to perform active and remote control among other different functionalities. For example, SSL are now integrated with occupancy sensors and indoor-positioning to allow optimal energy consumption. The number of new light emitting diode (LED) installations in the United States is estimated at 874 million new units in 2016. These have resulted in energy savings approximated at 137.45 TWh [14]. However, the potential energy saving is predicted to be as high as 1297.72 TWh by 2035 when all the lighting systems are converted into high efficacy LEDs [14]. This corresponds to huge savings in energy costs and reductions in CO_2 emmision. VLC has the potential to reuse

the existing SSL lighting infrastructure which could potentially increase these savings.

VLC offers a low-cost solution to the looming spectrum crunch due to the availability of inexpensive front-end devices. VLC is a unique option in scenarios where RF propagation is considered to be hazardous, such as hospital theaters and petrochemical plants[2]. The light propagation is confined by opaque objects. This allows VLC to reuse the same bandwidth in different rooms which further improves the spectral efficiency per unit area. In addition, it prevents eavesdropper from gaining access to the physical channel as long as they are not in the same room as a VLC transmitter. However, the major drawback of the propagation of light is the higher outage probability due to blockage.

The high speed bidirectional light-based networking solution that is proposed to work seamlessly with other RF access technologies is termed light fidelity (LiFi) [15, 16]. LiFi can support multiuser access and handover between light-based access points. The small cells in LiFi (attocells) improve the area spectral efficiency significantly due to the massive spatial reuse that allows LiFi to support cell radii between 1 and 4 meters [16]. It was estimated that the area spectral efficiency of LiFi can be 40 to 1800 times higher than the area spectral efficiency of femtocell networks [17]. The integration of SSL with sensors, smartphone applications and IoT enables a paradigm shift towards connected lights [13, 18]. LiFi has the potential to bridge the communications and lighting industries and enable the emergence of LaaS. The ubiquitous availability of light sources enables the opportunity of creating a dense network of access points that can enable a wider variety of applications such users density and location. There has been a recent increase in both research and commercial interest in LiFi. A task group has been formed to draft a new standard within the IEEE 802.11 standardization group based on LiFi [18]. The new standard has received the reference IEEE 802.11bb.

VLC and LiFi uses off-the-shelf incoherent optoelectronic components as front-end devices which restrict the signalling methods to intensity modulation and direct detection (IM/DD). Modulation techniques such as on-off keying (OOK), pulse position modulation (PPM), and pulse-amplitude modulation (PAM) can be straightforward to implement [19]. However, the performance of these techniques degrades as the data rate

---

[2]Note that shielding should be considered when designing the electronic circuitry of the transmitter and receiver since these elements are susceptible to RF interference.

increases due to the high inter-symbol interference (ISI). Optical orthogonal frequency division multiplexing (OFDM) is a promising candidate for OWC, since the equalization can be performed using the computationally efficient single-tap equalizer. The optical OFDM signal is required to be real and unipolar because of using IM/DD signalling. Therefore, Hermitian symmetry is used to enforce the OFDM output into the real domain [20]. The widely deployed DC-biased optical orthogonal frequency division multiplexing (DCO-OFDM) employs a direct current (DC)-bias to create a unipolar signal, but this incurs significant energy losses.

Unipolar OFDM modulation techniques were proposed to provide an energy efficient alternative to DCO-OFDM. Modulation techniques such as: asymmetrically clipped optical orthogonal frequency division multiplexing (ACO-OFDM) [21]; flipped OFDM [22]; and unipolar orthogonal frequency division multiplexing (U-OFDM) [23] exploit the OFDM input and output frame structures to realize a unipolar output. However, the spectral efficiency in all of these techniques is half of the spectral efficiency in DCO-OFDM due to the restrictions imposed on their frame structures. Therefore, the performance of M-ary quadrature amplitude modulation (M-QAM) DCO-OFDM should be compared to M^2-quadrature amplitude modulation (QAM) {ACO-OFDM; U-OFDM; flipped-OFDM}. Therefore, the energy efficiency of ACO-OFDM, U-OFDM and flipped-OFDM techniques become gradually inefficient as the modulation order, M, increases. In comparison with the other unipolar OFDM techniques, pulse-amplitude modulation discrete multitone modulation (PAM-DMT) employs M-ary pulse-amplitude modulation (M-PAM) as the modulation technique. PAM-DMT is a unipolar OFDM technique with an equivalent spectral efficiency to DCO-OFDM [24]. Since the bit error ratio (BER) performance of M-PAM is equivalent to M^2-QAM, the energy efficiency advantage of PAM-DMT also decreases as the spectral efficiency increases. An energy efficient solution to the spectral efficiency loss of U-OFDM was proposed in enhanced unipolar orthogonal frequency division multiplexing (eU-OFDM) [25, 26].

The concept of eU-OFDM is to superimpose multiple streams of U-OFDM waveforms so that the inter-stream-interference is distortion-less. The spectral efficiency of each additional stream decreases exponentially as the total number of streams increases. Therefore, achieving a spectral efficiency equivalent to DCO-OFDM would require a

relatively large number of streams to be superimposed. However, the practical implementation limits the number of superimposed streams due to the increased computational complexity and memory requirements [26]. Therefore, achieving both spectral and energy efficiency in OFDM-based IM/DD systems is still an active research area.

Commercially available LEDs have a limited frequency response due to the yellow phosphor coating on top of the blue LED chips. However, the slow response of the yellow phosphor can be filtered out using a blue filter in front of the receiver. Recent results for VLC using a phosphorescent white LED with adaptive bit and energy loading were reported at 2.32 Gb/s aided by a two-staged linear software equalizer [27]. The micrometer-sized Gallium Nitride light emitting diodes (m-LEDs) are promising candidates in enabling VLC due to their small active area that allows for a high modulation bandwidth [28]. A high speed OFDM-based VLC demonstration is presented in this thesis using m-LEDs, in addition to a proof-of-concept of the energy efficient modulation technique that was developed and presented in this work.

The effect of solar irradiance is considered to be one of the main misconceptions surrounding VLC [29]. It is generally assumed that it could prevent the operation of the communication system entirely due to interference. However, the effect of solar irradiance is more apparent as a strong shot noise source rather than an interference source as the sunlight intensity does not vary greatly over short periods of time. The impact of solar irradiance on VLC systems is investigated in this work.

1.2 Contributions

Novel superposition modulation techniques based on PAM-DMT and ACO-OFDM are proposed and investigated within this thesis. Multiple streams of PAM-DMT are superimposed in the enhanced pulse-amplitude modulation discrete multitone modulation (ePAM-DMT) to have a DCO-OFDM equivalent spectral efficiency with lower energy requirements. This technique demonstrates that superposition modulation can be achieved using the antisymmetry of PAM-DMT waveforms. Another novel and simplified technique is proposed to relax the complicated generation process of ePAM-DMT. The Augmented spectral efficiency discrete multitone (ASE-DMT) avoids the spectral efficiency losses of ePAM-DMT and provides significant energy efficiency improvement

over DCO-OFDM using the selective subcarrier modulation algorithm at each super-imposed depth. The proposed selective frequency domain loading of subcarriers allows low latency and simplified implementation of superposition modulation for PAM-DMT. The enhanced asymmetrically clipped optical orthogonal frequency division multiplexing (eACO-OFDM) is proposed as a power efficient solution to the spectral efficiency loss in ACO-OFDM. This technique utilizes the symmetry of ACO-OFDM subframes to allow multiple ACO-OFDM streams to be superimposed. The performance of all of the superposition OFDM-based modulation techniques is compared over an additive white Gaussian noise (AWGN) channel and a frequency selective VLC channel. The constellation size of each superimposed depth is selected so that the full spectral efficiency of DCO-OFDM is achieved at lower energy requirements. This makes the proposed modulation techniques promising candidates for future high-speed and energy efficient VLC and OWC systems. The contributions of this work are published in two conference papers *IEEE PIMRC* [30], *IEEE GlobalSIP* [31], and a journal paper in *OSA Optics–Express* [32].

A number of experimental works are presented in this thesis to demonstrate the high speed and energy savings capabilities of OFDM-based modulation techniques. A high bandwidth VLC link is demonstrated using a novel m-LED array that was developed by partners in Strathclyde University within the Ultra Parallel VLC (UP-VLC) project [33]. The transmitter consists of a single pixel of the segmented m-LED array emitting at 400 nm. A VLC system is realized using DCO-OFDM with a modulation bandwidth of 1.81 GHz using the computationally efficient single-tap equalizer. A data rate of 11.95 Gb/s is presented, when the nonlinear distortion noise of the m-LED is the major source of noise in the system. A record transmission rate at 7.91 Gb/s is presented in a more practical scenario when all the noise sources of the VLC system are considered. The contributions of this work are published in collaboration with partners from Strathclyde University in a journal paper at *OSA Photonics Research* [34]. The study is followed with a demonstration of the energy efficiency of the superposition modulation technique ASE-DMT. The contribution of this study was accepted in the *5th Workshop on Optical Wireless Communications of the 2019 IEEE International Conference on Communications (ICC)*. In addition, a record data rate of 15 Gb/s for a VLC system is demonstrated using a blue light amplification by stimulated emission of radiation diode (LD) at 450 nm. The contributions of this work are published in

collaboration with partners from Glasgow University in a conference paper at *SPIE Security + Defense* [35].

A framework to investigate the effect of sunlight on VLC at any given location and time is presented in this thesis. A proof of concept study is presented to demonstrate the effects of solar irradiance experimentally. The study demonstrates that the solar irradiance affects, but not significantly degrades, the performance of VLC. It is shown that a data rate in the order of 1 Gb/s can be experimentally achieved under the presence of sunlight without any optical filtering. In addition, the simulation results show that at least half of the loss in data rate performance can be recovered using an inexpensive commercially available bandpass blue filter. The contributions are published in a conference paper in *IEEE PIMRC* [36], and a journal paper in *IEEE/OSA Journal of lightwave technology* [37].

1.3 Thesis layout

The rest of this thesis is organized as follows. A background on the enabling technologies and modulation techniques for VLC is presented in Chapter 2. Three different digital modulation techniques are proposed in Chapter 3 based on superposition modulation, and experimental studies are demonstrated in Chapter 4 for high speed and energy efficient VLC systems. The impact of sunlight on practical VLC systems is considered in Chapter 5. The main findings and limitations of this work are given in Chapter 6.

In Chapter 2 a brief history of light is presented in Section 2.2. The developments that led to the advancement of OWC are presented in Section 2.3. Different types of light sources and detectors are discussed in Section 2.4 and a brief description of the OWC channel is presented in Section 2.5. A detailed discussion on the main modulation techniques in VLC is provided in Section 2.6 and Section 2.7 summarizes chapter 2.

The modulation concepts for ePAM-DMT, eACO-OFDM and ASE-DMT are presented in Chapter 3. The power efficiency of the proposed superposition modulation techniques is analyzed in Section 3.5.1 and the theoretical BER performance is derived in Section 3.5.2. A generalized solution to reduce the computation complexity is considered in Section 3.6. The results for all of the proposed techniques in Chapter 3 are presented in Section 3.7 and the chapter is summarized in Section 3.8.

Three experimental studies targeting spectral and energy efficiency are demonstrated in Chapter 4. High speed VLC studies are presented in Section 4.2 and Section 4.3 based on DCO-OFDM with a violet m-LED and a blue LD, respectively. Adaptive bit and energy loading is used for DCO-OFDM as detailed in Section 4.2.3. The experimental setups are presented for Study I and Study II in Section 4.2.4 and Section 4.3.2 and the the results are presented in Section 4.2.5 and Section 4.3.3, respectively. An investigation into the performance of ASE-DMT is presented in Section 4.4. The implementation of ASE-DMT is given in Section 4.4.2 and the experimental setup is presented in Section 4.4.3. The results of Study III are discussed in Section 4.4.4 and the summary of Chapter 4 is presented in Section 4.5.

The impact of sunlight on VLC is presented in Chapter 5. The solar irradiance is reviewed in Section 5.2. The assumptions of this study are specified in Section 5.3.1 and the signal-to-noise ratio (SNR), the maximum theoretical limit on the data rate and BER of the VLC system under the effect of the sunlight are derived in Section 5.3.2. An experimental proof-of-concept of a practical VLC system is presented in Section 5.4. The results are shown in Section 5.3.3 and Section 5.4.2. Finally, Section 5.5 concludes Chapter 5.

The summary and conclusions of this thesis are given in Section 6.1 and the limitations and future works are presented in Section 6.2.

1.4   Summary

The growth in mobile data traffic is rapidly increasing in an unsustainable regime due to the current capacity limits of the RF electromagnetic spectrum. VLC offers a lucrative solution based on an alternative license-free frequency band that is safe to use and inexpensive to utilize. There are still open challenges in the design of modulation techniques for VLC despite the ongoing research efforts. Improving the energy efficiency of spectrally efficient IM/DD-based systems is investigated in this thesis. In addition, a number of experimental studies are presented including a demonstration of record high-speed VLC systems. Lastly, the effect of sunlight on VLC is investigated and presented in this work. This chapter presents the motivations and contributions of this work and provides an outline of this thesis.

Chapter 2
Background

2.1 Introduction

The advances in the fields of optics and communications have enabled the concept of visible light communication (VLC) to be realized. The idea of using light to convey and transmit information was initially introduced by the pioneering work of Alexander Graham Bell and Charles Sumner Tainter in 1880 [38]. The photophone invention is considered to be the first practical optical wireless communication (OWC) system, which used sunlight to transmit voice messages. Gfeller and Bapst introduced the concept of modern OWC in 1979 by proposing and investigating an indoor wireless communication system via an infrared light emitting diode (LED) [8]. Modern advances in solid-state lighting (SSL) were enabled by the revolutionary invention of the blue LED by Isamu Akasaki, Hiroshi Amano and Shuji Nakamura in 1990. This has enabled the concept of communications using the visible light spectrum between wavelength $\lambda = 400$ nm and $\lambda = 700$ nm. The use of LEDs for VLC appeared early in the research work of Masso Nakagawa [9,10]. This was soon followed by establishing the visible light communication consortium (VLCC) in 2003 by major industrial and research parties in Japan.

Light fidelity (LiFi) is the bidirectional wireless networking solution using light. Optical attocells are developed within LiFi to enable seamless handover and multi-user mobility functionalities. LiFi is expected to be integrated with other radio frequency (RF) access technologies to enable higher spectral efficiency values per unit area. Visible and invisible light sources can be used in LiFi for downlink and uplink communication. Research on VLC has rapidly increased in the recent years. This is driven by the growing costs of licensing RF bands of the electromagnetic spectrum and also by the predicted spectrum crunch as detailed in Chapter 1. The emergence of VLC is also motivated by the low cost and widespread use of enabling technologies such as SSL sources.

Nowadays a wealth of optical sources and optical detectors can be used in VLC transmitters and receivers. The choice of the optical front-ends depends mainly on the considered application. For example, avalanche photodiodes (APDs) and single photon avalanche photodiodes (SPADs) are favorable detectors in VLC systems where the background illumination is limited and the expected received optical power is modest. Commercially available LEDs are the main optical front candidates in LiFi due to their vast availability and their low cost. Commercial LED-based optical luminaries are generally manufactured in arrays, due to the limited maximum optical power of individual LEDs that fall below the illumination requirements. Arrays of LEDs are also very beneficial from a communication system perspective, as each individual LED can transmit a different stream of data. Wavelength division multiplexing (WDM) improves the capacity of the communications system by enabling multi-streams of data to be transmitted on different wavelengths. For example, red, green and blue light emitting diodes (RGB-LEDs) and photodiodes (PDs) aided with optical filters can be used to enable multi-stream data communications, and at the same time realize white illumination.

Incoherent light sources limit the signaling in VLC to intensity modulation and direct detection (IM/DD). This imposes restrictions on the modulation techniques that can be applied. Pulse-based modulation techniques such as on-off keying (OOK) and pulse-amplitude modulation (PAM) can be applied straightforwardly in VLC. However, the performance of such techniques degrade at high speeds due to the increased inter-symbol interference (ISI) of the VLC channel [39]. Multi-carrier modulation (MCM) techniques such as orthogonal frequency division multiplexing (OFDM) are prominent candidates for VLC due to the computationally cost effective single tap equalizers and adaptive bit and energy loading algorithms.

In this chapter a brief history of light is presented in Section 2.2 to highlight the key achievements in the field of optics. The developments that led to the advancement of OWC alongside the concepts of VLC and LiFi are presented in Section 2.3. The major types of light sources and detectors and their characteristics are surveyed in Section 2.4. A brief description of the OWC channel and noise characterization is presented in Section 2.5. A detailed discussion of the main modulation techniques considered in VLC literature is provided in Section 2.6. Finally, Section 2.7 summarizes this chapter.

2.2   A brief short history of light

Humans have been exploiting light since the discovery of fire 0.5-1.5 million years ago. Lenses were developed by ancient Egyptians and Mesopotamians centuries before Christ (BC). The Nimrud lens is an oval lens made of rock crystal that was made 3000 years ago [40]. Although its objective remains controversial, the lens is argued to had been used as a magnifying lens [41]. Theories of light and vision were developed by ancient Greek philosophers. Two hypotheses were introduced to describe the visual perception. The emission theory was introduced by Euclid of Alexandria (325-265 BC) and supported by Claudius Ptolemy (AD 100-170) [40]. It claims that vision occurs due to rays being emitted from the eyes of an observer. The contradicting hypothesis is supported by Aristotle (384-322 BC) and Galen of Pergamum (AD 130-201) [40]. It claims that vision occurs due to rays of light being radiated by the visual object. Ibn al-Haytham (Alhazen) in his Book of Optics (*Kitāb al-Manāẓir*, AD 1027-1040) introduced the modernly accepted theory of visual perception [42]. He was the first to propose that vision occurs when reflections of light from surfaces of visual objects are observed by human eyes. A geometrical approach of studying optics and vision was introduced by Euclid of Alexandria. Alhazen's work had a great influence on the future development of optics. One of his geometrical solutions of light reflections in circular surfaces was only found analytically in 1998 [42, 43]. Ptolemy worked on calculating the refraction of optical rays in water. However, his empirical results were inaccurate. The law of refraction (Snell law) introduced by Willebrord Snellius in 1621 was also developed independently by Rene Descartes in 1637 [42].

Isaac Newton observed that white light can be decomposed into different spectral lights using a prism, and that another prism can recombine these colored lights into a white spectrum [42]. A mechanically oriented theory of light was initially introduced by Descartes and further developed and championed by Newton [40]. Light is claimed to be made up of small particles called corpuscles that travel in straight lines with finite velocity and impetus. Christiaan Huygens proposed the wave theory of light in 1690 [42]. However, the corpuscular theory of light survived until early 19th century. Thomas Young and Augustin-Jean Fresnel's experiments on light interference confirmed the wave nature of light mainly due to the failure of the corpuscular theory in describing the refraction and polarization of light [42]. This was followed by the pioneering work of

James Clarke Maxwell which confirmed the electromagnetism nature of optical waves in the 1860s [42]. Max Planck introduced the concept of *quanta* in which he claimed that light is quantized in nature. Based on this, Einstein proposed the law of photoelectric effect which confirmed the quantization nature of light [40]. Niels Bohr demonstrated that the wavelength of the emitted light depends on the *quanta* energy. These developments formed the basis of quantum optics. Nowadays, geometrical models of light are only considered as an approximation of wave-particle models when the considered wavelength of the light source is much smaller than the dimensions of the other system components. A detailed bibliography on the history of light and its applications can be found in [40].

2.3 Optical wireless communications

Smoke signals, beacon fires and semaphore are early forms of visual based communications. The optical telegraph developed by Claude Chappe in 1792 is considered to be the earliest practical visual based communication system [15]. Multiple towers were used to relay information between two ends using pre-agreed visual codes. A heliograph is a shutter-aided mirror that was used as an optical transmitter for Morse-coded messages using reflections of the sunlight [15]. William Grylls Adams discovered the photovoltaic property of selenium when exposed to light in 1876 [44]. Alexander Graham Bell utilized the light-sensitivity of selenium in his pioneering joint invention of the photophone with Charles Sumner Tainter in 1880 [38]. The photophone was demonstrated at a distance of 213 meters and is considered to be the first practical OWC system [38]. The air pressure caused by the voice variations is applied to a flexible mirror at the transmitter part of the photophone. This would alternately make the mirror concave and convex which would in turn condense and scatter the sunlight. These variations in sunlight intensity would be collected at the receiver end, which consists of a selenium cell at the focal point of a parabolic mirror [38]. Photophone based systems were eventually outperformed by their radio-based counterparts mainly due to their limited ranges and their dependencies on weather conditions.

The advances in semiconductor-based light sources facilitated the emergence and success of optical communications. The pioneering work of Gfeller and Bapst in 1979 introduced an infrared-based OWC system that was capable of achieving 260 Mb/s in short range

wireless indoor environments [8]. Long range OWC systems based on free space optical (FSO) communication were extensively investigated in backhauling applications [45]. The invention of the blue LED by Isamu Akasaki, Hiroshi Amano and Shuji Nakamura enabled the generation of white light using power efficient LED technologies [46]. This enabled researchers from Keio University in Japan led by Prof. Masso Nakagawa to consider the dual functionalities of white LEDs in general lighting and OWCs [9, 10]. Soon after that in 2003, the VLCC was established by major companies in Japan with the aim of promoting and standardizing VLC.

LiFi was proposed in 2011 by Prof. Harald Haas from University of Edinburgh as the high speed bidirectional networking solution based on light [38]. This extends the concept of VLC to a multi-user system that allows for handover and user mobility between small-area access points (attocells). The LiFi attocell concept improves the spectral efficiency per unit area due to the higher frequency reuse factor. The interest in LiFi has increased rapidly in the last few years. A standardization working group on light communications within the Institute of Electrical and Electronics Engineers (IEEE) 802.11.bb standard was formed recently. In addition, other standardization activities in IEEE 802.15.7 are being revised to be more focused on low rate optical camera communication (OCC) [18].

OWC is the broader category of light-based communications that is based on visible and invisible light sources such as infrared and ultraviolet. In that sense, OWC as a term covers FSO and VLC that is based on the visible light spectrum between wavelength $\lambda = 400$ nm and $\lambda = 700$ nm. The contributions of this thesis are generally discussed in a VLC context, although they are also applicable to OWC. In addition, the modulation techniques proposed in Chapter 3 of this thesis are applicable to wired optical communications.

2.4 Front-end

VLC transmitters incorporate a single or multiple light source emitting at a single or multiple wavelength bands with the aid of optical components such as reflectors, lenses and diffusers. On the other end, receivers consist of a single or multiple photodetectors with an optical system that may include lenses and filters. Electrical to optical (E-O)

conversion is performed by the transmitter of a VLC system. SSL sources such as LEDs and light amplification by stimulated emission of radiation diodes (LDs) are the main possible choices for VLC. Photodetectors used in optical wired and wireless communications such as silicon based P-type intrinsic N-type photodiodes (PIN-PDs) and APDs are suitable candidates for VLC due to their relatively high responsivity between wavelength $\lambda = 320$ nm and $\lambda = 1100$ nm. This section presents descriptions of the main categories of front-end devices in VLC.

2.4.1 Transmitters

The transmitter end of a VLC system is widely expected to be additionally used as a lighting device. Therefore, the VLC transmitter is expected to satisfy the illumination requirements[1] of the considered application. A VLC transmitter can be characterized by its radiation pattern, current-voltage-luminance characteristics, frequency response and spectral response. LEDs are prominent candidates for VLC due to their low cost and vast deployments as illumination sources. LEDs have started to replace other illumination sources such as incandescent and fluorescent light sources [13]. This is mainly due to their high luminance efficacy and their significant energy consumption reduction compared to incandescent and fluorescent light sources.

2.4.1.1 Basic optical source characteristics

The radiation pattern of LEDs is widely approximated by a generalized Lambertian model. The radiation pattern is characterized by the semiangle at half power representing the field of view of a LED, $\Phi_{1/2}$. The radiant intensity at angle ϕ is given by [19]:

$$R^{\text{LED}}(\phi) = \frac{m+1}{2\pi} \cos^m \phi, \tag{2.1}$$

where m is the Lambertian order given as: $m = -\log 2/\log(\cos \Phi_{1/2})$. Commercially available LEDs have a Lambertian order around $m = 1$, which corresponds to a semi-angle $\Phi_{1/2} = 60°$. The radiation pattern of a LED can be modified using optical components such as reflectors, lenses and diffusers. A LED-based luminaire uses multiple

---

[1]The illumination requirements are defined by the considered application. For example, the lighting system of an airplane must enable dimming when airplanes takeoff and land.
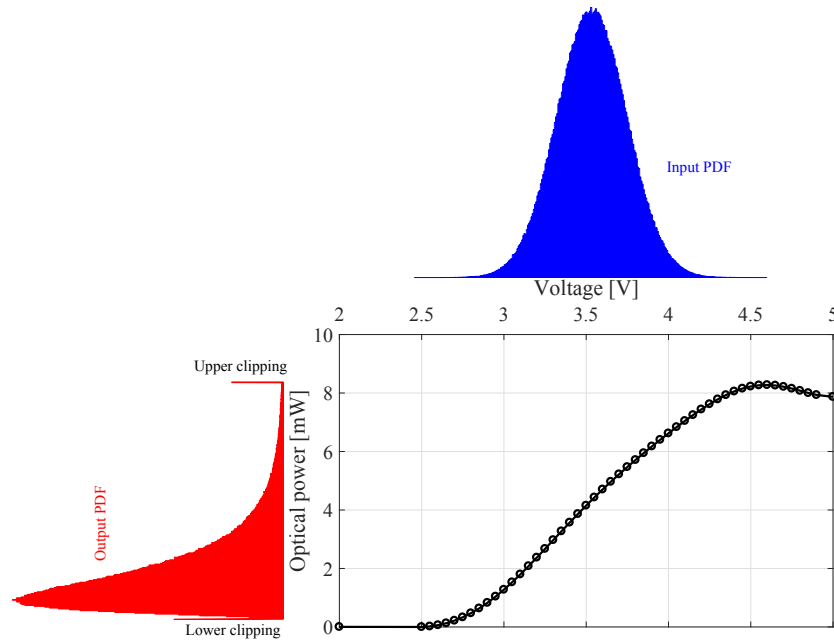
Figure 2.1: *The voltage-luminance characteristic of semiconductor-based light source. Input signal with a Gaussian PDF and an output signal with a truncated Gaussian PDF are considered.*

LEDs to satisfy the lighting requirements. A desired radiation pattern can be achieved using multiple LEDs and optical components to minimize interference and increase the system throughput based on the desired application. This allows for improved communications coverage and an increase in the spectral efficiency per unit area. LDs are much more directive than LEDs and their radiation beam is generally characterized with a Gaussian function.

The current-voltage (I-V) and luminance-current (L-I) transfer functions of a light source affects the overall performance of the VLC system. An ideal light source is assumed to have linear I-V and L-I transfer functions with double side clipping points representing the turn-on voltage and the saturated optical power. However, the I-V and L-I transfer functions of commercially available devices are mostly nonlinear. The non-linearity of the transmitter restricts the dynamic region where the transmitted signal can swing. The nonlinearity of the I-V and L-I characteristics distorts the modulation signal and impose degradation on the signal-to-noise ratio (SNR). The luminance-voltage (L-V) characteristic function of a blue LED (Vishay VLMB1500) is shown in Fig. 2.1. The probability density function (PDF) of a Gaussian distributed input to a LED is shown in blue color in Fig. 2.1 as a function of the forward voltage of the LED.

The PDF of the output signal is shown in red color as a function of the optical power of the LED. The output PDF is shown to be shaped by the nonlinearity of the light source. The statistics of the output signal can be investigated using Bussgang theorem [47, 48] as will be shown in Section 4.2.3. The turn-on voltage of the LED results in a clipping distortion for the lower part of the output signal PDF. Similarly, the saturation of the optical power of the LED results in a clipping distortion for the upper part of the output signal PDF. The transmitted signal power is the average power of the transmitter within the linear region of the dynamic range. The nonlinearity of LEDs have been empirically investigated in multiple studies [49–52]. A complete modelling of memory-less nonlinear distortion based on OFDM in IM/DD systems is presented in [53]. Signal pre-distortion was considered to mitigate the effects of nonlinearity. However, the I-V and L-I transfer functions of a device are not static and vary with the frequency of the transmitted signal [34]. Furthermore, the I-V and L-I characteristics are affected by the temperature variations of the device. Therefore, thermal management of VLC transmitters is essential to mitigate any performance degradation and ensure the reliability of the system.

The frequency response of the transmitter is directly proportional to the achievable data rate. The 3-dB bandwidth is commonly used to contrast the frequency profile of a device. However, the roll-off of the frequency response is important since the modulation bandwidth of VLC transmitters can exceed the 3-dB bandwidth when equalization techniques are used. Therefore, other metrics such as the 6-dB bandwidth are also used to reflect on the frequency response roll-off of a device. The frequency response of a LED is commonly approximated with a low pass filter. The 3-dB bandwidth of commercially available LEDs ranges between a few kHz and a few MHz (typically 2-3 MHz) [54], whereas the modulation bandwidth of LDs ranges between 200 MHz and 5 GHz [55]. The frequency response of LEDs is mostly affected by the carrier lifetime and the parasitic capacitance of the LED junction. Devices with high optical power are desired to relax the alignment constraints and enable longer transmission distances. Generally, this comes at the price of increasing the capacitance of the device which results in reducing the 3-dB bandwidth. On the other hand, devices with higher bandwidth are desired as the modulation bandwidth is directly proportional to the achievable data rate. This shows the potential of transmitters based on LDs in VLC systems. A relative comparison of the characterizations of phosphor coated light emitting diode (PC-LED),
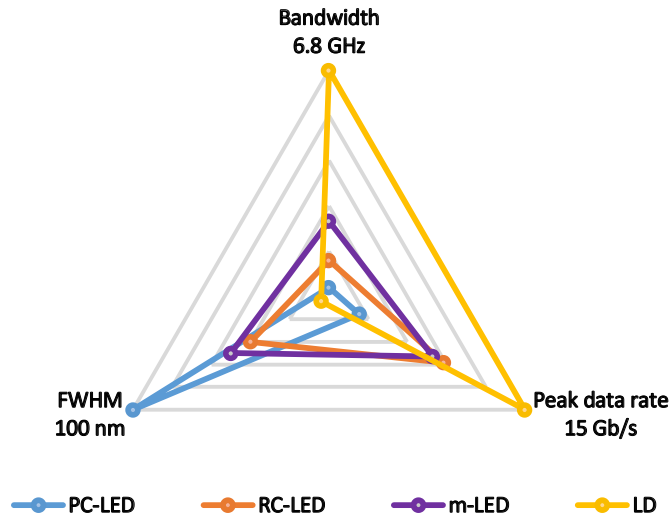
Figure 2.2: *A relative comparison of the characterizations of PC-LEDs [27, 54], RC-LEDs [56], m-LEDs [33, 34] and LDs [12, 35]*

LDs, micrometer-sized Gallium Nitride light emitting diodes (m-LEDs) and resonant cavity light emitting diodes (RC-LEDs) based on bandwidth, spectral width and the achieved peak data rate is presented in Fig. 2.2. The spectral width is given by the full width at half maximum (FWHM). Devices with small spectral width have the potential to increase the overall throughput in a WDM system. The divergence angle of a device can be modified using optical components.

2.4.1.2 White-colored LEDs

Monochromatic LEDs have a broad spectral width with the FWHM of commercially available LEDs ranging from 25-100 nm. Multiple streams can be transmitted using multiple LEDs emitting at different wavelength bands which increases the throughput in a WDM system. White illumination can be achieved using a combination of RGB-LED. The combined spectral response of multi-color LEDs can result in white illumination based on the color mixing concept that dates back to James Clarke Maxwell in 1861. Optical filters with spectral responses matching the wavelength bands of the LEDs are required in WDM systems. This is essential to reduce the interference resulting from the overlap of the adjacent wavelength bands of the used LEDs.

Yellow phosphor pumped with a blue-colored LED is most commonly used to generate white illumination due to the low cost of manufacturing. The process of converting high

energy short wavelengths into longer wavelengths is known as down-conversion. The white light output of a PC-LED has two components: a relatively narrow band in the blue spectrum (ranging from wavelength $\lambda = 425$ to $\lambda = 450$), and a relatively broad band in the spectrum ranging from $\lambda = 500$ to $\lambda = 650$ [15]. The yellow component endures a slow response which results in reducing the 3-dB bandwidth of the bare blue LED. A blue band pass filter is commonly used at the receiver to filter out the slow response of the phosphor. The 3-dB bandwidth of commercially available PC-LEDs is around 3 MHz [54]. However, this value can be increased up to 20 MHz when a blue filter is used [54]. Recent results reported 2.32 Gb/s using PC-LED with the aid of blue filters and two staged linear software equalizers [27]. The long photoluminance response of the phosphor has motivated the pursuit of fast down-conversion materials which allow for a better white light quality and a higher 3-dB bandwidth such as quantum dots [57, 58].

2.4.1.3 White-colored LDs

There has been an increasing interest in using LDs for general lighting due to their optical power efficiency at high current densities [59]. LDs have also gained an increasing interest in VLC recently, mainly due to their superior frequency response compared to LEDs reaching a 6.8 GHz of 3-dB bandwidth [12]. Recent results reported 15 Gb/s using a blue LD [35] with a 2.5 GHz modulation bandwidth. In addition, LDs have a spectral width as narrow as 1 nm [19]. This allows LDs to be used for a high dense deployment of the available visible spectrum. It has been reported that a 100 Gb/s link can be achieved using state-of-the-art sources when the whole visible spectrum is utilized [11]. The generation of white light using LDs is not straightforward due to eye safety concerns and speckle issues. The coherence of the LDs needs to be destroyed before a LD can be considered for illumination. Multiple LDs emitting at red, green and blue wavelengths can be used to generate white illumination [11]. Recent results reported more than 20 Gb/s using red, green and blue light amplification by stimulated emission of radiation diodes (RGB-LDs) [60]. Remote phosphor can be excited with a blue LD to achieve white illumination in a similar fashion to PC-LEDs. This has achieved a data rate at 5.2 Gb/s [61]. A combination of a conventional red phosphor and Perovskite nanocrystals were considered as down-converting materials for blue LDs, achieving a peak data rate at 2 Gb/s with a color rendering index (CRI) of 89 and a correlated color temperature (CCT) around 3200 K [62]. A violet LD is used with red,
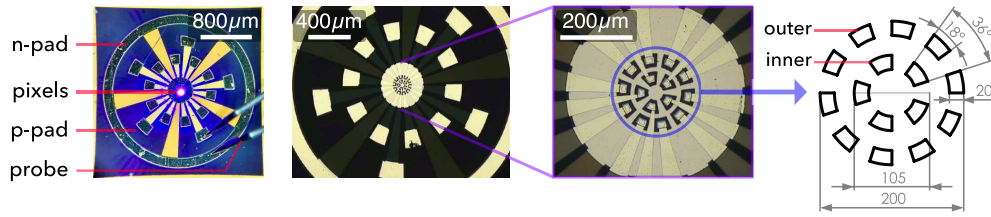
Figure 2.3: *Micrograph showing a segmented m-LEDs array that consists of inner and outer groups of pixels. The inner and outer pixels have active areas of 435 μm² and 465 μm² [34].*

green and blue phosphor to achieve white illumination at a CRI of 90, and CCT around 2700 K [63]. This has achieved a data rate above 1 Gb/s. Fig. 2.2 demonstrates the potential of LDs in future VLC systems compared with other light sources.

2.4.1.4   Micro-sized Gallium Nitride LEDs

LEDs with micro-sized pixels have attracted an increasing interest in the past few years mainly due to their high 3-dB bandwidth exceeding 800 MHz [33]. Recent results reported a data rate of 7.91 Gb/s using a violet m-LED with an active area of 435 μm^2 and a 3-dB bandwidth of 370 MHz [34]. A micrograph showing the design of this m-LEDs array is shown in Fig. 2.3 [34]. A reduction in junction size results in a high current density which allows for a short carrier life-time. However, the decrease in m-LED sizes results in a reduction in the optical power of m-LEDs. Multiple m-LEDs can be used to increase the optical power. However, this results in an increase of the junction temperature. The L-I and L-V characteristic functions of a m-LED are sensitive to the junction temperature. The random variations of the characteristic functions of a m-LED results in a significant nonlinearity that degrades the SNR. Therefore, thermal management is essential to avoid nonlinearity and to avoid the degradation in the m-LED lifetime.

2.4.1.5   Resonant cavity LEDs

RC-LEDs have a higher modulation bandwidth compared with conventional LEDs. A resonant cavity at the active region of RC-LED allows for an increased radiant intensity and improved directionality. Recent results reported a data rate of 8.76 Gb/s using an improved equalizer with a RC-LED that has a 100 MHz 3-dB bandwidth [56].

2.4.1.6 Organic LEDs

Organic light emitting diodes (OLEDs) are commonly used in display systems due to their low manufacturing cost, flexibility and wide radiation pattern. However a major drawback of using OLEDs for general lighting is their lifetime and brightness. Recently, there has been an interest in evaluating and characterizing OLEDs for VLC [64]. The 3-dB bandwidth of OLEDs is in the order of a 100 kHz due to their low carrier mobility [64]. However, the 3-dB bandwidth of OLEDs can be improved to 10 MHz by optimizing the used organic material [65].

2.4.2 Receivers

Photodetectors are characterized by the light collection pattern, frequency and spectral responses, detection area, sensitivity and noise figure. Commercially available PIN-PDs and APDs are the most commonly used receivers for VLC. SPADs have recently attracted an interest due to their high sensitivity [66]. Detectors capable of solar energy harvesting such as photo-voltaic (PV) cells have been recently considered for VLC systems [67]. Image sensors such as charge coupled device (CCD) and complementary metal oxide semiconductor (CMOS) cameras have been used for OCCs. However, the achievable data rates in OCCs are limited to a few hundred kb/s due to the low frames-per-second rate of these image sensors. This section is focused on PDs as detectors due to their capabilities in achieving multi-Gb/s VLC.

2.4.2.1 PIN-PDs and APDs

The light collection pattern of a PD is approximated with a generalized Lambertian model when a single PD is used without any optics [19]. The light collection pattern of the PD can be modified using optical elements that can change the field of view (FOV) of the PD based on the desired scenario. For example, it would be suitable to decrease the FOV in an interference-limited VLC system, whereas it would be more suitable to increase the FOV in a low-optical-power-limited VLC system. Optical elements such as concentrator lenses can be used to improve the light collection. The gain of the

concentrator is given as follows [19]:

$$g(\psi) = \begin{cases} \frac{n_c^2}{\sin^2 \Psi_c}, & 0 \leq \psi \leq \Psi_c \\ 0, & \psi > \Psi_c, \end{cases} \tag{2.2}$$

where ψ is the angle of incidence; n_c is the refractive index of the concentrator; and Ψ_c is the FOV of the concentrator. The light collection pattern can also be modified using multiple detectors which can be placed on a non-planer base with at least a single PD at each facet to allow for an angle diversity photoreceiver [68, 69]. This allows the photoreceiver to suppress interference signals and background light noise. Low power CMOS-based application-specific integrated circuit (ASIC) PDs were designed for LiFi applications [16]. Signal combing schemes can be used to maximize the SNR of such photoreceivers at the cost of increased implementation and operation complexity.

Photodetectors with high sensitivity are desired at the wavelength of interest. Silicon PDs are the most commonly used PDs due to their spectral responsivity in the visible spectrum which peaks at wavelengths longer than the red wavelength. A high reverse voltage is applied to PDs to achieve a multiplicative gain. This allows for an avalanche of photocurrent to be generated when triggered by a number of photons. Therefore, an APD is essentially a PD that has an internal gain. The gain results in a higher sensitivity for APDs compared with PIN-PDs. The high sensitivity of APDs promotes them to applications where low optical power is expected at the detector such as long range VLC systems and underwater optical wireless communications. Thermal noise and shot noise dominate the variance of the noise at the PD. Shot noise is affected by both the background intensity and the optical source intensity. Optical and electrical filters are commonly used at the receiver side to mitigate out of band noise [37]. The shot noise increases with the internal gain due to the multiplicative process in APDs. This limits their performance when strong background light is present at the detector. Optical power budgeting can be achieved using lenses, optical bandpass filters and neutral density (ND) filters. Spectral bandwidth with a FWHM as narrow as 1 nm are commercially available with a transmittance above 80% [19]. In addition, automatic gain control (AGC) can be used to adapt the multiplicative gain of the APD based on the achieved SNR.

The frequency response of a photodetector is inversely proportional to the active detec-

tion area. Increasing the detection area improves the received optical power. However, this increases the noise at the receiver and decreases the 3-dB bandwidth of the detector due to the increased capacitance. Most of the recent research efforts on front-ends in VLC focused on the transmitter. This is due to the fact that, in most practical cases, the bandwidth of the light source is the main limiting factor of high speed VLC systems. However, recent results on high speed VLC transmitters reported limitations in the modulation bandwidth of the system due to photodetectors [12, 34]. It is interesting to note that photodetectors with a higher modulation bandwidth could have been used in these studies. However, such PDs have a very small detection area. For example, the detection area of a commercially available 1 GHz PIN-PD is 0.283 mm^2 (ALPHALAS UPD-300-SP). This is 7 times larger than the detection area of a 10 GHz PIN-PD (ALPHALAS UPD-30-VSG-P). PDs with a small detection area limit the application of VLC to a very narrow FOV which requires tedious alignment and reduces the system reliability and practicality. There is an increasing demand to improve the 3-dB bandwidth of photodetectors while maintaining a relatively large detection area that would allow for VLC and LiFi applications to be feasible. Decoupling the light collection mechanism from the light detection has resulted in novel optical components that could improve the light detection area without significantly compromising the 3-dB bandwidth of the PDs [70, 71].

2.4.2.2 Single-photon APDs

A SPAD is a PD that is reverse biased beyond the breakdown voltage. SPADs are photon-counters that operate at photon level sensitivity. A single detected photon with a SPAD creates an avalanche of photocurrent [72]. SPADs have the highest sensitivity when compared with other types of PDs. Therefore, they are considered for scenarios where the received optical power is severely attenuated, such as downhole monitoring [73]. The bandwidth of SPADs is limited by the dead time which quantifies the recovery time required for the SPAD to detect newly arriving photons. Another major drawback of SPADs is their nonlinear response due to limitations in the maximum number of photons a SPAD can detect. A number of SPADs can be used in an array to mitigate this issue. Recent results reported 200 Mb/s using an array of SPADs [74].

2.4.2.3 PV solar cells

PV solar cells have recently gained an increasing interest as VLC photodetectors [67, 75–77]. PV cells offer an interesting solution for backhauling and internet of things (IoT) applications as they enable simultaneous wireless information and power transfer (SWIPT) [78]. A major drawback of using commercially available PV cells as photodetectors is their limited 3-dB bandwidths which is in the order of a few hundreds of kHz. However, recent results reported a data rate of 0.5 Gb/s for a VLC system using a GaAs PV cell with a 3-dB bandwidth of 24.5 MHz [76]. In addition, organic PV cells with a 3-dB bandwidth of 1.3 MHz were reported to achieve a data rate of 34.2 Mb/s while simultaneously harvesting 0.43 mW power [77].

2.5 OWC channel and noise

The received signal in an OWC system is given as follows:

$$y[n] = x[n] * h[n] + w[n], \tag{2.3}$$

where $x[n]$ is the discrete time transmitted waveform, $h[n]$ is the discrete time impulse response of the OWC channel, $w[n]$ is the discrete time additive white Gaussian noise at the receiver and $*$ denotes a convolution operation. The major noise factors at the receiver are shot noise and thermal noise [19]. Shot noise increases with the increased received intensity at the PD. The received intensity can be a result of both the background illumination and the optical power of the transmitter. Shot noise due to the high optical power of the transmitter can be the case in VLC systems where the light source is required to have high intensity to satisfy the illumination requirements. Shot noise can be modeled as an additive white Gaussian noise (AWGN) when the background illumination is larger than the desired signal at the receiver [79]. The power spectral density (PSD) of the shot noise is given as follows [19]:

$$N_o^{\text{sh}} = 2qRP_n \quad \text{A}^2/\text{Hz}, \tag{2.4}$$

where q is the electron charge given as $q = 1.60217662 \times 10^{-19}$ A $\times$ s, R is the average intrinsic responsivity of the photodetector over the used wavelength band given in A/W
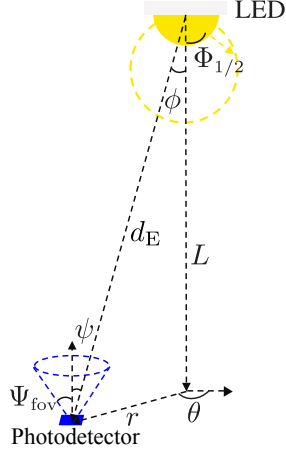
Figure 2.4: *The LOS channel model between an OWC transmitter and receiver*

and P_n is the average optical power of the background illumination. The thermal noise is related to the specific design of the transimpedance amplifier of the photodetector. However, it can also be modeled as an AWGN in most practical cases [19]. The PSD of the thermal noise is given as:

$$N_o^{\text{th}} = \frac{4k_{\text{B}}T_{\text{K}}}{R_{\text{L}}} \quad \text{A}^2/\text{Hz},\qquad(2.5)$$

where k_{B} is the Boltzmann constant given as $k_{\text{B}} = 1.381 \times 10^{-23}\,\text{J/K}$, T_{K} is the temperature given in K and R_{L} is the feedback resistor in Ω. Selecting a high value for R_{L} would decrease the thermal noise. However, this would also decrease the 3-dB bandwidth of the transimpedance amplifier.

The channel impulse response is determined by the front-ends low-pass frequency response and by the light reflections due to the multipath propagations of the OWC. Thus $h[n]$ in (2.3) is given as follows:

$$h[n] = h_{\text{fe}}[n] * h_{\text{mp}}[n],\qquad(2.6)$$

where $h_{\text{fe}}[n]$ is the discrete time channel impulse response function of the front-ends frequency response and $h_{\text{mp}}[n]$ is the discrete time channel impulse response function of the optical channel in OWC. The front-ends generally have a low-pass frequency response as described in Section 2.4. The front-ends frequency response can be experimentally obtained by estimating the overall channel in a line-of-sight (LoS) link which restricts
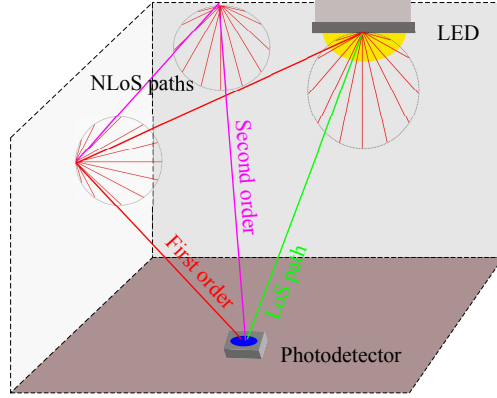
Figure 2.5: *LoS and NLoS propagation paths between an OWC transmitter and receiver*

the low-pass effect of the OWC channel into a scalar direct current (DC) channel gain. The channel DC gain in LoS scenario can be give as [19]:

$$H(0) = \begin{cases} \frac{A_{\mathrm{d}} R^{\mathrm{LED}}(\phi)}{d_{\mathrm{E}}^2} T(\psi) g(\psi) \cos\psi, & 0 \le \psi \le \Psi_{\mathrm{fov}} \\ 0, & \psi > \Psi_{\mathrm{fov}}, \end{cases} \tag{2.7}$$

where ϕ is the transmittance angle, ψ is the incidence angle, Ψ_{fov} is the FOV of the photodetector, $R^{\mathrm{LED}}(\phi)$ is the radiation pattern given in (2.1), A_{d} is the active detection area of the photodetector, d_{E} is the Euclidean distance between the transmitter and the receiver as shown in Fig. 2.4, $T(\psi)$ is the transmittance of the filter at the photodetector, $g(\psi)$ is the gain of the concentrator lens as given in (2.2). The channel DC gain can be increased by using photodetectors with larger detection area. Additionally, this can be achieved by improving the gain of the concentrator lens at the photodetector.

There could be multi-order non line-of-sight (NLoS) propagation paths due to light reflections in indoor environments as shown in Fig. 2.5. Room surfaces such as plaster walls introduce diffused reflections [19]. The calculation of the NLoS channel impulse response is dependent on the interiors of the considered environment. Ray tracing techniques are generally used to estimate the NLoS channel impulse response caused by multipath propagation. The room surfaces can be divided into sub-blocks and each sub-block can be considered to be receiving the optical rays as given in (2.7). Afterwards, each reflective sub-block re-emits the optical rays with a reflectivity factor ρ as a first order Lambertian emitter as given in (2.1) [80]. Replicas of the optical signal will be

received with different delays and different path losses as a result of the diffused channel. This can lead to ISI when the maximum delay spread of the channel approaches the symbol duration. However, the relative contribution of the multipath propagation into the ISI is small compared with the low-pass frequency response of the front-ends except when the receiver is very close to a reflective source [81].

2.6 Modulation techniques

It is widely believed that incoherent optical sources are the prominent choice for VLC transmitters due to their low cost and simple system design. Modulation techniques with high spectral efficiency are key elements in high speed OWC system design due to the limited bandwidth of these incoherent optical sources. Incoherent optical sources restrict the modulation techniques in VLC to IM/DD schemes. Spatial diversity can be achieved using IM/DD due to the relatively large-area detectors compared to the wavelength of the detected light. In comparison with coherent based RF modulation techniques, this feature completely avoids multipath fading and simplifies the VLC system design.

Single-carrier modulation (SCM) techniques such as OOK, pulse width modulation (PWM), pulse position modulation (PPM) and PAM can be easily implemented in VLC. The frequency response of the front-ends and the time dispersive visible light channel result in an ISI which degrades the SCM performance at high spectral efficiency. Equalizers with high computational complexity are required when the modulation bandwidth exceeds the 3-dB bandwidth of the VLC system.

MCM techniques, such as OFDM, have shown a great potential for high speed VLC systems [34, 35, 39, 82]. The achievable data rate of an OFDM-based VLC system can be maximized by adapting the system loading based on the frequency response of the considered channel. This can be achieved using the computationally efficient single-tap equalizers in addition to adaptive bit and energy loading algorithms. An improved throughput can be achieved by adaptively choosing the modulation order of M-ary quadrature amplitude modulation (M-QAM) based on the achieved SNR at each subcarrier. MCM techniques have a relatively high peak-to-average power ratio (PAPR) compared with SCM techniques due to the coincidence of multiple modulated symbols
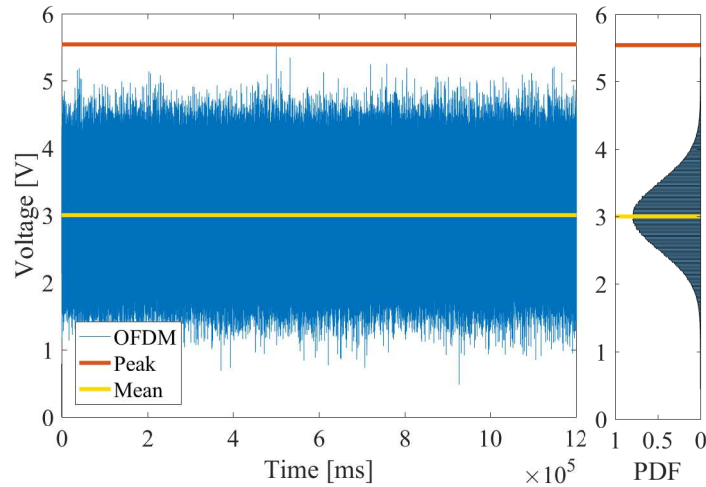
Figure 2.6: *The peak and average values of an OFDM waveform shown on the time-domain signal and the corresponding PDF.*

with a similar phase in the same frame[2]. This can cause degradation in a VLC system performance when the dynamic range of the light source is limited. The peak and average values of an OFDM waveform are shown in Fig. 2.6.

2.6.1 Single carrier modulation techniques

Binary bits are encoded in the presence and absence of light intensity in OOK, and similarly multilevel intensity levels can encode the incoming bits with M-ary pulse-amplitude modulation (M-PAM) [83]. Illumination control can be enabled by adjusting the light intensity of the two binary states in OOK without degrading the system performance. Compensation symbols are proposed in the VLC standard, IEEE 802.15.7 [84], to enable illumination control at the expense of reducing the spectral efficiency. The position of the optical pulse is modulated into shorter duration pulses in PPM with a position index that varies depending on the incoming bits. PPM is more power efficient than OOK, but it requires more bandwidth to support equivalent data rates [19]. Variable pulse position modulation (VPPM) was proposed in IEEE 802.15.7 to support dimming in conjunction with PPM and also to prevent any possible visible

---

[2]Note that MCM enables the use of phase modulation techniques in IM/DD systems. This includes but is not limited to binary phase-shift keying (BPSK), quadrature amplitude modulation (QAM), and M-ary phase shift keying (M-PSK).
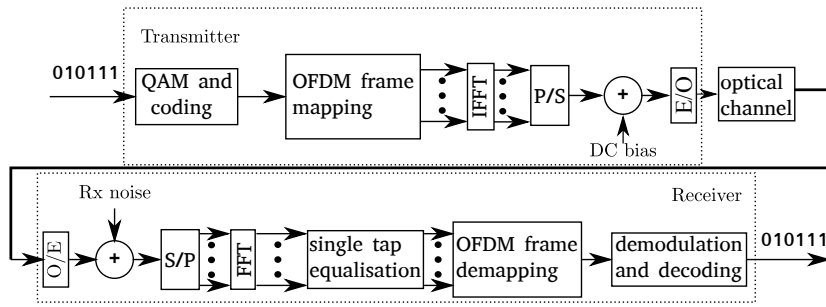
Figure 2.7: *A block diagram showing the main functions in DCO-OFDM transmitter and receiver.*

flicker. The pulse dimming in VPPM is controlled by the width of the pulse rather than the pulse amplitude. Therefore, VPPM can be considered as a combination of PPM and PWM techniques. Multiple pulse position modulation (MPPM) was proposed as a solution to the dimming capability of PPM, where it was reported that it achieves higher spectral efficiency values than VPPM with less optical power dissipation [85].

2.6.2   OFDM-based MCM

SCM techniques require computationally complicated equalization processes when employed at high data rates. In addition, flicker interference of background lights may influence the system performance at the low frequency regions of the used bandwidth. On the other hand, MCM techniques such as OFDM can equalize the VLC channel by using the computationally efficient single tap equalizers. Supporting multiple access is straightforward in orthogonal frequency division multiple access (OFDMA) as it can be achieved by allocating distinctive subcarriers to each individual user terminal. In addition, OFDM supports adaptive bit and energy loading which allocates different modulation orders based on the estimated SNR at each individual subcarrier. This allows subcarriers with high SNR values to be loaded with a higher modulation order. Therefore, OFDM can maximize the VLC system throughput by adapting the channel utilization to the low-pass frequency response of the VLC channel.

2.6.2.1   DCO-OFDM

A block diagram of the main functions in DC-biased optical orthogonal frequency division multiplexing (DCO-OFDM) transmitter and receiver is given in Fig. 2.7. Incoming

bits are modulated into modulation formats such as PAM or QAM. A number of bits that are encoded in each M-PAM and M-QAM symbols is given in b, where M is the modulation order $M = 2^b$. The modulated symbols are loaded into orthogonal subcarriers, $X[k]$, with a subcarrier spacing equal to $\Delta f = \frac{1}{N_{\text{FFT}}T_{\text{s}}}$, where N_{FFT} is the OFDM frame length, $T_{\text{s}} = \frac{1}{f_{\text{s}}}$ is the sampling period, $f_{\text{s}} = 2B$ is the Nyquist sampling rate and B is the single side bandwidth. Parallel to serial (P/S) transformation is then applied, usually using the inverse fast Fourier transform (IFFT) as given in (2.8). The time domain waveform output $x[n]$ can then be given as follows:

$$x[n] = \frac{1}{\sqrt{N_{\text{FFT}}}} \sum_{k=0}^{N_{\text{FFT}}-1} X[k] \times e^{j\frac{2\pi kn}{N_{\text{FFT}}}}, \tag{2.8}$$

where k is the subcarrier index. N_{FFT} is set to a value that is even power of two in order to simplify the computational complexity of fast Fourier transform (FFT) operation to $\mathcal{O}(N\log_2(N))$. The light intensity is real valued and strictly positive. Therefore, OFDM waveforms are required to be both unipolar and real valued. Hermitian symmetry is generally imposed on the frames of the modulated symbols such as: $X[k] = X^*[N_{\text{FFT}} - k]$, for $k = 1, 2, \cdots N_{\text{FFT}} - 1$ and $X[0] = X[N_{\text{FFT}}/2] = 0$. This forces the OFDM time domain output to be real valued. The time domain OFDM signal given in (2.8) is used to modulate the light source as an intensity modulation signal. The last N_{CP} symbols of each time domain frame are repeated at the beginning of each frame. This helps in transforming the linear convolution with the optical channel into a circular convolution, which can be efficiently equalized in the frequency domain. The cyclic prefix (CP) is required to be longer than the maximum delay spread of the channel T_d so that ISI can be mitigated using the single tap equalizer.

Different variants of optical OFDM were proposed to achieve a unipolar OFDM output. DC bias is used in DCO-OFDM to shift the OFDM signal to the linear region of a light source dynamic range [20]. However, OFDM signals have a high PAPR, which makes it practically impossible to convert all of the signal samples into unipolar ones. The PAPR is defined as:

$$\text{PAPR} \triangleq \frac{\max_{0 \leq n \leq N_{\text{FFT}}-1}|x^2[n]|}{\text{E}[x^2[n]]}, \tag{2.9}$$

where $\text{E}[\cdot]$ is the statistical expectation. The OFDM time-domain waveform can be approximated with a Gaussian distribution when the length of the input frame is greater
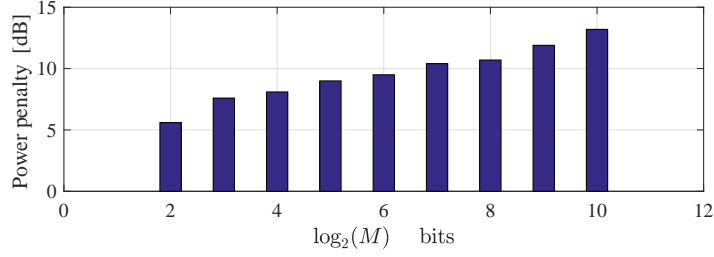
Figure 2.8: *Power penalty caused by the addition of DC bias in DCO-OFDM compared with bipolar OFDM as a function of the modulation order.*

than 64 [86]. The DC bias point would be ideally within the center of the linear region of the light source dynamic range. The dynamic range of a light source is the linear range between the turn-on voltage and the voltage at the saturation power of the light source. OFDM values that fall outside the dynamic range incur clipping distortion. The optimization of the DC bias point was studied in [48]. The DC bias can be defined as a k_{DC} multiple of the standard deviation of the time-domain OFDM signal σ_x. The electrical power penalty due to the addition of DC bias in DCO-OFDM compared with bipolar OFDM is written as follows:

$$B_{\mathrm{DC}}^{\mathrm{dB}} = 10 \log_{10}\left(k_{\mathrm{DC}}^2 + 1\right). \qquad (2.10)$$

The additional dissipation of electrical power caused by the DC bias in DCO-OFDM increases as the modulation order increases, which leads to electrical and optical power inefficiency. The electrical power penalty caused by the addition of DC bias is estimated in Fig. 2.8 using Monte Carlo simulation based on (2.10) at a bit error ratio (BER) of 1×10^{-4}. The DCO-OFDM optical power inefficiency can be justified for some VLC applications where a high luminance is desired. However, an alternative modulation approach is required to reduce the energy consumption. The spectral efficiency of DCO-OFDM is given by [53]:

$$\eta_{\mathrm{DCO}} = \frac{\log_2 M(N_{\mathrm{FFT}} - 2)}{2(N_{\mathrm{FFT}} + N_{\mathrm{CP}})} \quad \text{bits/s/Hz}. \qquad (2.11)$$

The definition of the achieved spectral efficiency is based on the definition of the bandwidth. Here it is assumed that the bandwidth is given as $2B$, where B is the single side bandwidth. A detailed analysis on the definition of the bandwidth in IM/DD-based VLC systems is presented in Appendix A.
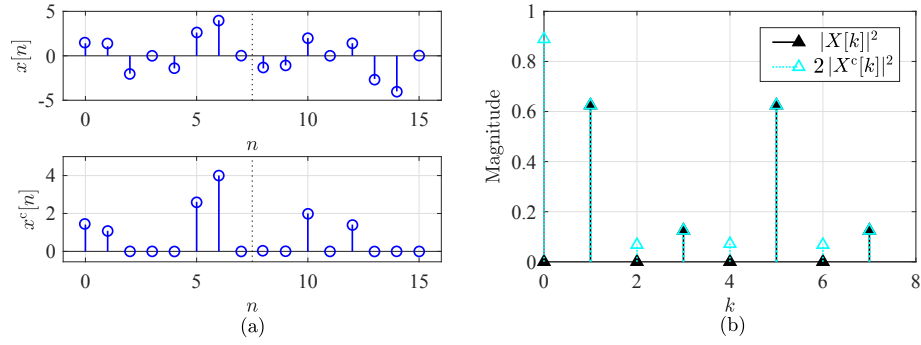
Figure 2.9: *(a) Time domain ACO-OFDM waveform before ($x[n]$) and after clipping ($x^{\mathrm{c}}[n]$). (b) Frequency domain representation of ACO-OFDM waveform before $|X[k]|^2$ and after clipping $2|X^{\mathrm{c}}[k]|^2$. The factor 2 is introduced to compensate for the attenuation that occurs due to the zero-level clipping as described in (2.16).*

The spectral efficiency given in (2.11) is based on the assumption that all the subcarriers are loaded with modulated symbols of M-QAM. Multiple LEDs can be used to spatially superimpose the modulation signal in the optical domain by transmitting discrete levels of the signal using multiple LEDs [87]. The spatial construction of the modulation signal in the optical domain overcomes the LED nonlinearity and dynamic range limitations. In addition, the digital control of LEDs simplifies the system design by bypassing any necessity of high resolution digital-to-analog converters (DACs). The OFDM waveform can also be transmitted by splitting the OFDM subcarriers into multiple groups of LEDs. The simplest case would be a sinusoid per each individual group of LEDs [87,88]. The OFDM subcarriers are modulated separately and transmitted through the multiple groups of LEDs. The OFDM signal can then be constructed in the optical domain through the spatial summation of streams. This approach decreases the PAPR by allowing the OFDM signal to be spatially formed in the optical domain. The necessity of multiple DACs and IFFT operations is a major drawback of this technique.

2.6.2.2 ACO-OFDM

A real-valued unipolar OFDM waveform can be achieved by exploiting the Fourier transformation properties. The principle of asymmetrically clipped optical orthogonal frequency division multiplexing (ACO-OFDM) is to skip loading the even subcarriers, and only load the odd subcarriers with useful information, as shown in Fig. 2.9(a) [21].

33

This creates a symmetry in the time domain OFDM signal, which allows the distortion-less clipping of the negative samples without adding any DC bias as shown in Fig. 2.9(b). The symmetry can be proven in (2.12) and (2.13), as follows:

$$x[n] = \frac{1}{\sqrt{N_{\text{FFT}}}} \sum_{k=0}^{N_{\text{FFT}}-1} X[k] \times e^{j\frac{2\pi kn}{N_{\text{FFT}}}}, \tag{2.12}$$

$$x\left[n + \frac{N_{\text{FFT}}}{2}\right] = \frac{1}{\sqrt{N_{\text{FFT}}}} \sum_{k=0}^{N_{\text{FFT}}-1} X[k] \times e^{j\frac{2\pi kn}{N_{\text{FFT}}}} \times e^{j\pi k}. \tag{2.13}$$

By setting the even-indexed subcarriers to be zeros, we can write:

$$x\left[n + \frac{N_{\text{FFT}}}{2}\right] = -x[n]. \tag{2.14}$$

However, if only odd-indexed subcarriers are loaded with modulated symbols, the following symmetry can be achieved:

$$x\left[n + \frac{N_{\text{FFT}}}{2}\right] = x[n]. \tag{2.15}$$

Clipping of the negative values is distortion-less since the distortion will only affect the even-indexed subcarriers. The clipping function of an OFDM waveform at zero is given as follows [53]:

$$x^{\text{c}}[n] = \text{f}_{\text{clip}}\{x[n]\} = \frac{1}{2}\left(x[n] + |x[n]|\right). \tag{2.16}$$

It is shown using (2.14), (2.15) and (2.16) that the clipping distortion $|x[n]|$ has the property $|x[n]| = |x[n + N_{\text{FFT}}/2]|$. This symmetry can be achieved when even-indexed subcarriers are only loaded with modulated symbols (2.15). This indicates that the clipping distorted symbols will only affect the even-indexed subcarriers [53].

Skipping half of the subcarriers reduces the spectral efficiency of ACO-OFDM to almost half of that in DCO-OFDM. The spectral efficiency of ACO-OFDM is given as follows:

$$\eta_{\text{ACO}} = \frac{\log_2 M(N_{\text{FFT}})}{4(N_{\text{FFT}} + N_{\text{CP}})} \quad \text{bits/s/Hz}. \tag{2.17}$$

This is based on the assumption that all the odd-indexed subcarriers are loaded with modulated symbols of M-QAM. A penalty of 3 dB should apply to the SNR of ACO-OFDM when compared with bipolar OFDM, since half of the signal power is
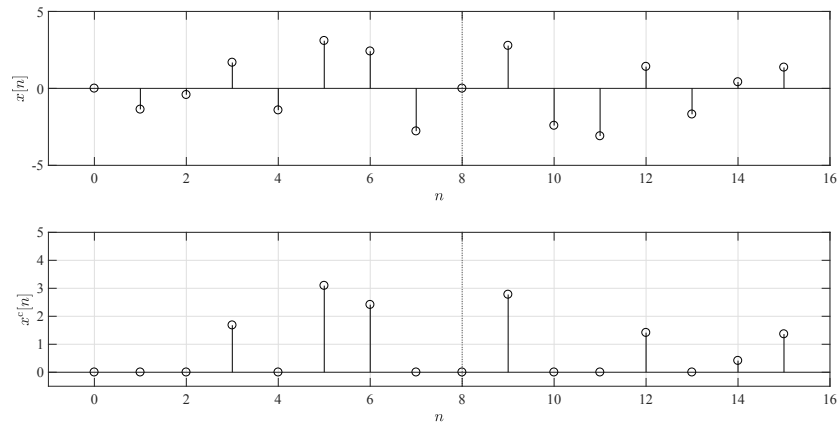
Figure 2.10: *Time domain PAM-DMT waveform before (x[n]) and after clipping (x^c[n]).*
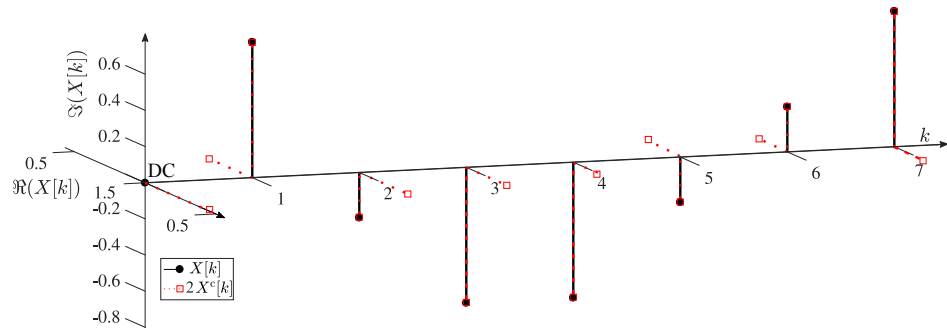
Figure 2.11: *The frequency representation of the transmitted PAM-DMT waveform before (X[k]) and after clipping (2X^c[k]). The factor 2 is introduced to compensate for the attenuation that occurs due to the zero-level clipping as described in (2.16).*

lost due to clipping. Hermitian symmetry is also used to guarantee a real valued ACO-OFDM output. At the receiver, the odd subcarriers are only considered after a FFT is applied on the incoming frame.

2.6.2.3 PAM-DMT

A real unipolar optical OFDM is achieved in pulse-amplitude modulation discrete multitone modulation (PAM-DMT) by exploiting the Fourier properties of imaginary signals [24]. The real component of the subcarriers is not used in PAM-DMT, which restricts the modulation scheme used to M-PAM. An antisymmetry in the time-domain waveform of PAM-DMT is achieved by only loading M-PAM modulated symbols on the imaginary components of the subcarriers $X[k] = jB^{\mathrm{PAM}}[k]$, as shown in Fig. 2.10.

The time domain PAM-DMT waveform is given as follows:

$$x[n] = \frac{1}{\sqrt{N_{\text{FFT}}}} \left(\sum_{k=1}^{N_{\text{FFT}}/2-1} X[k] e^{\frac{j2\pi kn}{N_{\text{FFT}}}} + \sum_{k=1}^{N_{\text{FFT}}/2-1} X[N_{\text{FFT}} - k] e^{\frac{-j2\pi kn}{N_{\text{FFT}}}} \right),$$

$$= \frac{-2}{\sqrt{N_{\text{FFT}}}} \sum_{k=1}^{N_{\text{FFT}}/2-1} B^{\text{PAM}}[k] \sin \frac{2\pi kn}{N_{\text{FFT}}}, \tag{2.18}$$

where $B^{\text{PAM}}[k]$ is the M-PAM modulated symbol that is loaded on the imaginary component of the subcarrier $X[k]$. The antisymmetry property $x[n] = -x[N_{\text{FFT}} - n]$ can be proven as follows:

$$x[N_{\text{FFT}} - n] = \frac{-2}{\sqrt{N_{\text{FFT}}}} \sum_{k=1}^{N_{\text{FFT}}/2-1} B^{\text{PAM}}[k] \sin \frac{2\pi k(N_{\text{FFT}} - n)}{N_{\text{FFT}}},$$

$$= \frac{-2}{\sqrt{N_{\text{FFT}}}} \sum_{k=1}^{N_{\text{FFT}}/2-1} B^{\text{PAM}}[k] \sin \left(2\pi k - \frac{2\pi kn}{N_{\text{FFT}}} \right),$$

$$= -x[n]. \tag{2.19}$$

It can be shown using (2.16) and (2.19) that the clipping distortion $|x[n]|$ has Hermitian symmetry $|x[n]| = |x[N_{\text{FFT}} - n]|$, which means that the zero level clipping distortion will only affect the real part of the subcarriers [53]. This is not to be confused with the Hermitian symmetry that is applied on the input frames of PAM-DMT to guarantee a real-valued output. PAM-DMT is more attractive than ACO-OFDM when bit loading techniques are considered, as the PAM-DMT performance can be optimally adapted to the frequency response of the channel since all of the subcarriers are used. PAM-DMT has a 3 dB fixed penalty when compared with bipolar OFDM at an appropriate constellation size, as half of the power is also lost due to clipping. At the receiver, the imaginary part of the subcarriers is only considered, while the real part is ignored. The spectral efficiency of PAM-DMT is similar to that of DCO-OFDM, and is given as follows:

$$\eta_{\text{PAM}} = \frac{\log_2 M (N_{\text{FFT}} - 2)}{2(N_{\text{FFT}} + N_{\text{CP}})} \quad \text{bits/s/Hz}. \tag{2.20}$$
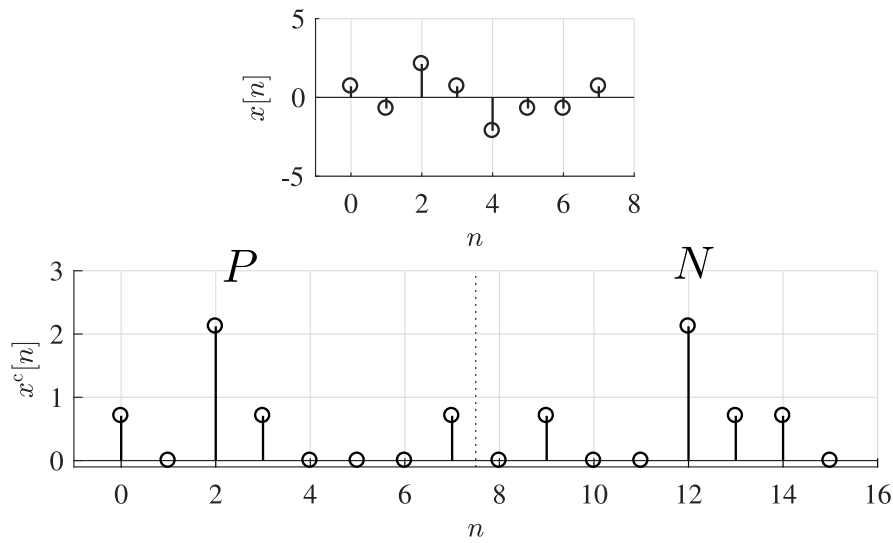
Figure 2.12: *The generation of two U-OFDM frames from one bipolar OFDM frame.*

2.6.2.4 U-OFDM

A novel inherent optical OFDM scheme was proposed in [22, 23] motivated by the fact that the polarity of a signal is only conveyed in a single bit. The concept and performance of unipolar orthogonal frequency division multiplexing (U-OFDM) [23] and flip orthogonal frequency division multiplexing (FLIP-OFDM) [22] is identical. The term U-OFDM is used in this thesis. However, the discussions and analysis are applicable to both schemes. Hermitian symmetry is applied on the incoming frames of M-QAM symbols as in the previously discussed schemes. Each bipolar OFDM time-domain frame is expanded into two time-domain frames in U-OFDM with similar sizes to the original OFDM frame as shown in Fig. 2.12. The bipolar OFDM time domain frame $x[n]$ is transmitted over two subsequent N_{FFT} frames. The first one, termed P, represents the positive values of $x[n]$ with zeros at the positions of the negative samples. The second, termed N, represents the absolute values of the originally negative values of $x[n]$ with zeros at the positions of the positive samples. A unipolar OFDM waveform can be achieved by clipping at zero-level. At the receiver, each second frame would be subtracted from the first frame of the same pair, in order to reconstruct the original bipolar OFDM frame. This would double the noise at the receiver, which leads to a 3 dB penalty when compared with bipolar OFDM at appropriate constellation sizes. The spectral efficiency of U-OFDM is half of the spectral efficiency of DCO-OFDM since two U-OFDM frames are required to convey the same information contained in a single
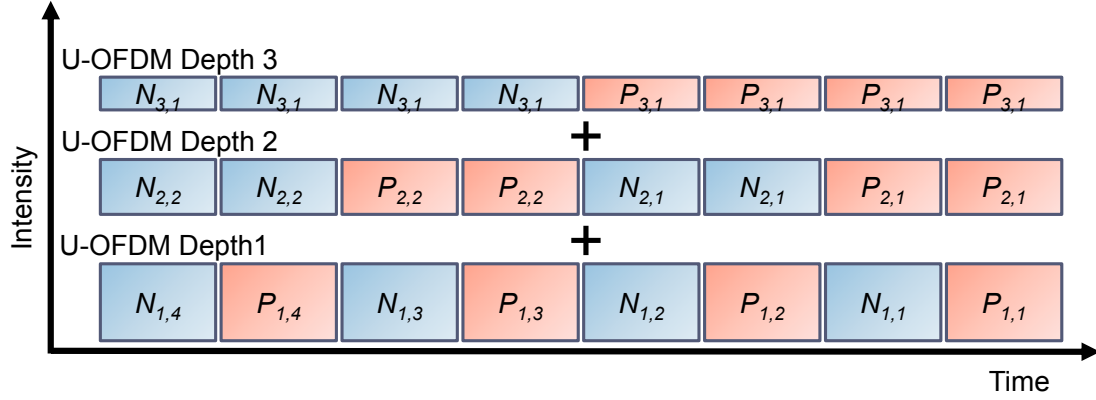
Figure 2.13: *Illustration of the enhanced U-OFDM concept with three information streams. $P_{d,l}$ represents the positive U-OFDM frame, and $N_{d,l}$ represents the negative frame of U-OFDM. The subscripts denote that the frame at depth-d belongs to the l-th original bipolar OFDM frame.*

DCO-OFDM frame. This is given as follows:

$$\eta_{\mathrm{U}} = \frac{\log_2 M (N_{\mathrm{FFT}} - 2)}{4(N_{\mathrm{FFT}} + N_{\mathrm{CP}})} \quad \text{bits/s/Hz.} \tag{2.21}$$

2.6.2.5 Enhanced U-OFDM

The concept of enhanced unipolar orthogonal frequency division multiplexing (eU-OFDM) is to superimpose multiple U-OFDM time domain streams in order to form a single time domain eU-OFDM stream [25]. Four bipolar OFDM frames are used to generated eight unipolar frames at depth-1 in Fig. 2.13. The subscripts of $P_{d,l}/N_{d,l}$ indicates that the current unipolar frame holds the positive/negative values of the l-th bipolar frame at depth-d, respectively.

The waveform at depth-1 is generated using a conventional U-OFDM modulator as described in Section 2.6.2.4. A second stream of U-OFDM frames is generated in depth-2. However, each unipolar frame in depth-2 is repeated twice. In addition, the amplitude of the U-OFDM stream at depth-2 is scaled by $1/\sqrt{2}$ in order to preserve the overall signal energy. The stream generated at depth-2 is superimposed on the previous stream at depth-1. A third stream of U-OFDM is generated in depth-3 and superimposed in a similar way to the stream at depth-2. However, each unipolar U-OFDM frame is replicated four times and scaled by $1/2$ in depth-3. Additional U-OFDM streams can be superimposed after they are replicated 2^{d-1} times and scaled by $1/\sqrt{2^{d-1}}$, where d

Frame index	Depth-1	Depth-2	Depth-3	eU-OFDM
1	$P_{1,1}$	$\frac{1}{\sqrt{2}}P_{2,1}$	$\frac{1}{2}P_{3,1}$	$P_{1,1} + \frac{1}{\sqrt{2}}P_{2,1} + \frac{1}{2}P_{3,1}$
2	$N_{1,1}$	$\frac{1}{\sqrt{2}}P_{2,1}$	$\frac{1}{2}P_{3,1}$	$N_{1,1} + \frac{1}{\sqrt{2}}P_{2,1} + \frac{1}{2}P_{3,1}$
3	$P_{1,2}$	$\frac{1}{\sqrt{2}}N_{2,1}$	$\frac{1}{2}P_{3,1}$	$P_{1,2} + \frac{1}{\sqrt{2}}N_{2,1} + \frac{1}{2}P_{3,1}$
4	$N_{1,2}$	$\frac{1}{\sqrt{2}}N_{2,1}$	$\frac{1}{2}P_{3,1}$	$N_{1,2} + \frac{1}{\sqrt{2}}N_{2,1} + \frac{1}{2}P_{3,1}$
5	$P_{1,3}$	$\frac{1}{\sqrt{2}}P_{2,2}$	$\frac{1}{2}N_{3,1}$	$P_{1,3} + \frac{1}{\sqrt{2}}P_{2,2} + \frac{1}{2}N_{3,1}$
6	$N_{1,3}$	$\frac{1}{\sqrt{2}}P_{2,2}$	$\frac{1}{2}N_{3,1}$	$N_{1,3} + \frac{1}{\sqrt{2}}P_{2,2} + \frac{1}{2}N_{3,1}$
7	$P_{1,4}$	$\frac{1}{\sqrt{2}}N_{2,2}$	$\frac{1}{2}N_{3,1}$	$P_{1,4} + \frac{1}{\sqrt{2}}N_{2,2} + \frac{1}{2}N_{3,1}$
8	$N_{1,4}$	$\frac{1}{\sqrt{2}}N_{2,2}$	$\frac{1}{2}N_{3,1}$	$N_{1,4} + \frac{1}{\sqrt{2}}N_{2,2} + \frac{1}{2}N_{3,1}$

Table 2.1: *Frames content of U-OFDM at each depth and their contribution to eU-OFDM generated in Fig. 2.13, where $P_{d,l}$ represents the positive U-OFDM frame, while $N_{d,l}$ represents the negative frame of U-OFDM. The subscripts refer that the frame at depth-d belongs to the l-th original bipolar OFDM frame*

is the depth of the respective information stream. Table 2.1 illustrates the contents of U-OFDM frames at each depth, and the contents of the overall eU-OFDM frames.

At the receiver, the demodulation process starts with the demodulation of the stream at depth-1 where a conventional U-OFDM receiver is used, as described in Section 2.6.2.4. Most of the inter-depth interference (IDI) caused by the superposition of multiple U-OFDM streams is removed by the subtraction operation in the demodulation process since the interference on each positive frame at depth-1 is equivalent to the interference on the correspondent negative frame. The recovered bits are remodulated at the receiver after the demodulation of the stream at depth-1. The remodulated stream of depth-1 is then subtracted from the overall received eU-OFDM signal. This results in removing most of the stream at depth-1. Afterwards, each two identical frames at depth-2 are summed. The demodulation process at depth-2 continues with the conventional U-OFDM demodulator. The recovered bits at depth-2 are remodulated in order to allow for the information stream at depth-2 to be subtracted from the overall received information signal. The demodulation process continues in the same way for all subsequent streams until the information at all depths is recovered.

The spectral efficiency of eU-OFDM can be written as the sum of the spectral efficiency
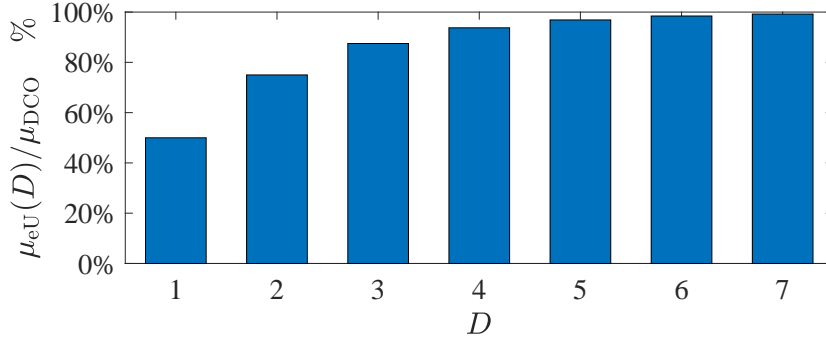
Figure 2.14: *The convergence of the spectral efficiency of eU-OFDM.*

values of the information signals at all depths. This is expressed as follows [25]:

$$\eta_{\text{eU}}(D) = \eta_{\text{U}} \sum_{d=1}^{D} \frac{1}{2^{d-1}} \tag{2.22}$$

where D is the total number of the used modulation depths. Therefore, the spectral efficiency of eU-OFDM approaches the spectral efficiency of DCO-OFDM as D increases, and as illustrated in Fig. 2.14. For example, more than 87.5% of the spectral efficiency of DCO-OFDM can be achieved using $D = 3$.

2.6.2.6 Hybrid OFDM techniques

Reverse polarity optical orthogonal frequency division multiplexing (RPO-OFDM) was proposed to allow a higher degree of illumination control in the OFDM-based VLC systems [89]. RPO-OFDM combines a real-valued unipolar optical OFDM technique with a slow PWM signal to control the dimming. Therefore, the spectral efficiency of RPO-OFDM is half of that in DCO-OFDM. In addition, the PWM duty cycle is assumed to be known at the receiver, which requires perfect synchronization between the transmitting and receiving ends.

The main principle of polar orthogonal frequency division multiplexing (P-OFDM) is to avoid Hermitian symmetry by converting the complex valued output of the IFFT from Cartesian coordinates into polar coordinates [90]. The radial and angular values can be sent instead of the magnitude and phase in two successive subframes. P-OFDM allocates the QAM modulated symbols into even indexed subcarriers which results in half-wave even symmetry [91]. This means that the first and second halves of the

complex valued IFFT frame output are identical. Therefore, it is sufficient to transmit half of the IFFT output. As a result, the spectral efficiency is reduced to be identical to that of DCO-OFDM since only half of the subcarriers are used. The performance of P-OFDM was compared to that of ACO-OFDM in [91]. It was reported that P-OFDM achieves better BER performance gains than ACO-OFDM when optimal values for the power allocation of the radial and angular information are used. However, the system performance in frequency selective channels should be investigated since any ISI between the radial and angular samples may deteriorate the BER performance.

A finite impulse response (FIR) filtering technique termed spectral factorization was used to create a unipolar optical OFDM signal [92]. The amplitude of the subcarriers in spectrally factorized optical orthogonal frequency division multiplexing (SFO-OFDM) were chosen to form an autocorrelation sequence that was shown to be sufficient to guarantee a unipolar OFDM output. The SFO-OFDM was reported to achieve 0.5 dB gain over ACO-OFDM with a 30% PAPR reduction [92].

Position modulation orthogonal frequency division multiplexing (PM-OFDM) avoids the Hermitian symmetry and splits the real and imaginary components of the OFDM output into two branches where a polarity separator is used to obtain the positive and negative samples of each branch [93]. The four frames composed of a real positive frame, a real negative frame, an imaginary positive frame and an imaginary negative frame are transmitted as unipolar OFDM frames. The spectral efficiency is exactly similar to other inherent unipolar OFDM techniques discussed in Sections 2.6.2.2-2.6.2.4. The performance of PM-OFDM was reported to be identical to U-OFDM in flat channels. However, it was reported to have better BER performance when compared to ACO-OFDM for frequency selective channels [93].

2.6.3 MCM based on other transformations

OFDM-based VLC systems have been mainly investigated based on FFT. Other transformations such as discrete Hartley transformation (DHT) [94], wavelet packet division multiplexing (WPDM) [95] and fast Walsh-Hadamard transformation (FWHT) [96] have also been considered for VLC. The output of a DHT transformation can be real-valued when modulation techniques such as BPSK and PAM are used. Similar to DCO-OFDM and ACO-OFDM, DC-biasing and asymmetrical clipping can also be
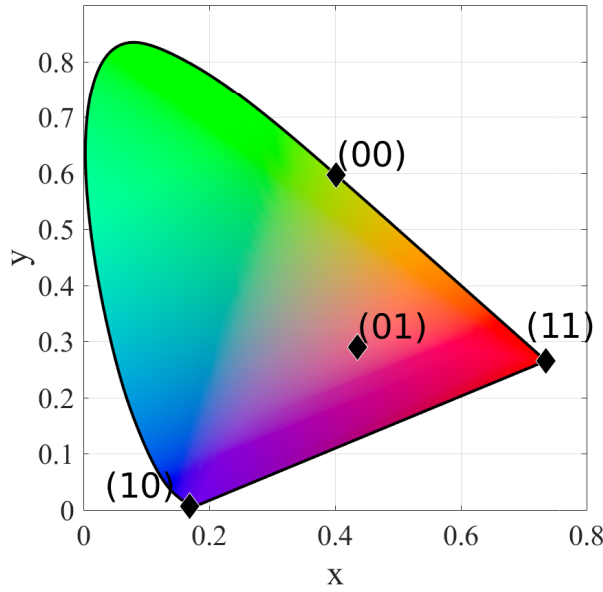
Figure 2.15: *The constellation of 4-CSK on the CIE color space.*

used to achieve a unipolar output in DHT-based MCM. DHT-based MCM does not require any Hermitian symmetry. However, it fails to improve the spectral efficiency of FFT-based OFDM. High illumination in DCO-OFDM requires a high DC bias level. This results in clipping distortion due to the peak power constraint of the LED as shown in Fig. 2.1. Hadamard coded modulation (HCM) was proposed based on FWHT as a solution to the limitation of DCO-OFDM at high illumination levels. HCM is reported to achieve modest performance improvement over RPO-OFDM.

2.6.4   Color-based transmission techniques

Color modulations allows for a new degree of freedom that is unique for VLC systems. Color tunable LEDs such as the RGB-LED can illuminate with different colors based on the intensity applied on each LED element. The IEEE 802.15.7 standard proposes color shift keying (CSK) for VLC [84]. The incoming bits are mapped into a constellation of colors from the chromatic Commission Internationale de l'Eclairage (CIE 1930) color space, as shown in Fig. 2.15. The CIE 1930 is the illumination model for human eye color perception [97]. Any color in the model can be represented by the chromaticity dimension $[x_C, y_C]$. The incoming bits are modulated using the instantaneous color of multi-color LEDs. The overall intensity of the LED is constant which allows for a

consistent optical power and color output. At the receiver side, the two coordinates can be recovered by detecting the instantaneous power of the received multicolor intensities. The color dimension in LiFi can also be used to drive a multicolor LED with different streams of data. The optical summation may turn this colored parallel streams into a single color stream output that can be optically filtered at the receiver into the original transmitted colored streams.

2.7   Summary

This chapter provides a background on OWC and the key developments behind its emergence. Advances in the fields of SSL and communication theory have enabled VLC and LiFi. Different types of light sources and detectors can be used in VLC to enable different applications such as downhole monitoring, high speed indoor communications, underwater communications and vehicular communications. Modulation techniques were developed to suit the VLC channels with different considerations such as illumination levels, energy efficiency and spectral efficiency. However, the choice of the modulation techniques is subject to the considered application and the desired system scenario.

OFDM-based modulation techniques are promising candidates for high speed and spectrum efficient VLC systems. The use of single tap equalizer and adaptive bit and energy loading algorithms allow OFDM-based techniques to utilize most of the available bandwidth in VLC systems. Energy efficiency is required to support dimming in VLC and uplink communications in LiFi systems. Inherently unipolar OFDM techniques are introduced as a solution to the significant power dissipation caused by the DC bias in DCO-OFDM. However, these techniques fail in reducing the energy requirements at high spectral efficiency values. Novel spectrum and energy efficient modulation techniques are proposed in this thesis as a solution to the energy inefficiency of inherently unipolar OFDM techniques at high spectral efficiency.

Chapter 3

Superposition modulation techniques

3.1 Introduction

Incoherent light sources such as light emitting diodes (LEDs) are prominent choices for visible light communication (VLC). This restricts the communication signals to real-valued unipolar intensity modulation and direct detection (IM/DD) signals. Adaptive bit and energy loading algorithms and the computationally efficient single-tap equalizer allow orthogonal frequency division multiplexing (OFDM) to be a promising candidate for VLC [15]. Hermitian symmetry is generally imposed on the OFDM input frames to achieve real-valued OFDM output. A direct current (DC) bias is used in DC-biased optical orthogonal frequency division multiplexing (DCO-OFDM) to shift the negative-valued OFDM samples into positive [20]. However, the OFDM signal has a high peak-to-average power ratio (PAPR) which makes it impossible to convert all of the signal samples into unipolar samples. The DC bias is defined as k_{DC} multiple of the standard deviation of the time-domain OFDM signal σ_x. The power penalty of DCO-OFDM compared with bipolar OFDM was given in (2.10). This penalty increases as the modulation order increases as shown in Fig. 2.8.

The additional DC power dissipation in DCO-OFDM can be justified when a high illumination level is required. However, a novel solution is essential when a reduction in the energy consumption is required. This is the case for most optical wireless communication (OWC) systems such as free space optical (FSO); infrared-based uplink in light fidelity (LiFi) systems and VLC systems with dimmed-illumination. The main objective of this chapter is to provide energy-efficient modulation techniques that are capable of supporting high-speed VLC systems.

3.1.1 Prior work

Inherently unipolar OFDM modulation techniques were introduced to provide energy efficient optical OFDM alternatives to DCO-OFDM. These schemes include asymmetrically clipped optical orthogonal frequency division multiplexing (ACO-OFDM) [21], pulse-amplitude modulation discrete multitone modulation (PAM-DMT) [24], flip orthogonal frequency division multiplexing (FLIP-OFDM) [22], and unipolar orthogonal frequency division multiplexing (U-OFDM) [23]. In order to avoid confusion with the U-OFDM modulation technique, the term 'inherent unipolar OFDM' is used to refer to (ACO-OFDM, PAM-DMT, FLIP-OFDM and U-OFDM). The concepts behind FLIP-OFDM and U-OFDM are identical. However, the term U-OFDM will be used to refer to both techniques throughout this thesis for simplicity.

Inherent unipolar OFDM modulation techniques exploit the OFDM input and output frame structures to produce a unipolar time domain waveform output. However, the energy efficiency of these techniques degrades at high modulation orders due to the restrictions imposed on their frame structures. For example, two time-domain U-OFDM frames are required to convey the information contained in a single DCO-OFDM frame. Similarly, half of the subcarriers are not loaded with modulated symbols in ACO-OFDM to guarantee a unipolar ACO-OFDM time-domain output. As a result, the performance of M-ary quadrature amplitude modulation (M-QAM) DCO-OFDM has to be compared with the bit error ratio (BER) performance of M^2-quadrature amplitude modulation (QAM) in ACO-OFDM and U-OFDM. Furthermore, PAM-DMT uses M-ary pulse-amplitude modulation (M-PAM) on the imaginary part of the subcarriers. Therefore, the BER of PAM-DMT is similar to other inherent unipolar schemes since the BER performance of M-PAM is equivalent to the performance of M^2-QAM [98]. When compared with DCO-OFDM at the same spectral efficiency, the BER performance gain of all of the inherent unipolar OFDM techniques degrades as the constellation size of M-QAM or M-PAM increases. For example, the performance of 1024-QAM in ACO-OFDM/U-OFDM and 32-pulse-amplitude modulation (PAM) in PAM-DMT would be required to be compared with the performance of 32-QAM in DCO-OFDM.

Improved receivers for the inherent unipolar OFDM techniques were proposed in [23, 99–106]. These improved receivers achieve BER performance gains at the price of additional computational complexities. Two main approaches are considered in the

design of these receivers. Amplitude comparison of waveform samples based on the time-domain symmetry is considered in the first approach. The diversity between the real and imaginary components of the received symbols is exploited in the second. For example, the even-indexed subcarriers in ACO-OFDM and the real part of the subcarriers in PAM-DMT can be exploited to improve the detection performance. Inherent unipolar optical OFDM waveforms utilize the lower part of the luminance-voltage (L-V) characteristic since they follow a truncated Gaussian statistical distribution. Therefore, these schemes are suitable candidates for dimming applications in VLC. However, these techniques are incapable of supporting high speed VLC applications given that their relative BER performance gain against DCO-OFDM degrades as the spectral efficiency increases.

There have been a number of studies to improve the spectral and energy efficiency of OFDM-based techniques. A technique that combines ACO-OFDM on the odd-indexed subcarriers with DCO-OFDM on the even-indexed subcarriers was proposed in asymmetrically DC-biased optical orthogonal frequency division multiplexing (ADO-OFDM) [107]. The clipping distortion of the negative-valued samples in ADO-OFDM falls only on the even-indexed subcarriers. This distortion can be estimated and canceled at the receiver at the cost of a 3 dB penalty to the signal-to-noise ratio (SNR). Similarly, hybrid asymmetrical clipped orthogonal frequency division multiplexing (HACO-OFDM) uses ACO-OFDM on the odd-indexed subcarriers and PAM-DMT on the even-indexed subcarriers to improve the spectral efficiency of inherent unipolar OFDM [108]. The symbols loaded on the odd-indexed subcarriers are demodulated first at the receiver to allow for the clipping distortion of ACO-OFDM to be estimated. The PAM-DMT symbols can then be demodulated with minimal distortion from ACO-OFDM. However, the real part of the even subcarriers remains unused in HACO-OFDM which leads to spectral efficiency loss when compared with DCO-OFDM. The asymmetrically and symmetrically clipping optical orthogonal frequency division multiplexing (ASCO-OFDM) is based on combining ACO-OFDM with symmetrical clipping optical orthogonal frequency division multiplexing (SCO-OFDM) [109]. Modulated symbols are loaded only on the even-indexed subcarriers in SCO-OFDM which creates a symmetry in the time domain OFDM signal output $x[n] = x[n + N_{\text{FFT}}/2]$. The clipping distortion of both ACO-OFDM and SCO-OFDM affects the even-indexed subcarriers. However, the clipping distortion of ACO-OFDM can be estimated and canceled at the receiver. The

clipping noise of SCO-OFDM can be removed using U-OFDM time domain processing techniques. The spectral efficiency of ASCO-OFDM is 75% of the spectral efficiency of DCO-OFDM. ASCO-OFDM was reported to have a better BER performance compared with ADO-OFDM since the ADO-OFDM uses the DC bias for the even-indexed subcarriers.

The theory of superposition modulation using inherently unipolar OFDM streams was first introduced by Tsonev *et al.* [25, 26]. The main objective of enhanced unipolar orthogonal frequency division multiplexing (eU-OFDM) is to double the spectral efficiency of U-OFDM by superimposing U-OFDM streams at multiple modulation depths [25]. The generation method and performance of eU-OFDM is described in detail in Section 2.6.2.5. However, the spectral efficiency gap between U-OFDM and DCO-OFDM can never be completely closed with eU-OFDM, as this would require a large number of information streams to be superimposed in the modulation signal. Implementation issues, such as latency, computational complexity, and memory requirements put a practical limit on the maximum number of depths that can be superimposed. The spectral efficiency gap between U-OFDM and DCO-OFDM can be completely closed when an appropriate selection of the constellation sizes is used at the different modulation depths. This has been investigated in generalized enhanced unipolar orthogonal frequency division multiplexing (GREENER-OFDM) [110].

3.1.2 Contribution

The principle behind superposition modulation in this thesis is to allow for a successful transmission of multiple OFDM-based streams by combining them into a single waveform. Additional superimposed streams are designed to avoid creating any distortion to the already existing streams. Therefore, the superposition of multiple OFDM-based streams does not hinder the recovery of any individual stream. Superposition modulation uses an inherent unipolar OFDM stream at depth $d = 1$, where d is the modulation depth index with values $d \geq 1$. Additional $D - 1$ OFDM-based streams are superimposed on top of this base stream, where D is the total number of used depths. The superimposed stream at depth d is designed to avoid distorting the $d - 1$ available streams. However, it may distort any future superimposed streams with a depth order higher than d. The receiver starts with the demodulation of the stream at depth $d = 1$.

A successive clipping distortion cancellation algorithm is used to estimate the clipping distortion created by the stream at depth $d = 1$ on the rest of the streams. This permits the receiver to remove this stream from the overall received signal. The recovery of the rest of the superimposed streams continues in the same way.

Three novel superposition modulation techniques based on inherent unipolar OFDM are proposed in this chapter. The proposed techniques are enhanced pulse-amplitude modulation discrete multitone modulation (ePAM-DMT) [30], enhanced asymmetrically clipped optical orthogonal frequency division multiplexing (eACO-OFDM) [31] and augmented spectral efficiency discrete multitone (ASE-DMT) [32]. The techniques rely on the frame structures of ACO-OFDM and PAM-DMT to superimpose multiple unipolar streams at different modulation depths while avoiding any inter-depth interference (IDI). For example, superposition modulation is achieved based on the anti-symmetry of PAM-DMT in the proposed ePAM-DMT [30]. The proposed ePAM-DMT is compared with DCO-OFDM in this chapter where it is shown to achieve a lower electrical energy dissipation at the same spectral efficiency. However, the cyclic prefixes are used in preserving the anti-symmetry of the superimposed streams in ePAM-DMT which reduces the spectral efficiency. Aligning the anti-symmetry of multiple PAM-DMT streams in the time domain is a complicated process. A novel solution is proposed based on superimposing multiple PAM-DMT streams in the frequency domain. The proposed ASE-DMT is based on the selective loading of M-PAM symbols on multiple modulation depths. It avoids the spectral efficiency losses of ePAM-DMT and provides energy efficiency gains over DCO-OFDM and ePAM-DMT.

A novel power efficient solution to the spectral efficiency loss of ACO-OFDM is proposed in eACO-OFDM [31]. The eACO-OFDM is shown to achieve BER performance gains when compared with DCO-OFDM and ePAM-DMT. The concept proposed by El-gala *et al.* [111] under the term spectrally and energy efficient orthogonal frequency division multiplexing (SEE-OFDM) is similar in principle to eACO-OFDM. However, SEE-OFDM implements the superposition of multiple ACO-OFDM streams with U-OFDM signal processing. This leads to an additional SNR penalty when SEE-OFDM is compared with eACO-OFDM. A similar concept to eACO-OFDM was also proposed by Wang *et al.* [112] under the term layered asymmetrically clipped optical orthogonal frequency division multiplexing (LACO-OFDM). However, it should be noted that the
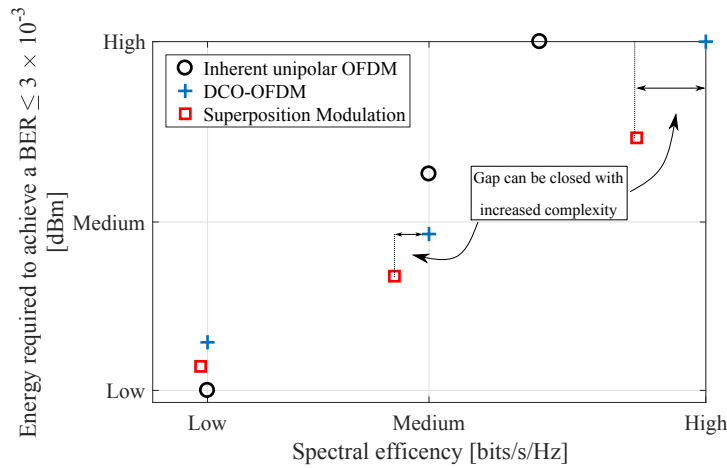
Figure 3.1: *An illustration of relative performance of the proposed modulation techniques.*

proposed eACO-OFDM technique was developed independently and concurrently to LACO-OFDM. An interesting analysis of eACO-OFDM and other related superposition techniques is presented in [113].

The energy efficiency is defined by the capability of a modulation technique to support a high spectral efficiency at low energy requirements. A modulation technique is said to be an energy efficient technique when it has less energy requirements than any other modulation technique that is compared to at the same spectral efficiency. The proposed modulation techniques are aimed to address the high energy requirements of the state-of-the-art modulation techniques in VLC. A relative performance comparison is presented in Fig. 3.1 for superposition modulation techniques, inherent unipolar modulation techniques, and DCO-OFDM. The term inherent unipolar modulation techniques is used to refer to ACO-OFDM, PAM-DMT and U-OFDM as described in Section 2.6.2. The performance of superposition modulation is presented for eACO-OFDM and ASE-DMT. Superposition modulation techniques offer a promising solution to the energy requirements at medium and high spectral efficiency values. The spectral efficiency gap between DCO-OFDM and superposition modulation can be decreased with an increased complexity. Inherent modulation techniques are suitable solutions for applications favoring low spectral efficiency below 1.5 bits/s/Hz. A similar but more detailed comparison is presented in Fig. 4.26 and Fig. 4.27. The relative complexity, spectral efficiency and energy efficiency of superposition modulation techniques, inherent unipolar modulation techniques, and DCO-OFDM are presented in table.3.1.

A detailed analysis and comparisons are provided in the rest of this chapter.

Modulation Technique	Complexity	Energy efficiency	Spectral efficiency
DCO-OFDM	low	low	high
Inherent unipolar	low	high	low
ePAM-DMT	high	medium	medium
eACO-OFDM and ASE-DMT	medium	high	high

Table 3.1: *A comparison between the proposed and the state-of-the-art modulation techniques. Low spectral efficiency is defined below 1.5 bits/s/Hz and high spectral efficiency is defined for values higher than 3 bits/s/Hz.*

The rest of this chapter is organized as follows. The modulation concept and associated spectral efficiency are presented in Section 3.2 for ePAM-DMT, Section 3.3 for eACO-OFDM and Section 3.4 for ASE-DMT. The theoretical study of the proposed superposition modulation techniques is presented in Section 3.5. The power efficiency is analyzed in Section 3.5.1, and the theoretical BER performance is derived in Section 3.5.2. A generalized solution to reduce the computation complexity is considered in Section 3.6. The results for all the proposed techniques are presented in Section 3.7. The results also include an investigation of the computation complexity and practical considerations of the proposed techniques in Section 3.7.4. The chapter is summarized in Section 3.8.

3.2 Superposition modulation based on PAM-DMT

The power efficiency improvement of PAM-DMT over DCO-OFDM decreases and quickly disappears at high spectral efficiency. The superposition modulation concept of ePAM-DMT is presented in this section to unlock the energy efficiency gains at high spectral efficiency based on PAM-DMT.

3.2.1 Modulation concept

The main objective in the design of ePAM-DMT is to convert all the clipping distortion of the superimposed PAM-DMT streams into the real-valued component of the subcarriers. This guarantees the distortion-less demodulation of all the superimposed streams at the receiver. A possible arrangement of the multiple PAM-DMT streams is given in Fig. 3.2 (e). The generation process starts with a PAM-DMT modulator at depth $d = 1$
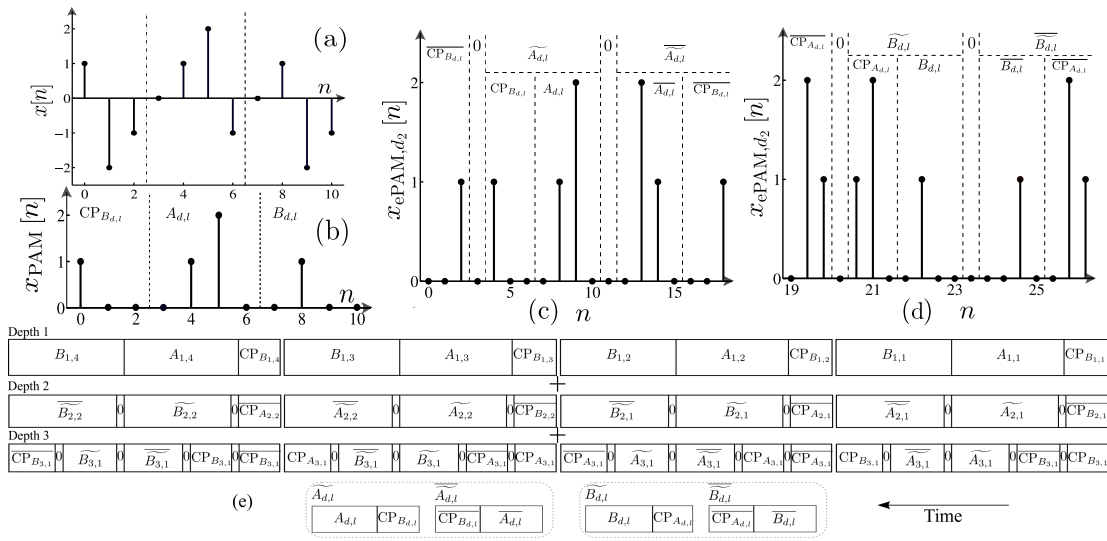
Figure 3.2: *(a) Original bipolar OFDM time domain waveform and its cyclic prefix before zero clipping. (b) PAM-DMT time domain waveform and its cyclic prefix. (c) and (d) Two successive ePAM-DMT frames at depth $d = 2$. (e) The complete frame structure arrangement for four ePAM-DMT frames using three information streams. At any depth, the first half of the PAM-DMT frame is denoted as $A_{d,l}$, while $B_{d,l}$ denotes the second half of the same PAM-DMT frame. The bar notation $\overline{F}$ refers that the subframe F is time-reversed $\overline{F}[n] = F[L_F - 1 - n]$, where L_F is the length of frame F. Modified subframes $\widetilde{A_{d,l}}$ and $\widetilde{B_{d,l}}$ are illustrated in the figure alongside their flipped versions $\overline{\widetilde{A_{d,l}}}$ and $\overline{\widetilde{B_{d,l}}}$, respectively. The subscripts denote that the subframe at modulation depth d belongs to the l-th PAM-DMT frame.*

where each generated frame is composed of a cyclic prefix $\text{CP}_{B_{d,l}}$ and two subframes $A_{d,l}$ and $B_{d,l}$, where d denotes the depth number and l denotes the frame number as shown in Fig. 3.2 (b). The bar notation $\overline{F}$ denotes that the subframe F is time reversed, *i.e.* $\overline{F}[n] = F[L_F - 1 - n]$, where L_F is the length of frame F. At depth $d = 2$, the frame is generated using a PAM-DMT modulator with a smaller OFDM frame length. The frame length at depth d is given by: $N_d^{\text{ePAM}} = N_{d-1}^{\text{ePAM}} - 2N_{\text{CP}} - 2 \ \forall d \geq 2$, where N_{CP} is the cyclic prefix length and $N_1^{\text{ePAM}} = N_{\text{FFT}}$ is the fast Fourier transform (FFT) length. The original subframe $A_{d,l}$ is combined with the cyclic prefix $\text{CP}_{B_{d,l}}$ to form a modified subframe $\widetilde{A_{d,l}}$. The modified subframe is flipped and repeated in $\overline{\widetilde{A_{d,l}}}$. Therefore, the two modified subframes at depth $d = 2$, $\widetilde{A_{d,l}}$ and $\overline{\widetilde{A_{d,l}}}$, form a new frame that is similar in length to the previous depth frames. Modified subframes at any depth $d > 1$ have a Hermitian symmetry that restricts their frequency representation to be real-valued. This allows distortion-free IDI with the stream at depth $d = 1$. This frame needs to be

guarded by a cyclic prefix that is identical to the last N_{CP} samples of that frame, $\overline{\text{CP}_{B_{d,l}}}$. Therefore, frames at depth $d = 2$ need three cyclic prefixes. The first one is intended to guard the modified frames from inter-symbol interference (ISI) at the demodulation process of stream-1. The other two prefixes are intended to guard the original frames from ISI at the demodulation process of stream-2. The use of zero padding instead of the cyclic prefix is a possible solution for the symmetry alignment in ePAM-DMT. However, zero padding cannot mitigate any ISI at the successive demodulation process of the superimposed streams. The subsequent frames in depth $d = 2$ are generated in a similar way to the first frame. The cyclic prefixes are also designed to preserve both the original and the modified subframes from ISI. The time-domain waveform for the first two frames at depth $d = 2$ is shown in Fig. 3.2 (c and d). Frames at depth $d = 2$ are scaled by $1/\sqrt{2}$ in order to preserve the overall signal energy at this depth. Frames at depth $d = 3$ are generated in the same way as the frames at depth $d = 2$. The frame length at $d = 3$ is smaller than the frame length at $d = 2$ and the cyclic prefixes are designed to create three tiers of ISI protection for each of the demodulation processes at the receiver. The information conveyed in subframes at depth $d = 3$ is repeated four times in a way that preserves the Hermitian symmetry for each demodulation process at higher depths. Frames at depth $d = 3$ are scaled by $1/2$ in order to preserve the overall signal energy at this depth. In addition to that, each of the streams is scaled by a parameter $1/\gamma_d$ to allocate different power settings to the streams based on the spectral loading. A possible design that requires a maximum of $D = 3$ depths to achieve the spectral efficiency of DCO-OFDM is investigated in Section 3.7.1.

The demodulation process starts by removing the first tier of cyclic prefixes at the receiver. Afterwards, the information carried at depth $d = 1$ can be extracted using a conventional PAM-DMT demodulator. The IDI caused by the superposition of multiple PAM-DMT streams affects only the real component of the frequency subcarriers since all of the superimposed streams have a Hermitian symmetry. After the information at depth $d = 1$ is demodulated, the recovered bits are remodulated at the receiver in order to reconstruct the information signal at depth $d = 1$, which is then subtracted from the overall received ePAM-DMT signal. After the removal of the first depth waveform, the second half of each frame is removed from the ePAM-DMT waveform. The length of the removed subframes is $N_1^{\text{ePAM}}/2$. Therefore the resulted waveform conveys the depth $d = 2$ and depth $d = 3$ information but with a hierarchy that is similar to the that

of depth $d = 1$ and depth $d = 2$ as shown in Fig. 3.2 (e). This allows the demodulation process at higher depths to be performed in a similar way to the demodulation of depth $d = 1$. The IDI caused by the superposition of multiple PAM-DMT streams is canceled at the receiver since it only affects the real component of the subcarriers. The multiple cyclic prefixes used at higher-depth streams are intended to protect the inner subframes at each demodulation process and are arranged to preserve the Hermitian symmetry required for this scheme. The demodulation process continues in a similar way for all subsequent streams until the information at all depths is recovered.

3.2.2 Spectral efficiency

The spectral efficiency of PAM-DMT at the first depth is equivalent to the spectral efficiency of DCO-OFDM for the same constellation size and the same frame length. The spectral efficiency of PAM-DMT at depth d is given as follows:

$$\eta_{\text{PAM}}(d) = \frac{(N_d^{\text{ePAM}} - 2) \log_2(M_{\text{ePAM},d})}{2^d \cdot (N_1^{\text{ePAM}} + N_{\text{CP}})} \quad \text{bits/s/Hz,} \tag{3.1}$$

where $M_{\text{ePAM},d}$ and N_d^{ePAM} are the constellation size and the OFDM frame length at depth d, respectively. The BER performance of M-QAM is equivalent to the BER performance of $\sqrt{M}$-PAM. When compared with M_{DCO}-QAM DCO-OFDM, ePAM-DMT uses multiple streams of PAM-DMT with smaller constellation sizes that are comparable to $\sqrt{M_{\text{DCO}}}$ to improve the energy efficiency. However, the BER performance of non-squared constellation orders of M-QAM cannot be matched with $\sqrt{M}$-PAM. Therefore, the resolution of constellation sizes that can be used at the different modulation depths of PAM-DMT is limited. The spectral efficiency of ePAM-DMT is given as the sum of the spectral efficiency values at the individual PAM-DMT streams. It can be written as follows:

$$\begin{aligned} \eta_{\text{ePAM}}(D) &= \sum_{d=1}^{D} \eta_{\text{PAM}}(d) \\ &= \sum_{d=1}^{D} \frac{\log_2 M_{\text{ePAM},d} \cdot \left(N_1^{\text{ePAM}} - 2 - 2 \cdot (N_{\text{CP}} + 1)(d-1) \right)}{2^d \cdot (N_1^{\text{ePAM}} + N_{\text{CP}})}. \end{aligned} \tag{3.2}$$

The spectral efficiency of ePAM-DMT cannot completely match the spectral efficiency of
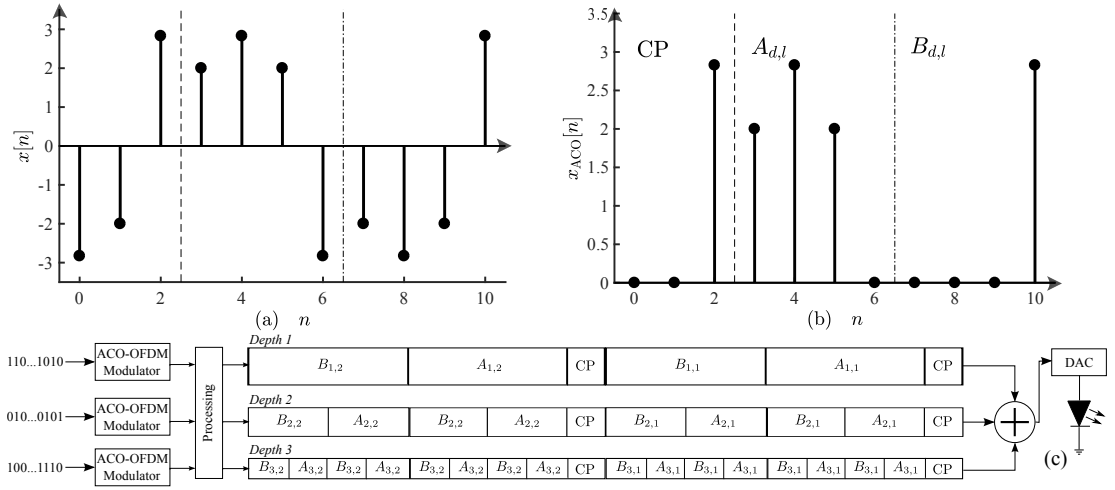
Figure 3.3: *(a) Original bipolar OFDM time domain waveform and its CP before zero clipping. (b) ACO-OFDM time domain waveform and its CP. (c) Illustration of eACO-OFDM modulation concept with three information streams. CP denotes the CP. The subframe $A_{d,l}$ represents the first half of ACO-OFDM unipolar frame, and the subframe $B_{d,l}$ represents the second half of the same ACO-OFDM unipolar frame. The subscripts denote that the frame at modulation depth d belongs to the l-th ACO-OFDM frame.*

DCO-OFDM since multiple cyclic prefixes are required to mitigate the ISI. The spectral efficiency ratio of ePAM-DMT and DCO-OFDM is a function of the combination of constellation sizes used as will be illustrated in Section 3.4.2. The spectral efficiency ratio of the ePAM-DMT to a PAM-DMT scheme with a similar constellation size is given as follows:

$$\alpha_\eta^{\text{ePAM}}(D,d) = \frac{\sum_{\acute{d}=1}^{D} \frac{\log_2 M_{\text{ePAM},\acute{d}}(N_{\text{FFT},\acute{d}}-2)}{2^{\acute{d}-1}}}{\log_2 M_{\text{ePAM},d}(N_{\text{FFT},1}-2)}. \tag{3.3}$$

3.3 Superposition modulation based on ACO-OFDM

The concept of superposition modulation can be implemented using ACO-OFDM. The asymmetry in the ACO-OFDM allows for multiple streams to be superimposed at multiple modulation depths without creating any IDI. The modulation concept and spectral efficiency of eACO-OFDM are presented in this section.
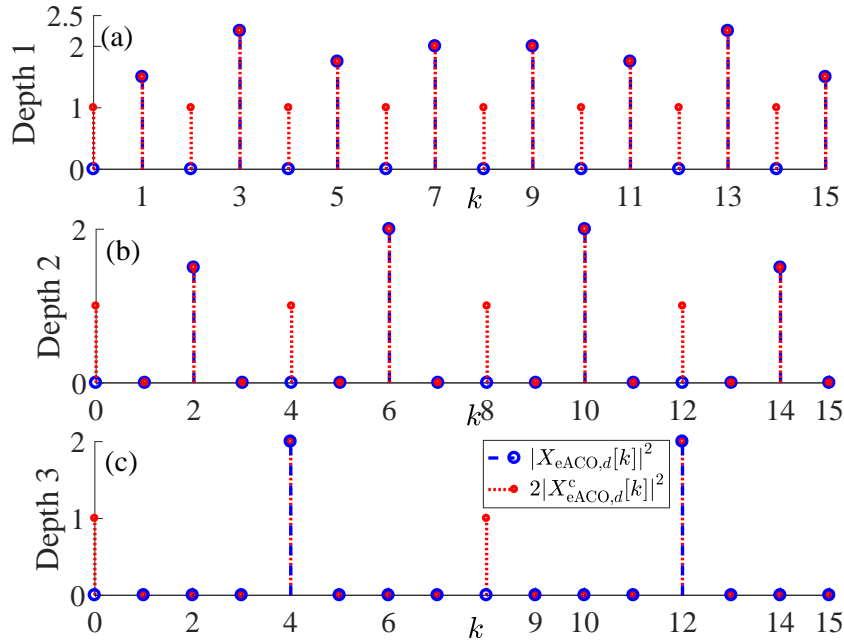
Figure 3.4: *An illustration of the frequency domain subcarrier loading at three depths eACO-OFDM and the effects of zero clipping. (a) and (b) and (d) shows the magnitude of the subcarriers before and after zero level time-domain clipping, $|X_{\text{eACO},d}[k]|^2$ and $2|X^{\text{c}}_{\text{eACO},d}[k]|^2$, respectively. The factor 2 is introduced to compensate for the attenuation that occurs due to the zero-level clipping as described in (2.16).*

3.3.1 Modulation concept

The main objective of the frame hierarchy design in eACO-OFDM is to convert all of the IDI of the superimposed streams into the even-indexed sub-carriers at the frequency domain, so that it becomes distortion-less to the ACO-OFDM stream at the first depth. A possible arrangement of the multiple ACO-OFDM signals is given in Fig. 3.3. The eACO-OFDM signal generation starts at the first depth with a conventional ACO-OFDM modulator. The subframes are defined to be half of the original ACO-OFDM frames in length. At depth $d = 2$, a second ACO-OFDM stream is superimposed on the first stream and generated in a similar fashion to depth $d = 1$. However, the OFDM frame length at depth $d = 2$ is $N_2^{\text{eACO}} = N_1^{\text{eACO}}/2$, where $N_1^{\text{eACO}} = N_{\text{FFT}}$ is the OFDM frame length at depth $d = 1$. The overall stream at depth $d = 2$ is scaled by $1/\sqrt{2}$ in order to preserve the overall signal energy at this depth and repeated 2 times. Furthermore, ACO-OFDM streams are superimposed at depth d with an OFDM frame length $N_d^{\text{eACO}} = N_{\text{FFT}}/2^{d-1}$ in a similar way as depth $d = 2$ and the overall stream

at that depth is scaled by $1/\sqrt{2^{d-1}}$ and repeated 2^{d-1} times. In addition, each of the streams is scaled by a parameter $1/\gamma_d$ to facilitate the allocation of different power levels as described in Section 3.2. At the receiver, the demodulation process starts with removing the cyclic prefixes. Then the information carried at depth $d = 1$ can be extracted using a conventional ACO-OFDM demodulator. The subframes in each individual frame at depth $d = 1$ are asymmetric. Therefore the information stream at this depth follows (2.14). At higher modulation depths, the subframes in each individual frame are identical. Therefore the information stream at this depth follows (2.15). As a result, the odd-indexed sub-carriers only convey the information of depth $d = 1$, and the IDI falls into the even-indexed sub-carriers. After the information at depth $d = 1$ is demodulated, the recovered bits are remodulated at the receiver in order to reconstruct the first depth stream, which is then distorted using the channel response and subtracted from the overall eACO-OFDM signal. After the removal of the depth $d = 1$ waveform, each two identical subsequent subframes are summed. The demodulation process at depth $d = 2$ continues with the conventional ACO-OFDM demodulation process and the recovered bits are remodulated in order to allow for the information stream at depth $d = 2$ to be subtracted from the overall received information signal. The demodulation process continues in a similar way for all subsequent streams until the information at the last depth is recovered.

The superposition of ACO-OFDM streams at multiple modulation depths is illustrated in the frequency domain diagram at Fig. 3.4. It can be shown that the subcarriers at modulation depths d' does not cause any distortion to the information-carrying subcarriers, $X_{\text{eACO},d}[k]$, at lower order modulation depths for any $d \leq d'$. For example, the clipping distortion $X_{\text{eACO},2}^{\text{c}}[k]$ that occurs due to the zero-level clipping of the ACO-OFDM stream at modulation depth 2 falls on the subcarriers $k = \{4, 8, 12\}$, which have null information symbols at modulation depths $d \leq 2$. The information-carrying subcarriers, $X_{\text{eACO},d}[k]$, are located at subcarriers indices $k = 2^{d-1}(2k' + 1)$ for $k' = 0, 1, 2, \cdots, N_{FFT}/2 - 1$. The clipping distortion, $X_{\text{eACO},d}^{\text{c}}[k]$, falls on the subcarriers indices $k = 2^d k'$ for $k' = 0, 1, 2, \cdots, N_{FFT}/2 - 1$.

3.3.2 Spectral efficiency

The spectral efficiency of eACO-OFDM is given as the summation of the spectral efficiency values of all the superimposed ACO-OFDM streams:

$$\eta_{\text{eACO}}(D) = \sum_{d=1}^{D} \eta_{\text{ACO}}(d) \quad \text{bits/s/Hz,} \tag{3.4}$$

where $\eta_{\text{ACO}}(d)$ is the spectral efficiency of ACO-OFDM at depth d:

$$\eta_{\text{ACO}}(d) = \frac{\log_2(M_{\text{eACO},d})(N_{\text{FFT},d})}{4(N_{\text{FFT}} + N_{\text{CP}})} \quad \text{bits/s/Hz.} \tag{3.5}$$

The spectral efficiency ratio of the eACO-OFDM to an ACO-OFDM scheme with a similar constellation size is expressed as follows:

$$\alpha_{\eta}^{\text{eACO}}(D, d) = \frac{\sum_{d=1}^{D} \left(\frac{\log_2 M_{\text{eACO},d}}{2^{d-1}} \right)}{\log_2 M_{\text{eACO},d}}. \tag{3.6}$$

The spectral efficiency of eACO-OFDM is exactly equivalent to η_{DCO} for large numbers of superimposed depths and any cyclic prefix length. However, the spectral efficiency of ePAM-DMT can never match the spectral efficiency of DCO-OFDM, since multiple cyclic prefixes are employed at higher order depths of ePAM-DMT. This trend will be illustrated in Section 3.4.2.

3.4 Superposition modulation based on ASE-DMT

The proposed ASE-DMT technique uses most of the available subcarriers in the OFDM frame. The ASE-DMT waveform can be generated by the selective loading of imaginary and real components of the subcarriers. The waveform generation starts with a typical PAM-DMT [24] modulator at the first depth. Additional streams can only be superimposed on the first depth stream if their frequency domain subcarriers are loaded on the real components of the subcarriers. Superposition modulation is achieved in ePAM-DMT by rearranging the PAM-DMT time domain waveforms to have a Hermitian symmetry as was shown in Section 3.2. A more efficient technique is achieved in ASE-DMT by using groups of subcarriers which allows for multiple streams of PAM-DMT waveforms to be superimposed without any IDI as will be shown in Sec-
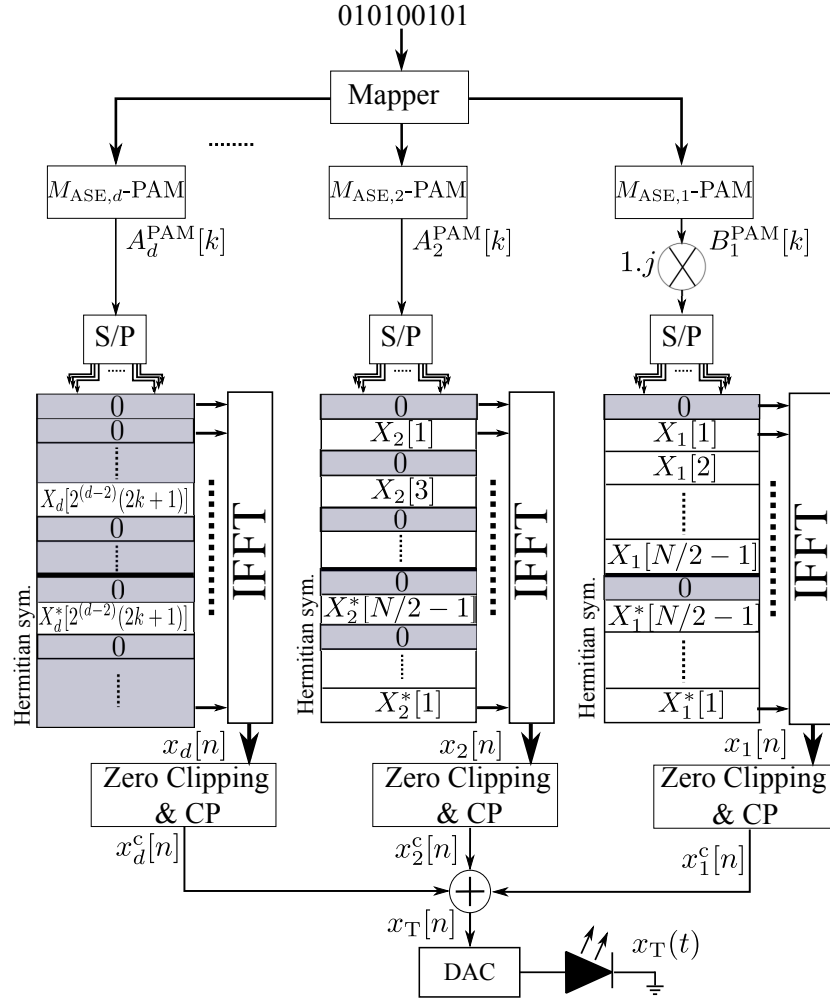
Figure 3.5: *ASE-DMT transmitter block diagram. $X_d[k]$ refers to the k-th subcarrier at depth d; S/P denotes for serial to parallel; DAC denotes for digital to analogue conversion; and CP refers to the cyclic prefixing.*

tion 3.4.1.

3.4.1 Modulation concept

The transmitter block diagram of ASE-DMT is shown in Fig. 3.5. At the first depth, the imaginary components of the subcarriers are loaded with PAM symbols while the real components are kept unused $X_1[k] = jB_1^{\text{PAM}}[k]$, where $B_1^{\text{PAM}}[k]$ is the PAM symbol at the k-th subcarrier of depth $d = 1$. Note that Hermitian symmetry is also required in the frequency domain to guarantee a real time-domain output, $B_1^{\text{PAM}}[0] = B_1^{\text{PAM}}[N_{\text{FFT}}/2] = 0$, and $B_1^{\text{PAM}}[k] = -B_1^{\text{PAM}}[N_{\text{FFT}} - k]$ for
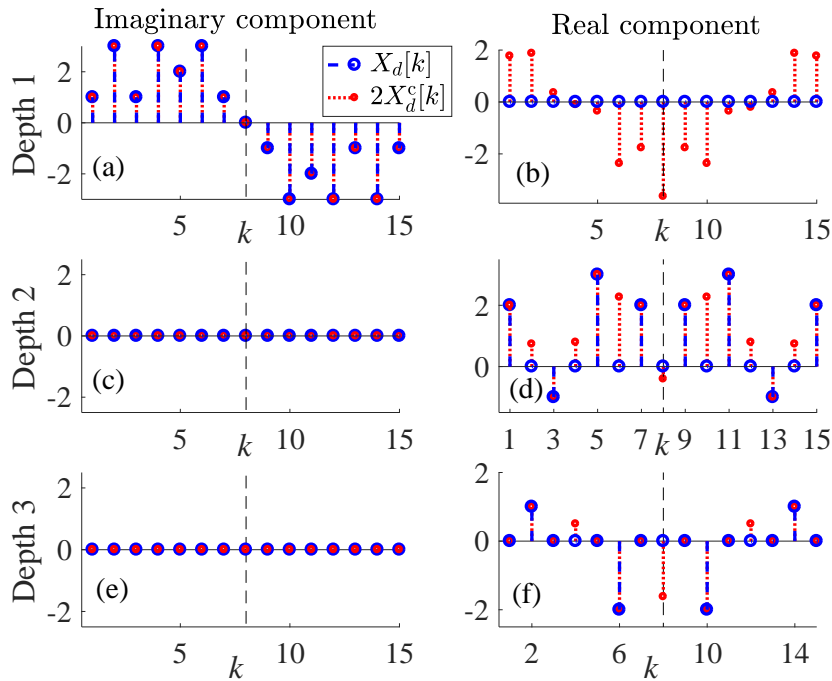
Figure 3.6: *An illustration of the frequency domain subcarrier loading at three depths ASE-DMT and the effects of zero clipping. (a) and (c) and (e) shows the imaginary components of the subcarriers before and after zero level time-domain clipping, $\Im[X_d[k]]$ and $\Im[2X_d^c[k]]$, respectively. (b) and (d) and (f) shows the real components of the subcarriers before and after zero level time-domain clipping, $\Re[X_d[k]]$ and $\Re[2X_d^c[k]]$, respectively. The factor 2 is introduced to compensate for the attenuation that occurs due to the zero-level clipping as described in (2.16).*

$k = 1, 2, \cdots, N_{\text{FFT}}/2 - 1$. As a result, the time domain PAM-DMT waveform $x_1[n]$ can be given in (2.19). The time domain PAM-DMT waveform in (2.19) exhibits the following antisymmetry: $x_1[n] = -x_1[N_{\text{FFT}} - n]$, where $x_1[0] = x_1[N_{\text{FFT}}/2] = 0$ as was shown in Section 2.6.2.3. The zero level clipping of the PAM-DMT waveform at depth d can be given in (2.16). The frequency domain transformation of the clipped waveform, $x_d^c[n]$, is given as follows:

$$X_d^c[k] = \frac{X_d[k] + \text{FFT}\{|x_d[n]|\}}{2}, \tag{3.7}$$

where the subscripts d denotes the depth order and $X_d[k] = \text{FFT}\{x_d[n]\}$. The effect of clipping is shown to be distortion-less to the information carrying subcarriers in Fig. 3.6. Clipping of the negative samples at depth $d = 1$ is distortion-less to the information at the same depth because all of the distortion transforms into the real

part of the subcarriers. The distortion term $|x_1[n]|$ has a Hermitian symmetry $|x_1[n]| = |x_1[N_{\text{FFT}} - n]|$, which can be illustrated by the following:

$$
\begin{aligned}
\text{FFT}\{|x_1[n]|\} &= \frac{1}{\sqrt{N_{\text{FFT}}}} \sum_{n=0}^{N_{\text{FFT}}-1} |x_1[n]| e^{-\frac{j2\pi kn}{N_{\text{FFT}}}} \\
&= \frac{2}{\sqrt{N_{\text{FFT}}}} \sum_{n=1}^{N_{\text{FFT}}/2-1} |x_1[n]| \cos \frac{2\pi kn}{N_{\text{FFT}}}.
\end{aligned}
\tag{3.8}
$$

At depth $d = 2$, the odd subcarriers are loaded with real valued PAM symbols $X_2[k] = A_2^{\text{PAM}}[k]$, while all of the other subcarriers are kept unused. The subcarriers at depth $d = 2$, $X_2[k]$, are given as follows:

$$
X_2[k'] = \begin{cases} A_2^{\text{PAM}}[k'], & \text{if } k' = 2k+1 \\ 0, & \text{Otherwise} \end{cases},
\tag{3.9}
$$

where $A_2^{\text{PAM}}[k']$ is the PAM symbol at the k'-th subcarrier of depth $d = 2$; and $k = 0, 1, \cdots, N_{\text{FFT}}/4 - 1$. Hermitian symmetry is also required to guarantee that $x_2[n]$ is real, $A_2^{\text{PAM}}[k] = A_2^{\text{PAM}}[N_{\text{FFT}} - k]$. As a result, the time domain waveform at depth $d = 2$, $x_2[n]$, would have the following symmetry: $x_2[n] = -x_2[n + N_{\text{FFT}}/2]$. Therefore, the distortion caused by the clipping at zero level would only affect the real domain even subcarriers. This is shown as follows:

$$
\text{FFT}\{|x_2[n]|\} = \frac{1}{\sqrt{N_{\text{FFT}}}} \sum_{n=0}^{N_{\text{FFT}}/2-1} |x_2[n]| e^{-\frac{j2\pi kn}{N_{\text{FFT}}}} (1 + e^{-j\pi k}),
\tag{3.10}
$$

which takes values only at $X_2^c[2k]$, for $k = 0, 1, \cdots, N_{\text{FFT}}/2 - 1$. Therefore, the distortion is orthogonal to the information content at both depth $d = 1$ and depth $d = 2$. Subsequent streams can be generated at depth d, where the subcarriers will be loaded with real valued PAM symbols:

$$
X_d[k'] = \begin{cases} A_d^{\text{PAM}}[k'], & \text{if } k' = 2^{d-2}(2k+1) \\ 0, & \text{Otherwise} \end{cases},
\tag{3.11}
$$

where $A_d^{\text{PAM}}[k']$ is the PAM symbol at the k'-th subcarrier of depth d; and $k = 0, 1, \cdots, N_{\text{FFT}}/2^d - 1$. Hermitian symmetry is also required to guarantee that $x_d[n]$

is real, $A_d^{\mathrm{PAM}}[k] = A_d^{\mathrm{PAM}}[N_{\mathrm{FFT}} - k]$. Using (2.16) and (3.11), it can be shown that:

$$x_d[n] = -x_d[n + N_{\mathrm{FFT}}/2^{d-1}] \quad \forall d > 1. \tag{3.12}$$

Using (3.7), $X_d[k]$ is written as follows:

$$X_d[k] = \frac{1}{\sqrt{N_{\mathrm{FFT}}}} \sum_{n=0}^{N_{\mathrm{FFT}}/2^{d-1}-1} x_d[n] e^{-\frac{j2\pi kn}{N_{\mathrm{FFT}}}} \kappa (1 - e^{\frac{-j\pi k}{2^{D-2}}}), \tag{3.13}$$

and the zero-level clipping distortion effect on the subcarriers in the frequency domain is written as follows:

$$\mathrm{FFT}\{|x_d[n]|\} = \frac{1}{\sqrt{N_{\mathrm{FFT}}}} \sum_{n=0}^{N_{\mathrm{FFT}}/2^{d-1}-1} |x_d[n]| e^{-\frac{j2\pi kn}{N_{\mathrm{FFT}}}} \kappa (1 + e^{\frac{-j\pi k}{2^{D-2}}}), \tag{3.14}$$

where D is the total number of used depths, and κ is written as follows:

$$\kappa = \prod_{d=2}^{D-1} (1 + e^{\frac{-j\pi k}{2^{d-2}}}). \tag{3.15}$$

Using (3.13) and (3.14), it can be shown that the zero-level clipping is distortion-less to the information content at $X_d^{\mathrm{c}}[2^{d-2}(2k+1)]$, and that all of the distortion will affect the subcarriers at $X_d^{\mathrm{c}}[2^{d-1}k]$. Similar analysis can be applied to eACO-OFDM. Using this technique of selective subcarrier loading at each depth will allow multiple PAM modulated waveforms to be superimposed without any IDI. The active subcarriers of each superimposed depth will not be affected by the zero-level clipping distortion of both the current depth and the higher order depths. However, it will be affected by the distortion of the zero-level clipping of the lower order depths. This distortion will be estimated and canceled at the receiver as will be shown below.

After generating the time domain waveforms of all depths, the generated waveforms are clipped and the cyclic prefixes are inserted. The overall ASE-DMT waveform can be obtained by superimposing the clipped waveforms of all depths:

$$x_{\mathrm{T}}[n] = \sum_{d=1}^{D} x_d^{\mathrm{c}}[n]. \tag{3.16}$$

Using (2.16) and (3.7), the ASE-DMT subcarriers is written as follows:

$$X_{\mathrm{T}}[k] = \frac{jB_1^{\mathrm{PAM}}[k] + \sum_{d=2}^{D} A_d^{\mathrm{PAM}}[k] + \sum_{d=1}^{D} \mathrm{FFT}\{|x_d[n]|\}}{2}. \tag{3.17}$$

The information content of depth $d = 1$ can be obtained by considering the imaginary-valued components and ignoring the real-valued components of the subcarriers. This can be given as $\hat{B}_1^{\mathrm{PAM}}[k] = 2\Im(X_{\mathrm{T}}[k] + W[k])$, where $W[k]$ is the frequency domain realization of the additive white Gaussian noise (AWGN) at the receiver [15]. The information of depth $d = 1$ can then be remodulated at the receiver to obtain $\hat{x}_1[n]$ which can be subtracted from the ASE-DMT received waveform. This would result in removing the imaginary component of $X_{\mathrm{T}}[n]$ and also removing the real domain distortion caused by the zero-level clipping of the depth $d = 1$ waveform, $\mathrm{FFT}\{|x_1[n]|\}$. Subsequent depths can be demodulated by selecting the appropriate frequency subcarrier indexes at each depth. The real component of the subcarriers at $2^{d-2}(2k + 1)$ for $k = 0, 1, \cdots, N_{\mathrm{FFT}}/2^d - 1$ can then be remodulated to obtain the waveform at depth d, $\hat{x}_d[n]$, which would be subtracted from the remaining ASE-DMT waveform.

The same process is repeated until the information at the last depth is demodulated. In this way the distortion of the previous depths is estimated and canceled from the higher depths in the successive clipping distortion cancellation process at the receiver.

3.4.2 Spectral efficiency

The spectral efficiency of the first depth of ASE-DMT is equivalent to the spectral efficiency of PAM-DMT, which is also similar to the spectral efficiency of DCO-OFDM. This is written as follows:

$$\eta_{\mathrm{ASE}}(1) = \frac{\log_2(M_{\mathrm{ASE},1})(N_{\mathrm{FFT}} - 2)}{2(N_{\mathrm{FFT}} + N_{\mathrm{CP}})} \quad \mathrm{bits/s/Hz}. \tag{3.18}$$

The spectral efficiency of higher depths $d \geq 2$ is expressed as follows:

$$\eta_{\mathrm{ASE}}(d) = \frac{\log_2(M_{\mathrm{ASE},d})N_{\mathrm{FFT}}}{2^d(N_{\mathrm{FFT}} + N_{\mathrm{CP}})} \quad \mathrm{bits/s/Hz}. \tag{3.19}$$
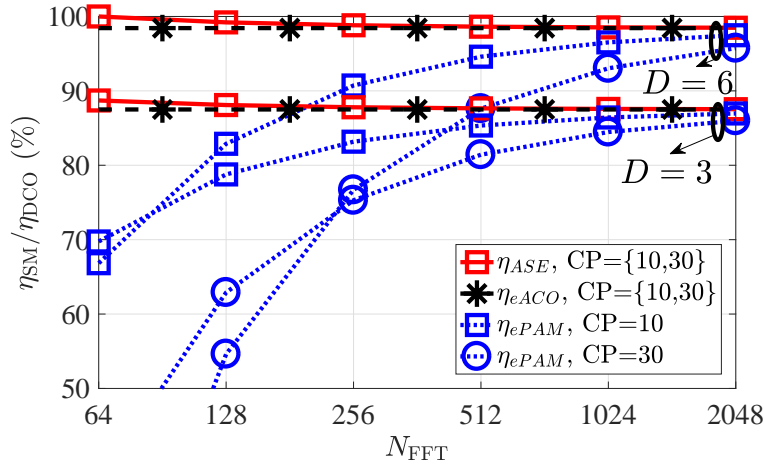
Figure 3.7: *The ratio of the spectral efficiency of the proposed superposition modulation techniques to the spectral efficiency of DCO-OFDM for different FFT and cyclic prefix lengths at $D = 3$ and $D = 6$. The term η_{SM} denotes the spectral efficiency of any of the proposed techniques ePAM-DMT, eACO-OFDM, and ASE-DMT as detailed in the legend.*

The spectral efficiency of ASE-DMT can then be calculated as follows:

$$\eta_{\mathrm{ASE,T}}(D) = \sum_{d=1}^{D} \eta_{\mathrm{ASE}}(d) \quad \text{bits/s/Hz} \tag{3.20}$$

$$= \frac{\log_2(M_{\mathrm{ASE,1}})(N_{\mathrm{FFT}} - 2) + \sum_{d=2}^{D} \frac{\log_2(M_{\mathrm{ASE},d})(N_{\mathrm{FFT}})}{2^{d-1}}}{2(N_{\mathrm{FFT}} + N_{\mathrm{CP}})}.$$

The spectral efficiency ratio of ASE-DMT to the spectral efficiency contribution of each individual depth is written as follows:

$$\alpha_\eta^{\mathrm{ASE}}(D, d) = \frac{\eta_{\mathrm{ASE,T}}(D)}{\eta_{\mathrm{ASE}}(d) 2^{d-1}}. \tag{3.21}$$

The spectral efficiency of ASE-DMT approaches twice the spectral efficiency of DCO-OFDM as the total number of depths increases. However, the energy efficiency comparison of both modulation schemes should be considered at an equivalent spectral efficiency. Therefore, the superimposed waveforms in ASE-DMT use smaller constellation sizes, $M_{\mathrm{ASE},d} = \sqrt{M_{\mathrm{DCO}}}$, which can lead to an overall spectral efficiency that is equivalent to DCO-OFDM. Since the system design of ePAM-DMT employs the cyclic prefixes in the symmetry alignment of the PAM-DMT time-domain frames, the spectral efficiency of ePAM-DMT is a function of the FFT/inverse fast Fourier transform (IFFT)

frame and cyclic prefix sizes.

The spectral efficiency of ePAM-DMT tends to increase as the FFT/IFFT frame length increases. Unlike ePAM-DMT, the spectral efficiency of ASE-DMT is independent of the cyclic prefix length and therefore, can be employed with smaller FFT/IFFT sizes. This allows ASE-DMT to operate at a lower computational complexity while avoiding any spectral efficiency loss. The spectral efficiency ratio of ePAM-DMT, eACO-OFDM and ASE-DMT to the spectral efficiency of DCO-OFDM is shown in Fig. 3.7 as a function of the OFDM frame and cyclic prefixes lengths. The spectral efficiency of ASE-DMT is slightly higher than the spectral efficiency of eACO-OFDM at small FFT/IFFT sizes. It is shown that the spectral efficiency of ePAM-DMT, η_{ePAM}, exceeds 80% of η_{DCO} for all of the presented cyclic prefix lengths when the OFDM frame length is $N_{\text{FFT}} \geq 512$. The spectral efficiency of ASE-DMT exactly matches the spectral efficiency of DCO-OFDM when $D = 6$ and $N_{\text{FFT}} = 64$.

3.5 Theoretical study

3.5.1 Power efficiency

The statistics of a real-valued bipolar OFDM time-domain waveform can be approximated with a Gaussian distribution, $x(t) \sim \mathcal{N}(0, \sigma_x^2)$ when $N_{\text{FFT}} \geq 64$, where σ_x is the standard deviation of $x(t)$ [15]. The waveforms of ACO-OFDM and PAM-DMT follow a truncated Gaussian distribution [53]. Therefore, the statistics of these techniques are identical. Moreover, the statistics of their superposition forms are also identical. Unless otherwise specified, the following discussion is applicable to all the proposed superposition modulation techniques of this thesis ePAM-DMT, eACO-OFDM and ASE-DMT. The superposition modulation signal $x_{\text{SM}}(t)$ can be given as the summation of the individual unipolar OFDM-based waveforms, which is written as follows:

$$x_{\text{SM}}(t) = \sum_{d=1}^{D} x_d^{\text{SM}}(t), \tag{3.22}$$

where D is the total number of used depths. Each superimposed stream at depth d is scaled by a parameter $1/\gamma_d$ to allow for an arbitrary allocation of power, based on the associated spectral efficiency of that depth. The time-domain waveform at depth d

follows a truncated Gaussian distribution with a statistical mean given as follows:

$$\text{E}[x_d^{\text{SM}}(t)] = \frac{\phi(0)\sigma_x}{\gamma_d\sqrt{2^{d-1}}}, \tag{3.23}$$

where $\text{E}[\cdot]$ is a statistical expectation and $\phi(x)$ is the probability density function (PDF) of the standard Gaussian distribution. As a result, the average electrical power of $x_{\text{SM}}(t)$ is written as follows:

$$
\begin{aligned}
P_{\text{elec}}^{\text{avg}}(D,\underline{\gamma}) &= \text{E}\left[x_{\text{SM}}^2(t)\right] = \text{E}\left[\left(\sum_{d=1}^{D} x_d^{\text{SM}}(t)\right)^2\right] \\
&= \sum_{d=1}^{D} \text{E}\left[\left(x_d^{\text{SM}}(t)\right)^2\right] + \sum_{d_1=1}^{D}\sum_{\substack{d_2=1\\d_1\neq d_2}}^{D} \text{E}\left[\left(x_{d_1}^{\text{SM}}(t)\right)^2\right]\text{E}\left[\left(x_{d_2}^{\text{SM}}(t)\right)^2\right] \\
&= \sigma_x^2\left(\sum_{d=1}^{D}\frac{\gamma_d^{-2}}{2^d} + 2\phi^2(0)\sum_{d_1=1}^{D}\sum_{\substack{d_2=1\\d_1\neq d_2}}^{D}\frac{(\gamma_{d_1}\gamma_{d_2})^{-1}}{\sqrt{2^{d_1+d_2}}}\right).
\end{aligned}
\tag{3.24}
$$

Similarly, the average optical power of $x_{\text{T}}(t)$ is given as follows:

$$
\begin{aligned}
P_{\text{opt}}^{\text{avg}}(D,\underline{\gamma}) &= \text{E}\left[x_{\text{SM}}(t)\right] = \text{E}\left[\sum_{d=1}^{D} x_d^{\text{SM}}(t)\right] \\
&= \sum_{d=1}^{D} \text{E}\left[x_d^{\text{SM}}(t)\right] \\
&= \phi(0)\sigma_x\sum_{d=1}^{D}\frac{\gamma_d^{-1}}{\sqrt{2^{d-1}}},
\end{aligned}
\tag{3.25}
$$

where $\underline{\gamma} = \{\gamma_d^{-1}; d = 1, 2, \ldots, D\}$ is the set of scaling factors applied to each corresponding stream. The ratio of the average electrical power of superposition modulation waveform to the average electrical power of an inherently unipolar waveform is given as follows:

$$\alpha_{\text{elec}}^{P}(D,\underline{\gamma}) = \frac{P_{\text{elec}}^{\text{avg}}(D,\underline{\gamma})}{P_{\text{elec},d}^{\text{avg}}(\gamma_d)}, \tag{3.26}$$

where the average electrical power of an inherently unipolar waveform is given as follows:

$$P_{\text{elec},d}^{\text{avg}}(\gamma_d) = \frac{\sigma_x^2}{2\gamma_d^2}. \tag{3.27}$$

The electrical and optical SNR of superposition modulations can be defined as [26]:

$$\frac{E_{\text{b,elec}}^{\text{SM}}}{N_o} = \frac{P_{\text{elec}}^{\text{avg}}(D,\underline{\gamma})}{2B\eta_{\text{SM}}N_o} = \frac{\text{E}[x_{\text{SM}}{}^2(t)]}{2B\eta_{\text{SM}}N_o}, \tag{3.28}$$

$$\frac{E_{\text{b,opt}}^{\text{SM}}}{N_o} = \frac{P_{\text{opt}}^{\text{avg}}(D,\underline{\gamma})}{2B\eta_{\text{SM}}N_o} = \frac{\text{E}[x_{\text{SM}}(t)]}{2B\eta_{\text{SM}}N_o}, \tag{3.29}$$

where $E_{\text{b,elec}}^{\text{SM}}$ is the electrical energy per bit of superposition modulation; B is the single sided bandwidth; N_o is the single sided power spectral density (PSD) of the noise at the receiver; and η_{SM} is the spectral efficiency of the considered superposition modulation. For example, this can be replaced with the spectral efficiency of ePAM-DMT given in (3.2) to calculate the electrical and optical SNR for ePAM-DMT. The optical SNR for a given system configuration can be calculated from the electrical SNR using the ratio of the electrical average power given in (3.28) to the optical average power given in (3.29). This is written as follows:

$$\alpha^{\text{EO}} = \frac{P_{\text{elec}}^{\text{avg}}(D,\underline{\gamma})}{P_{\text{opt}}^{\text{avg}}(D,\underline{\gamma})}. \tag{3.30}$$

The increase in the dissipated electrical energy per bit in ePAM-DMT compared with the electrical energy dissipation per bit of a PAM-DMT stream at depth d is given by the ratio of (3.26) to (3.3):

$$\alpha_{\text{elec}}^{\text{ePAM}}(D,d,\underline{\gamma}) = \frac{\alpha_{\text{elec}}^{P}(D,\gamma)}{\alpha_{\eta}^{\text{ePAM}}(D,d)}. \tag{3.31}$$

Similar quantity can be calculated for eACO-OFDM and ASE-DMT by taking the ratio of (3.26) to (3.6) and (3.21), respectively. These is given as follows:

$$\alpha_{\text{elec}}^{\text{eACO}}(D,d,\underline{\gamma}) = \frac{\alpha_{\text{elec}}^{P}(D,\gamma)}{\alpha_{\eta}^{\text{eACO}}(D,d)}, \tag{3.32}$$

$$\alpha_{\text{elec}}^{\text{ASE}}(D,d,\underline{\gamma}) = \frac{\alpha_{\text{elec}}^{P}(D,\underline{\gamma})}{\alpha_{\eta}^{\text{ASE}}(D,d)}. \tag{3.33}$$

3.5.2 Theoretical BER analysis

The received superposition modulation signal is given as follows:

$$\mathbf{y} = \mathbf{Hx} + \mathbf{w}, \tag{3.34}$$

where $\mathbf{x}$ and $\mathbf{y}$ are the transmitted and received waveforms; $\mathbf{w} = \{w_i | i = 0, 1, \cdots, N_{\text{FFT}} - 1\}$ is the discrete AWGN samples, $w_i \sim \mathcal{N}(0, N_o)$, where N_o is the single-sided PSD of the noise at the receiver; and $\mathbf{H}$ is a $N_{\text{FFT}} \times N_{\text{FFT}}$ circulant convolution channel matrix with the first column representing the channel impulse response $\mathbf{h}_{1 \times N_{\text{FFT}}} = [h_0, h_1, \cdots, h_{L-1}, 0, \cdots, 0]^{\text{T}}$, where L is the number of channel taps. The channel matrix $\mathbf{H}$ can be diagonalized as follows:

$$\mathbf{H} = \mathbf{F}^* \mathbf{\Lambda} \mathbf{F}, \tag{3.35}$$

where $\mathbf{F}$ is the normalized discrete Fourier transform (DFT) matrix with size $N_{\text{FFT}} \times N_{\text{FFT}}$, and $\mathbf{\Lambda}$ is an $N_{\text{FFT}} \times N_{\text{FFT}}$ diagonal matrix with the eigenvalues of the channel $\mathbf{\Lambda} = [\Lambda_0, \Lambda_1, \cdots, \Lambda_{N_{\text{FFT}}}]^{\text{T}}$.

The theoretical BER performance of superposition modulation can be derived using the analytical BER performance of M-QAM real-valued bipolar OFDM [98]. The BER of real-valued bipolar OFDM in frequency selective channels[1] is given as follows:

$$\text{BER}_{\text{QAM}} \left(M, \frac{E_{\text{b,elec}}}{N_o} \right) \cong$$
$$\cong \frac{4}{\log_2(M)} \left(1 - \frac{1}{\sqrt{M}} \right) \times \sum_{l=1}^{2} \sum_{k=1}^{N_{\text{FFT}}} Q \left((2l-1) \sqrt{\frac{3|\Lambda_k|^2 E_{\text{b,elec}} \log_2(M)}{N_o(M-1)}} \right), \tag{3.36}$$

where $Q(\cdot)$ is the Q-function and $E_{\text{b,elec}}/N_o$ is the electrical SNR of real-valued bipolar OFDM, which can be given as [26, 114]:

$$\frac{E_{\text{b,elec}}}{N_o} = \frac{\sigma_x^2}{2B\eta N_o}, \tag{3.37}$$

where B is the single sided bandwidth and η is the spectral efficiency of the bipolar OFDM.

---

[1]The eigenvalues of the channel response in (3.36) are set to $\mathbf{\Lambda} = I_N$ for frequency flat channels.

The BER of ePAM-DMT at depth d can be calculated using (3.36) since the BER performance of M-PAM is equivalent to the BER performance of M^2-QAM. However, the SNR should be scaled by $1/2$ to compensate for the energy loss caused by the zero-level clipping. This is consistent with the 3 dB loss of the BER performance of PAM-DMT that was shown in Section 2.6.2.3. In addition, the SNR should also be scaled by the energy loss per bit incurred by the ePAM-DMT given in (3.31). An additional scaling factor of $1/2^{d-1}$ is required since half of the frames are removed in the demodulation process at each depth. The theoretical bound on the BER performance of ePAM-DMT at depth d can be then expressed as follows:

$$
\begin{aligned}
\mathrm{BER}_{\mathrm{ePAM}}\left(M_{\mathrm{ePAM},d}, \frac{E_{\mathrm{b,elec}}^{\mathrm{ePAM}}}{N_o}\right) &\triangleq \mathrm{BER}_{\mathrm{QAM}}\left(M_{\mathrm{ePAM},d}^2, \frac{E_{\mathrm{b,elec}}}{2^d \alpha_{\mathrm{elec}}^{\mathrm{ePAM}}(D,d,\underline{\gamma})N_o}\right), \\
&\cong \frac{2}{\log_2(M_{\mathrm{ePAM},d})}\left(1 - \frac{1}{M_{\mathrm{ePAM},d}}\right) \times \\
&\sum_{l=1}^{2}\sum_{k=1}^{N_{\mathrm{FFT}}} \mathrm{Q}\left((2l-1)\sqrt{\frac{6|\Lambda_k|^2 E_{\mathrm{b,elec}}/N_o \log_2(M_{\mathrm{ePAM},d})}{2^d \alpha_{\mathrm{elec}}^{\mathrm{ePAM}}(D,d,\underline{\gamma})(M_{\mathrm{ePAM},d}^2 - 1)}}\right),
\end{aligned}
\tag{3.38}
$$

Similarly, the achieved electrical SNR for eACO-OFDM should be scaled by a factor of $1/2$ to account for the SNR loss in ACO-OFDM as was shown in Section 2.6.2.2, and by the dissipated electrical energy per bit $1/\alpha_{\mathrm{elec}}^{\mathrm{eACO}}(D,d,\underline{\gamma})$. The BER performance at depth d of eACO-OFDM can be then approximated as [26]:

$$
\begin{aligned}
\mathrm{BER}_{\mathrm{eACO}}\left(M_{\mathrm{eACO},d}, \frac{E_{\mathrm{b,elec}}^{\mathrm{eACO}}}{N_o}\right) &\triangleq \mathrm{BER}_{\mathrm{QAM}}\left(M_{\mathrm{eACO},d}, \frac{E_{\mathrm{b,elec}}}{2\alpha_{\mathrm{elec}}^{\mathrm{eACO}}(D,d,\underline{\gamma})N_o}\right), \\
&\cong \frac{4}{\log_2(M_{\mathrm{eACO},d})}\left(1 - \frac{1}{\sqrt{M_{\mathrm{eACO},d}}}\right) \times \\
&\sum_{l=1}^{2}\sum_{k=1}^{N_{\mathrm{FFT}}} \mathrm{Q}\left((2l-1)\sqrt{\frac{3|\Lambda_k|^2 E_{\mathrm{b,elec}} \log_2(M_{\mathrm{eACO},d})}{2\alpha_{\mathrm{elec}}^{\mathrm{eACO}}(D,d)(M_{\mathrm{eACO},d} - 1)N_o}}\right),
\end{aligned}
\tag{3.39}
$$

In a similar fashion, the BER bound on the performance of ASE-DMT at depth d is given as follows:

$$
\mathrm{BER}_{\mathrm{ASE}}\left(M_{\mathrm{ASE},d}, \frac{E_{\mathrm{b,elec}}^{\mathrm{ASE}}}{N_o}\right) \triangleq \mathrm{BER}_{\mathrm{QAM}}\left(M_{\mathrm{ASE},d}^2, \frac{E_{\mathrm{b,elec}}}{2\alpha_{\mathrm{elec}}^{\mathrm{ASE}}(D,d,\underline{\gamma})N_o}\right).
\tag{3.40}
$$

The improved design of ASE-DMT allows for an improved BER performance. In con-
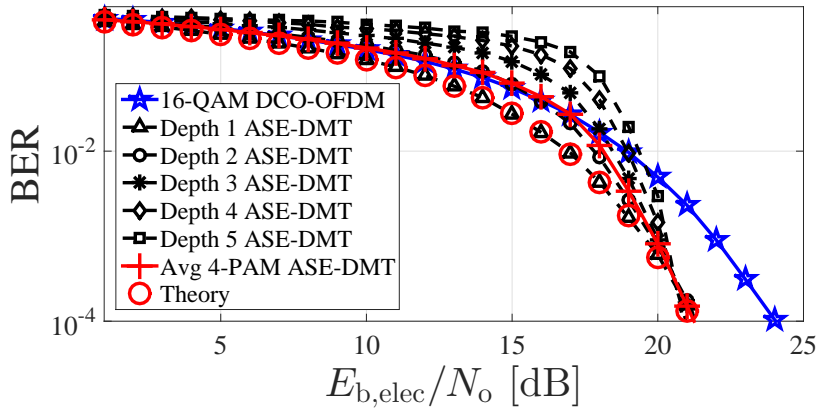
Figure 3.8: *The BER performance of 16-QAM ASE-DMT depths with a total number of depths $D = 5$. The BER of DCO-OFDM is only shown for comparison purposes.*

trast to ePAM-DMT, all of the received frame energy can be considered fully without any loss in the case of ASE-DMT.

The BER at each depth is weighted by the contribution of the same depth to the overall spectral efficiency. The average BER performance of all modulation depths in a superposition modulation as a function of the electrical SNR can then be expressed as follows:

$$\text{ABER}_{\text{SM}}^{\text{elec}}\left(\underline{M}_{\text{SM}}, \underline{\gamma}\right) \cong \sum_{d=1}^{D} \left(\frac{\text{BER}_{\text{SM}}\left(M_{\text{SM},d}, \frac{P_{\text{elec}}^{\text{avg}}(D,\gamma)}{2B\eta_{\text{SM}}N_o}\right)}{\alpha_{\eta}^{\text{SM}}(D,d)} \right), \tag{3.41}$$

where $\underline{M}_{\text{SM}} = [M_{\text{SM},1}, M_{\text{SM},2}, \cdots, M_{\text{SM},D}]$ is the vector of the constellation sizes used at the modulation depths, $\alpha_{\eta}^{\text{SM}}(D,d)$ is the spectral efficiency contribution at depth d to the overall spectral efficiency of the considered superposition modulation and $\text{BER}_{\text{SM}}(M_{\text{SM},d}, E_{\text{b,elec}}^{\text{SM}}/N_o)$ is the BER at depth d of the considered superposition modulation. The spectral efficiency ratio of depth d to the overall spectral efficiency can be given in (3.3) for ePAM-DMT, (3.6) for eACO-OFDM and (3.21) for ASE-DMT. The BER of depth d can be given in (3.38) for ePAM-DMT, (3.39) for eACO-OFDM and (3.40) for ASE-DMT. An equivalent bound for the BER performance as a function of the optical SNR can be established for all the proposed superposition modulation techniques by scaling the electrical SNR, $E_{\text{b,elec}}/N_o$ in (3.36), with the ratio of electrical average power to the optical average power given in (3.30).

The BER performance at higher depths is affected by the BER performance of the lower depths. Any incorrectly decoded bit at lower order depths results in more distortion

at all subsequent streams. The presented solution does not include the effects of the distortion caused by the incorrectly decoded bits at preceding streams, which underestimate the BER at low SNR values. However, the error propagation effect is assumed to be insignificant at high SNR values due to the low BER expected at each stream. This issue is investigated for ASE-DMT in Fig. 3.8. The analytical performance bound matches the BER performance of the first depth of ASE-DMT. The BER performance of other depths is shown to be affected by the wrongly decoded bits at the lower order depths. However, the BER performance of all depths converges to match with the analytical BER performance at high SNR as predicted. The BER performance of 4-PAM ASE-DMT is more efficient with a 3 dB gain in comparison with 16-QAM DCO-OFDM in terms of the electrical energy efficiency, as shown in Fig. 3.8. The spectral efficiency ratio of ASE-DMT to the spectral efficiency of DCO-OFDM is 97% in this example.

3.6 Superposition modulation with arbitrary constellation sizes

Implementation issues put a practical limit on the maximum number of depths that can be used with the proposed techniques. In addition, the energy per bit increases as the total number of modulation depths increases because each additional stream is added on top of an existing time domain signal. Considering that the spectral efficiency of each additional stream decreases exponentially, it can be assumed that the practical implementation of the proposed techniques is expected to be realized using only a few information streams.

Arbitrary constellation sizes are proposed to close the spectral efficiency gap between superposition modulation and DCO-OFDM with a maximum number of modulation depths $D = 3$. Moreover, the spectral efficiency achieved by non-squared constellation sizes in DCO-OFDM cannot be achieved with the constant loading of modulation depths in ePAM-DMT and ASE-DMT, as was shown in Section 3.2 and Section 3.4, respectively. The solution of arbitrary constellation sizes allows ePAM-DMT and ASE-DMT to achieve any desired spectral efficiency value. For example, to achieve the spectral efficiency of 8-QAM DCO-OFDM, it would be possible to use 4-PAM at the first depth, 2-PAM at the second depth and 4-PAM at the third depth of ASE-DMT. Different

power allocations are required at the different modulation depths when the arbitrary constellation sizes solution is adopted. The power allocation to each modulation stream is selected to maintain an equivalent energy per bit based on the used constellation size at each modulation depth $M_{\text{SM},d}$. Arbitrary constellation sizes offer a practical solution for superposition modulation without any spectral efficiency loss. For example, the computation complexity per bit of ASE-DMT with three modulation depths is around 1.67 times higher than the computation complexity per bit of DCO-OFDM. A detailed analysis of the computation complexity is given in Section 3.7.4.

The set $\mathcal{M}^{\text{can.}}_{(\varsigma,D)} = \{\underline{M}^{\text{can.}}_{(\eta,\varsigma,D)} \,|\, \forall \frac{\varsigma}{2} \leq \eta \leq 5\}$ of all possible candidates of constellation sizes $\underline{M}^{\text{can.}}_{(\eta,\varsigma,D)} = [M^{\text{can.}}_{\text{SM},1}, M^{\text{can.}}_{\text{SM},2}, \cdots, M^{\text{can.}}_{\text{SM},D}]_\eta$ that can achieve a spectral efficiency target η is obtained by an exhaustive search algorithm. The set $\mathcal{M}^{\text{can.}}_{(\varsigma,D)}$ is obtained for each of the proposed superposition modulation techniques, where ς is a variable that is set to $\varsigma = 1$ for eACO-OFDM and $\varsigma = 2$ for ePAM-DMT and ASE-DMT. The exhaustive search algorithm for $\mathcal{M}^{\text{can.}}_{(\varsigma,D)}$ is presented in Algorithm 1 for $D = 3$.

Two cases are investigated based on the total number of superimposed modulation depths D. The target spectral efficiency is proposed to be achieved with a maximum of $D = 2$ in the first solution or with a maximum of $D = 3$ in the second solution. The spectral efficiency targets are set in the range $0.5 \leq \eta \leq 5$ bits/s/Hz for eACO-OFDM and in the range from $1 \leq \eta \leq 5$ bits/s/Hz for ePAM-DMT and ASE-DMT. The spectral efficiency at $\eta = 0.5$ bits/s/Hz cannot be achieved in superposition modulation techniques based on M-PAM for $D > 1$ since there is no equivalent BER performance to M-QAM when $M = 2$. In order for the spectral efficiency of the proposed superposition modulation techniques to match the spectral efficiency of DCO-OFDM with a maximum number of depths D, the combination of constellation sizes at the different modulation depths should satisfy the following constraint:

$$\sum_{d=1}^{D} \frac{\log_2(M^{\text{can.}}_{\text{SM},d})}{2^d} = \frac{2\eta}{\varsigma}, \tag{3.42}$$

Where the spectral efficiency target is defined as $\eta = \log_2(M_{\text{DCO}})/2$. The set of possible candidates of constellation sizes should satisfy the constraint given in (3.42) and the

---

Algorithm 1: Exhaustive search algorithm for all the possible sets of constellation sizes $\mathcal{M}^{\text{can.}}_{(\varsigma,3)}$ that achieve the spectral efficiency values $\frac{\varsigma}{2} \leq \eta \leq 5$ with a total number of superimposed depths $D = 3$.

    Input : The number of superimposed depths $D = 3$ and the spectral efficiency variable ς

    Output: Set of possible candidates of constellation sizes $\mathcal{M}^{\text{can.}}_{(\varsigma,D)}$
         $= \{\underline{M}^{\text{can.}}_{(\eta,\varsigma,D)} \,|\, \forall \frac{\varsigma}{2} \leq \eta \leq 5\}$, for all candidates $\underline{M}^{\text{can.}}_{(\eta,\varsigma,D)}$ that satisfy (3.42), (3.43) and (3.44), with $D = 3$

1 **for** $\eta \leftarrow \frac{\varsigma}{2}$ **to** 5 **do**
2   **for** $\eta_1 \leftarrow 1$ **to** $\frac{4\eta}{\varsigma} - 1$ **do**
3   **for** $\eta_2 \leftarrow 1$ **to** $\frac{4\eta}{\varsigma}$ **do**
4   **for** $\eta_3 \leftarrow 1$ **to** $\frac{4\eta}{\varsigma}$ **do**
5 $\underline{M}^{\text{temp}}_{\text{SM},\eta} \leftarrow [2^{\eta_1}, 2^{\eta_2}, 2^{\eta_3}]$;
6   **if** $\underline{M}^{\text{temp}}_{\text{SM},\eta}$ *satisfy* (3.42), (3.43) **and** (3.44) **then**
7 $\underline{M}^{\text{can.}}_{(\eta,\varsigma,D)} \leftarrow \underline{M}^{\text{temp}}_{\text{SM},\eta}$;
8   Add $\underline{M}^{\text{can.}}_{(\eta,\varsigma,D)}$ to the set $\mathcal{M}^{\text{can.}}_{(\varsigma,D)}$;
9 $\eta_3 \leftarrow \eta_3 + 1$;
10 $\eta_2 \leftarrow \eta_2 + 1$;
11 $\eta_1 \leftarrow \eta_1 + 1$;
12 $\eta \leftarrow \eta + 0.5$;
13 Return $\mathcal{M}^{\text{can.}}_{(\varsigma,D)}$;

---

following additional constraints:

$$\log_2(M^{\text{can.}}_{\text{SM},d}) \leq \frac{\log_2 M^{\text{Max}}_{\text{SM},\eta}}{\varsigma} \quad \forall d > 1. \tag{3.43}$$

$$\log_2(M^{\text{can.}}_{\text{SM},1}) < \frac{4\eta}{\varsigma}, \tag{3.44}$$

where $M^{\text{Max}}_{\text{SM},\eta}$ is the maximum permitted constellation size at a spectral efficiency target η for the considered superposition modulation. For example, the constellation sizes above 4096-QAM and 64-PAM are relatively difficult to be realized. Therefore, the candidates of constellation sizes are constrained in (3.43) to a maximum permitted constellation size. The maximum permitted constellation size at all the considered spectral efficiency targets are given in Appendix B.

ACO-OFDM and PAM-DMT can be achieved as a special case of the proposed superposition modulation techniques when $D = 1$. The constraint in (3.44) is imposed to guarantee that the spectral efficiency of the proposed superposition modulation cannot

match the spectral efficiency of DCO-OFDM with one depth. This avoids the special case of $D = 1$ and restricts the generalized solution to superimposed modulation with $D > 1$. The sets of candidates of constellation sizes that satisfy theses constraints are provided in Appendix B for $D = 2$ and $D = 3$. The results for ePAM-DMT are presented in Table B.2, Table B.3 and Table B.4. The results for ASE-DMT are presented in Table B.5 and Table B.6. The results for eACO-OFDM are presented in Table B.7, Table. B.8, Table B.9, Table. B.10 and Table B.11.

The set $\mathcal{G}^{\text{can.}}_{(\varsigma,D)} = \{\underline{\gamma}^{\text{can.}}_{(\eta,\varsigma,D)} \mid \forall \frac{\varsigma}{2} \leq \eta \leq 5\}$ of optimal power scaling factors $\underline{\gamma}^{\text{can.}}_{(\eta,\varsigma,D)} = [\gamma^{\text{can.}}_{\text{SM},1}, \gamma^{\text{can.}}_{\text{SM},2}, \cdots, \gamma^{\text{can.}}_{\text{SM},D}]_\eta$ is obtained for each of the possible candidates $\underline{M}^{\text{can.}}_{(\eta,\varsigma,D)} \in \mathcal{M}^{\text{can.}}_{(\varsigma,D)}$ by exhaustive search for each of the proposed superposition modulation techniques as detailed in Algorithm 2 and Algorithm 3, for $D = 3$.

Power allocations are investigated for each of the possible candidates of constellation sizes $\underline{M}^{\text{can.}}_{(\eta,\varsigma,D)} \in \mathcal{M}^{\text{can.}}_{(\varsigma,D)} \forall \frac{\varsigma}{2} \leq \eta \leq 5$ using both coarse and fine exhaustive searches. The objective of the coarse search is to determine the scaling factors ranges $\underline{\gamma}^{\text{min,dB}}_{(\eta,\varsigma,D)} = [\gamma^{\text{dB}}_{\text{min},1}, \gamma^{\text{dB}}_{\text{min},2}, \cdots, \gamma^{\text{dB}}_{\text{min},D}]$ and $\underline{\gamma}^{\text{max,dB}}_{(\eta,\varsigma,D)} = [\gamma^{\text{dB}}_{\text{max},1}, \gamma^{\text{dB}}_{\text{max},2}, \cdots, \gamma^{\text{dB}}_{\text{max},D}]$ with a resolution of 1 dB between -30 dB and $+30$ dB at each of the associated candidates of constellation sizes, as shown in Algorithm 2. This range is wide enough to allow the optimal scaling factors to be obtained. The fine search determines the optimal values of the scaling factors $\underline{\gamma}^{\text{can.}}_{(\eta,\varsigma,D)}$ at each of the associated candidates of constellation sizes $\underline{M}^{\text{can.}}_{(\eta,\varsigma,D)} \in \mathcal{M}^{\text{can.}}_{(\varsigma,D)} \forall \frac{\varsigma}{2} \leq \eta \leq 5$ within the range that was determined in the coarse search $\underline{\gamma}^{\text{min,dB}}_{(\eta,\varsigma,D)}$ and $\underline{\gamma}^{\text{max,dB}}_{(\eta,\varsigma,D)}$ with a 0.1 dB resolution, as shown in Algorithm 3 for $D = 3$. The optimal scaling factors are determined by finding the sets of scaling factors that achieve the minimum average BER. This is achieved by comparing the average BER of the proposed superposition modulation technique at all of the possible configurations subject to the following constraints:

$$\text{ABER}^{\text{opt}}_{\text{SM}}\left(\underline{M}^{\text{can.}}_{(\eta,\varsigma,D)}, \underline{\gamma}^{\text{can.}}_{(\eta,\varsigma,D)}\right) \leq \text{ABER}^{\text{opt}}_{\text{SM}}\left(\underline{M}^{\text{can.}}_{(\eta,\varsigma,D)}, \mathbf{1}_{1 \times D}\right),$$
$$\text{ABER}^{\text{elec}}_{\text{SM}}\left(\underline{M}^{\text{can.}}_{(\eta,\varsigma,D)}, \underline{\gamma}^{\text{can.}}_{(\eta,\varsigma,D)}\right) \leq \text{ABER}^{\text{elec}}_{\text{SM}}\left(\underline{M}^{\text{can.}}_{(\eta,\varsigma,D)}, \mathbf{1}_{1 \times D}\right). \tag{3.45}$$

In addition, the power allocated to each stream is selected so that the average power of
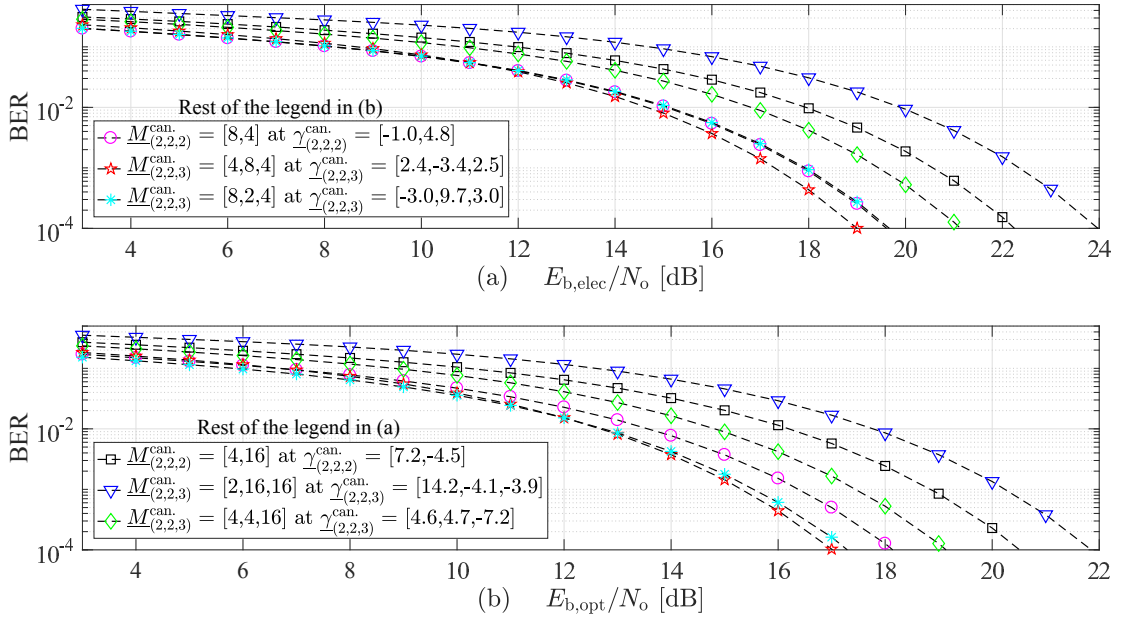
Figure 3.9: *The BER performance as function of all possible candidates of constellation sizes at the optimal scaling factors which can achieve a spectral efficiency target ($\eta = 2$ bits/s/Hz) with $D = 2$ and $D = 3$ in ASE-DMT. Note that the legend is shared between (a) electrical SNR and (b) optical SNR.*

the modulation signal satisfies the following two constraints:

$$P_{\text{elec}}^{\text{avg}}(D, \underline{\gamma}_{(\eta,\varsigma,D)}^{\text{can.}}) \leq P_{\text{elec}}^{\text{avg}}(D, \mathbf{1}_{1 \times D}),$$

$$P_{\text{opt}}^{\text{avg}}(D, \underline{\gamma}_{(\eta,\varsigma,D)}^{\text{can.}}) \leq P_{\text{opt}}^{\text{avg}}(D, \mathbf{1}_{1 \times D}). \tag{3.46}$$

The sets of optimal scaling factors at each of the candidates of constellation sizes are provided in Appendix B for $D = 2$ and $D = 3$ for the proposed superposition modulation techniques.

The optimal configurations $\mathcal{M}_D^{\text{SM}}$ and $\mathcal{G}_D^{\text{SM}}$ are obtained by comparing the BER performance of all possible candidates in the set $\mathcal{M}_{(\varsigma,D)}^{\text{can.}}$ at the associated set of optimal power scaling factors $\mathcal{G}_{(\varsigma,D)}^{\text{can.}}$ for $D = 2$ and $D = 3$, where $\mathcal{M}_D^{\text{SM}} \subset \mathcal{M}_{(\varsigma,D)}^{\text{can.}}$ and $\mathcal{G}_D^{\text{SM}} \subset \mathcal{G}_{(\varsigma,D)}^{\text{can.}}$. The BER performance comparisons are all performed at a BER level of 10^{-4} since most of the forward error correction (FEC) codes would be able to maintain a reliable communication link at such BER values [115]. The BER performance comparison of all the possible candidates of constellation sizes at $\eta = 2$ bits/s/Hz in

---

Algorithm 2: Exhaustive search algorithm for the scaling factors ranges $\underline{\gamma}_{(\eta,\varsigma,D)}^{\min,\mathrm{dB}}$ and $\underline{\gamma}_{(\eta,\varsigma,D)}^{\max,\mathrm{dB}}$ for each candidate of the set constellation sizes $\mathcal{M}_{(\varsigma,D)}^{\mathrm{can.}}$ that was obtained in Algorithm 1.

    Input : The number of superimposed depths $D = 3$, spectral efficiency variable ς and the set of possible candidates of constellation $\mathcal{M}_{(\varsigma,D)}^{\mathrm{can.}}$ sizes that was obtained in Algorithm 1

    Output: The scaling factors ranges $\underline{\gamma}_{(\eta,\varsigma,D)}^{\min,\mathrm{dB}} = [\gamma_{\min,1}^{\mathrm{dB}}, \gamma_{\min,2}^{\mathrm{dB}}, \cdots, \gamma_{\min,D}^{\mathrm{dB}}]$ and $\underline{\gamma}_{(\eta,\varsigma,D)}^{\max,\mathrm{dB}} = [\gamma_{\max,1}^{\mathrm{dB}}, \gamma_{\max,2}^{\mathrm{dB}}, \cdots, \gamma_{\max,D}^{\mathrm{dB}}]$ at each of the associated candidates of constellation sizes $\underline{M}_{(\eta,\varsigma,D)}^{\mathrm{can.}} \in \mathcal{M}_{(\varsigma,D)}^{\mathrm{can.}} \ \forall \ \frac{\varsigma}{2} \leq \eta \leq 5$

---

1 Initialize;

2 $\gamma_{\mathrm{res}}^{\mathrm{dB}} \leftarrow 1 \ \mathrm{dB}$;

3 $\gamma_{\min,d}^{\mathrm{dB}} \leftarrow -30 \ \mathrm{dB} \ | \forall \, 1 \leq d \leq D$;

4 $\gamma_{\max,d}^{\mathrm{dB}} \leftarrow +30 \ \mathrm{dB} \ | \forall \, 1 \leq d \leq D$;

5 for $\eta \leftarrow \frac{\varsigma}{2}$ **to** 5 **do**

6   **for** *each* $\underline{M}_{(\eta,\varsigma,D)}^{\mathrm{can.}} \in \mathcal{M}_{(\varsigma,D)}^{\mathrm{can.}}$ **do**

7   Calculate $P_{\mathrm{elec}}^{\mathrm{avg}}(D, \mathbf{1}_{1\times D})$ using (3.24) ;

8   Calculate $P_{\mathrm{opt}}^{\mathrm{avg}}(D, \mathbf{1}_{1\times D})$ using (3.25) ;

9   **for** $\gamma_1^{\mathrm{dB}} \leftarrow \gamma_{\min,1}^{\mathrm{dB}}$ **to** $\gamma_{\max,1}^{\mathrm{dB}}$ **do**

10   **for** $\gamma_2^{\mathrm{dB}} \leftarrow \gamma_{\min,2}^{\mathrm{dB}}$ **to** $\gamma_{\max,2}^{\mathrm{dB}}$ **do**

11   **for** $\gamma_3^{\mathrm{dB}} \leftarrow \gamma_{\min,3}^{\mathrm{dB}}$ **to** $\gamma_{\max,3}^{\mathrm{dB}}$ **do**

12 $\underline{\gamma}^{\mathrm{temp}} \leftarrow [10^{\gamma_1^{\mathrm{dB}}/20}, 10^{\gamma_2^{\mathrm{dB}}/20}, 10^{\gamma_3^{\mathrm{dB}}/20}]$;

13   Calculate $P_{\mathrm{elec}}^{\mathrm{avg}}(D, \underline{\gamma}^{\mathrm{temp}})$ using (3.24) ;

14   Calculate $P_{\mathrm{opt}}^{\mathrm{avg}}(D, \underline{\gamma}^{\mathrm{temp}})$ using (3.25) ;

15   **if** $P_{\mathrm{elec}}^{\mathrm{avg}}(D, \underline{\gamma}^{\mathrm{temp}})$ **and** $P_{\mathrm{opt}}^{\mathrm{avg}}(D, \underline{\gamma}^{\mathrm{temp}})$ *satisfy* (3.46) **then**

16   Calculate $\mathrm{ABER}_{\mathrm{SM}}^{\mathrm{elec}}\left(\underline{M}_{(\eta,\varsigma,D)}^{\mathrm{can.}}, \underline{\gamma}^{\mathrm{temp}}\right)$ using (3.41) ;

17   Calculate $\mathrm{ABER}_{\mathrm{SM}}^{\mathrm{opt}}\left(\underline{M}_{(\eta,\varsigma,D)}^{\mathrm{can.}}, \underline{\gamma}^{\mathrm{temp}}\right)$ using (3.41) ;

18   **if** $\mathrm{ABER}_{\mathrm{SM}}^{\mathrm{elec}}\left(\underline{M}_{(\eta,\varsigma,D)}^{\mathrm{can.}}, \underline{\gamma}^{\mathrm{temp}}\right)$ *satisfy* (3.45) **then**

19   **if** $\mathrm{ABER}_{\mathrm{SM}}^{\mathrm{opt}}\left(\underline{M}_{(\eta,\varsigma,D)}^{\mathrm{can.}}, \underline{\gamma}^{\mathrm{temp}}\right)$ *satisfy* (3.45) **then**

20   Add $20 \log_{10} \gamma_1^{\mathrm{temp}}$ to set $\mathcal{S}_1$;

21   Add $20 \log_{10} \gamma_2^{\mathrm{temp}}$ to set $\mathcal{S}_2$;

22   Add $20 \log_{10} \gamma_3^{\mathrm{temp}}$ to set $\mathcal{S}_3$;

23 $\gamma_3^{\mathrm{dB}} \leftarrow \gamma_3^{\mathrm{dB}} + \gamma_{\mathrm{res}}^{\mathrm{dB}}$;

24 $\gamma_2^{\mathrm{dB}} \leftarrow \gamma_2^{\mathrm{dB}} + \gamma_{\mathrm{res}}^{\mathrm{dB}}$;

25 $\gamma_1^{\mathrm{dB}} \leftarrow \gamma_1^{\mathrm{dB}} + \gamma_{\mathrm{res}}^{\mathrm{dB}}$;

26 $\underline{\gamma}_{(\eta,\varsigma,D)}^{\min,\mathrm{dB}} \leftarrow [\min(\mathcal{S}_1), \min(\mathcal{S}_2), \min(\mathcal{S}_3)]$;

27 $\underline{\gamma}_{(\eta,\varsigma,D)}^{\max,\mathrm{dB}} \leftarrow [\max(\mathcal{S}_1), \max(\mathcal{S}_2), \max(\mathcal{S}_3)]$;

28   Return $\underline{\gamma}_{(\eta,\varsigma,D)}^{\min,\mathrm{dB}}$ **and** $\underline{\gamma}_{(\eta,\varsigma,D)}^{\max,\mathrm{dB}}$ for each $\underline{M}_{(\eta,\varsigma,D)}^{\mathrm{can.}} \in \mathcal{M}_{(\varsigma,D)}^{\mathrm{can.}}$

Algorithm 3: Exhaustive search algorithm for the optimal scaling factors $\underline{\gamma}_{(\eta,\varsigma,D)}^{\text{can.}}$ at each candidate of the set constellation sizes $\mathcal{M}_{(\varsigma,D)}^{\text{can.}}$ that was obtained in Algorithm 1.

Input : The number of superimposed depths $D = 3$, spectral efficiency variable ς, the set of possible candidates of constellation $\mathcal{M}_{(\varsigma,D)}^{\text{can.}}$ sizes that was obtained in Algorithm 1 and the scaling factors ranges $\underline{\gamma}_{(\eta,\varsigma,D)}^{\text{min,dB}}$ and $\underline{\gamma}_{(\eta,\varsigma,D)}^{\text{max,dB}}$ that were obtained in Algorithm 2

Output: The optimal scaling factors $\underline{\gamma}_{(\eta,\varsigma,D)}^{\text{can.}}$ at each of the associated candidates of constellation sizes $\underline{M}_{(\eta,\varsigma,D)}^{\text{can.}} \in \mathcal{M}_{(\varsigma,D)}^{\text{can.}} \ \forall \ \frac{\varsigma}{2} \leq \eta \leq 5$

---

1 **Initialize**;

2 $\gamma_{\text{res}}^{\text{dB}} \leftarrow 0.1$ dB;

3 $\text{ABER}_{\text{opt}}^{\text{Least}} \leftarrow 1$;

4 $\text{ABER}_{\text{elec}}^{\text{Least}} \leftarrow 1$;

5 **for** $\eta \leftarrow \frac{\varsigma}{2}$ **to** 5 **do**

6   **for** *each* $\underline{M}_{(\eta,\varsigma,D)}^{\text{can.}} \in \mathcal{M}_{(\varsigma,D)}^{\text{can.}}$ **do**

7   Calculate $P_{\text{elec}}^{\text{avg}}(D, \mathbf{1}_{1 \times D})$ using (3.24) ;

8   Calculate $P_{\text{opt}}^{\text{avg}}(D, \mathbf{1}_{1 \times D})$ using (3.25) ;

9   **for** $\gamma_1^{\text{dB}} \leftarrow \gamma_{\text{min},1}^{\text{dB}}$ **to** $\gamma_{\text{max},1}^{\text{dB}}$ **do**

10   **for** $\gamma_2^{\text{dB}} \leftarrow \gamma_{\text{min},2}^{\text{dB}}$ **to** $\gamma_{\text{max},2}^{\text{dB}}$ **do**

11   **for** $\gamma_3^{\text{dB}} \leftarrow \gamma_{\text{min},3}^{\text{dB}}$ **to** $\gamma_{\text{max},3}^{\text{dB}}$ **do**

12 $\underline{\gamma}^{\text{temp}} \leftarrow [10^{\gamma_1^{\text{dB}}/20}, 10^{\gamma_2^{\text{dB}}/20}, 10^{\gamma_3^{\text{dB}}/20}]$;

13   Calculate $P_{\text{elec}}^{\text{avg}}(D, \underline{\gamma}^{\text{temp}})$ using (3.24) ;

14   Calculate $P_{\text{opt}}^{\text{avg}}(D, \underline{\gamma}^{\text{temp}})$ using (3.25) ;

15   **if** $P_{\text{elec}}^{\text{avg}}(D, \underline{\gamma}^{\text{temp}})$ **and** $P_{\text{opt}}^{\text{avg}}(D, \underline{\gamma}^{\text{temp}})$ *satisfy* (3.46) **then**

16   Calculate $\text{ABER}_{\text{SM}}^{\text{elec}}\left(\underline{M}_{(\eta,\varsigma,D)}^{\text{can.}}, \underline{\gamma}^{\text{temp}}\right)$ using (3.41) ;

17   Calculate $\text{ABER}_{\text{SM}}^{\text{opt}}\left(\underline{M}_{(\eta,\varsigma,D)}^{\text{can.}}, \underline{\gamma}^{\text{temp}}\right)$ using (3.41) ;

18   **if** $\text{ABER}_{\text{SM}}^{\text{elec}}\left(\underline{M}_{(\eta,\varsigma,D)}^{\text{can.}}, \underline{\gamma}^{\text{temp}}\right) < \text{ABER}_{\text{elec}}^{\text{Least}}$ **then**

19   **if** $\text{ABER}_{\text{SM}}^{\text{opt}}\left(\underline{M}_{(\eta,\varsigma,D)}^{\text{can.}}, \underline{\gamma}^{\text{temp}}\right) < \text{ABER}_{\text{opt}}^{\text{Least}}$ **then**

20 $\text{ABER}_{\text{elec}}^{\text{Least}} \leftarrow \text{ABER}_{\text{SM}}^{\text{elec}}\left(\underline{M}_{(\eta,\varsigma,D)}^{\text{can.}}, \underline{\gamma}^{\text{temp}}\right)$;

21 $\text{ABER}_{\text{opt}}^{\text{Least}} \leftarrow \text{ABER}_{\text{SM}}^{\text{opt}}\left(\underline{M}_{(\eta,\varsigma,D)}^{\text{can.}}, \underline{\gamma}^{\text{temp}}\right)$;

22 $\underline{\gamma}_{(\eta,\varsigma,D)}^{\text{can.}} \leftarrow \underline{\gamma}^{\text{temp}}$;

23 $\gamma_3^{\text{dB}} \leftarrow \gamma_3^{\text{dB}} + \gamma_{\text{res}}^{\text{dB}}$;

24 $\gamma_2^{\text{dB}} \leftarrow \gamma_2^{\text{dB}} + \gamma_{\text{res}}^{\text{dB}}$;

25 $\gamma_1^{\text{dB}} \leftarrow \gamma_1^{\text{dB}} + \gamma_{\text{res}}^{\text{dB}}$;

26   Return $\underline{\gamma}_{(\eta,\varsigma,D)}^{\text{can.}}$ for each $\underline{M}_{(\eta,\varsigma,D)}^{\text{can.}} \in \mathcal{M}_{(\varsigma,D)}^{\text{can.}}$

ASE-DMT $\underline{M}^{\text{can.}}_{(2,2,2)}$ is presented in Fig. 3.9 (a and b) for $D = 2$ and $D = 3$ as a function of the electrical and optical SNR, respectively. The optimal scaling factors are given as $\underline{\gamma}^{\text{can.,dB}}_{(\eta,\varsigma,D)} = 20 \log_{10} \underline{\gamma}^{\text{can.}}_{(\eta,\varsigma,D)}$. The set $\mathcal{M}^{\text{SM}}_D = \{\underline{M}^{\text{SM}}_{(\eta,D)} | \forall \frac{\varsigma}{2} \leq \eta \leq 5\}$ of optimal constellation sizes $\underline{M}^{\text{SM}}_{(\eta,D)} = [M_{\text{SM},1}, M_{\text{SM},2}, \cdots, M_{\text{SM},D}]_\eta$ and their associated optimal power scaling factors $\underline{\gamma}^{\text{SM}}_{(\eta,D)} = [\gamma_{\text{SM},1}, \gamma_{\text{SM},2}, \cdots, \gamma_{\text{SM},D}]_\eta$ are presented in Table 3.2 for ePAM-DMT, Table 3.3 for eACO-OFDM and Table 3.6 for ASE-DMT.

3.7 Results and discussions

The BER performance of all the proposed modulation techniques is compared with DCO-OFDM at the same spectral efficiency. The simulation results for the superposition modulation techniques are presented in a frequency flat AWGN channel because the proposed schemes are multicarrier techniques in the same way the benchmark technique against which they are compared, DCO-OFDM, is a multicarrier technique. The individual subcarriers between the OFDM-based techniques are subjected to the same attenuation when they are used in the same communication channel. As a result, the SNR penalty due to the channel in these techniques is the same. The results for a frequency selective channel are only valid for the specific channel conditions, which are specific to the communication scenario as described in Section 2.5. However, an investigation of ASE-DMT in a multipath frequency selective VLC channel with a zero-forcing equalizer is presented in Section 3.7.3 to prove this argument.

3.7.1 Simulation results of ePAM-DMT

There are many combinations of constellation sizes that can be used to achieve a specific spectral efficiency value. The performance of all the possible combinations of constellation sizes to achieve spectral efficiency values between 1 and 5 bits/s/Hz and their corresponding scaling factors for ePAM-DMT are investigated using the theoretical model and Monte Carlo simulations. The combinations that achieve the best BER performance are presented in Table 3.2. The performance of the optimum configurations in ePAM-DMT are compared with the performance of a spectrum equivalent DCO-OFDM in an AWGN channel with nonlinear clipping at zero level. The DCO-OFDM bias level for the different M-QAM constellation orders is selected using Monte Carlo simulations
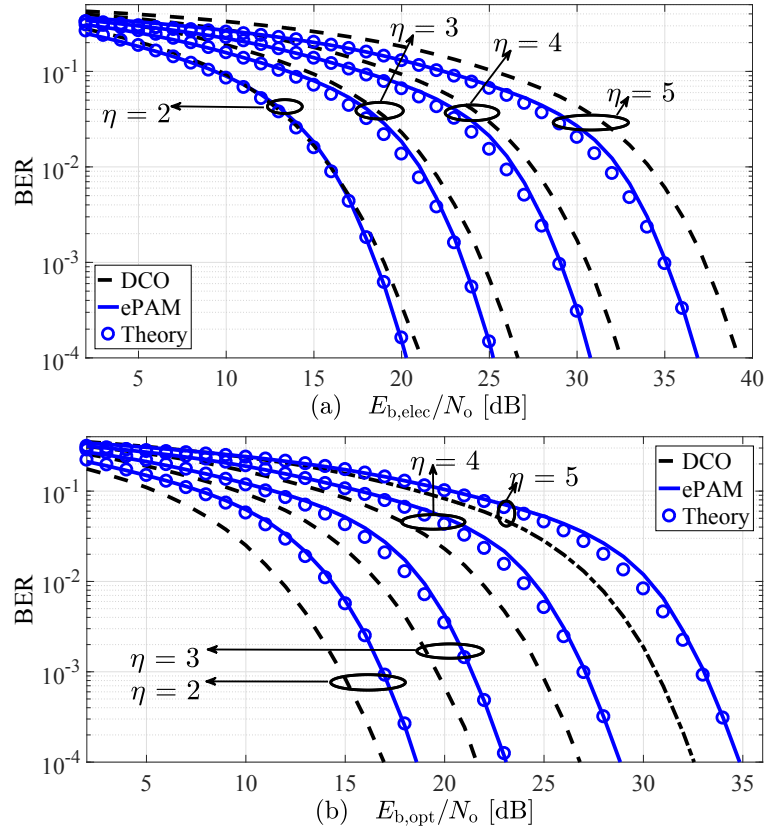
Figure 3.10: *The performance comparison of ePAM-DMT and DCO-OFDM for different spectral efficiency values in an AWGN channel as a function of (a) electrical SNR, and (b) optical SNR. The value of η is given in bits/s/Hz. Optimum biasing levels for DCO-OFDM at $\eta = \{2, 3, 4, 5\}$ are estimated through Monte Carlo simulations at respectively 7.5 dB, 9.5 dB, 11 dB, 13 dB as described in (2.10). The theoretical results for the first depth of ePAM-DMT are plotted as a lower bound on the BER performance.*

as given in Fig. 2.8.

The BER performance of non-squared constellation sizes of M-QAM cannot be achieved using $\sqrt{M}$-PAM. For example, the BER performance of 8-QAM can never be matched by any M-PAM constellation size. Therefore, the resolution of the possible constellation sizes that can be used at each depth in ePAM-DMT is limited because only square constellation sizes can be considered. Fig. 3.10 presents the BER performance of ePAM-DMT and DCO-OFDM as a function of electrical and optical SNR. In comparison with DCO-OFDM, ePAM-DMT is more energy efficient in terms of electrical SNR and less energy efficient in terms of optical SNR. Higher optical power dissipation is a disadvantage for dimming-based VLC applications. However, it can be

considered as a desirable characteristic when a high level of illumination is required. At a spectral efficiency of $\eta = 2$ bit/s/Hz, the energy efficiency of {8,4}-ePAM-DMT scaled at {-1,2.2} dB is higher than 16-QAM DCO-OFDM by 1.1 dB for the electrical SNR. However, it is shown to be less efficient by 1.65 dB for the optical SNR. At $\eta = 3$ bits/s/Hz, {16,8,4}-ePAM-DMT scaled at {-1.7,1.3,4.5} dB is more energy efficient than 64-QAM DCO-OFDM in terms of the electrical SNR with 1.5 dB energy savings and less efficient in terms of the optical SNR with a degradation of 2.1 dB. The inefficiency of ePAM-DMT in terms of the optical SNR is mainly attributed to the repetition of the cyclic prefixes. At $\eta = 4$ bits/s/Hz and by comparison with 256-QAM DCO-OFDM, {32,16,16}-ePAM-DMT scaled at {-0.8,2,-0.5} dB is more energy efficient in terms of electrical SNR with 1.75 dB energy savings, and less efficient in terms of optical SNR with a loss of 2 dB. At a higher spectral efficiency $\eta = 5$ bits/s/Hz, {64,64,16}-ePAM-DMT scaled at {0.2,-2.4,6.3} dB is more efficient in terms of electrical SNR with 2.3 dB gain, and less efficient in terms of optical SNR with 2.3 dB loss.

The theoretical curves show the BER performance obtained for depth $d = 1$ using (3.38). The BER performance of the first depth provides a lower bound on the BER performance of the proposed scheme. The theoretical curves of the BER performance approximate the actual BER results for all cases. The error propagation is apparent at some SNR values, however, the theoretical BER analysis matches the numerical simulations at higher SNR values and they are always lower than the actual BER values.

3.7.2 Simulation results of eACO-OFDM

All the possible combinations of constellation sizes at eACO-OFDM streams with all possible power allocations are investigated in this study. The maximum number of modulation depths used in this investigation is $D = 3$ and the range of spectral efficiency values is 0.5 to 5 bits/s/Hz. The performance of the optimum configurations in all superposition modulation techniques is compared with the performance of a spectrum equivalent DCO-OFDM in an AWGN channel. The comparison parameters and methodology is exactly similar to Section 3.2. The BER performance of eACO-OFDM is presented in Fig. 3.11 (a and b) Table 3.3. The electrical energy savings for eACO-OFDM start

DCO-OFDM	η	ePAM-DMT		Energy gains [dB]	
M_{DCO}-QAM	[bits/s/Hz]	$\underline{M}^{\text{ePAM}}_{(\eta,D)}$-PAM	$\underline{\gamma}^{\text{ePAM,dB}}_{(\eta,D)}$ [dB]	elec.	opt.
4-QAM	1	[2,4]	[5.2,-4]	1.35	-3.27
8-QAM	1.5	[4,4]	[1.1,-1.4]	1.75	-0.25
16-QAM	2	[8,4]	[-1,2.2]	1.1	-1.65
32-QAM	2.5	[8,8,4]	[0.7,-1.7,1.5]	1.25	-1.2
64-QAM	3	[16,8,4]	[-1.7,1.3,4.5]	1.5	-2.1
128-QAM	3.5	[32,8,4]	[-3,5.6,8.8]	0.5	-1.5
256-QAM	4	[32,16,16]	[-0.8,2,-0.5]	1.75	-2
512-QAM	4.5	[64,16,16]	[-2.6,5.9,3.2]	1.4	-2.5
1024-QAM	5	[64,64,16]	[0.2,-2.4,6.3]	2.3	-2.3

Table 3.2: *The optimal combination of constellation sizes and scaling factors for ePAM-DMT and the associated electrical and optical gains over DCO-OFDM at a BER of 10^{-4}, where $M_{\text{ePAM},d}$ and $\gamma_{\text{ePAM},d}$ denote the constellation size and the scaling factor for the modulation depth d, respectively.*

at 2 bit/s/Hz. As shown in Fig. 3.11 (a), eACO-OFDM is more efficient in terms of the electrical SNR requirements when compared with DCO-OFDM for all the considered spectral efficiency values. For the optical SNR values, the eACO-OFDM technique is shown to have an equivalent performance to DCO-OFDM for most of the presented cases. At high SNR values, the theoretical lower bound on BER is shown to be close with the Monte Carlo results for all the presented cases.

DCO-OFDM	η	eACO-OFDM		Energy gains [dB]	
M_{DCO}	[bits/s/Hz]	$\underline{M}^{\text{eACO}}_{(\eta,D)}$-QAM	$\underline{\gamma}^{\text{eACO,dB}}_{(\eta,D)}$ [dB]	elec.	opt.
2-QAM	0.5	[2,4]	[2.2,-2.4]	2.3	0.3
4-QAM	1	[8,2,4]	[-2.3,5.9,1.4]	0.3	-1.1
8-QAM	1.5	[16,8,4]	[-1.8,1.4,5]	3.4	1.53
16-QAM	2	[32,16,16]	[-1.4,1.7,2]	2.75	0.7
32-QAM	2.5	[64,64,16]	[-0.9,-0.7,5.3]	3.13	0.75
64-QAM	3	[128,128,64]	[0,-0.4,2.6]	3.2	0.06
128-QAM	3.5	[256,256,256]	[0,0,0]	3.27	-0.63
256-QAM	4	[512,1024,256]	[0.5,-2.2,3.8]	3.3	-0.4
512-QAM	4.5	[2048,1024,256]	[-1.9,1.1,6.8]	3.63	-0.37
1024-QAM	5	[4096,2048,1024]	[-1.7,1.4,4.3]	4.25	-0.15

Table 3.3: *The optimal combination of constellation sizes and scaling factors for eACO-OFDM and the associated electrical and optical gains over DCO-OFDM at a BER of 10^{-4}, where $M_{\text{eACO},d}$ and $\gamma_{\text{eACO},d}$ denote the constellation size and the scaling factor for the modulation depth d, respectively.*
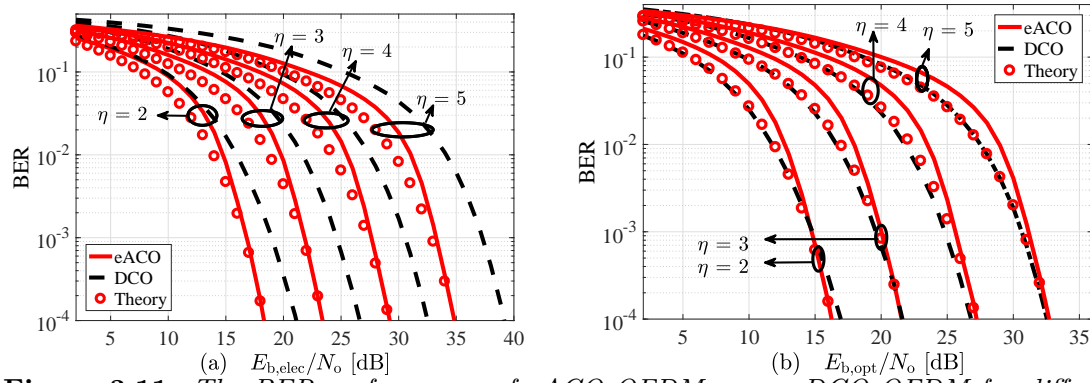
Figure 3.11: *The BER performance of eACO-OFDM versus DCO-OFDM for different spectral efficiency values, in both AWGN channel as a function of electrical SNR, and optical SNR. The values of η are given in bits/s/Hz. DC bias levels for DCO-OFDM at $\eta = \{2, 3, 4, 5\}$ are estimated through Monte Carlo simulations at respectively 7.5, 9.5, 11, and 13 dB as described in* (2.10).

3.7.3   Simulation results of ASE-DMT

The BER performance of ASE-DMT is compared with the BER performance of ePAM-DMT and DCO-OFDM. The simulation assumptions are similar to those presented in Section 3.7.1 and Section 3.7.2 for ePAM-DMT and eACO-OFDM, respectively. The disadvantage associated with the inability of ePAM-DMT to achieve the spectral efficiency of non-squared M-QAM constellation sizes is also present in ASE-DMT since both techniques use PAM-DMT.

The BER performance of $\sqrt{M_{\mathrm{DCO}}}$-PAM in ASE-DMT is compared with the BER performance of $\sqrt{M_{\mathrm{DCO}}}$-PAM in ePAM-DMT and M_{DCO}-QAM in DCO-OFDM as a function of the electrical SNR in an AWGN channel at Fig. 3.12 (a). ASE-DMT is more energy efficient than ePAM-DMT and DCO-OFDM for all of the presented cases. At different spectral efficiency values, the electrical energy savings ASE-DMT are between 2.24 dB and 8 dB when compared with DCO-OFDM, and almost constant at 2.5 dB when compared with ePAM-DMT at a BER of 10^{-4}. Similar trends are shown in Fig. 3.12 (b) for the optical SNR. The gain in terms of the optical SNR for ASE-DMT is between 0.6 dB and 3.25 dB when compared with DCO-OFDM at the considered spectral efficiency values. In addition, the savings in terms of the optical SNR are almost constant at 1.3 dB when compared with ePAM-DMT at a BER of 10^{-4}. The energy efficiency gains of ASE-DMT over DCO-OFDM at different spectral efficiency values are summarized in Table 3.4.
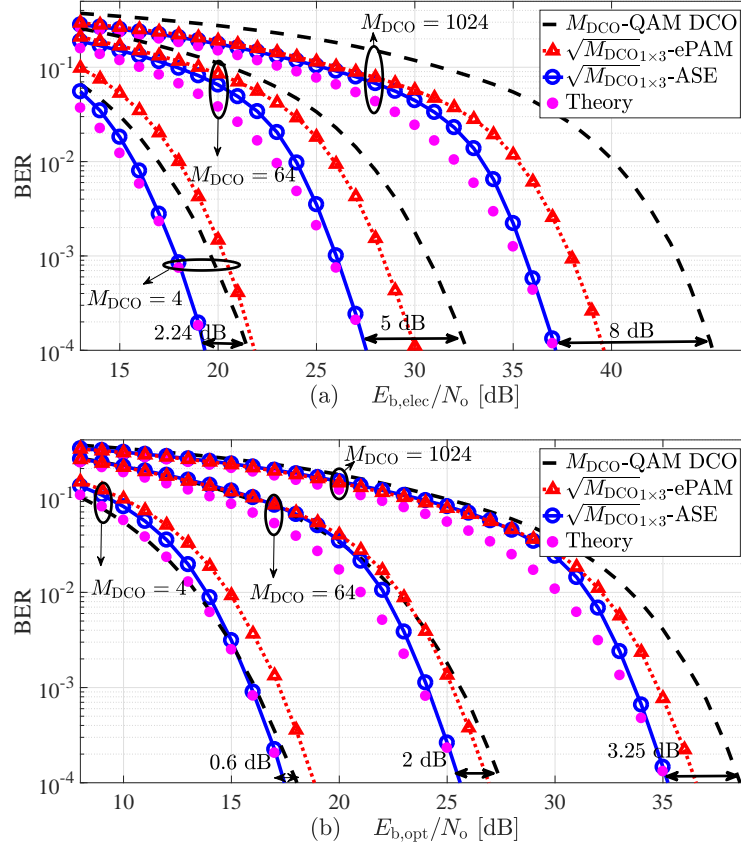
Figure 3.12: *The BER performance comparison of ASE-DMT, ePAM-DMT, and DCO-OFDM for different spectral efficiency values in an AWGN channel as a function of: (a) electrical SNR, and (b) optical SNR. The DC biasing levels for DCO-OFDM at $M = \{4, 64, 1024\}$ are estimated through Monte Carlo simulations at respectively 6 dB, 9.5 dB, and 13 dB as described in (2.10).*

ASE-DMT is more efficient than ePAM-DMT in terms of both the electrical and optical SNR. This is due to the fact that in ePAM-DMT, half of the frames are removed after each demodulation process as shown in Section 3.2. The frequency domain loading of PAM symbols in ASE-DMT does not require this process, which results in a performance gain of ASE-DMT over ePAM-DMT.

The theoretical BER bounds underestimate the BER at lower SNR due to the error propagation in the successive streams cancellation process at the receiver. However, the theoretical BER bounds match the Monte Carlo simulation results at high SNR values. This is consistent with eACO-OFDM and ePAM-DMT.

Spectral efficiency [bits/s/Hz]	1	2	3	4	5
Electrical SNR gains [dB]	2.24	4	5	5.75	8
optical SNR gains [dB]	0.6	1.7	2	2.5	3.25

Table 3.4: *Energy efficiency gains of ASE-DMT over DCO-OFDM at a BER of 10^{-4}.*

Parameter	Value
Room dimensions (Cartesian coordinates)	[5,5,3] m
Transmitter location (Cartesian coordinates)	[2.5,2.5,3] m
Receiver location (Cartesian coordinates)	[1,1.25,0.75] m
Ceiling reflectivity, ρ_c [116]	0.38
Floor reflectivity, ρ_f [116]	0.61
Walls reflectivity, ρ_w [116]	0.74
Receiver field of view (half angle), Ψ_c [19]	40°
Transmitter semi-angle, $\Phi_{1/2}$ [19]	60°
Photo-diode active area, A_d [19]	1 cm^2
Maximum number of reflections [19]	5
Cyclic prefix length, N_{CP}	30
OFDM frame length, N_{FFT}	2048

Table 3.5: *VLC channel model parameters*

Note that the BER performance of ASE-DMT is identical to the BER performance of eU-OFDM at the same spectral efficiency values [26], and to the BER performance of eACO-OFDM when identical constellation size and unitary scaling factors are used for eACO-OFDM. This is an expected result, because the BER performance of their inherently unipolar OFDM based-schemes forms (PAM-DMT, U-OFDM, and ACO-OFDM) is also identical [53].

The performance of ASE-DMT is investigated in a frequency selective VLC channel. The VLC channel model is obtained by a Monte Carlo ray tracing algorithm [19, 116, 117]. The parameters used to simulate the channel impulse response are presented in Table 3.5. The values in Table 3.5 are presented as examples and can be changed based on the studied scenario. The channel impulse response is obtained up to 80 ns, where the last notable contributions of the reflections appear to arrive at the destination. A cyclic prefixes length $N_{CP} = 30$ was found to be adequate for the ISI mitigation using a zero-forcing equalizer, given that the OFDM frame length is $N_{FFT} = 2048$. The comparison between ASE-DMT and DCO-OFDM has been presented for different M-QAM constellation sizes in Fig. 3.13. The performance difference between ASE-DMT and DCO-OFDM is almost equivalent for both the frequency flat
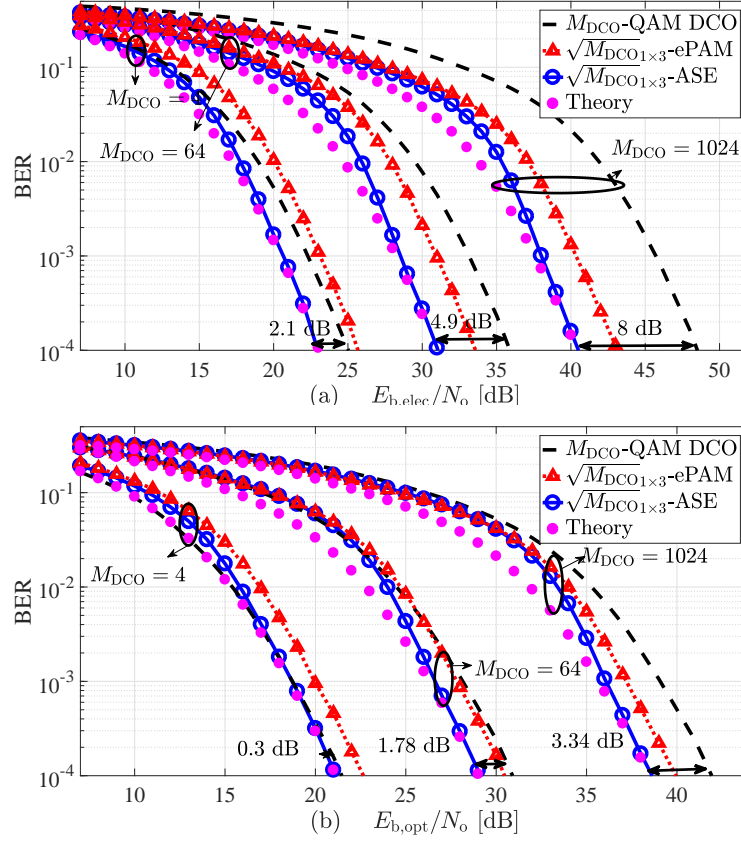
Figure 3.13: *The BER performance comparison of ASE-DMT, ePAM-DMT, and DCO-OFDM for different spectral efficiency values in a frequency selective channel as a function of: (a) electrical SNR, and (b) optical SNR. The DC biasing levels for DCO-OFDM at $M = \{4, 64, 1024\}$ are estimated through Monte Carlo simulations at respectively 6 dB, 9.5 dB, and 13 dB as described in* (2.10).

channel and the frequency selective channel for all of the presented cases. The cyclic prefix length in ePAM-DMT is limited by the total number of depths used. The maximum cyclic prefix length for ePAM-DMT with a total number of depths D is given as follows:

$$N_{\text{CP}}^{\text{ePAM,max}} = \lfloor N_{\text{FFT}}/(2D - 2) - 1 \rfloor. \tag{3.47}$$

This means that ePAM-DMT can be used for frequency selective channels only when the number of channel taps is less than $N_{\text{CP}}^{\text{ePAM,max}}$.

The performance of ASE-DMT is presented for arbitrary constellation sizes in Fig. 3.14 as a function of electrical and optical SNR. The results are outlined in Table 3.6. In comparison to results outlined in Table 3.4, the approach of arbitrary constellation
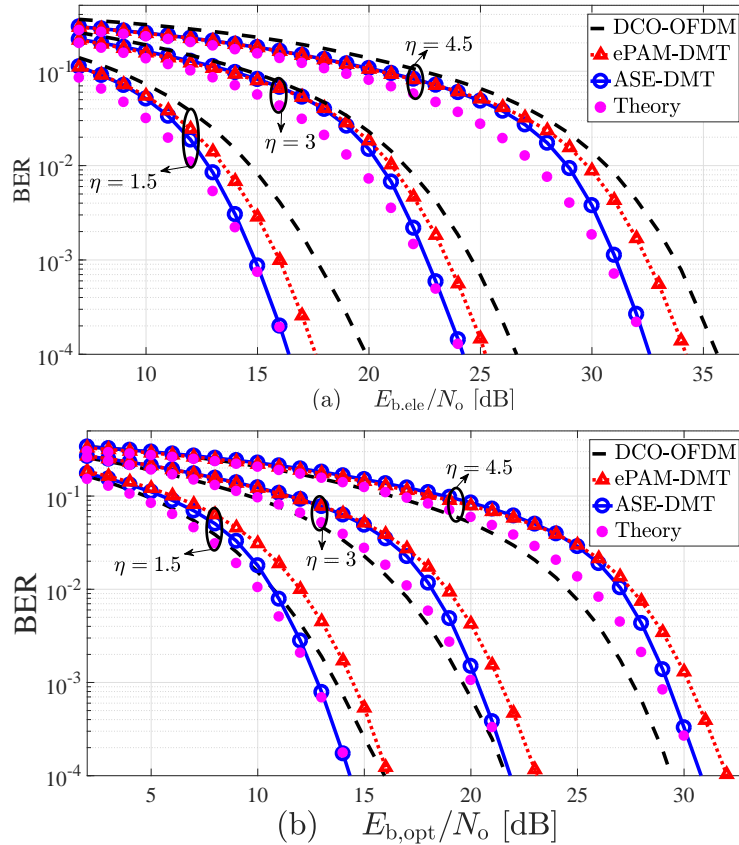
Figure 3.14: *The BER performance comparison of ASE-DMT, ePAM-DMT, and DCO-OFDM for different spectral efficiency values in an AWGN channel as a function of: (a) electrical SNR, and (b) optical SNR. The spectral efficiency η is given in [bits/s/Hz]. The DC biasing levels for DCO-OFDM at $\eta = \{1.5, 3, 4.5\}$ are estimated through Monte Carlo simulations at respectively 7 dB, 9.5 dB, and 12 dB as described in (2.10).*

sizes reduces the electrical and energy gains of ASE-DMT. However, it increases the spectral efficiency of ASE-DMT at a reduced computation complexity. Therefore, a trade-off between the computation complexity, spectral efficiency and energy efficiency for ASE-DMT should be considered based on the considered application.

3.7.4 Computation analysis and practical considerations

The computation complexity of ePAM-DMT, eACO-OFDM and ASE-DMT are studied and compared with the computation complexity of DCO-OFDM in this section. The computation complexity is dominated by the number of multiplications in FFT/IFFT operations. Therefore, the computation complexity in this thesis is defined as the

DCO-OFDM	η	ASE-DMT		Energy gains [dB]	
M_{DCO}-QAM	[bits/s/Hz]	$\underline{M}^{\mathrm{ASE}}_{(\eta,D)}$-PAM	$\underline{\gamma}^{\mathrm{ASE,dB}}_{(\eta,D)}$ [dB]	elec.	opt.
4-QAM	1	[2,2,4]	[1.9,2,-4.6]	0.6	-1
8-QAM	1.5	[4,2,4]	[-1.5,5.3,-1.2]	3.15	1.05
16-QAM	2	[4,8,4]	[2.4,-3.4,2.5]	2	0
32-QAM	2.5	[8,8,4]	[-0.9,-0.7,5.3]	3	0.75
64-QAM	3	[16,8,4]	[-2.7,3.2,9.4]	2.55	-0.25
128-QAM	3.5	[16,16,16]	[0,0,0]	3.28	0
256-QAM	4	[32,16,16]	[-2,3.6,3.7]	3.36	0
512-QAM	4.5	[32,32,64]	[1.5,1.7,-4]	3	-1.4
1024-QAM	5	[64,32,64]	[-1.3,4.3,-1.1]	4	-0.5

Table 3.6: *The optimal combination of constellation sizes and scaling factors for ASE-DMT and the associated electrical and optical gains over DCO-OFDM at a BER of 10^{-4}, where $M_{\mathrm{ASE},d}$ and $\gamma_{\mathrm{ASE},d}$ denote the constellation size and the scaling factor for the modulation depth d, respectively.*

number of complex multiplications required to perform a FFT/IFFT operation.

3.7.4.1 Computation complexity of DCO-OFDM

At the transmitter side, DCO-OFDM requires N_{FFT}-point complex multiplications which result in a computation complexity of $\mathcal{O}(N_{\mathrm{FFT}} \log_2 N_{\mathrm{FFT}})$. The FFT operation at the receiver side of DCO-OFDM is performed on real-valued frames. Two N_{FFT}-point FFT operations on two real-valued signals can be realized using one N_{FFT}-point FFT on one complex-valued signal [118]. Therefore, the computation complexity at the receiver of DCO-OFDM is $\mathcal{O}(N_{\mathrm{FFT}}/2 \log_2 N_{\mathrm{FFT}})$. The computation complexity per bit of DCO-OFDM is written as follows:

$$C_{\mathrm{DCO}} = \frac{2(3N/2 \log_2 N_{\mathrm{FFT}})}{\log_2(M_{\mathrm{DCO}})(N_{\mathrm{FFT}} - 2)}. \tag{3.48}$$

3.7.4.2 Computation complexity of ePAM-DMT

The cyclic prefix at each depth of ePAM-DMT is used in the symmetry alignment of superimposed depths. This reduces the frame lengths at higher order depths. The FFT frame length at depth-d of ePAM-DMT is given as $N^{\mathrm{ePAM}}_d = N^{\mathrm{ePAM}}_{d-1} - 2N_{\mathrm{CP}} - 2$, $\forall d \geq 2$, where $N^{\mathrm{ePAM}}_1 = N_{\mathrm{FFT}}$, and N_{FFT} is the frame length of DCO-OFDM. The frame lengths of all depths in ePAM-DMT are zero-padded to the next power of two.

At the transmitter side of ePAM-DMT, $\sum_{d=1}^{D} 2^{d-1}$ PAM-DMT frames are required to generate 2^{D-1} ePAM-DMT frames. Therefore, the computation complexity of the ePAM-DMT transmitter is given as follows:

$$C_{\mathrm{ePAM}}^{\mathrm{Tx}}(D) = \sum_{d=1}^{D} 2^{d-D} \left(N_{\mathrm{FFT}}/2 \log_2 N_{\mathrm{FFT}}\right)$$

$$= \left(1 - 2^{-D}\right) \times N_{\mathrm{FFT}} \log_2 N_{\mathrm{FFT}} \tag{3.49}$$

$$C_{\mathrm{ePAM}}^{\mathrm{Tx}} \approx \lim_{D \to \infty} C_{\mathrm{ePAM}}^{\mathrm{Tx}}(D) = \mathcal{O}\left(N_{\mathrm{FFT}} \log_2 N_{\mathrm{FFT}}\right). \tag{3.50}$$

This is equivalent to the computation complexity of a DCO-OFDM transmitter.

At the receiver side of ePAM-DMT, $\sum_{d=1}^{D} 2^{d-1}$ PAM-DMT frames are required to be demodulated and $\sum_{d=2}^{D} 2^{d-1}$ PAM-DMT frames are required to be remodulated in order for 2^{D-1} frames of ePAM-DMT to be demodulated. Therefore, the computation complexity of the ePAM-DMT receiver is given as follows:

$$C_{\mathrm{ePAM}}^{\mathrm{Rx}}(D) = \sum_{d=1}^{D} 2^{d-D} \left(N_{\mathrm{FFT}}/2 \log_2 N_{\mathrm{FFT}}\right) + \sum_{d=2}^{D} 2^{d-D} \left(N_{\mathrm{FFT}}/2 \log_2 N_{\mathrm{FFT}}\right)$$

$$= \left(1 - 2^{-D}\right) \times N_{\mathrm{FFT}} \log_2 N_{\mathrm{FFT}} + \left(1 - 2^{-D+1}\right) \times N_{\mathrm{FFT}} \log_2 N_{\mathrm{FFT}} \tag{3.51}$$

$$C_{\mathrm{ePAM}}^{\mathrm{Rx}} \approx \lim_{D \to \infty} C_{\mathrm{ePAM}}^{\mathrm{Rx}}(D) = \mathcal{O}\left(2 N_{\mathrm{FFT}} \log_2 N_{\mathrm{FFT}}\right). \tag{3.52}$$

Therefore the computation complexity of ePAM-DMT per bit is given as follows:

$$C_{\mathrm{ePAM}}(D) = \frac{2(C_{\mathrm{ePAM}}^{\mathrm{Tx}}(D) + C_{\mathrm{ePAM}}^{\mathrm{Rx}}(D))}{\log_2(M_{\mathrm{ePAM},1})(N_{\mathrm{FFT}} - 2) + \sum_{d=2}^{D} \log_2(M_{\mathrm{ePAM}_d}) N_d^{\mathrm{ePAM}}/2^{d-1}}, \tag{3.53}$$

where $M_{\mathrm{ePAM},d}$ is the constellation size used for depth d in ePAM-DMT, $M_{\mathrm{ePAM},d} = \sqrt{M_{\mathrm{DCO}}}$.

3.7.4.3 Computation complexity of eACO-OFDM

An IFFT operation is applied on the $N_{\mathrm{FFT}}/2$ complex symbols loaded on the odd-indexed subcarriers of an ACO-OFDM modulator. Therefore, the first modulation depth of an eACO-OFDM transmitter has a computation complexity of $\mathcal{O}(N_{\mathrm{FFT}}/2 \log_2 N_{\mathrm{FFT}})$. The rest of the modulation depths applies an IFFT operation only on $N_{\mathrm{FFT}}/2^d$ complex symbols. As a result the computation complexity of

eACO-OFDM is given as follows:

$$C_{\text{eACO}}^{\text{Tx}}(D) = \sum_{d=1}^{D} \left(N_{\text{FFT}}/2^d \log_2 N_{\text{FFT}} \right),$$

$$= \left(1 - 2^{-D} \right) \times N_{\text{FFT}} \log_2 N_{\text{FFT}}. \tag{3.54}$$

$$C_{\text{eACO}}^{\text{Tx}} \approx \lim_{D \to \infty} C_{\text{eACO}}^{\text{Tx}}(D) = \mathcal{O}\left(N_{\text{FFT}} \log_2 N_{\text{FFT}} \right). \tag{3.55}$$

The receiver starts with the demodulation of the $N_{\text{FFT}}/2$ complex symbols loaded on the odd subcarriers. However, the computation complexity associated with the demodulation of the first depth is similar to the computation complexity of DCO-OFDM since the FFT operation is applied on real-valued data. There is only $N_{\text{FFT}}/2^d$ subcarriers loaded with complex symbols at depth d. Therefore, algorithms such as Sparse FFT [119] can be applied to retrieve the symbols with a computational complexity of $\mathcal{O}(N_{\text{FFT}}/2^d \log_2 N_{\text{FFT}})$. The demodulated streams for all depths, except the last one, are required to be remodulated at the receiver. The associated complexity of remodulating the first depth is: $\mathcal{O}(N_{\text{FFT}}/2 \log_2 N_{\text{FFT}})$, and the associated complexity of remodulating the rest of the depths is $\sum_{d=1}^{D-1} \mathcal{O}(N_{\text{FFT}}/2^d \log_2 N_{\text{FFT}})$. As a result, the computation complexity associated with an eACO-OFDM receiver is given as follows:

$$C_{\text{eACO}}^{\text{Rx}}(D) = \sum_{d=1}^{D} \left(N_{\text{FFT}}/2^d \log_2 N_{\text{FFT}} \right) + \sum_{d=1}^{D-1} \left(N_{\text{FFT}}/2^d \log_2 N_{\text{FFT}} \right)$$

$$= \left(1 - 2^{-D} \right) \times N_{\text{FFT}} \log_2 N_{\text{FFT}} + \left(1 - 2^{-D+1} \right) \times N_{\text{FFT}} \log_2 N_{\text{FFT}} \tag{3.56}$$

$$C_{\text{eACO}}^{\text{Rx}} \approx \lim_{D \to \infty} C_{\text{eACO}}^{\text{Rx}}(D) = \mathcal{O}\left(2N_{\text{FFT}} \log_2 N_{\text{FFT}} \right). \tag{3.57}$$

3.7.4.4 Computation complexity of ASE-DMT

At the transmitter side of PAM-DMT, an IFFT operation is applied on imaginary-valued frames. At the receiver side, a single FFT operation is applied on real-valued frames. Therefore, the computation complexity of PAM-DMT for both of the transmitter and receiver is:

$$C_{\text{PAM}}^{\text{Tx/Rx}} = \mathcal{O}(N_{\text{FFT}}/2 \log_2 N_{\text{FFT}}). \tag{3.58}$$

The first depth of ASE-DMT has a computation complexity similar to that of a PAM-DMT transmitter. Higher depths of ASE-DMT are sparse as they have a low

number of active subcarriers. The number of active subcarriers at depth d is $N_{\text{FFT}}/2^{d-1}$, $\forall d \geq 2$. Therefore, the IFFT operation at higher order depths $d \geq 2$, can be optimized to avoid the calculations performed on zeros. This has been demonstrated by Q. Wang *et al.* in [120] by rearranging the inner operations of an IFFT operation. Given that the subcarriers in these depths are real-valued, the computation complexity at the transmitter of depth d is $\mathcal{O}(N_{\text{FFT}}/2^d \log_2 N_{\text{FFT}})$. Therefore, the computation complexity of ASE-DMT transmitter is given as follows:

$$C_{\text{ASE}}^{\text{Tx}}(D) = \sum_{d=1}^{D} \left(N_{\text{FFT}}/2^d \log_2 N_{\text{FFT}} \right),$$

$$C_{\text{ASE}}^{\text{Tx}} \approx \lim_{D \to \infty} C_{\text{ASE}}^{\text{Tx}}(D) = \mathcal{O}\left(N_{\text{FFT}} \log_2 N_{\text{FFT}} \right). \tag{3.59}$$

The first demodulation process at the receiver of ASE-DMT is applied on real-valued frames, therefore, the computation complexity associated with this process is equivalent to the computation complexity of a DCO-OFDM receiver. All the other demodulation process are also applied on real-valued frames. However, the frames at higher order depths are sparse in the frequency domain. There are only $N_{\text{FFT}}/2^d$ non-zero real-valued data symbols at a modulation depth $d > 1$. A specific set of subcarriers is only required at the output of each demodulation process. Therefore, the FFT operation at higher order depths, $d \geq 2$, is only evaluated at subcarriers given by (3.11). Algorithms such as Sparse FFT [119] can also be applied at depth d with a computational complexity of $\mathcal{O}(N_{\text{FFT}}/2^d \log_2 N_{\text{FFT}})$. Similar to eACO-OFDM, each modulation depth except the last one is required to be remodulated in order for the clipping distortion at the higher depth to be estimated as discussed in Section 3.4. Therefore, the computation complexity of an ASE-DMT receiver is given as follows:

$$C_{\text{ASE}}^{\text{Rx}}(D) = \sum_{d=1}^{D} \left(N_{\text{FFT}}/2^d \log_2 N_{\text{FFT}} \right) + \sum_{d=1}^{D-1} \left(N_{\text{FFT}}/2^d \log_2 N_{\text{FFT}} \right)$$

$$C_{\text{ASE}}^{\text{Rx}} \approx \lim_{D \to \infty} C_{\text{ASE}}^{\text{Rx}}(D) = \mathcal{O}\left(2N_{\text{FFT}} \log_2 N_{\text{FFT}} \right). \tag{3.60}$$

The computation complexity of ASE-DMT per bit is given as follows:

$$C_{\text{ASE}}(D) = \frac{2(C_{\text{ASE}}^{\text{Tx}}(D) + C_{\text{ASE}}^{\text{Rx}}(D))}{\log_2(M_{\text{ASE},1})(N_{\text{FFT}} - 2) + \sum_{d=2}^{D} \log_2(M_{\text{ASE},d}) N_{\text{FFT}}/2^{d-1}}, \tag{3.61}$$
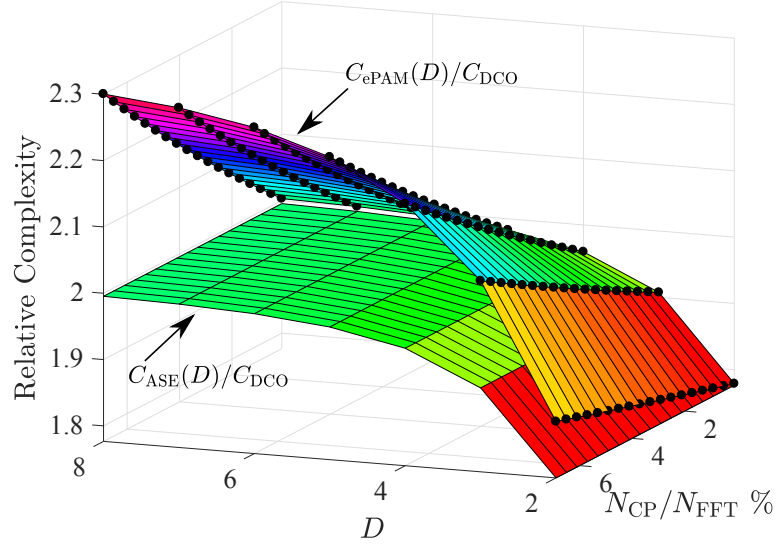
Figure 3.15: *The relative computation complexity of ASE-DMT and ePAM-DMT in comparison with the computation complexity of DCO-OFDM as a function of the total number of depths D, and the CP percentage of the frame length N_{CP}/N_{FFT}.*

where $M_{\mathrm{ASE},d}$ is the constellation size used at depth d in ASE-DMT, $M_{\mathrm{ASE},d} = \sqrt{M_{\mathrm{DCO}}}$.

3.7.4.5 Computation complexity comparison

The ratio of the computation complexities per bit of ASE-DMT to DCO-OFDM, $C_{\mathrm{ASE}}(D)/C_{\mathrm{DCO}}$, and the ratio of the computation complexities per bit of ePAM-DMT to DCO-OFDM, $C_{\mathrm{ePAM}}(D)/C_{\mathrm{DCO}}$ are presented in Fig. 3.15 as a function of the total number of used depths D and the cyclic prefix percentage of the overall frame length $N_{\mathrm{CP}}/N_{\mathrm{FFT}}$. The relative complexity of ASE-DMT is independent of the cyclic prefix and it increases as the total number of depths increases. However, it converges to twice the complexity of DCO-OFDM.

The relative complexity of ePAM-DMT increases as the cyclic prefix length and the total number of depths increase. The relative complexity of ePAM-DMT has a lower bound that is equivalent to the relative complexity of ASE-DMT when the cyclic prefix length is zero. The cyclic prefix length is limited by the total number of depths used. The maximum cyclic prefix length is less than 8% of the OFDM frame length for $D = 8$. When the cyclic prefix is 8%, the relative complexity of ePAM-DMT is 2.3 times higher than the computation complexity of DCO-OFDM.

3.7.4.6 Practical considerations

The transmission cannot be started in ePAM-DMT, unless $2^D - 1$ PAM-DMT frames are available at the transmitter side. In addition, frames at higher order modulation depths are required to be processed in the time domain to achieve the symmetry required for superposition modulation. This introduces an additional delay at the transmitter side. At the receiver side of ePAM-DMT, the demodulation of frames at depth-d can only happen after all lower modulation depths have been demodulated and remodulated. This is estimated at $\sum_{d'=2}^{d} 2^{D-d'+1}$ PAM-DMT frames. Moreover, 2^D frames are required to be buffered at the receiver, until the demodulation process of a full ePAM-DMT frame finishes.

There is no delay associated with the ASE-DMT transmitter, as all of the modulation depths can be generated at the same time. At the receiver side of ASE-DMT, the demodulation of frames at depth-d can only take place after all of the lower modulation depths have been demodulated and remodulated. This is estimated at a maximum of $D - 1$ PAM-DMT frames. Moreover, a maximum of $D - 1$ frames are required to be buffered at the receiver, so that the demodulation process of a full ASE-DMT frame can be finished. The associated delay and memory requirements of eACO-OFDM is exactly similar to ASE-DMT.

The spectral efficiency of each additional stream decreases exponentially. Therefore, it is more efficient to implement ASE-DMT with small number of modulation depths, $D = 2$ or $D = 3$. This would result in a small spectral efficiency gap between ASE-DMT and DCO-OFDM, 12.5% of the spectral efficiency of DCO-OFDM when $D = 3$. This gap can be closed when appropriate constellation sizes are used with a maximum number of modulation depths $D = 3$ as shown in Section 3.6.

Typical OFDM signals have high PAPR. This drives the LEDs into non-linear regions because of their limited dynamic range. However, the higher order modulation depths in ASE-DMT and eACO-OFDM are sparse in the frequency domain. This reduces the PAPR of higher order modulation depths. To exploit this property, the waveform at each modulation depth can be used to drive a single LED in an LED array. This allows the waveforms to be superimposed in the optical domain and reduces the PAPR which mitigates the non-linearity. The complementary cumulative distribution function
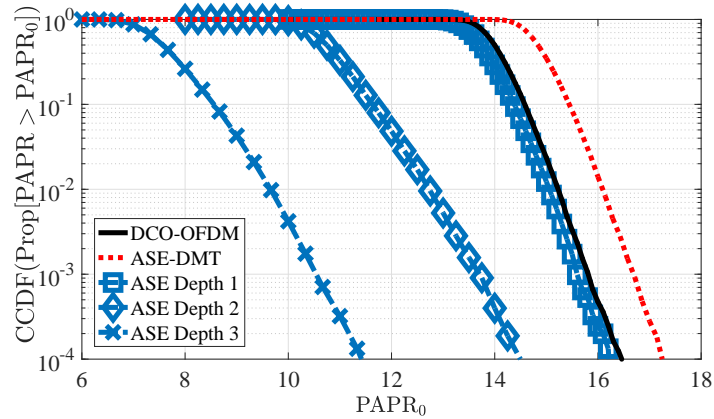
Figure 3.16: *The PAPR CCDF plot of DCO-OFDM and ASE-DMT (modulation depths and overall stream).*

(CCDF) as a function of reference peak-to-average-power ratio $PAPR_0$ of DCO-OFDM and ASE-DMT modulation depths is presented in Fig. 3.16 to illustrate the sparsity effect on the PAPR. The PAPR of the overall ASE-DMT waveform is shown to be higher than the PAPR of DCO-OFDM. However, The PAPR of the individual ASE-DMT modulation depths are shown to be lower than the PAPR of DCO-OFDM.

3.8 Summary

Three novel modulation techniques are proposed in this chapter based on the superposition of multiple inherently unipolar OFDM techniques. The proposed techniques offer solutions to the spectral efficiency loss in inherently unipolar OFDM without any DC bias[2]. The superposition of multiple PAM-DMT streams results in an improved spectral and electrical energy efficiency for ePAM-DMT when compared with DCO-OFDM. The anti-symmetry of PAM-DMT waveforms is used to avoid any IDI in ePAM-DMT. However, aligning the anti-symmetry of multiple PAM-DMT waveforms in the time domain was found to be computationally complex. An improved method to superimpose multiple PAM-DMT streams is proposed in ASE-DMT. The method is based on selective loading of M-PAM modulated symbols at multiple modulation depths. The selection of the loaded subcarriers is designed to allow the superposition of multiple PAM-DMT streams without any IDI. The proposed ASE-DMT offers improved spec-

---

[2]DC bias due to the turn-on voltage of the light source is required. However, it is neglected in our relative comparisons as it is required for all IM/DD techniques

tral and energy efficiency results when compared with ePAM-DMT and DCO-OFDM. Another superposition modulation technique is proposed based on ACO-OFDM. The asymmetry of ACO-OFDM waveforms is used to avoid any IDI in eACO-OFDM. The overall performance of eACO-OFDM is almost identical to ASE-DMT when a constant constellation order is used for all the modulation depths.

A generalized approach is presented for the proposed superposition modulation techniques. The objective of this approach is to reduce the implementation complexity by achieving the spectral efficiency of DCO-OFDM with up to three modulation depths. This is realized by selecting the appropriate constellation sizes for the used modulation depths. Theoretical bounds on the BER performance of the proposed techniques are derived and found to be in agreement with the Monte Carlo simulations at high SNR values. The performance of the proposed superposition OFDM-based techniques is compared with DCO-OFDM in both AWGN and frequency selective VLC channels.

The proposed techniques provide significant energy efficiency gains when compared to similar state-of-the-art IM/DD techniques at equivalent spectral efficiency values. This makes them promising candidates for future VLC and OWC systems.

Chapter 4

Experimental studies targeting spectral and energy efficiency

4.1 Introduction

General lighting is under a transformation to become semiconductor-based due to the increasing interest in energy savings. This shift has already enabled applications such as active energy consumption control and color tuning. Commercially available light emitting diodes (LEDs) have a limited frequency response due to the slow yellow color converting phosphor as detailed in Section 2.4.1.2. Nevertheless, recent results for visible light communication (VLC) using a phosphorescent white LED with adaptive bit and energy loading were reported at 2.32 Gb/s aided by a two-staged linear software equalizer and a blue filter [27].

Micrometer-sized Gallium Nitride light emitting diode (m-LED) are promising candidates in enabling light as a service (LaaS) and internet of things (IoT). The introduction of m-LEDs has enabled high-speed VLC and indoor positioning and tracking systems [121, 122]. Emerging m-LEDs are known for their small active areas enabling high current density injection which drives the modulation bandwidth to hundreds of MHz [28]. A 60 µm diameter pixel has achieved 3 Gb/s [121] and more recently a single pixel of a segmented array has demonstrated 5 Gb/s [33]. On the other hand, blue light amplification by stimulated emission of radiation diodes (LDs) are interesting solutions for general lighting due to their illumination quality and optical power efficiency at high current densities [59]. Additionally, LDs emitting at the blue wavelength around 450 nm are interesting choices for VLC-based underwater communications due to the lower optical attenuation at this wavelength [123].

Recently, a 40 µm diameter m-LED at 405 nm achieved a data rate of 3.32 Gb/s [124]. A high bandwidth VLC link at 400 nm is presented in Study I. The transmission rate is presented at 11.95 Gb/s, when the nonlinear distortion noise of the m-LED is the only

limiting factor in the system. A record transmission rate of 7.91 Gb/s is presented when all the noise sources of the VLC system are considered. Phosphors-pumped violet-based LEDs emitting at 400 nm offer better quality illumination at a higher color rendering index (CRI) when compared with blue-based LEDs emitting at 450 nm [125]. This is mainly a result of the higher light absorption of color converting materials. In addition to the main application in optical attocell access points, the VLC system in Study I offers a novel solution to the high speed data transmission requirement of board to board communication systems [126, 127].

A number of interesting experimental investigations were recently reported based on two of the proposed superposition modulations in Chapter 3 [120, 128–130]. The proposed enhanced asymmetrically clipped optical orthogonal frequency division multiplexing (eACO-OFDM) was investigated for short-haul optical fiber links in [128]. The received signal quality of eACO-OFDM and DC-biased optical orthogonal frequency division multiplexing (DCO-OFDM) is compared over a 19.8 km single mode fiber. It was found that eACO-OFDM offers 2 dB higher signal quality than DCO-OFDM at a data rate of 4.375 Gb/s [128]. A successful demonstration of augmented spectral efficiency discrete multitone (ASE-DMT) using a novel single inverse fast Fourier transform (IFFT) transmitter was also achieved over a 10 km single mode fiber and at a data rate of 18.4 Gb/s [120].

In this chapter we present three experimental studies demonstrating spectrum and energy efficient VLC systems. The works presented in Study I and Study II demonstrate a high speed VLC system based on DCO-OFDM. Computationally efficient single-tap equalizer and adaptive bit and energy loading in DCO-OFDM allows the channel utilization to approach the information capacity limit. A high bandwidth violet m-LED and blue LD are used in Study I and Study II. An investigation into the performance of the proposed superposition modulation scheme is presented in Chapter 3. The performance of ASE-DMT is investigated in a practical VLC system using blue LED and an infra-red (IR) vertical-cavity surface-emitting laser (VCSEL). The energy efficient ASE-DMT based VLC system presented in Study III offers an energy efficient solution to the IR based uplink of light fidelity (LiFi) systems. In addition, it offers a high speed solution for the dimming scenarios in VLC systems.

The rest of this chapter is organized as follows. Firstly, a high speed VLC study is

presented in Section 4.2 based on DCO-OFDM. The experiment is based on a violet m-LED which is described in Section 4.2.2. Adaptive bit and energy loading is implemented for DCO-OFDM as detailed in Section 4.2.3. The experimental setup and the results for Study I are presented in Section 4.2.4 and Section 4.2.5, respectively. An investigation into the range and alignment of the VLC system in Study I is presented in Section 4.2.6. Secondly, another experiment is presented in Section 4.3 based on a blue LD. Similar to Study I, the experiment in Study II is based on DCO-OFDM with adaptive bit and energy loading. The experimental setup and the results for Study I are presented in Section 4.3.2 and Section 4.3.3, respectively.

Thirdly, an investigation into the performance of ASE-DMT is presented in Section 4.4. The performance of ASE-DMT is compared with the performance of DCO-OFDM using a blue LED and an IR VCSEL. The implementation of ASE-DMT is detailed in Section 4.4.2 and the experimental setup is presented in Section 4.4.3. The results of Study III are discussed in Section 4.4.4. Finally, the summary of this chapter is presented in Section 4.5.

4.2 Study I: VLC system using a violet m-LED

A high bandwidth VLC system is demonstrated in this study using DCO-OFDM with adaptive bit and energy loading. The VLC system is realized using a violet m-LED emitting at 400 nm with a system modulation bandwidth of 1.81 GHz. A record transmission rate for the LED-based VLC system is presented at 7.91 Gb/s. In addition, the system transmission rate performance is considered when the nonlinear distortion noise of the m-LED is the major noise source in the VLC system.

4.2.1 The aim of this study

The aim of this study is to demonstrate a high speed VLC system based on DCO-OFDM using a novel low power m-LED device. DCO-OFDM is used with the computationally efficient single-tap equalizer. The adaptive bit and energy loading allows DCO-OFDM to increase the VLC system data rate.
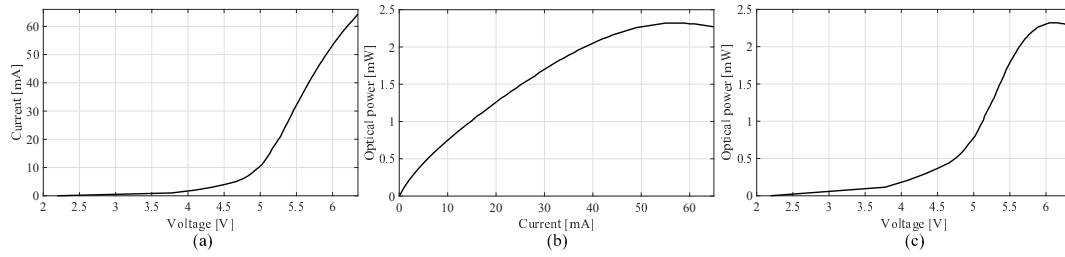
Figure 4.1: *(a) current-voltage, (b) luminescence-current and (c) luminescence-voltage characteristics of the used violet m-LED [34].*

4.2.2 Violet m–LED

The transmitter is a violet-based m-LED emitting at 400 nm from the m-LEDs array presented earlier in Fig. 2.3. The m-LEDs is originally designed by the Institute of Photonics at Strathclyde University in collaboration with prof. M. D. Dawson and his group to match with the geometry of plastic fibers [33]. The m-LEDs array consists of two sets of m-LEDs with different area sizes. The active area of the used m-LED is 435 μm^2. This compares with 1256 μm^2 active area for the 405 nm device in [124].

Solid-state lighting (SSL) devices with linear luminance-voltage (L-V) characteristics and high optical power allow for a large dynamic range that can accommodate large swings of the modulating signals. This subsequently improves the signal-to-noise ratio (SNR) of the VLC system. The current-voltage (I-V), luminance-current (L-I) and L-V characteristics for the used m-LED are presented in Fig. 4.1. The used m-LED achieves a maximum of 2.39 mW of optical power at the roll-over point.

The frequency response from 100 kHz to 1.5 GHz for direct current (DC)-bias current ranging from 10 mA to 50 mA are presented in Fig. 4.2. A high 3 dB bandwidth of the m-LED is measured at 370 MHz. This is enabled by the small active area of the device that allowed higher current density and shorter carrier lifetime.

4.2.3 An implementation of DCO-OFDM

Multiple variants of orthogonal frequency division multiplexing (OFDM) have been proposed for VLC as detailed in Section 2.6.2. DCO-OFDM is widely adopted in practical VLC implementations due to its relative simplicity in comparison with other optical OFDM-based modulation techniques. Conventional OFDM waveforms are both com-
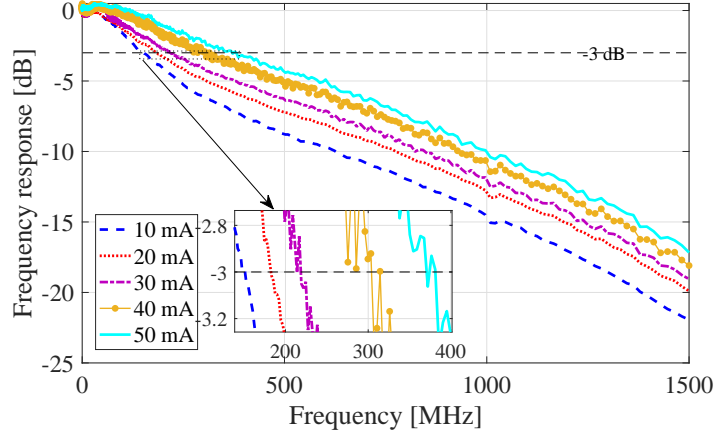
Figure 4.2: *Frequency response for the violet m-LED at DC bias values between 10 mA and 50 mA [34].*

plex and bipolar, however Hermitian symmetry can be imposed on the OFDM subcarriers to realize real-valued OFDM waveforms, $X[k] = X^*[N_{\text{FFT}} - k]$, where N_{FFT} is the OFDM frame length and k is the subcarrier index. A DC bias is used in DCO-OFDM to shift most of the negative valued OFDM samples to be positive, as discussed in Section 2.6.2.1. The generation of DCO-OFDM in this VLC experiment starts with generating a real-valued OFDM waveform in MATLAB$^®$. A pseudo random binary sequence (PRBS) is generated and modulated using quadrature amplitude modulation (QAM). The M_k-QAM constellation size at subcarrier k and its corresponding relative energy are adaptively selected based on the Levin-Campello bit and energy loading algorithm [131].

The QAM symbols are loaded onto orthogonal sub-carriers with sub-carrier spacing equal to $\Delta f = \frac{1}{T_{\text{Sym}}}$, where $T_{\text{Sym}} = N_{\text{FFT}} T_s$ and T_s is the sampling time. The OFDM frame length is set to $N_{\text{FFT}} = 1024$ subcarriers. Smaller sizes for the OFDM frame result in less statistcal significance and larger sizes result in a high peak-to-average power ratio (PAPR) and an increase in the computational complexity. The symbols can then be multiplexed into a serial time domain output using an IFFT. Cyclic prefixs (CPs) are inserted at the start of each OFDM frame. The adequate length of the CPs allows for the inter-symbol interference (ISI) to be mitigated by the computationally-efficient single-tap equalizer. A value of $N_{\text{CP}} = 5$ is found to be sufficient at less than 0.97% loss in the spectral efficiency. A root raised cosine (RRC) pulse shaping filter is used to realize a band limited communication since it allows a trade-off control between

the pulse duration and bandwidth requirements [53]. OFDM time domain waveforms have high PAPR due to the coincidence of multiple in-phase QAM symbols in the same OFDM frame. Extreme values for the OFDM modulating signal are clipped to minimize the effect of nonlinearity at acceptable error margins. The upper and lower clipping values are set to $+3\sigma_x$ and $-3.5\sigma_x$, respectively, where σ_x is the standard deviation of the bipolar OFDM waveform. Asymmetric values for the clipping points are used since the upper clipping was found to be higher than the lower clipping due to the saturation of the m-LED. In addition, asymmetric clipping allows for a higher DC bias to be used, which allows for a higher modulation bandwidth to be achieved by the m-LED[1]. The received waveform is processed with matched filters, fast Fourier transform (FFT) with CPs removal and single-tap equalizer and maximum likelihood decoder. The bit error ratio (BER) is calculated based on the demodulated binary stream.

The continuous-time received OFDM waveform $y(t)$ is given as follows:

$$y(t) = h(t) * z(x(t)) + w(t), \tag{4.1}$$

where $h(t)$ is the channel impulse response of the VLC system, $z(\cdot)$ is the nonlinear transformation of the m-LED and $w(t)$ is the noise process at the receiver. This can be approximated as an additive white Gaussian noise (AWGN) with a variance $\sigma_n^2 = BN_o$, where B and N_o are the single side bandwidth and single side noise power spectral density (PSD), respectively. The used arbitrary waveform generator (AWG) has 10 bits resolution for the digital-to-analog converter (DAC) and the used oscilloscope (MSO 73304DX) has 5.5 bits for the analog-to-digital converter (ADC). The nonlinearity effect from the amplifier is minimal at the operational frequencies and at the injected power levels. The harvested optical power at the photoreceiver is well below the saturation level. Therefore, the m-LED is assumed to be the main source of nonlinearity in the overall system due to the relatively limited dynamic range, compared to other system components. The nonlinear transformation $z(\cdot)$ can be described using the Bussgang theorem which is valid for Gaussian inputs such as the real-valued OFDM waveform. The nonlinear transformation $z(\cdot)$ is given as follows [47, 48]:

$$z(x) = \alpha x + w_c, \tag{4.2}$$

---

[1]High DC bias also results in nonlinearity due to the saturation power of the m-LED. Therefore, a trade-off is required for the DC bias setting

where α is an attenuation factor, w_{c} is the nonlinear distortion noise and $\mathrm{E}[\cdot]$ is the statistical expectation. Without loss of generality, the (t) notation is dropped for presentation simplicity. The nonlinear distortion w_{c} is uncorrelated with the transmitted signal x, $\mathrm{E}[x \cdot w_{\mathrm{c}}] = 0$. The attenuation factor α is a constant that is given as [47,48]:

$$\alpha = \frac{\mathrm{E}[z(x)x]}{\sigma_x^2}. \tag{4.3}$$

The nonlinear distortion w_{c} is a non-Gaussian noise. However, its representation in the frequency domain $W_{\mathrm{c}}(f)$ follows a Gaussian distribution with a mean $\mathrm{E}[w_{\mathrm{c}}]$ and a variance $\sigma_{w_{\mathrm{c}}}^2$. The standard deviation of the clipping noise is given as follows [47,48]:

$$\sigma_{w_{\mathrm{c}}}^2 = \mathrm{E}[w_{\mathrm{c}}^2] - \mathrm{E}[w_{\mathrm{c}}]^2, \tag{4.4}$$

$$\mathrm{E}[w_{\mathrm{c}}^2] = \mathrm{E}[z(x)^2] - \alpha^2 \mathrm{E}[x^2], \tag{4.5}$$

$$\mathrm{E}[w_{\mathrm{c}}] = \mathrm{E}[z(x)]. \tag{4.6}$$

The channel is first estimated using a pilot signal that is composed of multiple OFDM frames. Estimations for the channel and for the SNR are obtained using a conventional mean estimator as described in [26]. The estimated SNR is the ratio of the signal variance to the estimated noise, which is weighted by the estimated channel gain at each of the corresponding subcarriers. The estimated SNR is used to adaptively load the subcarriers with different constellation sizes based on the Levin-Campello algorithm [131]. The algorithm allows for more energy to be allocated to the subcarriers which require minimal additional power to be elevated into larger constellation sizes. This is achieved while preserving the probability of error target P_e^{T}. The adaptive bit and energy loading applies the following optimization problem on each single subcarrier:

$$\underset{b_k}{\text{maximize}} \qquad b_k = \log_2 M_k \quad \forall k = 1, 2, \cdots, \frac{N_{\mathrm{FFT}}}{2} - 1 \tag{4.7a}$$

$$\text{subject to} \qquad \mathrm{BER}\,(M_k, \nu_k) \leq P_e^{\mathrm{T}}, \tag{4.7b}$$

where b_k is the number of bits conveyed at subcarrier k and ν_k is the SNR per bit at

subcarrier k, which is given for large $N_{\text{FFT}} > 64$ as [48]:

$$\nu_k = \frac{\alpha^2}{\dfrac{\sigma_{w_c}^2 \log_2 M_k}{\sigma_x^2} + \dfrac{(1 + k_{\text{DC}}^2)}{E_{\text{b}k}/N_o|H(k)|^2}}, \tag{4.8}$$

where $E_{\text{b}k}$ is the energy per bit at subcarrier k, k_{DC} defines the DC bias in terms of σ_x as given in (2.10) and $|H(k)|^2$ is the channel gain at subcarrier k assuming that a zero forcing (ZF) equalizer is used. The theoretical BER at subcarrier k is given as [98]:

$$\text{BER}(M_k, \nu_k) \cong \frac{4}{\log_2(M_k)} \left(1 - \frac{1}{\sqrt{M_k}}\right) \times \sum_{l=1}^{2} Q\left((2l-1)\sqrt{\frac{3\log_2(M_k)\nu_k}{M_k - 1}}\right), \tag{4.9}$$

where $Q(\cdot)$ is the complementary cumulative distribution function (CCDF) for the standard normal distribution. The overall system BER can be given as:

$$\text{BER} = \frac{\displaystyle\sum_{\substack{k=1 \\ M_k>0}}^{N_{\text{FFT}}/2-1} \text{BER}(M_k, \nu_k) \log_2(M_k)}{\displaystyle\sum_{\substack{k=1 \\ M_k>0}}^{N_{\text{FFT}}/2-1} \log_2(M_k)}. \tag{4.10}$$

The adaptive bit and energy loading on each subcarrier is shown in Fig. 4.3 along with the theoretical limit on the spectral efficiency at subcarrier k which can defined using Shannon capacity as follows [132]:

$$\eta_k^{\text{Sh}} = \log_2\left(1 + \frac{\alpha^2 \sigma_x^2}{\sigma_{w_c}^2 + \dfrac{\sigma_n^2(1 + k_{\text{DC}}^2)}{|H(k)|^2}}\right). \tag{4.11}$$

It is shown that the gap between the exact loading and the capacity limit is already small, however, it can be closed when channel coding is employed. The cumulative distribution function (CDF) of the estimated SNR is presented in Fig. 4.4 for multiple QAM constellation sizes at a BER of 2.3×10^{-3}. The results show the distribution of the SNR values required to achieve a BER below the forward error correction (FEC) target based on the bit and energy loading algorithm.

The CDF of the SNR values that are required to realize a specified BER target is
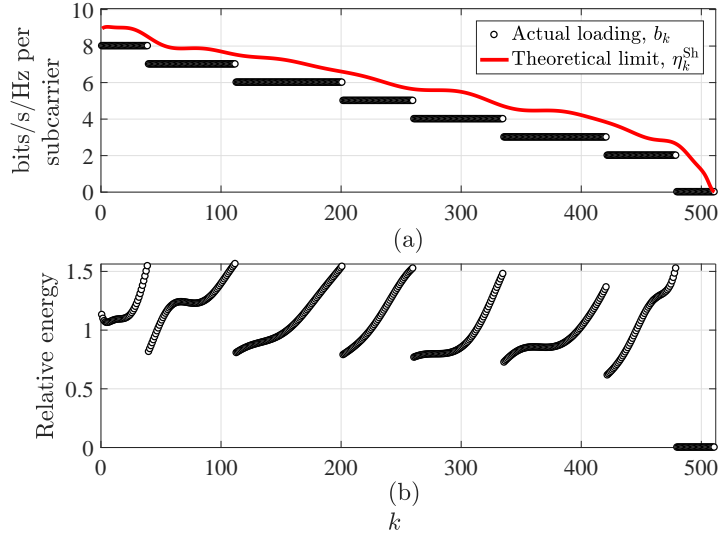
Figure 4.3: *(a) The bit loading and theoretical limit on the spectral efficiency per sub-carrier, both given in bits/s/Hz. (b) Energy loading per subcarrier.*

shown in Fig. 4.5(a) and Fig. 4.5(c) for 4-QAM and 64-QAM, respectively. In addition, the simulation results for real valued bipolar OFDM and DCO-OFDM is shown in Fig. 4.5(b) and Fig. 4.5(d) for 4-QAM and 64-QAM, respectively. The theoretical BER results for real valued OFDM are lower bounds for the CDF results of the experimentally achieved SNR.

4.2.4   Experimental setup

The experimental setup, shown in Fig. 4.6, starts with a laptop connected to an AWG (Tektronix AWG70001A) that has a maximum sampling frequency of 50 GS/s with an ADC resolution of 10 bits per sample. Bipolar OFDM waveforms are generated in MATLAB® as detailed in Section 4.2.3 and then transmitted to the AWG. The maximum peak-to-peak voltage (V_{PP}) of the AWG is 0.5 V. The output of the AWG is amplified with a broadband amplifier (SHF 100AP) that has a maximum gain of 20 dB in the bandwidth range (100 kHz–20 GHz). A 3 dB attenuator is used at the output of the amplifier to allow flexible control of V_{PP}. The power budget of the system is adjusted to allow complete utilization of the m-LED dynamic range shown in Fig. 4.1.

The amplified bipolar signal is DC-biased with a Bias-tee (Mini-Circuits ZFBT-4R2GW+). Low values for the DC bias result in a high zero-level clipping of the OFDM waveform which degrades the SNR. High values for the DC bias result in nonlinearity
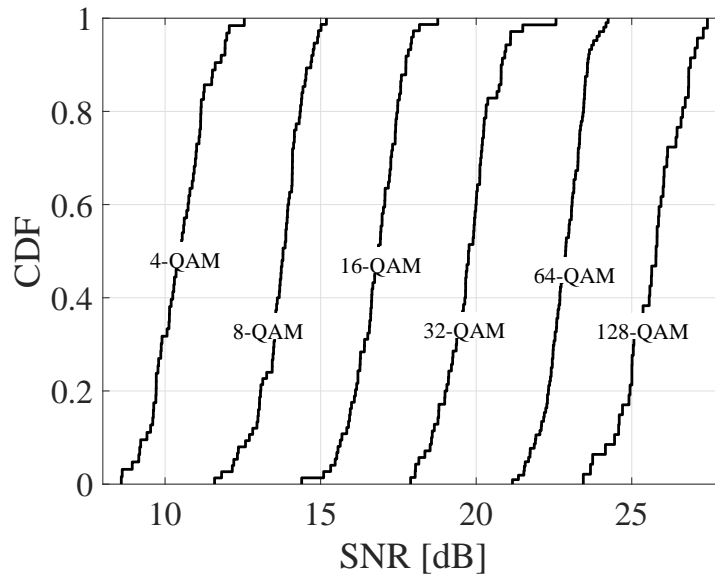
Figure 4.4: *The CDF for different QAM constellation sizes experimentally achieved at a BER=2.3×10^{-3}, below the FEC target.*

due to the optical power saturation at the m-LED which also degrades the SNR. After extensive experiments, the DC bias is set to $I_{DC} = 30$ mA which corresponds to a DC bias voltage of $V_{DC} = 5.23$ V. This value allows the OFDM bipolar signal to swing in the linear region of the L-V characteristic of the m-LED. The biased signal is then fed to the m-LED via a high speed probe. An optical plano-convex lens (Thorlabs LA1116) is used to collimate most of the light into a dielectric mirror (Thorlabs CM1-E02) that has more than 97% reflectance in the desired wavelength region. The reflected light is then focused onto the photoreceiver by a bi-convex lens (Thorlabs LB4879) followed by a microscopic objective lens (NewPort M-40x) with a numerical aperture (NA) of 0.65. A silicon P-type intrinsic N-type photodiode (PIN-PD) photoreceiver is used (Femto HSPR-X-I-1G4-SI) with a 3 dB bandwidth of 1.4 GHz and a responsivity of 0.135 A/W around 400 nm.

4.2.5 Results and discussions

The sampling frequency of the AWG is set to 29 GS/s with an over sampling factor of 8 samples per symbol, which results in a single-sided modulation bandwidth of 1.81 GHz. The subcarriers are equally spaced within the Nyquist rate of the modulation signal with a subcarrier spacing of 3.54 MHz. The high-speed equipment used in the measurements
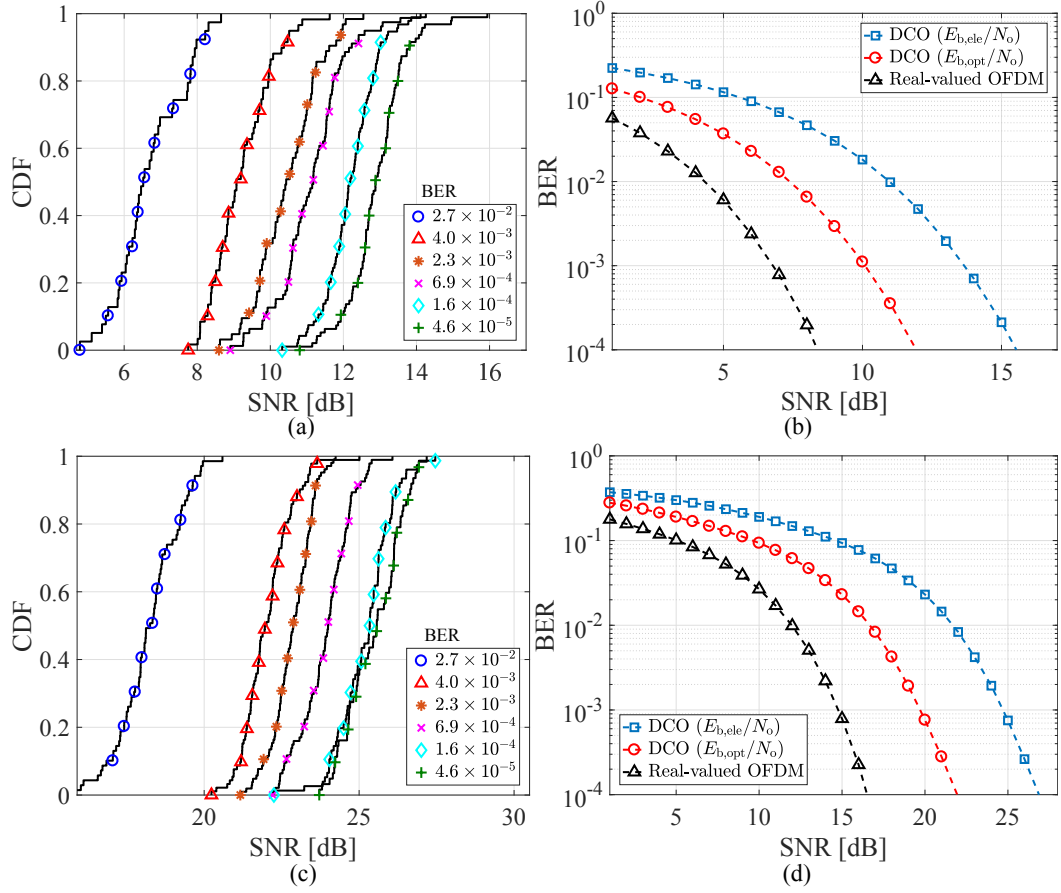
Figure 4.5: *(a) The CDF for 4-QAM at different realized BER. (b) Performance comparison between real-valued and DCO-OFDM (electrical and optical SNR) at 4-QAM. DC biasing levels is estimated at 6 dB as described in* (2.10). *(c) The CDF for 64-QAM at different realized BER. (d) Performance comparison between real-valued and DCO-OFDM (electrical and optical SNR) at 64-QAM. DC biasing levels is estimated at 9.5 dB as described in* (2.10).

allowed for the overall system bandwidth to be limited by the bandwidth of the m-LED. Fig. 4.7 shows the data rates and the corresponding experimentally obtained values for the BER values at different dimming levels. The data rates starts with 3.46 Gb/s at a received optical power, P^{opt} =-4.94 dBm, which corresponds to a DC bias of V_{DC} =4.16 V and a DC bias current of I_{DC} =10 mA. The data rate increases, but starts to saturate as the DC bias increases until it reaches a maximum of 4.91 Gb/s at P^{opt} =-2.29 dBm which corresponds to V_{DC} =5.21 V and I_{DC} =35 mA. The data rate starts to decrease as the DC bias increases beyond 35 mA. This result is expected due to the increased clipping distortion caused by the optical power saturation shown in Fig. 4.1(c).
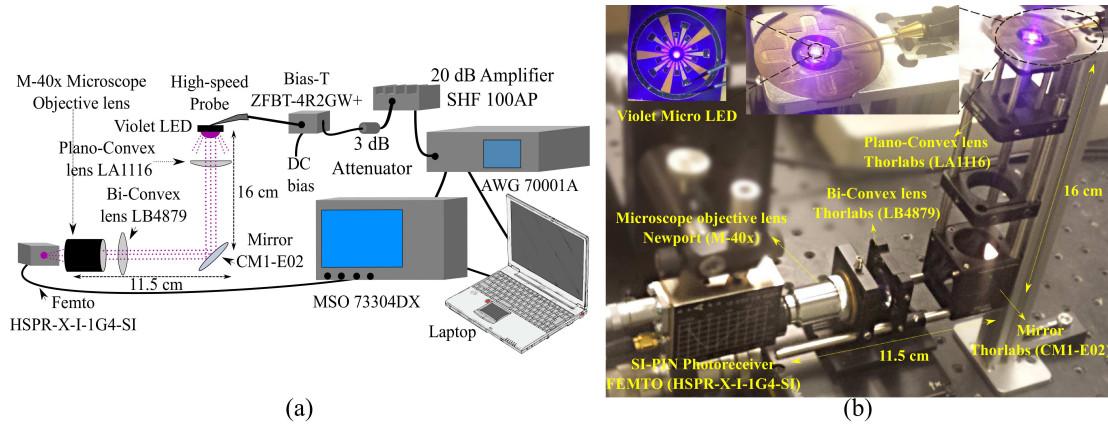
Figure 4.6: *The experimental setup of the violet m-LED based VLC system in Study I. (a) Schematic setup of the experiment showing the optical system, AWG, oscilloscope, amplifier, attenuator and Bias-tee. (b) Photograph of the optical system showing the m-LED, optical lenses system and the photoreceiver.*

The achieved BER for all of the studied cases in this test is well below the 3.8×10^{-3} FEC threshold. The optimized DC bias was selected for the rest of the measurements as V_{DC} =5.11 V and I_{DC} =30 mA, since the system performance for a larger swing of the peak-to-peak modulation signal starts to degrade at I_{DC} =35 mA. The theoretical lower bounds of the BER versus data rates at different dimming levels are shown in Fig. 4.8 with a comparison to the experimental results. The theoretical lower bounds for the BER estimations are calculated based on the experimentally estimated SNR as described in (4.10). These are shown to be close to the experimental results. The deviation between theoretical and experimental validation point at P^{opt} =-4.94 dBm is due to the severe clipping distortion at DC current I_{DC} =10 mA.

The system performance as a function of V_{PP} is investigated in Fig. 4.9. A large modulation signal swing is expected to increase the SNR due to the increased signal power, σ_x^2. Nevertheless, it incurs additional nonlinear distortion, $\sigma_{w_c}^2$, due to the increased clipping. It is shown in Fig. 4.9 that the SNR improves as the modulation depth increases. The nonlinear distortion is present on the first 250 MHz, however the improvement in the signal power σ_x^2 is more significant at higher frequencies. This result is justified by the fact that signals at higher frequencies are attenuated due to the lower channel gain at these high frequencies. Therefore, these values become less affected by the nonlinearity of the device. This result shows that tolerating additional nonlinearity by employing a controlled larger signal swing can improve the communication system

106
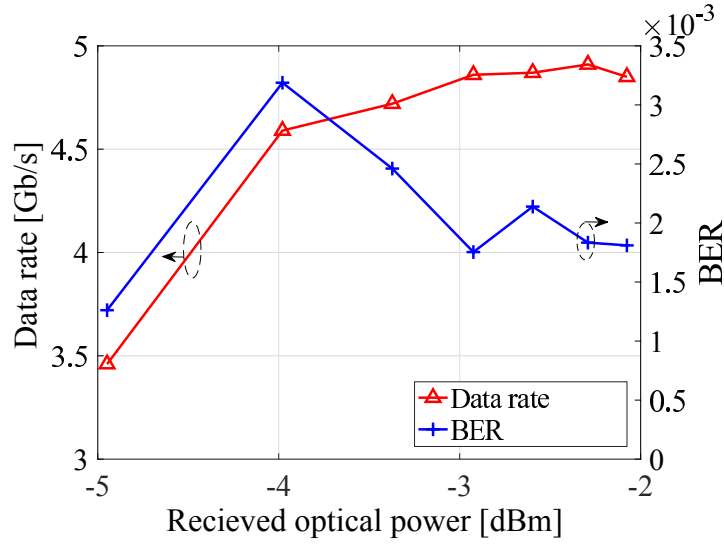
Figure 4.7: *Experimentally obtained results for the data rate and BER versus different dimming levels at a modulation depth of $V_{PP} = 2.36$ V. The values for the received optical power correspond to DC bias values ranging from 10 mA to 40 mA.*

performance.

The experimentally optimized values for the DC bias at 30 mA and the modulation signal swing at 3.88 V_{PP} are used to investigate the system data rate performance against BER. The experimentally obtained data rates versus BERs are presented with the theoretical lower bounds for the BER performance in Fig. 4.10. The theoretical lower bounds are shown to be very close to the experimentally obtained results. As shown in Fig. 4.10, a transmission data rate of 7.91 Gb/s is experimentally achieved at a BER below the FEC threshold, 3.8×10^{-3}. To guarantee reliable communications, the data rate is reduced to 7.36 Gb/s to allow for a 7% FEC overhead to be employed. This compares to 5 Gb/s for a device with a similar design, emitting at 450 nm [33]. To the best of the author's knowledge, this record is the highest for VLCs data transmission speeds using a single m-LED at the time of writing this thesis.

The system data rate performance is investigated when the waveform averaging acquisition mode of the oscilloscope is activated. The averaging acquisition is shown to be useful in drawing conclusions from experimental studies that could influence practical system design [133]. The averaging acquisition mode in this experiment allows for a better characterization of the m-LED by reducing the AWGN of the photoreceiver
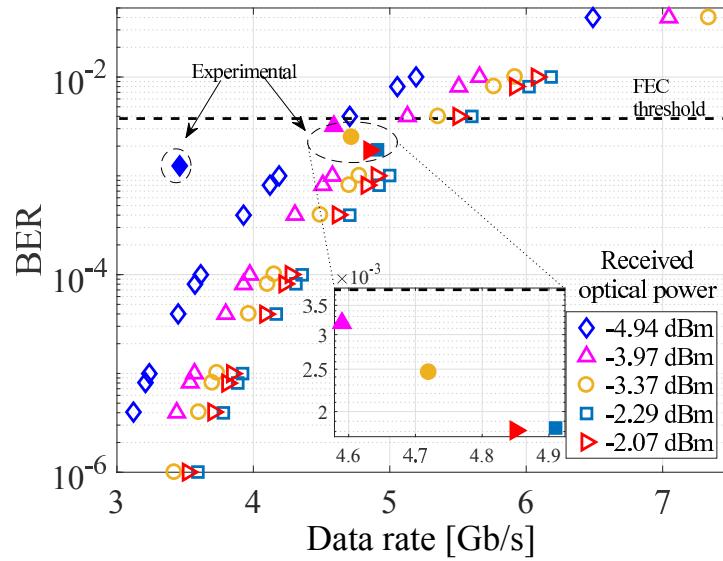
Figure 4.8: *Data rate versus theoretical BER* (4.10) *for different dimming levels at a modulation depth of V_{PP} =2.36 V. The values for the received optical power corresponds to DC bias values ranging from 10 mA to 40 mA. Filled markers denote experimental results.*

which limits the system performance to the nonlinear distortion noise of the m-LED. A detailed analysis on the effect of signal averaging on the SNR is given in Appendix C. It is shown in Fig. 4.10 that data rates up to 11.95 Gb/s are achieved at a BER below the FEC threshold. This is reduced to 11.12 Gb/s when 7% FEC overhead is used. The results for the waveform acquisition mode of the oscilloscope are only presented to show the effect of the nonlinear distortion in the absence of the photoreceiver AWGN noise. All other reported results are conducted without waveform averaging acquisition.

4.2.6 Range and alignment considerations

The VLC system is realized using an optical system to collect, collimate and focus the light on the photodiode (PD). The used optical system imposes restrictions on the link alignment and transmission range. Introducing optimized optics and deploying more m-LED pixels from the array can improve both the coverage and the range of the system. The feasibility of demonstrating long transmission distances was demonstrated at a free-space distance of 10 m and a data rate of 1.1 Gb/s in [134]. This is achieved using an avalanche photodiode (APD) with an integrated concentrator and a m-LED with an optical power of 4.5 mW, which is 1.96 times higher than the optical power of
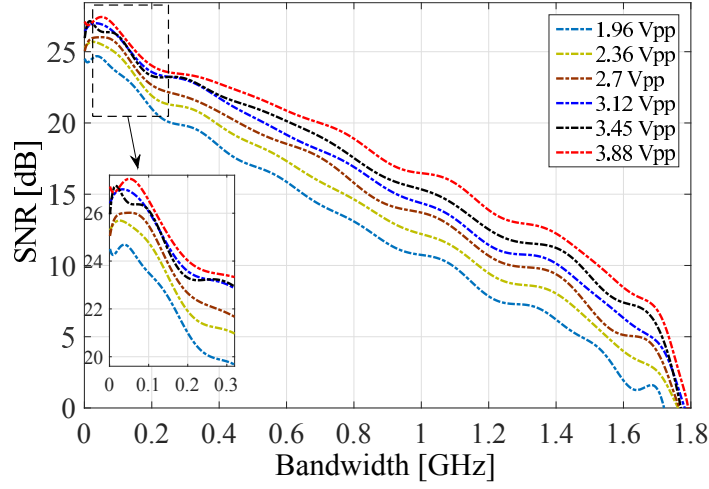
Figure 4.9: *SNR versus frequency for different modulation depths at DC bias current $I_{DC} = 30$ mA. The values for the modulation signal swings corresponds to feeding the m-LED with varying power levels from 5.85 dBm to 11.78 dBm.*

the m-LED pixel used in this chapter.

The obtained data rates and BERs for different received optical power presented in Fig. 4.7 enable us to investigate the system performance against the transmission range based on the widely accepted line-of-sight (LoS) optical wireless communication (OWC) propagation models [19]. The methodology is to compute the distances which result in the respective received optical power presented in Fig. 4.7. These distances are cross-mapped with the data rates achieved in Fig. 4.7. Note that the results shown in Fig. 4.7 are obtained at different dimming levels by varying the DC bias point which limits the operating bandwidth and the experimentally obtained data rates. An analysis of the system range is provided based on four studies: (I-A) using transmitter and receiver lenses; (I-B) using transmitter lens only; (I-C) using receiver lens only and (I-D) without using any optics. All of the array pixels are assumed to be used (15 m-LEDs) in a ganging OFDM mode for all of these studies. In practice, this increases the mutual heat between the pixels and consequently degrades the total aggregate data rates. However, the results in this section can be considered as upper bounds on the system performance in terms of data rates and BER as the device is assumed in this section to be working with idle thermal management.

The LoS channel gain is given in (2.7). The optical power after the transmitter lens
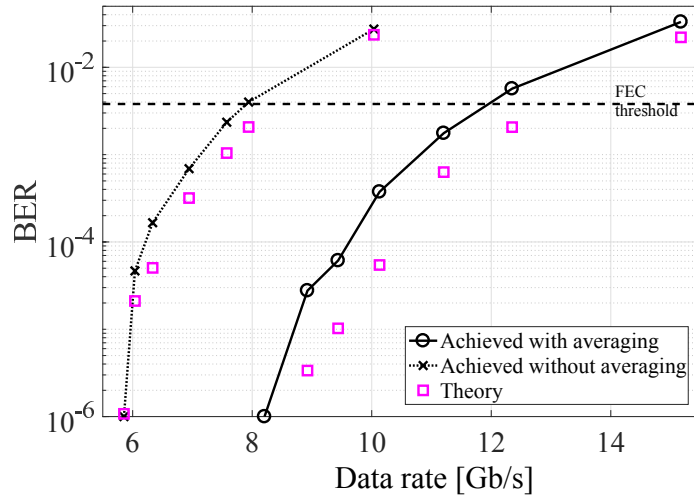
Figure 4.10: *Data rates versus BER for the experimentally obtained and the theoretical bounds at DC bias current I_{DC} =30 mA corresponding to P^{opt} =-2.6 dBm and modulation depth V_{PP} =3.88 V.*

can be given as [135]:

$$P_{\text{opt}}^{\text{R,lens}} = \frac{(m_{\text{mLED}} + 1)D_{\text{lens}}^2}{8d'^2}T_{\text{lens}}P_{\text{opt}}^{\text{T,mLED}}, \tag{4.12}$$

where $P_{\text{opt}}^{\text{T,mLED}}$ is the transmitted power by the m-LED, $m_{\text{mLED}} = -1/\log_2(\cos(\Phi_{1/2}))$ denotes the Lambertian order of the m-LED and $\Phi_{1/2}$ denotes its semi-angle, D_{lens} is the lens diameter, T_{lens} is the transmittance of the lens and d' is the distance between the m-LED and the transmitter lens. The existence of the transmitter lens affects the m-LED beam divergence. The semi-angle at half power $\Phi_{1/2}^{\text{lens}}$ can be given as [136]:

$$\Phi_{1/2}^{\text{lens}} = \frac{D_{\text{s}}}{2d'}, \tag{4.13}$$

where D_{s} is the diameter of the m-LED. The transmitter lens used in this investigation is an aspheric condenser lens (Thorlabs ACL7560U-A) with a diameter of $D_{\text{lens}} = 75$ mm and a focal length of lens $f_{\text{lens}} = 60$ mm.

A commercially available compound parabolic condenser (CPC) is assumed to be in front of the APD. The field of view (FOV) of the concentrator is 25°, with a refractive index of $n_{\text{c}} = 1.5$. We assume the use of a high speed commercially available APD at the receiver (Thorlabs APD210) instead of the used PIN-PD receiver (Femto HSPR-X-I-1G4-SI). The APD diameter is 0.5 mm and the modulation bandwidth is 1.6 GHz.
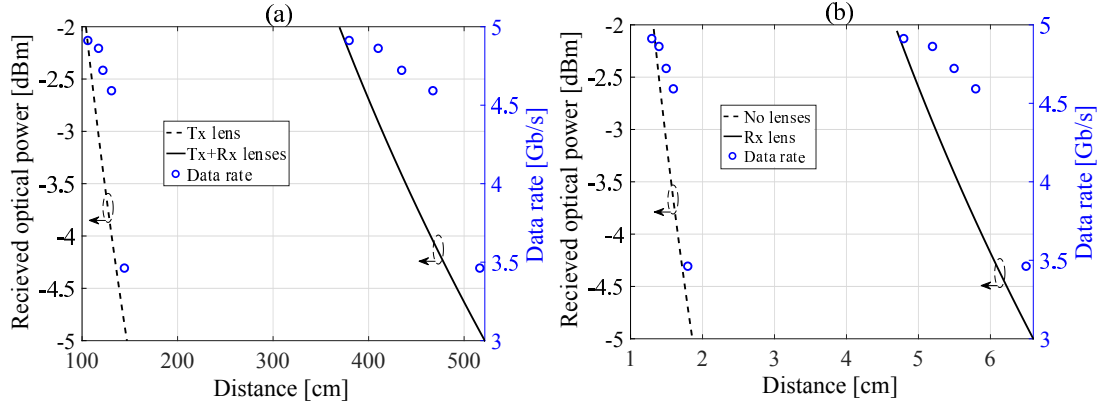
Figure 4.11: *(a) Distance versus received optical power (left axis – simulation) and data rate (right axis – simulation based on extrapolation) for Study I-A with transmitter and receiver lenses and Study I-B with transmitter lens only. (b) Distance versus received optical power (left axis) and data rate (right axis) for Study I-C with receiver lens only and Study I-D without any optics.*

The APD improves the sensitivity of the receiver, therefore an APD conversion gain factor is introduced to allow a fair comparison between the experimentally obtained results using the PIN-PD and the numerical results using the APD photoreceivers:

$$\Lambda^{\text{APD}} = \frac{G^{\text{APD}}}{G^{\text{PIN}}}, \tag{4.14}$$

where G^{APD} and G^{PIN} are the conversion gains of the APD and PIN-PD photoreceivers given in V/W, respectively. Using (2.2), (2.7), (4.12),(4.13) and (4.14), the received optical power at the APD can be given as:

$$P_{\text{opt}}^{\text{R,APD}} = \frac{(m_{\text{lens}} + 1)A_{\text{d}}}{2\pi d_{\text{E}}^2} \cos^{m_{\text{lens}}}(\phi)T(\psi)g(\psi)\cos(\psi)\Lambda^{\text{APD}} P_{\text{opt}}^{\text{R,lens}}, \tag{4.15}$$

where m_{lens} is the Lambertian order of the lens based on (4.13); A_{d} is the detection area of the APD; d_{E} is the Euclidean distance between the transmitter lens and the APD; ϕ is the angle of irradiance; ψ is the angle of incidence; $T(\psi)$ represents the gain of the optical filter used at the receiver and $g(\psi)$ represents the gain of the optical concentrator that is given in (2.2). The LoS propagation model is used to compute the transmission ranges that can achieve certain values for the received optical power between -5 dBm and -2 dBm. These values for the received optical power were demonstrated experimentally to achieve data rates between 3.46 Gb/s and 4.91 Gb/s using the experimentally realized

111
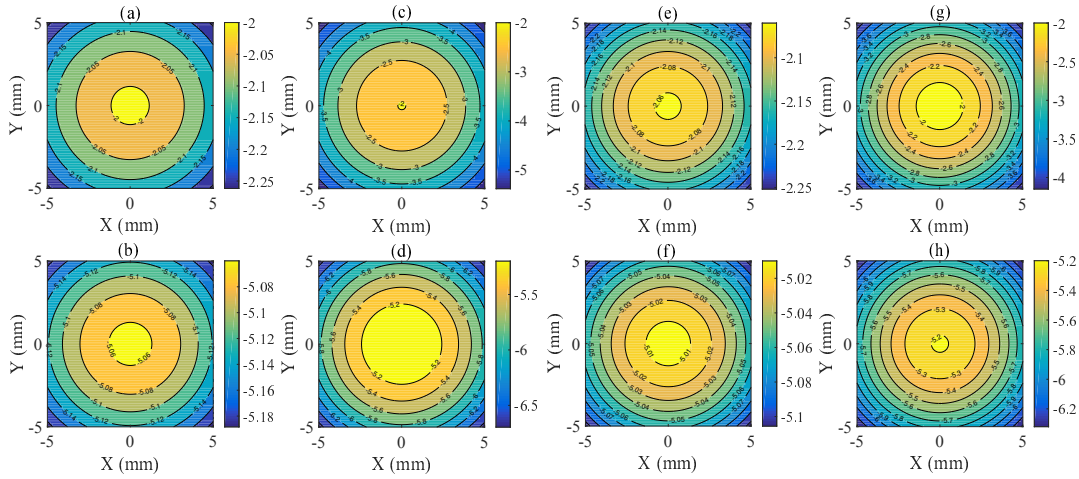
Figure 4.12: *Received optical power distribution in dBm as a function of vertical-horizontal displacements. (a) Study I-A at a distance of 369 cm; (b) Study I-A at a distance of 525 cm; (c) Study I-B at a distance of 104 cm; (d) Study I-B at a distance of 147 cm; (e) Study I-C at a distance of 4.7 cm;(f) Study I-C at a distance of 6.6 cm;(g) Study I-D at a distance of 1.3 cm; (h) Study I-D at a distance of 1.9 cm.*

VLC system. An upper bound on the data rates can be estimated by cross-mapping the computed received power at each distance, with the experimentally obtained data rates provided in Fig. 4.7. The distance versus received optical power and data rate for Study I-A and Study I-B are shown in Fig. 4.11(a), while Fig. 4.11(b) shows the same but for Study I-C and Study I-D. The longest distances can be achieved using the transmitter and receiver optics. Specifically, it was found that a data rate of 4.91 Gb/s can be achieved at a distance of 3.69 m. This data rate reduces to 3.46 Gb/s at 5.25 m distance. The transmitter lens is shown to boost the range more than the receiver concentrator lens. At a data rate of 4.91 Gb/s, the maximum distance is 1.04 m and 4.7 cm for studies I-B and I-C, respectively. At a data rate of 3.46 Gb/s, the maximum distance is 1.47 m and 6.6 cm for studies I-B and I-C, respectively. The transmission ranges that can be supported at data rates above 3.46 Gb/s are less than 2 cm when optics are not used.

The received optical power distribution is investigated as a function of the receiver's vertical-horizontal misalignment for the four considered studies, as shown in Fig. 4.12. The results are presented for the received optical power values that allow a maximum of -2 dBm and a minimum of -5 dBm, corresponding to data rates of 4.91 Gb/s and 3.46 Gb/s, respectively. The transmission range and the system robustness against

misalignment are both improved when optics are used for both front-end components in Study I-A, which makes this scenario suitable for high-speed point to point applications. The transmitter lens in Study I-B improves the transmission range but reduces the system robustness against misalignment. The receiver lens in Study I-C reduces the performance degradation caused by misalignment at the expense of a reduction in the system range. The transmission range and the system robustness against misalignment are both degraded in Study I-D. Studies I-C and I-D are suitable for applications such as board to board communication links [126, 127].

4.3   Study II: VLC system using a blue LD

There has been a growing interest in the use of LDs for VLC as detailed in Section 2.4.1.3. The motivation is mainly driven by the high modulation bandwidth of LDs which enables Gb/s VLC. An experimental investigation of a VLC system is presented in this study with a record data-rate reported at 15 Gb/s using a blue LD.

4.3.1   The aim of this study

The aim of this study is to demonstrate a high speed VLC system based on DCO-OFDM using a high bandwidth blue LD. There is an increasing interest in the use of blue LDs in underwater communications due to the relatively lower optical attenuation of the optical signals propagating around 450 nm compared to the other wavelength bands. In addition, they are also an emerging solution for general lighting when combined with yellow phosphor or other color converters.

4.3.2   Experimental setup

The used device is a commercially-available blue LD (Osram PL450B) with a peak optical power at 80 mW [137]. The frequency response of the LD is presented in Fig. 4.13. The 3 dB bandwidth is shown to be relatively similar for the considered DC bias. The highest 3 dB bandwidth is witnessed at 1.03 GHz with a DC current $I_{\text{DC}} = 65$ mA. A difference of 30 MHz exists between the 3 dB bandwidth of the considered lowest and highest used DC bias $I_{\text{DC}} = 55$ mA and $I_{\text{DC}} = 65$ mA. However, the frequency response at $I_{\text{DC}} = 65$ mA above 1 GHz is higher than the frequency
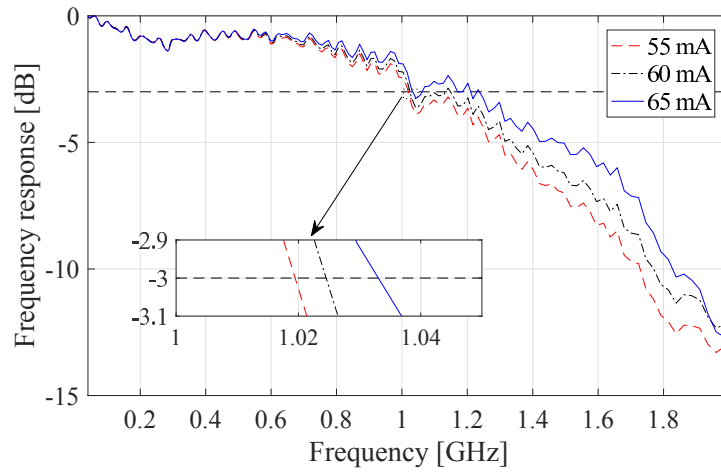
Figure 4.13: *Frequency response for the blue laser at different DC bias levels.*

response of the other considered DC bias levels. The device performance at higher DC bias values is degraded significantly and is not reliable to be utilized at values higher than $I_{DC} = 65$ mA due to heat.

The system performance was investigated at 15 cm and 197 cm link distances. The experiment at these two distances will be referred to throughout this section as Study II-A and Study II-B, respectively. The experimental setup is presented in Fig. 4.14(a) for Study II-A and the photograph of the setup is presented in Fig. 4.14(b) for Study II-B. A bipolar OFDM waveform is generated using (Tektronix AWG70001A) at a sampling frequency of F_s =40 GS/s. This corresponds to a single side modulation bandwidth of B =2.5 GHz as an oversampling factor of 8 samples per symbol is used. The used modulation technique in Study II is similar to the DCO-OFDM technique detailed in Section 4.2.3 for Study I. The generated OFDM waveform has a peak-to-peak voltage of $V_{PP} = 500$ mV. This was found to be a good choice after exhaustive tests based on the L-V characteristic of the used blue LD [137]. The generated waveform is biased afterwards using a bias-tee (Mini-Circuits ZFBT-4R2GW+), before it is fed to the blue LD. The DC bias is selected at $I_{DC} = 65$ mA because it achieves the highest frequency response compared to the other considered bias values. The used high speed receiver is similar to the photoreceiver used in Study I, (Femto HSPR-X-I-1G4-SI) with a 3 dB bandwidth at 1.4 GHz. The optical system for Study II-A is comprised of two microscopic objective lenses located at the LD side and at the receiver side. The small numerical aperture of these lenses results in a narrow FOV which requires a precise alignment. The only difference between the experimental setup of Study II-A and
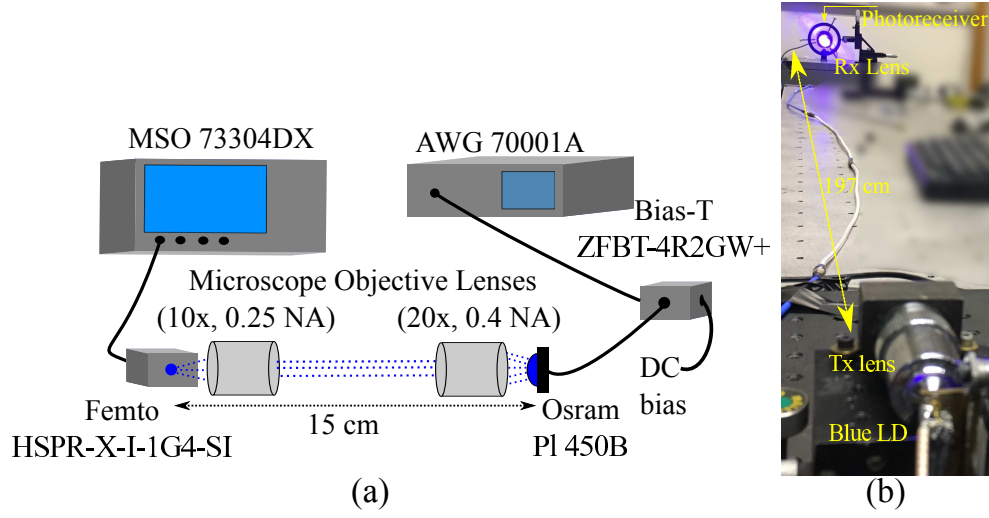
Figure 4.14: *The experimental setup of Study II. (a) Schematic setup of the experiment showing the optical system, AWG, oscilloscope, blue laser, photoreceiver and Bias-tee at 15 cm link distance. NA denotes numerical aperture (b) Photograph of the experiment at 197 cm link distance showing the Blue laser, optical lenses system and the photoreceiver.*

Study II-B is in the optical lens at the receiver. The objective lens used in Study II-A is replaced with an aspheric condenser lens with a diameter of 7.5 cm and a numerical aperture of 0.61 (Thorlabs ACL7560U) in Study II-B. This can enable a more relaxed FOV VLC link. The detected signal by the photoreceiver is captured at oscilloscope (MSO 73304DX) and processed afterwards using MATLAB$^{\circledR}$.

4.3.3 Results and discussions

Adaptive bit and energy loading is used as described in Section 4.2.3. This allows the system loading to be maximized based on the available SNR while preserving the probability of error target P_e^{T}. The SNR of the VLC system in Study II-B is shown in Fig. 4.15 at multiple received optical power levels P_{opt}. The DC bias is set at $I_{\mathrm{DC}} =65$ mA and the received optical power is controlled using optical neutral density filters. The increase in the SNR starts to saturate when the received optical power is higher than 1 dBm. This indicates that the SNR beyond 1 dBm of received optical power becomes limited by the noise floor of the photoreceiver. The dip at 1 GHz also appears in the frequency response diagram shown in Fig. 4.13, and therefore it can be attributed to the LD response.
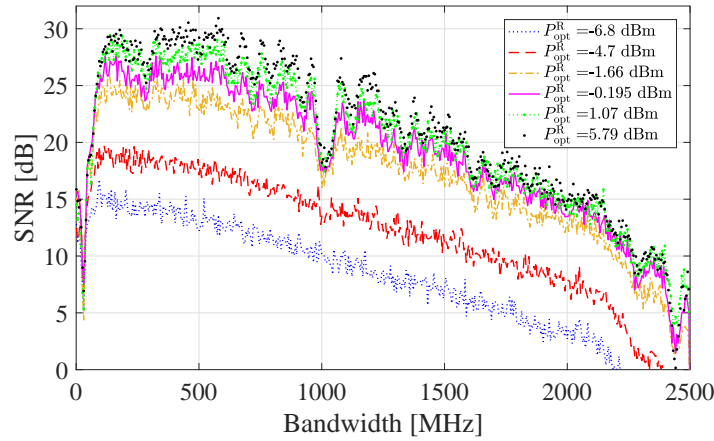
Figure 4.15: *SNR versus frequency at DC bias current $I_{DC} = 65$ mA for Study II.*
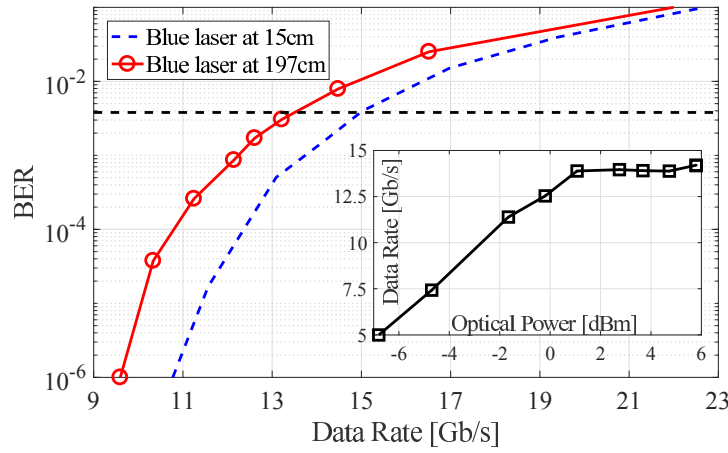
Figure 4.16: *Data rate versus BER for Study II at 15 cm and 197 cm. The inset shows the data rate versus the optical power Study II.*

The high SNR makes it possible for large constellation sizes of QAM modulation to be used. This allows for the high data rate at 15 Gb/s to be possible in Study II-A. The BER is presented in Fig. 4.16 as a function of the achieved data rate. A data rate of 15 Gb/s can be achieved below the FEC target at a link distance of 15 cm in Study II-A. This corresponds to an error-free data rate of 13.95 Gb/s after deducting the 7% FEC overhead. The achieved data rate is slightly reduced to a 13.5 Gb/s at a longer link distance of 197 cm in Study II-B. The system performance was analyzed at a range of received optical power levels as presented in the inset of Fig. 4.16. The increase in the achieved data rate is modest as the received optical power increases beyond 1 dBm. Therefore, the small reduction from 15 Gb/s to 13.5 Gb/s is expected as the received optical power at 197 cm is measured at 3 dBm.

4.4 Study III: spectrum and energy efficient superposition modulation

An experimental study on the performance of the superposition modulation technique that is proposed in Section 3.4 is presented in this section. The proposed ASE-DMT is compared with DCO-OFDM using two different transmitters, a blue LED (Vishay VLMB1500) and IR VCSEL (OPV300). The I-V, L-I and L-V characteristic functions for both the blue LED and the IR VCSEL are shown in Fig. 4.17(a-c) and Fig. 4.18(a-c), respectively. The forward voltage values for the blue LED and the IR VCSEL are 2.65 V and 1.7 V, respectively. The L-V characteristic function of the blue LED in Fig. 4.17(c) is shown to exhibit higher nonlinearity in comparison with the L-V characteristic function of the IR VCSEL in Fig. 4.18(c). Therefore, the sensitivity of ASE-DMT and DCO-OFDM to the nonlinearity can be investigated by comparing the results of the blue LED and the IR VCSEL.

4.4.1 The aim of this study

The aim of this study is to investigate and evaluate the experimental performance of the proposed superposition modulation scheme that is presented in Chapter 3. The energy efficiency of ASE-DMT is demonstrated as a solution to the IR based uplink of LiFi systems. In addition, it is shown that ASE-DMT offers a high speed solution for the dimming applications in VLC systems.
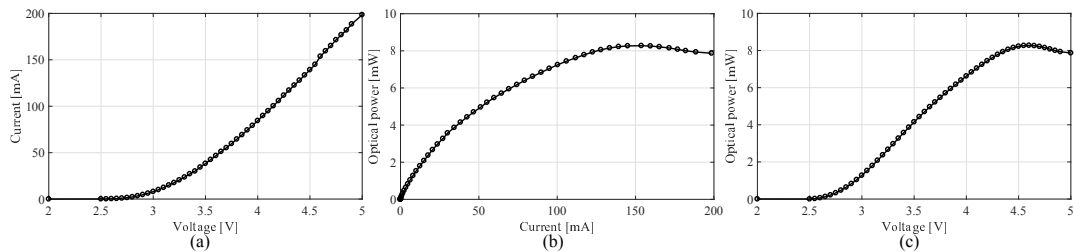
Figure 4.17: *(a) current-voltage, (b) luminescence-current and (c) luminescence-voltage characteristics of the blue LED used in Study III.*
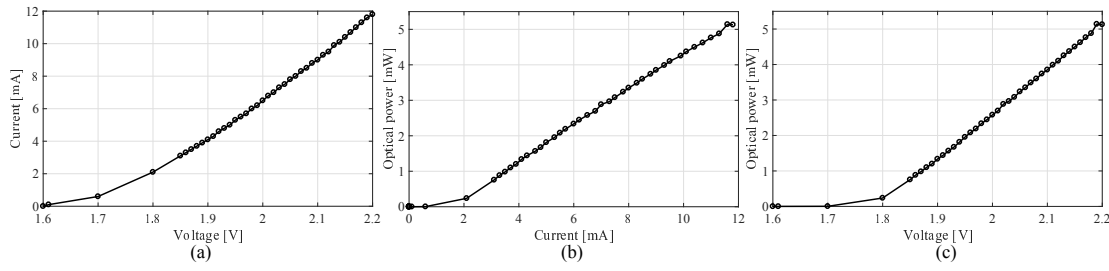
Figure 4.18: *(a) current-voltage, (b) luminescence-current and (c) luminescence-voltage characteristics of the IR VCSEL used in Study III.*

4.4.2 An implementation of ASE-DMT

The generation of both DCO-OFDM and ASE-DMT modulated signals is performed in MATLAB$^{\circledR}$. The implementation of DCO-OFDM is similar to implementation presented in Section 4.2.3 for Study I and Study II. A pseudo-random series of bits are encoded into M-ary pulse-amplitude modulation (M-PAM) symbols. The performance of M-PAM in ASE-DMT is compared with the performance of M^2-QAM DCO-OFDM in this section. The spectral efficiency of ASE-DMT increases as the total number of modulation depths D increases as shown in Fig. 4.19. For example, the spectral efficiency of ASE-DMT when $D = 4$ is 94% of the spectral efficiency of DCO-OFDM. Therefore, an excess bandwidth is allocated for the ASE-DMT signals to allow the performance comparison with DCO-OFDM to be performed at the same data rate.

The ASE-DMT stream at the first modulation depth $d = 1$ is exactly equivalent to a pulse-amplitude modulation discrete multitone modulation (PAM-DMT) stream [24]. Therefore, the implementation of ASE-DMT with one modulation depth $D = 1$ is identical to a PAM-DMT implementation. The modulated pulse-amplitude modulation (PAM) symbols are loaded on the imaginary component of the subcarriers at the first modulation depth of an ASE-DMT modulator. A further $D - 1$ streams can be superimposed on the first modulation depth without any distortion by loading the PAM symbols on the real-valued component of the subcarriers, as described in Section 3.4.

The modulation signals of DCO-OFDM and ASE-DMT are both clipped to fit within the dynamic range of the used DAC and the considered transmitter device. The clipping results in a limited distortion that is controlled by the upper and lower clipping points [86]. The DCO-OFDM modulation signal is clipped to both upper and a lower clipping points given at $\pm 3.2\sigma_x$. These values were experimentally found to achieve the best
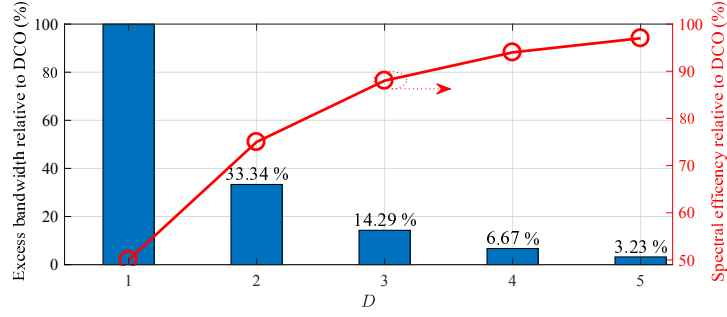
Figure 4.19: *The excess bandwidth required in ASE-DMT relative to DCO-OFDM as a function of the total number of modulation depths D.*

BER performance after exhaustive experiments. The ASE-DMT modulation signal is unipolar. Therefore, the lower clipping is set to zero and the upper clipping is set to $6.4\sigma_x$ to allow for a fair comparison at an equivalent quantization noise with DCO-OFDM.

The OFDM frame length is set to $N_{\text{FFT}} = 1024$ and the cyclic prefix length is set to $N_{\text{CP}} = 5$ for both DCO-OFDM and ASE-DMT. These values were selected based on the BER performance after extensive experiments. However, relatively small variations of these two values have marginal effect on the overall system performance.

An estimation of the channel and the achievable SNR over the utilized bandwidth is established for ASE-DMT and DCO-OFDM using a conventional mean estimator [26]. A zero-forcing equalizer is used to maintain a relatively constant SNR over all of the considered subcarriers. The equalization is performed on the frequency-domain representation of the received ASE-DMT signal. As a result, the demodulation of the symbols at the different modulation depths is performed in the frequency domain as detailed in Section 3.4.

4.4.3 Experimental setup

The experimental setup is shown in Fig. 4.20(a) for the VLC system using both the blue LED and the IR VCSEL. The photograph in Fig. 4.20(b) shows the experimental setup using the blue LED. The digital modulation signals are generated in MATLAB® and converted into analogue signals using the AWG (Agilent 81180A) which has a peak sampling frequency of 4.2 GS/s. The peak-to-peak voltage (V_{PP}) is set to 2 V for both the blue LED and to 125 mV for the IR VCSEL. The ASE-DMT modulation signal
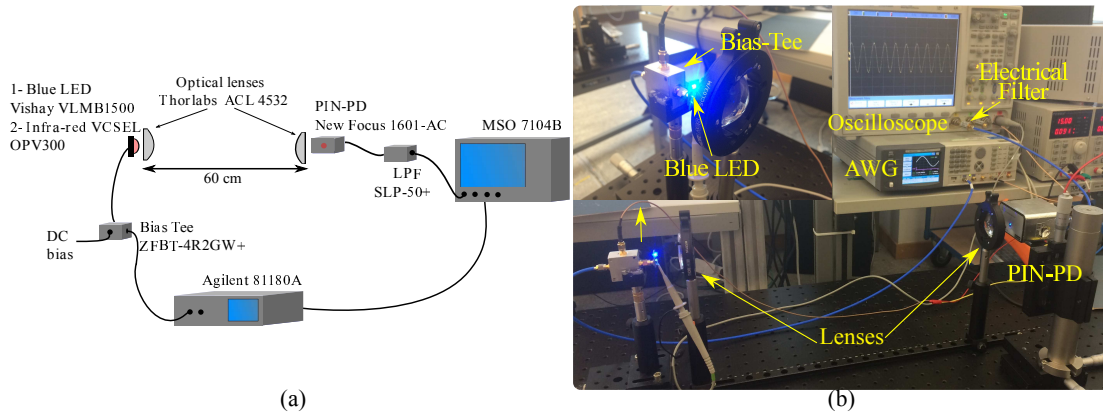
Figure 4.20: *The experimental setup of the ASE-DMT evaluation experiment in Study III. (a) Schematic setup of the experiment showing the optical system, AWG, oscilloscope, electrical filter and Bias-tee. (b) Photograph of the optical system showing the blue LED, optical lenses system and the photoreceiver.*

is inherently unipolar. However, it is mapped to a bipolar signal at the DAC as the AWG is unable to generate unipolar outputs. The AWG generates bipolar outputs with a DAC range between $-V_{\mathrm{PP}}/2$ and $V_{\mathrm{PP}}/2$. A DC bias is added to the modulation signals using a bias-tee (Mini-Circuits ZFBT-4R2GW+). The DC bias is required for the unipolar ASE-DMT signal due to the bipolarity of the AWG and the turn-on voltage of the used SSLs devices.

An optical system of two identical aspheric lenses (Thorlabs ACL 4532) is used at the photoreceiver and the transmitter ends. The communications link distance is 60 cm and the photoreceiver is a high speed PIN-PD with a 3-dB bandwidth of 1 GHz. An electrical low pass filter (SLP-50+) is used at the receiver with a pass-band between DC and 48 MHz to block any high-frequency radio frequency (RF) interference. The received signal is captured afterwards at the oscilloscope (Agilent MSO7104B) that has a 3-dB bandwidth of 1 GHz. The received signal is processed afterwards using MATLAB$^{\circledR}$.

The comparison between ASE-DMT and DCO-OFDM is achieved at the same data rate by increasing the sampling frequency of ASE-DMT based on the considered total number of modulation depths D. For example, the sampling frequency of ASE-DMT with $D = 4$ is set to 512 MS/s which corresponds to a single side bandwidth of 32 MHz since a RRC pulse shaping filter is used with an oversampling factor of 8 for both

DCO-OFDM and ASE-DMT. This is compared with a sampling frequency of 480 MS/s for DCO-OFDM which corresponds to a single side bandwidth of 30 MHz. The excess bandwidth required for ASE-DMT is shown in Fig. 4.19 as a function of the total number of modulation depths D.

ASE-DMT can additionally be realized by employing arbitrary constellation sizes to close any remaining spectral efficiency gap with a maximum of three modulation depths as detailed in Section 3.6. This solution is particularly useful for the cases where the excess bandwidth is not practically available due to the frequency profile constraints of the considered VLC system. However, the excess bandwidth required for $D > 3$ is marginal as shown in Fig. 4.19.

4.4.4 Results and discussions

The experiment is conducted using both the blue LED and the IR VCSEL for both DCO-OFDM and ASE-DMT. The performance of ASE-DMT is measured for a total number of depths $D = \{1, 3\}$ when using the IR VCSEL and for $1 \leq D \leq 5$ when using the blue LED. Note that D refers to the total number of modulation depths of the ASE-DMT waveform whereas d refers to the index of the superimposed stream at the modulation depth d, given that $1 \leq d \leq D$.

The BER and average SNR are measured for both DCO-OFDM and ASE-DMT against the DC bias voltage V_{DC}, average electrical power $P_{\mathrm{elec}}^{\mathrm{avg}}$ and average optical power $P_{\mathrm{opt}}^{\mathrm{avg}}$. The voltage signal applied on the considered transmitter device by the AWG is captured by the oscilloscope during the transmission period. The corresponding I-V curve is used to estimate the corresponding current values. These allow for the average electrical power to be estimated for each of the used modulation signals using both the blue LED and the IR VCSEL. The average optical power is measured using the spectral irradiance head (Labsphere E1000) and the monochromatic optical power meter (Thorlabs S121C).

The BER performance for each of the superimposed streams of a 4-PAM ASE-DMT modulation with $D = 5$ is presented as a function of the average electrical power of the blue LED in Fig. 4.21. The average BER is calculated based on the relative spectral efficiency contribution of each of the modulation depths as described in (3.41). The incorrectly decoded bits at lower order depths translates into further errors at
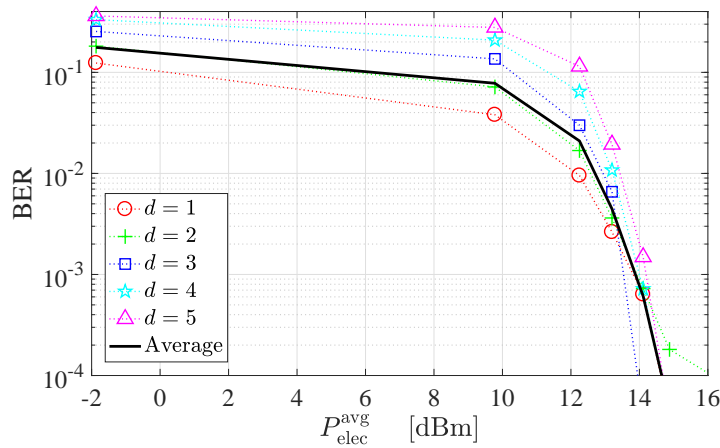
Figure 4.21: *The BER as a function of the average electrical power $P_{\text{elec}}^{\text{avg}}$ for each of the five superimposed modulation depths of a 4-PAM ASE-DMT waveform with $D = 5$. This is obtained for the blue LED based system in Study III.*

higher order depths. This is similar to error propagation shown for the theoretical and simulation-based results in Fig. 3.8.

The BER performance is shown to degrade as the modulation depth order d increases. However, the BER performance for all of the modulation depths converges to a similar BER value as the average electrical power increases. At high electrical average power, the error propagation becomes insignificant to affect the BER performance at the higher modulation depth orders. This is due to the decrease in the number of wrongly decoded bits at the lower modulation depth orders. The average BER performance is shown to be heavily affected by the BER performance of the lower orders of modulation depths due to their higher relative spectral efficiency contribution. However, it is also shown that the average BER converges to the same BER as the average electrical power increases. The number of transmitted PAM symbols at high modulation depth orders is small due to the selective loading algorithm described in Section 3.4 as well as the limited memory size of the AWG. This affects the statistical significance of the results at low BER values. In addition, it explains the slight deviation of the BER results of the stream at the modulation order $d = 4$ shown in Fig. 4.21.

The experimental BER performance for ASE-DMT and DCO-OFDM is investigated using the IR VCSEL in Fig. 4.22 as a function of the DC bias voltage. The performance is given in Fig. 4.22(a) for ASE-DMT with $D = 1$ and in Fig. 4.22(b) for ASE-DMT
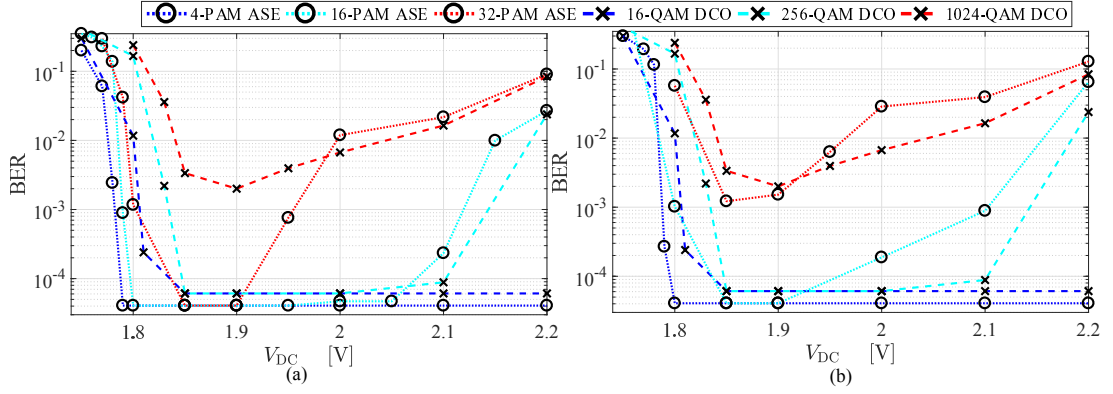
Figure 4.22: *The BER versus bias voltage V_{DC} of the IR VCSEL based system in Study III for 4-PAM ASE-DMT (120 Mb/s), 16-PAM ASE-DMT (240 Mb/s) and 32-PAM ASE-DMT (300 Mb/s) compared with 16-QAM DCO-OFDM (120 Mb/s), 256-QAM DCO-OFDM (240 Mb/s) and 1024-QAM DCO-OFDM (300 Mb/s), respectively. The total number of depths used for ASE-DMT is (a) $D = 1$ (b) $D = 3$. The forward voltage of the IR VCSEL is 1.7 V.*

with $D = 3$. The performance presented for ASE-DMT when $D = 1$ is equivalent to the performance of PAM-DMT.

The performance comparisons are presented at equivalent data rates for both ASE-DMT and DCO-OFDM. The BER performance of ASE-DMT with 4-PAM, 16-PAM and 32-PAM is compared with the BER performance of DCO-OFDM with 16-QAM, 256-QAM and 1024-QAM, respectively. These constellation sizes correspond to 120 Mb/s, 240 Mb/s and 300 MB/s, respectively. The BER performance of ASE-DMT when $D = 1$ is shown to be better than the BER performance of DCO-OFDM at DC bias below 2 V. The DC bias required to achieve a BER at 3.8×10^{-3} in 4-PAM ASE-DMT is 24.5 mV less than the bias required for 16-QAM DCO-OFDM. This is improved to 38.2 mV when 16-PAM ASE-DMT is compared with 256-QAM DCO-OFDM and to 52.25 mV when comparing 32-PAM ASE-DMT with 1024-QAM DCO-OFDM.

The BER performance of both ASE-DMT and DCO-OFDM improves as the DC bias increases up to the point where the increments in the DC bias results in significant signal clipping distortions which leads to an increased BER. The performance of DCO-OFDM at a DC bias higher than 2 V is shown to be better than the BER of ASE-DMT. The probability density function (PDF) of ASE-DMT when $D = 1$ is given as a truncated Gaussian distribution [53]. Therefore, the deterioration in the BER performance of

ASE-DMT at a high DC bias can be explained by the fact that the clipping distortion due to the upper clipping point is higher in ASE-DMT than it is in DCO-OFDM.

The performance of 4-PAM ASE-DMT and 16-QAM DCO-OFDM reaches the floor of the BER at a bias of 1.8 V. The floor of the BER is bounded by the number of transmitted symbols due to the limited memory size of the AWG. The clipping due to the upper clipping point of the L-V characteristic of the IR VCSEL does not deteriorate the performance of 4-PAM ASE-DMT and 16-QAM DCO-OFDM. Similar trends are shown in Fig. 4.22(b) for ASE-DMT with $D = 3$. The DC bias required to achieve a BER at 3.8×10^{-3} in 4-PAM ASE-DMT is 17.3 mV less than the bias required for 16-QAM DCO-OFDM. This is improved to 35.1 mV when 16-PAM ASE-DMT is compared with 256-QAM DCO-OFDM and to 13.75 mV when comparing 32-PAM ASE-DMT with 1024-QAM DCO-OFDM. The reduction in the DC bias requirements of ASE-DMT implies a reduction in the electrical and optical power requirements in comparison with DCO-OFDM.

The sensitivity of ASE-DMT to the limitation of the dynamic range of the LD is higher when $D = 3$ than it is when $D = 1$. This indicates that the clipping distortion is more detrimental to the performance of ASE-DMT as D increases. The BER performance of ASE-DMT when $D = 1$ is better than the BER performance of ASE-DMT when $D = 3$. However, this comes at the price of using 85.71% extra excess bandwidth as shown in Fig. 4.19.

The BER performance of 8-PAM ASE-DMT is given for $1 \leq D \leq 5$ in Fig. 4.23 as a function of the DC bias using the blue LED. This is compared at a data rate of 180 Mb/s with 64-QAM DCO-OFDM. The performance trends are similar to the results presented in Fig. 4.22. ASE-DMT requires less DC bias to achieve the same BER, as expected. However, the performance degrades at a high DC bias due to the clipping distortion. A bias at 3.5 V is shown to result in the lowest BER values for both ASE-DMT and DCO-OFDM. A bias above than 3.5 V is shown to degrade the BER due to the upper-level clipping of the L-V characteristic of the blue LED. The PDF of DCO-OFDM is symmetric around the biasing point. However, ASE-DMT has a heavy tail that results in a higher distortion due to the increased upper-level clipping. ASE-DMT is shown to be more sensitive to the upper-level clipping distortion of the blue LED due to the heavy tail of the PDF. The BER performance of ASE-DMT with
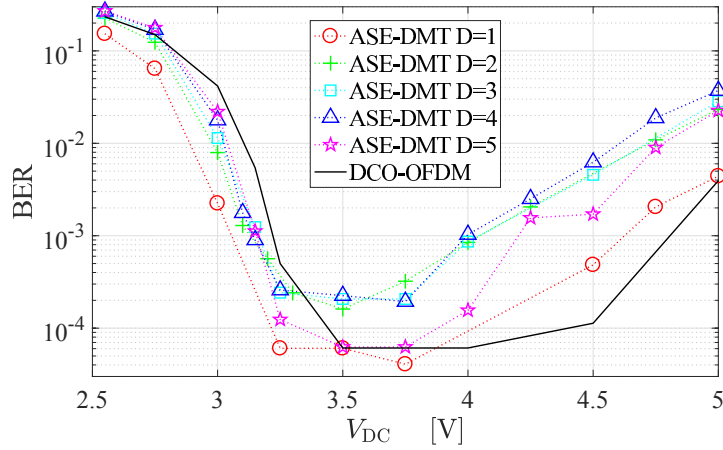
Figure 4.23: *The BER versus bias voltage V_{DC} of the blue LED based system in Study III for 8-PAM ASE-DMT with a total number of depths used for ASE-DMT $1 \leq D \leq 5$ (180 Mb/s) compared with a 64-QAM DCO-OFDM (180 Mb/s). The forward voltage of the blue LED is 2.65 V.*
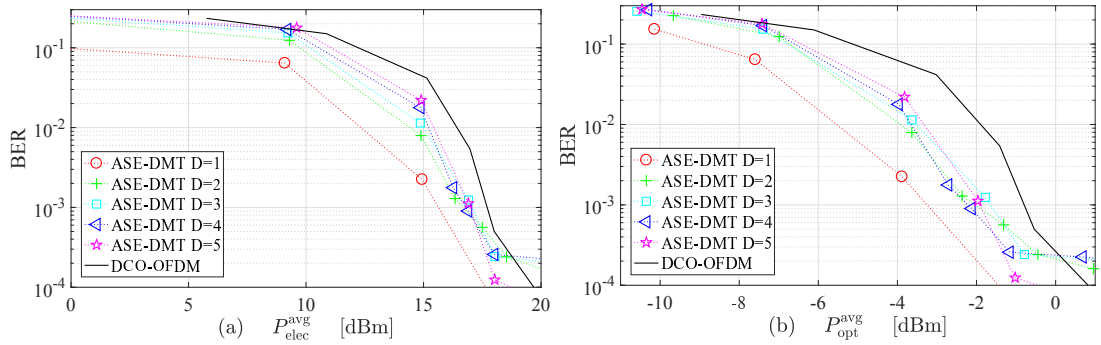
Figure 4.24: *The BER of the blue LED based system in Study III for 8-PAM ASE-DMT with a total number of depths used for ASE-DMT $1 \leq D \leq 5$ (180 Mb/s) compared with a 64-QAM DCO-OFDM (180 Mb/s). (a) average electrical power $P_{\mathrm{elec}}^{\mathrm{avg}}$ (b) average electrical power $P_{\mathrm{opt}}^{\mathrm{avg}}$.*

$D = 5$ for $V_{\mathrm{DC}} > 3.18$ V is notably better than the BER performance of ASE-DMT when $1 < D < 5$. This is a promising results since ASE-DMT with $D = 5$ requires a marginal excess bandwidth given at 3.23% of the DCO-OFDM bandwidth.

The BER performance of ASE-DMT is presented as a function of the electrical and optical average power of the blue LED in Fig. 4.24(a) and Fig. 4.24(b), respectively. The BER performance of 8-PAM ASE-DMT is compared for $1 \leq D \leq 5$ with the BER of 64-QAM DCO-OFDM at a data rate of 180 Mb/s. ASE-DMT achieves a lower BER when compared with DCO-OFDM at the same electrical and optical average power levels. In other words, ASE-DMT requires less power than DCO-OFDM to operate at
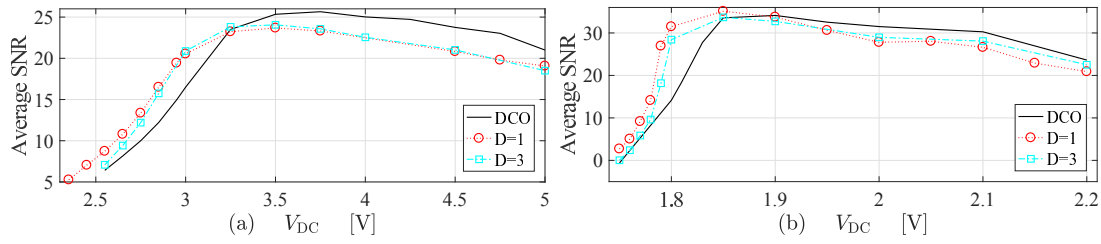
Figure 4.25: *The average SNR versus bias voltage V_{DC} for DCO-OFDM and ASE-DMT with a total number of depths $D = 1$ and $D = 3$. (a) using the blue LED. (b) using the IR VCSEL. The forward voltage values for the blue LED and the IR VCSEL are 2.65 V and 1.7 V, respectively.*

the same data rate and the same BER target. The electrical and optical energy savings decreases as the total number of modulation depths increases, as expected in Section 3.4. The electrical energy savings of ASE-DMT in comparison with DCO-OFDM are given at 3.13 dB when $D = 1$, 1.63 dB when $D = 2$, 1.25 dB when $D = 3$, 1.33 dB when $D = 4$ and 1.04 dB when $D = 5$. The optical energy savings on the other hand are given in Fig. 4.24(b) at 3.19 dB when $D = 1$, 1.84 dB when $D = 2$, 1.44 dB when $D = 3$, 1.84 dB when $D = 4$ and 1.44 dB when $D = 5$. The results are consistent with the electrical energy savings presented in Fig. 4.24(a). At $P_{\text{elec}}^{\text{avg}} = 18$ dB and $P_{\text{opt}}^{\text{avg}} = -1$ dB, the performance of ASE-DMT reaches the BER floor when $D = 1$ while it converges at 2×10^{-4} for $D = \{2, 3, 4\}$. The performance of ASE-DMT when $D = 5$ outperforms the rest of the presented cases in consistency with Fig. 4.23.

The BER performance gain of ASE-DMT against DCO-OFDM is shown to decrease as D increases. However, the improvement of ASE-DMT when $D < 3$ comes at the price of a higher excess bandwidth. ASE-DMT implementations are expected to be achieved with a total number of modulation depths $D \geq 3$ since the excess bandwidth decreases significantly as D increases. The BER performance of ASE-DMT with $D < 3$ is presented for comparison purposes only.

The average SNR of ASE-DMT and DCO-OFDM is shown in Fig. 4.25(a-b) for the blue LED and the IR VCSEL, respectively. The average SNR of ASE-DMT is presented for $D = 1$ and $D = 3$. The SNR is estimated using a conventional mean estimator based on the channel and noise estimation in agreement with Study I and Study II. The proposed ASE-DMT achieves higher SNR levels at low DC bias levels. The SNR gain of using ASE-DMT with the blue LED increases to reach a peak of 4.47 dB at 2.95 V
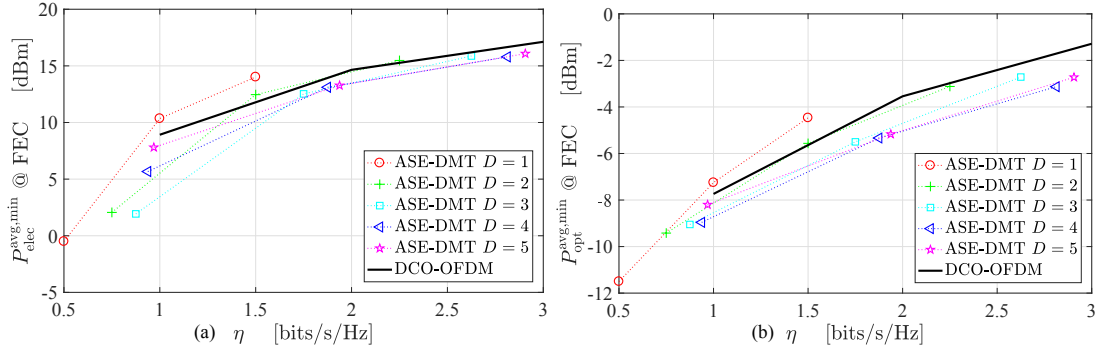
Figure 4.26: *The minimum average power required at a BER equals to the FEC thresh-old 3.8×10^{-3} versus the spectral efficiency of DCO-OFDM and ASE-DMT with a total number of depths $1 \leq D \leq 5$ using the blue LED. (a) average electrical power $P_{\text{elec}}^{\text{avg,min}}$, (b) average electrical power $P_{\text{opt}}^{\text{avg,min}}$.*

for $D = 1$ and 4.38 dB at 3 V for $D = 3$. The SNR gain drops due to the clipping distortion and diminishes at 3.23 V for $D = 1$ and 3.3 V for $D = 3$. Similar trends are shown in Fig. 4.25(b) for the IR VCSEL. Higher SNR gain is achieved when comparing ASE-DMT and DCO-OFDM at low DC bias levels. The peak gain reaches 17.33 dB at 1.8 V for $D = 1$ and 14.27 dB at the same DC bias for $D = 3$. The SNR gain drops as the DC bias increases beyond 1.8 V and diminishes at 1.89 V for $D = 1$ and 1.85 V for $D = 3$. The difference in the SNR gain of ASE-DMT between the blue LED and the IR VCSEL is attributed to the improved linearity of the L-V characteristic of the IR VCSEL.

The degradation of the achieved SNR in ASE-DMT is in agreement with the SNR degradation in DCO-OFDM due to clipping distortion at a high DC bias. However, the peak value of the average SNR in DCO-OFDM is achieved at 25.65 dB when $V_{\text{DC}} = 3.75$ V using the blue LED. This is higher than the peak SNR of ASE-DMT which is achieved at 24 dB when $V_{\text{DC}} = 3.5$ V. Therefore, DCO-OFDM is capable of achieving a higher data rate than ASE-DMT at high DC bias levels. However, DCO-OFDM has higher energy consumption and it is unable to support dimming applications in VLC systems. The difference at high DC bias levels between the achieved SNR of ASE-DMT and DCO-OFDM is smaller when using the IR VCSEL. This is also due to the better linearity of the L-V characteristic of the IR VCSEL.

The minimum required power to achieve the FEC threshold are compared for ASE-DMT and DCO-OFDM in this section. The results are presented as a function of the spectral
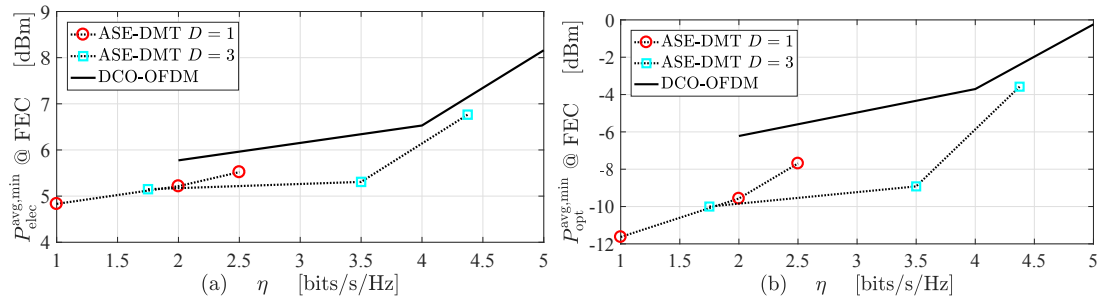
Figure 4.27: *The minimum average power required at a BER equals to the FEC thresh-old 3.8×10^{-3} versus the spectral efficiency of DCO-OFDM and ASE-DMT with a total number of depths $D = 1$ and $D = 3$ using the IR VC-SEL. (a) average electrical power $P_{\text{elec}}^{\text{avg,min}}$, (b) average electrical power $P_{\text{opt}}^{\text{avg,min}}$.*

efficiency when using the blue LED and the IR VCSEL in Fig. 4.26 and Fig. 4.27, respectively. The results of ASE-DMT are presented for $1 \le D \le 5$ when using the blue LED and for $D = 1$ and $D = 3$ when using the IR VCSEL. The results for the IR VCSEL are presented for two representative cases to allow for a comparison with the trends obtained using the blue LED.

There is a noticeable improvement in the performance of ASE-DMT when $D = 1$ in comparison with the performance of ASE-DMT with other values of D as shown in Fig. 4.22(a), Fig. 4.23 and Fig. 4.24. This is because the spectral efficiency of ASE-DMT when $D = 1$ is exactly half of that in DCO-OFDM. For example, the performance of 8-PAM ASE-DMT when $D = 1$ is compared with the performance of 64-QAM DCO-OFDM, despite that the spectral efficiency of 8-PAM ASE-DMT when $D = 1$ is half of that in 64-QAM DCO-OFDM. The comparison in Fig. 4.22(a), Fig. 4.23 and Fig. 4.24 is performed at the same data rate. Therefore, a considerable excess bandwidth equal to the whole utilized bandwidth in DCO-OFDM is required for ASE-DMT when $D = 1$. The spectral efficiency of ASE-DMT increases with the increase of D. Therefore, a comparison between the performance of ASE-DMT with $D = 1$ and $D = 3$ at the same spectral efficiency is expected to result in a better BER performance for $D = 3$. The results in Fig. 4.26 and Fig. 4.27 are presented at a normalized bandwidth to allow for a fair comparison between the different values of D in ASE-DMT.

The minimum required electrical average power $P_{\text{elec}}^{\text{avg,min}}$ for ASE-DMT is shown to be lower than the required power for DCO-OFDM in Fig. 4.26(a). ASE-DMT is shown
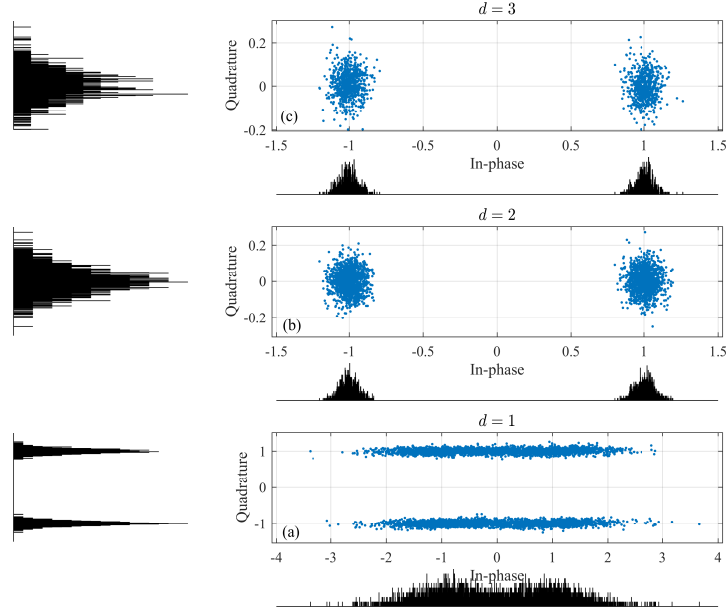
Figure 4.28: *The constellation diagram of the demodulated symbols of 2-PAM ASE-DMT with a total number of depths $D = 3$. The constellations are shown for the superimposed modulation depths $d = \{1, 2, 3\}$. The demodulated symbols are obtained for the blue LED based system in Study III with a bias voltage $V_{\mathrm{DC}} = 3.25\,V$. The histogram of the demodulated symbols is shown for the in-phase and quadrature components to the left and below each plot.*

to offer a spectrum and energy efficient alternative to DCO-OFDM. The required electrical average power in ASE-DMT when $D = 1$ is estimated at 1.43 dB higher than the required power for DCO-OFDM at a spectral efficiency $\eta = 1$ bits/s/Hz. However, the electrical average power savings of ASE-DMT are estimated at 3.39 dB when $D = 2$, 5.48 dB when $D = 3$, 2.76 dB when $D = 4$ and 0.94 dB when $D = 5$. The savings are reduced at higher spectral efficiency. However, reductions up to 2.28 dB at $\eta = 1.5$ bits/s/Hz when $D = 3$ and 1 dB at $\eta = 2.5$ bits/s/Hz when $D = 5$ are achieved. Similar trends are shown in Fig. 4.27(a) for the required electrical average power with the IR VCSEL. A peak reduction in the required electrical power can be achieved with ASE-DMT when $D = 3$ at $\eta = 3.5$ bits/s/Hz. There is a sharp increase in the electrical and optical power requirements of ASE-DMT at $\eta = 4.375$ bits/s/Hz and of DCO-OFDM at $\eta = 5$ bits/s/Hz. This is because of the high SNR requirements of 32-PAM and 1024-QAM, respectively.

The required optical average power $P_{\mathrm{opt}}^{\mathrm{avg,min}}$ is shown in Fig. 4.26(b) for the blue
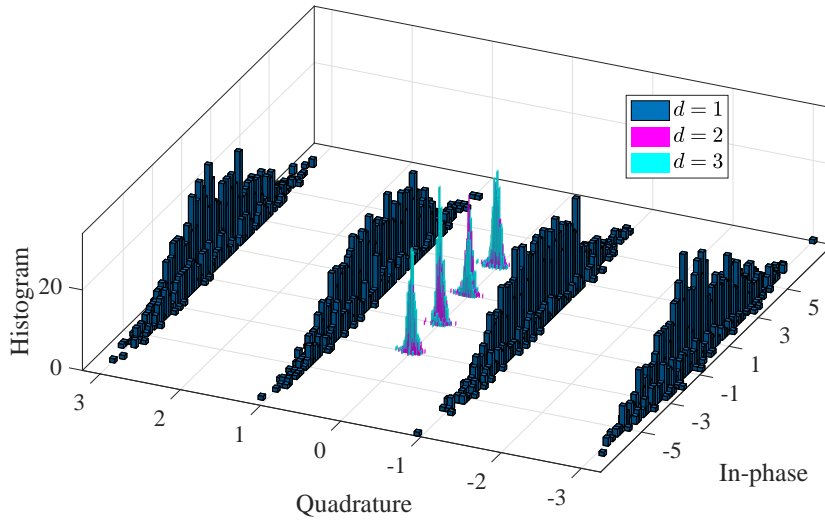
Figure 4.29: *The histogram of the demodulated symbols constellations of 4-PAM ASE-DMT with a total number of depths $D = 3$. The constellations are shown for the superimposed modulation depths $d = \{1, 2, 3\}$. The demodulated symbols are obtained for the IR VCSEL based system in Study III with a bias voltage $V_{\mathrm{DC}} = 1.85\,V$.*

LED. The improvement in the optical average power of ASE-DMT with $D = 4$ at $\eta = 1$ bits/s/Hz approaches 1 dB when compared with DCO-OFDM. However, the optical power savings increases as the spectral efficiency increases. The reduction in the required optical power reaches 1.5 dB at $\eta = 2$ bits/s/Hz and 1.45 dB at $\eta = 2.5$ bits/s/Hz when $D = 4$. The improvements in the optical power requirements are higher for the case of the IR VCSEL as shown in Fig. 4.27(b). The optical power gain is estimated at 3.63 dB for ASE-DMT when $D = 3$. This is mainly due to the improved linearity of the L-V characteristic in the IR VCSEL. The differences in the optical power requirements for the same modulation technique between the blue LED and the IR VCSEL are also attributed to the higher responsivity of the photoreceiver at the IR band. This allows the optical power levels of the IR VCSEL shown in Fig. 4.27(b) to be lower than the optical power levels of the blue LED shown in Fig. 4.26(b). ASE-DMT needs less optical power than DCO-OFDM to operate at the same data rate and the same BER. Therefore, ASE-DMT can support longer distance VLC links with more relaxed alignment/orientation constraints at the receiver.

The demodulated constellation diagrams in ASE-DMT are presented for 2-PAM, 4-PAM and 16-PAM in Fig. 4.28, Fig. 4.29 and Fig. 4.30, respectively. The demodulated symbols are shown in the constellation diagrams with a total number of modulation
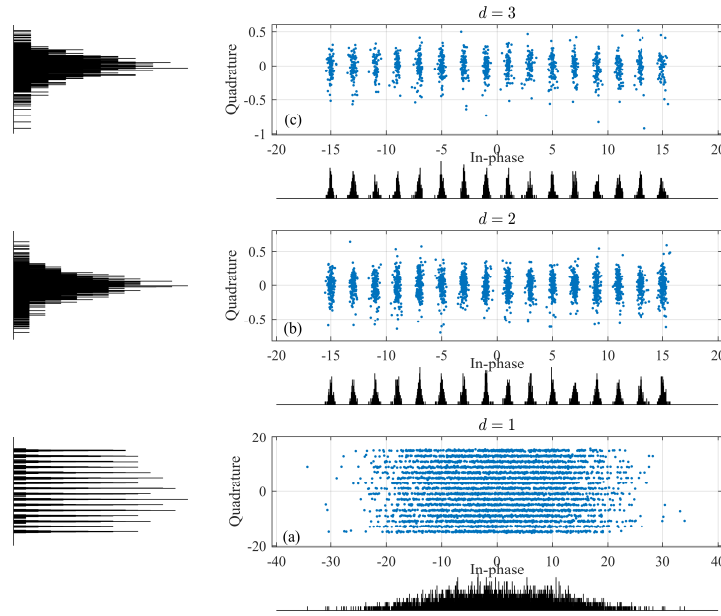
Figure 4.30: *The constellation diagram of the demodulated symbols of 16-PAM ASE-DMT with a total number of depths $D = 3$. The constellations are shown for the superimposed modulation depths $d = \{1, 2, 3\}$. The demodulated symbols are obtained for the IR VCSEL based system in Study III with a bias voltage $V_{DC} = 1.85\,V$. The histogram of the demodulated symbols is shown for the in-phase and quadrature components to the left and below each plot.*

depths $D = 3$. The constellation points are given for the superimposed modulation depths $d = \{1, 2, 3\}$ in each of the figures. The histogram of the constellation diagrams are shown for the real and imaginary components of the demodulated symbols below and on the left of each of the diagrams, respectively. The histogram reveals the distribution of the constellation points against the number of demodulated symbols. The information bits are conveyed in the imaginary component of the symbols at the first modulation depth when $d = 1$. The rest of the superimposed modulation depths are conveyed in the real component of the symbols.

The constellation points for 2-PAM ASE-DMT are displayed with a bias voltage $V_{DC} = 3.25$ V for the blue LED. The constellation points for 4-PAM and 16-PAM ASE-DMT are displayed with bias voltage $V_{DC} = 1.85$ V for the IR VCSEL. These bias levels represent the optimal bias points for ASE-DMT with the used transmitter devices. That explains the good representation of the constellation points which allows for ASE-DMT performance to reach the BER floor.

131

4.5   Summary

A VLC system based on DCO-OFDM and adaptive bit and energy loading is realized using a violet m-LED in Study I. The nonlinear distortion is found to affect the low frequency region of the overall system bandwidth due to the limited dynamic range of the m-LED. A transmission rate of 11.12 Gb/s, including the 7% FEC overhead is achieved when the overall VLC system noise is limited to the nonlinear distortion noise of the m-LED. This is achieved by averaging out the thermal and shot noise of the photoreceiver at the oscilloscope. This particular result represents an upper bound on the proposed m-LED performance that can be approached when higher quality system components with lower noise margins are used. A data transmission rate of 7.36 Gb/s, including the 7% FEC overhead is also reported when all the noise sources of the VLC system are considered. The presented theoretical bounds are in good approximation with the experimental results. The numerical investigation of the range and alignment highlight the role of optimized optics in increasing the transmission distance and improving system robustness against misalignment.

Additionally, a record data rate is demonstrated for a VLC system based on a high bandwidth blue LD in Study II. The high modulation bandwidth of the used LD is estimated at 1.03 GHz. DCO-OFDM with the adaptive bit and energy loading algorithm enabled an error free VLC link at a distance of 15 cm and a data rate of 13.95 Gb/s. A longer distance link at 197 cm is achieved at a 12.55 Gb/s error free data rate. The utilized modulation bandwidth at 2.5 GHz is well beyond the 3 dB bandwidth of the photoreceiver given at 1.4 GHz. A photoreceiver with a higher modulation bandwidth is expected to improve the SNR, modulation bandwidth and data rate. The results presented in this chapter demonstrate both the capabilities and the potentials of VLC systems as high-speed communication solutions.

The proposed ASE-DMT is demonstrated in Study III as a promising choice for energy efficient VLC systems. The BER performance gain of ASE-DMT at low DC bias in comparison with DCO-OFDM results in reduced electrical and optical power requirements. Therefore, the proposed ASE-DMT is a promising choice for any intensity modulation and direct detection (IM/DD) system where the reduction of the energy consumption is required. An example of such a system is the IR-based uplink of a LiFi system. ASE-DMT is also a better choice than DCO-OFDM at low DC bias where

the dimming of the light source is required. ASE-DMT requires less optical power to operate at the same data rate of DCO-OFDM. The reduced optical power requirement translates to a higher capability of supporting longer distance links with more relaxed alignment/orientation constraints at the receiver. Therefore, ASE-DMT is a promising solution for long distances IM/DD systems.

The degradation of ASE-DMT at high optical power restricts the capability of the system to satisfy high illumination requirements. In addition, the inability to derive the transmitter device at a high DC bias results in a reduced 3-dB bandwidth of the considered transmitter. Therefore, it can be concluded that ASE-DMT is a less favorable choice when compared with DCO-OFDM at high DC bias points where the energy efficiency of the system is not the main concern.

Chapter 5
The impact of sunlight on VLC

5.1 Introduction

The effect of solar irradiance on visible light communication (VLC) is considered to be one of the main misconceptions surrounding the practical implementation of VLC systems [29]. It is generally assumed that it could halt the operation of the communication system entirely due to interference. However, the effect of solar irradiance is more apparent as a strong shot noise source rather than an interference source as the sunlight intensity does not vary greatly over short periods of time. This allows multicarrier schemes such as orthogonal frequency division multiplexing (OFDM) to allocate the symbols over the usable frequency subcarriers of the modulation bandwidth. Adaptive bit and energy loading allows OFDM to be more robust against direct current (DC) wandering and low-frequency flickering of the background illumination [138].

The effect of solar irradiance on the performance of optical wireless communication (OWC) and VLC has been investigated in a limited number of works in the literature [139–143]. A simplified model was adopted in some of these works by approximating the solar irradiance with a black body radiation [139]. Other works adopted a standardized solar irradiance model [144] which is used as a reference model in the research on solar energy harvesting [140]. However, the location and time of the considered system play important roles in characterizing the effect of solar irradiance on the performance of VLC systems. These important factors were considered using Monte Carlo simulations in [141]. However, the direct solar irradiance was not used to characterize the system performance. The sunlight was assumed to be transmitted through a window and reflected to multiple walls before it is collected at the photoreceivers. The impact of solar irradiance on the performance of underwater OWC links was investigated for P-type intrinsic N-type photodiodes (PIN-PDs), avalanche photodiodes (APDs) and photo-multiplier tubes (PMTs) using Monte Carlo simulation methods in [140]. It was shown that the sunlight degrades the bit error ratio (BER) performance at relatively low depths up to 80 m.

The use of optical filters with a light control film to mitigate the effect of sunlight was proposed in [139, 142]. A filter with a light control film known as microlouver is used to restrict the field of view (FOV) and to reduce the background light collected at the photoreceiver. However, the microlouver cannot adapt to the changes of the photoreceiver's orientation and location which limits this solution to fixed point-to-point systems. The objective of this chapter is to provide a theoretical and experimental characterization of the solar irradiance effect on high-speed OFDM-based VLC systems. The investigation compares the use of a bandpass optical blue filter to the case where a filter is not considered in front of the photoreceiver. The performance is compared to a benchmark scenario of a dark room where background light does not reach the photoreceiver.

A complete framework to investigate the sunlight effect on VLC at any given location and time is presented in this chapter. Prior works on this topic were mainly based on pulsed modulation techniques [142, 143]. However, an outdoor underwater VLC demonstration achieving a data rate of 58 Mb/s was considered in [145] using discrete multi-tone (DMT). An experimental proof of concept study of a high speed OFDM-based VLC system is demonstrated in Edinburgh, UK at data rates above 1 Gbps in the presence of a solar illuminance measured at 50350 lx. Two locations are considered for the theoretical study: (55°55'20.4" North, 3°10'23.3" West) in Edinburgh, UK and (23°27'16.1" South, 70°26'21.4" West) in Antofagasta, Chile. The first location is used in Edinburgh for comparison purposes with the experimental results and the second is used in Antofagasta as this location has the highest solar radiation on Earth [146].

The rest of this chapter is organized as follows. In Section 5.2, the solar position and irradiance calculations based on the location and time are reviewed and the results in two geographical locations are presented. The assumptions of the theoretical study are specified in Section 5.3.1. The signal-to-noise ratio (SNR), the maximum theoretical limit on the data rate and BER of the system are derived and the system modeling is discussed in Section 5.3.2. An experimental proof-of-concept is presented in Section 5.4. The system performance is analyzed and the results are shown in Section 5.3.3 and Section 5.4.2, respectively. Section 5.5 concludes the chapter.

5.2 Solar irradiance and position

The solar constant flux density P_{SC} is given as 1366.1 W/m^2 outside the Earth's atmosphere by the American society for testing and materials (ASTM) standard (ASTM E-490) [147]. The solar irradiance is not limited to the visible spectrum as it spans the wavelengths from 250 nm to 2500 nm. The solar irradiance is unequally attenuated at various wavelengths due to the different absorption and scattering coefficients of the air molecules and aerosols. The shortest path for the sunlight exists when the Sun is located at the zenith point (imaginary point above the head of an observer). The optical air mass (AM) is approximated as the ratio of the actual sunlight path to the minimum path at the zenith point. It is given as AM0 for the extraterrestrial irradiance. When the Sun is at an angle θ_Z relative to the zenith, the optical AM is given by using the following approximation:

$$\text{AM} \simeq \frac{1}{\cos\theta_Z}. \tag{5.1}$$

The solar irradiance at $\theta_Z = 48.2°$ is defined as the reference AM1.5 in the standard (ASTM E-490) to help the solar energy community in testing and comparing the performance of various solar cells [144]. However, the solar irradiance varies based on the geographical location; seasonal and diurnal variations arising from the rotation of the Earth around the Sun; and the rotation of the Earth around its own axis. The effect of solar irradiance on VLC varies based on the location and time. Therefore, it is essential to calculate the position of the Sun in the sky in order for the solar irradiance at a particular location and time to be estimated. Various algorithms with different complexities and accuracies for calculating the solar position exist in the astrophysics literature [148]. An algorithm proposed by the astronomical applications department of the U.S. naval observatory to calculate the solar position is reviewed in Appendix D [149, 150].

The horizontal coordinate system is typically used for solar energy applications where the horizon of the observer is considered to be the fundamental plane. The solar position can be described using two angles: the altitude Al and the azimuth Az. The solar altitude $Al \in [0°, 90°]$ is given as the elevation of the Sun above the horizon. A solar altitude of $Al = 90°$ means that the Sun is at the zenith point. The solar altitude can also be given as $Al = 90° - \theta_Z$. The solar azimuth $Az \in [0°, 360°]$ is given as the angle between the north and the horizontal projection of the line-of-sight (LoS) between the Sun and the observer. Both angles are illustrated in Fig. 5.1(a) and demonstrated
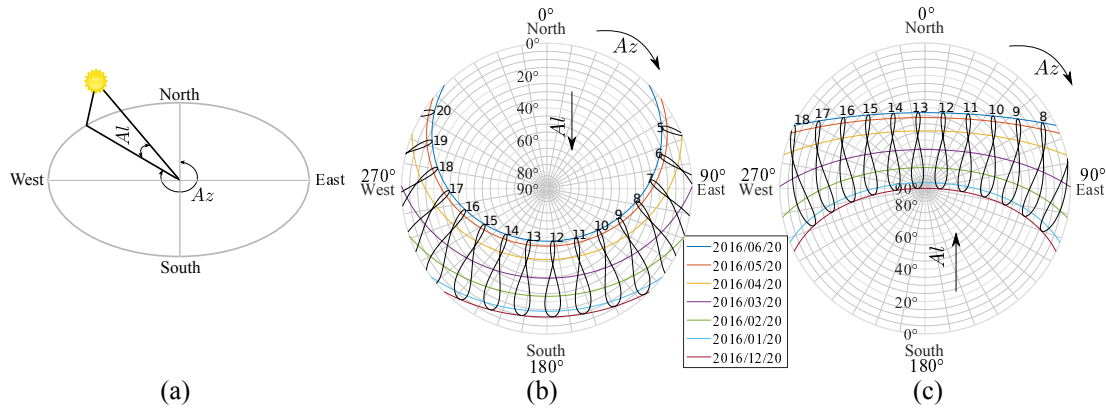
Figure 5.1: *(a) Solar position described by the altitude and the azimuth. (b) and (c) Solar position in Edinburgh and Antofagasta, respectively, for each 20th day of each considered month. The time of the day is listed above the elliptical shapes representing the analemma diagrams.*

in Fig. 5.1(b and c) for Edinburgh, UK and Antofagasta, Chile on the 20th of each considered month, respectively. The solar altitude is shown to reach the zenith $Al = 90°$ around 13:00 on the 20th of December 2016 for Antofagasta in Fig. 5.1(c). The time of the day is shown above the analemma diagrams in Fig. 5.1(b and c), which depict the Sun's motion throughout the year when observed at the same location and the same hour of day.

Direct solar irradiance is the sunlight that is directly reaching the surface of the Earth. Global solar irradiance is the combination of the direct and diffused solar irradiance. The simple model of the atmospheric radiative transfer of sunshine (SMARTS) is a transmittance model to evaluate the solar irradiance at any particular location and time [151,152]. The model is used to generate the ASTM standard (ASTM E-490) with a resolution between 0.5 nm and 1 nm [147]. The solar irradiance is typically higher than the information signal irradiance when the total solar irradiance is taken into account over the whole visible spectrum. Fortunately, VLC is realized using optical sources that have a fixed and predefined spectral irradiance. This allows inexpensive commercially available optical filters to be practical solutions for the degradation in VLC system performance that is caused by the solar irradiance. The total predicted solar irradiance is shown in Fig. 5.2(a and b) for Antofagasta and Edinburgh at the noon of the 21th of December and the 20th of June, respectively. These particular dates are considered due to their astronomical interest. The 20th of June 2016 is the summer solstice in Edinburgh and the winter solstice in Antofagasta, and the 21th of December 2016 is

the winter solstice in Edinburgh and the summer solstice in Antofagasta. The summer solstice is the date of the year when the maximum tilt is experienced at one of the Earth's hemispheres towards the Sun. As the considered locations lie in the Northern and Southern hemispheres, the winter solstice in Edinburgh would be summer solstice in Antofagasta and vice versa. The 20$^{\text{th}}$ of June 2016 and the 21$^{\text{th}}$ of December 2016 are referred to as June and December solstices throughout this chapter, respectively.

Monthly comparisons for the total solar irradiance are shown in Fig. 5.3. The total spectral irradiance is calculated for the spectrum between 400 nm and 760 nm. The blue component of the solar irradiance for the wavelengths between 425 nm and 475 nm shows the importance of optical filtering in improving the overall performance of VLC. Optical filtering is also beneficial for other objectives in VLC. White illumination is generally achieved by coating the blue light emitting diode (LED) with a yellow phosphor which introduces a slow component into the frequency response of the LED. Blue filters are required to eliminate the slow response component of the yellow phosphor as described in Section 2.4.1.2. Monochromatic light sources have a narrow spectral linewidth and, thus, can guarantee a robust VLC system against solar irradiance with the potential of achieving data rates in the orders of multiple Gb/s.
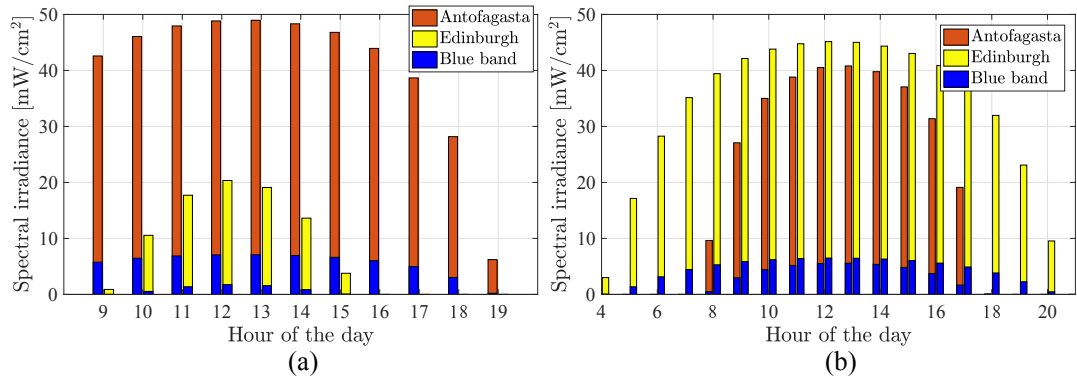
Figure 5.2: *Total solar irradiance estimated in Antofagasta and Edinburgh on: (a) 21th of December 2016 and (b) 20th of June 2016. The blue spectral component of the solar irradiance is shown in blue. The blue band is given between 425 nm and 475 nm.*
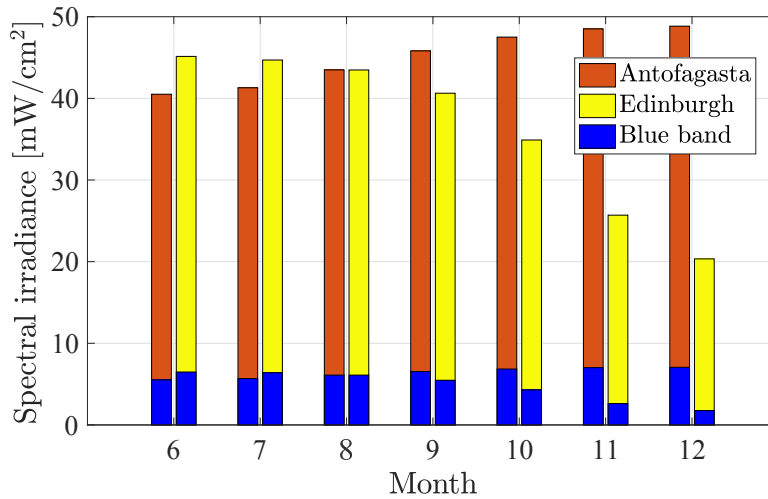
Figure 5.3: *Total solar irradiance estimated in Antofagasta and Edinburgh during the noon of each 20th day of the second half of the year. The blue spectral component of the solar irradiance is shown in blue.*

5.3   Theoretical study

A complete framework to estimate the effects of solar irradiance on OFDM-based VLC systems is presented in this section. The theoretical performance of a VLC system using a blue LED as a transmitter is presented. The modeling assumptions are presented in two different geographical locations and for different operating scenarios. The system model for the solar irradiance is based on the predicted solar irradiance using SMARTS [151,152]. The results are provided and discussed in terms of three metrics: BER, SNR and maximum theoretical limit on the data rate.

5.3.1   Modeling assumptions

An OFDM-based VLC system is used due to its robustness against background illumination flickering. The OFDM waveform is required to be both unipolar and real valued. Hermitian symmetry is imposed on the quadrature amplitude modulation (QAM) symbols, to enforce the OFDM time domain signal output into the real domain as discussed in Section 2.6.2. A real-valued OFDM waveform with a DC bias is used to modulate the intensity of the LED as described in Section 2.6.2.1. Binary inputs are encoded into multiple QAM symbols which are allocated to N_{FFT} subcarriers over a single-sided bandwidth of B. Three scenarios are considered:

Parameter	Value	Unit
APD detection area, A_d	19.6	mm^2
Bandwidth, B	60	MHz
APD gain, M_APD	100	-
Dark current, I_d	3	nA
Blue filter FWHM	50	nm
Maximum transmitted optical power, $P_\mathrm{Max}^\mathrm{L}$	8	mW
Transmission distance, d_E	63.85	cm
Half-power semi-angle of the transmitter, $\Phi_{1/2}$	25°	degrees

Table 5.1: *Modeling assumptions*

- *Scenario I (dark room)*: this is assumed to be an optimal case where no background illumination reaches the photoreceiver. This is an ideal scenario as the dominant noise source is the thermal noise.

- *Scenario II (with a blue filter)*: it is assumed that the solar irradiance is collected with a bandpass blue filter in front of the photoreceiver. This is a practical scenario as the useful information signal is transmitted and any out-of-band signal is filtered. Part of the solar irradiance within the transmittance band of the optical filter is passed since the solar irradiance covers a wide wavelength band.

- *Scenario III (without a blue filter)*: this is assumed to be a worst case scenario where the solar irradiance is collected without any optical filtering in front of the photoreceiver.

The modeling assumptions are presented in Table 5.1. The system uses a blue micrometer-sized Gallium Nitride light emitting diode (m-LED) with a pixel size of 100×100 μm^2 and a maximum optical power of 8 mW. Due to the reduced emission area of m-LEDs, the capacitance decreases and the current density increases allowing for higher 3-dB bandwidths compared to off-the-shelf LEDs as described in Section 2.4.1.4 [81]. The transmission distance is used at $d_\mathrm{E} = 63.85$ cm to match with the distance that was used to measure the spectral irradiance of the m-LED. The system performance is also investigated at longer distances up to 3 m in Section 5.3.3. A focusing aspheric condenser optical lens (Thorlabs, ACL4532U-A) is used at the transmitter side, which allows for a small half-power semi-angle at the transmitter $\Phi_{1/2} = 25°$ as given in (4.13). An optical bandpass blue filter from Edmund Optics is assumed in Scenario II with a central wavelength of 450 nm, a transmittance higher than 90% and

a full width at half maximum (FWHM) of 50 nm. The photoreceiver is an APD (Hamamatsu, S8664-50K) that is assumed to be aligned with the m-LED. APDs operate at a high reverse bias to create an amplification effect that allows incident photons to create an avalanche of electrons as described in Section 2.4.2.1. APDs are more sensitive to background noise compared to other photodiodes. However, APDs are used as a worst case choice in this investigation as they are shot-noise limited [153]. The APD will not always be collecting the solar irradiance due to the orientation of the communication link in practical situations. However, the APD is always assumed to be collecting the sunlight in this investigation.

The locations considered for the theoretical study are (55°55'20.4" North, 3°10'23.3" West) in Edinburgh, UK and (23°27'16.1" South, 70°26'21.4" West) in Antofagasta, Chile. The system model considers two dates: the December solstice and June solstice. The solar position is used to estimate the hourly solar irradiance as discussed in Section 5.2 [151, 152]. The model assumes a clear sky scenario due to the irregular variations in the local weather conditions which influence the solar irradiance. This allows us to consider the maximum possible solar irradiance in a pessimistic approach.

5.3.2 System modeling

The continuous time OFDM waveform $x(t)$ is transmitted over the VLC channel with an impulse response $h(t)$, before it is distorted by a noise signal $w(t)$ at the receiver. The received signal $y(t)$ is then sampled at a sampling rate of $1/T_s$, where T_s is the sampling period. The fast Fourier transform (FFT) is then applied on the samples after a serial to parallel (S/P) conversion. Assuming that the OFDM frame length is sufficiently large ($N_{FFT} > 64$) [154], the central limit theorem (CLT) can be applied on the combination of shot, thermal and dark noise generated at the receiver. This can be modeled as zero-mean additive white Gaussian noise (AWGN) with a variance σ_n^2. The discrete time received OFDM waveform $y[n]$ can then be given in (2.3). The average photocurrent generated at the APD due to the average optical power received from sunlight is given as:

$$I_b = A_d \int_{350}^{750} P_D^S(\lambda) R(\lambda) T_{bf}(\lambda) d\lambda, \tag{5.2}$$

where A_d is the APD detection area, $P_\mathrm{D}^\mathrm{S}(\lambda)$ is the direct solar irradiance given in W/m^2/nm, $T_\mathrm{bf}(\lambda)$ is the transmittance of the bandpass optical blue filter, $R(\lambda)$ is the intrinsic responsivity of the APD given in A/W and λ is the wavelength considered for the APD detectable light spectrum mainly from 350 nm to 750 nm.

Similarly, the average photocurrent generated at the APD due to the average optical power received from the m-LED is given as:

$$I_x = \frac{(m+1)A_\mathrm{d}}{2\pi d_\mathrm{E}^2} \int_{350}^{750} P_\mathrm{T}^\mathrm{L}(\lambda)R(\lambda)T_\mathrm{bf}(\lambda)d\lambda, \tag{5.3}$$

where m is the Lambertian order of the m-LED; d_E is the Euclidean distance between the m-LED and the APD; and $P_\mathrm{T}^\mathrm{L}(\lambda)$ is the transmitted optical irradiance from the m-LED, which is given as:

$$P_\mathrm{T}^\mathrm{L}(\lambda) = P_\mathrm{Max}^\mathrm{L} \frac{P_\mathrm{Measured}^\mathrm{L}(\lambda)}{\int_{350}^{750} P_\mathrm{Measured}^\mathrm{L}(\lambda)d\lambda}, \tag{5.4}$$

where $P_\mathrm{Max}^\mathrm{L}$ is the maximum transmitted optical power of the m-LED and $P_\mathrm{Measured}^\mathrm{L}(\lambda)$ is the measured optical irradiance of the m-LED given in W/m^2/nm. This was measured at a distance of $d_\mathrm{E} = 63.85$ cm using a Labsphere spectral irradiance head (E1000).

The random arrival of incident photons results in shot noise which can be modeled by a Poisson distribution. However, when the number of incident photons increases, the shot noise is approximated by a Gaussian distribution [79]. The shot noise variance is given by [155]:

$$\sigma_\mathrm{sh}^2 = 2qM_\mathrm{APD}^2 F'(I_\mathrm{b} + I_x)B, \tag{5.5}$$

where M_APD is the average gain of the APD, q is the electron charge, B is the bandwidth of the APD and F' is the excess noise given as [156]:

$$F' = \kappa M_\mathrm{APD} + (2 - 1/M_\mathrm{APD})(1 - \kappa), \tag{5.6}$$

where κ is the holes/electrons ionization rate. The SNR per symbol at subcarrier k can be given by:

$$\Gamma_k = \frac{M_\mathrm{APD}^2 I_x^2}{\sigma_n^2/|H(k)|^2}, \tag{5.7}$$

where $H(k)$ is the frequency response of the VLC channel, $\sigma_n^2 = \sigma_\mathrm{sh}^2 + \sigma_\mathrm{th}^2 + \sigma_\mathrm{d}^2$ and σ_d^2

is the variance of the dark current noise which is given as follows [155]:

$$\sigma_{\mathrm{d}}^2 = 2qM_{\mathrm{APD}}^2 F' I_{\mathrm{dg}} B + 2q I_{\mathrm{ds}} B, \tag{5.8}$$

where I_{ds} is the surface dark current and I_{dg} is the bulk dark current that experience the avalanche effect of the APD and where $I_{\mathrm{d}} = I_{\mathrm{ds}} + M_{\mathrm{APD}} I_{\mathrm{dg}}$. The variance of the thermal noise σ_{th}^2 is given by [19]:

$$\sigma_{\mathrm{th}}^2 = 4 \left(\frac{K_{\mathrm{B}} T_{\mathrm{K}}}{R_L} \right) F_n B, \tag{5.9}$$

where K_{B} is Boltzmann constant, T_{K} is the temperature in Kelvin, R_L is the load resistance given as 50 Ω and F_n is the photodiode noise figure.

Adaptive bit and energy loading algorithms such as the Levin-Campello algorithm [131] can be used to maximize the data rate by assigning larger constellation sizes on the subcarriers that have higher SNR. The maximum theoretical limit of the data rate of DC-biased optical orthogonal frequency division multiplexing (DCO-OFDM) can be calculated using the channel capacity defined by the Shannon-Hartley theorem [132] when neglecting the DC bias and the optical source nonlinearity [48]. These are valid assumptions as we are interested in the relative results of the considered scenarios. This is given as:

$$R_{\mathrm{Max}} = B \sum_{l=1}^{N_{\mathrm{FFT}}/2-1} \log_2 \left(1 + \Gamma_l \right). \tag{5.10}$$

The system performance in terms of BER can be calculated using the theoretical BER of real-valued OFDM as described in (4.10).

5.3.3   Results and discussions

The spectral irradiance of the m-LED and the amplified responsivity of the APD $MR(\lambda)$ are shown in Fig. 5.4 with the presence and absence of the bandpass blue filter. In addition, the predicted spectral irradiance of the sunlight in Antofagasta is shown at three different times during the December solstice. It is shown that the solar irradiance is high at the ultra-violet (UV) and blue spectrum bands at sunrise. At sunset it becomes higher at the red and infra-red (IR) spectrum bands. The blue filter captures 70% of the m-LED irradiance.
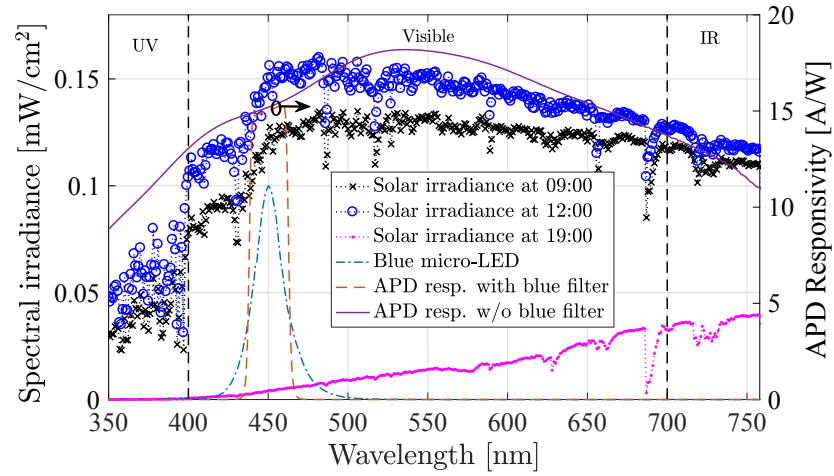
Figure 5.4: *The predicted solar irradiance in Antofagasta at 9 AM, 12 PM and 19 PM (local time) during the December solstice (left), alongside the spectral irradiance of the modeled m-LED centred at 450 nm (left) and response of the APD with and without considering the transmittance of the blue filter (right).*

The system performance is presented in Fig. 5.5(a and b) as a function of the SNR degradation against the time of the day for the December and June solstice, respectively. The degradation is calculated with respect to the benchmark case of the dark room in Scenario I. It is shown that the SNR degrades by a maximum of -13.4 dB and -9.7 dB during the noon of the December solstice in Scenario III in Antofagasta and Edinburgh, respectively. However, when a blue filter is used in front of the APD, this degradation is reduced to -6.2 dB and -3.2 dB in Scenario II in Antofagasta and Edinburgh, respectively. The high degradation in SNR in Antofagasta is expected due to the higher solar irradiance in the December solstice in comparison with Edinburgh as shown in Fig. 5.2. The SNR degradation in Edinburgh for the June solstice increases in comparison with the December solstice by a maximum increases of 3.4 dB. The SNR degradation is 0.8 dB lower for the June solstice compared with the December solstice in Antofagasta. The SNR increases by at least 6.5 dB when blue filters are used in Scenario II. The SNR degradation in Edinburgh was witnessed for longer hours during the June solstice due to the longer hours of daylight, which is shown in Fig. 5.1(b).

The system performance as a function of the BER against the time of the day is shown in Fig. 5.6(a and b) for 128-QAM DCO-OFDM during the December and June solstices, respectively. The results show the SNR degradation effect on the BER performance for
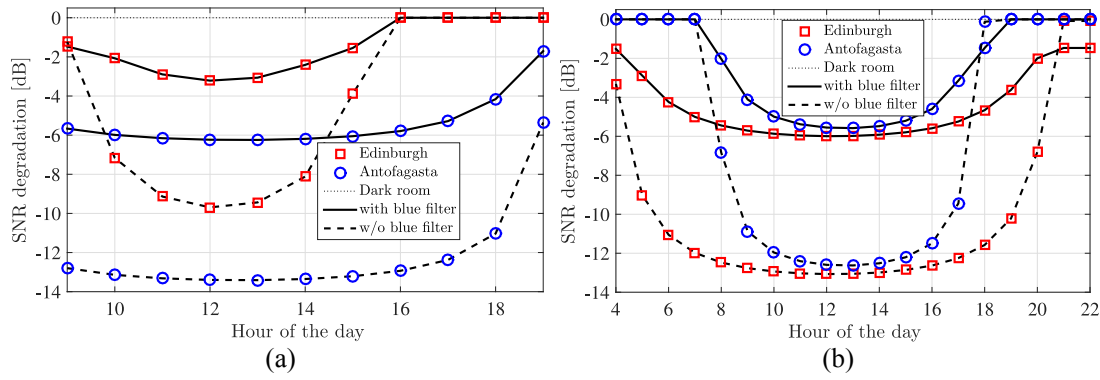
Figure 5.5: *The SNR for the three considered scenarios in Antofagasta and Edinburgh versus time on: (a) December solstice and (b) June solstice.*
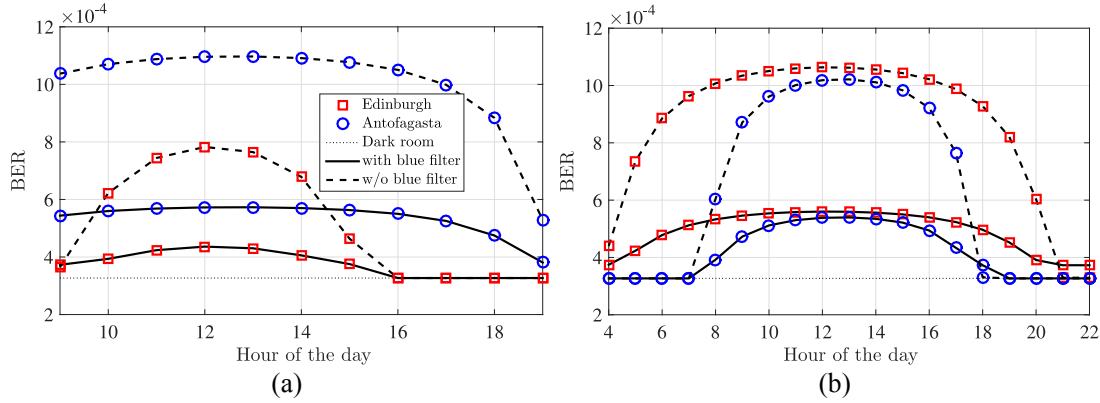
Figure 5.6: *The BER for the three considered scenarios in Antofagasta and Edinburgh versus time on: (a) December solstice and (b) June solstice.*

the OFDM-based VLC system. Both Scenario II and Scenario III in Antofagasta and Edinburgh are shown to allow the use of forward error correction (FEC) during both the December and June solstice, although a significant improvement is shown to be achieved when the blue filter is used.

The system performance is investigated as a function of the maximum theoretical limit on the data rate versus the time of the day in Fig. 5.7(a and b) for the December and June solstices, respectively. The performance of Scenario II and the performance of Scenario III are compared to the benchmark performance recorded at 1.25 Gb/s of Scenario I for Antofagasta and Edinburgh. It is shown that the data rate degrades by 21.35% and by 15.49% during the noon of the December solstice when the blue filter is not used in Antofagasta and Edinburgh, respectively. However, this degradation is reduced to 10% and 5.22% for Scenario II in Antofagasta and Edinburgh, respectively.

146
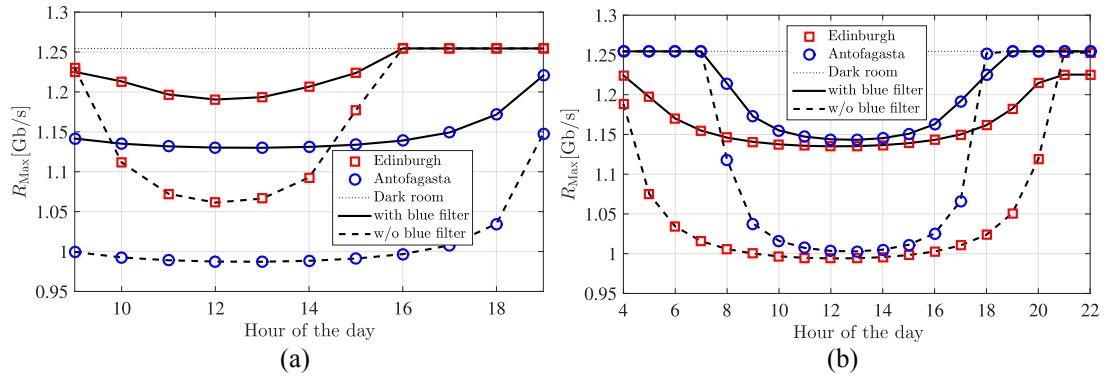
Figure 5.7: *The maximum theoretical limit on the data rate for the three considered scenarios in Antofagasta and Edinburgh versus time on: (a) December solstice and (b) June solstice.*
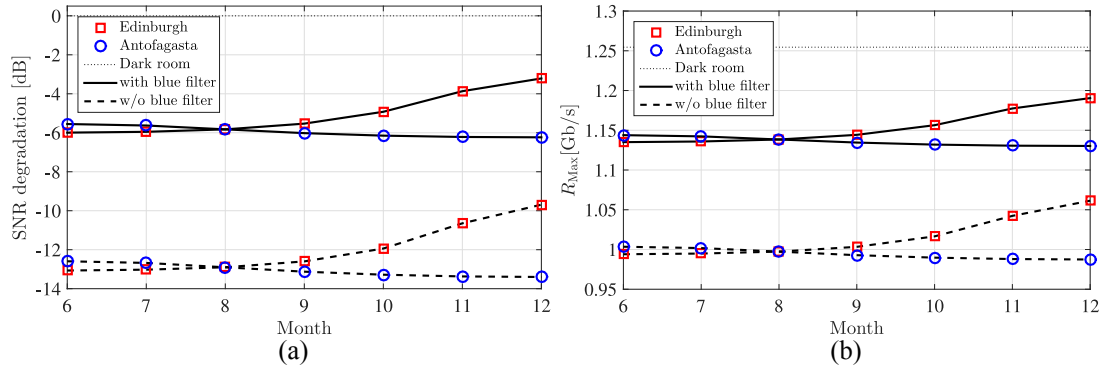
Figure 5.8: *The system performance presented on monthly basis during the noon of each 20ᵗʰ day of the considered months for the three considered scenarios in Antofagasta and Edinburgh. (a) SNR and (b) Maximum theoretical limit on data rate.*

A maximum theoretical limit on the data rate for the June solstice under the solar irradiance is estimated to be 1.03 Gb/s and 0.99 Gb/s for Scenario III in Antofagasta and Edinburgh, respectively; and 1.14 Gb/s and 1.13 Gb/s for Scenario II in Antofagasta and Edinburgh, respectively.

The SNR degradation in Antofagasta and Edinburgh at the noon on the 20ᵗʰ day for the last six months in 2016 is presented in Fig. 5.8(a). The degradation decreases noticeably as we approach the December solstice in Edinburgh, while SNR degradation variations are less noticeable for Antofagasta. A comparison of the maximum data rate performance in both Antofagasta and Edinburgh at the noon on the 20ᵗʰ day for the last six months in 2016 is presented in Fig. 5.8(b). The variations in data rates are more noticeable for Edinburgh, where it increases to reach a maximum of 1.19 Gb/s for

147
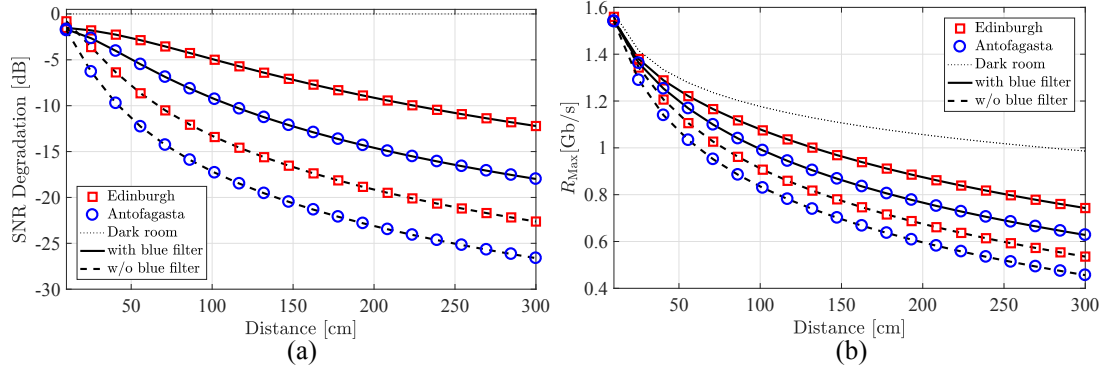
Figure 5.9: *System performance versus transmission distance d_{E} during the noon during the December solstice for the three considered scenarios in Antofagasta and Edinburgh. (a) SNR and (b) Maximum theoretical limit on data rate.*

Scenario II and 1.06 Gb/s for Scenario III in December.

The SNR degradation and the maximum theoretical limit on the data rate are given in Fig. 5.9(a and b) as functions of the transmission distance. The results in Fig. 5.9 are presented for the three considered scenarios in Antofagasta and Edinburgh at noon during the December solstice. The SNR degrades as the transmission distance increases in all considered scenarios, including the dark room Scenario I, as expected. However, the SNR degradation for Scenario II and III are calculated with reference to the dark room in Scenario I to highlight the solar irradiance effect in comparison with the benchmark Scenario I. It is shown that the SNR degradation reaches -26.6 dB and -22.6 dB when the blue filter is not used in Scenario III at a transmission distance of 3 m in Antofagasta and Edinburgh, respectively. Although the SNR degradation appears to be high, the SNR gain of using the blue filter in Scenario II reaches 8.6 dB and 10.4 dB at a transmission distance of 3 m for Antofagasta and Edinburgh, respectively. Similarly, the maximum theoretical limit on the data rate is shown to decrease as the transmission distance increases. The maximum theoretical limit on the data rate at a transmission distance of 3 m for the dark room in Scenario I is 986.3 Mb/s. This is degraded by 53.74% for Antofagasta and 45.71% for Edinburgh in Scenario III. However, it is shown that the degradation is reduced to 36.33% and 24.7% in Antofagasta and Edinburgh when the blue filter is used in Scenario II. Despite the degradation in SNR, high-speed VLC can still be available at sufficiently long distances.
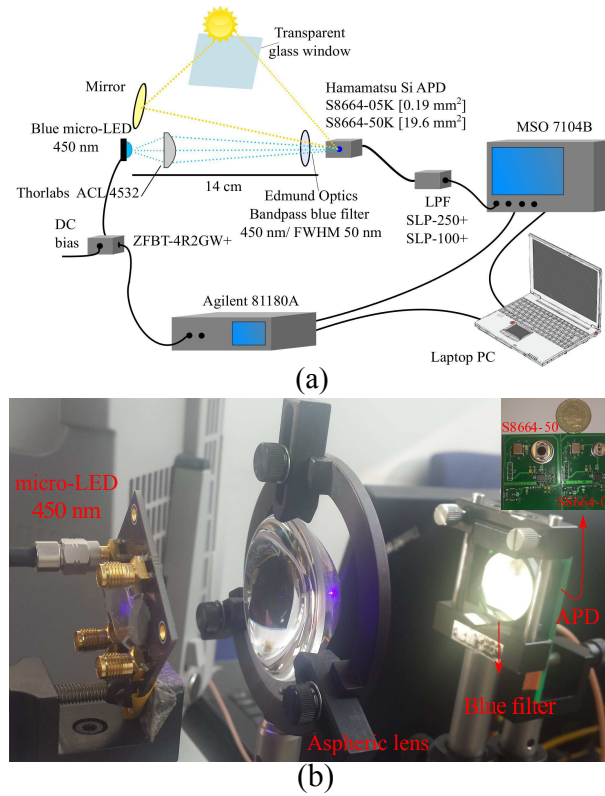
Figure 5.10: *The experimental set-up. (a) Schematic set-up of the experiment showing the optical system, arbitrary waveform function generator, oscilloscope, electrical and optical filters and Bias-Tee. (b) Photograph of the optical system showing the m-LED, optical lenses system and the used APDs. At the top right corner (left): large APD S8664-50k; (right): small APD S8664-05k*

5.4 Experimental study

An experimental investigation on the effects of solar irradiance on an OFDM-based VLC system is presented in this section. A blue m-LED is used at the VLC transmitter side and the performance of two APDs with different sizes is compared at the receiver side. The results are presented in terms of SNR and achieved data rates in Section 5.4.2.

5.4.1 Experimental set-up

The measurements were conducted between 11:00-17:00 (local time) of the 6th and 9th of June 2016 under clear sky weather conditions demonstrated by very good visibility estimated above 21 km and a solar illuminance measured at 50350 lx. The measurements were carried at (55°55'20.4" North, 3°10'23.3" West) in Edinburgh, UK. The
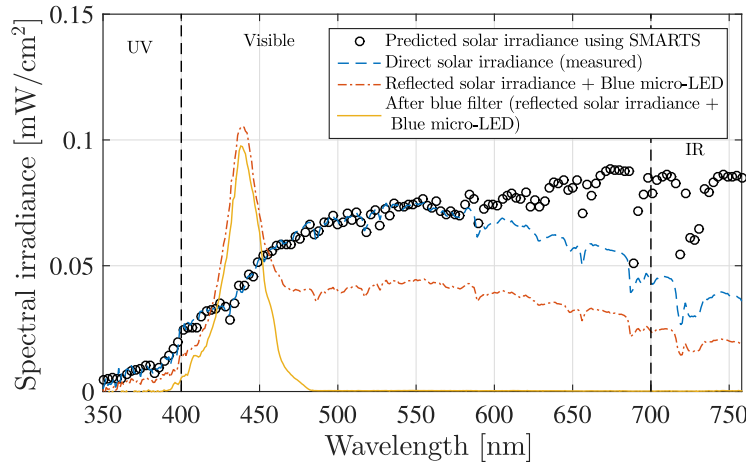
Figure 5.11: *The spectral distribution of the solar irradiance measured and predicted using SMARTS [151, 152] for Edinburgh (direct, reflected and filtered) in the presence and absence of the desired signal at 450 nm.*

experimental setup is shown in Fig. 5.10(a-b). The system elements used in the experiment are the same components described in Section 5.3.1. The OFDM modulation waveform is generated and processed off-line using MATLAB®. The OFDM digital waveform is converted into an analog waveform using the arbitrary waveform generator Agilent 81180A, which sends the bipolar OFDM waveform to the m-LED using a Bias-Tee ZFBT-4R2GW. The DC bias is selected after exhaustive tests at $V_{DC} = 4.1$ Volts to minimize the clipping distortion. The optical power of the m-LED is 4.5 mW and the 3-dB bandwidth is 30 MHz, both measured at a DC current $I_{DC} = 50$ mA. An aspheric lens ACL 4532 is used to focus the light on the photoreceiver. Two Silicon APDs are used in this experiment (Hamamatsu, S8664-05k) and (Hamamatsu, S8664-50k), as shown at the top-right corner of Fig. 5.10(b). These APDs are referred to as 'small' APD and 'large' APD, respectively. The small APD has a smaller active area of 0.19 mm^2 and therefore, has a lower capacitance that leads to a higher 3-dB bandwidth of 680 MHz. The large APD has a larger active area of 19.6 mm^2 that leads to a higher capacitance and a lower 3-dB bandwidth of 60 MHz.

The received signal at the APDs is filtered using a low pass electrical filter (Mini-circuits, SLP-100+) with a cut-off of 98 MHz for the large APD; and (Mini-circuits, SLP-250+) with a cut-off of 225 MHz for the small APD. A system modulation bandwidth of 100 MHz and 250 MHz is used for the large and small APDs, respectively. This is the maximum bandwidth for which the experimental SNR is higher than 0 dB. The electrical

Scenario		Average SNR [dB]	Data rate [Mbps] @ BER $<3.8 \times 10^{-3}$
Dark room (I)	Large APD	17.57	416.44
	Small APD	18.58	1139.26
with blue filter (II)	Large APD	16.64	396.71
	Small APD	17.36	1080
w/o blue filter (III)	Large APD	12.42	313.35
	Small APD	16.42	1015

Table 5.2: *Achievable SNR values and data rates for the small and large APDs for the three considered scenarios.*

signal is then captured using an oscilloscope (Agilent, MSO7104B) and then processed using MATLAB®. The overall distance between the m-LED and the photodetector is 14 cm. The received optical power by the APD decreases at longer distances due to the geometrical losses. This is the reason why the achievable SNR decrases and not because of the shot noise caused by the sunlight. The maximum link distance is limited by the optical power of the m-LED and it can be improved by using more advanced collimation optics or using m-LEDs with multiple pixels in a ganging mode [81]. The three scenarios described in Section 5.3.1 are considered in the experimental study. The SNR of the channel is first estimated and then the constellation sizes and the associated power of M-QAM symbols are adaptively allocated to each subcarrier based on the estimated SNR. The adaptive bit and energy loading algorithm avoids the use of low-frequency subcarriers, where the interference of ambient light can be strong. In addition, it avoids any other subcarrier, where the SNR is expected to result in a BER below the FEC target.

5.4.2 Results and discussions

The measured solar irradiance is given in Fig. 5.11 for the wavelengths between 350 and 750 nm covering the visible spectrum and part of the infrared and ultraviolet spectra. Four cases are presented: direct sunlight; reflected sunlight from a mirror, reflected sunlight + blue m-LED (Scenario III); and reflected sunlight + blue m-LED with a blue optical filter (Scenario II). The experiment was conducted inside a building where the direct sunlight is passed through a transparent glass window before it is collected at the photoreceiver. It was not practically feasible to realize the experimental setup while the direct solar irradiance is always focused into the APD due to the varying solar position
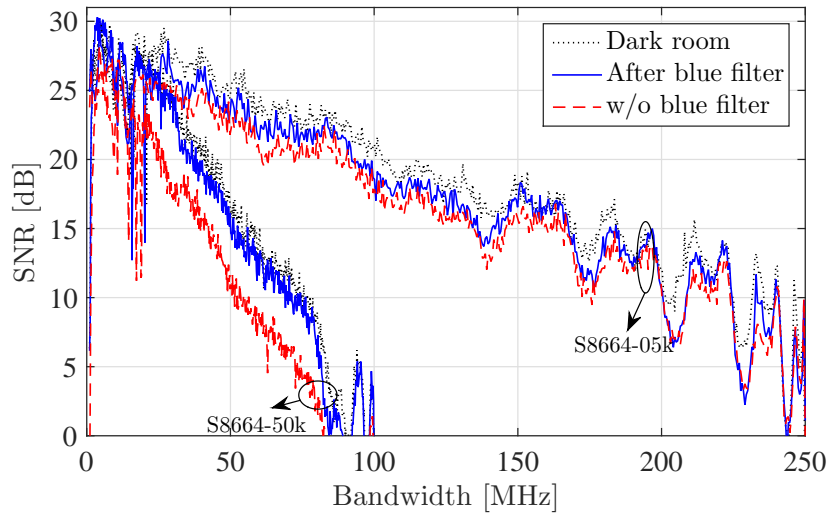
Figure 5.12: *Experimentally estimated SNR versus the system bandwidth when small and large APDs are used for the three considered scenarios.*

throughout the experiment duration. A mirror was used to work around this issue at the expense of reduced solar irradiance. This was shown to have a small impact on the blue band below 450 nm as it is shown in Fig. 5.11. The experimentally measured direct solar irradiance is shown to be identical to the simulated solar irradiance below 580 nm. The mismatch at longer wavelengths is attributed to the high reflectance of mirror glazing in the infrared spectrum that aims to improve building heat insulation [157].

The experimentally estimated SNR is presented in Fig. 5.12 for the small and large APDs for all of the considered scenarios. All the performance comparisons are presented with reference to the optimal dark room (Scenario I). It is shown that the performance of the VLC system degrades in the presence of direct sunlight for both APDs. The degradation in the average SNR is estimated to be 2.2 dB for the small APD and 5.2 dB for the large APD in Scenario III. The photocurrents generated by both signal and background noise generally increase as the detection area of the APD increases. However, an optical source with a small emission area and an imaging lens are used in this experiment to focus the light on the APD. The spot size of the focused light at the APD can ideally be as small as the emission area of the m-LED (0.01 mm^2) [136]. Therefore, the signal photocurrent does not increase when the detection area becomes larger than the focused light spot at the APD. This validates the result that the SNR degradation is higher for the large APD because it collects more background light. When the blue filter is used to restrict the unwanted irradiance, the degradation in the

average SNR is reduced to 1.2 dB for the small APD and 0.9 dB for the large APD. Similar trends are presented in Table 5.2 for the achieved data rates. All the presented data rates are achieved below the FEC limit of 3.8×10^{-3}. The data rate decreases in the presence of solar irradiance. However, most of this reduction can be recovered using the blue filter. It is shown that a data rate of 1.015 Gb/s can be achieved under the presence of solar irradiance for the small APD in Scenario III. This is equivalent to a 10.4% reduction of the data rate compared to Scenario I. This degradation can be reduced to 5.2% when the blue filter is used. A reduction of 24.75% in the data rates is witnessed in Scenario II for the large APD. This is improved to 4.73% when using the blue filter in Scenario II.

5.5   Summary

The impact of sunlight on the performance of VLC systems is investigated. An accurate model for the solar irradiance is used to determine the exact effect based on the location and time of the system. In addition, an experimental study is used to demonstrate that a practical VLC system can be realized under the effect of solar irradiance. The experimental study confirms the theoretical and Monte Carlo simulation results. The effect of sunlight on the performance of DCO-OFDM is examined in both Edinburgh, the United Kingdom and Antofagasta, Chile. The results are presented at multiple times of the year with a particular interest in the June and December solstices due to their corresponding solar position.

A pessimistic approach is assumed for the simulation study in terms of location, time and used devices to consider a worst case scenario for the impact of sunlight on VLC. A blue m-LED is employed at the transmitter and a shot-noise limited APD is used at the receiver. The total solar irradiance is higher than the information signal at the photoreceiver. However, the blue spectral band between 425 nm and 475 nm is affected by a maximum of 15% of the total solar irradiance. That is why a blue filter is found to be beneficial in improving the SNR of the VLC system.

A high speed VLC system is found to be feasible in the presence of sunlight. Shot noise caused by sunlight reduces the data rate of VLC systems. However, optical bandpass blue filters can limit the degradation caused by solar irradiance. Data rates above

1 Gb/s were experimentally achieved in the presence of solar irradiance without optical filtering. Simulation results show that an SNR improvement of at least 6.5 dB can be achieved using off-the-shelf blue filters.

Chapter 6
Conclusions and future work

6.1 Summary and conclusions

Three different intensity modulation and direct detection (IM/DD) techniques are proposed based on superposition modulation in this thesis. The proposed techniques offer spectrum and energy efficient solutions for visible light communication (VLC) based on asymmetrically clipped optical orthogonal frequency division multiplexing (ACO-OFDM) and pulse-amplitude modulation discrete multitone modulation (PAM-DMT). Additionally, a number of experimental studies are presented including a demonstration of spectrum and power efficient VLC systems. Lastly, the effect of sunlight on practical VLC systems is investigated.

Superposition modulation of multiple PAM-DMT streams is proposed in this thesis. It is found that enhanced pulse-amplitude modulation discrete multitone modulation (ePAM-DMT) compensates for the spectral efficiency loss of PAM-DMT. The spectral efficiency of the proposed ePAM-DMT is higher than 95% of the spectral efficiency in DC-biased optical orthogonal frequency division multiplexing (DCO-OFDM) for most practical cases. It is shown that multiple unipolar streams can be superimposed on a PAM-DMT stream as long as they have a Hermitian symmetry in the time-domain. The symmetry properties of the proposed ePAM-DMT allow for a distortion-free demodulation of the multiple superimposed streams at the receiver. This thesis has shown for the first time that the superposition of multiple PAM-DMT streams is more efficient in terms of the electrical power when compared with DCO-OFDM. However, aligning the anti-symmetry of the first modulation depth in ePAM-DMT with the Hermitian symmetry of the additional superimposed streams is computationally complex. In addition, it leads to spectral efficiency losses which results in a higher optical power dissipation when compared with DCO-OFDM.

It is also found that multiple unipolar streams can be superimposed on an ACO-OFDM stream as long as their frequency representation occupies the even-indexed subcarriers.

This is achieved in enhanced asymmetrically clipped optical orthogonal frequency division multiplexing (eACO-OFDM) by imposing an additional symmetry on the time-domain frames of the superimposed streams. This constraints the data symbols of the additional superimposed streams onto the even-indexed subcarriers and allows for a distortion-free demodulation of the independent streams at the receiver. In addition, the proposed eACO-OFDM has a better bit error ratio (BER) performance in comparison with DCO-OFDM in terms of the electrical and optical signal-to-noise ratio (SNR). A novel and computationally efficient method to apply the superposition modulation is introduced in this thesis. The signal generation of augmented spectral efficiency discrete multitone (ASE-DMT) occurs in the frequency domain. The technique is based on selective frequency domain loading of pulse-amplitude modulation (PAM) symbols, so that multiple streams can be superimposed and transmitted without any inter-depth interference (IDI). The selective frequency domain loading of subcarriers allows for a simplified implementation of superposition modulation for PAM-DMT. This simplifies the computational complexity and enables practical IM/DD systems based superposition modulation. The proposed digital modulation techniques in Chapter 3 provides significant energy efficiency gains when compared with DCO-OFDM at equivalent spectral efficiency values. The techniques proposed in this thesis are also promising for both wired and wireless optical communications based on IM/DD.

The experimental VLC studies presented in Chapter 4 provide a proof-of-concept that energy efficient VLC systems can be achieved at high speed communication links. An implementation of DCO-OFDM with adaptive bit and energy loading is demonstrated using a violet micrometer-sized Gallium Nitride light emitting diode (m-LED) and a blue light amplification by stimulated emission of radiation diodes (LDs) in Study I and Study II, respectively. Record data rates are presented in this thesis at 7.81 Gb/s and 15 Gb/s for Study I and Study II, respectively. An improved photoreceiver is found to improve the VLC system throughput in Study I to 11.95 Gb/s. This is achieved by averaging the noise generated by the used photoreceiver and limiting the noise of the system to the nonlinear distortion of the m-LED.

The proposed ASE-DMT is demonstrated as a promising choice for energy efficient IM/DD systems in Study III. The experimental results for ASE-DMT are in close agreement with the theoretical performance. The SNR performance gain of ASE-DMT at low

direct current (DC) bias results in reduced electrical and optical power requirements in comparison with DCO-OFDM and PAM-DMT. However, it is shown that ASE-DMT is more affected than DCO-OFDM by the clipping distortion of the upper clipping point of the used optical source. Therefore, DCO-OFDM is a more preferred choice than ASE-DMT when there is an interest in satisfying the illumination requirements with a high DC bias. Nevertheless, significant energy savings with up to 14.27 dB gain in SNR are achieved in comparison with DCO-OFDM at low DC bias. This highlights the potential of ASE-DMT in spectrum and energy efficient IM/DD systems.

The proposed experimental studies in this thesis present proof-of-concepts for spectrum and energy efficient VLC systems. In addition to the main application in optical attocell access points, the presented studies demonstrate the applicability of VLC systems to a number of other application scenarios. The VLC system in Study I offers a novel solution to the high speed data transmission requirement of board to board communication systems [126, 127]. VLC is a prominent solution for such an application when wired communications cannot be used due to the mechanical requirements of these boards. The LD-based VLC system in Study II can also be envisaged for underwater VLC-based communication systems due to the lower attenuation at the blue wavelength around 450 nm [123]. Finally, the energy efficient ASE-DMT based VLC system presented in Study III offers an energy efficient solution to the infra-red (IR)-based uplink of light fidelity (LiFi) systems where ASE-DMT is shown to be a favorable solution for long distance IM/DD systems. In addition, the experimental system in Study III offers a high speed solution for the dimming application in VLC systems.

The impact of sunlight on VLC is investigated in Chapter 5. The myth that VLC cannot work under the effect of sunlight is refuted for the first time based on simulation and experimental based studies. Worst-case scenarios are considered in the simulation-based study in a pessimistic approach. The simulation and experimental results show that the sunlight degrades the VLC link performance in terms of SNR and BER, but the effects are gradual and depend on a number of other parameters such as the link margin and the location and time of the considered system. The simulation results show that half of the sunlight-caused losses in the data rate performance can be recovered using an inexpensive commercially available bandpass blue filter.

A practical VLC link is proved to be feasible under the effect of sunlight. A high speed

VLC system based on DCO-OFDM is demonstrated and a data rate of 1.01 Gb/s is achieved in the experimental study under a solar illuminance measured at 50350 lux. Therefore, the results of this thesis prove the feasibility of outdoor VLC systems.

6.2 Limitations and future work

The proposed superposition modulation techniques offer spectrum and power efficient solutions for IM/DD. However, the improved spectral and power performance results in an increased signal processing cost. The computational complexity, memory requirements and delay of superposition modulation techniques is expected to grow as the number of superimposed streams increases. A computationally efficient solution is proposed in ASE-DMT where the transmitter is expected to have an equivalent computational complexity as DCO-OFDM. This is proved in [120] using a novel inverse fast Fourier transform (IFFT) architecture. However, the computational complexity at the receiver is expected to be twice of that in DCO-OFDM. Therefore, a solution to the increased complexity of superposition modulation is required in future studies.

The performance comparisons of the proposed modulation techniques are performed in a linear IM/DD channel. However, it is well known that IM/DD channels are nonlinear due to the luminance-voltage (L-V) characteristic function of optical sources. However, the performance comparisons of the superposition modulation techniques are investigated in an experimental study with practical optical sources such as a light emitting diode (LED) and a LD. Therefore, the performance of the proposed modulation technique against the nonlinearity of the optical source is considered. Nevertheless, a detailed theoretical analysis of the proposed solutions against nonlinearity is an open research topic.

The detection error propagation between the lower and the higher order modulation depths in ASE-DMT fades as the SNR increases. However, it would still be interesting to analyze the detection error propagation in order to understand the system performance at low SNR. In addition, it can be useful to apply forward error correction (FEC) coding at each modulation depth to suppress the error propagation. On the other hand, improved receivers with iterative demodulation processes can improve the system performance. For example, the demodulation of the first modulation depth in the

proposed ASE-DMT considers only the imaginary-valued component of the subcarriers. The demodulation of the rest of the superimposed modulation depths considers only the real-valued component of the subcarriers. However, the real-valued component of the subcarriers in the first modulation depth and the imaginary-valued component of the subcarriers in the rest of the superimposed modulation depths hold information that could improve the detection of the data symbols. Improved receivers have appeared in the literature for eACO-OFDM [158]. However, an iterative receiver for ASE-DMT is yet to be investigated.

The experimental studies presented in this thesis are all performed under ideal synchronization between the transmitter and the receiver ends. In addition, multiple training frames are employed to simplify the channel estimation at the receiver. This results in an overhead which reduces the achieved throughput. The perfect synchronization is not always possible in practical scenarios which results in channel estimation errors. On the other hand, the experimental studies are limited by the physical properties of the used system components. For example, the link distance of each considered study is limited by the link budget which is determined by the used optical source, lens system and photoreceiver. The used m-LED in Study I is a power-efficient device to enable communications. However, such devices are still beyond the illuminance levels that allow them to enable general lighting. The low optical power per pixel in m-LEDs is a challenge when combined illumination and communication is considered. This problem can be addressed by using a large arrays of pixels. However, the temperature effects may reduce the maximum total power and degrade the linearity of the L-V curve. Therefore, it is expected to degrade the communication system performance and to curb the lifetime of the device. The m-LED is used in Study I without a heat sink which increases the device degradation due to the continuous modulation at high-speeds and large modulation depths. The effect of VLC on the lifetime of the m-LED is outside the scope of this thesis and should be studied in future works.

The nonlinearity of the m-LED in study I is found to affect the lower frequency bands of the utilized bandwidth. This experimental result shows that the nonlinear distortion differs based on the considered frequency band. The frequency dependency of the nonlinear distortion should be considered theoretically in future works. In addition, nonlinearity mitigation techniques that take into account this frequency dependency

would be interesting to investigate.

The Gaussian probability density function (PDF) of the orthogonal frequency division multiplexing (OFDM)-based modulation techniques results in assigning most of the signal samples around the DC point in DCO-OFDM. Therefore, the signal is not equally distributed in the digital-to-analog converter (DAC) dynamic range. This results in an increased sensitivity to the quantization noise especially when the number of bits at the DAC is low. A solution is proposed in our earlier work on OFDM with discrete power levels [159] by using the Lloyd-Max quantisation method [160]. An improved quantisation method is expected to result in a better immunity against the quantisation noise.

The experimental results in Chapter 4 shows a superior SNR performance for ASE-DMT in comparison with DCO-OFDM at low DC bias. However, the comparison is only limited to constant loading of the subcarriers. Future research on ASE-DMT should consider adaptive bit and energy loading algorithms. In addition, the performance of ASE-DMT is found to be worse than DCO-OFDM at high DC bias. Therefore, a solution for employing ASE-DMT with a DC bias at high illumination levels can be investigated by inverting the polarity of the ASE-DMT waveform. However, the details of such an investigation is open for research.

The main objective of the sunlight study presented in Chapter 5 is to investigate the solar irradiance effect on VLC systems based on the widely used state-of-the-art DCO-OFDM. This approach was adopted to offer a general framework to the research community that allows researchers to consider the solar irradiance effect on their system performance. However, it is natural to claim that once the sunlight illuminance is high, indoor illumination would be dimmed. This makes the proposed superposition modulation technique a suitable solution under high sunlight illuminance scenario. The performance of the proposed superposition modulation technique is not considered under sunlight irradiance. This is because the experimental work on the sunlight irradiance preceded the implementation of the proposed superposition modulation technique. However, the investigation of the sunlight irradiance on the performance of the proposed superposition modulation technique will be considered in future works.

Saturation is a major drawback for photodiodes in the presence of strong background

noise. Automatic gain control (AGC) can be used to reduce the likelihood of performance outage due to avalanche photodiode (APD) saturation. However, this is not considered in this thesis and will be considered in future research. Bandpass optical filtering is considered as a technique to mitigate solar irradiance noise. However, the results of the study presented in Chapter 5 can be used to build upon and to develop new solar irradiance noise mitigation techniques. An interesting solution could be envisaged to use angle-diversity receiver with signal combining techniques. However, the details of such investigation is out the scope of this thesis and will be considered in future research.

Appendix A

The Definition of Bandwidth in IM/DD-based VLC Systems

A.1 Introduction

The definition of bandwidth is fundamental to any communication system as it is directly related to the spectral efficiency and the bit error ratio (BER) performance. There is a confusion about the definition of bandwidth in the literature of optical wireless communication (OWC) [161]. However, this confusion becomes more apparent when using incoherent sources in intensity modulation and direct detection (IM/DD)-based visible light communication (VLC) systems. IM/DD-based systems are usually used in short-to-medium optical wired and wireless communications systems since they offer a cost-effective low-complexity solutions in comparison with coherent-based optical communication systems. In this appendix, we aim to clear the ambiguity that surround the definition of the bandwidth and the spectral efficiency of IM/DD-based systems.

We first compare IM/DD-based systems with coherent based systems. Afterwards, we distinguish between the case of using coherent sources in IM/DD-based OWC systems and the case where incoherent sources in IM/DD-based VLC systems are used. The discussion in this appendix is focused on baseband orthogonal frequency division multiplexing (OFDM)-based systems. However, it can be generalized to any other digital modulation technique straightforwardly.

We argue in this appendix that all of the available bandwidth of the front-end devices in VLC can be utilized without any loss. This appendix explains the differences between one-sided band and double sided bandwidth (DSB) definitions of bandwidth that are adopted in the literature. In addition, we explain why the definition of the one-sided band should be used for IM/DD-based VLC systems.
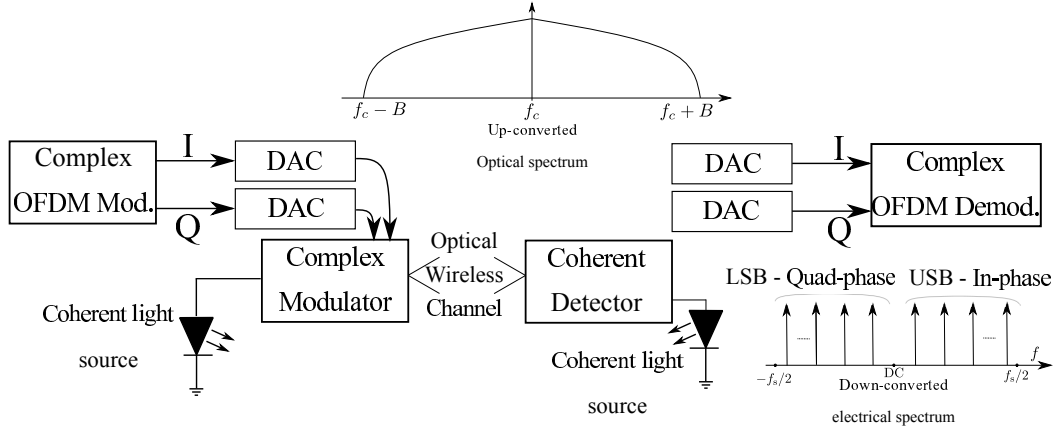
Figure A.1: *Coherent-based OWC system. f_s is the sampling frequency of the DAC. f_c is the carrier frequency of the CW Laser.*

A.2   IM/DD and coherent modulation

Two popular signaling schemes are commonly used in optical communications. The main confusion around the definition of the bandwidth arises when comparing IM/DD-based systems with coherent based systems. Such comparisons usually assume the use of a continuous wave laser (CW Laser) to allow for a fair comparison between IM/DD-based and coherent-based OWC systems. The intensity of a CW Laser is directly modulated in IM/DD-based systems, while the amplitude and phase of the electric field of a CW Laser beam is externally modulated in coherent-based systems. The definition of the bandwidth in most of the published research on IM/DD-based OWC systems is inherently based on the assumption that a CW Laser is used at the transmitter. However, the definition is completely different for IM/DD systems which are based on incoherent sources as will be discussed in Section A.3 for VLC systems.

A coherent-based OFDM communication system is presented in Fig. A.1. The in-phase and quadrature-phase digital outputs of a complex-valued OFDM modulator are converted into analog waveforms using two independent digital-to-analog converters (DACs). The outputs of the DACs are then used to modulate the amplitude and phase of the electric field of a CW Laser using a complex modulator. This up-converts the DSB electrical spectrum of the OFDM to be centered around the optical carrier as shown in Fig. A.1.

The used CW Laser is desired to have a narrow linewidth to allow for a higher spectral
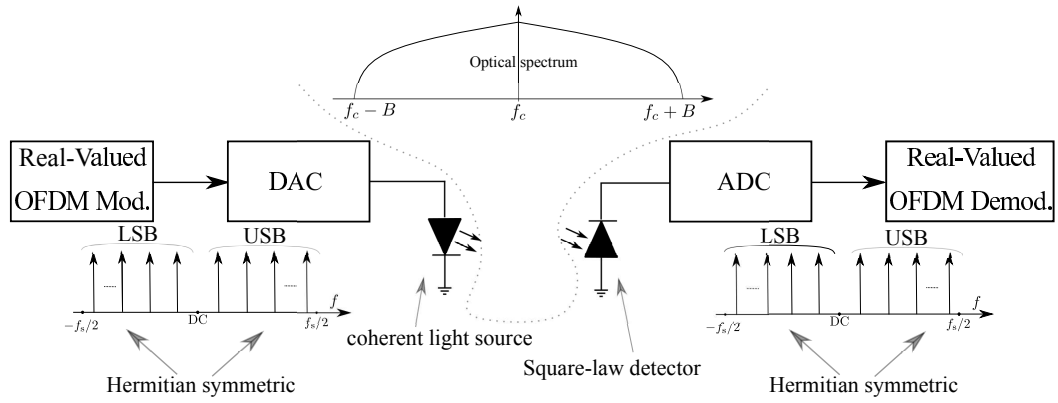
Figure A.2: *IM/DD-based OWC system using a coherent source. f_s is the sampling frequency of the DAC. f_c is the carrier frequency of the CW Laser.*

efficiency in the optical domain. The communication system bandwidth is given as $2B$. Note that the data rate of coherent-based OWC systems is mostly influenced by the bandwidth of the complex modulator[1]. This is an important difference to IM/DD-based systems where the data-rate of the system is mostly influenced by the bandwidth of the light source[2].

Coherent detectors are required at the optical receiver. An additional CW Laser is usually required at the detector because it is capable of down-converting the optical spectrum to the electrical spectrum while linearly mapping the in-phase and quadrature-phase components. Afterwords, two independent analog-to-digital converters (ADCs) are used before a complex-valued demodulator.

An IM/DD-based OWC system is shown in Fig. A.2. A CW Laser is used to allow for a fair comparison with coherent-based systems. One could ask if there are any better ways to modulate a CW Laser, and the answer is: yes. The amplitude and phase of the electric field of a CW Laser can be modulated as it is in coherent-based OWC systems. That would be a complex-valued modulation that would allow for a better use of the channel bandwidth at the expense of using an external complex modulator and a coherent detector. However, IM/DD-based OWCs are attractive for their simplicity and low-cost.

---

[1]This assumes that the bandwidth of the complex modulator is the lowest bandwidth within the coherent-based system.

[2]This assumes that the bandwidth of the light source is the lowest bandwidth within the IM/DD-based system.

The output of an OFDM modulator is a base-band signal which is both complex and bipolar, therefore modifications are required to use OFDM in IM/DD-based systems. The intensity of a CW Laser is directly modulated in IM/DD-based systems. Therefore, real-valued modulating waveforms are only possible. A real-valued OFDM modulator is used with a single DAC operating at a sampling frequency f_s. A CW Laser up-converts the electrical spectrum of the OFDM waveform to the optical domain around the optical carrier as in coherent-based OWC systems. However, the OFDM spectrum is Hermitian symmetric since the modulating waveform is real-valued. Intensity modulation allows for a simplified square-law detectors to be used at the receiver. The detector down-converts the optical spectrum to the electric domain.

The bandwidth of IM/DD-based systems is widely believed to occupy a DSB in both the optical and electrical spectra [162, 163]. However, this assumption is based on the fact that a coherent light source is directly modulated at the transmitter. CW Lasers are directly modulated to up-convert the signal spectrum around the optical carrier frequency. Therefore, the up-converted signal occupies a DSB around a CW Laser optical carrier as discussed in [163].

In this particular case, it can be said that the Hermitian symmetry in IM/DD-based systems leads to a loss that is equal to half of the optical spectrum in comparison with coherent-based OWC systems. However, this is only valid when using a CW Laser source. This is due to the fact that a CW Laser has the capability to utilize both sides of the spectrum, and therefore it can enable a communication bandwidth of[3] $2B$. The claim that IM/DD loses half of the spectrum is not valid in the case of using incoherent sources in VLC-based systems. This is because IM/DD-based VLC systems utilize all of the available spectrum as will be shown in the following section.

The DSB optical spectrum in IM/DD is not desirable in wired optical communications as it limits the transmission distance due to the chromatic distortion of the fiber [162, 164]. Converting the DSB spectrum of IM/DD-based systems to a single sided bandwidth (SSB) is an effective solution to mitigate this distortion [162, 164]. The term upper side band (USB) is used to refer to the one-sided bandwidth definition that we will adopt for IM/DD-based VLC systems to avoid any confusion with the SSB

---

[3]The full $2B$ bandwidth can only be utilized in full when an external modulator and coherent detectors are used.

achieved in the aforementioned solutions.

A.3 IM/DD-based VLC systems

VLC communication transmitters are commonly believed to use incoherent light sources such as light emitting diodes (LEDs), phosphorous-diffused light amplification by stimulated emission of radiation diodes (LDs) or red, green and blue laser diodes (RGB-LDs). In the case of the latter, a diffuser is used to allow for an eye-safe illumination of the LDs which destruct their coherency. Therefore, it is possible to assume that all VLC transmitters are incoherent. IM/DD-based OWC systems which use coherent light sources are referred to as 'IM/DD-based OWC systems', while IM/DD-based OWC systems which use incoherent light sources, which are referred to as 'IM/DD-based VLC systems' for simplicity.

A baseband real-valued waveform is used in IM/DD-based systems to modulate the intensity of the light source. Therefore, the frequency representation of such a waveform is Hermitian symmetric and occupies a DSB as shown in Fig. A.3. The USB conveys the transmitted information and the lower side band (LSB) is redundant. This is similar to the IM/DD-based OWC system detailed in the previous section. However, the only difference is that an incoherent source is used at the transmitter of the VLC system as shown in Fig. A.3. Without loss of generality, the bandwidth of the incoherent light source is assumed to be the minimum bandwidth in comparison with the other system components. The available communication system bandwidth is given as B for IM/DD-based VLC systems. The VLC channel is assumed to be be mainly determined by the frequency response of the incoherent light source. The VLC channel gain can be modeled with a low pass filter (LPF) as presented in Fig. A.3. Therefore, the baseband spectrum will be filtered by this LPF, and a USB consisting of the positive frequencies will only pass through the channel. The LSB is generated again at the detector. However, it is ignored digitally as it conveys no useful information. It is almost impossible to utilize the LSB so that it conveys any additional information in VLC. Incoherent light sources can never preserve the coherency that would allow for independent streams of data to be loaded on the in-phase and quadrature-phase of the spectrum. Coherent-based OWC systems utilize two degrees of freedom (DoF) out of the available two DoF since a complex modulator is used to modulate the amplitude and phase of the electric
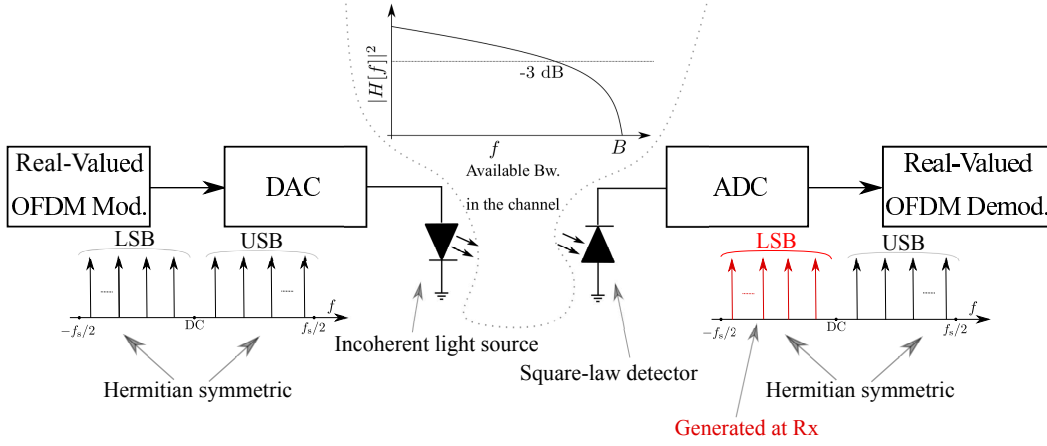
Figure A.3: *IM/DD-based OWC system using an Incoherent source. f_s is the sampling frequency of the DAC.*

field of a CW Laser beam. IM/DD-based OWC systems utilize one DoF out of the available two DoF enabled by the optical carrier. Incoherent sources occupy a very wide optical spectral density in comparison with coherent sources. Therefore, a narrow linewidth optical carrier does not exist in VLC. In contrast to IM/DD-based OWC systems, IM/DD-based VLC systems utilize one DoF out of the single available DoF. A simpler explanation can be given by the fact that coherent sources enable a double sided bandwidth, while incoherent sources are only capable of enabling a single sided bandwidth. Therefore, IM/DD-based VLC systems utilizes all the available bandwidth.

A.3.1 A detailed analysis of an IM/DD-based VLC system

An OFDM signal can be generated as follows: data bits are digitally modulated, usually using an M-ary quadrature amplitude modulation (M-QAM) scheme, where $M = 2^b$ represents the constellation size, and b represents the number of bits per symbol. These symbols are then converted from serial-to-parallel (S/P) streams. An inverse fast Fourier transform (IFFT) operation is usually used for this purpose. A real-valued waveform can be obtained at the output of the IFFT by imposing a Hermitian symmetry on the M-QAM symbols input, $X[k] = X^*[N - k]$ for $k = 1, 2, ..., N - 1$ and by setting $X[\mathrm{DC}] = X[N/2] = 0$.

OFDM uses multiple orthogonal sub-carriers at different frequencies to convey the information bits. Orthogonality is guaranteed by transmitting the OFDM symbols with a subcarrier spacing equal to $\Delta f = \frac{1}{T_\mathrm{Sym}}$, where T_Sym is the symbol duration given as

follows:

$$T_{\text{Sym}} = NT_{\text{s}}, \tag{A.1}$$

where N is the OFDM frame length which represents the number of subcarriers within an OFDM frame, $T_{\text{s}} = \frac{1}{f_{\text{s}}}$ is the sampling period, $f_{\text{s}} \geq 2B$ is the Nyquist sampling rate and B is the available bandwidth of the IM/DD-based VLC system. In practical systems an oversampling factor is used to minimize the likelihood of anti-aliasing. However, the Nyquist sampling rate is used $f_{\text{s}} = 2B$ in this appendix for simplicity. We also define the available bandwidth of the VLC system by the USB as discussed in the previous section. This is determined by the bandwidth of the used optical front-end, which is generally limited by the bandwidth of the incoherent light source. The spectrum of a real-valued OFDM DAC output is given in baseband as shown in Fig. A.4.
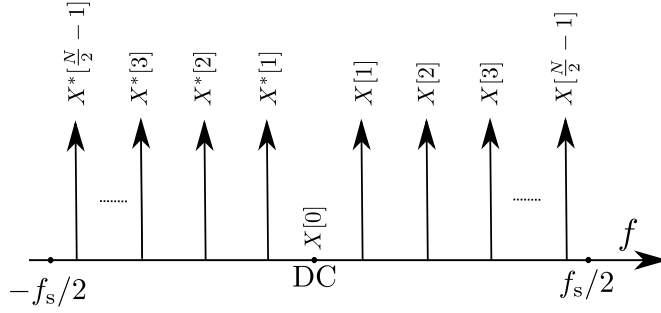
Figure A.4: *The frequency domain representation of a baseband real-valued OFDM waveform.*

The statistics of a real-valued bipolar OFDM time-domain waveform can be approximated with a Gaussian distribution, $x(t) \sim \mathcal{N}(0, \sigma_x^2)$ when $N \geq 64$, where σ_x is the standard deviation of $x(t)$ [86]. The average power of an OFDM frame is given as $P^{\text{avg}} = \text{E}[x^2(t)] = \sigma_x^2$. The energy per bit can be defined as follows:

$$E_{\text{b}} = \frac{\text{Average power of the OFDM frame} \times \text{Duration of the frame}}{\text{Number of bits within a frame}}. \tag{A.2}$$

This can be given as follows:

$$E_{\text{b}} = \frac{\sigma_x^2 N T_{\text{s}}}{\frac{N-2}{2} \log_2 M}. \tag{A.3}$$

This can be approximated for large values of N as follows:

$$E_{\text{b}} = \frac{\sigma_x^2}{B \log_2 M} \tag{A.4}$$

The signal-to-noise ratio (SNR) per bit can then be give as follows:

$$\frac{E_{\text{b}}}{N_o} = \frac{\sigma_x^2}{BN_o \log_2 M} = \frac{\sigma_x^2}{\sigma_n^2 \log_2 M}, \tag{A.5}$$

where N_o is the single sided power spectral density (PSD) of the additive white Gaussian noise (AWGN) at the receiver, and σ_n is the variance of the noise.

The spectral efficiency of the system can be defined as:

$$\eta = \frac{\frac{\text{Number of bits within the OFDM frame}}{\text{Duration of the frame}}}{\text{Available bandwidth}}. \tag{A.6}$$

This can be given as:

$$\eta = \frac{\frac{\frac{N-2}{2} \log_2 M}{(N+N_{\text{CP}})T_{\text{s}}}}{B}, \tag{A.7}$$

where N_{CP} is the length of the cyclic prefix (CP). A constant loading of symbols with a constellation size M is assumed for simplicity. This can be approximated to $\eta \approx \log_2 M$ for large values for the OFDM frame length N.

A.4 Summary

Hermitian symmetry does not lead to any spectral efficiency loss in IM/DD-based VLC systems. The definition of the bandwidth in IM/DD-based systems is examined for OWC and VLC. IM/DD-based OWC systems are commonly assumed to utilize a CW Laser source at the transmitter. Such types of LDs enables a double-sided optical bandwidth. This optical bandwidth is not achievable with incoherent sources in IM/DD-based VLC systems. Therefore, a one-sided bandwidth is the only available room for the signal spectrum in VLC systems.

Adopting the DSB definition limits the performance of the VLC system to the performance of the DAC and the electronic driving circuitry. High speed DACs are commercially available and they should not become the barrier in satisfying the anticipated potentials of VLC-based systems.

Appendix B
Possible candidates for arbitrary constellation sizes

The set of all the possible candidates of constellation sizes that can achieve a spectral efficiency target η and their associated optimal scaling factors are presented in this appendix for all of the proposed superposition modulation techniques in Chapter 3.

The set $\mathcal{M}_{(\varsigma,D)}^{\mathrm{can.,SM}}$ of all the possible candidates of constellation sizes $\underline{M}_{(\eta,\varsigma,D)}^{\mathrm{can.,SM}}$ is obtained by Algorithm 1 in Chapter 3, where D is the total number of superimposed depths and ς is a variable that is set to $\varsigma = 1$ for enhanced asymmetrically clipped optical orthogonal frequency division multiplexing (eACO-OFDM) and $\varsigma = 2$ for enhanced pulse-amplitude modulation discrete multitone modulation (ePAM-DMT) and augmented spectral efficiency discrete multitone (ASE-DMT). The optimal scaling factors $\underline{\gamma}_{(\eta,\varsigma,D)}^{\mathrm{can.,SM}}$ for each of the associated candidates of constellation sizes $\underline{M}_{(\eta,\varsigma,D)}^{\mathrm{can.,SM}} \in \mathcal{M}_{(\varsigma,D)}^{\mathrm{can.,SM}}$ are obtained using Algorithm 2 and Algorithm 3 presented in Chapter 3. The maximum permitted constellation size at each of the considered spectral efficiency values $M_{\mathrm{SM},\eta}^{\mathrm{Max}}$ is presented in Table. B.1. The values were chosen to avoid any large constellation size that can lead to a performance degradation.

The set $\mathcal{M}_{(2,2)}^{\mathrm{can.,ePAM}}$ is shown in Table B.2 for spectral efficiency targets $\eta = \{1, 1.5, 2, 2.5, 3, 3.5, 4, 4.5\}$ bits/s/Hz when $D = 2$. The set $\mathcal{M}_{(2,3)}^{\mathrm{can.,ePAM}}$ is shown in Table B.3 for spectral efficiency targets $\eta = \{1, 1.5, 2, 2.5\}$ bits/s/Hz when $D = 3$ and in Table B.4 for spectral efficiency targets $\eta = \{3, 3.5, 4, 4.5, 5\}$ bits/s/Hz when $D = 3$.

Similarly, the sets $\mathcal{M}_{(2,2)}^{\mathrm{can.,ASE}}$ and $\mathcal{M}_{(2,3)}^{\mathrm{can.,ASE}}$ are shown in Table B.5 for spectral efficiency targets $\eta = \{1, 1.5, 2, 2.5, 3, 3.5, 4, 4.5\}$ bits/s/Hz when $D = 2$ and for spectral efficiency targets $\eta = \{1, 1.5, 2, 2.5\}$ bits/s/Hz when $D = 3$. The set $\mathcal{M}_{(2,3)}^{\mathrm{can.,ASE}}$ is shown in Table B.6 for spectral efficiency targets $\eta = \{3, 3.5, 4, 4.5, 5\}$ bits/s/Hz when $D = 3$.

The set $\mathcal{M}_{(1,2)}^{\mathrm{can.,eACO}}$ is shown in Table B.7 for spectral efficiency targets $\eta = \{0.5, 1, 1.5, 2\}$ bits/s/Hz when $D = 2$ and in Table. B.8 for spectral efficiency targets $\eta = \{2.5, 3,$

3.5, 4, 4.5\} bits/s/Hz when $D = 2$. Lastly, the set $\mathcal{M}_{(1,3)}^{\text{can.,eACO}}$ is shown in Table B.9 for spectral efficiency targets $\eta = \{1, 1.5, 2, 2.5\}$ bits/s/Hz when $D = 3$, Table. B.10 for spectral efficiency targets $\eta = \{0.5, 4.5, 5\}$ bits/s/Hz when $D = 3$, and Table B.11 for spectral efficiency targets $\eta = \{3, 3.5, 4\}$ bits/s/Hz when $D = 3$.

M_{DCO}	η [bits/s/Hz]	$M_{\text{eACO},\eta}^{\text{Max}}$	$M_{\text{ePAM},\eta}^{\text{Max}}$ $M_{\text{ASE},\eta}^{\text{Max}}$
2	0.5	8	—
4	1	32	4
8	1.5	128	8
16	2	256	16
32	2.5	512	16
64	3	1024	32
128	3.5	2048	32
256	4	4096	64
512	4.5	4096	64
1024	5	4096	64

Table B.1: *The maximum permitted arbitrary constellation size in ePAM-DMT, eACO-OFDM and ASE-DMT for any modulation depth $d > 1$*

$\underline{M}^{\mathrm{can.,ePAM}}_{(1,2,2)}$	$\underline{\gamma}^{\mathrm{can.,dB}}_{(1,2,2)}$	$\underline{M}^{\mathrm{can.,ePAM}}_{(1.5,2,2)}$	$\underline{\gamma}^{\mathrm{can.,dB}}_{(1.5,2,2)}$	$\underline{M}^{\mathrm{can.,ePAM}}_{(2,2,2)}$	$\underline{\gamma}^{\mathrm{can.,dB}}_{(2,2,2)}$	$\underline{M}^{\mathrm{can.,ePAM}}_{(2.5,2,2)}$	$\underline{\gamma}^{\mathrm{can.}}_{(2.5,2,2)}$
[2,4]	[5.2,-4]	[4,4]	[1.1,-1.4]	[4,16]	[9.2,-4.9]	[8,16]	[4.4,-3.7]
—	—	—	—	[8,4]	[-1,2.2]	[16,4]	[-2,6.8]

$\underline{M}^{\mathrm{can.,ePAM}}_{(3,2,2)}$	$\underline{\gamma}^{\mathrm{can.,dB}}_{(3,2,2)}$	$\underline{M}^{\mathrm{can.,ePAM}}_{(3.5,2,2)}$	$\underline{\gamma}^{\mathrm{can.,dB}}_{(3.5,2,2)}$	$\underline{M}^{\mathrm{can.,ePAM}}_{(4,2,2)}$	$\underline{\gamma}^{\mathrm{can.,dB}}_{(4,2,2)}$	$\underline{M}^{\mathrm{can.,ePAM}}_{(4.5,2,2)}$	$\underline{\gamma}^{\mathrm{can.,dB}}_{(4.5,2,2)}$
[16,16]	[1.1,-1.4]	[32,16]	[-0.9,1.9]	[32,64]	[4.4,-3.7]	[64,64]	[1.1,-1.4]
[32,4]	[-2,12.6]	—	—	[64,16]	[-2,-6.6]	—	—

Table B.2: *The set $\mathcal{M}^{\mathrm{can.,ePAM}}_{(2,2)}$ of all possible candidates of constellation sizes and their associated optimal scaling factors in ePAM-DMT that can achieve spectral efficiency targets $\eta = \{1, 1.5,\ 2, 2.5, 3,\ 3.5, 4, 4.5\}$ bits/s/Hz with a total number of superimposed depths $D = 2$.*

$\underline{M}^{\mathrm{can.,ePAM}}_{(1,2,3)}$	$\underline{\gamma}^{\mathrm{can.,dB}}_{(1,2,3)}$	$\underline{M}^{\mathrm{can.,ePAM}}_{(1.5,2,3)}$	$\underline{\gamma}^{\mathrm{can.,dB}}_{(1.5,2,3)}$	$\underline{M}^{\mathrm{can.,ePAM}}_{(2,2,3)}$	$\underline{\gamma}^{\mathrm{can.,dB}}_{(2,2,3)}$	$\underline{M}^{\mathrm{can.,ePAM}}_{(2.5,2,3)}$	$\underline{\gamma}^{\mathrm{can.}}_{(2.5,2,3)}$
[2,2,4]	[4.7,2.2,-6.6]	[2,8,4]	[10,-4.7,-1.5]	[2,16,16]	[17,-3.3,-5.4]	[4,16,16]	[11,-2.8,-5]
—	—	[4,2,4]	[0.4,4.3,-4.3]	[4,4,16]	[8.2,5.5,-8.3]	[8,4,16]	[3.4,6.6,-7.2]
—	—	—	—	[4,8,4]	[4.5,-3.6,-0.5]	[8,8,4]	[0.7,-1.7,1.5]
—	—	—	—	[8,2,4]	[-1.9,8,-1.3]	[16,2,4]	[-3,13,3.1]

Table B.3: *The set $\mathcal{M}^{\mathrm{can.,ePAM}}_{(2,3)}$ of all possible candidates of constellation sizes and their associated optimal scaling factors in ePAM-DMT that can achieve spectral efficiency targets $\eta = \{1, 1.5,\ 2, 2.5\}$ bits/s/Hz with a total number of superimposed depths $D = 3$.*

$M^{\text{can.,ePAM}}_{(3,2,3)}$	$\gamma^{\text{can.,dB}}_{(3,2,3)}$	$M^{\text{can.,ePAM}}_{(3.5,2,3)}$	$\gamma^{\text{can.,dB}}_{(3.5,2,3)}$	$M^{\text{can.,ePAM}}_{(4,2,3)}$	$\gamma^{\text{can.,dB}}_{(4,2,3)}$	$M^{\text{can.,ePAM}}_{(4.5,2,3)}$	$\gamma^{\text{can.,dB}}_{(4.5,2,3)}$	$M^{\text{can.,ePAM}}_{(5,2,3)}$	$\gamma^{\text{can.,dB}}_{(5,2,3)}$
[8,16,16]	[5.8,-2,-4.2]	[16,16,16]	[1.8,-0.4,-2.4]	[16,32,64]	[8.9,0.7,-7.2]	[32,32,64]	[4.3,1.7,-6.2]	[64,32,64]	[0.5,3.4,-4]
[8,32,4]	[8,-5.9,8.5]	[16,32,4]	[3.3,-4.8,9.6]	[16,64,16]	[8.4,-5.5,3]	[32,64,16]	[3.7,-4.4,4.1]	[64,64,16]	[0.2,-2.4,6.3]
[16,4,16]	[-0.1,8.5,-4.9]	[32,4,16]	[-2,12,-1.9]	[32,8,64]	[3.1,12,-7.6]	[64,8,64]	[-0.4,14,-5.2]	—	—
[16,8,4]	[-1.7,1.3,4.5]	[32,8,4]	[-3,5.6,8.8]	[32,16,16]	[-0.8,2,-0.5]	[64,16,16]	[-2.6,5.9,3.2]	—	—
[32,2,4]	[-3.8,18,8]	—	—	[32,32,4]	[-0.2,-2.6,12]	[64,32,4]	[-2,0.7,15]	—	—
—	—	—	—	[64,2,64]	[-0.7,26,-5.4]	—	—	—	—
—	—	—	—	[64,4,16]	[-3,17,2.8]	—	—	—	—
—	—	—	—	[64,8,4]	[-3.8,11,14]	—	—	—	—

Table B.4: *The set $\mathcal{M}^{\text{can.,ePAM}}_{(2,3)}$ of all possible candidates of constellation sizes and their associated optimal scaling factors in ePAM-DMT that can achieve spectral efficiency targets $\eta = \{3,\ 3.5, 4, 4.5,\ 5\}$ bits/s/Hz with a total number of superimposed depths $D = 3$.*

$\underline{M}^{\text{can.,ASE}}_{(1,2,2)}$	$\underline{\gamma}^{\text{can.,dB}}_{(1,2,2)}$	$\underline{M}^{\text{can.,ASE}}_{(1.5,2,2)}$	$\underline{\gamma}^{\text{can.,dB}}_{(1.5,2,2)}$	$\underline{M}^{\text{can.,ASE}}_{(2,2,2)}$	$\underline{\gamma}^{\text{can.,dB}}_{(2,2,2)}$	$\underline{M}^{\text{can.,ASE}}_{(2.5,2,2)}$	$\underline{\gamma}^{\text{can.}}_{(2.5,2,2)}$
[2,4]	[3.3,-3.2]	[4,4]	[0,0]	[4,16]	[7.2,-4.5]	[8,16]	[2.8,-2.9]
—	—	—	—	[8,4]	[-1,4.8]	[16,4]	[-2,9.7]
$\underline{M}^{\text{can.,ASE}}_{(3,2,2)}$	$\underline{\gamma}^{\text{can.,dB}}_{(3,2,2)}$	$\underline{M}^{\text{can.,ASE}}_{(3.5,2,2)}$	$\underline{\gamma}^{\text{can.,dB}}_{(3.5,2,2)}$	$\underline{M}^{\text{can.,ASE}}_{(4,2,2)}$	$\underline{\gamma}^{\text{can.,dB}}_{(4,2,2)}$	$\underline{M}^{\text{can.,ASE}}_{(4.5,2,2)}$	$\underline{\gamma}^{\text{can.,dB}}_{(4.5,2,2)}$
[16,16]	[0,0]	[32,16]	[-1,4.6]	[32,64]	[2.8,-2.9]	[64,64]	[0,0]
[32,4]	[-2,15.5]	—	—	[64,16]	[-2,9.4]	—	—
$\underline{M}^{\text{can.,ASE}}_{(1,2,3)}$	$\underline{\gamma}^{\text{can.,dB}}_{(1,2,3)}$	$\underline{M}^{\text{can.,ASE}}_{(1.5,2,3)}$	$\underline{\gamma}^{\text{can.,dB}}_{(1.5,2,3)}$	$\underline{M}^{\text{can.,ASE}}_{(2,2,3)}$	$\underline{\gamma}^{\text{can.,dB}}_{(2,2,3)}$	$\underline{M}^{\text{can.,ASE}}_{(2.5,2,3)}$	$\underline{\gamma}^{\text{can.}}_{(2.5,2,3)}$
[2,2,4]	[1.9,2,-4.6]	[2,8,4]	[7.7,-5,1]	[2,16,16]	[14.2,-4.1,-3.9]	[4,16,16]	[8.1,-3.4,-3.4]
—	—	[4,2,4]	[-1.5,5.3,-1.2]	[4,4,16]	[4.6,4.7,-7.2]	[8,4,16]	[0.6,6.6,-5.2]
—	—	—	—	[4,8,4]	[2.4,-3.4,2.5]	[8,8,4]	[-0.9,-0.7,5.3]
—	—	—	—	[8,2,4]	[-3,9.7,3]	[16,2,4]	[-3.7,14.8,8.1]

Table B.5: *The sets $\mathcal{M}^{\text{can.,ASE}}_{(2,2)}$ and $\mathcal{M}^{\text{can.,ASE}}_{(2,3)}$ of all possible candidates of constellation sizes and their associated optimal scaling factors in ASE-DMT that can achieve spectral efficiency targets $\eta = \{1, 1.5, \ 2, 2.5, 3, \ 3.5, 4\}$ bits/s/Hz when the total number of superimposed depths $D = 2$, or spectral efficiency targets $\eta = \{1, 1.5, \ 2, 2.5\}$ bits/s/Hz when the total number of superimposed depths $D = 3$.*

$\underline{M}^{\mathrm{can.,ASE}}_{(3,2,3)}$	$\underline{\gamma}^{\mathrm{can.,dB}}_{(3,2,3)}$	$\underline{M}^{\mathrm{can.,ASE}}_{(3.5,2,3)}$	$\underline{\gamma}^{\mathrm{can.,dB}}_{(3.5,2,3)}$	$\underline{M}^{\mathrm{can.,ASE}}_{(4,2,3)}$	$\underline{\gamma}^{\mathrm{can.,dB}}_{(4,2,3)}$	$\underline{M}^{\mathrm{can.,ASE}}_{(4.5,2,3)}$	$\underline{\gamma}^{\mathrm{can.,dB}}_{(4.5,2,3)}$	$\underline{M}^{\mathrm{can.,ASE}}_{(5,2,3)}$	$\underline{\gamma}^{\mathrm{can.,dB}}_{(5,2,3)}$
[8,16,16]	[3.4,-2.2,-2]	[16,16,16]	[0,0,0]	[16,32,64]	[5.7,-0.1,-5.8]	[32,32,64]	[1.5,1.7,-4]	[64,32,64]	[-1.3,4.3,-1.1]
[8,32,4]	[5.9,-5.7,12.1]	[16,32,4]	[1.5,-4.1,13.5]	[16,64,16]	[6.1,-5.4,6.2]	[32,64,16]	[1.8,-3.9,7.7]	[64,64,16]	[-1,-1.3,10.2]
[16,4,16]	[-1.9,9.8,-1.9]	[32,4,16]	[-3,14.4,2.8]	[32,8,64]	[0.1,11.8,-5.6]	[64,8,64]	[-2.2,14.9,-2]	—	—
[16,8,4]	[-2.7,3.2,9.4]	[32,8,4]	[-3,8.5,14.6]	[32,16,16]	[-2,3.6,3.7]	[64,16,16]	[-3,8.4,8.5]	—	—
[32,2,4]	[-4,20.3,13.5]	—	—	[32,32,4]	[-1.4,-1.2,16]	[64,32,4]	[-3,3,20.4]	—	—
—	—	—	—	[64,2,64]	[-2.4,27.3,-2.3]	—	—	—	—
—	—	—	—	[64,4,16]	[-3.8,19.5,7.7]	—	—	—	—
—	—	—	—	[64,8,4]	[-4,13.3,19.4]	—	—	—	—

Table B.6: *The set $\mathcal{M}^{\mathrm{can.,ASE}}_{(2,3)}$ of all possible candidates of constellation sizes and their associated optimal scaling factors in ASE-DMT that can achieve spectral efficiency targets $\eta = \{3, 3.5, 4, 4.5, 5\}$ bits/s/Hz when the total number of superimposed depths $D = 3$.*

$\underline{M}^{\mathrm{can.,eACO}}_{(0.5,1,2)}$	$\underline{\gamma}^{\mathrm{can.}}_{(0.5,1,2)}$	$\underline{M}^{\mathrm{can.,eACO}}_{(1,1,2)}$	$\underline{\gamma}^{\mathrm{can.,dB}}_{(1,1,2)}$	$\underline{M}^{\mathrm{can.,eACO}}_{(1.5,1,2)}$	$\underline{\gamma}^{\mathrm{can.,dB}}_{(1.5,1,2)}$	$\underline{M}^{\mathrm{can.,eACO}}_{(2,1,2)}$	$\underline{\gamma}^{\mathrm{can.,dB}}_{(2,1,2)}$
[2,4]	[2.2,-2.4]	[4,16]	[3.3,-3.2]	[8,64]	[5.1,-3.9]	[16,256]	[7.2,-4.5]
—	—	[8,4]	[-1,2.5]	[16,16]	[0,0]	[32,64]	[1.3,-1.6]
—	—	—	—	[32,4]	[-2,7.7]	[64,16]	[-1,4.8]
—	—	—	—	—	—	[128,4]	[-2,13.5]

Table B.7: *The set $\mathcal{M}^{\mathrm{can.,eACO}}_{(1,2)}$ of all possible candidates of constellation sizes and their associated optimal scaling factors in eACO-OFDM that can achieve spectral efficiency targets $\eta = \{0.5, 1, 1.5, 2\}$ bits/s/Hz with a total number of superimposed depths $D = 2$.*

$\underline{M}^{\text{can.,eACO}}_{(2.5,1,2)}$	$\underline{\gamma}^{\text{can.}}_{(2.5,1,2)}$	$\underline{M}^{\text{can.,eACO}}_{(3,1,2)}$	$\underline{\gamma}^{\text{can.,dB}}_{(3,1,2)}$	$\underline{M}^{\text{can.,eACO}}_{(3.5,1,2)}$	$\underline{\gamma}^{\text{can.,dB}}_{(3.5,1,2)}$	$\underline{M}^{\text{can.,eACO}}_{(4,1,2)}$	$\underline{\gamma}^{\text{can.,dB}}_{(4,1,2)}$	$\underline{M}^{\text{can.,eACO}}_{(4.5,1,2)}$	$\underline{\gamma}^{\text{can.,dB}}_{(4.5,1,2)}$
[64,256]	[2.8,-2.9]	[128,1k]	[4.7,-3.8]	[512,1k]	[1.2,-1.5]	[1k,4k]	[2.8,-2.9]	[4k,4k]	[0,0]
[128,64]	[-0.9,1.9]	[256,256]	[0,0]	[1k,256]	[-1,4.6]	[2k,1k]	[-0.9,1.9]	—	—
[256,16]	[-2,9.7]	[512,64]	[-2,6.6]	[2k,64]	[-2,12.3]	[4k,256]	[-2,9.4]	—	—
[512,4]	[-2,19.3]	[1k,16]	[-2,15.5]	—	—	—	—	—	—

Table B.8: *The set $\mathcal{M}^{\text{can.,eACO}}_{(1,2)}$ of all possible candidates of constellation sizes and their associated optimal scaling factors in eACO-OFDM that can achieve spectral efficiency targets $\eta = \{2.5, 3, 3.5, 4, 4.5\}$ bits/s/Hz with a total number of superimposed depths $D = 2$.*

$\underline{M}^{\text{can.,eACO}}_{(1,1,3)}$	$\underline{\gamma}^{\text{can.,dB}}_{(1,1,3)}$	$\underline{M}^{\text{can.,eACO}}_{(1.5,1,3)}$	$\underline{\gamma}^{\text{can.,dB}}_{(1.5,1,3)}$	$\underline{M}^{\text{can.,eACO}}_{(2,1,3)}$	$\underline{\gamma}^{\text{can.,dB}}_{(2,1,3)}$	$\underline{M}^{\text{can.,eACO}}_{(2.5,1,3)}$	$\underline{\gamma}^{\text{can.}}_{(2.5,1,3)}$
[2,16,16]	[7.7,-3.4,-3.3]	[4,32,64]	[7.6,-2.1,-4.9]	[4,256,256]	[14.2,-4.1,-3.9]	[16,256,256]	[8.1,-3.4,-3.4]
[4,4,16]	[1.9,2,-4.6]	[4,64,16]	[7.7,-5,1]	[8,64,256]	[8.6,-0.6,-6.4]	[16,512,64]	[9,-5.6,3.1]
[4,8,4]	[1.2,-2.2,1.4]	[8,8,64]	[3.1,3.1,-6.1]	[8,128,64]	[7.6,-4.3,-1.3]	[32,64,256]	[3.6,0.7,-5.1]
[8,2,4]	[-2.3,5.9,1.4]	[8,16,16]	[1.7,-1.3,-1.2]	[8,256,16]	[9,-5.9,6]	[32,128,64]	[2.8,-2.9,0]
—	—	[8,32,4]	[2.2,-3.9,5.9]	[16,16,256]	[4.6,4.7,-7.2]	[32,256,16]	[3.8,-4.8,7]
—	—	[16,2,64]	[0.2,11.8,-5.7]	[16,32,64]	[2.5,-0.4,-3.2]	[32,512,4]	[5.8,-5.8,15.9]
—	—	[16,4,16]	[-1.5,5.3,-1.2]	[16,64,16]	[2.4,-3.4,2.5]	[64,16,256]	[0.6,6.6,-5.2]
—	—	[16,8,4]	[-1.8,1.4,5]	[16,128,4]	[3.7,-5,10.7]	[64,32,64]	[-0.8,2.1,-0.6]
—	—	[32,2,4]	[-3,11.4,6.8]	[32,4,256]	[1.8,11.7,-7]	[64,64,16]	[-0.9,-0.7,5.3]
—	—	—	—	[32,8,64]	[-0.6,5.7,-3.4]	[64,128,4]	[-0.1,-2.8,13.1]
—	—	—	—	[32,16,16]	[-1.4,1.7,2]	[128,4,256]	[-1.3,14.4,-4]
—	—	—	—	[32,32,4]	[-1,-1.2,8.8]	[128,8,64]	[-2.6,9.6,0.7]
—	—	—	—	[64,2,64]	[-2.2,15.1,-2]	[128,16,16]	[-3,6.2,6.3]
—	—	—	—	[64,4,16]	[-3,9.7,3]	[128,32,4]	[-2.9,3.3,13.2]
—	—	—	—	[64,8,4]	[-3,6.1,9.8]	[256,2,64]	[-3,20.2,2.8]
—	—	—	—	[128,2,4]	[-3.9,16.4,11.7]	[256,4,16]	[-3.7,14.8,8.1]
—	—	—	—	—	—	[256,8,4]	[-3.8,11.1,14.8]
—	—	—	—	—	—	[512,2,4]	[-4,22.1,17.4]

Table B.9: *The set $\mathcal{M}^{\text{can.,eACO}}_{(1,3)}$ of all possible candidates of constellation sizes and their associated optimal scaling factors in eACO-OFDM that can achieve spectral efficiency targets $\eta = \{1, 1.5, 2, 2.5\}$ bits/s/Hz with a total number of superimposed depths $D = 3$.*

$\underline{M}^{\text{can.,eACO}}_{(0.5,1,3)}$	$\underline{\gamma}^{\text{can.,dB}}_{(0.5,1,3)}$	$\underline{M}^{\text{can.,eACO}}_{(4.5,1,3)}$	$\underline{\gamma}^{\text{can.,dB}}_{(4.5,1,3)}$	$\underline{M}^{\text{can.,eACO}}_{(5,1,3)}$	$\underline{\gamma}^{\text{can.,dB}}_{(5,1,3)}$
[2,2,4]	[1.2,1.2,-3.3]	[512,4k,4k]	[5.4,-2.9,-2.8]	[2k,4k,4k]	[1.5,-1.2,-1]
—	—	[1k,1k,4k]	[1.5,1.7,-4]	[4k,1k,4k]	[-1.3,4.3,-1.1]
—	—	[1k,2k,1k]	[0.9,-1.8,1.2]	[4k,2k,1k]	[-1.7,1.4,4.3]
—	—	[1k,4k,256]	[1.8,-3.9,7.7]	[4k,4k,256]	[-1,-1.3,10.2]
—	—	[2k,256,4k]	[-0.9,7.9,-3.6]	—	—
—	—	[2k,512,1k]	[-1.9,4,1.3]	—	—
—	—	[2k,1k,256]	[-1.9,1.1,6.8]	—	—
—	—	[2k,2k,64]	[-1.3,-1.2,13.3]	—	—
—	—	[2k,4k,16]	[-0.2,-3,20.7]	—	—
—	—	[4k,64,4k]	[-2.2,14.9,-2]	—	—
—	—	[4k,128,1k]	[-3,11.3,2.8]	—	—
—	—	[4k,256,256]	[-3,8.4,8.5]	—	—
—	—	[4k,512,64]	[-3,5.5,14.3]	—	—
—	—	[4k,1k,16]	[-3,3,20.4]	—	—
—	—	[4k,2k,4]	[-2.4,0.6,27.7]	—	—

Table B.10: *The set $\mathcal{M}^{\text{can.,eACO}}_{(1,3)}$ of all possible candidates of constellation sizes and their associated optimal scaling factors in eACO-OFDM that can achieve spectral efficiency targets $\eta = \{0.5, 4.5, 5\}$ bits/s/Hz with a total number of superimposed depths $D = 3$.*

$\underline{M}^{\mathrm{can.,eACO}}_{(3,1,3)}$	$\underline{\gamma}^{\mathrm{can.,dB}}_{(3,1,3)}$	$\underline{M}^{\mathrm{can.,eACO}}_{(3.5,1,3)}$	$\underline{\gamma}^{\mathrm{can.,dB}}_{(3.5,1,3)}$	$\underline{M}^{\mathrm{can.,eACO}}_{(4,1,3)}$	$\underline{\gamma}^{\mathrm{can.,dB}}_{(4,1,3)}$
[32,512,1k]	[9.3,-2.4,-5.2]	[64,2k,1k]	[9.8,-4.6,-1.7]	[128,4k,4k]	[10.4,-3.8,-3.6]
[32,1k,256]	[9.3,-5.2,0.6]	[128,512,1k]	[4.4,-1.3,-4]	[256,1k,4k]	[5.7,-0.1,-5.8]
[64,128,1k]	[5,2,-6.6]	[128,1k,256]	[4.4,-4.2,1.6]	[256,2k,1k]	[4.8,-3.6,-0.8]
[64,256,256]	[3.4,-2.2,-2]	[128,2k,64]	[5.9,-5.6,9]	[256,4k,256]	[6.1,-5.4,6.2]
[64,512,64]	[4,-4.5,4.2]	[256,128,1k]	[0.9,3.9,-4.7]	[512,256,4k]	[2.3,5.3,-6.3]
[64,1k,16]	[5.9,-5.7,12.1]	[256,256,256]	[0,0,0]	[512,512,1k]	[0.6,0.7,-2]
[128,32,1k]	[2,8,-6.6]	[256,512,64]	[0.3,-2.5,6.3]	[512,1k,256]	[0.5,-2.2,3.8]
[128,64,256]	[-0.1,2.9,-2.8]	[256,1k,16]	[1.5,-4.1,13.5]	[512,2k,64]	[1.6,-4,10.5]
[128,128,64]	[0,-0.4,2.6]	[256,2k,4]	[3.4,-5.2,22.3]	[512,4k,16]	[3.4,-5.2,18.4]
[128,256,16]	[0.1,-2.7,9.4]	[512,32,1k]	[-1.1,10.6,-3.8]	[1k,64,4k]	[0.1,11.8,-5.6]
[128,512,4]	[1.4,-4.2,17.3]	[512,64,256]	[-2,6.5,0.8]	[1k,128,1k]	[-1.7,6.8,-1.4]
[256,8,1k]	[-0.1,15.1,-5.7]	[512,128,64]	[-2.5,3.3,6.4]	[1k,256,256]	[-2,3.6,3.7]
[256,16,256]	[-1.9,9.8,-1.9]	[512,256,16]	[-2,0.7,12.6]	[1k,512,64]	[-2,0.8,9.5]
[256,32,64]	[-2.7,6.3,3.5]	[512,512,4]	[-1.4,-1.4,20.2]	[1k,1k,16]	[-1.4,-1.2,16]
[256,64,16]	[-2.7,3.2,9.4]	[1k,8,1k]	[-2.3,18.2,-2.1]	[1k,2k,4]	[-0.2,-3,24.2]
[256,128,4]	[-2,0.7,16.5]	[1k,16,256]	[-3,14.4,2.8]	[2k,16,4k]	[-1.4,19.1,-4.1]
[512,2,1k]	[-1.5,24.8,-4.2]	[1k,32,64]	[-3,11.4,8.6]	[2k,32,1k]	[-2.8,14.4,0.2]
[512,4,256]	[-2.9,18.4,0]	[1k,64,16]	[-3,8.5,14.6]	[2k,64,256]	[-3,11.3,5.6]
[512,8,64]	[-3,14.8,5.7]	[1k,128,4]	[-3,5.6,21.4]	[2k,128,64]	[-3,8.4,11.4]
[512,16,16]	[-3.7,10.9,11]	[2k,2,1k]	[-3,28.7,-0.1]	[2k,256,16]	[-3,5.5,17.4]
[512,32,4]	[-3,8.5,18.5]	[2k,4,256]	[-3.7,23.4,5]	[2k,512,4]	[-3,2.8,24.2]
[1k,2,64]	[-3.9,25.3,7.7]	[2k,8,64]	[-4,20,11]	[4k,4,4k]	[-2.4,27.3,-2.3]
[1k,4,16]	[-4,20.3,13.5]	[2k,16,16]	[-4,16.3,16.4]	[4k,8,1k]	[-3,23.4,2.8]
[1k,8,4]	[-4,16.7,20.4]	[2k,32,4]	[-4,13.3,23.3]	[4k,16,256]	[-3.8,19.5,7.7]
—	—	—	—	[4k,32,64]	[-4,16.4,13.5]
—	—	—	—	[4k,64,16]	[-4,13.3,19.4]
—	—	—	—	[4k,128,4]	[-3.9,10.4,26.3]

Table B.11: *The set $\mathcal{M}^{\mathrm{can.,eACO}}_{(1,3)}$ of all possible candidates of constellation sizes and their associated optimal scaling factors in eACO-OFDM that can achieve spectral efficiency targets $\eta = \{3, 3.5, 4\}$ bits/s/Hz with a total number of superimposed depths $D = 3$.*

Appendix C
The averaging effect on SNR of DCO-OFDM

The effect of oscilloscope averaging on the signal-to-noise ratio (SNR) of DC-biased optical orthogonal frequency division multiplexing (DCO-OFDM) is analyzed in this appendix. Averaging can be used in repetitive communications when similar replicas of the transmitted waveform are repeatedly transmitted. Averaging acquisition is considered to be useful in extracting results from experimental studies that could influence practical system design [133]. The averaging acquisition mode was used in one of the scenarios of Study I in Chapter 4 to analyze the visible light communication (VLC) system performance when it is only limited to the nonlinearity of the optical source.

The received averaged waveform $y^{\text{Avg}}[n]$ at the discrete time index n is given as follows:

$$y^{\text{Avg}}[n] = \frac{1}{N^{\text{Avg}}} \sum_{j=1}^{N^{\text{Avg}}} y_j[n], \tag{C.1}$$

where N^{Avg} is the total number of averaged waveforms at the oscilloscope and $y_j[n]$ is the j–th sample of the received waveform at discrete time index n, which is given as follows:

$$y_j[n] = h[n] * z(x_j[n]) + w_j[n], \tag{C.2}$$

where $h[n]$ is the VLC channel impulse response[1] at discrete-time sample n, $z(\cdot)$ is the nonlinear transformation of the light source, $w_j[n]$ is the j–th sample of the additive white Gaussian noise (AWGN) at discrete time index n and $x_j[n]$ is the j–th sample of the transmitted waveform at discrete time index n, which is given as: $x_j[n] = x[n] \, \forall \, j = 1, 2, \cdots, N^{\text{Avg}}$.

The nonlinear transformation $z(\cdot)$ can be described using the Bussgang theorem as detailed in Chapter 4. The averaged received waveform given in (C.1) can then be

---

[1]The VLC channel gain at subcarrier k is assumed to remain constant for the duration of capturing the N^{Avg} waveforms

given as follows:

$$y^{\text{Avg}}[n] = \frac{h[n]}{N^{\text{Avg}}} \sum_{j=1}^{N^{\text{Avg}}} (\alpha x[n] + w_{\text{c}}) + \frac{1}{N^{\text{Avg}}} \sum_{j=1}^{N^{\text{Avg}}} w_j[n], \tag{C.3}$$

where α is an attenuation factor that is given in (4.3), w_{c} is the nonlinear distortion noise which is a non-Gaussian noise. However, its representation in the frequency domain $W_{\text{c}}(f)$ follows a Gaussian distribution with a mean $\text{E}[w_{\text{c}}]$ given in (4.6) and a variance $\sigma_{w_{\text{c}}}^2$ given in (4.5), where $\text{E}[\cdot]$ is the statistical expectation. The nonlinear distortion w_{c} is uncorrelated with the transmitted signal x, $\text{E}[x \cdot w_{\text{c}}] = 0$. The averaged AWGN noise is defined as follows:

$$w[n] = \frac{1}{N^{\text{Avg}}} \sum_{j=1}^{N^{\text{Avg}}} w_j[n]. \tag{C.4}$$

The noise samples at the discrete time index n, $w_j[n] \, \forall \, j = 1, 2, \cdots, N^{\text{Avg}}$ are independent identically distributed (i.i.d.) Gaussian noise with zero mean and variance σ_n^2. Therefore, the central limit theorem (CLT) applies on (C.4), and the variance of the averaged AWGN noise can be given as $\frac{\sigma_n^2}{N^{\text{Avg}}}$. The averaged noise is uncorrelated with the transmitted signal x, $\text{E}[x \cdot w] = 0$.

The SNR of DCO-OFDM for the averaged received waveforms can then be given as follows:

$$\text{SNR}_{\text{Avg}} = \frac{\alpha^2 \sigma_x^2}{\sigma_{w_{\text{c}}}^2 + \frac{\sigma_n^2(1 + k_{\text{DC}}^2)}{N^{\text{Avg}}|H(k)|^2}}. \tag{C.5}$$

The SNR given in (C.5) becomes limited by the nonlinearity of the optical source for large values of N^{Avg}, as shown below:

$$\lim_{N^{\text{Avg}} \to \infty} \text{SNR}_{\text{Avg}} = \frac{\alpha^2 \sigma_x^2}{\sigma_{w_{\text{c}}}^2}. \tag{C.6}$$

Appendix D
Solar Position

Three coordinate systems are used to calculate the position of the Sun in Chapter 5: ecliptic coordinates; equatorial coordinates; and horizontal coordinates. These coordinate systems can be illustrated on the celestial sphere that is shown in Fig. D.1. The parameters corresponding to each coordinate system are mapped in Table D.1. The arbitrary coordinates in Fig. D.1 is defined by Θ which is the angle between the principle and the projection of the Sun at the fundamental plane and by Ξ which is the angle between the Sun and the fundamental plane. Celestial coordinate systems can be converted into Cartesian coordinates using:

$$
\begin{pmatrix} X_{\mathrm{C}} \\ Y_{\mathrm{C}} \\ Z_{\mathrm{C}} \end{pmatrix} = \begin{pmatrix} \cos\Xi\cos\Theta \\ \cos\Xi\sin\Theta \\ \sin\Xi \end{pmatrix}.
\tag{D.1}
$$

Arbitrary	Ecliptic	Equatorial	Horizontal
center	center of the Earth	center of the Earth	observer
north pole	north ecliptic pole	north celestial pole	zenith
fundamental plane	ecliptic	celestial equator	horizon
principle	March equinox	March equinox	geographic north pole
Θ	ecliptic longitude (λ_{el})	right ascension (α^{ra})	azimuth (Az)
Ξ	ecliptic latitude (β)	declination (δ)	altitude (Al)
$\begin{pmatrix} X_{\mathrm{C}} \\ Y_{\mathrm{C}} \\ Z_{\mathrm{C}} \end{pmatrix}$	$\begin{pmatrix} X_{\mathrm{Ecl}} \\ Y_{\mathrm{Ecl}} \\ Z_{\mathrm{Ecl}} \end{pmatrix}$	$\begin{pmatrix} X_{\mathrm{Equ}} \\ Y_{\mathrm{Equ}} \\ Z_{\mathrm{Equ}} \end{pmatrix}$	$\begin{pmatrix} X_{\mathrm{Hor}} \\ Y_{\mathrm{Hor}} \\ Z_{\mathrm{Hor}} \end{pmatrix}$

Table D.1: *Coordination systems corresponding parameters*

The horizontal coordinate system is usually used for solar cell applications where the horizon of the observer is the fundamental plane. The solar position can be projected on a celestial sphere using two angles: altitude Al and azimuth Az. The Earth revolves around the Sun in an elliptic orbit in which a complete revolution takes a year, a motion of around 1° per day. This motion can be best described using the ecliptic coordinates
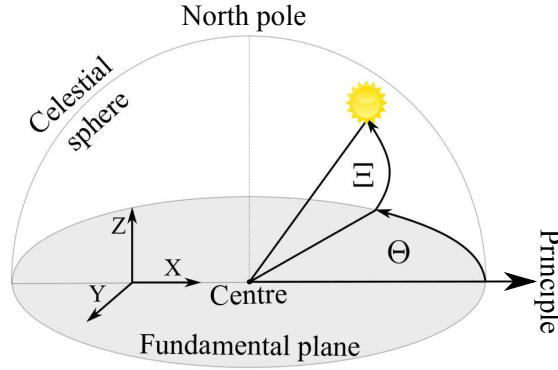
Figure D.1: *An illustration of an arbitrary coordinate system on a celestial sphere.*

where the principle is the position of the Sun during the spring equinox (the date of the year when the Earth's equator is aligned with the center of the Sun ecliptic). The angular ecliptic coordinates are the ecliptic longitude, λ_{el} and ecliptic latitude, β, which is given as $\beta \approx 0$ [150]. The ecliptic longitude can be given as follows [150]:

$$\lambda_{\mathrm{el}} = q_{\mathrm{ml}} + 1.915° \sin g_{\mathrm{o}} + 0.020° \sin 2g_{\mathrm{o}}, \tag{D.2}$$

where q_{ml} is the mean longitude given as follows [150]:

$$q = 280.459° + 0.98564736° D_{\mathrm{o}}, \tag{D.3}$$

and g_{o} is the mean anomaly of the Sun, which accounts for the varying speeds of the Earth motion throughout the year. This is given as follows [150]:

$$g_{\mathrm{o}} = 357.529° + 0.98560028° D_{\mathrm{o}}, \tag{D.4}$$

where D_{o} is the time elapsed since the Greenwich noon of the 1$^{\mathrm{st}}$ of January 2000.

The equatorial coordinate system is required as a translational stage when transforming the ecliptic coordinates into equatorial coordinates, as follows:

$$\begin{pmatrix} X_{\mathrm{Equ}} \\ Y_{\mathrm{Equ}} \\ Z_{\mathrm{Equ}} \end{pmatrix} = \begin{pmatrix} 1 & 0 & 0 \\ 0 & \cos \epsilon & -\sin \epsilon \\ 0 & \sin \epsilon & \cos \epsilon \end{pmatrix} \begin{pmatrix} X_{\mathrm{Ecl}} \\ Y_{\mathrm{Ecl}} \\ Z_{\mathrm{Ecl}} \end{pmatrix}, \tag{D.5}$$

where ϵ is the axial tilt between the equatorial plane and the ecliptic plane. The axial

tilt is zero in March and September equinox and takes its maximum value of $\pm 23.429°$ in June and December solstices (the days when the maximum tilt is experienced at the north and south hemisphere, respectively). The axial tilt is given as follows [150]:

$$\epsilon = 23.429° - 0.00000036° D_{\mathrm{o}}. \tag{D.6}$$

The equatorial coordinates are given by the right ascension α^{ra} which is the angle between the March equinox and the projection of the Sun on the Earth's equator and by the declination δ which is the angle between the Sun and the Earth equator. The Sun moves $15°$ of longitude per hour. The hour angle is defined as the angle between the projection of the Sun on the fundamental plane and the meridian given at longitude of $0°$ (an imaginary circle passing through the north and south poles and the zenith of an observer). The hour angle is given as follows:

$$h_{\mathrm{o}} = \theta_L - \alpha^{\mathrm{ra}}, \tag{D.7}$$

where θ_L is the angle between the meridian and the March equinox. It can also be defined as the local mean sidereal time (LMST). A sidereal day is the time that the Earth takes to complete a $360°$ rotation on its own axis. It is slightly shorter than the solar day mainly due to the rotation of the Earth around the Sun. The LMST can be given as:

$$\theta_L = \mathrm{GMST}\frac{15°}{\mathrm{hour}} + \lambda_0, \tag{D.8}$$

where λ_0 is the longitude of the observer and GMST is the Greenwich mean sidereal time (GMST), which is defined as the hour angle between the March equinox and the meridian at Greenwich. The GMST is calculated as follows [150]:

$$\mathrm{GMST} = 18.697374558\mathrm{h} + 24.06570982441908\mathrm{h}D_{\mathrm{o}}, \tag{D.9}$$

where it is scaled to values between 0 and 24.

The principle of the coordinates can be transformed from the March equinox to the

LMST using [150]:

$$\begin{pmatrix} \cos \delta \cos h \\ \cos \delta \sin h \\ \sin \delta \end{pmatrix} = \begin{pmatrix} \cos \theta_L & \sin \theta_L & 0 \\ \sin \theta_L & -\cos \theta_L & 0 \\ 0 & 0 & 1 \end{pmatrix} \begin{pmatrix} X_{\text{Equ}} \\ Y_{\text{Equ}} \\ Z_{\text{Equ}} \end{pmatrix}, \tag{D.10}$$

In addition, the center of the coordinates can be transformed from the center of the Earth to the position of the observer using [150]:

$$\begin{pmatrix} X'_{\text{Hor}} \\ Y'_{\text{Hor}} \\ Z'_{\text{Hor}} \end{pmatrix} = \begin{pmatrix} \sin \phi_0 & 0 & -\cos \phi_0 \\ 0 & 1 & 0 \\ \cos \phi_0 & 0 & \sin \phi_0 \end{pmatrix} \begin{pmatrix} \cos \delta \cos h \\ \cos \delta \sin h \\ \sin \delta \end{pmatrix}, \tag{D.11}$$

where ϕ_0 is the latitude angle of the observer. Following the prior calculations, the directions of X'_{Hor} and Y'_{Hor} are directed towards south and west, respectively. The following can be applied to adjust the reference direction to north and east [150]:

$$\begin{pmatrix} X_{\text{Hor}} \\ Y_{\text{Hor}} \\ Z_{\text{Hor}} \end{pmatrix} = \begin{pmatrix} -1 & 0 & 0 \\ 0 & -1 & 0 \\ 0 & 0 & 1 \end{pmatrix} \begin{pmatrix} X'_{\text{Hor}} \\ Y'_{\text{Hor}} \\ Z'_{\text{Hor}} \end{pmatrix} \tag{D.12}$$

The horizontal coordinates can then be calculated using [150]:

$$\sin Al = \cos \phi_0 \cos \theta_L \cos \lambda_{\text{el}} + (\cos \phi_0 \sin \theta_L \cos \epsilon + \sin \phi_0 \sin \epsilon) \sin \lambda_{\text{el}} \tag{D.13}$$

$$\tan Az = \frac{\Gamma_1}{\Gamma_2 - \Gamma_3}, \tag{D.14}$$

where:

$$\Gamma_1 = -\sin \theta_L \cos \lambda_{\text{el}} + \cos \theta_L \cos \epsilon \sin \lambda_{\text{el}}, \tag{D.15}$$

$$\Gamma_2 = -\sin \phi_0 \cos \theta_L \cos \lambda_{\text{el}}, \tag{D.16}$$

$$\Gamma_3 = \sin \lambda_{\text{el}}(\sin \phi_0 \sin \theta_L \cos \epsilon - \cos \phi_0 \sin \epsilon), \tag{D.17}$$

Appendix E
Selected publications

E.1   Journal publications

- M. S. Islim and H. Haas, "Augmenting the spectral efficiency of enhanced pam-dmt-based optical wireless communications," *OSA Opt. Express*, vol. 24, pp. 11932–11949, May 2016.

- M. S. Islim, R. X. Ferreira, X. He, E. Xie, S. Videv, S. Viola, S. Watson, N. Bamiedakis, R. V. Penty, I. H. White, A. E. Kelly, E. Gu, H. Haas, and M. D. Dawson, "Towards 10 Gb/s Orthogonal Frequency Division Multiplexing-based Visible Light Communication Using a GaN Violet Micro-LED," *OSA Photon. Res.*, vol. 5, pp. A35–A43, Apr 2017.

- M. S. Islim, S. Videv, M. Safari, E. Xie, J. J. D. McKendry, E. Gu, M. D. Dawson, and H. Haas, "The Impact of Solar Irradiance on Visible Light Communications," *IEEE/OSA J. Lightw. Technol.*, vol. 36, pp. 2376–2386, Jun 2018.

E.2   Magazine publications

- M. S. Islim and H. Haas, "Modulation Techniques for Li-Fi," *ZTE Communications*, vol. 14, pp. 29–40, Apr 2016.

E.3   Book chapter

- D. Tsonev, M. S. Islim, and H. Haas, 2016. OFDM-based visible light communications. In *Optical Wireless Communications* (pp. 255–298). Springer, Cham.

E.4   Conference publications

- M. S. Islim, D. Tsonev, and H. Haas, "Spectrally Enhanced PAM-DMT for IM/DD

Optical Wireless Communications," in *Proc. of the 25th Int. Symp. Pers. Indoor and Mobile Radio Commun. (PIMRC)*, (Hong Kong, China), pp. 927–932, IEEE, Aug. 30–Sept. 2 2015.

- M. S. Islim, D. Tsonev, and H. Haas, "On the Superposition Modulation for OFDM-based Optical Wireless Communication," in *Signal and Information Processing (GlobalSIP), 2015 IEEE Global Conference on*, (Orlando, USA), IEEE, Dec., 14–16 2015.

- S. Viola, M. S. Islim, S. Watson, S. Videv, H. Haas, and A. E. Kelly, "15 Gb/s OFDM-based VLC Using Direct Modulation of 450 GaN Laser Diode," in *Proc. SPIE*, vol. 10437, (Warsaw, Poland), pp. 10437 – 10437, Oct. 6 2017.

- M. S. Islim and H. Haas, "An Investigation of the Sunlight Irradiance Effect on Visible Light Communications," in *2017 IEEE 28th Annual International Symposium on Personal, Indoor, and Mobile Radio Communications (PIMRC)*, (Montreal, Canada), pp. 1–6, Oct., 8–13 2017.

- M. S. Islim and H. Haas, "An Experimental Demonstration of a Superposition-based DMT Technique for IM/DD." *Accepted in 2019 IEEE International Conference on Communication Workshop (ICCW)*, 2019.

E.5   Patents

- M. S. Islim and H. Haas, "Communication Scheme for Intensity Modulated Systems", *international patent application*: PCT/GB2017/051423, May 2016.

- M. S. Islim and H. Haas, "Mobile Hand-held LiFi Device or Cover", *international patent application:* PCT/GB2017/053797, Dec. 2016.

Augmenting the spectral efficiency of enhanced PAM-DMT-based optical wireless communications

Mohamed Sufyan Islim,* **and Harald Haas**

Institute for Digital Communications, Li-Fi R&D Centre, the University of Edinburgh, King's Buildings, Mayfield Road, Edinburgh, EH9 3JL, UK

*m.islim@ed.ac.uk

Abstract: The energy efficiency of pulse-amplitude-modulated discrete multitone modulation (PAM-DMT) decreases as the modulation order of *M*-PAM modulation increases. Enhanced PAM-DMT (ePAM-DMT) was proposed as a solution to the reduced energy efficiency of PAM-DMT. This was achieved by allowing multiple streams of PAM-DMT to be superimposed and successively demodulated at the receiver side. In order to maintain a distortion-free unipolar ePAM-DMT system, the multiple time-domain PAM-DMT streams are required to be aligned. However, aligning the antisymmetry in ePAM-DMT is complex and results in efficiency losses. In this paper, a novel simplified method to apply the superposition modulation on *M*-PAM modulated discrete multitone (DMT) is introduced. Contrary to ePAM-DMT, the signal generation of the proposed system, termed augmented spectral efficiency discrete multitone (ASE-DMT), occurs in the frequency domain. This results in an improved spectral and energy efficiency. The analytical bit error rate (BER) performance bound of the proposed system is derived and compared with Monte-Carlo simulations. The system performance is shown to offer significant electrical and optical energy savings compared with ePAM-DMT and DC-biased optical orthogonal frequency division multiplexing (DCO-OFDM).

OCIS codes: (060.4510) Optical communications; (170.4090) Modulation techniques; (220.4830) Systems design.

References and links

1. Cisco Visual Networking Index, "The Zettabyte era: trends and analysis," White Paper, Cisco (2015), http://www.cisco.com/c/en/us/solutions/collateral/service-provider/visual-networking-index-vni/VNI_Hyperconnectivity_WP.pdf.
2. S. Dimitrov and H. Haas, *Principles of LED Light Communications: Towards Networked Li-Fi*, (Cambridge University, 2015).
3. D. Tsonev, S. Videv, and H. Haas, "Towards a 100 Gb/s visible light wireless access network," Opt. Express **23**, 1627–1637 (2015).
4. J. Armstrong and A.J. Lowery, "Power efficient optical OFDM," Elect. Lett. **42**, 370–372 (2006).
5. S. C. J. Lee, S. Randel, F. Breyer, and A. M. J. Koonen, "PAM-DMT for intensity-modulated and direct-detection optical communication systems," IEEE Photonics Technology Letters **21**, 1749–1751 (2009).
6. D. Tsonev, S. Sinanovic, and H. Haas, "Novel unipolar orthogonal frequency division multiplexing (U-OFDM) for optical wireless," in *Proceedings of IEEE Vehicular Technology Conference (VTC Spring)*, (IEEE, 2012). pp. 1–5.
7. N. Fernando, Y. Hong; E. Viterbo, "Flip-OFDM for Unipolar Communication Systems," IEEE Tran. on Commun. **60**, 3726–3733 (2012).

8. D. Tsonev, S. Videv, and H. Haas, "Unlocking spectral efficiency in intensity modulation and direct detection systems," IEEE J. Sel. Areas Commun. **33**, 1758–1770 (2015).

9. M. Islim, D. Tsonev, and H. Haas, "Spectrally enhanced PAM-DMT for IM/DD optical wireless communications," in *Proceedings of IEEE Personal, Indoor, and Mobile Radio Communication*, (IEEE, 2015), pp. 877–882.

10. M. Islim, D. Tsonev, and H. Haas, "On the superposition modulation for OFDM-based optical wireless Communication," in *Proceedings of IEEE Global Signal and Information Processing conference*, (IEEE, 2015). pp. 1022–1026.

11. H. Elgala and T. Little, "SEE-OFDM: spectral and energy efficient OFDM for optical IM/DD systems," in *Proceedings of IEEE Personal, Indoor, and Mobile Radio Communication*, (IEEE, 2014), pp. 851–855.

12. Q. Wang, C. Qian, X. Guo, Z. Wang, D. G. Cunningham, and I. H. White, "Layered ACO-OFDM for intensity-modulated direct-detection optical wireless transmission," Opt. Express **23**, 12382–12393 (2015).

13. A.J. Lowery, "Enhanced asymmetrically-clipped optical OFDM," Opt. Express **24**, 3950–3966 (2016).

14. D. Tsonev, S. Sinanovic, and H. Haas, "Complete modelling of nonlinear distortion in OFDM-based optical wireless communication," J. Lightw. Technol. **31**, 3064–3076 (2013).

15. M. Islim, D. Tsonev, and H. Haas, "A generalized solution to the spectral efficiency loss in unipolar optical OFDM-based systems," in *Proceedings of IEEE International Conference on Communications (ICC)*, (IEEE, 2015). pp. 5126–3131.

16. F. Xiong, *Digital Modulation Techniques*, (Artech House Publishers, 2006), 2nd ed.

17. J. Proakis and G. Manolakis, *Digital Signal Processing* (Pearson, 2013), Chap. 8.

18. H. Hassanieh, P. Indyk, D. Katabi, and E. Price, "Nearly optimal sparse fourier transform," in *Proceedings of the forty-fourth annual ACM symposium on Theory of computing*, (ACM, 2012), pp. 563–578.

19. J. Armstrong and B. J. C. Schmidt, "Comparison of asymmetrically clipped optical OFDM and DC-biased optical OFDM in AWGN," IEEE Commun. Lett. **12**, 343–345 (2008).

1. Introduction

As the demand for higher data rate broadband access increases, the limited availability of the electromagnetic spectrum becomes an ever more important challenge. It is predicted that the annual global internet traffic will be in the order of the Zettabyte (1000 exabytes) by the end of 2016, and will be 2 Zettabytes per year by 2019 [1]. The increasing number of interconnected digital devices and online services highlights the necessity of new access technologies that could meet these demands. The visible light spectrum offers an abundant, unregulated communication bandwidth [2]. Visible light communication (VLC) is an emerging technique that is predicted to offer data rates of 100 Gb/s at very high deployment devices in the near future [3].

VLC is realized using off-the-shelf optoelectronic light emitting diodes (LEDs) and photodiodes (PDs). Due to the nature of these optoelectronic devices, the optical signal is required to be both real and positive. Optical orthogonal frequency division multiplexing (OFDM) is a promising candidate for high-speed VLCs and optical wireless communications (OWCs) [2]. Optical OFDM imposes Hermitian symmetry on the incoming frames to achieve a real time-domain waveform. The direct current (DC)-biased optical OFDM (DCO-OFDM) employs a DC bias to shift the signal samples to become positive. Unipolar OFDM schemes, such as asymmetrically clipped optical OFDM (ACO-OFDM) [4]; pulse-amplitude-modulated discrete multitone (PAM-DMT) [5]; unipolar orthogonal frequency division multiplexing (U-OFDM) [6]; and flip OFDM (FLIP-OFDM) [7], achieve unipolar OFDM time-domain waveforms by exploiting the frequency/time domain symmetries of the OFDM frames. As a result, all of these unipolar schemes, except PAM-DMT, have a reduced spectral efficiency in comparison with DCO-OFDM. The bit error rate (BER) performance of M-ary quadrature amplitude modulation (M-QAM) DCO-OFDM, should be compared with M^2-QAM {ACO-OFDM; U-OFDM; flipped-OFDM}, and M-PAM PAM-DMT. Since the BER performance of M-PAM is equivalent to the BER performance M^2-QAM at a given signal-to-noise ratio (SNR), the BER performance of all of the aforementioned unipolar OFDM schemes is identical. More importantly, the power efficiency of unipolar OFDM schemes decreases as the constellation size M increases, which makes it impracticable to employ these schemes for high data rate applications.

A novel superposition modulation technique termed, enhanced U-OFDM (eU-OFDM), was introduced in [8] as a solution to the spectral efficiency gap between U-OFDM and DCO-OFDM. Enhanced U-OFDM compensates for the spectral efficiency loss of U-OFDM by superimposing multiple U-OFDM frames. The superimposed U-OFDM streams are arranged so that the inter-stream-interference is null. The superposition concept was also extended to other unipolar OFDM techniques such as PAM-DMT in [9] and ACO-OFDM in [10–13]. The superposition optical OFDM techniques close the spectral efficiency gap between unipolar OFDM and DCO-OFDM, but require increased computational complexity and memory requirements. Enhanced asymmetrically clipped optical OFDM (eACO-OFDM) [10] utilizes the symmetry of ACO-OFDM subframes to allow multiple ACO-OFDM streams to be superimposed. A similar concept was also proposed by Elgala *et al.* [11] and Wang *et al.* [12] under the terms spectrally and energy efficient OFDM (SEE-OFDM), and layered asymmetrically clipped optical OFDM (Layered ACO-OFDM), respectively. The receiver proposed in SEE-OFDM [11] results in a SNR penalty that could have been avoided by using the symmetry properties of ACO-OFDM streams. The symmetry arrangement in Layered ACO-OFDM [12] is described in the frequency domain, however, it is shown in [12, Fig. 2] that it takes place in the time-domain. An alternative method to achieve superposition modulation based on aclaco was proposed by Lawery [13]. This is similar in principle to [10–12], however the superposition is performed in the frequency domain which results in simpler system implementation compared with the time domain processing of eACO-OFDM, SEE-OFDM and Layered ACO-OFDM. The constellation size of each superimposed depth in eACO-OFDM is optimized so that the full spectral efficiency of DCO-OFDM is achieved.

The enhanced pulse-amplitude-modulated discrete multitone (ePAM-DMT) [9] demonstrates that superposition modulation can also be utilized using the antisymmetry of PAM-DMT waveforms. However, aligning the antisymmetry of multiple PAM-DMT waveforms in the time domain is a complex process and results in spectral efficiency losses. The antisymmetry of PAM-DMT waveforms incorporates the cyclic prefix (CP) in aligning the symmetry. In addition ePAM-DMT requires flipping the PAM-DMT subframes in the time domain, which requires lengthy time-domain processing.

In this paper, a novel simplified technique is proposed to generate the superimposed PAM-DMT waveforms in the frequency domain, and it is termed augmented spectral efficiency discrete multitone (ASE-DMT). The proposed technique, ASE-DMT, avoids the spectral efficiency losses of ePAM-DMT and provides energy efficiency improvements over ePAM-DMT and DCO-OFDM by using the selective subcarrier modulation algorithm at each superimposed depth.

The paper is organized as follows. The proposed technique is described in Section 2, where the modulation concept of ASE-DMT and its spectral and power efficiencies are analysed. The theoretical analysis of the BER performance is derived in Section 3. A detailed study on the additional computation complexity of the proposed technique is presented in Section 4. A Performance comparison with ePAM-DMT and DCO-OFDM and simulation results of the proposed scheme are presented in Section 5. A simplified approach for implementing the proposed modulation technique is presented in Section 5.2. Finally, conclusions are given in Section 6.

2. Augmented spectral efficiency discrete multitone (ASE-DMT)

The augmented spectral efficiency discrete multitone (ASE-DMT) technique uses most of the available subcarriers in the OFDM frame. The ASE-DMT waveform can be generated by a selective loading of the imaginary and real components of the subcarriers. The waveform generation starts with a typical PAM-DMT [5] modulator at the first depth. Additional streams can only be superimposed on the first depth stream if their frequency domain subcarriers are
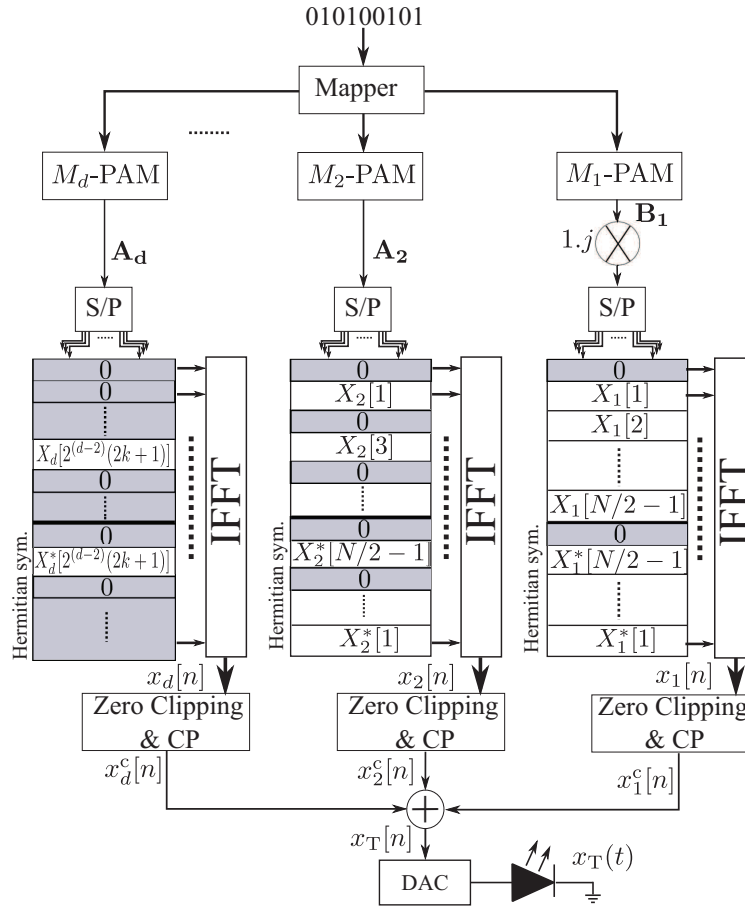
Fig. 1. ASE-DMT transmitter block diagram. $X_d[k]$ refers to the kth subcarrier at depth d; S/P denotes for serial to parallel; DAC denotes for digital to analogue conversion; and CP refers to the cyclic prefixing.

loaded on the real components of the subcarriers. This constraint was fulfilled in ePAM-DMT by rearranging the ePAM-DMT time domain waveforms to have a Hermitian symmetry [9]. Alternatively, in ASE-DMT, the frames alignment is arranged in the frequency domain.

2.1. Modulation concept

The transmitter block diagram of ASE-DMT is shown in Fig. 1. At the first depth, the imaginary components of the subcarriers are loaded with M-ary pulse-amplitude modulation (M-PAM) symbols while the real components are kept unused $X_1[k] = jB_1[k]$, where $B_1[k]$ is the M-PAM symbol at the kth subcarrier of depth 1. Note that Hermitian symmetry is also required in the frequency domain to guarantee a real time-domain output, $B_1[0] = B_1[N/2]$, and $B_1[k] = -B_1[N-k]$ for $k = 1, 2, ..., N/2 - 1$. As a result, the time domain PAM-DMT waveform $x_1[n]$
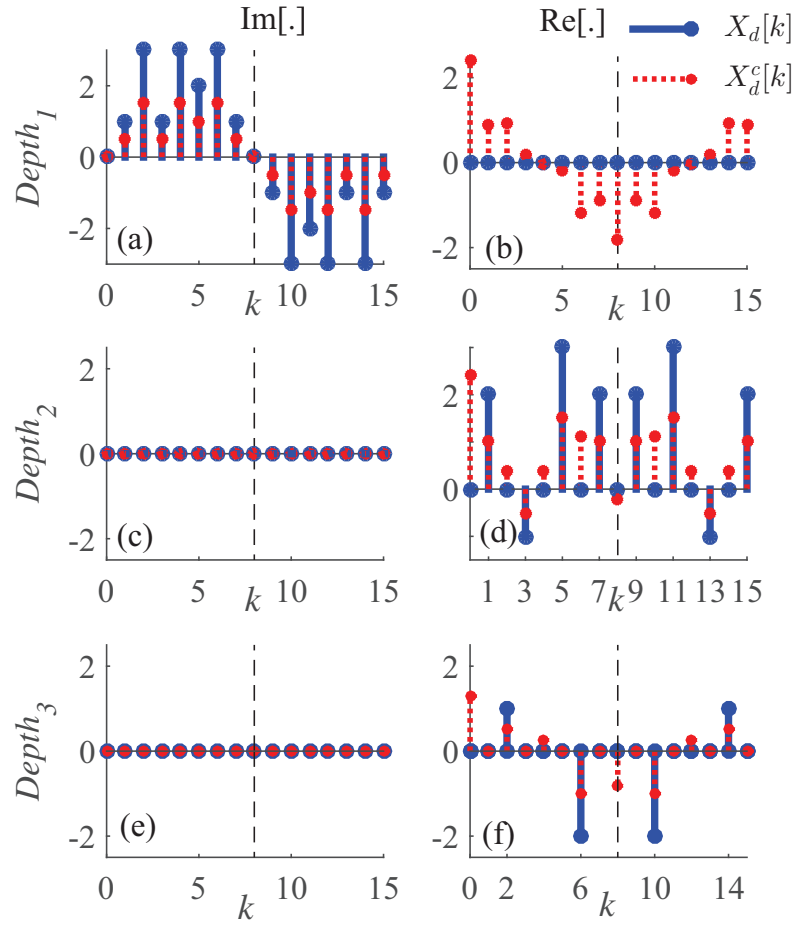
Fig. 2. An illustration of the frequency domain subcarrier loading at three depths ASE-DMT and the effects of zero clipping. (a) and (c) and (e) shows the imaginary components of the subcarriers before and after zero level time-domain clipping, $\Im[X_d[k]]$ and $\Im[X_d^c[k]]$, respectively. (b) and (d) and (f) shows the real components of the subcarriers before and after zero level time-domain clipping, $\Re[X_d[k]]$ and $\Re[X_d^c[k]]$, respectively.

can be written as:

$$x_1[n] = \frac{1}{\sqrt{N}} \sum_{k=0}^{N-1} X_1[k] e^{\frac{j2\pi kn}{N}}$$
$$= \frac{-2}{\sqrt{N}} \sum_{k=1}^{N/2-1} B[k] \sin \frac{2\pi kn}{N}. \tag{1}$$

It is straightforward to conclude that the time domain PAM-DMT waveform in (1) exhibits the following antisymmetry: $x_1[n] = -x_1[N-n]$, where $x_1[0] = x_1[N/2] = 0$. Following [14], the clipping at zero level is described as:

$$x_d^c[n] = \frac{x_d[n] + |x_d[n]|}{2}, \tag{2}$$

and the frequency domain transformation of the clipped waveform, $x_d^c[n]$, can be shown as:

$$X_d^c[k] = \frac{X_d[k] + \text{FFT}\{|x_d[n]|\}}{2}, \tag{3}$$

where the subscripts d denotes the depth d index, and $X_d[k] = \text{FFT}\{x_d[n]\}$. The effects of clipping on the subcarriers are shown in Fig. 2. Clipping of the negative samples at depth 1 is distortion-less to the information at the same depth because all of the distortion transforms into the real part of the subcarriers. As a simple proof, the distortion term $|x_1[n]|$ has a Hermitian symmetry $|x_1[n]| = |x_1[N-n]|$, which can also be proved by:

$$\text{FFT}\{|x_1[n]|\} = \frac{1}{\sqrt{N}} \sum_{n=0}^{N-1} |x_1[n]| e^{-\frac{j2\pi kn}{N}}$$

$$= \frac{2}{\sqrt{N}} \sum_{n=1}^{N/2-1} |x_1[n]| \cos \frac{2\pi kn}{N}. \tag{4}$$

At depth 2, the odd subcarriers are loaded with real valued M-PAM symbols $X_2[k] = A_2[k]$, while all of the other subcarriers are kept unused. The subcarriers at depth 2, $X_2[k]$, can be written as:

$$X_2[k'] = \begin{cases} A_2[k'], & \text{if } k' = 2k+1 \\ 0, & \text{Otherwise} \end{cases}, \tag{5}$$

where $A_2[k']$ is the M-PAM symbol at the k'^{th} subcarrier of depth 2; and $k = 0, 1, ..., N/4 - 1$. Hermitian symmetry is also required to guarantee that $x_2[n]$ is real, $A_2[k] = A_2[N-k]$. As a result, the time domain waveform at depth 2, $x_2[n]$, would have the following symmetry: $x_2[n] = -x_2[n + N/2]$. Therefore, the distortion caused by clipping at zero level would only affect the real domain even subcarriers. This can be shown as:

$$\text{FFT}\{|x_2[n]|\} = \frac{1}{\sqrt{N}} \sum_{n=0}^{N/2-1} |x_2[k]| e^{-\frac{j2\pi kn}{N}} (1 + e^{-j\pi k}), \tag{6}$$

which takes values only at $X_2^c[2k]$, for $k = 0, 1, ..., N/2 - 1$. Therefore, the distortion is orthogonal to the information content at depth 1 and depth 2. Subsequent streams can be generated at depth d, where the subcarriers will be loaded with real valued M-PAM symbols:

$$X_d[k'] = \begin{cases} A_d[k'], & \text{if } k' = 2^{d-2}(2k+1) \\ 0, & \text{Otherwise} \end{cases}, \tag{7}$$

where $A_d[k']$ is the M-PAM symbol at the k'^{th} subcarrier of depth d; and $k = 0, 1, ..., N/2^d - 1$. Hermitian symmetry is also required to guarantee that $x_d[n]$ is real, $A_d[k] = A_d[N-k]$. Using (7), it can be shown that:

$$x_d[n] = -x_d[n + N/2^{d-1}] \quad \forall d > 1. \tag{8}$$

Using (3), $X_d[k]$ can be written as:

$$X_d[k] = \frac{1}{\sqrt{N}} \sum_{n=0}^{N/2^{d-1}-1} x_d[k] e^{-\frac{j2\pi kn}{N}} \kappa \left(1 - e^{\frac{-j\pi k}{2^{D-2}}}\right), \tag{9}$$

and the zero level clipping distortion effect on the subcarriers in the frequency domain can be written as:

$$\text{FFT}\{|x_d[n]|\} = \frac{1}{\sqrt{N}} \sum_{n=0}^{N/2^{d-1}-1} |x_d[k]| e^{-\frac{j2\pi kn}{N}} \kappa (1 + e^{\frac{-j\pi k}{2^{D-2}}}), \tag{10}$$

where D is the total number of used depths, and κ can be written as:

$$\kappa = \prod_{d=2}^{D-1} (1 + e^{\frac{-j\pi k}{2^{d-2}}}). \tag{11}$$

Using (9) and (10), it can be shown that the zero level clipping is distortion-less to the information content at $X_d^c[2^{d-2}(2k+1)]$, and that all of the distortion will affect the subcarriers at $X_d^c[2^{d-1}k]$. Using this technique of selective subcarrier indexes loading at each depth will allow multiple *M*-PAM modulated waveforms to be superimposed without any inter-stream-interference. The active subcarriers of each superimposed depth will not be affected by the zero level clipping distortion of the current and subsequent depths. However, it will be affected by the distortion of the zero level clipping of the previous depths. This distortion will be estimated and cancelled at the receiver, as shown below.

After generating the time domain waveforms of all depths, the generated waveforms are clipped and the cyclic prefixes are prefixed. The overall ASE-DMT waveform can be obtained by superimposing the clipped waveforms of all depths:

$$x_\text{T}[n] = \sum_{d=1}^{D} x_d^c[n]. \tag{12}$$

Using (2) and (3), the ASE-DMT subcarriers can be written as:

$$X_\text{T}[k] = \frac{jB_1[k] + \sum_{d=2}^{D} A_d[k] + \sum_{d=1}^{D} \text{FFT}\{|X_d[n]|\}}{2}. \tag{13}$$

The information content of depth 1 can be obtained by considering only the imaginary components of the subcarriers. This can be given as $\hat{B}_1[k] = 2\Im(X_\text{T}[k]) + W[k]$, where $W[k]$ is the frequency domain realization of the additive white Gaussian noise (AWGN) at the receiver [2]. The information of depth 1 can then be remodulated at the receiver to obtain $\hat{x}_1[n]$ which can be subtracted from the ASE-DMT received waveform, $x_\text{T}[n]$. This would result in removing the imaginary component of $X_\text{T}[n]$ and also removing the real domain distortion caused by the zero level clipping of the depth 1 waveform, $\text{FFT}\{|x_1[n]|\}$. Subsequent depths can be demodulated by selecting the appropriate frequency subcarrier indexes at each depth. The real component of the subcarriers at $2^{d-2}(2k+1)$ for $k = 0, 1, ..., N/2^d - 1$ can then be remodulated to obtain the waveform at depth d, $\hat{x}_d[n]$, which would be subtracted from the remaining ASE-DMT waveform.

The same process is repeated until the information at the last depth is demodulated. In this way the distortion of the previous depths is estimated and cancelled from the higher depths in this successive receiver process.

2.2. Spectral efficiency

The spectral efficiency of the first depth of ASE-DMT is equivalent to the spectral efficiency of PAM-DMT, which is also similar to the spectral efficiency of DCO-OFDM. This can be written as:

$$\eta_\text{PAM}(1) = \frac{\log_2(M_1)(N-2)}{2(N+N_\text{CP})} \quad \text{bits/s/Hz}, \tag{14}$$
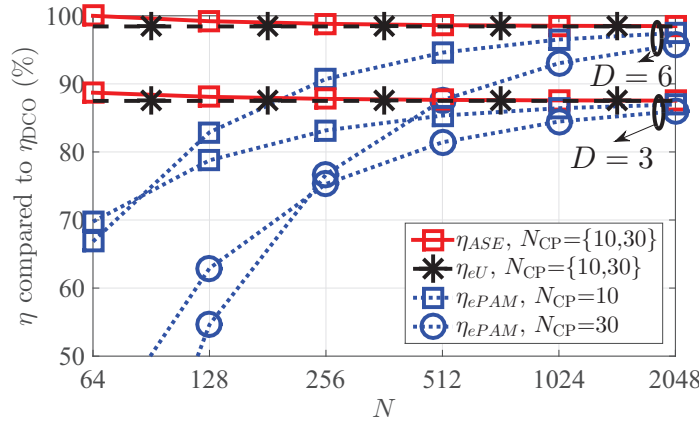
Fig. 3. The spectral efficiency of ASE-DMT, eU-OFDM, and ePAM-DMT compared to the spectral efficiency of DCO-OFDM for different FFT and CP lengths at $D = 3$ and $D = 6$.

where N is the FFT/inverse fast Fourier transform (IFFT) frame length, M_1 is the constellation size at first depth of ASE-DMT, and N_{CP} is the cyclic prefix length. The spectral efficiency of higher depths $d \geq 2$ can be expressed as:

$$\eta_{PAM}(d) = \frac{\log_2(M_d)N}{2^d(N+N_{CP})} \quad \text{bits/s/Hz}, \tag{15}$$

where M_d is the constellation size at depth d. As a result, the spectral efficiency of ASE-DMT can be calculated as:

$$\eta_{ASE}(D) = \sum_{d=1}^{D} \eta_{PAM}(d) \quad \text{bits/s/Hz} \tag{16}$$

$$= \frac{\log_2(M_1)(N-2) + \sum_{d=2}^{D} \frac{\log_2(M_d)(N)}{2^{d-1}}}{2(N+N_{CP})}.$$

The spectral efficiency ratio of ASE-DMT to the spectral efficiency contribution of each individual depth can be written as:

$$\alpha_\eta(D,d) = \frac{\eta_{ASE}(D)}{\eta_{PAM}(d)2^{d-1}}. \tag{17}$$

The spectral efficiency of ASE-DMT approaches twice the spectral efficiency of DCO-OFDM as the total number of depths increase. However, the energy efficiency comparison of both modulation schemes should be considered at an equivalent spectral efficiency. Therefore, the superimposed waveforms in ASE-DMT use smaller constellation sizes, $M_d = \sqrt{M_{DCO}}$, that can build-up a DCO-OFDM equivalent spectral efficiency. Since the system design of ePAM-DMT employs the cyclic prefixes in the symmetry alignment of the PAM-DMT time-domain frames, the spectral efficiency of ePAM-DMT is a function of the FFT/IFFT frame and cyclic prefix sizes.

The spectral efficiency of ePAM-DMT tends to increase as the FFT/IFFT frame size increases. Unlike ePAM-DMT, the spectral efficiency of ASE-DMT is independent of the cyclic prefix length and therefore, can be employed with smaller FFT/IFFT sizes. The spectral efficiency ratio of ASE-DMT, ePAM-DMT and eU-OFDM to the spectral efficiency of DCO-OFDM is shown in Fig. 3. The spectral efficiency of ASE-DMT is slightly higher than the

spectral efficiency of eU-OFDM at small FFT/IFFT sizes. It is shown that when $D = 6$ and $N = 64$, the spectral efficiency of ASE-DMT exactly matches the spectral efficiency of DCO-OFDM.

2.3. *Power efficiency*

The real bipolar OFDM time-domain waveform can be approximated with a Normal distribution, $x(t) \sim \mathcal{N}(0, \sigma_x^2)$ when $N \geq 64$, where σ_x is the standard deviation of $x(t)$ [2]. It was shown in [14] that PAM-DMT follows a truncated normal distribution. The stream at depth D is scaled by a parameter $1/\gamma_d$ to facilitate the optimization of the allocated power at that stream. The ASE-DMT time-domain waveform at depth d follows a truncated normal distribution with a mean $E[x_d(t)] = \phi(0)\sigma_x/(\gamma_d\sqrt{2^{d-1}})$, where $1/\gamma_d$ is the scaling factor at depth d, $E[\cdot]$ is a statistical expectation, and $\phi(x)$ is the probability density function (PDF) of the standard normal distribution. As a result, the average electrical and optical power of ASE-DMT is equivalent to the electrical and optical power of eU-OFDM which can be written as [15]:

$$P_{\text{Ele}}^{\text{avg}}(D, \underline{\gamma}) = E\left[x_T^2(t)\right] = E\left[\left(\sum_{d=1}^{D} x_d(t)\right)^2\right]$$

$$= \sigma_s^2 \left(\sum_{d=1}^{D} \frac{\gamma_d^{-2}}{2^d} + 2\phi^2(0) \sum_{d_1=1}^{D} \sum_{\substack{d_2=1 \\ d_1 \neq d_2}}^{D} \frac{(\gamma_{d_1}\gamma_{d_2})^{-1}}{\sqrt{2^{d_1+d_2}}} \right), \tag{18}$$

$$P_{\text{Opt}}^{\text{avg}}(D, \underline{\gamma}) = \sum_{d=1}^{D} E[s_d(t)] = \phi(0)\sigma_s \sum_{d=1}^{D} \frac{\gamma_d^{-1}}{\sqrt{2^{d-1}}}, \tag{19}$$

where $x_T(t)$ is the time domain ASE-DMT waveform; $x_d(t)$ is the time domain PAM-DMT at depth d; and $\underline{\gamma} = \{\gamma_d^{-1}; d = 1, 2, \ldots, D\}$ is the set of scaling factors applied to each corresponding stream. The ratio of the average electrical power of ASE-DMT waveform to the average electrical power of a PAM-DMT stream, $P_{\text{Ele},d}^{\text{avg}}(\gamma_d) = \sigma_x^2/(2\gamma_d^2)$, is given by:

$$\alpha_{\text{Ele}}^P(D, \underline{\gamma}) = \frac{P_{\text{Ele}}^{\text{avg}}(D, \underline{\gamma})}{P_{\text{Ele},d}^{\text{avg}}(\gamma_d)}. \tag{20}$$

3. Theoretical BER analysis

The ASE-DMT received signal is given by:

$$\mathbf{y} = \mathbf{Hx} + \mathbf{w}, \tag{21}$$

where $\mathbf{x}$ and $\mathbf{y}$ are the transmitted and received ASE-DMT waveforms; $\mathbf{w} = \{w_i; i = 0, 1, \ldots, N-1\}$ is the AWGN samples, $w_i \sim \mathcal{N}(0, N_o)$, where N_o is the double-sided power spectral density (PSD) of the noise at the receiver; and $\mathbf{H}$ is a $N \times N$ circulant convolution channel matrix with the first column representing the channel impulse response $\mathbf{h} = [h_0, h_1, \ldots, h_L, 0, \ldots, 0]^T$, where L is the number of channel taps. The channel matrix $\mathbf{H}$ can be diagonalized as:

$$\mathbf{H} = \mathbf{F}^* \mathbf{\Lambda} \mathbf{F}, \tag{22}$$

where $\mathbf{F}$ is an $N \times N$ Discrete Fourier transform (DFT) matrix, and $\mathbf{\Lambda}$ is an $N \times N$ diagonal matrix with the eigenvalues of the channel $\mathbf{\Lambda} = [\Lambda_0, \Lambda_1, \ldots, \Lambda_N]^T$.
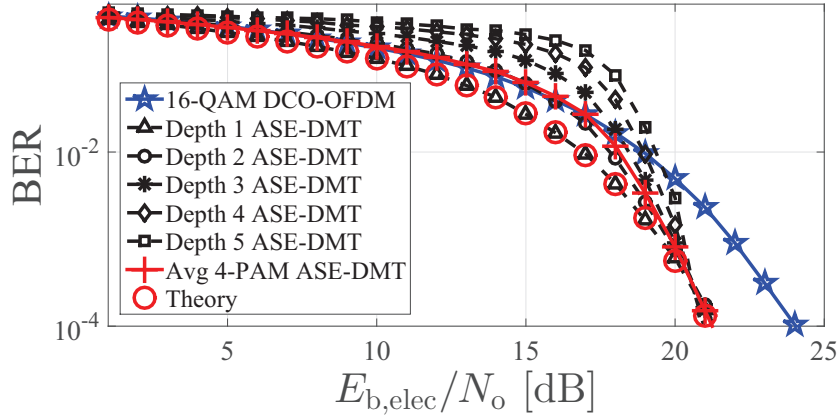
Fig. 4. The BER performance of 16-QAM ASE-DMT depths with a total number of depths $D = 5$. The BER of DCO-OFDM is only shown for comparison purposes.

The theoretical BER performance of ASE-DMT can be derived using the analytical BER performance of real M-QAM OFDM [16]. However, the SNR should be scaled by half to compensate for the energy loss of zero level clipping at each depth. This is consistent with the 3 dB loss of the BER performance of PAM-DMT. In addition, the SNR should also be scaled by the energy loss per bit incurred by the superposition modulation of ASE-DMT, which can be written as:

$$\alpha_{\text{Ele}}(D, d, \underline{\gamma}) = \frac{\alpha_{\text{Ele}}^P(D, \underline{\gamma})}{\alpha_\eta(D, d)}. \tag{23}$$

Since the BER performance of M-PAM is equivalent to the BER performance of M^2-QAM in an AWGN channel, the analytical BER performance bound of ASE-DMT in the AWGN channel can be derived as:

$$\text{BER}_{(D,d,\underline{\gamma})} \cong \frac{2}{\log_2(M_d)} \left(1 - \frac{1}{M_d}\right) \times \sum_{l=1}^{2} \sum_{k=1}^{N} Q\left((2l-1)\sqrt{\frac{3|\Lambda_k|^2 E_{\text{b,elec}} \log_2(M_d)}{N_o \alpha_{\text{Ele}}(D, d, \underline{\gamma})(M_d^2 - 1)}}\right), \tag{24}$$

where $E_{\text{b,elec}}/N_o$ is the electrical SNR of real M-QAM OFDM, and N_o is the double side noise PSD. An equivalent bound for the ASE-DMT BER performance as a function of the optical SNR can be established by scaling the electrical SNR, $E_{\text{b,elec}}/N_o$ in (24), with the ratio of electrical average power (18) to the optical average power (19).

As shown in Fig. 4, the analytical performance bound matches the BER performance of the first depth. The BER performance of other depths tends to be affected by the wrongly decoded bits at the lower order depths. Any incorrectly decoded bit at the lower order depths translates into further incorrect bits at higher order depths. However, at high SNR, the BER performance of all depths converges to match with the analytical performance of ASE-DMT.

As shown in Fig. 4, the BER performance of 4-PAM ASE-DMT is more efficient, with a 3 dB gain, than 16-QAM DCO-OFDM in terms of the electrical energy efficiency. The spectral efficiency ratio of ASE-DMT to the spectral efficiency of DCO-OFDM is 97%.

4. Computational complexity

The computation complexity of ASE-DMT and ePAM-DMT are studied and compared with the computation complexity of DCO-OFDM in this section. The computation complexity is

dominated by the number of multiplications in FFT/IFFT operations. Therefore, the computation complexity in this paper is defined as the number of complex multiplications required to perform a FFT/IFFT operation.

4.1. Computation complexity of DCO-OFDM

At the transmitter side, DCO-OFDM requires N-point complex multiplications which result in a computation complexity of $\mathscr{O}(N\log_2(N))$. The FFT operation at the receiver side of DCO-OFDM is performed on real-valued frames. Two N-point FFT operations on two real-valued signals can be realized using one N-point FFT on one complex-valued signal [17]. Therefore, the computation complexity at the receiver of DCO-OFDM is $\mathscr{O}(N/2\log_2(N))$. The computation complexity per bit of DCO-OFDM can be written as:

$$C_{\mathrm{DCO}} = \frac{2\mathscr{O}(3N/2\log_2(N))}{\log_2(M_{\mathrm{DCO}})(N-2)}, \tag{25}$$

where M_{DCO} is the constellation size of DCO-OFDM.

4.2. Computation complexity of ASE-DMT

At the transmitter side of PAM-DMT, an IFFT operation is applied on imaginary-valued frames. At the receiver side, a single FFT operation is applied on real-valued frames. Therefore, the computation complexity of PAM-DMT for each of the transmitter and receiver is $\mathscr{O}(N/2\log_2(N))$.

The first depth of ASE-DMT has a computation complexity similar to the computation complexity of a PAM-DMT transmitter. Higher depths of ASE-DMT are sparse as they have a low number of active subcarriers. The number of active subcarriers at depth d is: $N/2^{d-1}, \forall d \leq 2$. Therefore, the IFFT operation at higher order depths $d \leq 2$, can be optimized to avoid the calculations performed on zeros. Given that the subcarriers in these depths are real-valued, the computation complexity at the transmitter of depth d is $\mathscr{O}(N/2^d\log_2(N))$. Therefore, the computation complexity of ASE-DMT transmitter is given as:

$$C_{\mathrm{ASE}}^{\mathrm{Tx}} = \mathscr{O}(N/2\log_2(N)) + \sum_{d=2}^{D} \mathscr{O}(N/2^d\log_2(N))$$
$$\approx \mathscr{O}(N\log_2(N)), \tag{26}$$

where D is the total number of depths.

The first demodulation process at the receiver of ASE-DMT is applied on real-valued frames, therefore, the computation complexity associated with this process is equivalent to the computation complexity of a DCO-OFDM receiver. All the other demodulation process are also applied on real-valued frames. However, the frames at higher order depths are sparse in the frequency domain. A specific set of subcarriers is only required at the output of each demodulation process. Therefore, the FFT operation at higher order depths, $d \leq 2$, is only evaluated at subcarriers given by (7). Algorithms such as Sparse FFT [18] can also be applied for depth d with a computational complexity of $\mathscr{O}(N/2^d\log_2(N))$. The demodulated streams for all depths, except the last one, are required to be remodulated at the receiver. The associated complexity of remodulating the first depth is: $\mathscr{O}(N/2\log_2(N))$, and the associated complexity of remodulating other depths is $\sum_{d=2}^{D} \mathscr{O}(N/2^d\log_2(N))$. Therefore, the computation complexity of a ASE-DMT receiver is given as:

$$C_{\mathrm{ASE}}^{\mathrm{Rx}} = \mathscr{O}(N/2\log_2(N)) + \sum_{d=2}^{D} \mathscr{O}(N/2^d\log_2(N)) + \sum_{d=2}^{D-1} \mathscr{O}(N/2^d\log_2(N))$$
$$\approx \mathscr{O}(2N\log_2(N)). \tag{27}$$
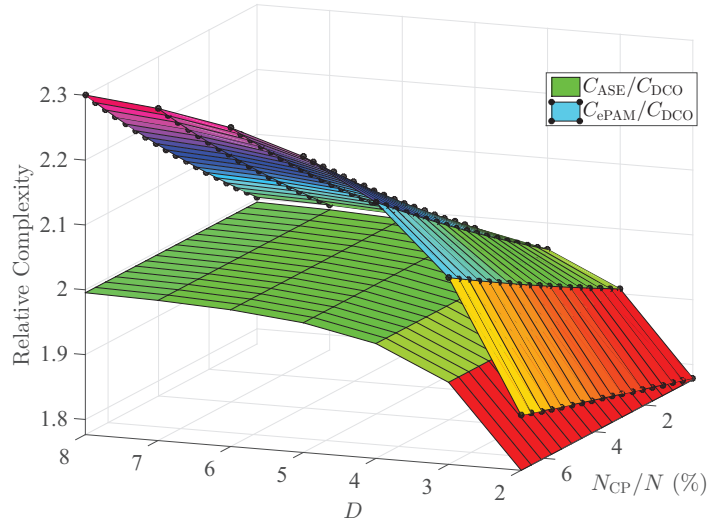
Fig. 5. The relative computation complexity of ASE-DMT and ePAM-DMT in comparison with the computation complexity of DCO-OFDM as a function of the total number of depths D, and the cyclic prefix percentage of the frame size N_{CP}/N.

The computation complexity of ASE-DMT per bit is given as:

$$C_{ASE} = \frac{2(C_{ASE}^{Tx} + C_{ASE}^{Rx})}{\log_2(M_d)(N-2) + \sum_{d=2}^{D} \log_2(M_d)N/2^{d-1}}, \tag{28}$$

where M_d is the constellation size used for all depths in ASE-DMT, $M_d = \sqrt{M_{DCO}}$.

4.3. Computation complexity of ePAM-DMT

The cyclic prefix at each depth of ePAM-DMT is used in the symmetry alignment of superimposed depths. This reduces the frame sizes at higher order depths. The FFT frame size at depth-d of ePAM-DMT is given as $N_d = N_{d-1} - 2N_{CP} - 2$, $\forall d \geq 2$, where $N_1 = N$, and N is the frame size of DCO-OFDM. The frame sizes of all depths in ePAM-DMT are zero-padded to the next power of two.

At the transmitter side of ePAM-DMT, $\sum_{d=1}^{D} 2^{d-1}$ PAM-DMT frames are required to generate 2^{D-1} ePAM-DMT frames. Therefore, the computation complexity of the ePAM-DMT transmitter can be given as:

$$C_{ePAM}^{Tx} = \sum_{d=1}^{D} 2^{d-D} \mathcal{O}(N/2 \log_2(N))$$
$$\approx \mathcal{O}(N \log_2(N)). \tag{29}$$

This is equivalent to the computation complexity of DCO-OFDM transmitter.

At the receiver side of ePAM-DMT, $\sum_{d=1}^{D} 2^{d-1}$ PAM-DMT frames are required to be demodulated and $\sum_{d=2}^{D} 2^{d-1}$ PAM-DMT frames are required to be remodulated in order for 2^{D-1} frames of ePAM-DMT to be demodulated. Therefore, the computation complexity of

the ePAM-DMT receiver can be given as:

$$C_{\text{ePAM}}^{\text{Rx}} = \frac{\mathscr{O}(N/2\log_2(N)) + 2\sum_{d=2}^{D} 2^{d-1}\mathscr{O}(N/2\log_2(N))}{2^{D-1}}$$

$$\approx \mathscr{O}(2N\log_2(N)), \tag{30}$$

which is equivalent to twice the computation complexity of DCO-OFDM transmitter. Therefore the computation complexity of ePAM-DMT per bit is given as:

$$C_{\text{ePAM}} = \frac{2(C_{\text{ePAM}}^{\text{Tx}} + C_{\text{ePAM}}^{\text{Rx}})}{\log_2(M)(N-2) + \sum_{d=2}^{D} \log_2(M)N_d/2^{d-1}}, \tag{31}$$

where N_d is the frame size at depth-d and M is the constellation size used for all depths in ePAM-DMT, $M = \sqrt{M_{\text{DCO}}}$.

4.4. Computation complexity comparison

The ratio of the computation complexities per bit of ASE-DMT to DCO-OFDM, $C_{\text{ASE}}/C_{\text{DCO}}$, and the the ratio of the computation complexities per bit of ePAM-DMT to DCO-OFDM, $C_{\text{ePAM}}/C_{\text{DCO}}$. are presented in Fig. 5 as a function of the total number of used depths D and the cyclic prefix percentage of the overall frame size N_{CP}/N. The relative complexity of ASE-DMT is independent of the cyclic prefix and it increases as the total number of depths increases. However, it converges to twice the complexity of DCO-OFDM.

Table 1. Computational complexity of the Transmitter and receiver of DCO-OFDM, ePAM-DMT and ASE-DMT.

Modulation technique	Computational complexity	
	Transmitter	Receiver
DCO-OFDM	$\mathscr{O}(N\log_2(N))$	$\mathscr{O}(N/2\log_2(N))$
ASE-DMT	$\mathscr{O}(N\log_2(N))$	$\mathscr{O}(2N\log_2(N))$
ePAM-DMT	$\mathscr{O}(N\log_2(N))$	$\mathscr{O}(2N\log_2(N))$

The relative complexity of ePAM-DMT increases as the cyclic prefix length increases and as the total number of depths increases. The relative complexity of ePAM-DMT has a lower bound that is equivalent to the relative complexity of ASE-DMT when the cyclic prefix length is zero. The cyclic prefix length is limited by the total number of depths used. The maximum cyclic prefix length for $D = 8$ is only 8% of the OFDM frame size. When the cyclic prefix is 8%, the relative complexity of ePAM-DMT is 2.3 times the complexity of DCO-OFDM. The computation complexities of DCO-OFDM, ePAM-DMT and ASE-DMT are summarized in Table 1.

4.5. Practical considerations

The transmission cannot be started in ePAM-DMT, unless $2^D - 1$ PAM-DMT frames are available at the transmitter side. In addition, frames at higher order depths are required to be processed in the time domain to achieve the symmetry required for superposition modulation. This introduces additional delay at the transmitter side. At the receiver side of ePAM-DMT, the demodulation of frames at depth-d can only happen after all lower depths have been demodulated and remodulated. This is estimated at $\sum_{d'=2}^{d} 2^{D-d'+1}$ PAM-DMT frames. Moreover, 2^D frames are required to be buffered at the receiver, until the demodulation process of a full ePAM-DMT frame finishes.
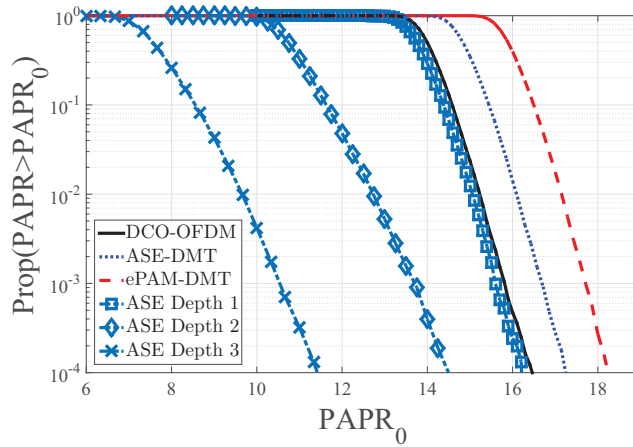
Fig. 6. The peak to average power ratio of ASE-DMT (depths and overall), ePAM-DMT and DCO-OFDM.

There is no delay associated with the ASE-DMT transmitter, as all of the depths are generated at the same time. At the receiver side of ASE-DMT, the demodulation of frames at depth-d can only take place after all of the lower depths have been demodulated and remodulated. This is estimated at $(d-1)$ PAM-DMT frames. Moreover, $(d-1)$ frames are required to be buffered at the receiver, until the demodulation process of a full ASE-DMT frame finishes.

The spectral efficiency of each additional stream decreases exponentially. Therefore, it is more efficient to implement ASE-DMT with small number of depths, $D = 2$ or $D = 3$. This would result in a small spectral efficiency gap between ASE-DMT and DCO-OFDM, 12.5% of the spectral efficiency of DCO-OFDM when $D = 3$. A solution to this issue is given in Section 5.2

5. Performance comparison

Typical OFDM signals attain high peak-to-average power ratios (PAPRs). This drives the LEDs into non-linear regions because of their limited dynamic range. However, the higher order depths in ASE-DMT are sparse in the frequency domain. This reduces the PAPR of higher order depths. To exploit this property, the waveform at each depth can be used to drive a single LED in an LED array. This allows the waveforms to be superimposed in the optical domain and reduces the PAPR, and this will mitigate any non-linearity. The PAPR of ASE-DMT depths is presented in Fig. 6 to illustrate the sparsity effect on the PAPR. The PAPR of ASE-DMT depths increases as the depth order, d, increases. The PAPR of the overall ASE-DMT waveform is shown to be higher than the PAPR of DCO-OFDM but lower than the PAPR of ePAM-DMT.

The BER performance of ASE-DMT is compared with the BER performance of ePAM-DMT and DCO-OFDM in an AWGN channel. An ideal LED model is used, therefore, the only non-linear operation considered is the clipping at the zero level. The DC bias is defined to be a multiple of the standard deviation of the bipolar OFDM signal $k_{M_{\mathrm{DCO}}}\sigma_s$. The energy dissipation of DCO-OFDM compared with bipolar OFDM can be written as [19]:

$$B_{\mathrm{DC}}^{\mathrm{dB}} = 10\log_{10}(k_{M_{\mathrm{DCO}}}^2 + 1).\qquad(32)$$

The DC bias for DCO-OFDM is estimated through Monte-Carlo simulations. Since the BER performance of $\sqrt{M}$-PAM is equivalent to the BER performance of M-QAM at a given SNR, it would not be possible for ASE-DMT to achieve the spectral efficiency of a non-squared
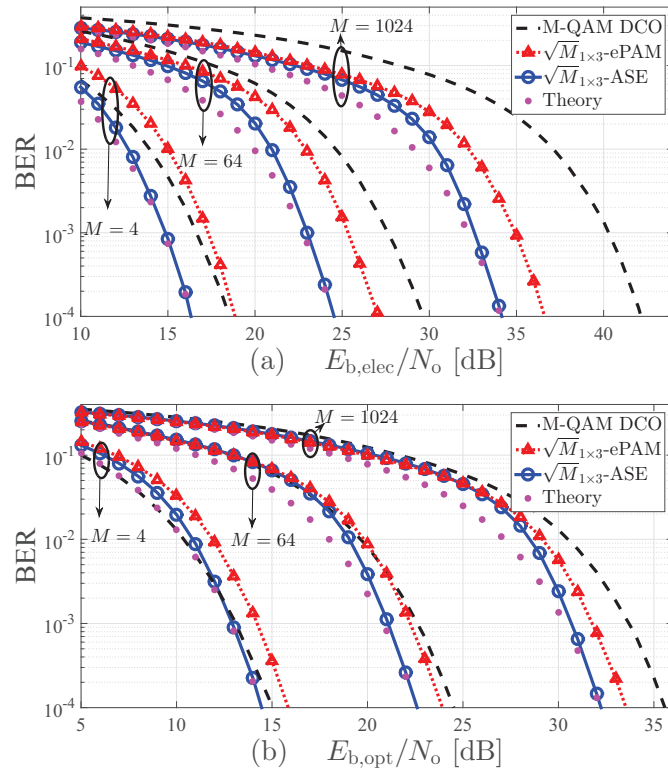
Fig. 7. The BER performance comparison of ASE-DMT, ePAM-DMT, and DCO-OFDM for different spectral efficiencies in an AWGN channel as a function of: (a) electrical SNR, and (b) optical SNR. The DC biasing levels for DCO-OFDM at $M = \{4, 64, 1024\}$ are estimated through Monte Carlo simulations at respectively 6 dB, 9.5 dB, and 13 dB as described in (32).

M-QAM constellation size. When equal constellation size is used at each modulation depth of ASE-DMT, only integer spectral efficiencies, $\eta_{\text{ASE}}(D) = \{1, 2, 3, ...\}$ bits/s/Hz, can be achieved.

5.1. Simulation results

The BER performance of the proposed scheme $\sqrt{M}$-PAM ASE-DMT is compared with the BER performance of $\sqrt{M}$-PAM ePAM-DMT and M-QAM DCO-OFDM as functions of the electrical SNR in an AWGN channel at Fig. 7(a). The proposed scheme, ASE-DMT, is more energy efficient than ePAM-DMT and DCO-OFDM for all of the presented cases as a function of the electrical SNR. At different spectral efficiencies, the electrical energy savings ASE-DMT are between 2.24 dB and 8 dB when compared with DCO-OFDM, and almost constant at 2.5 dB when compared with ePAM-DMT at a BER of 10^{-4}. Similar trends are shown in Fig. 7 (b) for the optical SNR. At different spectral efficiencies, the optical energy savings of ASE-DMT are between 0.6 dB and 3.25 dB when compared with DCO-OFDM, and are almost constant at 1.3 dB when compared with ePAM-DMT at a BER of 10^{-4}. The energy efficiency gains of ASE-DMT over DCO-OFDM at different spectral efficiencies are summarized in Table 2.

ASE-DMT is more efficient than ePAM-DMT in terms of both the electrical and optical SNR. This is due to the fact that in ePAM-DMT half of the frames are removed after each

demodulation process [9]. The frequency domain loading of *M*-PAM symbols in ASE-DMT does not require this process, which results in a performance gain of ASE-DMT over ePAM-DMT.

The theoretical BER bounds underestimate the BER at lower SNR due to the propagation errors in the successive streams cancellation process at the receiver. However, the theoretical BER bounds match the Monte-Carlo simulation results at high SNR values.

Table 2. Energy efficiency gains of ASE-DMT over DCO-OFDM at a BER of 10^{-4}.

Spectral efficiency [bits/s/Hz]	Electrical energy gains [dB]	Optical energy gains [dB]
1	2.24	0.6
2	4	1.7
3	5	2
4	5.75	2.5
5	8	3.25

Note that the BER performance of ASE-DMT is identical to the BER performance of eU-OFDM [8], and to the BER performance of eACO-OFDM [10] when identical constellation size and unitary scaling factors are used for eACO-OFDM. This is an unsurprising result, because the BER performance of their unipolar OFDM based-schemes forms (PAM-DMT, U-OFDM, and ACO-OFDM) is also identical [14]. A detailed comparison between the superposition OFDM modulation schemes will be the subject of future research on this topic.

The performance difference between ASE-DMT and DCO-OFDM is almost equivalent for both flat channels and frequency selective channels. When subjected to the same communication channel, the individual subcarriers between the OFDM-based techniques are subjected to the same attenuation by the channel. As a result, the SNR penalty due to the channel in both techniques is the same. The results for a frequency selective channel are only valid for the specific channel conditions, which are specific to the communication scenario. Therefore, the results for frequency selective channels are not presented in this paper.

The cyclic prefix length in ePAM-DMT is limited by the total number of depths used. The maximum cyclic prefix length for ePAM-DMT, with a total number of depths D, can be given as:

$$N_{CP}^{ePAM,max} = \lfloor N/(2D-2) - 1 \rfloor. \tag{33}$$

This means that ePAM-DMT can be used for frequency selective channels only when the number of channel taps is less than $N_{CP}^{ePAM,max}$.

5.2. ASE-DMT with arbitrary constellation sizes

Arbitrary constellation sizes are proposed to close the remaining spectral efficiency gap between DCO-OFDM and ASE-DMT, when small number of depths is used for ASE-DMT. This would allow the spectral efficiency of ASE-DMT to be exactly similar to the spectral efficiency of DCO-OFDM with only few number of superimposed depths. Arbitrary constellation sizes offer a practical solution for ASE-DMT without any spectral efficiency loss. The computation complexity per bit associated with this approach is around 1.67 times higher than the computation complexity per bit of DCO-OFDM. Arbitrary constellation sizes would allow the non-squared constellation sizes of *M*-QAM DCO-OFDM to be achieved. For example, to achieve the spectral efficiency of 8-QAM DCO-OFDM, it would be possible to use 4-PAM at the first depth, 2-PAM at the second depth, and 4-PAM at the third depth of ASE-DMT. In order for the spectral efficiency of ASE-DMT to match the spectral efficiency of DCO-OFDM, the

204
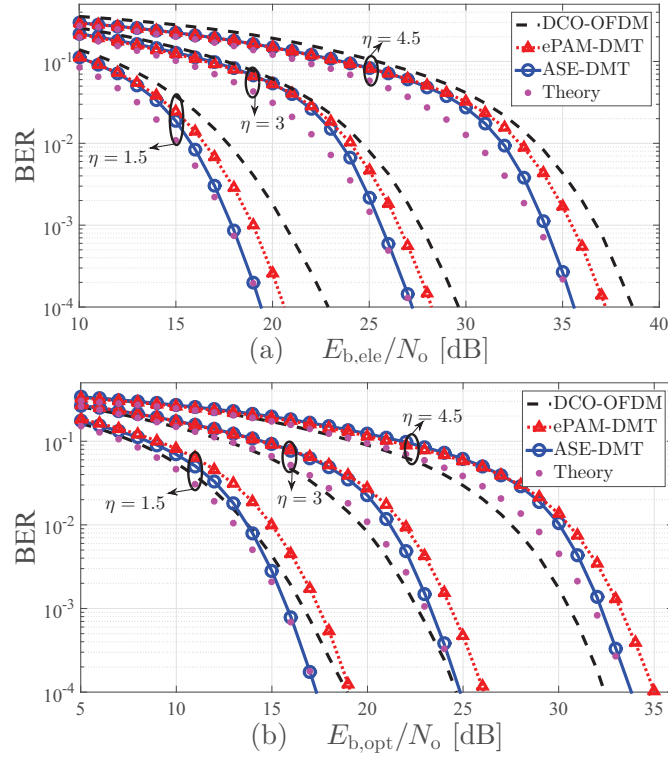
Fig. 8. The BER performance comparison of ASE-DMT, ePAM-DMT, and DCO-OFDM for different spectral efficiencies in an AWGN channel as a function of: (a) electrical SNR, and (b) optical SNR. The spectral effiency η is given in [bits/s/Hz]. The DC biasing levels for DCO-OFDM at $\eta = \{1.5, 3, 4.5\}$ are estimated through Monte Carlo simulations at respectively 7 dB, 9.5 dB, and 12 dB as described in (32).

combination of constellation sizes used should satisfy the following constraint:

$$\log_2(M_{\text{DCO}}) = 2 \sum_{d=1}^{D} \frac{\log_2(M_d)}{2^d}. \tag{34}$$

In addition, the power is allocated to each stream so that the average power of the modulation signal satisfies the following two constraints:

$$P_{\text{Ele}}^{\text{avg}}(D, \underline{\gamma}) \leq P_{\text{Ele}}^{\text{avg}}(D, \mathbf{1}_{1 \times D}),$$
$$P_{\text{Opt}}^{\text{avg}}(D, \underline{\gamma}) \leq P_{\text{Opt}}^{\text{avg}}(D, \mathbf{1}_{1 \times D}). \tag{35}$$

The BER at each depth is weighted by the contribution of that depth to the overall spectral efficiency. The average BER performance can then be expressed as:

$$\text{BER} \cong \sum_{d=1}^{D} \left(\frac{\text{BER}_{(D,d,\underline{\gamma})}}{\alpha_\eta(D,d)} \right). \tag{36}$$

All possible combinations of constellation sizes at the different ASE-DMT depths with all possible power allocations are investigated for a maximum depth of $D = 3$, where spectral efficiency in the range from 1 to 5 bits/s/Hz is achieved. The optimal configurations were obtained

using Monte Carlo simulation comparisons of all the possible sets. The optimal configurations are presented in Table 3.

Since the performance of $\sqrt{M}$-PAM is equivalent to the performance of M-QAM, the resolution of the possible constellation sizes at each depth is limited. Fig. 8 presents the BER performance of ASE-DMT and DCO-OFDM as a function of electrical and optical SNR when arbitrary constellation sizes and scaling factors are used. The results are outlined in Table 3. In comparison to results outlined in Table 2, the approach of arbitrary constellation sizes reduces the electrical and energy gains of ASE-DMT. However, it increases the spectral efficiency of ASE-DMT at a reduced computation complexity. Therefore, a trade-off between the complexity and spectral and energy efficiencies for ASE-DMT is a function of the application required.

Table 3. The optimal combination of constellation sizes and scaling factors for ASE-DMT and the associated electrical and optical gains over DCO-OFDM at a BER of 10^{-4}, where M_d and γ_d denote the constellation size and the scaling factor for the modulation depth-d, respectively.

DCO-OFDM M_{DCO}-QAM	η [b/s/Hz]	ASE-DMT $\{M_1, M_2, ..., M_D\}$-PAM	γ [dB]	Energy gains [dB] Ele.	Opt.
4-QAM	1	{2,2,4}-PAM	{1.9,2,-4.6}	0.6	-1
8-QAM	1.5	{4,2,4}-PAM	{-1.5,5.3,-1.2}	3.15	1.05
16-QAM	2	{4,8,4}-PAM	{2.4,-3.4,2.5}	2	0
32-QAM	2.5	{8,8,4}-PAM	{-0.9,-0.7,5.3}	3	0.75
64-QAM	3	{16,8,4}-PAM	{-2.7,3.2,9.4}	2.55	-0.25
128-QAM	3.5	{16,16,16}-PAM	{0,0,0}	3.28	0
256-QAM	4	{32,16,16}-PAM	{-2,3.6,3.7}	3.36	0
512-QAM	4.5	{32,32,64}-PAM	{1.5,1.7,-4}	3	-1.4
1024-QAM	5	{64,32,64}-PAM	{-1.3,4.3,-1.1}	4	-0.5

6. Conclusion

A novel energy efficient superposition modulation scheme for intensity modulation and direct detection (IM/DD) OWC is proposed. The scheme is based on selective frequency domain loading of M-PAM symbols, so that multiple streams can be superimposed and transmitted with no inter-stream-interference. The selective frequency domain loading of subcarriers allows low latency and simplified implementation of superposition modulation for PAM-DMT. The proposed scheme avoids the spectral and energy efficiency losses of ePAM-DMT.

The analytical bounds for BER performance are derived as a function of the electrical and optical SNR. The analytical bounds converge to match the Monte-Carlo simulations at high SNR values. The performance comparison shows the improvement of ASE-DMT over ePAM-DMT for the same spectral efficiency, and over DCO-OFDM at 87.5% of the spectral efficiency of DCO-OFDM for both electrical and optical SNR. A novel approach of arbitrary constellation sizes for ASE-DMT is proposed. This approach offers a simplified implementation of ASE-DMT with a reduced total number of depths. Future studies will include detailed comparisons with other superposition OFDM modulation schemes.

Acknowledgment

Towards 10 Gb/s orthogonal frequency division multiplexing-based Visible Light Communication using a GaN Violet micro-LED

Mohamed Sufyan Islim,[1,*] Ricardo X. Ferreira,[2,*] Xiangyu He,[2,*] Enyuan Xie,[2]

Stefan Videv,[1] Shaun Viola,[3] Scott Watson,[3] Nikolaos Bamiedakis,[4] Richard V. Penty,[4]

Ian H. White,[4] Anthony E. Kelly,[3] Erdan Gu,[2] Harald Haas,[1] and Martin D. Dawson[2]

[1]*Li–Fi R&D Centre, the University of Edinburgh, Institute for Digital Communications,*

King's Buildings, Mayfield Road, Edinburgh, EH9 3JL, UK

[2]*Institute of Photonics, Department of Physics, University of Strathclyde, Glasgow G1 1RD, UK*

[3]*School of Engineering, University of Glasgow, Glasgow G12 8LT, UK*

[4]*Centre for Advanced Photonics and Electronics,*

Electrical Engineering Division, Department of Engineering,

University of Cambridge, Cambridge CB3 0FA, UK

compiled: February 21, 2017

Visible light communication (VLC) is a promising solution to the increasing demands for wireless connectivity. Micro-sized Gallium Nitride (GaN) light emitting diodes (mirco-LEDs) are strong candidates for VLC due to their high bandwidths. Segmented violet mirco-LEDs are reported in this work with electrical-to-optical bandwidths up to 655 MHz. An orthogonal frequency division multiplexing (OFDM) based VLC system with adaptive bit and energy loading is demonstrated and a data transmission rate of 11.95 Gb/s is achieved with a violet mirco-LED, when the nonlinear distortion of the mirco-LED is the dominant noise source of the VLC system. A record 7.91 Gb/s data transmission rate is reported below the forward error correction threshold using a single pixel of the segmented array when all the noise sources of the VLC system are present.

OCIS codes: (060.4510) Optical communications; (060.2605) Free-space optical communication; (230.3670) Light-emitting diodes; (230.3990) Micro-optical devices.

http://dx.doi.org/10.1364/XX.99.099999

1. Introduction

The increasing demands of communication services are challenging radio frequency (RF) wireless communications technologies. The overall number of networked devices is expected to reach 26.3 billion in 2020 [1]. Visible light communication (VLC) is a promising solution to the limited availability of the RF spectrum as the visible light spectrum offers abundant bandwidth that is unlicensed and free to use. VLC improves the spectral efficiency per unit area, which enhances the quality of service in crowded environments and allows for secure and localized services to be provided.

General lighting is under a rapid transformation to become semiconductor based due to huge energy savings. This transformation has already enabled applications such as active energy consumption control and color tuning. Solid state lighting devices such as Gallium Nitride

(GaN)-based inorganic light emitting diodes (LEDs) are ubiquitous power-efficient devices to enable illumination and communications. Commercially available LEDs have a limited frequency response due to the yellow phosphor coating on top of the blue LEDs chips. However, the slow response of the yellow phosphor can be filtered out using a blue filter in front of the receiver. Recent results for VLC using a phosphorescent white LED with adaptive bit and energy loading were reported at 2.32 Gb/s aided by a two-staged linear software equalizer [2].

Micro LEDs (micro-LEDs) are promising candidates in enabling lighting as a service (LaaS) and internet of things (IoT). The introduction of micro-LEDs has enabled high-performance value-added lighting functions such as VLC, and indoor positioning and tracking [3]. micro-LEDs are known for their small active areas enabling high current density injection which drives the modulation bandwidth to hundreds of MHz [4, 5]. At 450 nm, micro-LEDs have set the standard for high–speed VLC. A 60 μm diameter pixel has achieved

* Contributed equally to this work.   Corresponding author: m.islim@ed.ac.uk
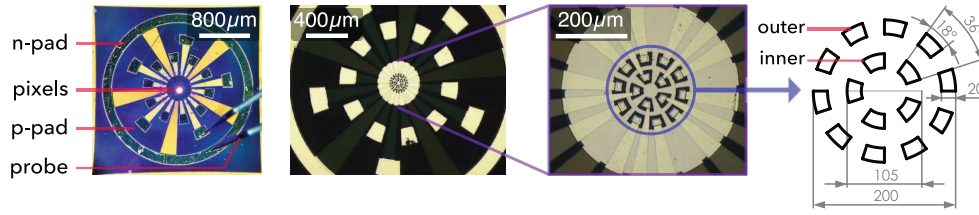
Fig. 1. Plan view micrographs of the segmented micro-LED arrays. The magnified micrographs on the right show the array configuration and individual pixel design. A diagram is also included noting inner and outer pixels (dimensions in micron).

3 Gb/s [6], and more recently a single pixel of a new segmented array has demonstrated 5 Gb/s [7]. The novel micro-LEDs emitting at 400 nm featured in the current work offer a number of advantages over the 450 nm devices previously reported [7]. From typical trends concerning the internal quantum efficiency (IQE) of indium gallium nitride-based active regions, comparable IQEs are expected at 400 nm and 450 nm, whereas IQE decreases steeply at shorter emission wavelengths [8]. For generation of white light for illumination, use of violet-emitting LEDs exciting tricolour (red, green, blue) phosphors also offers advantages over the widely used method of combining blue direct LED emission with a yellow-emitting phosphor. These include much superior colour rendering indices [9, 10], and the absence of a direct blue component, which has proven to be disruptive to the human circadian rhythm [11]. The micro-LED die shapes employed in this work are also expected to be advantageous for efficient light extraction, by analogy with previous designs employing non-circular emitting areas [12].

VLC is enabled by incoherent illumination from the light sources. Therefore, only real and positive modulating waveforms can be realized. Single carrier modulation schemes such as on-off keying (OOK), pulse amplitude modulation (PAM), and pulse width modulation (PWM) are straightforward to be implemented. However, the performance of these modulation schemes degrades as the transmission speed increases due to the increased inter-symbol interference (ISI). Equalization techniques can be used to improve the system performance at significant computation cost [13]. Multi-carrier modulation techniques such as orthogonal frequency division multiplexing (OFDM) are promising candidates for VLC. Computationally efficient single-tap equalizers are straightforward to be realized in OFDM. Adaptive bit and energy loading in OFDM allows the channel utilization to approach the information capacity limit. In addition, multiple access can be easily supported in OFDM by assigning groups of sub-carriers to multiple users, which is known as orthogonal frequency division multiple access (OFDMA).

Previously, a 40 μm diameter micro-LED at 405 nm achieved a data rate of 3.32 Gb/s at an optical power of 2.5 mW with electrical–optical bandwidth up to

307 MHz [14]. In this paper, we present a high bandwidth VLC link at 400 nm. The emitter consists of a single pixel of the segmented micro-LED array design introduced in [7]. This device achieves 2.3 mW of optical output power while maintaining an E-O bandwidth of 655 MHz. A VLC system is realized with a modulation bandwidth of 1.81 GHz, evaluated beyond the 3 dB bandwidth of the system. Transmission rate of 11.95 Gb/s is presented, when the nonlinear distortion noise of the micro-LED is the major source of noise in the system. A record transmission rate at 7.91 Gb/s is presented when all the noise sources of the VLC system are considered.

2. Violet Micro–LED

2.A. Design and Fabrication

The design of standard GaN LEDs is based on a large-area chip assembled on a package that maximises heat extraction through an n-pad at the bottom for a flip-chip configuration. This creates two limitations: a large capacitance due to the package contact area and an upper limit on the current density due to the rapid self heating of a large-area chip. The design and fabrication process of the micro-LED array used in this work are as reported in our previous work [7]. It consists of two circular micro-LED arrays, an inner and outer, containing 5 and 10 pixels, respectively. Originally designed to match the geometry of plastic optical fibre, the inner and outer pixels have active areas of 435 μm^2 and 465 μm^2, respectively. This compares with 1256 μm^2 active area for the 405 nm device in [14]. Fig. 1 shows optical images of this micro-LED array, together with a schematic of the pixel layout.

The wafer used in this work is for commercially available GaN-based LEDs emitting at 400 nm. In order to fabricate these arrays, micro-LEDs emitters are etched by inductively coupled plasma to expose n-type GaN. An annealed *Pd* layer is used as metal contact to p-type GaN. Each emitter is isolated by a layer of *SiO$_2$*. The metallization on the n-type GaN is formed by depositing a *Ti/Au* metal bilayer, which fills the area between each micro-LED and enables an improved current spreading. This bilayer connects each micro-LED emitter in order to individually address them. The micro-LED array allows increasing the total output power with minimal re-
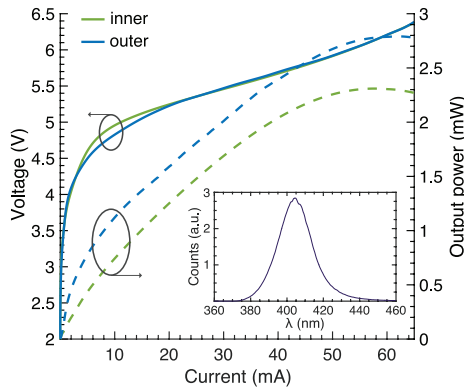
Fig. 2. Combined current-voltage (*I-V*), left, and luminescence-current (*L-I*), right, characteristics of both inner and outer pixels. The inset shows the emission spectrum of an inner pixel at 50 mA.

Fig. 3. Small signal frequency response for the inner pixel at 5 mA and 50 mA. The inset shows 6 dB electrical-optical (E-O) bandwidth at different values for the current density *J*, corresponding to DC bias values of 5-50 mA.

duction in performance due to mutual heating between pixels. The low optical power per pixel in micro-LEDs is a challenge when combined illumination and communication is considered. This problem can be addressed by using large arrays of pixels, where a system capable of handing the communication link over multiple pixels can be designed to reduce duty cycle, reduce junction temperature on individual pixels and maintain high efficiency. These investigations are subject to future work.

2.B. Performance Measurements

The electrical performance of the micro-LED arrays was measured by a semiconductor analyser (HP 4155). The optical power of the arrays under direct current (DC) conditions was measured using a Si detector placed in close proximity to the polished sapphire substrate. A spectrometer and charge coupled device detection system was used for the collection of electroluminescence spectra. The small signal frequency response was measured by a network analyser with a 20 mV AC frequency sweep signal combined in a bias-tee with a DC-bias current ranging from 5 mA to 50 mA. The optical response was collected by a lens system and focused onto a fast photodiode and fed to the network analyser. All the measurements were performed at room temperature with the device directly probed on chip with a high-speed probe to guarantee minimal parasitic effects.

2.B.1. *I–V* and *L–I* Characteristics

Devices with linear luminescence-voltage (*L-V*) characteristics and high optical power allow for a large dynamic range that can accommodate large swings of modulating signals and this subsequently improves the signal-to-noise ratio (SNR) of the VLC system. The current-voltage (*I–V*) and luminescence-current (*L–I*) character-

istics for the micro-LED are presented in Fig. 2. The pixels present a shunt resistance responsible for a sub-threshold turn-on, this is attributed to damaged regions in the junction and by surface imperfections. Differences between the inner and the outer pixels are minimal in *I–V* with a series resistance of 27 Ω and 26 Ω and threshold turn on voltage of 4.60 V and 4.64 V for the inner and outer pixels, respectively. In terms of optical power, at the roll-over point, the outer pixels achieve a maximum of 2.79 mW, 17% higher than the inner pixel, which is expected given the larger active area. This compares to 2.5 mW from a pixel at 405 nm with a 2.88 times larger active area [14]. The improvement in the optical power is due to the improved *Pd* p-type contact, resulting in 50% higher optical power compared to [14]. In addition, the commercially supplied wafer for this micro-LED gives better IQE.
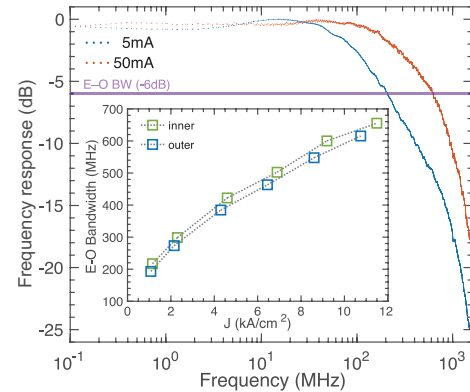
2.B.2. Frequency response

The frequency response from 100 kHz to 1.5 GHz for the lowest and highest bias currents of the testing set are presented in Fig. 3. At 1.5 GHz modulation the pixels do not reach the noise floor of the system, thus providing a large useful bandwidth for data transmission. The calculated electrical-optical (E-O) bandwidth against current density is shown in the inset of Fig. 3 for the set of bias currents covering the full operating range. The current densities for these pixels are in line with what was previously seen at 450 nm [7], meaning that the pixels achieve similar bandwidth at the same current density. This is also compared with 307 MHz bandwidth for the 405 nm device in [14]. The improvement in bandwidth over [14] is due to the smaller active area of the device that allowed higher current density and shorter carrier lifetime. With a bandwidth of 655 MHz for the inner pixel, to the authors' best knowledge, this micro-LED has the highest
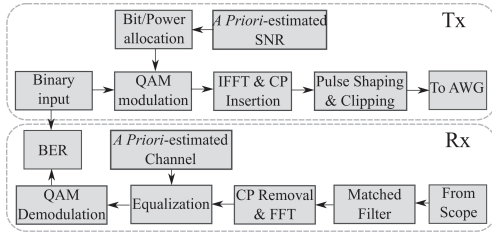
Fig. 4. Block diagram for OFDM transmitter and receiver

bandwidth yet shown in the violet wavelength band.

3. VLC System

3.A. Optical OFDM

Multiple variants of OFDM have been proposed for VLC [15]. Conventional OFDM waveforms are both complex and bipolar, however Hermitian symmetry can be imposed on the OFDM subcarriers frame to realize real-valued OFDM waveforms, $X[k] = X^*[N_{\text{FFT}} - k]$, where N_{FFT} is the OFDM frame size, and k is the subcarrier index. In addition, subcarriers at $X[0]$ and $X[N_{\text{FFT}}/2]$ are set to zero. DC-biased optical OFDM (DCO-OFDM) uses a DC bias to shift most of the negative real-valued OFDM samples into positive. The block diagram for OFDM is shown in Fig. 4. The generation of DCO-OFDM in this VLC experiment starts with generating a real-valued OFDM waveform in MATLAB®. A pseudo-random bit sequence (PRBS) is generated and then modulated using quadrature amplitude modulation (QAM). Given the *a priori* estimated SNR, the M_k-QAM constellation size at subcarrier k and its corresponding realtive energy, ν_k^2, are adaptively allocated based on the probability of error target, P_e^{T}.

The QAM symbols are loaded into orthogonal subcarriers with sub-carrier spacing equal to the symbol duration. The OFDM frame size is set to $N_{\text{FFT}} = 1024$ subcarriers. Smaller sizes for the OFDM frame result in less statistcal significance, larger sizes result in an increased peak-to-average power ratio (PAPR). The symbols can then be multiplexed into a serial time domain output using an inverse fast Fourier transform (IFFT). Cyclic prefixes (CPs) are inserted at the start of each OFDM frame. Adequate length of the CPs, N_{CP}, allows for ISI to be eliminated by the computationally-efficient single-tap equalizer. A value of $N_{\text{CP}} = 5$ is found to be sufficient for the ISI to be removed at less than 0.97% loss in the spectral efficiency. Root-raised cosine (RRC) pulse shaping filter is used to achieve band limited communication since it allows a trade-off control between pulse duration and bandwidth requirements [16]. OFDM time domain waveforms have high PAPR due to the coincidence of multiple in-phase QAM symbols in the same OFDM frame. Extreme values for the OFDM modulating signal are clipped to minimize the effect of nonlinearity at acceptable error margins. The upper and

lower clipping values are set to $+3\sigma_x$ and $-3.5\sigma_x$, respectively, where σ_x is the standard deviation of the OFDM waveform. Asymmetric values for the clipping points are used since the upper clipping due to the saturation of the micro-LED is higher than the lower clipping. The received waveform is processed with matched filters, fast Fourier transform (FFT) with CPs removal, single-tap equalizer using the *a priori* estimated channel, and demodulator. Bit error rate (BER) is calculated based on the demodulated binary stream.

Before any data tranmission, the channel is first estimated by pilots composed of multiple OFDM frames. A conventional mean estimator is used with random pilots that would take the nonlinearity effects into account. Details about the used estimation method can be found in [17]. An estimation of the SNR is also obtained using the same method. The received OFDM waveform, $y(t)$, can be expressed as follows:

$$y(t) = h(t) * z(x(t)) + n(t), \qquad (1)$$

where $h(t)$ is the VLC system channel, $n(t)$ is the additive white Gaussian noise (AWGN) at the receiver with a variance σ_n^2, and $z(.)$ is the nonlinear transformation of the micro-LED. For Gaussian inputs such as the real-valued OFDM waveform, the Bussgang theorem can be applied and the nonlinear transformation can be expressed as [18]:

$$z(x(t)) = \alpha x(t) + d(t), \qquad (2)$$

given that the processes $x(t)$ and $d(t)$ are uncorrelated $\text{E}[x(t)d(t)] = 0$, where $\text{E}[.]$ is the statistical expectation and $d(t)$ is the distortion noise. The constant α can be calculated as [18]:

$$\alpha = \frac{\text{E}[z(x(t)).x(t)]}{\sigma_x^2}. \qquad (3)$$

The distortion noise $d(t)$ is a non-Gaussian noise. However, its representation in the frequency domain $D(f)$ follows a Gaussian distribution with a DC mean and a variance σ_d^2 [18]. Detailed analysis of the nonlinear distortion noise effect on DCO-OFDM can be found in [19]. The used arbitrary waveform generator (AWG) has 10 bits resolution for the digital-to-analog converter (DAC), and the oscilloscope used has an effective number of bits 5.5 for the analog-to-digital converter (ADC). The nonlinearity effect from the amplifier is minimal at the operational frequencies and at the injected power levels. The harvested optical power at the photoreceiver is well below the saturation level. Therefore, the micro-LED is assumed to be the main source of nonlinearity in the overall system due to the relatively limited dynamic range, compared to other system components.

The estimated SNR is used to adaptively load the subcarriers with variable constellation sizes at different energy levels based on the Levin-Campello algorithm [20]. The algorithm allows more energy to be allocated to the
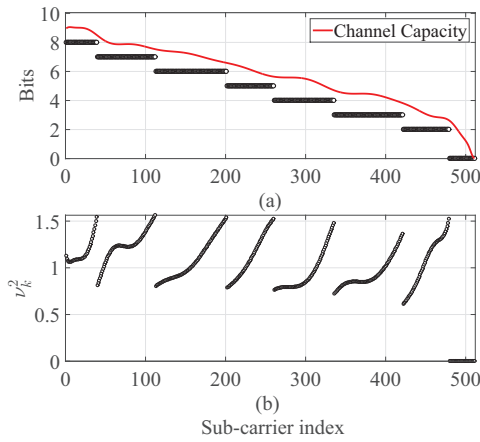
Fig. 5. (a) The bit loading and channel capacity per subcarrier, both given in bits per subcarrier. (b) Energy loading per subcarrier.

Fig. 6. The statistical CDF for different QAM constellation sizes experimentally achieved at a BER=2.3×10^{-3}, below the FEC target.

subcarriers which require minimal additional power to be elevated into larger constellation sizes, while preserving the probability of error target, P_e^{T}. Assuming that $N_{\mathrm{FFT}} > 64$, the adaptive bit and energy loading can be formulated in the following optimization problem:

$$\underset{\eta}{\text{maximize}} \quad \eta = \frac{\sum_{\substack{k=1 \\ M_k>0}}^{\frac{N_{\mathrm{FFT}}}{2}-1} \log_2 M_k}{(N_{\mathrm{FFT}} + N_{\mathrm{CP}})(1 + \beta)}, \quad (4a)$$

$$\text{subject to} \quad \mathrm{BER}\left(M_k, \frac{\nu_k^2 \alpha^2 E_{\mathrm{b}k}}{N_o/|H(k)|^2 + \sigma_d^2}\right) \leq P_e^{\mathrm{T}}, \quad (4b)$$

$$\sum_{\substack{k=1 \\ M_k>0}}^{\frac{N_{\mathrm{FFT}}}{2}-1} \frac{\nu_k^2}{\frac{N_{\mathrm{FFT}}}{2}-1} = 1, \quad (4c)$$

where β is the roll-off factor of the RRC filter, $E_{\mathrm{b}k}$ is the energy per bit at subcarrier k, N_o is the double-sided power spectral density (PSD) of the noise at the receiver, $|H(k)|^2$ is the channel gain at subcarrier k when a zero forcing (ZF) equilzer is used, η is the spectral efficiency given in bits/s/Hz, and $\mathrm{BER}(M_k, \gamma_k)$ is the theoretical BER equation of M_k-QAM at subcarrier k and SNR per bit γ_k, given in non-flat channels as [21]:

$$\mathrm{BER}(M_k, \gamma_k) \cong \frac{4}{\log_2(M_k)}\left(1 - \frac{1}{\sqrt{M_k}}\right) \times$$
$$\sum_{l=1}^{R} \sum_{k=1}^{N_{\mathrm{FFT}}} Q\left((2l-1)\sqrt{\frac{3\log_2(M_k)\gamma_k}{2(M_k-1)}}\right), \quad (5)$$

where $Q(.)$ is the complementary cumulative distribu-

tion function (CCDF) for the standard normal distribution, and $R = \min(2, \sqrt{M_d})$.

The adaptive bit and energy loading on each subcarrier is shown in Fig. 5 along with the channel capacity limit defined by Shannon as [22]:

$$C = \log_2\left(1 + \frac{\alpha^2 E_{\mathrm{b}k}}{N_o/|H(k)|^2 + \sigma_d^2}\right), \quad (6)$$

It is shown that the gap between the exact loading and the capacity limit is already small, however, it can be closed when channel coding is employed. The cumulative distribution function (CDF) of the estimated SNR for multiple QAM constellation sizes are presented in Fig. 6. The results show the distribution of the SNR values required to achieve a BER below the forward error correction (FEC) target based on the bit and energy loading algorithm.

3.B. Experimental Set-up

The experimental set-up, shown in Fig. 7, starts with a laptop connected to a Tektronix AWG (AWG70001A) that has a maximum sampling frequency of 50 GS/s with an ADC resolution of 10 bits per sample. Bipolar OFDM waveforms are generated in MATLAB® as detailed in Section 3.A and then transmitted to the AWG. The maximum peak-to-peak voltage (V_{PP}) of the AWG is 0.5 V_{PP}. The output of the AWG is amplified with a broadband amplifier (SHF 100AP) that has a maximum gain of 20 dB in the bandwidth range (100 kHz–20 GHz). A 3 dB attenuator is used at the output of the amplifier to allow flexible control of the signal modulation depth, V_{PP}. The power budget of the system is adjusted to allow complete utilization of the micro-LED dynamic range shown in Fig. 2.

The amplified bipolar signal is DC-biased with a Bias-tee (Mini-Circuits ZFBT-4R2GW+). Low values

(a) Schematic

(b) Photograph

Fig. 7. The experimental set-up. (a) Schematic set-up of the experiment showing the optical system, AWG, oscilloscope, amplifier, attenuator, and Bias-tee. (b) Photograph of the optical system showing the micro-LED, optical lenses system, and the photoreceiver.

Fig. 8. Experimentally obtained results and theoretical bounds of data rate and BER versus different dimming levels at a modulation depth of $V_{PP} = 2.36$ V. The values for the received optical power correspond to DC bias values ranging from 10 mA to 40 mA.

4. Results and Discussion

The VLC data transmission experiment was only conducted on the inner pixels due to their higher E-O bandwidth compared to the outer pixels. The sampling frequency of the AWG is set to 29 GS/s with an over sampling factor of 8 samples per symbol, which results in a single-sided modulation bandwidth of 1.81 GHz. The subcarriers are equally spaced within the Nyquist rate of the modulation signal with a subcarrier spacing of 3.54 MHz. The high-speed equipment used in the measurements allowed for the overall system bandwidth to be limited by the bandwidth of the micro-LED. Figure 8 shows the data rates, and the corresponding theoretical lower bounds and experimentally obtained values for the BERs at different dimming levels. The theoretical lower bounds for the BER estimations are calculated based on the experimentally estimated SNR as described in (5) and they are shown to be close to the experimental results. The data rates starts with 3.46 Gb/s at a received optical power, P^{opt} =-4.94 dBm, which corresponds to a DC bias of V_{DC} =4.16 V and a DC current of I_{DC} =10 mA. The data rate increases, but starts to saturate as the DC bias increases until it reaches a maximum of 4.91 Gb/s at P^{opt} =-2.29 dBm corresponding to V_{DC} =5.21 V and I_{DC} =35 mA. The data rate starts to decrease as the DC bias increases beyond 35 mA. This result is expected due to the increased clipping distortion caused by the optical power saturation shown in Fig. 2. The achieved BER for all the studied cases in this test is well below the 3.8×10^{-3} FEC threshold. The optimized DC bias was selected for the rest of the measurements as V_{DC} =5.11 V and I_{DC} =30 mA, since the system performance for a larger swing of the peak-to-peak modulation signal starts to degrade at I_{DC} =35 mA. The theoretical lower bounds of the BER versus data rates at different dimming levels are shown in Fig. 9 with a

for the DC bias results in high zero-level clipping of the OFDM waveform which degrades the SNR. High values for the DC bias results in optical power saturation at the micro-LED which also degrades the SNR. After extensive experiments, the DC bias is set to I_{DC} = 30 mA corresponding to a measured DC voltage of V_{DC} = 5.23 V. This value allows the OFDM bipolar signal to swing in the linear region of the L-V characteristic of the micro-LED. The biased signal is then fed to the micro-LED via a high speed probe. An optical plano-convex lens (Thorlabs LA1116) is used to collimate most of the light into a dielectric mirror (Thorlabs CM1-E02) with higher than 97% reflectance in the desired wavelength region. The reflected light is then focused onto the photoreceiver by a bi-convex lens (Thorlabs LB4879) followed by a microscopic objective lens (NewPort M-40x) with a numerical aperture (NA) of 0.65. A silicon positive-intrinsic-negative (PIN) photoreceiver is used (Femto HSPR-X-I-1G4-SI) with a 3 dB bandwidth of 1.4 GHz and a responsivity of 0.135 A/W around 400 nm.

Fig. 9. Theoretical bounds on the data rate versus BER for different dimming levels at a modulation depth of V_{PP} =2.36 V. The values for the received optical power corresponds to DC bias values ranging from 10 mA to 40 mA. Filled markers denote experimental results.

Fig. 10. SNR versus frequency for different modulation depths at DC bias current I_{DC} =30 mA. The values for the modulation signal swings corresponds to feeding the micro-LED with varying power levels from 5.85 dBm to 11.78 dBm.

Fig. 11. Data rates versus BER for the experimentally obtained and the theoretical bounds at DC bias current I_{DC} =30 mA corresponding to P^{opt} =-2.6 dBm and modulation depth V_{PP} =3.88 V.

comparison to the experimental results. The deviation between theoretical and experimental validation point at P^{opt} =-4.94 dBm is due to the severe clipping distortion at DC current I_{DC} =10 mA.

The system performance as a function of the modulation signal depth, V_{PP} is investigated. Large modulation signal swing is expected to increase the SNR due to the increased signal power, σ_x^2. Nevertheless, it incurs additional nonlinear distortion, σ_d^2, due to the increased clipping. It is shown in Fig. 10 that the SNR improves as the modulation depth increases. The nonlinear distortion is present on the first 250 MHz, however the improvement in the signal power σ_x^2 is more significant at higher frequencies. This result is justified by the fact that signals at higher frequencies are attenuated due to the lower channel gain at these high frequencies. Therefore, these values become less affected by the nonlinearity of the device. This result shows that tolerating additional nonlinearity by employing a larger signal swing can improve the communication system performance.

The experimentally optimized values for the DC bias at 30 mA and the modulation signal swing at 3.88 V_{PP} are used to investigate the system data rate performance against BER. The experimentally obtained data rates versus BERs are presented with the theoretical lower bounds for the BER performance in Fig.11. The theoretical lower bounds are shown to be very close to the experimentally obtained results. As shown in Fig. 11, transmission data rate of 7.91 Gb/s is experimentally achieved at a BER below the FEC threshold, 3.8×10^{-3}. To guarantee reliable communications, the data rate is reduced to 7.36 Gb/s to allow for a 7% FEC overhead to be employed. This compares to 5 Gb/s for a device with similar design emitting at 450 nm [7]. To the best of the authors' knowledge, this record is the highest for VLCs data transmission speeds using single micro-LED.
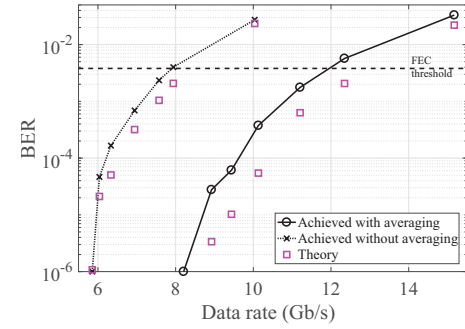
The system data rate performance is investigated when waveform averaging acquisition mode of the oscilloscope is activated. Averaging acquisition was shown to be useful in drawing conclusions from experimental studies that could influence practical system design [23]. The averaging acquisition mode in this experiment allows for a better characterization of the micro-LED by reducing the AWGN of the photoreceiver which limits the system performance to the nonlinear distortion noise of the micro-LED. It is shown in Fig. 11 that data rates up to 11.95 Gb/s can be achieved at a BER below the FEC threshold. This is reduced to 11.12 Gb/s when 7% FEC overhead is used. The results for the waveform acquisition mode of the oscilloscope are only presented to show the effect of the nonlinear distortion in the absence of the photoreceiver AWGN noise. All other reported results were conducted without waveform averaging acquisition.
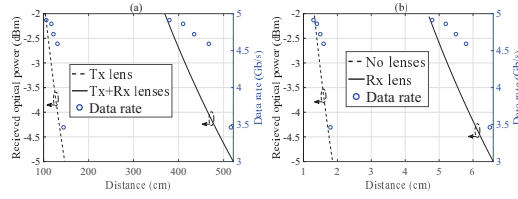
Fig. 12. Distance versus received optical power (left) and data rate (right). (a) for Study I with transmitter and receiver lenses and Study II with transmitter lens only. (b) for Study III with receiver lens only and Study IV without any optics.

5. Range and Alignment Considerations

The VLC system was realized using an optical system to collect, collimate, and focus the light on the photodiode (PD). The used optical system imposes restrictions on the link alignment and transmission range. Introducing optimized optics and deploying more micro-LED pixels from the array can improve both the coverage and the range of the system. The feasibility of demonstrating long transmission distances was demonstrated at a free-space distance of 10 m and a data rate of 1.1 Gb/s in [24]. This was achieved using an avalanche photodiode (APD) with an integrated concentrator, and a micro-LED with an optical power of 4.5 mW, which is 1.96 times higher than the optical power of the micro-LED pixel used in this work.

The obtained data rates and BERs for different received optical power presented in Fig. 8 enable us to investigate the system performance against the transmission range based on the widely accepted line-of-sight (LoS) optical wireless communication (OWC) propagation models [25]. The methodology is to compute the distances which result in the respective received optical power presented in Fig. 8, and the distances are then cross-mapped with the data rates achieved in Fig. 8. Note that the results shown in Fig. 8 are obtained at different dimming levels by varying the DC bias point which limits the operating bandwidth and the experimentally obtained data rates. An analysis of the system range is provided based on four studies: (I) with transmitter and receiver lenses; (II) with transmitter lens only; (III) with receiver lens only; (IV) without any optics. In all cases we assume that all array pixels are used (15 micro-LEDs) in a ganging OFDM mode. This can increase the mutual heat between the pixels and consequently degrades the total aggregate data rates, therefore the results in this section can be considered as upper bounds on the system performance.

The LoS channel gain can be given as [25]:

$$H(0) = \frac{(m+1)A}{2\pi d^2} \cos^m(\phi) T(\psi) g(\psi) \cos(\psi), \quad (7)$$

where $m = -1/\log_2(\cos(\Phi_{1/2}))$ is the Lambertian order of the optical source and $\Phi_{1/2}$ denotes its semi-angle;

ϕ is the angle of irradiance; A is the detection area of the APD; d is the Euclidean distance between the optical source and the APD; ψ is the angle of incidence; $T(\psi)$ represents the gain of the optical filter used at the receiver; and $g(\psi)$ represents the gain of the optical concentrator, given as [25]:

$$g(\psi) = \begin{cases} \frac{n^2}{\sin^2(\Psi_{\text{fov}})}, & 0 \leq \psi \leq \Psi_{\text{fov}} \\ 0, & \psi > \Psi_{\text{fov}} \end{cases}, \quad (8)$$

where n is the refractive index of the optical concentrator used at the APD. The optical power after the transmitter lens can be given as [26]:

$$P_{\text{opt}}^{\text{R,lens}} = \frac{(m_{\text{LED}} + 1)D_{\text{lens}}^2}{8d'^2} T_{\text{lens}} P_{\text{opt}}^{\text{T,LED}}, \quad (9)$$

where m_{LED} denotes the Lambertian order of the micro-LED, D_{lens} is the lens diameter, T_{lens} is the transmittance of the lens, and d' is the distance between the micro-LED and the transmitter lens. The existence of the transmitter lens affect the micro-LED beam divergence. The half power semi-angle $\Phi_{1/2}^{\text{lens}}$ can be given as [26]:

$$\Phi_{1/2}^{\text{lens}} = \frac{D_{\text{s}}}{2d'}, \quad (10)$$

where D_{s} is the diameter of the micro-LED. The transmitter lens used in this investigation is aspheric condenser lens (Thorlabs ACL7560U-A) with a diameter of $D_{\text{lens}} = 75$ mm, and a focal length of lens $f = 60$ mm.

A commercially available compound parabolic concentrator (CPC) is assumed to be in front of the APD. The field-of-view (FOV) of the concentrator is 25°, with a refractive index of $n = 1.5$. We assume the use of a high speed commercially available APD at the receiver (Thorlabs APD210) instead of the used positive-intrinsic-negative (PIN) receiver (Femto HSPR-X-I-1G4-SI). The APD diameter is 0.5 mm and the modulation bandwidth is 1.6 GHz. The APD improves the sensitivity of the receiver, therefore an APD conversion gain factor is introduced to allow a fair comparison between the experimentally obtained results using the PIN and the numerical results using the APD photoreceivers:

$$\Lambda^{\text{APD}} = \frac{G^{\text{APD}}}{G^{\text{PIN}}}, \quad (11)$$

where G^{APD} and G^{PIN} are the conversion gains of the APD and PIN photoreceivers given in V/W, respectively. Using Equations (7) to (11), the received optical power at the APD can be given as:

$$P_{\text{opt}}^{\text{Rx,APD}} = \frac{(m_{\text{lens}} + 1)A}{2\pi d^2} \cos^{m_{\text{lens}}}(\phi) \times \\ T(\psi) g(\psi) \cos(\psi) \Lambda^{\text{APD}} P_{\text{opt}}^{\text{R,lens}}, \quad (12)$$

where m_{lens} is the Lambertian order of the lens based on (10).
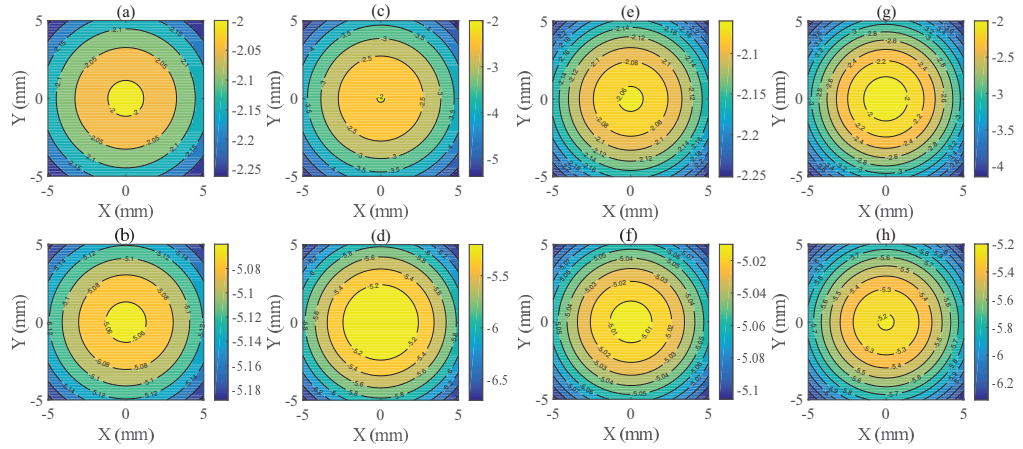
Fig. 13. Received optical power distribution in dBm as a function of vertical-horizontal displacements. (a) Study I at a distance of 369 cm; (b) Study I at a distance of 525 cm; (c) Study II at a distance of 104 cm; (d) Study II at a distance of 147 cm; (e) Study III at a distance of 4.7 cm;(f) Study III at a distance of 6.6 cm;(g) Study IV at a distance of 1.3 cm; (h) Study IV at a distance of 1.9 cm.

The LoS propagation model is used to compute the transmission ranges that can achieve certain values for the received optical power between -5 dBm and -2 dBm. These values for the received optical power were demonstrated experimentally to achieve data rates between 3.46 Gb/s and 4.91 Gb/s using the experimentally realized VLC system. An upper bound on the data rates can be estimated by cross-mapping the computed received power at each distance, with the experimentally obtained data rates provided in Fig.8. The distance versus received optical power and data rate for Studies I and II and studies III and IV are shown in Fig. 12, respectively. The largest distances can be achieved using transmitter and receiver optics. Specifically, it was found that at 3.69 m distance a data rate of 4.91 Gb/s can be achieved, and at 5.25 m distance the data rates reduces to 3.46 Gb/s. As expected, the transmitter lens is shown to boost the range more than the receiver concentrator lens. At a data rate of 4.91 Gb/s, the maximum distance is 1.04 m and 4.7 cm for studies II and III, respectively. At a data rate of 3.46 Gb/s, the maximum distance is 1.47 m and 6.6 cm for studies II and III, respectively. The transmission ranges that can be supported at data rates above 3.46 Gb/s are less than 2 cm when optics are not used.

The received optical power distribution is investigated as a function of the receiver's vertical-horizontal misalignments for the four considered studies, as shown in Figure 13. The results are presented for the received optical power values that allow a maximum of -2 dBm and a minimum of -5 dBm, corresponding to data rates of 4.91 Gb/s and 3.46 Gb/s, respectively. The transmission range and the system robustness against misalignments are both improved when optics are used for both front-end components in Study I, which makes this scenario suitable for high-speed point to point applications. The transmitter lens in Study II improves the transmission range but reduces the system robustness against misalignments. The receiver lens in Study III is reducing the performance degradation caused by misalignment at the expense of reducing the system range. The transmission range and the system robustness against misalignments are both degraded in Study IV. However, Studies III and IV are suitable for board to board communication links, where wired links are not possible because of the rotational requirements between the boards for example.

6. Conclusion

A novel violet micro-LED array with two sets of inner and outer pixels is reported in this paper. The inner pixels allow very high current densities due to the small active area, enabling E-O bandwidth up to 655 MHz at an optical output power of 2.3 mW.

An OFDM-based VLC system using a single pixel of the proposed violet micro-LED is realized using adaptive bit and energy loading. The nonlinear distortion is found to affect the slow frequency region of the overall system bandwidth due to the limited dynamic range of the micro-LED. A transmission rate of 11.12 Gb/s, including the 7% FEC overhead is achieved by averaging out thermal and shot noise of the photoreceiver and limiting the overall VLC system noise to the nonlinear distortion of the micro-LED. This result represents an upper bound on the proposed micro-LED performance that can be approached when higher quality system components with lower noise margins are used. A data transmission rate of 7.36 Gb/s, including the 7% FEC over-

head is also reported when all the noise sources of the VLC system are considered. The theoretical bounds are in good approximation with the experiment results.

The numerical investigation of the range and alignment highlight the role of optimized optics in increasing the transmission distance and improving system robustness.

Acknowledgement

References

[1] Cisco Visual Networking Index, "The Zettabyte era: trends and analysis," White Paper, Cisco (2015), `http://www.cisco.com/c/en/us/solutions/collateral/service-provider/visual-networking-index-vni/VNI_Hyperconnectivity_WP.pdf`.

[2] Y. Zhou, J. Zhao, M. Zhang, J. Shi and N. Chi, "2.32 Gbit/s phosphorescent white LED visible light communication aided by two-staged linear software equalizer," in *10th International Symposium on Communication Systems, Networks and Digital Signal Processing (CSNDSP)*, (IEEE, 2016), pp. 1–4.

[3] J. Herrnsdorf, J.J.D. McKendry, E. Xie, M.J. Strain, E. Gu, I.M. Watson, and M.D. Dawson, "Gallium Nitride structured illumination light sources," in Light, Energy and the Environment conference, (Optical Society of America, 2016), paper SSM2C.1.

[4] J.J.D. McKendry, R.P. Green, A.E. Kelly, Z. Gong, B. Guilhabert, D. Massoubre, E. Gu, M.D. Dawson, "High-speed visible light communications using individual pixels in a Micro light-emitting diode array," IEEE Photon. Technol. Lett. **22**, 1346–1348 (2010).

[5] P.P. Maaskant, H. Shams, M. Akhter, W. Henry, M.J. Kappers, D. Zhu, C.J. Humphreys, and B. Corbett, "High-speed substrate-emitting Micro-light-emitting diodes for applications requiring high radiance," Appl. Phys. Expr. **6**, 022102 (2013).

[6] D. Tsonev, H. Chun, S. Rajbhandari, J.J.D. McKendry, S. Videv, E. Gu, M. Haji, S. Watson, A.E. Kelly, G. Faulkner, M.D. Dawson, H. Haas, and D. O'Brien, "A 3-Gb/s single-LED OFDM-based wireless VLC link using a Gallium Nitride µLED," IEEE Photon. Technol. Lett. **26**, 637–640 (2014).

[7] R. Ferreira, E. Xie, J. McKendry, S. Rajbhandari, H. Chun, G. Faulkner, S. Watson, A.E. Kelly, E. Gu, R. Penty, I. White, D. O'Brien, and M.D. Dawson, "High bandwidth GaN-based micro-LEDs for multi-Gbps visible light communications," IEEE Photon. Technol. Lett., **28**, 2023–2026, (2016).

[8] C.J. Humphreys, "Solid-state lighting," MRS bulletin, Cambridge Univ Press **33**, 459–470 (2008).

[9] A. Zukauskas, R. Vaicekauskas and M.S. Shur, "Colour-rendition properties of solid-state lamps," J. Appl. Phys. D **43**, 354006 (2010).

[10] J.M. Phillips, M.E. Coltrin, M.H. Crawford, A.J. Fischer, M.R. Krames, R. Mueller-Mach, G.O. Mueller, Y. Ohno, L.E.S. Rohwer, J.A. Simmons and J.Y. Tsao, "Research challenges to ultra-efficient inorganic solid-state lighting," Laser and Photon Rev. **1**, 307-333 (2007).

[11] Q. Dai, Q. Shan, H. Lam, L. Hao, Y. Lin and Z. Cui, "Circadian-effect engineering of solid-state lighting spectra for beneficial and tunable lighting," Opt. Exp. **24**, 20049-20058 (2016).

[12] Z. Gong, Y.F. Zhang, P. Kelm, I.M. Watson, E. Gu, and M.D. Dawson, "InGaN micro-pixellated light-emitting diodes with nano-textured surfaces and modified emission profiles," Appl. Phys. A **103**, 389-393 (2011).

[13] D.J.F. Barros, S.K. Wilson and J.M. Kahn, "Comparison of orthogonal frequency-division multiplexing and pulse-amplitude modulation in indoor optical wireless links," IEEE Trans. Commun. **60**, 153–163 (2012).

[14] J. McKendry, D. Tsonev, R. Ferreira, S. Videv, A. Griffiths, S. Watson, E. Gu, A. Kelly, H. Haas, and M. Dawson, "Gb/s single-LED OFDM-based VLC using violet and UV Gallium Nitride µLEDs," in *IEEE Summer Topicals Meeting Series (SUM)*, (IEEE, 2015), paper TuD4.3.

[15] M.S. Islim, and H. Haas, "Modulation techniques for Li–Fi," ZTE COMMUNICATIONS **14**, 29–40 (2016).

[16] D. Tsonev, S. Sinanovic, and H. Haas, "Complete modelling of nonlinear distortion in OFDM-based optical wireless communication," J. Lightwave Technol. **31**, 3064–3076 (2013).

[17] D. Tsonev, S. Videv, and H. Haas, "Unlocking spectral efficiency in intensity modulation and direct detection systems," IEEE J. Sel. Areas Commun. **33**, 1758–1770 (2015).

[18] P. Banelli and S. Cacopardi, "Theoretical analysis and performance of OFDM signals in nonlinear AWGN channels," IEEE Trans. Commun. **48**, 430–441 (2000).

[19] S. Dimitrov and H. Haas, "Information rate of OFDM-based optical wireless communication systems with nonlinear distortion," J. Lightwave Technol. **31**, 918–929 (2013).

[20] H.E. Levin, "A complete and optimal data allocation method for practical discrete multitone systems," in *Proceedings of IEEE Global Telecommunications Conference* (IEEE, 2001), pp. 369–374.

[21] F. Xiong, *Digital Modulation Techniques*, (Artech House Publishers, 2006), 2nd ed.

[22] CE. Shannon, "A mathematical theory of communication," Bell System Technical Journal **27**, 379–423 (1948).

[23] L. Peng, S. Haese and M. Hèlard, "Optimized discrete multitone communication over polymer optical fiber," IEEE J. Opt. Commun. Netw. **5**, 1313–1327 (2013).

[24] J. Jiang, Y. Huo, F. Jin, P. Zhang, Z. Wang, Z. Xu, H. Haas, and L. Hanzo, "Video streaming in the multiuser indoor visible light downlink," IEEE Access **3**, 2959–2986 (2015).

[25] J. M. Kahn and J. R. Barry, "Wireless Infrared Communications," Proc. IEEE **85**, 265–298 (1997).

[26] J. Fakidis, M. Ijaz, S. Kucera, H. Claussen, and H. Haas, "On the Design of an Optical Wireless Link for Small Cell Backhaul Communication and Energy Harvesting," in *Proc. IEEE 25th Annu. Int. Symp. Personal Indoor Mobile Radio Commun.*, (IEEE, 2014), pp. 58–62.

The Impact of Solar Irradiance on Visible Light Communications

Mohamed Sufyan Islim, *Graduate Student Member, IEEE,* Stefan Videv, Majid Safari, Enyuan Xie, Jonathan J. D. McKendry, Erdan Gu, Martin D. Dawson, *Fellow, IEEE,* and Harald Haas, *Fellow, IEEE* .

Abstract—This work aims to address the perception that visible light communication (VLC) systems cannot work under the presence of sunlight. A complete framework is presented to evaluate the performance of VLC systems in the presence of solar irradiance at any given location and time. The effect of solar irradiance is investigated in terms of degradations in signal to noise ratio (SNR), data rate and bit error rate (BER). Direct current (DC) optical orthogonal frequency division multiplexing (DCO-OFDM) is used with adaptive bit and energy loading to mitigate DC wander interference and low-frequency ambient light noise. It was found that reliable communication can be achieved under the effect of solar irradiance at high-speed data rates. An optical bandpass blue filter is shown to compensate for half of the reduced data rate in the presence of sunlight. This work demonstrates data rates above 1 Gb/s of a VLC link under strong solar illuminance measured at 50350 lux in clear weather conditions.

Index Terms—Visible light communication (VLC), Light fidelity (LiFi), OFDM, solar irradiance.

I. INTRODUCTION

TRAFFIC from wireless and mobile devices will account for two-thirds of the total internet traffic by 2020 [1]. The radio frequency (RF) bandwidth is a scarce resource costing above \$1.28m per 1 MHz in the 2.4 GHz frequency band in the UK [2]. Visible light communication (VLC) offers a much larger frequency bandwidth that is unlicensed and safe to use. VLC has the potential to reuse the existing lighting infrastructure based on light emitting diode (LED) for communications purposes [3]. Light fidelity (LiFi) is the network solution for VLC that is proposed to work seamlessly beside other RF access technologies [3]. A record data rate of 7.91 Gb/s was reported for orthogonal frequency division multiplexing (OFDM)-based VLC using single violet micro-scale GaN LED (micro-LED) [4]. Data rates above 100 Gb/s can be achieved when the complete visible spectrum is utilized [5].

The effect of solar irradiance is considered to be one of the main misconceptions surrounding VLC [6]. It is generally

assumed that it could halt the operation of the communication system entirely due to interference. However, the effect of solar irradiance is more apparent as a strong shot noise source rather than an interfererence source as the sunlight intensity does not vary greatly over short periods of time. This allows multicarrier schemes such as OFDM to allocate the symbols over the usable frequency subcarriers of the deployed bandwidth [7].

The effect of solar irradiance on the performance of optical wireless communications (OWC) and VLC has been investigated in a limited number of works in the litrature [8]–[12]. A simplified model was adopted in some of these works by approximating the solar irradiance to a black body radiation [8]. Other works adopted a standarized solar irradiance model [13] that is being used as a reference model in the research on solar energy harvesting [9]. However, the location and time of the studied system play important roles in characterizing the solar irradiance effect on VLC system performance. These important parameters were considered using computer simulation in [10]. However, the direct solar irradiance was not used to characterize the system performance. The solar irradiance was assumed to be incident from a window and reflected on multiple walls before it is collected by the photoreceivers. The impact of solar irradiance on the performance of underwater OWC links was investigated for positive-intrinsic-negative (PIN), avalanche photodiode (APD) and photomultiplier tube (PMT) using Monte Carlo simulaiton in [9]. It was shown that sunlight degrades the system performance at relatively low depths below 80 meters.

The use of optical filters with a light control film to mitigate the effects of sunlight was proposed in [8], [11]. A filter with a light control film called microlouver is used to restrict the field of view (FOV) and to reduce the background light collected at the photoreceiver. However, the light control film can not adapt to the changes of the photoreceiver orientation and location which limits the solution to fixed point-to-point systems. The objective of this paper is to provide a theoretical and experimental characterization of the solar irradiance effect on high-speed OFDM-based VLC systems. The investigation compares the use of a bandpass optical blue filter to the case where a filter is not considered in front of the photoreceiver. The performance is compared to a benchmark scenario of a dark room where background light does not reach the photoreceiver.

In our previous work [14], we investigated the solar irradiance effect on VLC in Antofagasta, Chile based on worst-case scenarios in terms of location, link orientation and choice of photoreceiver. In this paper, we present a complete framework to investigate the sunlight effect on VLC at any given location and time. The previous literture were manily

Fig. 1. (a) Solar position described by altitude and azimuth. (b) and (c) Solar position at Edinburgh and Antofagasta, respectively, for each 20th day of each considered month. The time of the day is listed above the elliptical shapes representing the Analemma diagrams
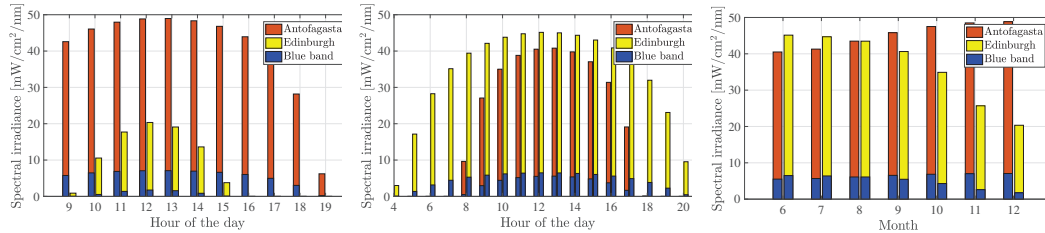
Fig. 2. Total solar irradiance estimated at Antofagasta and Edinburgh on the 20th of December 2016 (left) and on the 20th of June 2016 (center); and at the noon of each 20th day of the second half of the year (right). The blue spectral component of the solar irradiance is shown in blue.

based on pulsed modulation techniques [11], [12]. However, an outdoor underwater VLC demonstration acheiving a data rate of 58 Mb/s was considered using discrete multi-tone (DMT) [15]. In this work, we demonstrate our results by an experimental proof of concept of a high speed OFDM-based VLC system in Edinburgh, UK achieving data rate above 1 Gbps in the presence of solar irradiance without any optical filtering. The simulation and experimental results show that the solar irradiance affects VLC link performance, but the effects are gradual and depend on a number of other parameters such as link margin. The simulation results show that at least half of the losses in data rate performance can be recovered using an inexpensive commercially available bandpass blue filter.

The rest of this paper is organized as follows. In Section II, we review the solar position and irradiance calculations based on location and time and present the results of two geographical locations. The assumptions of the theoretical study are specified in Section III-A. The signal-to-noise ratio (SNR), the maximum theoretical limit to the data rate and bit error rate (BER) of the system are derived and the system modelling is discussed in Section III-B. An experimental proof-of-concept is presented in Section IV. The system performance is analyzed and the results are shown in Section III-C and Section IV-B. Section V concludes the paper.

II. SOLAR IRRADIANCE AND POSITION

The solar constant flux density P_{SC} is given as 1366.1 W/m^2 outside the Earth's atmosphere by the American society for testing and materials (ASTM) standard (ASTM E-490) [16]. The solar irradiance is not limited to the visible spectrum as it spans the wavelengths from 250 nm to 2500 nm. The solar irradiance at different wavelengths is non-equally attenuated as it travels through the atmosphere due to the different

absorption and scattering effects of the air molecules and aerosols. The shortest path for the sunlight exists when the Sun is located at the zenith point (imaginary point above the head of the observer). The optical air mass (AM) is approximated as the ratio of the actual sunlight path to the minimum path at the zenith point. It is given as AM0 for the extraterrestrial irradiance. When the Sun is at angle θ_Z relative to the zenith, the optical AM is approximated as:

$$\text{AM} \simeq \frac{1}{\cos\theta_Z}. \tag{1}$$

The solar irradiance at $\theta_Z = 48.2°$ is given at an AM1.5 by the standard (ASTM E-490) [13] as a reference to help the solar energy community in testing and comparing the performance of various solar cells. However, the solar irradiance varies based on the geographical location; seasonal and diurnal variations arising from the rotation of the Earth around the Sun; and the rotation of the Earth around its own axis. The effect of solar irradiance on VLC varies based on the location and time. Therefore, it is essential to calculate the position of the Sun in the sky in order for the solar irradiance at a particular location and time to be estimated. Various algorithms with different complexities and accuracies for calculating the solar position exist in the astrophysics literature [17]. In Appendix A, we review a simple algorithm based on the ecliptic coordinates with an accuracy of $(1/60)°$ presented in [18] and proposed by the astronomical applications department of the U.S. naval observatory [19].

The horizontal coordinate system is usually used for solar energy applications where the horizon of the observer is considered to be the fundamental plane. The solar position can be described using two angles: altitude Al and azimuth Az. The solar altitude $Al \in [0°, 90°]$ is given as the elevation of the Sun above the horizon. A solar altitude of $Al = 90°$

means that the Sun is at the zenith point. The solar altitude can also be given as $Al = 90° - \theta_Z$. The solar azimuth $Az \in [0°, 360°]$ is given as the angle between the north and the horizontal projection of the line-of-sight (LoS) between the Sun and the observer. Both angles are illustrated in Fig. 1(a) and demonstrated in Fig. 1(b and c) for Edinburgh, UK and Antofagasta, Chile on the 20th of each considered month, respectively. The solar altitude is shown to reach the zenith $Al = 90°$ around 13:00 on the 20th of December 2016 for Antofagasta in Fig. 1(c). The time of the day is shown above the analemma diagrams in Fig. 1(b and c), which depict the Sun's motion throughout the year when observed at the same location and the same hour of day.

Direct solar irradiance is the sunlight that is directly reaching the surface of the Earth. Global solar irradiance is the combination of the direct and diffused solar irradiance. The simple model of the atmospheric radiative transfer of sunshine (SMARTS) is a transmittance model to evaluate the direct solar irradiance at any particular location and time [20], [21]. The model is used in generating the ASTM standard (ASTM E-490) with a resolution of 0.5-1 nm [16]. The direct solar irradiance is typically stronger than the signal of interest when the total solar irradiance is taken into account. Fortunately, VLC is realized using mono-chromatic or multi-chromatic optical sources that has fixed and pre-defined spectral irradiance. This allows inexpensive commercially available optical filters to be a practical solution for the degradations caused by solar irradiance. The total predicted solar irradiance is shown in Fig.2(a and b) for Antofagasta and Edinburgh at the noon of December and June solstices, respectively. Monthly comparisons for the total solar irradiance are shown in Fig.2(c). The total spectral irradiance is calculated for the visible spectrum between 400 nm and 760 nm. The blue component of the solar irradiance for the wavelengths between 425 nm and 475 nm shows the importance of optical filtering in improving the VLC communications performance. Optical filtering is also beneficial for other objectives in VLC. White illumination is generally achieved by coating the blue LED with a yellow phosphor which introduces a slow component into the frequency response of the LED. Blue filters are required to eliminate the slow response component of the yellow phosphor. Monochromatic light sources with narrowband spectral distributions can guarantee a robust VLC system against solar irradiance with the potential of achieving data rates in the orders of multiple Gb/s.

III. THEORETICAL STUDY

A. Modelling Assumptions

An OFDM-based VLC system is assumed due to its robustness against background illumination flickering. The OFDM waveform is required to be both unipolar and real valued. Hermitian symmetry is imposed on the M-ary quadrature amplitude modulation (M-QAM) symbols, to enforce the OFDM time domain signal output into the real domain. This can be written as: $X[k] = X^*[N_{FFT} - k]$, where N_{FFT} is the OFDM frame size. The subcarriers $X[0]$ and $X[N_{FFT}/2]$ are both set to zero. A real-valued OFDM waveform with a direct current (DC) bias is used to modulated the intensity of the LED in what is known as DC-biased optical OFDM (DCO-OFDM).

TABLE I
MODELLING ASSUMPTIONS

Locations	Edinburgh, UK, 55°55'20.4"N 3°10'23.3"W
	Antofagasta, Ch, 23°27'16.1"S 70°26'21.4"W
Dates	Every 20th of each considered month
APD model	Hamamatsu S8664-50K
APD detection area, A	19.6 mm^2
Bandwidth, B	60 MHZ
APD gain, M	100
Dark current, I_d	3 nA
Blue filter FWHM	50 nm
Maximum transmitted optical power, P_{Max}^L	8 mW
Transmission distance, d	63.85 cm
Half-power semi-angle of the transmitter, $\Phi_{1/2}$	25°

Binary inputs are encoded into multiple M-QAM symbols which are allocated into N_{FFT} subcarriers over a single-sided bandwidth of B. DC bias is used to shift the negative signal samples into positive values. Three scenarios are considered:

- *Dark room (Scenario I)*: assumes an optimal case where no background illumination is reaching the photoreceiver. This is an ideal scenario as the dominant noise source is the thermal noise.
- *With blue filter (Scenario II)*: assumes that the solar irradiance is collected with a bandpass blue filter in front of the photoreceiver. This is a practical scenario as the useful transmitted signal is passed and any out-of-band signal is filtered. Part of the solar irradiance is passed since it covers a wide wavelength band.
- *Without blue filter (Scenario III)*: assumes a worst case scenario where the solar irradiance is collected without any optical filtering in front of the photoreceiver.

The modeling assumptions are presented in Table I. The system uses a blue micro-LED with a pixel size of $100 \times 100 \ \mu m^2$ and a maximum optical power of 8 mW. Due to the reduced emission area of micro-LEDs, the capacitance decreases and current density increases allowing for higher 3-dB bandwiths compared to off-the-shelf LEDs [22]. The transmission distance is specified at $d = 63.85$ cm to match with the distance that we have used to measure the spectral irradaince of the micro-LED. The system performance is also investigated at longer distances up to 3 meters in Section III-C. A focusing aspheric condenser optical lens (Thorlabs, ACL4532U-A) is used at the transmitter side, which allows for a small half-power semi-angle at the transmitter $\Phi_{1/2} = 25°$. An optical bandpass blue filter from Edmund Optics is assumed in Scenario II with a center wavelength of 450 nm, a transmittance higher than 90% and a full width at half maximum (FWHM) of 50 nm. The photoreceiver is an APD (Hamamatsu, S8664-50K) where it is assumed to be aligned with the micro-LED. APDs operate at high reverse bias to create an amplification effect that allows incident photons to create an avalanche of electrons. APDs are more sensitive to background noise compared to other photodiodes. However, APDs are used as a worst case choice in this investigation as they are shot-noise limited [23]. The APD will not always be collecting the solar irradiance due to the orientation of the communication link in practical situations. However, the APD is always assumed to

be collecting the sunlight in this investigation.

The locations considered are 55°55'20.4"N 3°10'23.3"W in Edinburgh, UK and 23°27'16.1"S 70°26'21.4"W in Antofagasta, Chile. The former location is used to compare with the experimtal results and the latter is claimed to have the highest solar radiation on Earth [24]. The model considers two dates: summer solstice and winter solstice where the solar position is calculated and used in SMARTS [20], [21] to estimate the hourly solar irradiance data. The model assumes a clear sky scenario due to the irregular variations in the local weather conditions which influence the solar irradiance. This allows us to consider the maximum possible solar irradiance in a pessimistic approach. As the considered locations lies in the north and south hemispheres, the summer solstice at Edinburgh would be winter solstice at Antofagasta and similarly the opposite is true.

B. System modeling

The OFDM waveform $x(t)$ is transmitted over the VLC channel $h(t)$, before it is distorted with noise $n(t)$ at the receiver. The received signal $r(t)$ is then sampled at $1/T$ with an analog-to-digital converter (ADC), where T is the sampling perid. Fast Fourier transform (FFT) is then applied on the samples after serial to parallel (S/P) conversion. Assuming that the OFDM frame size is large ($N_{\text{FFT}} > 64$) [25], central limit theorem (CLT) can be applied on the combination of noise generated at the receiver. This can be modeled as zero mean additive white Gaussian noise (AWGN) with variance σ_n^2. The received OFDM waveform $r(t)$ can be given as:

$$r(t) = h(t) * x(t) + n(t). \qquad (2)$$

The average photocurrent generated at the APD due to the average optical power received from sunlight is given as:

$$I_{\text{b}} = A_{\text{d}} \int_{350}^{750} P_{\text{D}}^{\text{S}}(\lambda) R(\lambda) T_{\text{bf}}(\lambda) d\lambda, \qquad (3)$$

where A_{d} is the APD detection area, $P_{\text{D}}^{\text{S}}(\lambda)$ is the direct solar irradiance given in W/m²/nm, $T_{\text{bf}}(\lambda)$ is the transmittance of the bandpass optical filter, $R(\lambda)$ is the intrinsic responsivity of the APD given in A/W and λ is the wavelength considered for the visible light spectrum mainly from 350 nm to 750 nm.

Similarly, the average photocurrent generated at the APD due to the average optical power received from the micro-LED is given as:

$$I_x = \frac{(m+1)A_{\text{d}}}{2\pi d^2} \int_{350}^{750} P_{\text{T}}^{\text{L}}(\lambda) R(\lambda) T_{\text{bf}}(\lambda) d\lambda, \qquad (4)$$

where $m = -1/\log_2(\cos(\Phi_{1/2}))$ is the Lambertian order of the micro-LED; d is the Euclidean distance between the micro-LED and the APD; and $P_{\text{T}}^{\text{L}}(\lambda)$ is the transmitted optical irradiance from the micro-LED, which is given as:

$$P_{\text{T}}^{\text{L}}(\lambda) = P_{\text{Max}}^{\text{L}} \frac{P_{\text{Measured}}^{\text{L}}(\lambda)}{\int_{350}^{750} P_{\text{Measured}}^{\text{L}}(\lambda) d\lambda}, \qquad (5)$$

where $P_{\text{Max}}^{\text{L}}$ is the maximum transmitted optical power of the micro-LED and $P_{\text{Measured}}^{\text{L}}(\lambda)$ is the measured optical irradiance of the micro-LED given in W/m²/nm. This was

measured at a distance of $d = 63.85$ cm using a Labsphere spectral irradiance head (E1000).

The random arrival of incident photons results in shot noise which can be modeled by a Poisson distribution. However, when the number of incident photons increases, the shot noise is approximated by a Gaussian distribution [26]. The shot noise variance is given by [27]:

$$\sigma_s^2 = 2qM^2 F(I_b + I_x)B, \qquad (6)$$

where M is the average gain of the APD, q is the electron charge, B is the bandwidth of the APD and F is the excess noise given as [28]:

$$F = \kappa M + (2 - 1/M)(1 - \kappa), \qquad (7)$$

where κ is the holes/electrons ionization rate. The SNR at subcarrier k can be given by:

$$\gamma_k = \frac{M^2 I_x^2}{\sigma_n^2/|H(k)|^2}, \qquad (8)$$

where $H(k)$ is the frequency domain realization of the VLC channel, $\sigma_n^2 = \sigma_s^2 + \sigma_t^2 + \sigma_d^2$ and σ_d^2 is the variance of the dark noise which is given as [27]:

$$\sigma_d^2 = 2qM^2 F I_{dg}B + 2qI_{ds}B, \qquad (9)$$

where I_{ds} is the surface dark current and I_{dg} is the bulk dark current that experience the avalanche effect of the APD and where $I_{\text{d}} = I_{ds} + MI_{dg}$. The variance of the thermal noise σ_T^2 is given by [29]:

$$\sigma_T^2 = 4\left(\frac{K_B T}{R_L}\right) F_n B, \qquad (10)$$

where K_B is Boltzmann constant, T is the temperature in Kelvin, R_L is the load resistance given as 50 Ω and F_n is the photodiode noise figure.

Adaptive bit and energy loading algorithms such as the Levin-Campello algorithm [30] can be used to maximize the data rate by assigning larger constellation sizes on the subcarriers that have higher SNR. The maximum theoretical limit to the data rate of DCO-OFDM can be calculated using the channel capacity defined by Shannon-Hartley theorem [31]
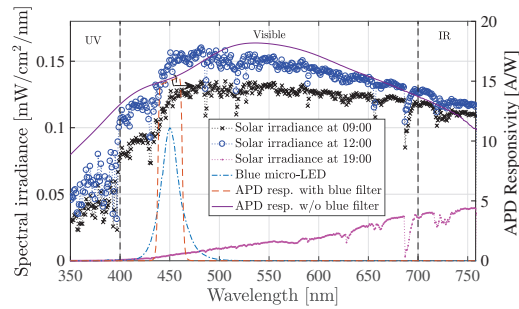
Fig. 3. The predicted solar irradiance in Antofagasta at 9 AM, 12 PM and 19 PM (local time) of the 20th on December 2016 (left), alongside the spectral irradiance of the modeled micro-LED centred at 450 nm (left) and response of the APD with and without considering the transmittance of the blue filter (right).
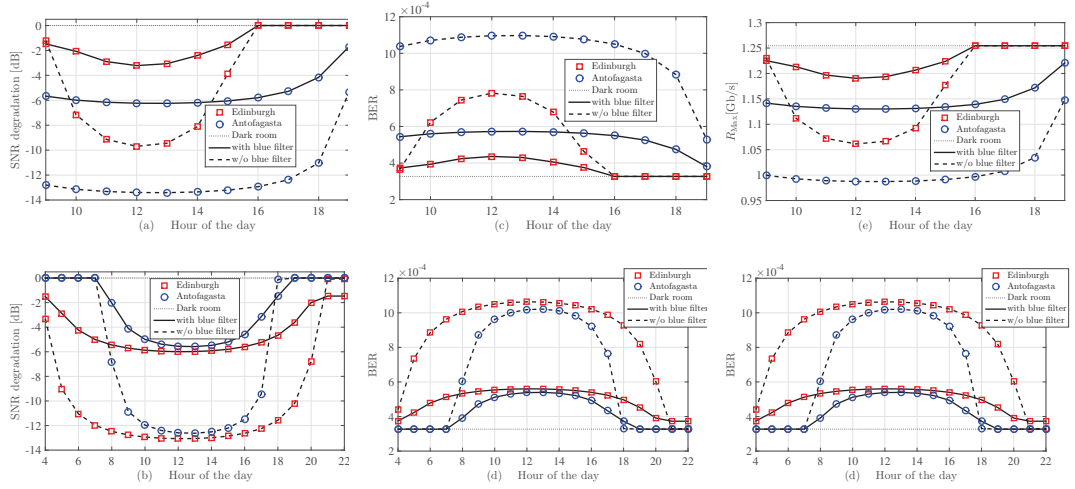
Fig. 4. (a and b) SNR; (c and d) BER; (e and f) maximum theoretical limit to the data rate. All results are presented for the three considered scenarios in Antofagasta and Edinburgh versus time at the 20th of December 2016 (a, c, e) and 20th of June 2016 (b, d, f).

when negecting the DC bias and the optical source nonlinearity [32]. This is given as:

$$R_{\text{Max}} = B \sum_{\substack{k=1 \\ M'_k>0}}^{N_{\text{FFT}}/2-1} \log_2 \left(1 + \gamma_k\right), \qquad (11)$$

where M'_k is the constellation order of M'_k-QAM used at subcarrier k.

The system performance in terms of BER can be calculated using the theoretical BER of real-valued OFDM given for frequency selective channels [33]. The BER at subcarrier k can be given as:

$$\text{BER}(M'_k, \gamma_k) \cong \frac{4}{\log_2(M'_k)} \left(1 - \frac{1}{\sqrt{M'_k}}\right) \times \\ \sum_{l=1}^{R} \text{Q}\left((2l-1)\sqrt{\frac{3\gamma_k}{2(M'_k-1)}}\right), \quad (12)$$

where $Q(.)$ is the complementary cumulative distribution function (CCDF) for the standard normal distribution and $R = \min(2, \sqrt{M'_k})$. The overall system BER can be given as:

$$\text{BER} = \frac{\displaystyle\sum_{\substack{k=1 \\ M'_k>0}}^{N_{\text{FFT}}/2-1} \text{BER}(M'_k, \gamma_k) \log_2(M'_k)}{\displaystyle\sum_{\substack{k=1 \\ M'_k>0}}^{N_{\text{FFT}}/2-1} \log_2(M'_k)} \qquad (13)$$

C. Results and Discussions

The spectral irradiance of the micro-LED and the amplified responsivity of the APD $MR(\lambda)$ are shown in Fig. 3 with the presence and absence of the optical bandpass blue filter. In addition, the predicted spectral irradiance of the sunlight at

Antofagasta is shown at three different times of the summer solstice. It is shown that the solar irradiance is high at the ultra-violet (UV) and blue spectrum bands at sunrise. At sunset it becomes higher at the red and infra-red (IR) spectrum bands. The blue filter captures 70% of the micro-LED irradiance.

The system performance is presented in Fig. 4(a and b) as a function of the SNR degradation against the time of the day for both December and June solstice, respectively. The degradation is calculated with reference to the benchmark case of the dark room in Scenario I. It is shown that the SNR degrades by a maximum of -13.4 dB and -9.69 dB at the noon of December solstice in Scenario III at Antofagasta and Edinburgh, respectively. However, when a blue filter is used in font of the APD, this degradation is reduced to -6.23 dB and -3.214 dB in Scenario II at Antofagasta and Edinburgh, respectively. The high degradation in SNR at Antofagasta is expected due to the higher solar irradiance in December solstice in comparison with Edinburgh as shown in Fig.2(a). The SNR degradations at Edinburgh for June solstice increase in comparison with December solstice by a maximum increase of 3.38 dB. The SNR degradation is 0.8 dB lower for June solstice compared with December solstice at Antofagasta. A minimum of 6.47 dB improvement in SNR is achieved when blue filters are used in Scenario II. The SNR degradation at Edinburgh are witnessed for longer hours during June solstice due to the longer daylight that is shown in Fig .1(b). The SNR degradation at Antofagasta and Edinburgh at the 20th day of the noon of the last six months of 2016 is presented in Fig. 5(a). The degradation decreases noticeably as we approach December solstice at Edinburgh, while SNR degradation variations are less noticeable for Antofagasta.

The system performance as a function of the BER against the time of the day is shown in Fig.4(c and d) for 128-QAM DCO-OFDM at December and June solstices, respectively. The results show the SNR degradation effect on the BER performance for the OFDM-based VLC system. Both sce-

(a) SNR

(b) Maximum theoretical limit on data rate
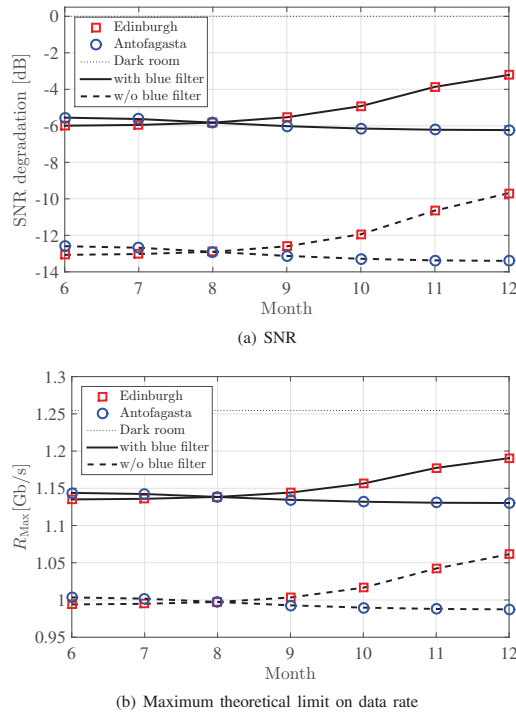
Fig. 5. The system performance presented on monthly basis at the noon of each 20th day of the considered months for the three considered scenarios in Antofagasta and Edinburgh. (a) SNR and (b) Maximum theoretical limit on data rate.

(a) SNR

(b) Maximum theoretical limit on data rate
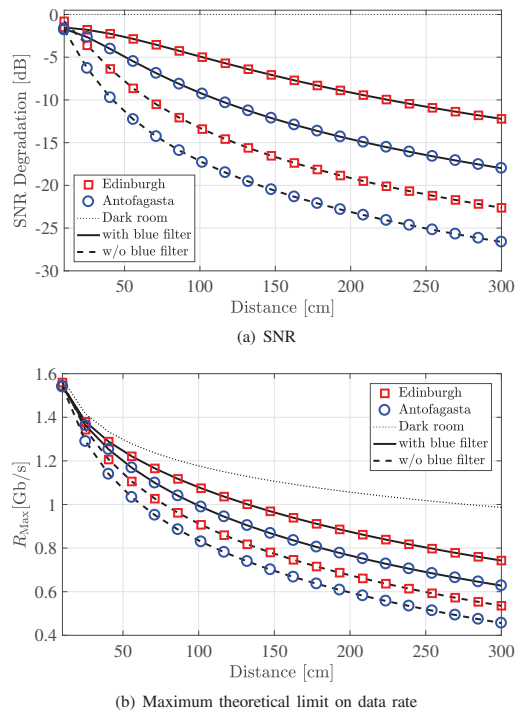
Fig. 6. System performance versus transmission distance d at the noon of the 20th of December 2016 for the three considered scenarios in Antofagasta and Edinburgh. (a) SNR and (b) Maximum theoretical limit on data rate.

nario II and scenario III at Antofagasta and Edinburgh are shown to allow the use of forward error correction (FEC) in both December and June solstice, although a significant improvement is shown to be achieved when the blue filter is used. The system performance is investigated as a function of the maximum theoretical limit to the data rate versus the time of the day in Fig. 4(e and f) for December and June solstices, respectively. The performance of Scenario II and the performance of Scenario III are compared to the benchmark performance recorded at 1.25 Gb/s of Scenario I for Antofagasta and Edinburgh. It is shown that the data rate degrades by 21.35% and by 15.49% at the noon of December solstice when the blue filter is not used in Antofagasta and Edinburgh, respectively. However, this degradation is reduced to 10% and 5.22% for Scenario II at Antofagasta and Edinburgh, respectively. This is equivalent to a significant 53.16% and 66.30% improvement that is achieved by placing a blue filter in front of the APD. A maximum theoretical limit to the data rate for June solstice under the solar irradiance is estimated at 1.03 Gb/s and 0.99 Gb/s for Scenario III at Antofagasta and Edinburgh, respectively and at 1.14 Gb/s and 1.13 Gb/s for Scenario II at Antofagasta and Edinburgh, respectively. A comparison of the maximum data rate performance at both Antofagasta and Edinburgh at noons of the last six months of 2016 is presented in Fig. 5(b). The variations in data rates are more noticeable for Edinburgh, where it increases to reach

a maximum of 1.19 Gb/s for Scenario II and 1.06 Gb/s for Scenario III in December.

The SNR degradation and the maximum theoretical limit on the data rate are given in Fig. 6(a and b) as functions of the transmission distance. The results in Fig. 6 are presented for the three considered scenarios at Antofagasta and Edinburgh at noon of the 20th of December 2016. The SNR degrades as the transmission distance increases in all considered scenarios, including the dark room scenario I, as expected. However, the SNR degradation for Scenario II and III are calculated with reference to the dark room in scenario I to highlight the solar irradiance effect in comparison with the benchmark Scenario I. It is shown that the SNR degradation reaches -26.61 dB and -22.63 dB when the blue filter is not used in Scenario III at a transmission distance of 3 meters at Antofagasta and Edinburgh, respectively. Although the SNR degradation appears to be high, the SNR gain of using the blue filter in Scenario II reaches 8.6 dB and 10.41 dB at a transmission distance of 3 meters for Antofagasta and Edinburgh, respectively. Similarly, the maximum theoretical limit on the data rate is shown to decrease as the transmission distance increases. The maximum theoretical limit on the data rate at a transmission distance of 3 meters for the dark room in Scenario I is 986.3 Mb/s. This is degraded by 53.74% for Antofagasta and 45.71% for Edinburgh in Scenario III. However, it is shown that the degradation is reduced to 36.33%

(a) Schematic
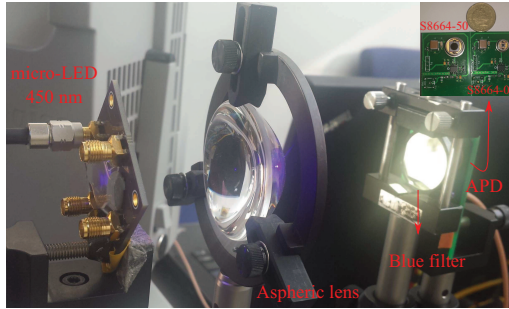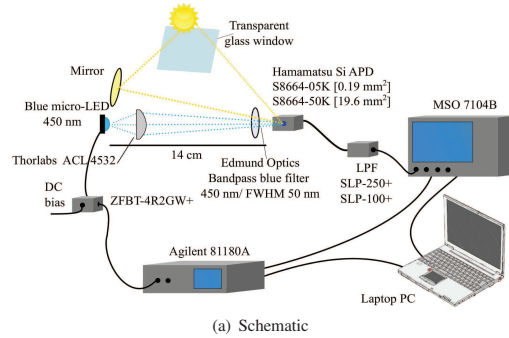
(b) Photograph

Fig. 7. The experimental set-up. (a) Schematic set-up of the experiment showing the optical system, arbitrary waveform function generator, oscilloscope, electrical and optical filters and Bias-T. (b) Photograph of the optical system showing the micro-LED, optical lenses system and the used APDs. In the top right corner (left): large APD s8664-50k; (right): small APD S8664-05k

and 24.7% in Antofagasta and Edinburgh when the blue filter is used in Scenario II. Despite the degradation in SNR, high-speed VLC can still be available at sufficiently long distances.

IV. EXPERIMENTAL STUDY

A. Experimental Set-up

The measurements were conducted between 11:00-17:00 (local time) of the 6th and 9th of June 2016 under clear sky weather conditions demonstrated by very good visibility estimated above 21 km and a solar illuminance measured at 50350 lux. The measurements were carried at 55°55'20.4"N 3°10'23.3"W in Edinburgh, UK. The experimental setup is shown in Fig. 7(a-b). The system elements used in the experiment are the same components described in Section III-A. The OFDM modulation waveform is generated and processed off-line using MATLAB®. The OFDM digital waveform is converted into an analog waveform using the arbitrary waveform generator Agilent 81180A, which sends the bipolar OFDM waveform to the micro-LED using a Bias-Tee ZFBT-4R2GW. The DC bias is selected after exhaustive tests at $V_{DC} = 4.1$ Volts to minimize the clipping distortion. The optical power of the micro-LED is 4.5 mW and the 3-dB bandwidth is 30 MHz, both measured at DC current $I_{DC} = 50$ mA. An aspheric collimation lens ACL 4532 is used to focus the light on the photoreceiver. Two Silicon APDs are used in this experiment
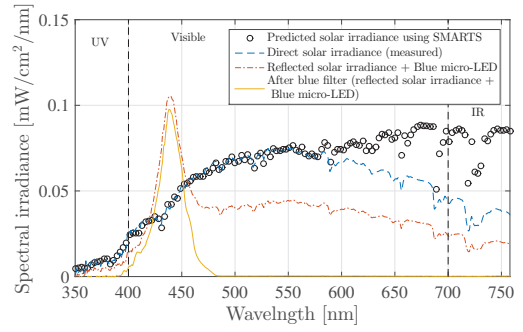
Fig. 8. The spectral distribution of the solar irradiance measured and predicted using SMARTS [20], [21] for Edinburgh (direct, reflected and filtered) in the presence and absence of the desired signal at 450 nm.

(Hamamatsu, S8664-05k) and (Hamamatsu, S8664-50k), as shown in the top-right corner of Fig. 7(b). These APDs are referred to as "small" APD and "large" APD, respectively. The small APD has a smaller active area of 0.19 mm² and therefore, has a lower capacitance that leads to a higher 3-dB bandwidth of 680 MHz. The large APD has a larger active area of 19.6 mm² that leads to a higher capacitance and lower 3-dB bandwidth of 60 MHz.

The received signal at the APDs is filtered using a low pass electrical filter (Mini-circuits, SLP-100+) with a cut-off of 98 MHz for the large APD; and (Mini-circuits, SLP-250+) with a cut-off of 225 MHz for the small APD. Both filters are shown in Fig. 7(a). The system modulation bandwidth is used at 100 MHz and 250 MHz for the large and small APDs, respectively. This is experimentally determined as the maximum bandwidth that allows for a SNR higher than 0 dB to be achieved. The electrical signal is then captured using an oscilloscope (Agilent, MSO7104B) and then processed using MATLAB®. The overall distance between the micro-LED and the photodetector is 14 cm. The received optical power from the micro-LED would decrease at longer distances and consequently this would degrade the SNR because the SNR diminishes as the desired signal diminishes, but not because of noise due to sunlight. The distance is limited by the optical power of the micro-LED and it can be improved using more advanced collimation optics or using micro-LEDs with multiple pixels in a ganging mode [22]. The three scenarios described in Section III-A are considered in the experimental study. The SNR of the channel is first estimated and then the constellation sizes and the associated power of M-QAM symbols are adaptively allocated to each subcarrier based on the estimated SNR. The adaptive bit and energy loading algorithm avoids the use of low-frequency subcarriers, where the interference of ambient light can be strong. In addition, it avoids any other subcarrier, where the SNR is expected to result in a BER below the FEC target.

B. Results and Discussions

The measured solar irradiance is given in Fig. 8 for the wavelengths between 350 and 750 nm covering the visible spectrum and part of the infrared and ultraviolet spectra. Four

TABLE II
ACHIEVABLE SNR VALUES AND DATA RATES FOR THE SMALL AND LARGE APDS FOR THE THREE CONSIDERED SCENARIOS.

	Dark room (Scenario I)		with blue filter (Scenario II)		w/o blue filter (Scenario III)	
	Large APD	Small APD	Large APD	Small APD	Large APD	Small APD
Average SNR [dB]	17.57	18.58	16.64	17.36	12.42	16.42
Data rate @ BER<3.8e-3 [Mb/s]	416.44	1139.26	396.71	1080	313.35	1015
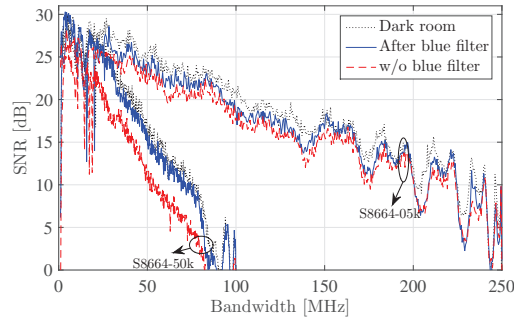
Fig. 9. Experimentally estimated SNR versus the system bandwidth when small and large APDs are used for the three considered scenarios.

cases are presented: direct sunlight; reflected sunlight from a mirror, reflected sunlight and blue micro-LED (Scenario III); and reflected sunlight and blue micro-LED with a blue optical filter (Scenario II). The experiment was conducted inside a building where the direct sunlight is passed through a transparent glass window before it is collected at the photoreceiver. It was practically infeasible to realize the experimental setup while the direct solar irradiance is always focused into the APD due to the varying solar position throughout the experiment duration. A mirror was used to work around this issue at the expense of reduced solar irradiance. This was shown to have little impact on the blue band below 450 nm as it is shown in Fig. 8. The experimentally measured direct solar irradiance is shown to be identical to the simulated solar irradiance below 580 nm. The mismatch at longer wavelengths is attributed to the high reflectance and less transmittance characteristics of heat mirrors glazing in the infrared band that aim to improve building heat insulation [34].

The experimentally estimated SNR is presented in Fig. 9 for the small and large APDs at all the considered scenarios. All the performance comparisons are presented with reference to the the optimal dark room (Scenario I). It is shown that the performance of the VLC system degrades in the presence of direct sunlight for both APDs. The degradation in the average SNR is estimated at 2.16 dB for the small APD and 5.15 dB for the large APD in Scenario III. The photocurrents generated by both signal and background noise generally increase as the detection area of the APD increases. However, an optical source with small emission area and an imaging lens are used in this experiment to focus the light into the APD. The focused light spot size at the APD can ideally be as small as the emission area of the micro-LED (0.01 mm^2) [35]. Therefore, The signal photocurrent does not increase when the detection area becomes larger than the focused light spot at the APD. This validates the result that the SNR degradation is higher

for the large APD, because it collects more background light. When the blue filter is used to restrict the unwanted irradiance, the degradation in the average SNR is reduced to 1.22 dB for the small APD and 0.93 dB for the large APD. Similar trends are presented in Table II for the achieved data rates. All the presented data rates are achieved below the FEC limit of 3.8×10^{-3}. The data rate decreases in the presence of solar irradiance. However, most of this reduction can be recovered using the blue filter. It is shown that a data rate of 1.015 Gb/s can be achieved under the presence of solar irradiance for the small APD in Scenario III. This is equivalent to a 10.4% reduction in data rate compared to Scenario I. This degradation can be reduced to 5.2% when the blue filter is used. A reduction of 24.75% in the data rates is witnessed in Scenario II for the large APD. This is improved to 4.73% when using the blue filter in Scenario II.

V. CONCLUSION

VLC system is feasible in the presence of solar irradiance. Worst-case scenarios are considered in this study to prove the concept that VLC systems can work under the influence of strong solar irradiance. Shot noise caused by sunlight reduces the data rate of VLC systems. However, optical bandpass blue filters can limit the degradation caused by solar irradiance. Data rates above 1 Gb/s were experimentally achieved in the presence of solar irradiance without optical filtering. Simulation results have shown that an improvement of at least 6.47 dB can be achieved for SNR using off-the-shelf blue filters.

Saturation is a major drawback for photodiodes in the presence of strong background noise. Automatic gain controller (AGC) can be used to reduce the likelihood of performance outage due to APD saturation. However, this is not considered in the current work and will be considered in future research. Bandpass optical filtering was considered as a technique to mitigate solar irradiance noise. However, the results of this study can be used to build upon and to develop new solar irradiance noise mitigation techniques. An interesting solution could be envisaged to use angle-diversity receiver with signal combining techniques. However, the details of such investigation is out the scope of this paper and will be considered in future research.

APPENDIX A
SOLAR POSITION

Three coordinate systems are used to calculate the position of the Sun: ecliptic coordinates; equatorial coordinates; and horizontal coordinates. These coordinate systems can be illustrated on the celestial sphere shown in Fig. 10. The parameters corresponding to each coordinate system are mapped in Table III. The arbitrary coordinates in Fig. 10 is defined by Θ which is the angle between the principle and the projection of the Sun at the fundamental plane and by Ξ which is the
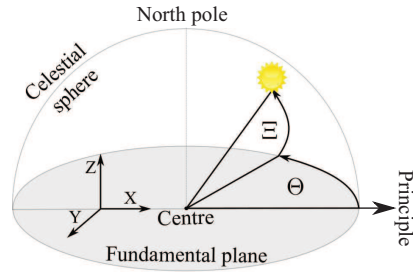
Fig. 10. An illustration of an arbitrary coordinate system on a celestial sphere.

TABLE III
COORDINATION SYSTEMS CORRESPONDING PARAMETERS

Arbitrary	Ecliptic	Equatorial	Horizontal
center	center of the Earth	center of the Earth	observer
north pole	north ecliptic pole	north celestial pole	zenith
fundamental plane	ecliptic	celestial equator	horizon
principle	March equinox	March equinox	geographic north pole
Θ	ecliptic longitude (λ)	right ascension (α)	azimuth (Az)
Ξ	ecliptic latitude (β)	declination (δ)	altitude (Al)
$\begin{pmatrix} X \\ Y \\ Z \end{pmatrix}$	$\begin{pmatrix} X_{\mathrm{Ecl}} \\ Y_{\mathrm{Ecl}} \\ Z_{\mathrm{Ecl}} \end{pmatrix}$	$\begin{pmatrix} X_{\mathrm{Equ}} \\ Y_{\mathrm{Equ}} \\ Z_{\mathrm{Equ}} \end{pmatrix}$	$\begin{pmatrix} X_{\mathrm{Hor}} \\ Y_{\mathrm{Hor}} \\ Z_{\mathrm{Hor}} \end{pmatrix}$

angle between the Sun and the fundamental plane. Celestial coordinate systems can be converted into Cartesian coordinates using:

$$\begin{pmatrix} X \\ Y \\ Z \end{pmatrix} = \begin{pmatrix} \cos \Xi \cos \Theta \\ \cos \Xi \sin \Theta \\ \sin \Xi \end{pmatrix}. \quad (14)$$

The horizontal coordinate system is usually used for solar cell applications where the horizon of the observer is the fundamental plane. The solar position can be projected on a celestial sphere using two angles: altitude Al and azimuth Az. The Earth revolves around the Sun in an elliptic orbit in which a complete revolution takes a year, a motion of around $1°$ per day. This motion can be best described using the ecliptic coordinates where the principle is the position of the Sun during the spring equinox (the date of the year when the Earth's equator is alligned with the center of the Sun ecliptic). The angular ecliptic coordinates are the ecliptic longitude, λ and ecliptic latitude, β, which is given as $\beta \approx 0$ [18]. The ecliptic longitude can be given as [18]:

$$\lambda = q + 1.915° \sin g + 0.020° \sin 2g, \quad (15)$$

where q is the mean longitude given as [18]:

$$q = 280.459° + 0.98564736°D, \quad (16)$$

and g is the mean anomaly of the Sun, which accounts for the varying speeds of the Earth motion throughout the year. This is given as [18]:

$$g = 357.529° + 0.98560028°D, \quad (17)$$

where D is the time elapsed since the Greenwich noon of the 1st of January 2000.

The equatorial coordinate system is required as a translational stage when transforming the ecliptic coordinates into horizontal coordinates, as follows:

$$\begin{pmatrix} X_{\mathrm{Equ}} \\ Y_{\mathrm{Equ}} \\ Z_{\mathrm{Equ}} \end{pmatrix} = \begin{pmatrix} 1 & 0 & 0 \\ 0 & \cos \epsilon & -\sin \epsilon \\ 0 & \sin \epsilon & \cos \epsilon \end{pmatrix} \begin{pmatrix} X_{\mathrm{Ecl}} \\ Y_{\mathrm{Ecl}} \\ Z_{\mathrm{Ecl}} \end{pmatrix}, \quad (18)$$

where ϵ is the axial tilt between the equatorial plane and the ecliptic plane. The axial tilt is zero in March and September equinox and takes its maximum value of $\pm 23.429°$ in June and December solstices (the days when the maximum tilt is experinced at the north and south hemisphere, respectively). The axial tilt is given as [18]:

$$\epsilon = 23.429° - 0.00000036°D. \quad (19)$$

The equatorial coordinates are given by the right ascension α which is the angle between the March equinox and the projection of the Sun on the Earth's equator and by the declination δ which is the angle between the Sun and the Earth equator. The Sun moves $15°$ of longitude per hour. The hour angle is defined as the angle between the projection of the Sun on the fundamental plane and the meridian given at longitude of $0°$ (an imaginary circle passing through the north and south poles and the zenith of an observer). The hour angle is given by:

$$h = \theta_L - \alpha, \quad (20)$$

where θ_L is the angle between the meridian and the March equinox. It can also be defined as the local mean sidereal time (LMST). A sidereal day is the time that the Earth takes to complete a $360°$ rotation on its own axis. It is slightly shorter than the solar day mainly due to the rotation of the Earth around the Sun. The LMST can be given as:

$$\theta_L = \mathrm{GMST} \frac{15°}{\mathrm{hour}} + \lambda_0, \quad (21)$$

where λ_0 is the longitude of the observer and GMST is the Greenwich mean sidereal time (GMST), which is defined as the hour angle between the March equinox and the meridian at Greenwich. GMST is calculated as [18]:

$$\mathrm{GMST} = 18.697374558\mathrm{h} + 24.06570982441908\mathrm{h}D, \quad (22)$$

where it is scaled to values between 0 and 24.

The principle of the coordinates can be transformed from the March equinox to the LMST using:

$$\begin{pmatrix} \cos \delta \cos h \\ \cos \delta \sin h \\ \sin \delta \end{pmatrix} = \begin{pmatrix} \cos \theta_L & \sin \theta_L & 0 \\ \sin \theta_L & -\cos \theta_L & 0 \\ 0 & 0 & 1 \end{pmatrix} \begin{pmatrix} X_{\mathrm{Equ}} \\ Y_{\mathrm{Equ}} \\ Z_{\mathrm{Equ}} \end{pmatrix}, \quad (23)$$

In addition, the center of the coordinates can be transformed from the center of the Earth to the position of the observer using:

$$\begin{pmatrix} X'_{\mathrm{Hor}} \\ Y'_{\mathrm{Hor}} \\ Z'_{\mathrm{Hor}} \end{pmatrix} = \begin{pmatrix} \sin \phi_0 & 0 & -\cos \phi_0 \\ 0 & 1 & 0 \\ \cos \phi_0 & 0 & \sin \phi_0 \end{pmatrix} \begin{pmatrix} \cos \delta \cos h \\ \cos \delta \sin h \\ \sin \delta \end{pmatrix} \quad (24)$$

Following the prior calculations, the directions of X'_{Hor} and Y'_{Hor} are directed towards south and west, respectively. The

following can be applied to adjust the reference direction to north and east [18]:

$$\begin{pmatrix} X_{\text{Hor}} \\ Y_{\text{Hor}} \\ Z_{\text{Hor}} \end{pmatrix} = \begin{pmatrix} -1 & 0 & 0 \\ 0 & -1 & 0 \\ 0 & 0 & 1 \end{pmatrix} \begin{pmatrix} X'_{\text{Hor}} \\ Y'_{\text{Hor}} \\ Z'_{\text{Hor}} \end{pmatrix} \quad (25)$$

The horizontal coordinates can then be calculated using [18]:

$$\sin Al = \cos\phi_0 \cos\theta_L \cos\lambda_{\text{S}} +$$
$$(\cos\phi_0 \sin\theta_L \cos\epsilon + \sin\phi_0 \sin\epsilon)\sin\lambda_{\text{S}} \quad (26)$$

$$\tan Az = \frac{\Gamma_1}{\Gamma_2 - \Gamma_3}, \quad (27)$$

where:

$$\Gamma_1 = -\sin\theta_L \cos\lambda_{\text{S}} + \cos\theta_L \cos\epsilon \sin\lambda_{\text{S}}, \quad (28)$$
$$\Gamma_2 = -\sin\phi_0 \cos\theta_L \cos\lambda_{\text{S}}, \quad (29)$$
$$\Gamma_3 = \sin\lambda_{\text{S}}(\sin\phi_0 \sin\theta_L \cos\epsilon - \cos\phi_0 \sin\epsilon), \quad (30)$$

REFERENCES

[1] Cisco Visual Networking Index, "Global Mobile Data Traffic Forecast Update, 2015-2020," CISCO, White Paper, Feb. 2016. [Online]. Available: http://www.cisco.com/c/en/us/solutions/collateral/service-provider/visual-networking-index-vni/mobile-white-paper-c11-520862.pdf

[2] OFCOM report, "Award of the 2.3 and 3.4 GHz Spectrum Bands: Competition Issues and Auction Regulations," OFCOM, Consultation , Jan. 2017. [Online]. Available: https://www.ofcom.org.uk/__data/assets/pdf_file/0026/93545/award-of-the-spectrum-bands-consultation.pdf

[3] S. Dimitrov and H. Haas, *Principles of LED Light Communications: Towards Networked Li-Fi*. Cambridge University Press, 2015.

[4] M. S. Islim, R. X. Ferreira, X. He, E. Xie, S. Videv, S. Viola, S. Watson, N. Bamiedakis, R. V. Penty, I. H. White, A. E. Kelly, E. Gu, H. Haas, and M. D. Dawson, "Towards 10 Gb/s Orthogonal Frequency Division Multiplexing-based Visible Light Communication Using a GaN Violet Micro-LED," *Photon. Res.*, vol. 5, no. 2, pp. A35–A43, Apr 2017. [Online]. Available: http://www.osapublishing.org/prj/abstract.cfm?URI=prj-5-2-A35

[5] D. Tsonev, S. Videv, and H. Haas, "Towards a 100 Gb/s Visible Light Wireless Access Network," *Opt. Express*, vol. 23, no. 2, pp. 1627–1637, Jan 2015. [Online]. Available: http://www.opticsexpress.org/abstract.cfm?URI=oe-23-2-1627

[6] G. Povey, "Top 10 Li-Fi Myths," June 2012. [Online]. Available: http://visiblelightcomm.com/top-10-li-fi-myths/

[7] M. S. Islim and H. Haas, "Modulation Techniques for Li-Fi," *ZTE Communications*, vol. 14, no. 2, pp. 29–40, April 2016.

[8] Y. H. Chung and S. B. Oh, "Efficient Optical Filtering for Outdoor Visible Light Communications in the Presence of Sunlight or Articifical Light," in *Intelligent Signal Processing and Communications Systems (ISPACS), 2013 International Symposium on*, Nov 2013, pp. 749–752.

[9] T. Hamza, M.-A. Khalighi, S. Bourennane, P. Léon, and J. Opderbecke, "Investigation of Solar Noise Impact on the Performance of Underwater Wireless Optical Communication Links," *Opt. Express*, vol. 24, no. 22, pp. 25 832–25 845, Oct 2016. [Online]. Available: http://www.opticsexpress.org/abstract.cfm?URI=oe-24-22-25832

[10] M. Beshr, C. Michie, and I. Andonovic, "Evaluation of Visible Light Communication system performance in the presence of sunlight irradiance," in *2015 17th International Conference on Transparent Optical Networks (ICTON)*, July 2015, pp. 1–4.

[11] Y.-h. C. Yong-hyeon Kim, "Experimental Outdoor Visible Light Data Communication System using Differential Decision Threshold with Optical and Color Filters," *Optical Engineering*, vol. 54, pp. 54 – 54 – 3, 2015. [Online]. Available: http://dx.doi.org/10.1117/1.OE.54.4.040501

[12] D. R. Kim, S. H. Yang, H. S. Kim, Y. H. Son, and S. K. Han, "Outdoor Visible Light Communication for inter-vehicle Communication using Controller Area Network," in *2012 Fourth International Conference on Communications and Electronics (ICCE)*, Aug 2012, pp. 31–34.

[13] ASTM, *Standard Tables for Reference Solar Spectral Irradiances: Direct Normal and Hemispherical on 37 Tilted Surface*, ASTM G173-03 Std., 2014. [Online]. Available: https://doi.org/10.1520/G0173-03R12

[14] M. Islim and H. Haas, "An Investigation of the Sunlight Irradiance Effect on Visible Light Communications," Oct., 8–13 2017, accepted for Publication in *Proc. of the 27th Int. Symp. Pers. Indoor and Mobile Radio Commun. (PIMRC)*, (Montereal, Canada).

[15] G. Cossu, R. Corsini, A. M. Khalid, S. Balestrino, A. Coppelli, A. Caiti, and E. Ciaramella, "Experimental Demonstration of High Speed Underwater Visible Light Communications," in *2013 2nd International Workshop on Optical Wireless Communications (IWOW)*, Oct 2013, pp. 11–15.

[16] ASTM, *Standard Solar Constant and Zero Air Mass Solar Spectral Irradiance Tables*, ASTM-E490-00a Std., 2014. [Online]. Available: https://doi.org/10.1520/E0490

[17] W. B. Stine and M. Geyer, *Power from the Sun*, 2001. [Online]. Available: http://Powerfromthesun.net

[18] A. Smets, K. Jäger, O. Isabella, M. Zeman, and R. van Swaaij, *Solar Energy: The Physics and Engineering of Photovoltaic Conversion, Technologies and Systems*. UIT Cambridge, 2016. [Online]. Available: https://books.google.co.uk/books?id=vTkdjgEACAAJ

[19] I. Reda and A. Andreas, "Solar Position Algorithm for Solar Radiation Applications," *Solar energy*, vol. 76, no. 5, pp. 577–589, 2004.

[20] C. A. Gueymard, "Parameterized Transmittance Model for Direct Beam and Circumsolar Spectral Irradiance," *Solar Energy*, vol. 71, no. 5, pp. 325–346, 2001.

[21] C. Gueymard, *SMARTS2: a Simple Model of the Atmospheric Radiative Transfer of Sunshine: Algorithms and Performance Assessment*. Florida Solar Energy Center Cocoa, FL, 1995.

[22] S. Rajbhandari, J. J. D. McKendry, J. Herrnsdorf, H. Chun, G. Faulkner, H. Haas, I. M. Watson, D. O'Brien, and M. D. Dawson, "A Review of Gallium Nitride LEDs for Multi-Gigabit-per-second Visible Light Data Communications," *Semiconductor Science and Technology*, vol. 32, no. 2, p. 023001, 2017. [Online]. Available: http://stacks.iop.org/0268-1242/32/i=2/a=023001

[23] F. Xu, M. A. Khalighi, and S. Bourennane, "Impact of Different Noise Sources on the Performance of PIN- and APD-based FSO Receivers," in *Proceedings of the 11th International Conference on Telecommunications*, June 2011, pp. 211–218.

[24] R. Rondanelli, A. Molina, and M. Falvey, "The Atacama Surface Solar Maximum," *Bulletin of the American Meteorological Society*, vol. 96, no. 3, pp. 405–418, 2015. [Online]. Available: https://doi.org/10.1175/BAMS-D-13-00175.1

[25] S. Dimitrov, S. Sinanovic, and H. Haas, "Signal Shaping and Modulation for Optical Wireless Communication," *Lightwave Technology, Journal of*, vol. 30, no. 9, pp. 1319–1328, May 2012.

[26] F. M. Davidson and X. Sun, "Gaussian Approximation Versus Nearly Exact Performance Analysis of Optical Communication Systems with PPM Signaling and APD Receivers," *IEEE Transactions on Communications*, vol. 36, no. 11, pp. 1185–1192, Nov 1988.

[27] Hamamatsu Photonics K.K, "Characteristics and Use of SI-APD (avalanche photodiode)," May 2004. [Online]. Available: http://neutron.physics.ucsb.edu/docs/Characteristics_and_use_of_SI_APD.pdf

[28] G. Keiser, *Optical Communications Essentials*. McGraw-Hill, 2003.

[29] J. M. Kahn and J. R. Barry, "Wireless Infrared Communications," *Proc. IEEE*, vol. 85, no. 2, pp. 265–298, Feb. 1997.

[30] H. E. Levin, "A Complete and Optimal Data Allocation Method for Practical Discrete Multitone Systems," in *Proc. IEEE Global Telecommun. Conf.*, vol. 1, San Antonio, TX , USA, 25–29 Nov. 2001, pp. 369–374.

[31] C. Shannon, "A Mathematical Theory of Communication," *Bell System Technical Journal*, vol. 27, pp. 379–423 & 623–656, Jul. & Oct. 1948.

[32] S. Dimitrov and H. Haas, "Information Rate of OFDM-Based Optical Wireless Communication Systems With Nonlinear Distortion," *IEEE J. Lightw. Technol.*, vol. 31, no. 6, pp. 918–929, Mar. 2013.

[33] F. Xiong, *Digital Modulation Techniques*, 2nd ed. Artech House Publishers, 2006.

[34] C. M. Lampert, "Heat Mirror Coatings for Energy Conserving Windows," *Solar Energy Materials*, vol. 6, no. 1, pp. 1 – 41, 1981. [Online]. Available: http://www.sciencedirect.com/science/article/pii/0165163381900472

[35] E. Diaz and M. Knobl, "Prototyping Illumination Systems with Stock Optical Components," Photonik International, 2012.

1□

Modulation Techniques for Li-Fi

Mohamed Sufyan Islim and Harald Haas

（Li-Fi Research and Development Centre, Institute for Digital Communications，University of Edinburgh, Edinburgh EH9 3JL, UK）

Abstract:

Modulation techniques for light fidelity (Li-Fi) are reviewed in this paper. Li-Fi is the fully networked solution for multiple users that combines communication and illumination simultaneously. Light emitting diodes (LEDs) are used in Li-Fi as visible light transmitters, therefore, only intensity modulated direct detected modulation techniques can be achieved. Single carrier modulation techniques are straightforward to be used in Li-Fi, however, computationally complex equalization processes are required in frequency selective Li-Fi channels. On the other hand, multicarrier modulation techniques offer a viable solution for Li-Fi in terms of power, spectral and computational efficiency. In particular, orthogonal frequency division multiplexing (OFDM) based modulation techniques offer a practical solution for Li-Fi, especially when direct current (DC) wander, and adaptive bit and power loading techniques are considered. Li-Fi modulation techniques need to also satisfy illumination requirements. Flickering avoidance and dimming control are considered in the variant modulation techniques presented. This paper surveys the suitable modulation techniques for Li-Fi including those which explore time, frequency and colour domains.

Keywords: light fidelity (Li-Fi); optical wireless communications (OWC); visible light communication (VLC); intensity modulation and direct detection (IM/DD); orthogonal frequency division multiplexing (OFDM)

1 Introduction

More than half a billion new communication devices were added to the network services in 2015. Globally, mobile data traffic is predicted to reach 30.6 exabytes per month by 2020 (the equivalent of 7641 million DVDs each month), up from 3.7 exabytes per month in 2015 [1]. The radio frequency bandwidth currently used is a very limited resource. The increasing dependency on cloud services for storage and processing means that new access technologies are necessary to allow this huge increase in network utilization. The visible light spectrum on the other hand offers a 10,000 times larger unlicensed frequency bandwidth that could accommodate this expansion of network capacity. Visible light communication (VLC) is the point-to-point high speed communication and illumination system. Light fidelity (Li-Fi) is the complete wireless, bi-directional, multi-user network solution for visible light communications that would operate seamlessly alongside other Long Term Evolution (LTE) and wireless fidelity (Wi-Fi) access technologies [2]. Li-Fi is a green communication method as it reuses the existing lightning infrastructure for communications. Information is transmitted by the rapid subtle changes of light intensity that is unnoticeable by the human eye. Recent studies have demonstrated data rates of 14 Gbps for Li-Fi using three off-the-shelf laser diodes (red, green and blue) [3]. It was also predict that a data rate of 100 Gbps is achievable for Li-Fi when the whole visible spectrum is utilized [3]. Li-Fi offers inherent security, and also it can be employed in areas where sensitive electronic devices are present, such as in hospitals. In addition, Li-Fi is a potential candidate for other applications such as underwater communications, intelligent transportation systems, indoor positioning, and the Internet of Things (IoT) [2].

Modulation techniques developed for intensity modulation and direct detection (IM/DD) optical wireless communication (OWC) systems are suitable for Li-Fi communications systems. However, these modulation techniques may not be suitable for all lightning regimes. Li-Fi transceivers are illumination devices enabled for data communications. Therefore adapting IM/DD modulation technique should first satisfy certain illumination requirements before being Li-Fi enabled. For example, modulation techniques should support dimmable illumination so that communication would be still available when the illumination is not required. Li-Fi uses off-the-shelf light emitting diodes (LEDs) and photodiodes (PDs) as channel front-end devices. This restricts signals propagating throughout the channel to strictly positive signals. Single carrier modulation (SCM) techniques are straight forward to implement in Li-Fi. Modulation techniques, such as on-off keying (OOK), pulse-position modulation (PPM), and M-ary pulse-amplitude modulation (M-PAM), can be easily implemented. However, due to the dispersive nature of optical wireless channels, such schemes require complex equalizers at the receiver. Therefore, the performance of these schemes degrades as their spectral efficiency (SE) increases. On the other hand, multiple carrier modulation (MCM) techniques, such as the orthogonal frequency division multiplexing (OFDM), have been shown to be potential candidates for optical wireless channels since they only require single tap equalizer at the receiver. Adaptive bit and power loading can maximize the achievable data

rates of OFDM-based Li-Fi systems by adapting the system loading to the channel frequency response. Moreover, the DC wander and low frequency interference can be easily avoided in OFDM by optimizing the adaptive bit/power loading to avoid the low frequency subcarriers. Colour modulation techniques are unique to Li-Fi communication systems as the information is modulated on the instantaneous colour changes. The colour dimension adds a new degree of freedom to Li-Fi. The various modulation Li-Fi modulation techniques discussed in this paper are shown in **Fig. 1**.
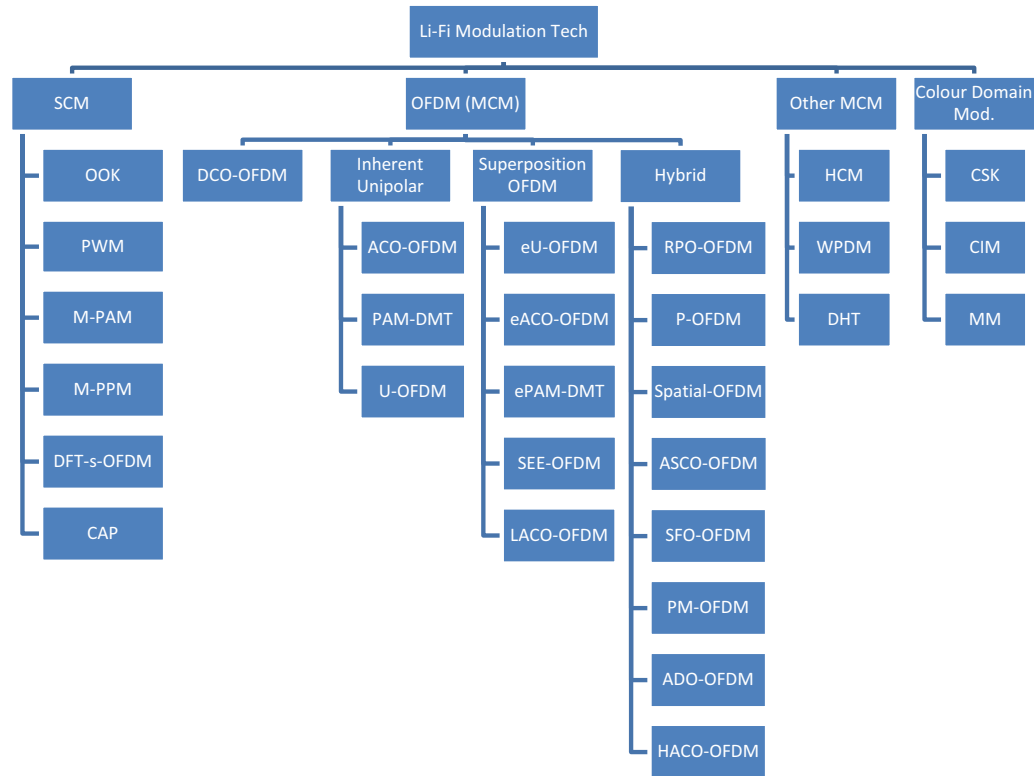
Li-Fi: light fidelity

OFDM: orthogonal frequency modulation

SCM: single carrier modulation

OOK: on-off keying

PWM: pulse width modulation

M-PAM: M-ary pulse amplitude modulation

M-PPM: M-ary pulse position modulation

DFT-s-OFDM: discrete Fourier transformation spread OFDM

CAP: carrier-less amplitude modulation

DCO-OFDM: DC biased OFDM

ACO-OFDM: asymmetrically clipped optical OFDM

PAM-DMT: pulse amplitude modulation discrete multitone

eU-OFDM: enhanced unipolar OFDM

eACO-OFDM: enhanced ACO-OFDM

ePAM-DMT: enhanced PAM-DMT

SEE-OFDM: spectrally and energy efficient OFDM

LACO-OFDM: layered ACO-OFDM

RPO-OFDM: reverse polarity optical OFDM

P-OFDM: polar OFDM

ASCO-OFDM: asymmetrically and symmetrically clipped optical OFDM

SFO-OFDM: spectrally factorized optical OFDM

PM-OFDM: position modulation OFDM

ADO-OFDM: asymmetrically clipped DC biased optical OFDM

HACO-OFDM: hybrid asymmetrically clipped optical OFDM

MCM: multicarrier modulation

HCM: Hadamard coded modulation.

WPDM: wavelet packet division multiplexing

DHT: discrete Hartley transform

CSK: colour shift keying

CIM: colour intensity modulation

MM: metameric modulation

Figure 1. Li-Fi modulation techniques considered in this paper.

This paper is organized as follows: The main challenges for Li-Fi modulation techniques are summarized in Section 2. SCM techniques for Li-Fi are detailed in Section 3. OFDM-based modulation techniques for Li-Fi are discussed in details in Section 4, including inherent unipolar OFDM techniques, hybrid OFDM modulation techniques and superposition OFDM modulation techniques. Other MCM techniques are revised in Section 5. The unique colour domain modulation techniques are discussed in Section 6. Finally the conclusion is presented in Section 7. The paper is limited to single input – single output (SISO) Li-Fi communication systems. The space dimension of Li-Fi is not considered in this paper.

2 Li-Fi Modulation Techniques Challenges

Li-Fi is an emerging high-speed, low-cost solution to the scarcity of the radio frequency (RF) spectrum, therefore it is expected to be realized using the widely deployed off-the-shelf optoelectronic LEDs. Due to the mass production of these inexpensive devices, they lack accurate characterizations. In Li-Fi, light is modulated on the subtle changes of the light intensity, therefore, the communication link would be affected by the non-linearity of the voltage-luminance characteristic. As a solution, pre-distortion techniques were proposed to mitigate non-linear distortion [4]. However, as the LED temperature increases the voltage-luminance (V-L) characteristic experiences memory-effects. Therefore, the LED non-linearity mitigation is still an open research problem. The limited bandwidth of Li-Fi communication channel leads to inter-symbol interference (ISI) at high data rates. The LED frequency response is modeled as a low-pass filter, and it is the major contributor to the frequency selectivity of Li-Fi channels. The modulation bandwidth over which the frequency response of most commercially available LEDs can be considered flat is around 2–20 MHz [5], [6]. However, the usable bandwidth in Li-Fi could be extended beyond the 3 dB cut-off frequency.

Therefore, modulation techniques with higher spectral efficiencies are key elements in a Li-Fi system design. Satisfying the illumination requirements is a key element in Li-Fi. Most of the research on modulation techniques has been on the communication system performance of Li-Fi system. Factors such as dimming, illumination level control and flickering have been analyzed as secondary parameters of a Li-Fi system. The Li-Fi systems should be also considered as an illumination system with communications capability, not the reverse.

3 Single Carrier Modulation Techniques

Single carrier modulation techniques were first proposed for IM/DD optical wireless communications based on infrared communications [7]. Modulation techniques, such as OOK, pulse amplitude modulation (PAM), pulse width modulation (PWM), and PPM, are straightforward to implement for Li-Fi systems. In general, single carrier modulation techniques are suitable candidates for Li-Fi when low-to-moderate data rates applications are required. By switching the LED between "on" and "off" states, the incoming bits can be modulated into the light intensity. Illumination control can be supported by adjusting the light intensities of the "on" and "off" states, without affecting the system performance. Compensation symbols are proposed in the visible light communications standard, IEEE 802.15.7 [8], to facilitate the illumination control at the expense of reducing the

SE. If the link budget offers high signal to noise ratios (SNR), M-PAM can be used to modulate the incoming bits on the amplitude of the optical pulse [9].The position of the optical pulse is modulated into shorter duration chips in PPM with a position index that varies depending on the incoming bits. The PPM is more power efficient than OOK, however, it requires more bandwidth than OOK to support equivalent data rates. Differential PPM (DPPM) was proposed to achieve power and/or SE gains [10], however the effect of unequal bit duration for the different incoming symbols could affect the illumination performance. A solution was proposed in [11] to ensure that the duty cycle is similar among the different symbols to prevent any possible flickering. Variable PPM (VPPM) was proposed in the VLC standard IEEE 802.15.7 to support dimming for the PPM technique and prevent any possible flickering. The pulse dimming in VPPM is controlled by the width of the pulse rather than the pulse amplitude. Therefore, VPPM can be considered as a combination of PPM and PWM techniques. Multiple PPM (MPPM) was proposed [12] as a solution to the dimming capability of PPM, where it was reported that it achieves higher spectral efficiencies than VPPM with less optical power dissipation. The advantages of PAM and PPM are combined in pulse amplitude and position modulation (PAPM) [13].

The performance comparison between single carrier and multicarrier modulation techniques was studied in [14]−[18] for different scenarios and considerations. The results may differ depending on the major considerations and assumptions of each study. However in general, the performance of single carrier modulation techniques deteriorate as the data rates increase, due to the increased ISI. Equalization techniques, such as optimum maximum likelihood sequence detection (MLSD), frequency domain equalizers (FDE), nonlinear decision feedback equalizers (DFE), and linear feed forward equalizer (FFE), are suitable candidates for equalization processes, with different degrees of performance and computational complexity [7], [19], [20]. The single carrier frequency domain equalizer (SC-FDE) was proposed for OWC as a solution to the high peak to average power ratio (PAPR) of OFDM in [12], [21]. PPM-SCFDE was considered in [22], and OOK-SCFDE was considered in [23]. The performance of OOK with minimum mean square error equalization (MMSE) was compared with the performance of asymmetrically clipped optical (ACO)-OFDM and the performance of complex modulation M-ary quadrature amplitude modulation (M-QAM) ACO-SCFDE in [18]. It was reported that the performance of ACO-SCFDE outperforms asymmetrically clipped optical OFDM (ACO-OFDM) and OOK-MMSE due to the high PAPR of ACO-OFDM when the nonlinear characteristics of the LED are considered. The performance of PAM-SCFDE is compared with OFDM in [12], without consideration of the LED nonlinearity. It was shown that PAM-SCFDE achieves higher performance gains when compared with OFDM at spectral efficiencies less than 3 bits/s/Hz.

Discrete Fourier transformation spread (DFT-s) OFDM was also considered for Li-Fi as a SCM that has the benefits of an OFDM multicarrier system with lower PAPR [24]. An extra pair of DFT and inverse discrete Fourier transformation (IDFT) operations are required to achieve DFT-s OFDM. Multiple independent streams of DFT-s OFDM modulated waveforms are separately transmitted through multiple LEDs in a single array. The performance of DFT-s OFDM is reported to be better when compared with DC-biased optical OFDM (DCO-OFDM) in terms of both PAPR and bit error rate (BER) [24]. A novel carrier-less amplitude and phase (CAP) modulation was proposed for Li-Fi in [25]. In order for CAP to suit the frequency response of LEDs, the spectrum of CAP was divided into m subcarriers by the aid of finite impulse response (FIR) filter. Although CAP is computationally complex, it could offer high spectral efficiencies in band-limited Li-Fi channel.

4 Optical OFDM

Single carrier modulation techniques require a complex equalization process when employed at high data rates. In addition, effects such as DC wandering and flickering interference of florescent lights may influence the system performance at the lower frequency regions of the used bandwidth. On the other hand, multicarrier modulation techniques such as OFDM can convert the frequency selective fading of the communication channel into a flat fading by employing the computationally efficient single tap equalizer. In addition, OFDM supports adaptive power and bit loading which can adapt the channel utilization to the frequency response of the channel. This can maximize the system performance. Supporting multiuser communication systems is an inherent advantage of OFDM, where each user could be allocated certain subcarriers. At the OFDM transmitter, the incoming bits are modulated into specific modulation formats such as M-QAM. The M-QAM symbols are loaded afterwards into orthogonal subcarriers with subcarrier spacing equal to multiple of the symbol duration. The parallel symbols can then be multiplexed into a serial time domain output, generally using inverse fast Fourier transformation (IFFT). The physical link of Li-Fi is achieved using off-the-shelf optoelectronic devices such as LED and photo-detectors (PD). Due to the fact that these light sources produce an incoherent light, the OFDM time-domain waveforms are used in Li-Fi to modulate the intensity of the LED source. Therefore, these waveforms are required to be both unipolar and real valued.

Hermitian symmetry is generally imposed on the OFDM input frame to enforce the OFDM time domain signal output into the real domain. Different variants of optical OFDM were proposed to achieve a unipolar OFDM output. DC bias is used in the widely deployed DCO-OFDM [26] to realize a unipolar time-domain OFDM output. However, OFDM signals have a high PAPR, which makes it practically impossible to convert all of the signal samples into unipolar ones. The OFDM time-domain waveform can be approximated with a Normal distribution when the length of the input frame is greater than 64. The DC bias point would be dependent on the V-L characteristic of the LED. Zero level clipping of the remaining negative samples after the biasing would result in a clipping distortion that could deteriorate the system performance. High DC bias would also incur some

distortion as a result of the upper clipping of the OFDM waveform due to the V-L characteristic of the ideal LED. The forward-output current characteristic of an LED is shown in **Fig. 2**. Pre-distortion is used to linearize the dynamic range of the LED. The LED input and output probability distribution function (PDF) of the OFDM modulation signal are also shown. The dynamic range of the LED is between the turn-on bias and the maximum allowed current points of the LED. The input signal is biased and the output signal is clipped for values outside the dynamic range. The optimization of the DC biasing point was studied in [27]–[29]. The additional dissipation of electrical power in DCO-OFDM compared with bipolar OFDM increases as the modulation order increases. This leads to electrical and optical power inefficiency when DCO-OFDM is used with high M-QAM modulation orders. Illumination is an essential part of VLC, therefore, the DCO-OFDM optical power inefficiency can be justified for some VLC applications. However, when energy efficiency is required, an alternative modulation approach is required.

LED: light emitting diode

PDF: probability distribution function
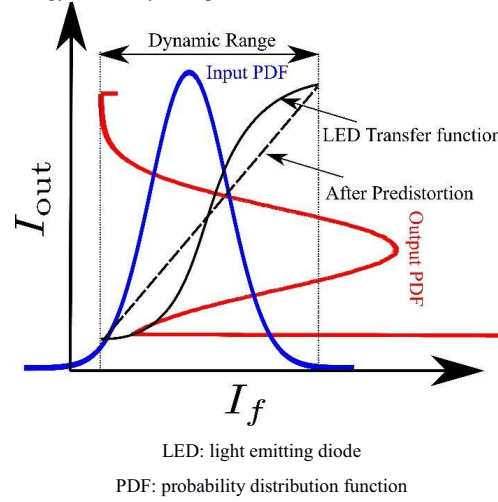
Figure 2:The forward-output current characteristic of an LED.

4.1 Inherent Unipolar Optical OFDM Techniques

Unipolar OFDM modulation schemes were mainly introduced to provide energy efficient optical OFDM alternatives to DCO-OFDM. These schemes include ACO-OFDM [30], pulse-amplitude-modulated discrete multitone modulation (PAM-DMT) [31], flipped OFDM (Flip-OFDM) [32], and unipolar orthogonal frequency division multiplexing (U-OFDM) [33]. They exploit the OFDM input/output frame structure to produce a unipolar time domain waveform output. However, all of these schemes have a reduced SE compared with DCO-OFDM due to the restrictions imposed on their frame structures. In this section, ACO-OFDM, PAM-DMT and U-OFDM/Flip-OFDM modulation schemes are discussed.

4.1.1 ACO-OFDM

A real unipolar OFDM waveform can be achieved by exploiting the Fourier transformation properties on the frequency domain input OFDM frames. The principle of ACO-OFDM [30] is to skip the even subcarriers of an OFDM frame, by only loading the odd subcarriers with useful information (**Fig. 3**). This creates a symmetry in the time domain OFDM signal, which allows the distortion-less clipping of the negative samples without the need of any DC biasing (**Fig. 4**). Clipping of the negative values is distortion-less since all of the distortion will only affect the even-indexed subcarriers. However, skipping half of the subcarriers reduces the SE of ACO-OFDM to half of that in DCO-OFDM. A penalty of 3 dB should applied to the signal-to-noise ratio (SNR) of ACO-OFDM when compared with bipolar OFDM, since half of the signal power is lost due to clipping. Hermitian symmetry is also used to guarantee a real valued ACO-OFDM output. At the receiver, after a fast Fourier transformation (FFT) is applied on the incoming frame, only odd subcarriers are considered.

DCO-OFDM

Hermitian symmetry

DC	X_1	X_2	X_3	0	X_3^*	X_2^*	X_1^*

ACO-OFDM

Hermitian symmetry

0	X_1	0	X_3	0	X_3^*	0	X_1^*

PAM-DMT

Hermitian symmetry

0	P_1	P_2	P_3	0	P_3	P_2	P_1

ACO-OFDM: asymmetrically clipped optical OFDM

DC: direct current

DCO-OFDM: DC-biased optical OFDM

PAM-DMT: pulse-amplitude-modulated discrete multi-tone modulation
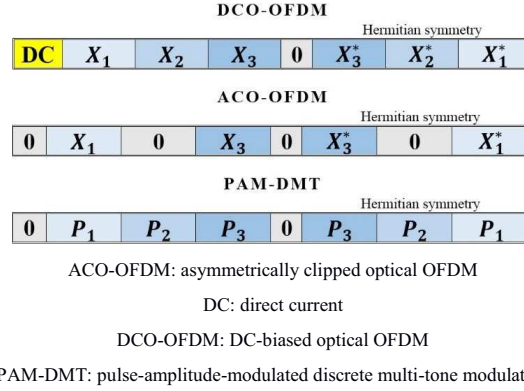
Figure 3. Subcarriers mapping of the input frames for DCO-OFDM, ACO-OFDM and PAM-DMT. X_i represents the M-QAM symbol at the ith subcarrier and P_i represents the M-PAM symbol at the ith subcarrier.
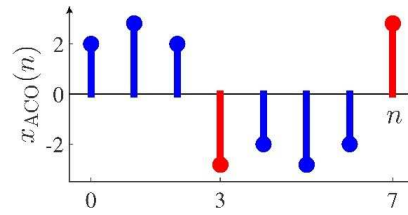
Figure 4. The time-domain ACO-OFDM waveform.

4.1.2 PAM-DMT

A real unipolar optical OFDM is realized in PAM-DMT by exploiting the Fourier properties of imaginary signals. The real component of the subcarriers is not used in PAM-DMT, which restricts the modulation scheme used to M-PAM (**Fig. 3**). By only loading M-PAM modulated symbols on the imaginary components of the subcarriers, an antisymmetry in the time-domain waveform of PAM-DMT would be achieved (**Fig. 5**). This would facilitate the distortion-less zero level clipping of PAM-DMT waveform, as all of the distortion would only affect the real component of the subcarriers. Hermitian symmetry is also used to guarantee a real valued PAM-DMT output. PAM-DMT is more attractive than ACO-OFDM when bit loading techniques are considered, as the PAM-DMT performance can be optimally adapted to the frequency response of the channel since all of the subcarriers are used. The SE of PAM-DMT is similar to that of DCO-OFDM. PAM-DMT has a 3 dB fixed penalty when compared with bipolar OFDM at an appropriate constellation size, as half of the power is also lost due to clipping. At the receiver, the imaginary part of the subcarriers is only considered, while the real part is ignored.
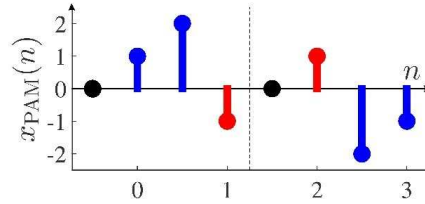
Figure 5. The time-domain PAM-DMT waveform.

4.1.3 U-OFDM/Flip-OFDM

The concept and performance of U-OFDM and Flip-OFDM is identical. In this paper, the term U-OFDM is used, however, all discussion and analysis is applicable to both schemes. Hermitian symmetry is applied on the incoming frame of M-QAM symbols. The bipolar OFDM time-domain frame obtained afterwards is expanded into two time-domain frames in U-OFDM with similar sizes to the original OFDM frame (**Fig. 6**). The first frame is identical to the original frame, while the second is a flipped replica of the original frame. A unipolar OFDM waveform can be achieved by zero-level clipping without the need of

232

any DC biasing. At the receiver, each second frame would be subtracted from the first frame of the same pair, in order to reconstruct the original bipolar OFDM frame. This would double the noise at the receiver, which leads to a 3 dB penalty when compared with bipolar OFDM at equivalent constellation sizes. The SE of U-OFDM is half of the SE of DCO-OFDM since two U-OFDM frames are required to convey the same information conveyed in a single DCO-OFDM frame. The single tap equalizer can be used for U-OFDM, providing that the ISI effects on the first frame are identical to the ISI effects on the second frame.
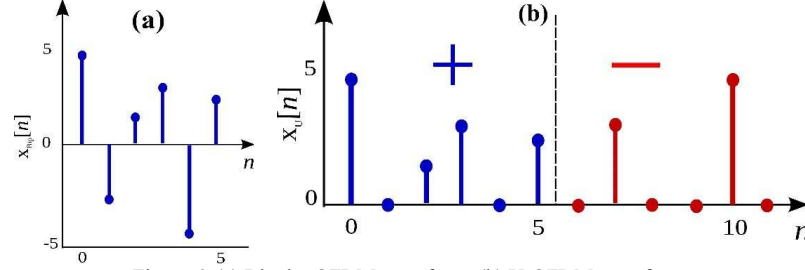
Figure 6. (a) Bipolar OFDM waveform; (b) U-OFDM waveform.

4.1.4 Performance of Inherent Unipolar OFDM Techniques

The inherent unipolar OFDM schemes (ACO-OFDM, U-OFDM, and Flip-OFDM) were introduced as power efficient alternatives to DCO-OFDM. However because two time-domain U-OFDM/Flip-OFDM frames are required to convey the information contained in a single DCO-OFDM frame, and because half of the subcarriers are skipped in ACO-OFDM, the performance of M-QAM DCO-OFDM should be compared with the performance of M^2-QAM (ACO-OFDM, U-OFDM, and Flip-OFDM). Additionally, PAM-DMT uses M-PAM on the imaginary part of the subcarriers instead of M-QAM. Since the performance of M-PAM is equivalent to the performance of M^2-QAM, the BER of PAM-DMT is similar to that of the inherent unipolar schemes. When compared with DCO-OFDM at the same SE, the performance of all of the inherent unipolar OFDM techniques degrades as the constellation size of M-QAM or M-PAM increases. For example, the performance of 1024-QAM ACO-OFDM/U-OFDM/Flip-OFDM and 32-PAM PAM-DMT would be required to be compared with the performance of 32-QAM DCO-OFDM.

Improved receivers for all of the inherent unipolar OFDM techniques were proposed in [33]−[41]. Most of these improved receivers would either require a flat channel to operate or incur additional computational complexities. Two main methods are considered in the design of these improved receivers. In the first method, the time-domain symmetry can be exploited at the receiver to achieve performance gains. An amplitude comparison between the symmetric received signal samples can improve the receiver detection in flat fading channels at the expense of increased computational complexity. The second method is based on the frequency diversity. The even subcarriers in ACO-OFDM and the real part of the subcarriers in PAM-DMT were exploited, respectively, to achieve improved performance at the receiver [33]−[41]. The frequency diversity method can be used in the frequency selective channel, however it has a higher computational complexity. In addition, it cannot be used for U-OFDM/Flip-OFDM because both schemes are based on the time-domain processing of the OFDM frames. Based on their statistical distribution, the inherent unipolar optical OFDM waveforms utilize the lower part of the V-L characteristic. Therefore, these schemes are suitable candidates for Li-Fi dimmable applications since they can operate with lower optical power dissipation. Adaptive bit loading techniques were studied for MCM techniques, DCO-OFDM and ACO-OFDM, and compared with SC-FDE in [42]. It was found that the performance of SC-FDE is worse than ACO-OFDM but better than DCO-OFDM. In addition, SC-FDE is less complex than DCO-OFDM and ACO-OFDM.

4.2 Hybrid OFDM Techniques

OFDM was modified in many studies to tailor several specific aspects of the Li-Fi system parameters. The natural spatial signal summing in the optical domain was proposed in [43]. An array of multiple LEDs is used to transmit the OFDM signal so that the subcarriers are allocated to different LEDs. As the number of the LEDs in the array increases, the PAPR of the electrical OFDM signals reduces. When the number of subcarriers is equal to the number of the LEDs in the array, the PAPR would reach its minimum value of 3 dB as the electrical signal would be an ideal sine wave. The spatial optical OFDM (SO-OFDM) is reported to have BER performance gains over DCO-OFDM at high SNR due to the reduced PAPR and the robustness against LED nonlinearities [43]. Reverse polarity optical OFDM (RPO-OFDM) was proposed to allow a higher degree of illumination control in the OFDM-based Li-Fi systems [44]. RPO-OFDM combines a real-valued optical OFDM broadband technique with slow PWM to allow dimming. The dynamic range of the LED is fully used in RPO-OFDM to minimize any nonlinear distortion. The RPO-OFDM is reported to achieve higher performance gains compared with DCO-OFDM at a large fraction of dimming ranges without limiting the data rate of the system. RPO-OFDM offers a practical solution for the illumination and dimming control for Li-Fi communication systems, however the OFDM signal in RPO-OFDM is based on unipolar OFDM. This means that the SE of RPO-OFDM is half of that of DCO-OFDM. As a result, the power efficiency advantage over DCO-OFDM starts to diminish as the SE increases. In addition, the PWM duty cycle is assumed to be known at the receiver, which means that side-information

should be sent before any transmission and this requires perfect synchronization between the transmitting and receiving ends. A novel technique that combines ACO-OFDM on the odd subcarriers with DCO-OFDM on the even subcarriers was proposed in asymmetrically DC-biased optical OFDM (ADO-OFDM) [45]. The clipping noise of the ACO-OFDM falls only into the even subcarriers, and can be estimated and canceled with a 3 dB penalty at the receiver. The power allocation for different constellation sizes between ACO-OFDM and DCO-OFDM streams in ADO-OFDM was investigated in [15]. The optical power efficiency of the optimal settings for ADO-OFDM was better than ACO-OFDM and DCO-OFDM for different configurations. Hybrid asymmetrical clipped OFDM (HACO-OFDM) uses ACO-OFDM on the odd subcarriers and PAM-DMT on the even subcarriers to improve the SE of unipolar OFDM modulation techniques [46]. The asymmetrical clipping of the ACO-OFDM on the odd symbols would only distort the even subcarriers. At the receiver, ACO-OFDM symbols are demodulated first by only considering the odd subcarriers and then remodulated to estimate the ACO-OFDM distortion on the even subcarriers. This allows the PAM-DMT symbols on the even subcarrier to be demodulated without any distortion. The SE achieved in HACO-OFDM is identical to that of DCO-OFDM, however PAM-DMT uses M-PAM modulation on half of the subcarriers. Equal power was allocated to ACO-OFDM and PAM-DMT. As the performance of M^2-QAM is equivalent to the performance of M-PAM, the power requirements for both ACO-OFDM and PAM-DMT to achieve the same performance is different. The problem also appears when different modulation orders are used for both schemes. Unequal power allocation for both schemes was investigated in [47] to guarantee that the performance of both schemes in HACO-OFDM is equal. An improved, but computationally complex, receiver was also proposed in [47] based on the time domain symmetry of both ACO-OFDM and PAM-DMT.

Polar OFDM (P-OFDM) is a new method to achieve the IM/DD for OFDM [48]. The main principle of P-OFDM is to convert the complex valued output of the IFFT from the Cartesian coordinates into the polar coordinates. Therefore, the radial and angular coordinate can be sent in the first and second halves of the OFDM frame, successively. It avoids the use of Hermitian symmetry, however, it allocates the M-QAM symbols into the even indexed subcarriers. As a result, P-OFDM has half-wave even symmetry which states that the first half of the complex valued time-domain frame is identical to the other half. Therefore, it is sufficient to transmit the first half of the IFFT output. As a result, the SE is reduced to be identical to that of DCO-OFDM since only half of the subcarriers are used. The performance of P-OFDM was compared to that of ACO-OFDM in [49]. It was reported that P-OFDM achieves better BER performance gains than ACO-OFDM under narrow dynamic ranges when optimal values for the power allocation of the radial and angular information are used. Note that any ISI between the radial and angular samples may deteriorate the system performance, therefore the system performance in frequency selective channels should be investigated. Asymmetrical and symmetrical clipping optical OFDM (ASCO-OFDM) was proposed in [50] for IM/DD Li-Fi systems. The ACO-OFDM is combined with symmetrical clipping optical OFDM (SCO-OFDM) that uses the even subcarriers. The clipping distortion of both ACO-OFDM and SCO-OFDM affects the even subcarriers. However, the clipping distortion of ACO-OFDM can be estimated and canceled at the receiver. The SCO-OFDM clipping noise can be removed at the receiver using U-OFDM/Flip-OFDM time domain processing techniques. The SE of ASCO-OFDM is 75% of the SE of DCO-OFDM. ASCO-OFDM was reported to have better symbol error rate (SER) compared with ADO-OFDM since the ADO-OFDM uses the DC bias for the even subcarriers. FIR filtering technique termed spectral factorization was used to create a unipolar optical OFDM signal [51]. The amplitude of the subcarriers in spectral factorized optical OFDM (SFO-OFDM) were chosen to form an autocorrelation sequence that was shown to be sufficient to guarantee a unipolar OFDM output. The SFO-OFDM was reported to achieve 0.5 dB gain over ACO-OFDM with 30% PAPR reduction [51]. The position modulation OFDM (PM-OFDM) avoids the Hermitian symmetry and splits the real and imaginary components of the OFDM output into two branches where a polarity separator is used to obtain the positive and negative samples of each branch [52]. The four frames composed of a real positive frame, a real negative one, an imaginary positive one and an imaginary negative one are transmitted as unipolar OFDM frames. The SE is exactly similar to other inherent unipolar OFDM techniques discussed in section 4.1. The performance of PM-OFDM was reported to be identical to U-OFDM in flat channels. However, it was reported to have better BER performance when compared to ACO-OFDM for frequency selective channels [52].

4.3 Superposition OFDM Techniques

Superposition OFDM based modulation techniques rely on the fact that the SE of U-OFDM/Flip-OFDM, ACO-OFDM, and PAM-DMT can be doubled by proper superimposing of multiple layers of OFDM waveforms. Superposition modulation was first introduced for OFDM-based OWC and has led to enhanced U-OFDM (eU-OFDM) [53]. The eU-OFDM compensates for the spectral efficiency loss of U-OFDM by superimposing multiple U-OFDM streams so that the inter-stream-interference is null. The generation method of the first depth in eU-OFDM is exactly similar to that in U-OFDM. Subsequent depths can be generated by U-OFDM modulators before each unipolar OFDM frame is repeated 2^{d-1} times and scaled by $1/2^{d-1}$, where d is the depth number. At the receiver, the information conveyed in the first depth is demodulated and then remodulated to be subtracted from the overall received signal. Then repeated frames which are equivalent at higher depths are recombined and the demodulation procedure continues the same as for the stream at the first depth. Afterwards, the information conveyed in latter depths is demodulated in a similar way. The SE gap between U-OFDM and DCO-OFDM can never be completely closed with eU-OFDM, as this would require a large number of information streams to be superimposed in the modulation signal. Implementation issues, such as latency, computational complexity, power penalty, and memory requirements put a practical limit on the maximum number of available depths. The eU-OFDM was generalized in the Generalized Enhanced Unipolar OFDM (GREENER-OFDM) for configurations where arbitrary constellation sizes and arbitrary power allocations are used [54]. As a

result, the SE gap between U-OFDM and DCO-OFDM can be closed completely with an appropriate selection of the constellation sizes in different information streams. The symmetry in U-OFDM lies in frames, whilst in ACO-OFDM and PAM-DMT, it lies in subframes.

The superposition concept has also been extended to other unipolar OFDM techniques such as PAM-DMT [55] and ACO-OFDM [56]−[60]. The enhanced asymmetrically clipped optical OFDM (eACO-OFDM) [56] uses the symmetry of ACO-OFDM subframes to allow multiple ACO-OFDM streams to be superimposed. A similar concept was also proposed by Elgala et al. and Wang et al. under the names of spectrally and energy efficient OFDM (SEE-OFDM) [57] and layered asymmetrically clipped optical OFDM (Layered ACO-OFDM) [58], respectively. The receiver proposed in SEE-OFDM [57] results in SNR penalty that could have been avoided by using the symmetry properties of ACOOFDM streams. The symmetry arrangement in Layered ACO-OFDM [58] is described in the frequency domain, however, it is shown in [58, Fig.2] that it takes place in the time-domain. Recently, an alternative method to achieve superposition modulation based on ACO-OFDM was proposed by Kozu et al. [59] for two ACO-OFDM streams, and Lawery [60] for Layered ACO-OFDM. This is similar in principle to the solutions in [56]−[58], however the superposition is performed in the frequency domain which results in simpler system design. The concept of eACO-OFDM was generalized to close the SE gap between ACO-OFDM and DCO-OFDM. The generation of eACO-OFDM signal starts at the first depth with an ACO-OFDM modulator. Additional depths are generated in a similar way to the first depth, but with an OFDM frame length equal to half of the previous depth frames. Similar to eU-OFDM, all of the generated frames are repeated 2^{d-1} times and appropriately scaled. The demodulation process at the receiver is applied in a similar way as the eU-OFDM. The information at Depth-1 can be recovered directly as in conventional ACO-OFDM because all of the inter-stream-interference falls into the even-indexed subcarriers. After the first stream is decoded, the information can be remodulated again and subtracted from the overall received signal. Then, the frames that are equivalent can be recombined and the demodulation procedure continues as for the stream at first depth.

The enhanced pulse-amplitude-modulated discrete multi-tone (ePAM-DMT) [55] demonstrates that superposition modulation can also be utilized when the antisymmetry of PAM-DMT waveforms is used. Analogous to eU-OFDM and eACO-OFDM, unique time-domain structures are also present in PAM-DMT. If the interference over a single PAM-DMT frame possesses a Hermitian symmetry in the time-domain, its frequency profile falls on the real component of the subcarriers. Hence, the interference is completely orthogonal to the useful information which is encoded in imaginary symbols of the PAM-DMT frames. The concept of superposition modulation was extended to ePAM-DMT for an arbitrary modulation order and an arbitrary power allocation at each depth [55]. The theoretical BER analysis of eACO-OFDM is similar to the analysis of GREENER-OFDM, therefore the optimal modulation sizes and scaling factors are identical. This is an expected result because the performance of their unipolar OFDM forms, ACO-OFDM and U-OFDM, is also similar. The ePAM-DMT is less energy efficient than GREENER-OFDM and eACO-OFDM, because ePAM-DMT has 3 dB loss in each depth demodulation process and the optimal configurations of ePAM-DMT are suboptimal as the non-squared M-QAM BER performance can never be achieved using the $\sqrt{M}$-PAM modulation scheme. The ePAM-DMT is more energy efficient than DCO-OFDM in terms of the electrical SNR at SE values above 1 bit/s/Hz. In terms of the optical SNR, the ePAM-DMT is less energy efficient than DCO-OFDM for all of the presented values. Higher optical energy dissipation is a desirable property for illumination based Li-Fi applications, but it is considered as a disadvantage for dimmable-based Li-Fi applications. However, GREENER-OFDM and eACO-OFDM are suitable candidates for dimmable-based Li-Fi applications due to their optical SNR performance.

5 Other Multi-Carrier Modulation Techniques

OFDM has been mainly studied in the context of Li-Fi channels based on FFT. Other transformations such as discrete Hartley transformation (DHT) [61], wavelet packet division multiplexing (WPDM) [62] and Hadamard coded modulation (HCM) [63] have also been considered for Li-Fi channels. A multicarrier IM/DD system based on DHT was proposed in [61]. It was shown that DHT output can be real when an input frame of real modulated symbols such as binary phase shift keying (BPSK) and M-PAM is used. Similar to DCO-OFDM and ACO-OFDM, DC-biasing and asymmetrical clipping can also be used to achieve unipolar output in DHT-based multicarrier modulation technique. As a major advantage over FFT-based conventional OFDM, the DHT-based multicarrier modulation does not require any Hermitian symmetry. However, this fails to improve the SE as real modulated symbols such as M-PAM are used in DHT-based multicarrier modulation. WPDM uses orthogonal wavelet packet functions for symbol modulation where the basis functions are wavelet packet functions with finite length. It was reported that the performance of WPDM is better than that of OFDM in terms of the spectral and power efficiencies when LED nonlinear distortion and channel dispersion are taken into account [62]. The high illumination level of OFDM Li-Fi systems require higher optical power, which may result in clipping due to the peak power constraint of the V-L transfer function of the LED (Fig. 2). HCM was proposed for multicarrier modulation Li-Fi as a solution to the limitation of OFDM modulation at higher illumination levels. The technique is based on fast Walsh-Hadamard transformation (FWHT) as an alternative to the FFT. HCM is reported to achieve higher performance gains when compared with ACO-OFDM and DCO-OFDM at higher illumination levels [63]. However, the performance improvement over RPO-OFDM is modest. An alternative variant of HCM, termed DC reduced HCM (DCR-HCM), was also proposed to reduce the power consumption of HCM to support dimmable Li-Fi applications, and interleaving with MMSE equalization is used for HCM in dispersive Li-Fi channels.
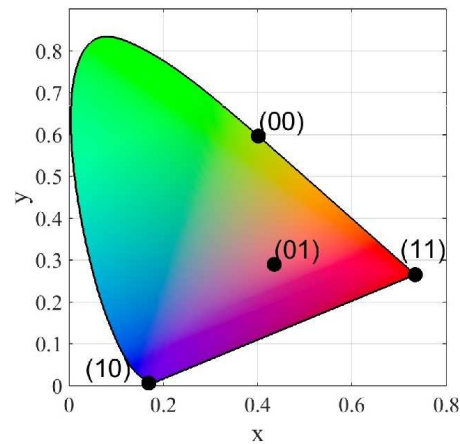
Figure 7. The symbol mapping of 4-CSK on the CIE 1931 colour model based on IEEE 802.15.7.

6 Li-Fi Unique Modulation Technique

The modulation frequency in Li-Fi systems does not correspond to the carrier frequency of the LED. All the aforementioned modulation techniques are baseband modulation techniques. It is practically difficult to modulate the carrier frequency of the LEDs, however, it is practically straightforward to change its colour. This feature adds a new degree of freedom to Li-Fi systems. Colour tunable LEDs such as the red green blue LED (RGB-LED) can illuminate with different colours based on the intensity applied on each LED element. The IEEE 802.15.7 standard proposes colour shift keying (CSK) as a modulation technique for VLC [8]. The incoming bits are mapped into a constellation of colours from the chromatic CIE 1931 colour space [64], as shown in **Fig. 7**. The CIE 1931 is the widely used illumination model for human eye colour perception. Any colour in the model can be represented by the chromaticity dimension [x, y]. In CSK, the overall intensity of the output colour is constant, however, the relative intensities between the multiple used colours are changed. Therefore the instantaneous colour of the multicolour LED is modulated. Seven wavelengths are defined in IEEE 802.15.7 specify the vertices of a triangle where the constellation point lies in. The intensity of each RGB-LED element is changed to match the constellation point while maintaining a constant optical power and a constant illumination colour. This is desirable in Li-Fi systems, since the constant illumination colour naturally mitigates any flickering. An amplitude dimming is used for brightness control in CSK while the center colour of the colour constellation constant is kept. However, colour shift is possible due to the presence of any improper driving current used for dimming control. Constellation sizes up to 16-CSK were proposed in the IEEE 802.15.7 standard based on tri-colour LEDs. Constellation points design based on CIE 1931 was also investigated by Drost and Sadler using billiard algorithms [65], by Monterio and Hranilovic using interior point method [66], by Singh et al. using quad LED (QLED) [67], and by Jiang et al. using extrinsic transfer (EXIT) charts for an iterative CSK transceiver design [68].

A generalized CSK (GCSK) that operates under varying target colours independent from the number of used LEDs was proposed in [69]. Colour intensity modulation (CIM) was proposed to improve the communication capacity without any loss to the illumination properties (dimming and target colour matching) [70]. The instantaneous intensity of the RGB LED was modulated in CIM while only maintaining a constant perceived colour. Therefore, CIM can be considered as a relaxed version of CSK since a constant perceived power is additionally required in CSK. Metameric modulation (MM) constrains the CSK to have a constant instantaneous perceived ambient light with the aid of an external green LED [70]. An improved control of the RGB output colour was achieved in MM by improving the colour rendering and reducing the colour flickering [71]. A four colour system was used in [67] with the aid of additional IM/DD signaling as a fourth dimension signal. Higher order modulation techniques of 2^{12}-CSK for QLED were achieved in [67].The CSK was combined with constant rate differential PPM in [72] to simplify the synchronization while maintaining the illumination control and avoiding flickering. A similar approach of combining CSK with complementary PPM was proposed by [73]. A digital CSK (DCSK) was proposed in [74]. Multiple multicolour LEDs were used in DCSK where only one colour is activated in each multicolour LED at a single time. Therefore the information is encoded in the combinations of activated colours. The main advantage of DCSK over conventional CSK is avoiding the need of any digital-to-analog converters, while the main disadvantage is rendering the activated colours which may result in slight changes of the colour perception over time.

The receiver architecture has not been fully addressed in most of the published research on colour domain modulation. CSK is considered to be an expensive and complex modulation technique when compared with OFDM. The colour dimension in Li-Fi can also be used to derive a multicolour LED with different streams of data. The optical summation may turn this coloured parallel stream into a single colour stream output that can be filtered at the receiver into the original transmitted coloured stream.

Table 1. Comparison of multicarrier modulation schemes for Li-Fi

Mod. Tech.	SE as a function of DCO-OFDM	Illumination		Computational Complexity	Remarks	Ref.
		Control	Level			
ADO-OFDM	100%	No	Dimmed-Medium	High	Requires DC bias	[15]
DCO-OFDM	100%	No	Medium	Low	Requires DC bias	[26]
Inherent unipolar	50%	No	Dimmed	Low	Power efficient at low SE	[30]-[33]
Spatial OFDM	100%	Limited	Medium	High	Low PAPR	[43]
RPO-OFDM	50%	Yes	Dimmed-High	Medium	Requires Sync.	[44]
HACO-OFDM	100%	No	Dimmed	High	Power efficient at low-medium SE	[46]
P-OFDM	50%	No	Medium	High	-	[48]
ASCO-OFDM	75%	No	Dimmed	High	-	[50]
SFO-OFDM	Variable	No	Medium	High	Low PAPR	[51]
PM-OFDM	50%	No	Medium	High	-	[52]
Superposition	100%	No	Dimmed	High	Power efficient at low-high SE	[53]-[60]
DHT	50%-100%	No	Dimmed-Medium	Low	-	[61]
WPDM	100%	No	Medium	High	-	[62]
HCM	100%	Yes	High	Low	Power inefficient	[63]

7 Conclusion

The modulation techniques suitable for Li-Fi are presented in this paper. These techniques should satisfy illumination and communication requirements. Single carrier modulation techniques offer a simple solution for frequency-flat Li-Fi channels. Low-to-medium data rates can be achieved using single carrier modulation techniques. Multicarrier modulation techniques offer high data rates solution that can adapt the system performance to the channel frequency response. Many variants of optical OFDM modulation techniques have been proposed in published research to satisfy certain illumination and/or communication requirements. A summary of Li-Fi multicarrier modulation techniques is presented in **Table. 1**. The colour dimension offers unique modulation formats for Li-Fi and adds to the degrees of freedom of Li-Fi systems. Time, frequency, space, colour dimensions, and the combinations of them can be used for Li-Fi modulation. Li-Fi modulation techniques should offer a high speed communication and be suitable for most illumination regimes.

Acknowledgment

References

[1] Cisco Visual Networking Index, "Global Mobile Data Traffic Forecast Update, 2015-2020," CISCO, White Paper, Feb. 2016. [Online]. Available: http://www.cisco.com/c/en/us/solutions/collateral/service-provider/visual-networking-index-vni/-mobile-white-paper-c11-520862.pdf
[2] S. Dimitrov and H. Haas, *Principles of LED Light Communications: Towards Networked Li-Fi*. Cambridge, England: Cambridge University Press, 2015.
[3] D. Tsonev, S. Videv, and H. Haas, "Towards a 100 Gb/s Visible Light Wireless Access Network," *Opt. Express*, vol. 23, no. 2, pp. 1627–1637, Jan 2015. [Online]. Available: http://www.opticsexpress.org/abstract.cfm?URI=oe-23-2-1627. doi: 10.1364/OE.23.001627.

[4]   H. Elgala, R. Mesleh, and H. Haas, "A Study of LED Nonlinearity Effects on Optical Wireless Transmission using OFDM," in *Proceedings of the 6th IEEE International Conference on wireless and Optical communications Networks (WOCN)*, Cairo, Egypt, Apr. 28–30, 2009. doi: 10.1109/WOCN.2009.5010576.

[5]   A. M. Khalid, G. Cossu, R. Corsini, et al., "1-Gb/s transmission over a phosphorescent white LED by using rate-adaptive discrete multitone modulation," *IEEE Photon. J.*, vol. 4, no. 5, pp. 1465–1473, Oct. 2012. doi: 10.1109/JPHOT.2012.2210397.

[6]   G. Cossu, A. M. Khalid, P. Choudhury, et al., "3.4 Gbit/s visible optical wireless transmission based on RGB LED," *Optics Express*, vol. 20, pp. B501–B506, 2012. doi: 10.1364/OE.20.00B501.

[7]   J. M. Kahn and J. R. Barry, "Wireless Infrared Communications," *Proc. IEEE*, vol. 85, no. 2, pp. 265–298, Feb. 1997.

[8]   IEEE Std. 802.15.7-2011, *IEEE Standard for Local and Metropolitan Area Networks, Part 15.7: Short-Range Wireless Optical Communication Using Visible Light*, IEEE Std., 2011. doi: 10.1109/IEEESTD.2011.6016195

[9]   S. Randel, F. Breyer, S. C. J. Lee, et al., "Advanced Modulation Schemes for Short-Range Optical Communications," *IEEE Journal of Selected Topics in Quantum Electronics*, vol. PP, no. 99, pp. 1 –10, 2010. doi: 10.1109/JSTQE.2010.2040808.

[10] D. shan Shiu and J. Kahn, "Differential pulse-position modulation for power-efficient optical communication," *Communications, IEEE Transactions on*, vol. 47, no. 8, pp. 1201–1210, Aug 1999. doi: 10.1109/26.780456.

[11] F. Delgado, I. Quintana, J. Rufo, et al., "Design and implementation of an ethernet-vlc interface for broadcast transmissions," *Communications Letters, IEEE*, vol. 14, no. 12, pp. 1089–1091, December 2010. doi: 10.1109/LCOMM.2010.12.100984.

[12] S. H. Lee, S.-Y. Jung, and J. K. Kwon, "Modulation and coding for dimmable visible light communication," *Communications Magazine, IEEE*, vol. 53, no. 2, pp. 136–143, Feb 2015. doi: 10.1109/MCOM.2015.7045402.

[13] Y. Zeng, R. Green, and M. Leeson, "Multiple Pulse Amplitude and Position Modulation for the Optical Wireless Channel," in *Proc. 10th Anniversary International Conference on Transparent Optical Networks (ICTON'08)*, vol. 4, Athens, Greece, Jun. 22–26 2008, pp. 193–196. doi: 10.1109/ICTON.2008.4598766.

[14] R. Mesleh, H. Elgala, and H. Haas, "On the Performance of Different OFDM Based Optical Wireless Communication Systems," *IEEE/OSA Journal of Optical Communications and Networking*, vol. 3, no. 8, pp. 620–628, Aug. 2011. doi: 10.1364/JOCN.3.000620.

[15] S. Dissanayake and J. Armstrong, "Comparison of aco-ofdm, dco-ofdm and ado-ofdm in im/dd systems," *J. Lightwave Technol.*, vol. 31, no. 7, pp. 1063–1072, Apr 2013. [Online]. Available: http://jlt.osa.org/abstract.cfm?URI=jlt-31-7-1063. doi: 10.1109/JLT.2013.2241731.

[16] D. Barros, S. Wilson, and J. Kahn, "Comparison of orthogonal frequency-division multiplexing and pulse-amplitude modulation in indoor optical wireless links," *IEEE Transactions on Communications*, vol. 60, no. 1, pp. 153–163, 2012. doi: 10.1109/TCOMM.2011.112311.100538.

[17] J. Armstrong and B. J. C. Schmidt, "Comparison of Asymmetrically Clipped Optical OFDM and DC-Biased Optical OFDM in AWGN," *IEEE Commun. Lett.*, vol. 12, no. 5, pp. 343–345, May 2008. doi: 10.1109/LCOMM.2008.080193.

[18] M. Kashani and M. Kavehrad, "On the performance of single- and multi-carrie modulation schemes for indoor visible light communication systems," in *Global Communications Conference (GLOBECOM), 2014 IEEE*, Dec 2014, Austin, USA, pp. 2084–2089. doi: 10.1109/GLOCOM.2014.7037115.

[19] J. B. Carruthers and J. M. Kahn, "Angle Diversity for Nondirected Wireless Infrared Communication," *IEEE Transactions on Communications*, vol. 48, no. 6, pp. 960–969, Jun. 2000. doi: 10.1109/26.848557.

[20] J. G. Proakis, *Digital Communications*, 4th ed. New York, NY, USA: McGraw–Hill, 2000.

[21] K. Acolatse, Y. Bar-Ness, and S. K. Wilson, "Novel techniques of single-carrier frequency-domain equalization for optical wireless communications," *EURASIP J. Adv. Signal Process*, vol. 2011, pp. 4:1–4:13, Jan. 2011. [Online]. Available: http://-dx.doi.org/10.1155/2011/393768

[22] C. chen Hsieh and D. shan Shiu, "Single carrier modulation with frequency domain equalization for intensity modulation-direct detection channels with intersymbol interference," in *17th IEEE International Symposium on Personal, Indoor and Mobile Radio Communications*, Sept. 2006, Helsinki, Finland, pp. 1–5. doi: 10.1109/PIMRC.2006.254418.

[23] A. Nuwanpriya, J. Zhang, A. Grant, et al., "Single carrier frequency domain equalization based on on-off-keying for optical wireless communications," in *IEEE Wireless Communications and Networking Conference (WCNC)*, April 2013, Shanghai, China, pp. 4272–4277. doi: 10.1109/WCNC.2013.6555264.

[24] C. Wu, H. Zhang, and W. Xu, "On visible light communication using led array with dft-spread ofdm," in *IEEE International Conference on Communications (ICC)*, June 2014, Sydney, Australia, pp. 3325–3330. doi: 10.1109/ICC.2014.6883834.

[25] P. Haigh, S. T. Le, S. Zvanovec, et al., "Multi-band carrier-less amplitude and phase modulation for bandlimited visible light communications systems," *IEEE Wireless Communications*, vol. 22, no. 2, pp. 46–53, April 2015. doi: 10.1109/MWC.2015.7096284.

[26] J. B. Carruthers and J. M. Kahn, "Multiple-subcarrier Modulation for Nondirected Wireless Infrared Communication," *IEEE Journal on Selected Areas in Communications*, vol. 14, no. 3, pp. 538–546, Apr. 1996. doi: 10.1109/49.490239.

[27] S. Dimitrov and H. Haas, "Information Rate of OFDM-Based Optical Wireless Communication Systems with Nonlinear Distortion," *IEEE J. Lightw. Technol.*, vol. 31, no. 6, pp. 918–929, Mar. 2013. doi: 10.1109/JLT.2012.2236642.

[28] X. Ling, J. Wang, X. Liang, et al., "Offset and power optimization for dco-ofdm in visible light communication systems," *Signal Processing, IEEE Transactions on*, vol. 64, no. 2, pp. 349–363, Jan 2016. doi: 10.1109/TSP.2015.2477799.

[29] M. Zhang and Z. Zhang, "An optimum dc-biasing for dco-ofdm system," *Communications Letters, IEEE*, vol. 18, no. 8, pp. 1351–1354, Aug 2014. doi: 10.1109/LCOMM.2014.2331068.

[30] J. Armstrong and A. Lowery, "Power Efficient Optical OFDM," *Electronics Letters*, vol. 42, no. 6, pp. 370–372, Mar. 16, 2006. doi: 10.1049/el:20063636.

[31] S. C. J. Lee, S. Randel, F. Breyer, et al., "PAM-DMT for Intensity-Modulated and Direct-Detection Optical Communication Systems," *IEEE Photonics Technology Letters*, vol. 21, no. 23, pp. 1749–1751, Dec. 2009. doi: 10.1109/LPT.2009.2032663.

[32] N. Fernando, Y. Hong, and E. Viterbo, "Flip-OFDM for Unipolar Communication Systems," *IEEE Transactions on Communications*, vol. 60, no. 12, pp. 3726–3733, Dec. 2012. doi: 10.1109/TCOMM.2012.082712.110812.

[33] D. Tsonev, S. Sinanovic, and H. Haas, "Novel Unipolar Orthogonal Frequency Division Multiplexing (U-OFDM) for Optical Wireless," in *Proc. of the Vehicular Technology Conference (VTC Spring)*, IEEE. Ýokohama, Japan: IEEE, May 6–9 2012. doi: 10.1109/VETECS.2012.6240060.

[34] L. Chen, B. Krongold, and J. Evans, "Diversity combining for asymmetrically clipped optical ofdm in im/dd channels," in *Global Telecommunications Conference, 2009. GLOBECOM 2009. IEEE*, Nov 2009, Hawaii, USA, pp. 1–6. doi: 10.1109/GLOCOM.2009.5425293.

[35] J. Dang, Z. Zhang, and L. Wu, "A novel receiver for aco-ofdm in visible light communication," *Communications Letters, IEEE*, vol. 17, no. 12, pp. 2320–2323, December 2013. doi: 10.1109/LCOMM.2013.111113.132223.

[36] N. Huang, J.-B. Wang, C. Pan, et al., "Iterative receiver for flip-ofdm in optical wireless communication," *Photonics Technology Letters, IEEE*, vol. 27, no. 16, pp. 1729–1732, Aug 2015. doi: 10.1109/LPT.2015.2438338.

[37] Y. Zheng, Z. Zhang, J. Dang, et al., "A novel receiver for filp-ofdm in optical wireless communication," in *Communication Technology (ICCT), 2015 IEEE 16th International Conference on*, Oct 2015, Mumbai, India, pp. 620–625. doi: 10.1109/ICCT.2015.7399914.

[38] J. Dang, Z. Zhang, and L. Wu, "Frequency-domain diversity combining receiver for aco-ofdm system," *Photonics Journal, IEEE*, vol. 7, no. 6, pp. 1–10, Dec 2015. doi: 10.1109/JPHOT.2015.2496865.

[39] J. Xu, W. Xu, H. Zhang, et al., "Asymmetrically reconstructed optical ofdm for visible light communications," *Photonics Journal, IEEE*, vol. 8, no. 1, pp. 1–18, Feb 2016. doi: 10.1109/JPHOT.2016.2520818.

[40] N. Huang, J.-B. Wang, J. Wang, et al., "Receiver design for pam-dmt in indoor optical wireless links," *Photonics Technology Letters, IEEE*, vol. 27, no. 2, pp. 161–164, Jan 2015. doi: 10.1109/LPT.2014.2363876.

[41] N. Xiang, Z. Zhang, J. Dang, et al., "A novel receiver design for pam-dmt in optical wireless communication systems," *Photonics Technology Letters, IEEE*, vol. 27, no. 18, pp. 1919–1922, Sept 2015. doi: 10.1109/LPT.2015.2445793.

[42] L. Wu, Z. Zhang, J. Dang, et al., "Adaptive modulation schemes for visible light communications," *J. Lightwave Technol.*, vol. 33, no. 1, pp. 117–125, Jan 2015. [Online]. Available: http://jlt.osa.org/abstract.cfm?URI=jlt-33-1-117. doi: 10.1109/JLT.2014.2374171.

[43] M. Mossaad, S. Hranilovic, and L. Lampe, "Visible light communications using ofdm and multiple leds," *Communications, IEEE Transactions on*, vol. 63, no. 11, pp. 4304–4313, Nov 2015. doi: 10.1109/TCOMM.2015.2469285.

[44] H. Elgala and T. D. C. Little, "Reverse polarity optical-ofdm (rpo-ofdm): dimming compatible ofdm for gigabit vlc links," *Opt. Express*, vol. 21, no. 20, pp. 24288–24299, Oct 2013. [Online]. Available: http://www.opticsexpress.org/-abstract.cfm?URI=oe-21-20-24288. doi: 10.1364/OE.21.024288..

[45] S. Dissanayake, K. Panta, and J. Armstrong, "A Novel Technique to Simultaneously Transmit ACO-OFDM and DCO-OFDM in IM/DD Systems," in *IEEE GLOBECOM Workshops (GC Wkshps)*. Houston, TX, USA: IEEE, Dec. 5–9 2011, pp. 782–786. doi: 10.1109/GLOCOMW.2011.6162561.

[46] B. Ranjha and M. Kavehrad, "Hybrid asymmetrically clipped ofdm-based im/dd optical wireless system," *Optical Communications and Networking, IEEE/OSA Journal of*, vol. 6, no. 4, pp. 387–396, April 2014. doi: 10.1364/JOCN.6.000387.

[47] Q. Wang, Z. Wang, and L. Dai, "Iterative receiver for hybrid asymmetrically clipped optical ofdm," *Lightwave Technology, Journal of*, vol. 32, no. 22, pp. 4471–4477, Nov 2014. doi: 10.1109/JLT.2014.2358611.

[48] H. Elgala and T. Little, "P-ofdm: Spectrally efficient unipolar ofdm," in *Optical Fiber Communications Conference and Exhibition (OFC), 2014*, March 2014, San Francisco, USA, pp. 1–3. doi:10.1364/OFC.2014.Th3G.7.

[49] H. Elgala and T. D. C. Little, "Polar-based ofdm and sc-fde links toward energy-efficient gbps transmission under im-dd optical system constraints invited," *J. Opt. Commun. Netw.*, vol. 7, no. 2, pp. A277–A284, Feb 2015. [Online]. Available: http://-jocn.osa.org/abstract.cfm?URI=jocn-7-2-A277. doi: 10.1364/JOCN.7.00A277.

[50] N. Wu and Y. Bar-Ness, "A novel power-efficient scheme asymmetrically and symmetrically clipping optical (asco)-ofdm for im/dd optical systems," *EURASIP Journal on Advances in Signal Processing*, vol. 2015, no. 1, pp. 1–10, 2015. [Online]. Available: http://dx.doi.org/10.1186/1687-6180-2015-3

[51] K. Asadzadeh, A. Farid, and S. Hranilovic, "Spectrally Factorized Optical OFDM," in *12th Canadian Workshop on Information Theory (CWIT 2011)*. IEEE, May 17–20 2011, British Columbia, Canada, pp. 102–105. doi: 10.1109/CWIT.2011.5872134.

[52] T. Mao, C. Qian, Q. Wang, et al., "Pm-dco-ofdm for papr reduction in visible light communications," in *Opto-Electronics and Communications Conference (OECC), 2015*, June 2015, Shanghai, China, pp. 1–3. doi: 10.1109/OECC.2015.7340207.

[53] D. Tsonev and H. Haas, "Avoiding Spectral Efficiency Loss in Unipolar OFDM for Optical Wireless Communication," in *Proc. of the International Conference on Communications (ICC)*. Sydney, Australia: IEEE, Jun., 10–14 2014. doi: 10.1109/ICC.2014.6883836.

[54] M. Islim, D. Tsonev, and H. Haas, "A Generalized Solution to the Spectral Efficiency Loss in Unipolar Optical OFDM-based Systems," in *Proc. of the International Conference on Communications (ICC)*. London, UK: IEEE, Jun., 8–12 2015. doi: 10.1109/ICC.2015.7249137.

[55] M. Islim, D. Tsonev, and H. Haas, "Spectrally Enhanced PAM-DMT for IM/DD Optical Wireless Communications," in *Proc. of the 25th Int. Symp. Pers. Indoor and Mobile Radio Commun. (PIMRC)*. Hong Kong, China: IEEE, Aug. 30–Sep. 2 2015, pp. 927–932. doi: 10.1109/PIMRC.2015.7343421.

[56] M. Islim, D. Tsonev, and H. Haas, "On the Superposition Modulation for OFDM-based Optical Wireless Communication," in *Signal and Information Processing (GlobalSIP), 2015 IEEE Global Conference on*. Orlando, USA: IEEE, Dec., 14–16 2015. doi: 10.1109/GlobalSIP.2015.7418352.

[57] H. Elgala and T. Little, "SEE-OFDM: Spectral and energy efficient OFDM for optical IM/DD systems," in *Personal, Indoor, and Mobile Radio Communication (PIMRC), 2014 IEEE 25th Annual International Symposium on*, Washington DC, USA, 2–5 2014, pp. 851–855. doi: 10.1109/PIMRC.2014.7136284.

[58] Q. Wang, C. Qian, X. Guo, et al., "Layered ACO-OFDM for intensity-modulated direct-detection optical wireless transmission," *Opt. Express*, vol. 23, no. 9, pp. 12382–12393, May 2015. [Online]. Available: http://www.opticsexpress.org/-abstract.cfm?URI=oe-23-9-12382. doi: 10.1364/OE.23.012382.

[59] T. Kozu and K. Ohuchi, "Proposal for superposed aco-ofdm using several even subcarriers," in *Signal Processing and Communication Systems (ICSPCS), 2015 9th International Conference on*, Dec 2015, Cairns, Australia, pp. 1–5. doi: 10.1109/ICSPCS.2015.7391762.

[60] Arthur James Lowery, "Comparisons of spectrally-enhanced asymmetrically-clipped optical OFDM systems," Opt. Express 24, 3950-3966 (2016). doi: 10.1364/OE.24.003950.

[61] M. S. Moreolo, R. M. noz, and G. Junyent, "Novel power efficient optical ofdm based on hartley transform for intensity-modulated direct-detection systems," *J. Lightwave Technol.*, vol. 28, no. 5, pp. 798–805, Mar 2010. [Online]. Available: http://-jlt.osa.org/abstract.cfm?URI=jlt-28-5-798. doi: 10.1109/JLT.2010.2040580.

[62] W. Huang, C. Gong, and Z. Xu, "System and waveform design for wavelet packet division multiplexing-based visible light communications," *Lightwave Technology, Journal of*, vol. 33, no. 14, pp. 3041–3051, July 2015. doi: 10.1109/JLT.2015.2418752.

[63] M. Noshad and M. Brandt-Pearce, "Hadamard coded modulation for visible light communications," *Communications, IEEE Transactions on*, vol. PP, no. 99, pp. 1–1, 2016. doi: 10.1109/TCOMM.2016.2520471.

[64] The International Commission on Illumination (CIE), "CIE 1931 Standard Colorimetric Observer," Retrieved from http://www.cie.co.at, Aug. 2008.

[65] R. Drost and B. Sadler, "Constellation design for color-shift keying using billiards algorithms," in *GLOBECOM Workshops (GC Wkshps), 2010 IEEE*, Dec 2010, Miami, USA, pp. 980–984. doi: 10.1109/GLOCOMW.2010.5700472.

[66] E. Monteiro and S. Hranilovic, "Design and implementation of color-shift keying for visible light communications," *Lightwave Technology, Journal of*, vol. 32, no. 10, pp. 2053–2060, May 2014. doi: 10.1109/JLT.2014.2314358.

[67] R. Singh, T. O'Farrell, and J. P. R. David, "An enhanced color shift keying modulation scheme for high-speed wireless visible light communications," *J. Lightwave Technol.*, vol. 32, no. 14, pp. 2582–2592, Jul 2014. [Online]. Available: http://-jlt.osa.org/abstract.cfm?URI=jlt-32-14-2582. doi: 10.1109/JLT.2014.2328866.

[68] J. Jiang, R. Zhang, and L. Hanzo, "Analysis and design of three-stage concatenated color-shift keying," *Vehicular Technology, IEEE Transactions on*, vol. 64, no. 11, pp. 5126–5136, Nov 2015. doi: 10.1109/TVT.2014.2382875.

[69] N. Murata, H. Shimamoto, Y. Kozawa, et al., "Performance evaluation of digital colour shift keying for visible light communications," in *Communication Workshop (ICCW), 2015 IEEE International Conference on*, June 2015, London, UK, pp. 1374–1379. doi: 10.1109/ICCW.2015.7247370.

[70] K.-I. Ahn and J. Kwon, "Color intensity modulation for multicolored visible light communications," *Photonics Technology Letters, IEEE*, vol. 24, no. 24, pp. 2254–2257, Dec 2012. doi: 10.1109/LPT.2012.2226570.

[71] P. Butala, J. Chau, and T. Little, "Metameric modulation for diffuse visible light communications with constant ambient lighting," in *Optical Wireless Communications (IWOW), 2012 International Workshop on*, Oct 2012, Pisa, Italy, pp. 1–3. doi: 10.1109/IWOW.2012.6349697

[72] J. Luna-Rivera, R. Perez-Jimenez, V. Guerra-Yañez, et al., "Combined csk and pulse position modulation scheme for indoor visible light communications," *Electronics Letters*, vol. 50, no. 10, pp. 762–764, May 2014. doi: 10.1049/el.2014.0953.

[73] S. Pergoloni, M. Biagi, S. Colonnese, et al., "Merging color shift keying and complementary pulse position modulation for visible light illumination and communication," in *Euro Med Telco Conference (EMTC),* Nov 2014, Naples, Italy, pp. 1–6. doi: 10.1109/EMTC.2014.6996621.

[74] F. Delgado Rajoì, V. Guerra, J. RabadaÌn Borges, et al., "Color shift keying communication system with a modified ppm synchronization scheme," *IEEE on Photonics Technology Letters*, vol. 26, no. 18, pp. 1851–1854, Sept. 2014. doi: 10.1109/LPT.2014.2337953.

Biographies

Mohamed Sufyan Islim (m.islim@ed.ac.uk) received his BSc (1st Hons) in communications technology engineering in 2009, and MSc (Distinction) in communications engineering from Aleppo University, Syria in 2012. Among several scholarships he was awarded in 2013, he was awarded the Global Edinburgh Scholarship from Edinburgh University, UK. In 2014, he received another MSc (Distinction) in signal processing and communications from Edinburgh University. He was the recipient of the 2014 IEEE Communications Chapter Best Master Project Prize. Currently, he is a PhD student, under the supervision of Professor Harald Haas, at the Li-Fi Research and Development Centre, University of Edinburgh. His research interests include optical OFDM, Li-Fi, and optical wireless communications.

Harald Haas (h.haas@ed.ac.uk) holds the chair for Mobile Communications at the School of Engineering, and is the director of the Li-Fi Research and Development Centre, University of Edinburgh, UK. Professor Haas has been working in wireless communications for 20 years and has held several posts in industry. He was an invited speaker at TED Global in 2011 where he demonstrated and coined 'Li-Fi'. Li-Fi was listed among the 50 best inventions in *TIME Magazine* 2011. Moreover, his work has been covered in other international media such as the *New York Times*, BBC, MSNBC, CNN International, Wired UK, and many more. He is initiator, co-founder and chief scientific officer (CSO) of pureLiFi Ltd. Professor Haas holds 31 patents and has more than 30 pending patent applications. He has published 300 conference and journal papers including a paper in *Science Magazine*. He published two textbooks with Cambridge University Press. His h-index is 43 (Google). In 2015 he was co-recipient of three best paper awards including the IEEE Jack Neubauer Memorial Award. He is CI of programme grant TOUCAN (EP/L020009/1), and CI of SERAN (EP/L026147/1). He currently holds an EPSRC Established Career Fellowship (EP/K008757/1). In 2014, Professor Haas was selected as one of ten EPSRC UK RISE Leaders.

Spectrally Enhanced PAM-DMT for IM/DD Optical Wireless Communications

Mohamed Sufyan Islim, Dobroslav Tsonev and Harald Haas

Li-Fi Research and Development Centre, Institute for Digital Communications
University of Edinburgh, King's Buildings, Mayfield Road, Edinburgh, EH9 3JL, UK
Email: {m.islim, d.tsonev, h.haas}@ed.ac.uk

Abstract—For the same spectral efficiency, pulse-amplitude-modulated discrete multitone modulation (PAM-DMT) has a lower power efficiency in comparison with direct current (DC)-biased optical orthogonal frequency division multiplexing (DCO-OFDM). A power efficient spectrally enhanced PAM-DMT (ePAM-DMT) is proposed in this paper. Superposition modulation of multiple PAM-DMT streams is used to improve the spectral efficiency of PAM-DMT. The ePAM-DMT allows the spectral efficiency gap between DCO-OFDM and other unipolar OFDM schemes to be completely closed. The proposed system is compared with DCO-OFDM in the context of an additive white Gaussian noise (AWGN) channel. A closed-form theoretical bound on the bit error rate (BER) performance of the proposed scheme is derived and verified by Monte Carlo simulations. The proposed scheme is energy efficient in terms of the electrical power consumption. The high optical energy dissipation of the proposed scheme makes it suitable for the illumination-based visible light communications (VLC) applications.

I. INTRODUCTION

As the demand for higher data rate mobile access increases, the limited availability of the electromagnetic spectrum becomes an ever more important challenge. It is predicted that the average smartphone will generate 4 Gigabyte of traffic per month by 2019 [1]. As a solution, the visible light spectrum offers an abundant, available, unregulated communication bandwidth. Visible light communications (VLC) is an emerging technique that is predicted to offer an excess of 100 Gb/s data rates at very high deployment devices in the near future [2]. Light-fidelity (Li-Fi) is the bidirectional, fully networked, high-speed VLC solution for wireless personal area networks (PAN). Also, VLC is a good candidate for other applications, including: indoor positioning; internet of things (IoT); and intelligent transportation systems (ITS) [3].

VLC uses off-the-shelf optoelectronic components as front-end devices. Incoherent intensity modulation and direct detection (IM/DD) is employed as a signalling method. Modulation techniques such as on-off keying (OOK), pulse-position modulation (PPM), and M-ary pulse-amplitude modulation (M-PAM) can be straightforward to implement [4]. However, due to the dispersive nature of the optical wireless communications (OWC) channels, the performance of these schemes degrades as the data rate increases. Optical orthogonal frequency division multiplexing (OFDM) is a good candidate for OWC, since the equalization can be performed using single-tap equalizer. Due to the nature of the OWC channels,

the OFDM signal is required to be real and unipolar. Therefore, Hermitian symmetry is used to enforce the OFDM output into the real domain [5]. The widely deployed direct current (DC)-biased optical OFDM (DCO-OFDM) employs a DC-bias to create a unipolar signal, but this incurs significant energy losses. Unipolar OFDM schemes, such as asymmetrically clipped optical OFDM (ACO-OFDM) [6]; flipped OFDM [7]; and unipolar orthogonal frequency division multiplexing (U-OFDM) [8], offer alternative solutions to address the energy requirements of DCO-OFDM. However, in all these schemes, the spectral efficiency is half that of the DCO-OFDM spectral efficiency. Therefore, the power efficiency advantage of unipolar OFDM schemes in comparison with DCO-OFDM, for the same spectral efficiency, becomes less as the spectral efficiency increases. The pulse-amplitude-modulated discrete multitone modulation (PAM-DMT) is a unipolar OFDM scheme with an equivalent spectral efficiency to DCO-OFDM [9]. In comparison with other unipolar OFDM schemes, PAM-DMT employs M-PAM as a modulation technique. Since the performance of M-PAM is equivalent to M^2-QAM, the power advantage of PAM-DMT also decreases as the spectral efficiency increases.

The enhanced U-OFDM (eU-OFDM) scheme was proposed to compensate for the spectral efficiency loss in U-OFDM by superimposing multiple U-OFDM streams [10]. Due to some implementation complexities, the spectral efficiency gap between eU-OFDM and DCO-OFDM can never be closed completely. The GeneRalizEd ENhancEd UnipolaR OFDM (GREENER-OFDM) was proposed to close the spectral efficiency gap with an appropriate selection of the employed constellation sizes at the different superimposed information streams [11]. In this paper, the concept of GREENER-OFDM is extended to allow multiple streams of PAM-DMT to have a DCO-OFDM equivalent spectral efficiency with lower energy requirements. The proposed scheme is compared with DCO-OFDM in the context of a linear flat additive white Gaussian noise (AWGN) channel.

The rest of this paper is organized as follows. The principles of PAM-DMT are revised in Section II. The concept of superposition modulation for enhanced pulse-amplitude-modulated discrete multitone modulation (ePAM-DMT) and its spectral efficiency analysis are given in Section III. Theoretical bit error rate (BER) performance bound is derived in Section IV and verified in Section V. The optimal sets of constellation

sizes and their corresponding scaling factors are presented in Section V, and the proposed system performance is compared with a spectrally equivalent DCO-OFDM in the same section. Conclusions are given in Section VI.

II. PAM-DMT

In order to realize a unipolar signal, DCO-OFDM employs a DC bias. However, OFDM signals attain a high peak-to-average power ratio (PAPR), which makes it practically impossible to convert all of the signal samples into unipolar ones. Following [12], the DC bias can be defined as a k multiple of the standard deviation of the time-domain OFDM signal σ_s. Therefore, the additional dissipation of electrical power in the DCO-OFDM compared with bipolar OFDM can be written as [12]:

$$B_{\text{DC}}^{\text{dB}} = 10 \log_{10}(k^2 + 1). \tag{1}$$

This power penalty increases as the spectral efficiency increases, which leads to an electrical power inefficiency when DCO-OFDM is used with high M-ary quadrature amplitude modulation (M-QAM) orders.

Unipolar OFDM modulation schemes were mainly introduced to provide energy efficient optical OFDM alternatives to DCO-OFDM. Such schemes exploit the OFDM frame structure to generate a unipolar time domain waveform. Due to the restrictions imposed on their frame structures, all of these schemes have a lower power efficiency when compared with DCO-OFDM for the same spectral efficiency.

In PAM-DMT [9], the subcarriers are loaded with imaginary symbols Z_k: $X[k] = jZ_k$. This restricts the modulation schemes that can be used to M-PAM. Due to the Hermitian symmetry, the PAM-DMT time domain signal $x[n]$ can be written as:

$$\begin{aligned}
x[n] &= \frac{1}{\sqrt{N}} \sum_{k=0}^{N-1} X[k] e^{\frac{j2\pi kn}{N}} \\
&= \frac{1}{\sqrt{N}} \sum_{k=0}^{N-1} jX[k] \sin \frac{2\pi kn}{N} \\
&= \frac{-2}{\sqrt{N}} \sum_{k=1}^{N/2-1} Z_k \sin \frac{2\pi kn}{N}.
\end{aligned} \tag{2}$$

As a result, the time domain OFDM signal $x[n]$ in (2) exhibits an antisymmetry where $x[0] = x[N/2] = 0$, and $x[n] = -x[N-n]$ as illustrated in Fig.1 (a). Following [13], clipping is described as:

$$\text{CLIP}(x(n)) = \frac{(x[n] + |x[n]|)}{2}. \tag{3}$$

Clipping of the negative samples is distortion-less as all of the distortions transform into the real domain of the subcarriers. This is because the distortion term, $|x[n]|$, has a Hermitian symmetry.

III. ENHANCED PAM-DMT

The power efficiency improvement of PAM-DMT over DCO-OFDM decreases and quickly disappears as the constellation size M increases. This is because in an AWGN, M-PAM performs equivalently to M^2-QAM. The situation is similar to U-OFDM and ACO-OFDM. Motivated by this, eU-OFDM was proposed as a unipolar solution to the spectral efficiency loss of other unipolar OFDM schemes [10]. The concept of eU-OFDM is to superimpose multiple streams of U-OFDM waveforms such that the inter-stream interference is zero in the resulted time domain unipolar signal. Achieving a DCO-OFDM equivalent spectral efficiency would require a large number of streams to be superimposed (an infinite number in theory). Due to the computational complexity, practical implementation of eU-OFDM restricts the number of superimposed streams to three. Therefore, in order for the spectral efficiency gap between eU-OFDM and DCO-OFDM to be completely closed, an alternative setting of constellation sizes at the different modulation depths was proposed in [11]. In this paper, the concept of superposition modulation proposed in [10] and [11] is extended to ePAM-DMT for an arbitrary modulation order and an arbitrary power allocation at each depth.

A. Modulation Concept

The main aim of the frame hierarchy design is to convert all of the inter-stream interference into the real component of the frequency subcarriers, so that it becomes distortion-less in the demodulation process at the receiver. A possible arrangement of the multiple PAM-DMT streams is given in Fig.2 (d). The generation process starts with a PAM-DMT modulator at depth-1 where each generated frame is composed of a cyclic prefix, $\text{CP}_{B_{dl}}$, and two subframes, A_{dl} and B_{dl}, where d denotes the depth number, and l denotes the frame number. The bar notation $\overline{F}$ denotes that the subframe F is flipped, *i.e.* $F[n] = \overline{F}[N_F - 1 - n]$, where N_F is the length of F. At depth-2, the information is generated using a PAM-DMT modulator with a smaller OFDM frame size. The frame size at depth-d is given by: $N_d = N_{d-1} - 2N_{\text{CP}} - 2$, $\forall d \geq 2$. The original subframe A_{dl} is combined with the cyclic prefix $\text{CP}_{B_{dl}}$ to form a modified subframe $\widetilde{A_{dl}}$. The modified subframe is flipped and repeated in $\widetilde{\overline{A_{dl}}}$. Therefore, the two modified subframes at depth-2 $\widetilde{A_{dl}}$ and $\widetilde{\overline{A_{dl}}}$ each prefixed with a zero sample form a new frame that is similar in length to the previous depth frames. Moreover, these two modified subframes have a Hermitian symmetry that allows distortion-free inter-stream interference at lower depths. Intuitively this frame needs to be guarded by a cyclic prefix that is identical to the last N_{CP} samples of that frame, $\overline{\text{CP}_{B_{dl}}}$. Therefore, frames at depth-2 need three cyclic prefixes. The first one is intended to guard the modified frames from inter-symbol interference (ISI) at the demodulation process of stream-1. The other two prefixes are intended to guard the original frames from ISI at the demodulation process of stream-2. The subsequent frames in depth-2 are generated in a similar way to the first
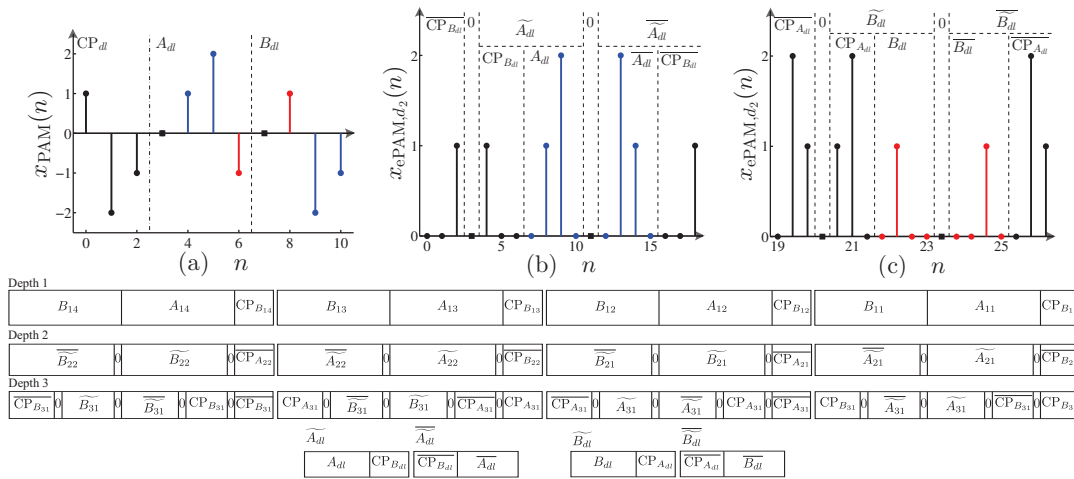
Fig. 1. (a) presents the PAM-DMT time domain waveform and its cyclic prefix before zero clipping. (b) and (c) present two unipolar ePAM-DMT frames at depth-2. (d) presents the complete frame structure arrangement for three information streams. At any depth, the first half of the PAM-DMT frame is denoted as A_{dl}, while B_{dl} denotes the second half of the same PAM-DMT frame. The bar notation $\overline{F}$ refers that the subframe F is flipped $F[n] = \overline{F}[N_F - 1 - n]$, where N_F is the length of F. Modified subframes $\widetilde{A_{dl}}$ and $\widetilde{B_{dl}}$ are shown in the figure alongside their flipped versions $\widetilde{\overline{A_{dl}}}$ and $\widetilde{\overline{B_{dl}}}$, respectively. The subscripts denote that the frame at depth-d belongs to the l-th PAM-DMT frame.

frame. The cyclic prefixes are also designed to preserve both the original and the modified subframes from ISI. The time-domain waveform for the first two frames at depth-2 are shown in Fig.1 (b) and (c). Frames at depth-2 are scaled by $1/\sqrt{2}$ in order to preserve the overall signal energy at this depth. At depth-3, frames are generated in a similar way to depth-2 frames. The frame length is smaller than the previous stream frame length and the cyclic prefixes are designed to create three layers of ISI protection for each of the demodulation processes at the receiver. The information conveyed in depth-3 subframes are repeated four times in a way that preserve the Hermitian symmetry for each demodulation process at higher depths. Frames at depth-3 are scaled by $1/2$ in order to preserve the overall signal energy at this depth. In addition to that, each of the streams is scaled by a parameter $1/\gamma_d$ to facilitate the optimization of the allocated power at that stream. The proposed design requires a maximum of $D = 3$ depths to achieve the spectral efficiency of DCO-OFDM. The complete hierarchy is presented in Fig.1 (d).

At the receiver, the demodulation process starts by removing the first layer of the cyclic prefixes of the ePAM-DMT frames. Afterwards, the information carried at depth-1 can be extracted using a PAM-DMT demodulator. Since all of the streams at higher depths follow a Hermitian symmetry, the inter-stream interference caused by the superposition of multiple PAM-DMT streams affects only the real component of the frequency subcarriers. After the information at depth-1 is demodulated, the recovered bits are remodulated at the receiver in order to reconstruct the information signal at depth-1, which is then subtracted from the overall received ePAM-DMT signal. After the removal of the depth-1 waveform, the second half of each

frame is removed from the ePAM-DMT waveform. The length of the removed subframes is $N_1/2$. Therefore the resulted waveform conveys the depth-2 and depth-3 information but with a hierarchy that is similar to depth-1 and depth-2 as shown in Fig.1 (d). This allows the demodulation process at higher depths to be performed in a similar way to depth-1 demodulation. The inter-stream interference caused by the superposition of multiple PAM-DMT streams is cancelled at the receiver since it only affects the real component of the subcarriers. The multiple cyclic prefixes used at higher-depth streams are intended to protect the inner subframes at each demodulation process and are arranged to preserve the Hermitian symmetry required for this scheme. The demodulation process continues in a similar way for all subsequent streams until the information at all depths is recovered.

B. Spectral Efficiency

The spectral efficiency of PAM-DMT at the first depth is equivalent to the spectral efficiency of DCO-OFDM for the same constellation size and the same frame length. The spectral efficiency of PAM-DMT at depth-d can be given by:

$$\eta_{\text{PAM}}(d) = \frac{\log_2(M_d)(N_d - 2)}{2^d(N_1 + N_{\text{CP}})} \quad \text{bits/s/Hz}, \quad (4)$$

where M_d and N_d are the constellation size and the OFDM frame length at depth-d, respectively, and N_{CP} is the cyclic prefix length. The resolution of constellation sizes that can be used at the different modulation depths of PAM-DMT is a limiting factor. In order to improve the power efficiency, the ePAM-DMT employs multiple streams of PAM-DMT with small constellation sizes. Therefore, the combination

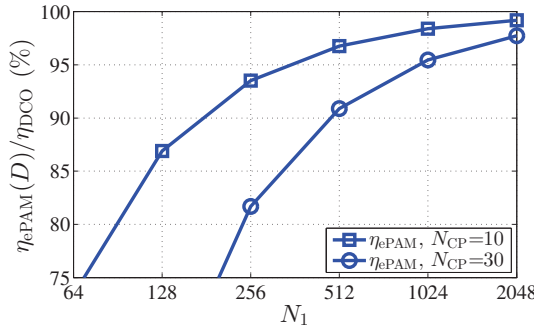Fig. 2. The spectral efficiency of ePAM-DMT, η_{ePAM}, compared to the spectral efficiency of DCO-OFDM, η_{DCO}, as a function of depth-1 frame length N_1 and cyclic prefix length N_{CP}.

IV. THEORETICAL ANALYSIS

The PAM-DMT waveform follows a truncated Gaussian distribution. The mean value of any stream at depth-d can be written as $\text{E}[\text{s}_d(t)] = \phi(0)\sigma_s/(\gamma_d\sqrt{2^{d-1}})$ where $1/\gamma_d$ is a scaling parameter at depth-d; σ_s^2 is twice the average electrical power of the unscaled PAM-DMT signal at the same depth; and $\phi(x)$ is the probability density function (pdf) of the standard normal distribution. The average power of the ePAM-DMT waveform can be expressed as [11]:

$$P_{\text{elec}}^{\text{avg}}(D, \underline{\gamma}) = \text{E}\left[\text{s}^2(t)\right] = \text{E}\left[\left(\sum_{d=1}^{D} \text{s}_d(t)\right)^2\right]$$

$$= \sigma_s^2 \left(\sum_{d=1}^{D} \frac{\gamma_d^{-2}}{2^d} + 2\phi^2(0) \sum_{d_1=1}^{D} \sum_{\substack{d_2=1 \\ d_1 \neq d_2}}^{D} \frac{(\gamma_{d_1}\gamma_{d_2})^{-1}}{\sqrt{2^{d_1+d_2}}} \right), \quad (8)$$

where $\text{s}(t)$ is the time domain ePAM-DMT waveform; $\text{s}_d(t)$ is the time domain PAM-DMT at depth d; and $\underline{\gamma} = \{\gamma_d^{-1}; d = 1, 2, \ldots, D\}$ is the set of scaling factors applied to each corresponding stream. The power is allocated to each stream so that the average power of the modulation signal satisfies the following two constraints:

$$P_{\text{elec}}^{\text{avg}}(D, \underline{\gamma}) \leq P_{\text{elec}}^{\text{avg}}(D, \mathbf{1}_{1 \times D}),$$
$$P_{\text{opt}}^{\text{avg}}(D, \underline{\gamma}) \leq P_{\text{opt}}^{\text{avg}}(D, \mathbf{1}_{1 \times D}), \quad (9)$$

where $P_{\text{opt}}^{\text{avg}}(D, \underline{\gamma})$ is average optical power of the ePAM-DMT waveform. It can be given by [11]:

$$P_{\text{opt}}^{\text{avg}}(D, \underline{\gamma}) = \sum_{d=1}^{D} \text{E}[\text{s}_d(t)] = \phi(0)\sigma_s \sum_{d=1}^{D} \frac{\gamma_d^{-1}}{\sqrt{2^{d-1}}}. \quad (10)$$

The ratio of the average electrical power of a ePAM-DMT waveform to the average electrical power of a PAM-DMT stream at depth-d, $P_{\text{elec},d}^{\text{avg}}(\gamma_d)$, is given by:

$$\alpha_{\text{elec}}^P(D, \underline{\gamma}) = \frac{P_{\text{elec}}^{\text{avg}}(D, \underline{\gamma})}{P_{\text{elec},d}^{\text{avg}}(\gamma_d)}. \quad (11)$$

The increase in the dissipated electrical energy per bit in ePAM-DMT compared with the electrical energy dissipation per bit in PAM-DMT stream at depth-d is given by the ratio of (11) to (7):

$$\alpha_{\text{elec}}^{\text{ePAM}}(D, d, \underline{\gamma}) = \frac{\alpha_{\text{elec}}^P(D, \underline{\gamma})}{\alpha_\eta^{\text{ePAM}}(D, d)}. \quad (12)$$

A theoretical bound on the BER performance of the ePAM-DMT streams is derived using the formula for the BER performance of real bipolar M-QAM OFDM [14]. The achieved electrical SNR at the receiver should be scaled by a factor of $1/2$ to account for the SNR loss in M-PAM, and by a factor of $1/\alpha_{\text{elec}}^{\text{ePAM}}(D, d)$ to account for the electrical signal-to-noise ratio (SNR) penalty in ePAM-DMT. An additional scaling factor of $1/2^{d-1}$ is required, since half of the frames are removed in the demodulation process at each depth. Although

of constellation sizes are required to follow the following constraint:

$$\log_2(M_{\text{DCO}}) = 2 \sum_{d=1}^{D} \frac{\log_2(M_d)}{2^d}. \quad (5)$$

The spectral efficiency of ePAM-DMT is given as the sum of the spectral efficiencies at the individual PAM-DMT streams. It can be written as:

$$\eta_{\text{ePAM}}(D) = \sum_{d=1}^{D} \eta_{\text{PAM}}(d)$$

$$= \sum_{d=1}^{D} \frac{\log_2(M_d)\left(N_1 - 2 - 2(N_{\text{CP}} + 1)(d - 1)\right)}{2^d(N_1 + N_{\text{CP}})}. \quad (6)$$

Since multiple cyclic prefixes are required to compact the ISI effects, the spectral efficiency of ePAM-DMT cannot match the spectral efficiency of DCO-OFDM exactly. The spectral efficiency ratio of ePAM-DMT and DCO-OFDM is a function of the combination of constellation sizes used. Among all of the possible sets of constellation sizes obtained in this paper, the worst case scenario is presented in Fig.2. The spectral efficiency ratio is shown as a function of the OFDM frame and cyclic prefixes lengths. It is shown that $\eta_{\text{ePAM}}(D)$ is higher than 90% of η_{DCO} for all of the presented cyclic prefix lengths when the frame size $N_1 \geq 512$.

The spectral efficiency ratio of the ePAM-DMT to a PAM-DMT scheme with a similar constellation size can be expressed as:

$$\alpha_\eta^{\text{ePAM}}(D, d) = \frac{\eta_{\text{ePAM}}(D)}{\eta_{\text{PAM}}(d)}$$

$$= \frac{\sum_{\hat{d}=1}^{D} \log_2(M_{\hat{d}})(N_{\hat{d}} - 2)/2^{\hat{d}}}{\log_2(M_d)(N_1 - 2)/2}, \quad (7)$$

where D is the total number of depths, and N_1 is the size of the OFDM frame at depth-1.

this could be avoided in AWGN channels, here it has been considered to expand the versatility of the proposed system. The theoretical bound on the BER performance of ePAM-DMT can be expressed as:

$$\text{BER}_{(D,d,\underline{\gamma})} \cong \frac{2}{\log_2(M_d)} \left(1 - \frac{1}{M_d}\right) \times$$
$$\sum_{l=1}^{R} Q\left((2l-1)\sqrt{\frac{6E_{\text{b,elec}}/N_o \log_2(M_d)}{2^d \alpha_{\text{elec}}^{\text{ePAM}}(D,d)(M_d^2-1)}}\right), \quad (13)$$

where $E_{\text{b,elec}}/N_o$ is the electrical SNR of real bipolar OFDM, and $R = \min(2, \sqrt{M_d})$.

The BER performance at higher depths is affected by the BER performance of the lower depths. Any incorrectly decoded bit at lower order depths translates into more distortion in all subsequent streams. The presented solution does not include the effects of the distortion caused by incorrectly decoded bits at preceding streams, which underestimate the BER at certain SNR values. However, for high SNR values, this error propagation effect is assumed to be insignificant due to the low BER expected at each stream, and the proposed bounds are expected to be close to the actual BER performance at each depth. A closed-form bound on the average BER performance of the overall ePAM-DMT scheme can be obtained by considering the spectral contribution of each individual stream. The BER bounds for each stream, given in (13), are weighted by their contribution to the overall spectral efficiency. The average BER performance can then be expressed as:

$$\text{BER} \cong \sum_{d=1}^{D} \left(\frac{\text{BER}_{(D,d,\underline{\gamma})}}{\alpha_\eta^{\text{ePAM}}(D,d)}\right). \quad (14)$$

The BER performance bound as a function of the optical SNR can be obtained by inserting the ratio of (10) and (8) into (14).

V. SIMULATION RESULTS

The optimal combinations of constellation sizes and their corresponding scaling factors for ePAM-DMT are obtained using both the theoretical model and Monte Carlo simulations. In addition, the performance of the optimum configurations in ePAM-DMT are compared with the performance of a spectrally equivalent DCO-OFDM in a linear AWGN channel. The only non-linear effect considered is the negative clipping of the modulation signal due to the characteristics of the ideal light emitting diode (LED). The non-flat channel effects on the proposed scheme would be equivalent to the same effects on any other conventional OFDM scheme. Therefore, the performance of the proposed scheme in frequency selective channels is not required for comparison purposes. The DCO-OFDM optimum bias level for the different M-QAM DCO-OFDM is estimated using Monte Carlo simulations [15]. Results are presented for BER values down to 10^{-4} since most of the forward error correction (FEC) codes would be able to maintain a reliable communication link at such BER values [16]. The negative values for the scaling factor denote
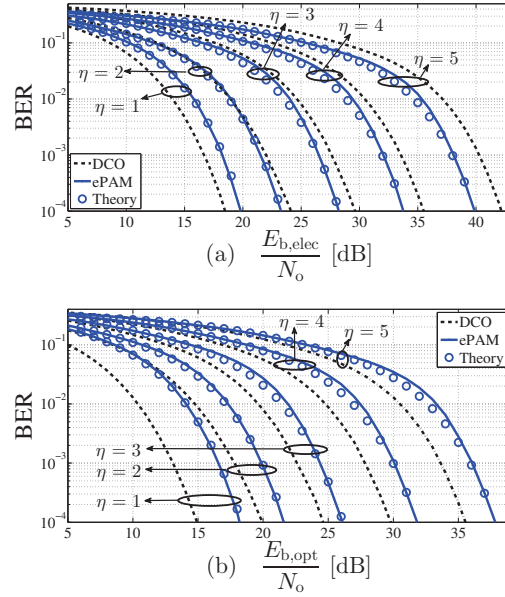
Fig. 3. The performance comparison of ePAM-DMT and DCO-OFDM for different spectral efficiencies in an AWGN channel as a function of (a) electrical SNR, and (b) optical SNR. The value of η is given in bits/s/Hz. Optimum biasing levels for DCO-OFDM at $\eta = \{1, 2, 3, 4, 5\}$ are estimated through Monte Carlo simulations at respectively 6 dB, 7.5 dB, 9.5 dB, 11 dB, 13 dB as described in (1). The theoretical results for the first depth of ePAM-DMT are plotted as a lower bound on the BER performance.

that the corresponding streams are amplified, and similarly, the positive values denote that the corresponding streams are attenuated [11].

Since the performance of $\sqrt{M}$-PAM is equivalent to the performance of M-QAM, the resolution of the possible constellation sizes at each depth is limited. The performances of non-square constellation sizes of M-QAM cannot be achieved using $\sqrt{M}$-PAM. Fig. 3 presents the BER performance of ePAM-DMT and DCO-OFDM as a function of electrical and optical SNR. In comparison with DCO-OFDM, ePAM-DMT is more energy efficient in terms of electrical SNR and less energy efficient in terms of optical SNR. Higher optical energy dissipation is a desirable property for illumination based VLC applications. However, it is considered as a disadvantage for dimmable-based VLC applications. At a spectral efficiency of $\eta = 1$ bit/s/Hz, the energy dissipation of 4-QAM DCO-OFDM is shown to be better than {2,4}-PAM scaled at {5.2,-4} dB with 1.35 dB for the electrical SNR and 3.27 dB for the optical SNR. In comparison with 16-QAM DCO-OFDM at $\eta = 2$ bit/s/Hz, the electrical energy efficiency improvement of {8,4}-PAM scaled at {-1,2.2} dB is 1.1 dB, while the optical energy efficiency loss is 1.65 dB. At $\eta = 3$ bits/s/Hz, {16,8,4}-PAM scaled at {-1.7,1.3,4.5} dB is more efficient in terms of

TABLE I

THE OPTIMAL COMBINATION OF CONSTELLATION SIZES AND SCALING
FACTORS FOR ENHANCED PAM-DMT, WHERE M_d AND γ_d DENOTE THE
CONSTELLATION SIZE AND THE SCALING FACTOR FOR THE MODULATION
DEPTH-d, RESPECTIVELY.

DCO-OFDM	ePAM-DMT		η
M_{DCO}-QAM	$\{M_1, M_2, ..., M_D\}$-PAM	γ [dB]	[b/s/Hz]
8-QAM	$\{4,4\}$-PAM	$\{1.1,-1.4\}$	1.5
32-QAM	$\{8,8,4\}$-PAM	$\{0.7,-1.7,1.5\}$	2.5
128-QAM	$\{32,8,4\}$-PAM	$\{-3,5.6,8.8\}$	3.5
512-QAM	$\{64,16,16\}$-PAM	$\{-2.6,5.9,3.2\}$	4.5

the electrical energy dissipation with 1.5 dB and less efficient in terms of the optical energy dissipation with 2.1 dB compared with 64-QAM DCO-OFDM. At $\eta = 4$ bits/s/Hz and by comparison with 256-QAM DCO-OFDM, $\{32,16,16\}$-PAM scaled at $\{-0.8,2,-0.5\}$ dB is more energy efficient in terms of electrical energy saving with 1.75 dB, and less efficient in terms of optical energy dissipation with 2 dB. At higher spectral efficiency $\eta = 10$ bits/s/Hz, $\{64,64,16\}$-PAM scaled at $\{0.2,-2.4,6.3\}$ dB is more efficient in terms of electrical energy savings with 2.3 dB gain, and less efficient in terms of optical energy consumption with 2.3 dB loss. The theoretical curves show the BER performance obtained for depth-1 using (13). The BER performance of the first depth provides a lower bound on the BER performance of the proposed scheme. The theoretical curves of the BER performance approximate the actual BER results for all cases. The propagation error is apparent at some SNR values, however, the theoretical BER analysis matches the numerical simulations at higher SNR values and they are always lower than the actual BER values. The optimal combinations of constellation sizes for other spectral efficiency values are given in Table I.

VI. CONCLUSION

Superposition modulation of multiple unipolar streams of PAM-DMT is proposed in this paper. The spectral efficiency of the proposed ePAM-DMT is approximately the same as the spectral efficiency of DCO-OFDM. The optimal combinations of constellation sizes at each depth and their corresponding scaling factors have been determined at different spectral efficiencies. A closed form theoretical bound on the BER performance of the proposed scheme is derived and verified in comparisons with Monte Carlo simulations. The proposed scheme is shown to be more efficient in terms of the electrical energy consumption and less efficient in terms of optical energy dissipation when compared with DCO-OFDM in the context of a line-of-sight (LoS) AWGN channel. The proposed scheme attains a high optical energy dissipation for less electrical power consumption, which makes it very suitable for illumination-based VLC applications. Future studies will extend and compare the superposition modulation for all unipolar OFDM-based optical wireless communications in more realistic VLC channels.

REFERENCES

[1] Cisco Visual Networking Index, "Global Mobile Data Traffic Forecast Update, 2014-2019," CISCO, White Paper, Feb. 2015. [Online]. Available: http://www.cisco.com/c/en/us/solutions/collateral/service-provider/visual-networking-index-vni/white_paper_c11-520862.pdf

[2] D. Tsonev, S. Videv, and H. Haas, "Towards a 100 Gb/s Visible Light Wireless Access Network," *Opt. Express*, vol. 23, no. 2, pp. 1627–1637, Jan 2015. [Online]. Available: http://www.opticsexpress.org/abstract.cfm?URI=oe-23-2-1627

[3] H. Burchardt, N. Serafimovski, D. Tsonev, S. Videv, and H. Haas, "VLC: Beyond Point-to-Point Communication," *Communications Magazine, IEEE*, vol. 52, no. 7, pp. 98–105, July 2014.

[4] J. M. Kahn and J. R. Barry, "Wireless Infrared Communications," *Proc. IEEE*, vol. 85, no. 2, pp. 265–298, Feb. 1997.

[5] J. B. Carruthers and J. M. Kahn, "Multiple-subcarrier Modulation for Nondirected Wireless Infrared Communication," *IEEE Journal on Selected Areas in Communications*, vol. 14, no. 3, pp. 538–546, Apr. 1996.

[6] J. Armstrong and A. Lowery, "Power Efficient Optical OFDM," *Electronics Letters*, vol. 42, no. 6, pp. 370–372, Mar. 16, 2006.

[7] N. Fernando, Y. Hong, and E. Viterbo, "Flip-OFDM for Unipolar Communication Systems," *IEEE Transactions on Communications*, vol. 60, no. 12, pp. 3726–3733, Dec. 2012.

[8] D. Tsonev, S. Sinanović, and H. Haas, "Novel Unipolar Orthogonal Frequency Division Multiplexing (U-OFDM) for Optical Wireless," in *Proc. of the Vehicular Technology Conference (VTC Spring)*, IEEE. Yokohama, Japan: IEEE, May 6–9 2012.

[9] S. C. J. Lee, S. Randel, F. Breyer, and A. M. J. Koonen, "PAM-DMT for Intensity-Modulated and Direct-Detection Optical Communication Systems," *IEEE Photonics Technology Letters*, vol. 21, no. 23, pp. 1749–1751, Dec. 2009.

[10] D. Tsonev and H. Haas, "Avoiding Spectral Efficiency Loss in Unipolar OFDM for Optical Wireless Communication," in *Proc. of the International Conference on Communications (ICC)*. Sydney, Australia: IEEE, Jun., 10–14 2014.

[11] M. Islim, D. Tsonev, and H. Haas, "A Generalized Solution to the Spectral Efficiency Loss in Unipolar Optical OFDM-based Systems," in *Proc. of the International Conference on Communications (ICC)*. London, UK: IEEE, Jun., 8–12 2015.

[12] J. Armstrong and B. J. C. Schmidt, "Comparison of Asymmetrically Clipped Optical OFDM and DC-Biased Optical OFDM in AWGN," *IEEE Commun. Lett.*, vol. 12, no. 5, pp. 343–345, May 2008.

[13] D. Tsonev, S. Sinanovic, and H. Haas, "Complete Modeling of Nonlinear Distortion in OFDM-based Optical Wireless Communication," *J. Lightw. Technol.*, vol. 31, no. 18, pp. 3064–3076, Sep. 15 2013.

[14] F. Xiong, *Digital Modulation Techniques*, 2nd ed. Artech House Publishers, 2006.

[15] S. Dimitrov, S. Sinanovic, and H. Haas, "Clipping Noise in OFDM-Based Optical Wireless Communication Systems," *IEEE Transactions on Communications*, vol. 60, no. 4, pp. 1072–1081, April 2012.

[16] ITU-T, "Forward error correction for high bit-rate DWDM submarine systems," ITU, Tech. Rep. ITU-T G.975.1, Retrieved Nov. 19, 2013 from http://www.itu.int/rec/T-REC-G.975.1-200402-I/en, 2004.

On the Superposition Modulation for OFDM-based Optical Wireless Communication

Mohamed Sufyan Islim, Dobroslav Tsonev and Harald Haas

Li-Fi Research and Development Centre, Institute for Digital Communications
University of Edinburgh, King's Buildings, Mayfield Road, Edinburgh, EH9 3JL, UK
Email: {m.islim, d.tsonev, h.haas}@ed.ac.uk

Abstract—Inherent unipolar orthogonal frequency division multiplexing (OFDM) schemes have a reduced spectral efficiency (SE) when compared with direct current (DC)-biased optical OFDM (DCO-OFDM). The concept of superposition modulation was proposed as a solution to the SE loss of unipolar orthogonal frequency division multiplexing (U-OFDM) and the power efficiency loss of pulse-amplitude-modulated discrete multitone modulation (PAM-DMT). In this paper, we demonstrate that the superposition modulation can also be applied to asymmetrically clipped optical OFDM, and we refer to it as enhanced asymmetrically clipped optical OFDM (eACO-OFDM). The eACO-OFDM results in a new power and spectrally efficient scheme for intensity modulation and direct detection (IM/DD) systems. The bit error ratio (BER) performance of the proposed scheme is derived and obtained results agree with Monte Carlo simulations. The performance of the superposition OFDM-based modulation schemes is compared and presented for both additive white Gaussian noise (AWGN) and non-flat visible light communication (VLC) channels.

I. INTRODUCTION

The demand for wireless communication capacity is rapidly increasing. Monthly global mobile data traffic will exceed 24.3 exabytes by 2019 [1]. However, the radio frequency (RF) spectrum is a limited resource. The visible light spectrum offers licence-free bandwidth that can meet these increasing capacity demands. Therefore, visible light communication (VLC) is a promising technique that offers significant energy and cost savings, physical-link level security, and high speed communication links.

VLC employs off-the-shelf light emitting diodes (LEDs) and photodiodes (PDs) as channel front-end devices. The communication signals are restricted to intensity modulation and direct detection (IM/DD) signals. Orthogonal frequency division multiplexing (OFDM) is a good candidate for optical wireless communications due to the simplicity of the single-tap equalizer at the receiver [2]. Hermitian symmetry is generally imposed on the OFDM input frame to enforce the OFDM modulator output to be real. The widely deployed direct current (DC)-biased optical OFDM (DCO-OFDM) uses a DC bias to realize a unipolar signal [3]. However, OFDM signals attain a high peak-to-average power ratio (PAPR) which makes it impossible to convert all of the signal samples into unipolar samples. Following [4], the DC bias is defined as k_M multiple of the standard deviation of the time-domain OFDM signal σ_s,

where M is the M-ary quadrature amplitude modulation (M-QAM) modulation order. Therefore, the dissipation of electrical power in DCO-OFDM compared with bipolar OFDM can be written as [4]:

$$B_{\text{DC}}^{\text{dB}} = 10 \log_{10}(k_M^2 + 1). \tag{1}$$

This power penalty increases as the modulation order, M, increases, in order to ensure an equivalent lower clipping distortion for all the modulation orders. Unipolar OFDM modulation schemes were introduced to provide an energy efficient alternative to DCO-OFDM. Schemes such as: ACO-OFDM [5]; pulse-amplitude-modulated discrete multitone modulation (PAM-DMT) [6]; flipped OFDM [7]; and unipolar orthogonal frequency division multiplexing (U-OFDM) [8] exploit the OFDM input/output frame structure to realize a unipolar output. However, due to the restrictions imposed on their frame structures, the performance of M-QAM DCO-OFDM, should be compared to M^2-QAM {ACO-OFDM; U-OFDM; flipped-OFDM}, and M-PAM PAM-DMT. Therefore, the power efficiency of these schemes become gradually inefficient as the modulation order, M, increases. Enhanced U-OFDM (eU-OFDM) was proposed as an energy efficient solution to the SE loss of U-OFDM [9]. The concept of eU-OFDM is to superimpose multiple streams of U-OFDM waveforms so that the inter-stream-interference is distortion-less. The SE of each additional stream decreases exponentially as the total number of streams increases. Therefore, achieving a SE equivalent to DCO-OFDM would require a large number of streams to be superimposed. However, due to the computational complexity and memory requirements, practical implementation limits the number of superimposed streams to three typically [10]. Alternatively, different configuration arrangements were exploited in GeneRalizEd ENhancEd UnipolaR OFDM (GREENER-OFDM) to close the SE gap between U-OFDM and DCO-OFDM [11]. In [12], enhanced pulse-amplitude-modulated discrete multitone modulation (ePAM-DMT) was proposed as a superposition modulation for PAM-DMT. In this paper enhanced asymmetrically clipped optical OFDM (eACO-OFDM) is proposed as a power efficient solution to the SE loss of ACO-OFDM. It uses superposition modulation to achieve performance gains. The performance of all of the superposition OFDM-based modulation schemes is compared
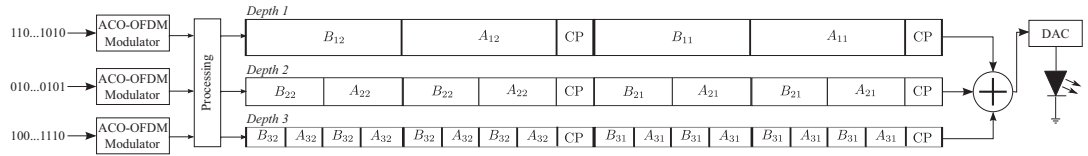
Fig. 1. Illustration of the eACO-OFDM concept with three information streams. CP denotes the cyclic prefix. Subframe A_{dl} represents the first half of unipolar frame, and subframe B_{dl} represents the second half of the unipolar frame. The subscripts denote that the frame at depth-d belongs to the l-th ACO-OFDM frame.

for both the additive white Gaussian noise (AWGN) channel and the non-flat dispersive VLC channel.

A review of ACO-OFDM is given in Section II. The modulation concept and the SE of eACO-OFDM are discussed in Section III. The theoretical analysis is derived in Section IV, and the simulation results and the system comparison are presented in Section V. Conclusions are given in Section VI.

II. ACO-OFDM

The ACO-OFDM scheme exploits the Fourier transformation properties to realize a unipolar signal. If only odd-indexed sub-carriers are loaded with information, the OFDM waveform would have the following property:

$$x[n] = -x[n + N/2], \qquad (2)$$

where N is the OFDM frame size. Similarly, if only the even-indexed sub-carriers are used, then the OFDM waveform would have the following property:

$$x[n] = x[n + N/2] \qquad (3)$$

A symmetric time domain waveform that follows (2) is achieved in ACO-OFDM [5]. As a result, clipping of the negative values is distortion-less due to the symmetry and all of the distortion will affect the even-indexed sub-carriers. However, skipping half of the sub-carriers results in reducing the SE of ACO-OFDM to half of that in DCO-OFDM. A scaling factor of $\sqrt{2}$ is required to normalize the power as the clipped signal is half of that in the bipolar signal. Therefore, a penalty of 3 dB is applied to the signal-to-noise ratio (SNR) of ACO-OFDM when compared with bipolar OFDM.

III. ENHANCED ACO-OFDM

A. Modulation Concept

The symmetry in U-OFDM lies in frames, while in ACO-OFDM and PAM-DMT, it lies in subframes. The main objective of the frame hierarchy design is to convert all of the inter-stream-interference of the superimposed streams into the even-indexed sub-carriers at the frequency domain, so that it becomes distortion-less. A possible arrangement of the multiple ACO-OFDM signals is given in Fig. 1. The eACO-OFDM signal generation starts at the first depth with a conventional ACO-OFDM modulator. The subframes are defined to be half of the original ACO-OFDM frames in length and they are the basic elements of eACO-OFDM streams. At depth-2, a second ACO-OFDM stream is superimposed on the first stream and

generated in a similar fashion to depth-1, the OFDM frame length at depth-2 is $N_2 = N_{\mathrm{FFT}}/2$, where N_{FFT} is the OFDM frame length at depth-1. The overall stream at depth-2 is scaled by $1/\sqrt{2}$ in order to preserve the overall signal energy at this depth. Furthermore, ACO-OFDM streams are superimposed at depth-d with an OFDM frame length $N_d = N_{\mathrm{FFT}}/2^{d-1}$ in a similar way as depth-2 and the overall stream at that depth is scaled by $1/\sqrt{2^{d-1}}$. In addition, each of the streams is scaled by a parameter $1/\gamma_d$ to facilitate the optimization of the allocated power to that stream. At the receiver, the demodulation process starts with removing the cyclic prefixes. Then the information carried at depth-1 can be extracted using a traditional ACO-OFDM demodulator. The subframes in each individual frame are symmetric at depth-1. Therefore the information stream at this depth follows (2). At higher depths, the subframes in each individual frame are identical. Therefore the information stream at this depth follows (3). As a result, the odd-indexed sub-carriers only convey the depth-1 information, and the inter-stream-interference falls into the even-indexed sub-carriers. After the information at depth-1 is demodulated, the recovered bits are remodulated at the receiver in order to reconstruct the depth-1 stream, which is then distorted using the channel response and subtracted from the overall eACO-OFDM signal. After the removal of the depth-1 waveform, each two identical subsequent subframes are summed. The demodulation process at depth-2 continues with the conventional ACO-OFDM demodulation process and the recovered bits are remodulated in order to allow for the information stream at depth-2 to be subtracted from the overall received information signal. The demodulation process continues in a similar way for all subsequent streams until the information at the last depth is recovered.

B. Spectral Efficiency

The spectral efficiency of eACO-OFDM is given as the sum of the spectral efficiencies of all ACO-OFDM streams:

$$\eta_{\mathrm{eACO}}(D) = \sum_{d=1}^{D} \eta_{\mathrm{ACO}}(d) \quad \text{bits/s/Hz}, \qquad (4)$$

where $\eta_{\mathrm{ACO}}(d)$ is the SE of ACO-OFDM at depth-d:

$$\eta_{\mathrm{ACO}}(d) = \frac{\log_2(M_d)(N_d)}{4(N_1 + N_{\mathrm{CP}})} \quad \text{bits/s/Hz}, \qquad (5)$$

where M_d is the constellation size at depth-d. In order for the SE of eACO-OFDM to match that of DCO-OFDM, the
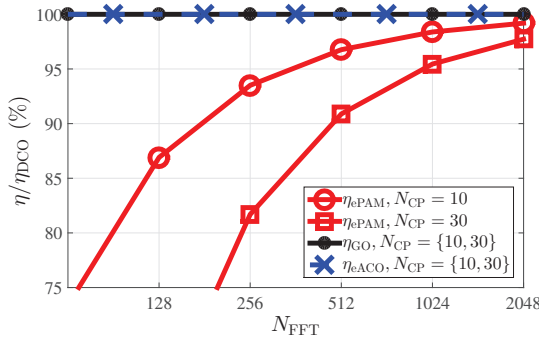
Fig. 2. The spectral efficiency of eACO-OFDM (η_{eACO}), ePAM-DMT (η_{ePAM}), and GREENER-OFDM (η_{GO}) compared to the spectral efficiency of DCO-OFDM (η_{DCO}), as a function of the frame length N and cyclic prefix length N_{CP}.

following criterion should be fulfilled [11]:

$$\log_2(M_{\text{DCO}}) = \sum_{d=1}^{D} \frac{\log_2(M_d)}{2^d}, \tag{6}$$

where M_{DCO} is the constellation size of M_{DCO}-QAM DCO-OFDM. The SE of eACO-OFDM and GREENER-OFDM, η_{GO}, is exactly equivalent to η_{DCO} for any cyclic prefix length. However, The spectral efficiency of ePAM-DMT can never match the spectral efficiency of DCO-OFDM, since multiple cyclic prefixes are employed at higher order depths of ePAM-DMT. This trend is shown in Fig. 2 as a function of the OFDM frame and cyclic prefixes lengths. It is shown that the spectral efficiency of ePAM-DMT, η_{ePAM}, exceeds 90% of η_{DCO} for all of the presented cyclic prefix lengths when the frame size $N \geq 512$.

IV. THEORETICAL ANALYSIS

The VLC channel model is given by:

$$\mathbf{y} = \mathbf{H}\mathbf{x} + \mathbf{w}, \tag{7}$$

where $\mathbf{x}$ and $\mathbf{y}$ are the transmitted and received superposition-modulated time domain waveforms; $\mathbf{w} = \{w_i; i = 0, 1, ..., N-1\}$ is the AWGN samples, $w_i \sim \mathcal{N}(0, N_o)$, where N_o is the double-sided power spectral density (PSD) of the noise at the receiver; and $\mathbf{H}$ is a $N \times N$ circulant convolution channel matrix with the first column representing the channel impulse response $\mathbf{h} = [h_0, h_1, ..., h_L, 0, ..., 0]^{\text{T}}$, where L is the number of channel taps. The channel matrix $\mathbf{H}$ can be diagonalized as:

$$\mathbf{H} = \mathbf{F}^* \mathbf{\Lambda} \mathbf{F}, \tag{8}$$

where $\mathbf{F}$ is an $N \times N$ discrete Fourier transform (DFT) matrix, and $\mathbf{\Lambda}$ is an $N \times N$ diagonal matrix with the eigenvalues of the channel $\mathbf{\Lambda} = [\Lambda_0, \Lambda_1, ..., \Lambda_N]^{\text{T}}$.

ACO-OFDM, PAM-DMT and U-OFDM waveforms follow a truncated Gaussian distribution. Therefore, the statistics of

these schemes are identical. The statistics of their superposition forms are also identical. The power is allocated to each stream so that the average electrical and optical power of the modulation signal satisfy the following constraint:

$$P_{\text{elec}}^{\text{avg}}(D, \underline{\gamma}) \leq P_{\text{elec}}^{\text{avg}}(D, \mathbf{1}_{1 \times D}),$$
$$P_{\text{opt}}^{\text{avg}}(D, \underline{\gamma}) \leq P_{\text{opt}}^{\text{avg}}(D, \mathbf{1}_{1 \times D}), \tag{9}$$

where $\underline{\gamma} = \{\gamma_d^{-1}; d = 1, 2, ..., D\}$ is the set of scaling factors applied to each corresponding stream; $P_{\text{elec}}^{\text{avg}}(D, \underline{\gamma})$ and $P_{\text{opt}}^{\text{avg}}(D, \underline{\gamma})$ are the average electrical and optical power for the superposition-modulated OFDM-based waveform, respectively.

A theoretical bound on the bit error ratio (BER) performance of the superposition-modulated streams can be derived using the formula for the BER performance of real bipolar M-QAM-OFDM [13]. For eACO-OFDM, the achieved electrical SNR at the receiver should be scaled by a factor of $1/2$ to account for the SNR loss in ACO-OFDM, and by $1/\alpha_{\text{elec}}^{\text{eACO}}(D, d)$ to account for the electrical SNR penalty in eACO-OFDM, where $\alpha_{\text{elec}}^{\text{eACO}}(D, d)$ denotes the increase in the dissipated electrical energy per bit in eACO-OFDM compared with the electrical energy dissipation per bit in ACO-OFDM stream at depth-d [11]. A multipath dispersive VLC channel is adopted [14, Fig. 3] and a zero-forcing equalizer is used for simplicity as the objective is to prove the validity of superposition OFDM-based schemes in non-flat channels. The BER performance at depth-d can be expressed as:

$$\text{BER}_{(D,d,\underline{\gamma})}^{\text{eACO}} \cong \frac{4}{\log_2(M_d)} \left(1 - \frac{1}{\sqrt{M_d}}\right) \times$$
$$\sum_{l=1}^{R} \sum_{k=1}^{N} \text{Q}\left((2l-1)\sqrt{\frac{3|\Lambda_k|^2 E_{\text{b,elec}} \log_2(M_d)}{2\alpha_{\text{elec}}^{\text{eACO}}(D, d)(M_d - 1)N_{\text{o}}}}\right), \tag{10}$$

where $E_{\text{b,elec}}/N_{\text{o}}$ is the SNR of real bipolar OFDM, and $R = \min(2, \sqrt{M_d})$. For flat channels, $\mathbf{\Lambda} = I_N$.

The BER performance at higher depths is affected by the BER performance of the streams at the lower depths. Any incorrectly decoded bit at lower order depths translates into more distortion for all subsequent streams. The presented solution does not include the effects of the error propagation due to errors in preceding streams which results in an underestimation of the BER at low SNR values. However, for high SNR values, this error propagation effect is assumed to be insignificant due to the low BER expected at each stream. A closed-form bound on the average BER performance of the overall eACO-OFDM scheme can be obtained by considering the spectral contribution of each individual stream to the overall BER. The average BER performance can then be expressed as:

$$\text{BER}^{\text{eACO}} \cong \sum_{d=1}^{D} \left(\text{BER}_{(D,d,\underline{\gamma})}^{\text{eACO}} \xi_d\right), \tag{11}$$

where ξ_d is the effective spectral contribution of the stream at depth-d to the overall SE. The BER performance bound as a function of the optical SNR can be obtained by inserting
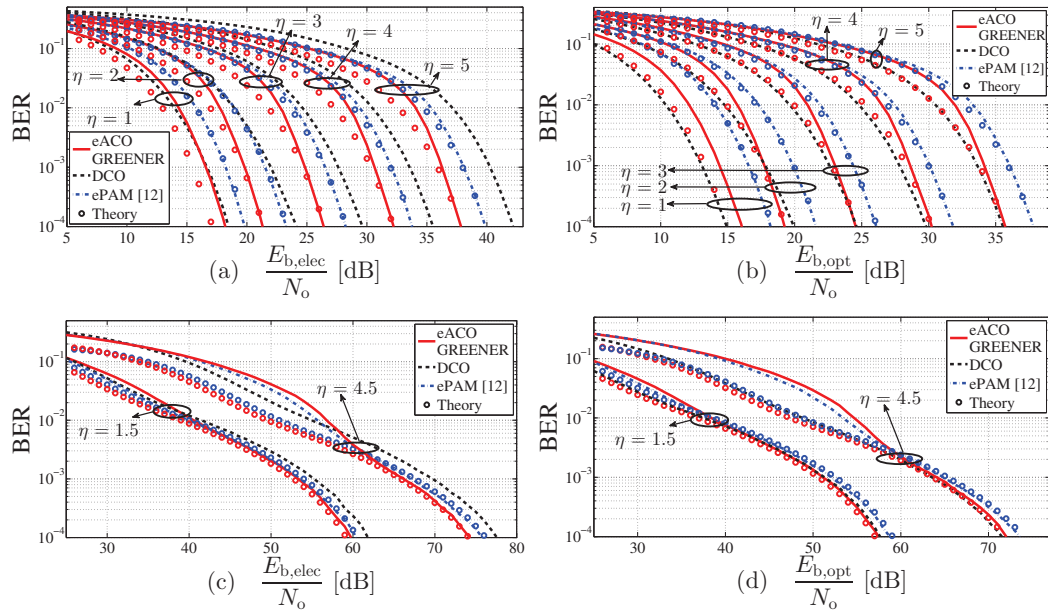
Fig. 3. The BER performance of eACO-OFDM versus ePAM-DMT versus GREENER-OFDM versus DCO-OFDM for different spectral efficiencies, in both AWGN channel (a and b) and dispersive channel (c d), as a function of electrical SNR, and optical SNR. The value of η is given in bits/s/Hz. DC bias levels for DCO-OFDM at $\eta = \{1, 1.5, 2, 3, 4, 4.5, 5\}$ are estimated through Monte Carlo simulations at respectively 6, 7, 7.5, 9.5, 11, 12, and 13 dB as described in (1).

the ratio of average optical power to the the average electrical power, defined in [11], into (10).

V. SIMULATION RESULTS

The optimal configurations (optimal combinations of constellation sizes and their corresponding scaling factors) for eACO-OFDM are identical to GREENER-OFDM due to the similarity in signal statistics and system design; and the optimal configurations for ePAM-DMT are different due to the different system design [12]. The performance of the optimum configurations in all superposition modulation schemes is compared with the performance of a spectrally equivalent DCO-OFDM in both the AWGN channel and the dispersive VLC channel. The only non-linear effect considered is the negative clipping of the modulation signal due to the characteristics of an ideal LED. The DCO-OFDM DC bias levels for the different M-QAM DCO-OFDM are estimated using Monte Carlo simulations [15]. The performance results are presented for BER values down to 10^{-4} since most of the forward error correction (FEC) codes would be able to maintain a reliable communication link at such BER values [16]. The BER performance of the superposition OFDM schemes in an AWGN channel is presented in Fig. 3(a and b), and equivalent trends are shown in Fig. 3(c and d) for the non-flat dispersive VLC channel [14]. The SE for all of the presented schemes is higher than 97% of the SE of DCO-OFDM. The eACO-OFDM/GREENER-OFDM performances are equivalent for

all cases, since the optimal configurations used are identical. The electrical energy savings for eACO-OFDM/GREENER-OFDM start at 1 bit/s/Hz, while for ePAM-DMT [12, eq. (15)], the electrical energy savings start at 1.5 bits/s/Hz. As shown in Fig. 3(a and c), the superposition OFDM-based schemes are more efficient in terms of the electrical SNR requirements when compared with DCO-OFDM, with an advantage for eACO-OFDM/GREENER-OFDM over ePAM-DMT. For the optical SNR values, the eACO-OFDM/GREENER-OFDM schemes are shown to have an equivalent performance to DCO-OFDM for most of the presented cases, however, the performance of DCO-OFDM is more efficient when compared with the ePAM-DMT, as shown Fig. 3(b and d). At high SNR values, the theoretical BER values are in close agreement with Monte Carlo results for all the presented cases.

VI. CONCLUSION

The superposition modulation concept is extended to ACO-OFDM. The spectral efficiency (SE) of the proposed scheme, eACO-OFDM, is equivalent to DCO-OFDM. A theoretical bound on the BER performance of eACO-OFDM is derived and agrees with Monte Carlo simulations. The performance of all superposition OFDM-based schemes is compared with DCO-OFDM in both AWGN and in multipath dispersive channels. The BER performance of eACO-OFDM and GREENER-OFDM are equivalent. Future research will consider the LED non-linearity and PAPR.

REFERENCES

[1] Cisco Visual Networking Index, "Global Mobile Data Traffic Forecast Update, 2014-2019," CISCO, White Paper, Feb. 2015. [Online]. Available: http://www.cisco.com/c/en/us/solutions/collateral/service-provider/visual-networking-index-vni/white_paper_c11-520862.pdf

[2] S. Dimitrov and H. Haas, *Principles of LED Light Communications: Towards Networked Li-Fi*. Cambridge University Press, 2015.

[3] J. B. Carruthers and J. M. Kahn, "Multiple-subcarrier Modulation for Nondirected Wireless Infrared Communication," *IEEE Journal on Selected Areas in Communications*, vol. 14, no. 3, pp. 538–546, Apr. 1996.

[4] J. Armstrong and B. J. C. Schmidt, "Comparison of Asymmetrically Clipped Optical OFDM and DC-Biased Optical OFDM in AWGN," *IEEE Commun. Lett.*, vol. 12, no. 5, pp. 343–345, May 2008.

[5] J. Armstrong and A. Lowery, "Power Efficient Optical OFDM," *Electronics Letters*, vol. 42, no. 6, pp. 370–372, Mar. 16, 2006.

[6] S. C. J. Lee, S. Randel, F. Breyer, and A. M. J. Koonen, "PAM-DMT for Intensity-Modulated and Direct-Detection Optical Communication Systems," *IEEE Photonics Technology Letters*, vol. 21, no. 23, pp. 1749–1751, Dec. 2009.

[7] N. Fernando, Y. Hong, and E. Viterbo, "Flip-OFDM for Unipolar Communication Systems," *IEEE Transactions on Communications*, vol. 60, no. 12, pp. 3726–3733, Dec. 2012.

[8] D. Tsonev, S. Sinanović, and H. Haas, "Novel Unipolar Orthogonal Frequency Division Multiplexing (U-OFDM) for Optical Wireless," in *Proc. of the Vehicular Technology Conference (VTC Spring)*, IEEE. Yokohama, Japan: IEEE, May 6–9 2012.

[9] D. Tsonev and H. Haas, "Avoiding Spectral Efficiency Loss in Unipolar OFDM for Optical Wireless Communication," in *Proc. of the International Conference on Communications (ICC)*. Sydney, Australia: IEEE, Jun., 10–14 2014.

[10] D. Tsonev, S. Videv, and H. Haas, "Unlocking Spectral Efficiency in Intensity Modulation and Direct Detection Systems," *IEEE J. Sel. Areas Commun.*, vol. PP, no. 99, pp. 1–1, 2015.

[11] M. Islim, D. Tsonev, and H. Haas, "A Generalized Solution to the Spectral Efficiency Loss in Unipolar Optical OFDM-based Systems," in *Proc. of the International Conference on Communications (ICC)*. London, UK: IEEE, Jun., 8–12 2015.

[12] ——, "Spectrally Enhanced PAM-DMT for IM/DD Optical Wireless Communications," in *Proc. of the 25th Int. Symp. Pers. Indoor and Mobile Radio Commun. (PIMRC)*. Hong Kong, China: IEEE, Aug. 30–Sep. 2 2015, pp. 927–932.

[13] F. Xiong, *Digital Modulation Techniques*, 2nd ed. Artech House Publishers, 2006.

[14] K. Lee, H. Park, and J. Barry, "Indoor channel characteristics for visible light communications," *IEEE Communications Letters*, vol. 15, no. 2, pp. 217 – 219, Feb. 2011.

[15] S. Dimitrov, S. Sinanovic, and H. Haas, "Clipping Noise in OFDM-Based Optical Wireless Communication Systems," *IEEE Transactions on Communications*, vol. 60, no. 4, pp. 1072–1081, April 2012.

[16] ITU-T, "Forward error correction for high bit-rate DWDM submarine systems," ITU, Tech. Rep. ITU-T G.975.1, Retrieved Nov. 19, 2013 from http://www.itu.int/rec/T-REC-G.975.1-200402-I/en, 2004.

15 Gb/s OFDM-based VLC using Direct Modulation of 450 nm GaN Laser Diode

Shaun Viola[a], Mohamed Sufyan Islim[b], Scott Watson[a], Stefan Videv[b], Harald Haas[b], and Anthony E. Kelly[a]

[a] School of Engineering, University of Glasgow, Glasgow, G12 8LT, U.K.
[b] Li–Fi R&D Centre, Institute for Digital Communications, the University of Edinburgh, King's Buildings, Mayfield Road, Edinburgh, EH9 3JL, U.K.

ABSTRACT

A record data rate for visible light communications (VLC) using a transistor outline (TO) packaged Gallium Nitride (GaN) laser diode is reported. Using a system 3 dB bandwidth of 1.4 GHz data transmission at 15 Gb/s is reported. This is achieved due to the use of orthogonal frequency division multiplexing (OFDM) in combination with a high system signal to noise ratio (SNR) and adaptive bit loading extending the effective bandwidth to 2.5 GHz. To the best of authors knowledge this is the highest reported data rate for single channel VLC.

Keywords: Optical Communications, Visible Light Communications, Digital Communications

1. INTRODUCTION

GaN-based semiconductors are a safe and efficient means of modernizing our existing lighting infrastructure and could reduce lighting energy requirements to 1/5 of their current consumption.[1] The prospective ubiquity of GaN based lighting has given rise to research into using VLC as the data demand grows on the already congested radio frequency (RF) spectrum.[2] GaN based lighting devices are of interest due to their high speed modulation capabilities and in tandem with OFDM light emitting diodes (LED) have demonstrated data rates up to 5 Gb/s.[3] However, LED bandwidth is limited by the material carrier lifetime and efficiency is lowered when increasing the carrier density.[1] Laser-based VLC alleviates these problems and using laser diodes for free space VLC with non-return-to-zero on-off keying (NRZ-OOK) has shown data rates of up to 4 Gb/s.[4,5] Using multicarrier modulation schemes such as OFDM for laser-based VLC has achieved transmission speeds as high as 9 Gb/s.[6] Recently, a laser-based VLC system with a bandwidth of 3.5 GHz was demonstrated, with additional hardware for impedance matching and limited spectral efficiency 14 Gb/s was achieved.[7] Additionally, it is possible to combine different colour laser sources to increase data rates with wavelength division multiplexing (WDM) whilst providing standard white light illumination levels.[8] Recently, distributed feedback (DFB) lasers in GaN have been demonstrated making high channel density in WDM VLC systems possible.[9] Laser-based illumination has already been shown to produce high quality colour rendering for white light illumination using mutiple coloured sources and using phosphor colour converters.[10,11]

In this paper we surpass the highest data rate for single transmitter VLC using a GaN blue laser diode for free space transmission. 15 Gb/s over 15 cm using a commercial blue laser with a system 3 dB bandwidth of 1.4 GHz is demonstrated with a bit error rate (BER) below the forward error correction (FEC) limit. Successful transmission was also achieved over a distance of 197 cm at 13.5 Gb/s with a BER below the FEC limit.

The rest of the paper is organized as follows. In Section 2, the device characterization is presented. The OFDM modulation parameters are discussed in Section 3, experimental results are provided in Section 4 and conclusions are drawn in Section 5.

Further author information: (Send correspondence to S. V.)
S.V.: E-mail: s.viola.1@research.gla.ac.uk, Telephone:
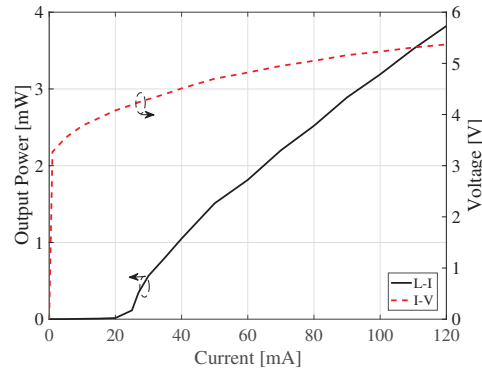
Figure 1. LVI characteristics of GaN laser at 17 ^{o}C.
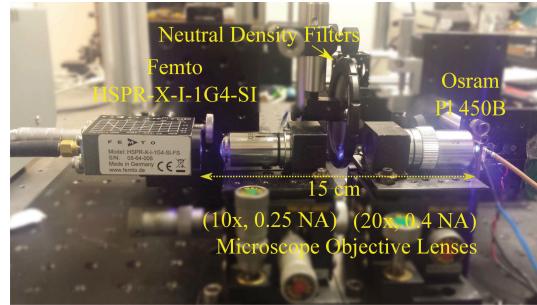
Figure 2. The optical system showing the laser, optical lens system and the photoreceiver.

2. DEVICE CHARACTERISATION

The laser diode used for transmission is OSRAMs PL450B device with a nominal emission wavelength of 450 nm. The luminance-voltage-current (LVI) characteristics of the device were experimentally obtained at 17 ^{o}C and are shown in Fig.1. The temperature was maintained with the use of a temperature controller (ILX Lightwave LDT-5910).

The threshold current of the device is 25 mA at a turn-on voltage of 4.29 V. The laser diode output was collected and collimated with a microscope lens (0.40 NA, x20 magnification) before being transmitted over a free space link 15 cm from source to photoreceiver. It was then focused onto the power meter (Newport 1918-R) with a second microscope lens (0.25 NA, x10 magnification). The laser and lens setup are depicted in Fig.2. After surpassing the threshold, the power received at the power meter increased from 0.1 uW until a maximum reading of 3.82 mW.

The power meter was then replaced with a spectrometer (Ocean Optics USB 4000 Miniature Fibre Optic), whilst the lens configuration was maintained, and the wavelength of the laser light was measured at varying drive currents. The results are exhibited in Fig.3. The laser spectral width is around 2 nm and exhibited the typical Fabry-Perot red shift in wavelength with increasing current. The optical bandwidth and the frequency response were then measured using a network analyser (Agilent HP 8753ES).

A direct-current (DC) power supply and RF signal from the network analyser are combined via a bias-T and fed to the laser diode. After collecting and collimating as per LVI and Spectra measurements, the light is focussed onto the 0.4 mm effective active diameter of a high-speed silicon positive-intrinsic-negative (PIN) photoreceiver
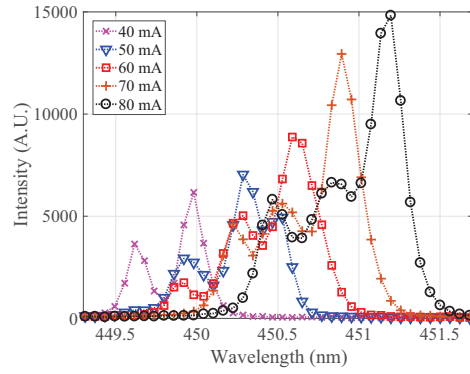
Figure 3. Spectra of the GaN laser at increasing drive currents.
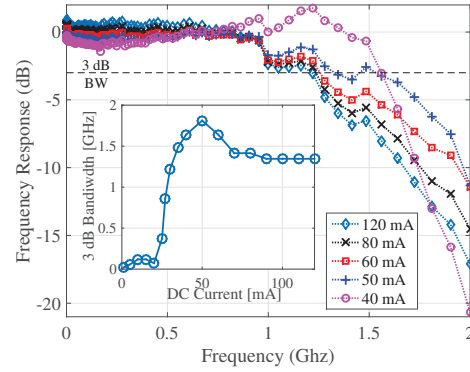
Figure 4. Frequency response at different drive currents. Inset shows 3 dB frequency at different drive currents.

(Femto, HSA-X-S-1G4-SI), with a 3 dB bandwidth of 1.4 GHz, shown in Fig.2. The system frequency response at drive currents from 40 mA to 120 mA is shown in Fig.4. The maximum optical bandwidth of the system was found at a drive current of 50 mA shown in the inset of Fig.4. However, at higher drive currents where the laser bandwidth is expected to continue to increase, the system response is limited by the photoreceiver.

3. OFDM PARAMETERS

The OFDM waveform must be real and positive to utilize the intensity of the light source. To achieve this Hermitian symmetry must be imposed on the subcarriers.[12] The useful bandwidth of a system utilizing OFDM is limited to the positive frequency band therefore N_{FFT} subcarriers are evenly separated across the frequency range $-\frac{1}{2T_s}$ to $\frac{1}{2T_s}$ where T_s is the sampling period which corresponds to the Nyquist rate. The spectral efficiency of OFDM can be described as:[8]

$$\eta = \frac{\sum_{\substack{k=1 \\ M_k>0}}^{\frac{N_{\text{FFT}}}{2}-1} \log_2 M_k}{N_{\text{FFT}} + NCP(1+\beta)} \text{ bits/s/Hz,} \tag{1}$$
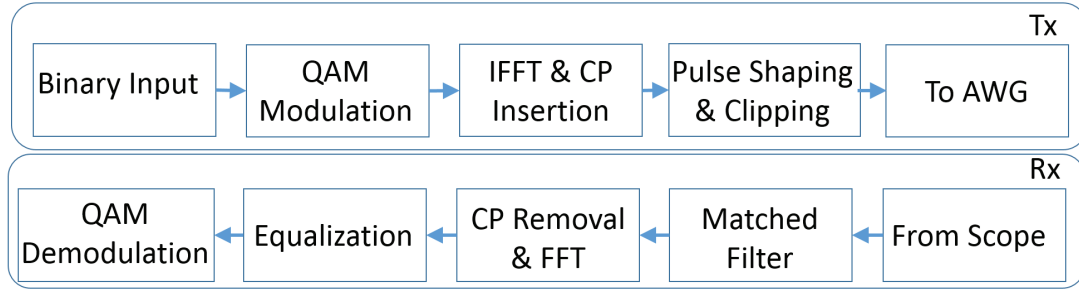
Figure 5. Block diagram showing OFDM transmitter and receiver components.

Where N_{FFT} is the number of subcarriers, M_k is the quadrature amplitude modulation (QAM) constellation size at the subcarrier k, N_{CP} is the length of the cyclic prefix (CP) and β is roll-off factor for the employed root-raised cosine (RRC) pulse shaping filter. The filter is chosen to satisfy bandwidth limitation and pulse duration requirements.

The number of subcarriers in the fast Fourier transformation (FFT), N_{FFT}, is equal to 1024 in this experiment. After exhaustive experimental measurements the cyclic prefix length, N_{CP}, was set to 5 which prevented any significant intersymbol interference (ISI). It is possible to use a bipolar OFDM signal to modulate a laser diode if a suitable DC bias is selected around which the signal will be centred. This is known as DC-biased optical OFDM (DCO-OFDM). The time domain OFDM signal has high peak to average power ratio (PAPR) which degrades the system performance due to non-linearities. Clipping of the time domain waveform is employed at marginal clipping noise distortion. In this experiment the upper and lower clipping was set as $+3\sigma$ and -3.5σ respectively. Where σ is the standard deviation of the time domain signal. Eqn.2 shows the square of σ given as:[8]

$$\sigma^2 = 2 \sum_{\substack{k=1 \\ M_k>0}}^{\frac{N_{\text{FFT}}}{2}-1} \frac{E_{\text{b}k} \log_2 M_k}{N_{\text{FFT}}} \tag{2}$$

Where $E_{\text{b}k}$ is defined as the electrical energy per bit on the k_{th} subcarrier. The OFDM transmitter and receiver are shown in the block diagram of Fig.5. The SNR from *a priori* estimation is used to determine the bit and energy allocation at each subcarrier. The binary data is encoded using M-QAM modulation before the inverse fast Fourier transformation (IFFT) converts the QAM symbols into the serial time domain waveform. The repition of the cyclic prefix helps the receiver mitigate any ISI effects, finally pulse shaping and waveform clipping alleviate ISI and nonlinearity distortion, respectively. The receiver then filters and removes the CP from the time domain waveform before the FFT converts it back to the frequency domain. Compensation of the effect from the channel is performed by equalization before QAM demodulation. The estimated SNR is used to adaptively load the subcarriers with bit and energy loading determined by the Levin-Campello algorithm.[13] Fig.6 shows the bit and energy loading of subcarriers and the channel capacity. The channel capacity is shown in Eqn.3 as described by Shannon:[14]

$$C = \log_2(1 + \frac{\alpha^2 E_{bk}}{\sigma_n^2/|H(k)|^2 + \sigma_d^2}) \tag{3}$$

Where α is a constant, σ_n^2 is the variance of the additive white Gaussian noise at the receiver, σ_d^2 is the frequency domain variance of the distortion noise and $|H(k)|^2$ is the channel gain at subcarrier k.
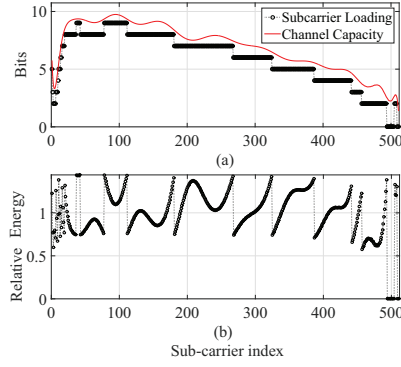
Figure 6. (a) The bit loading and channel capacity per subcarrier, both given in bits per subcarrier. (b) Energy loading per subcarrier.

4. EXPERIMENTAL RESULTS

The OFDM signal is generated using MATLAB. The analog OFDM waveform is then produced using an arbitrary waveform generator (Tektronix AWG70001A), with a DC bias added via a bias-T and used to modulate the laser. The lens configuration is maintained from the device characterization stage described in Section 2 and a FEMTO photoreceiver is placed at the receiver (HSPR-X-1G4-SI-FS). The output from the detector is fed to the oscilloscope (Tektronix MSO73304DX) and analyzed by MATLAB. Fig.7 shows the SNR over the 15 cm free space link at different drive currents. Data was transmitted using the optimal modulation voltage of 500 mV at varying drive currents and the MATLAB receiver code measured the end to end system SNR of each subcarrier. We can see that by increasing the drive current from 60 mA to 70 mA there is a noticeable improvement in the SNR of the high frequency subcarriers due to the increase in laser bandwidth with current. However, the inset in Fig.7 also details the reduction in SNR at lower subcarriers. We found 65 mA to be the optimum drive current at which the combination of increased high frequency SNR, and low frequency SNR reduction, resulted in the highest system data rate.

The channel performance was characterized as a function of channel attenuation. The optical power at the receiver was varied using a neutral density filter wheel. This varies the SNR and, therefore, the achievable data
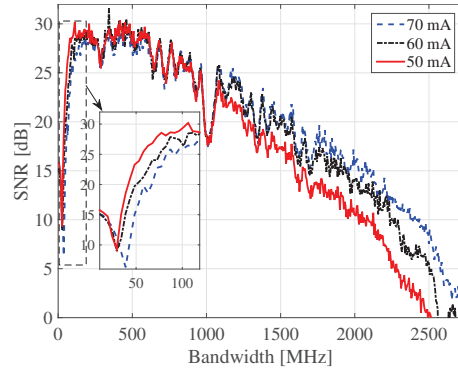
Figure 7. The SNR across the utilized bandwidth for different biasing levels.

257
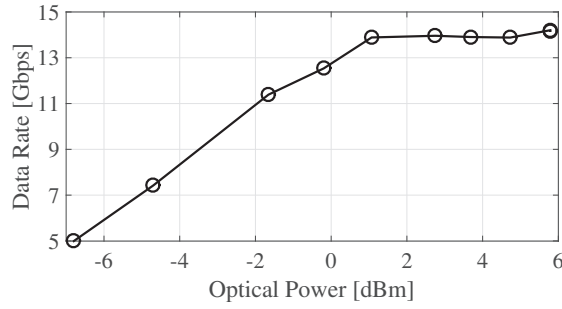
Figure 8. Data rate versus optical power over 15 cm link.

rate. Fig.8 shows the optical power required for different data rates whilst maintaining the BER below the FEC limit. This shows that the optical power can be reduced to 1 dBm and still transmit successfully at 14 Gb/s with the BER set below the FEC limit at $2.8 * 10^{-3}$. The data rate saturates at optical powers higher than 1 dBm and therefore it is possible to increase the transmission distance and maintain 14 Gb/s.

Fig.9 shows BER versus data rate for the 15 cm free space link. The black horizontal line illustrates the BER required to meet the FEC limit. From the figure it can be seen that 15 Gb/s data transmission can be achieved below the FEC limit. The transmission distance was then increased to 197 cm which was deemed a practical distance for dual purpose lighting VLC systems or remotely operated underwater vehicles. The receiver lens, previously a microscope lens, was replaced by a larger aspheric lens (Thorlabs ACL7560U-A). The laser bias and modulation voltage were unchanged. The maximum successful data rate is reduced to 13.5 Gb/s as shown in Fig.9 due to the increased losses and therefore decreased SNR. The relatively small decrease in maximum bit rate for this distance is due to the use of a near collimated laser output and the fact that the maximum bit rate at 15 cm was invariant with receiver powers between 1 dBm and 6 dBm.

5. CONCLUSIONS

The high bandwidth and high data rate capabilities of the OSRAM PL450B laser in the context of a VLC transmission system have been demonstrated. With a system 3dB bandwidth of 1.4 GHz, record data transmission system capacity has been demonstrated with data transmission over a 15 cm free space link at 15 Gb/s. This has been achieved through high system SNR and adaptive bit loading. The optical power required for achieving
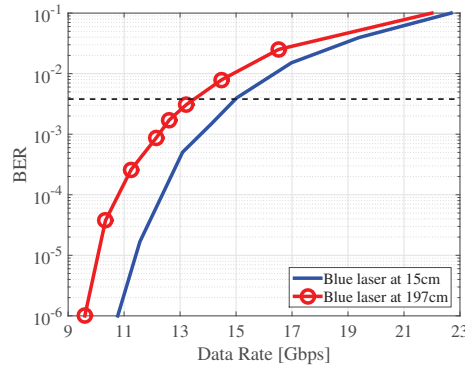
Figure 9. Data rate versus BER over 15 cm and 197cm link.

14 Gb/s over the 15 cm link was found to be 1 dBm. Over a 197 cm free space link, successful transmission was achieved at 13.5 Gb/s. Given the system is currently limited by the photoreceiver bandwidth, we believe that the overall system bandwidth could be improved without sacrificing spectral efficiency as long as the SNR of the detected signal is maintained.

ACKNOWLEDGMENTS

REFERENCES

[1] Nakamura, S., [*The Blue Laser Diode*], Springer, Berlin, Germany (1997).

[2] O'Brien, D., Parry, G., and Stavrinou, P., "Optical hotspots speed up wireless communication," *Nature Photonics* **1**(5), 245–247 (2007).

[3] Ferreira, R. X. G., Xie, E., McKendry, J. J. D., Rajbhandari, S., Chun, H., Faulkner, G., Watson, S., Kelly, A. E., Gu, E., Penty, R. V., White, I. H., O'Brien, D. C., and Dawson, M. D., "High bandwidth gan-based micro-leds for multi-gb/s visible light communications," *IEEE Photonics Technology Letters* **28**, 2023–2026 (Oct 2016).

[4] Watson, S., Tan, M., Najda, S. P., Perlin, P., Leszczynski, M., Targowski, G., Grzanka, S., and Kelly, A., "Visible light communications using a directly modulated 422 nm gan laser diode," *Optics letters* **38**(19), 3792–3794 (2013).

[5] Lee, C., Zhang, C., Cantore, M., Farrell, R. M., Oh, S. H., Margalith, T., Speck, J. S., Nakamura, S., Bowers, J. E., and DenBaars, S. P., "4 gbps direct modulation of 450 nm gan laser for high-speed visible light communication," *Optics express* **23**(12), 16232–16237 (2015).

[6] Chi, Y.-C., Hsieh, D.-H., Tsai, C.-T., Chen, H.-Y., Kuo, H.-C., and Lin, G.-R., "450-nm gan laser diode enables high-speed visible light communication with 9-gbps qam-ofdm," *Optics express* **23**(10), 13051–13059 (2015).

[7] Huang, Y.-F., Wu, T.-C., Chi, Y.-C., Tsai, C.-T., Wang, W., Shih, T.-T., Kuo, H.-C., and Lin, G.-R., "Impedance matched gan ld package for direct ofdm communication at 14 gbps," in [*OptoElectronics and Communications Conference (OECC) held jointly with 2016 International Conference on Photonics in Switching (PS), 2016 21st*], 1–3, IEEE (2016).

[8] Tsonev, D., Videv, S., and Haas, H., "Towards a 100 Gb/s Visible Light Wireless Access Network," *Opt. Express* **23**, 1627–1637 (Jan 2015).

[9] Slight, T. J., Odedina, O., Meredith, W., Docherty, K. E., and Kelly, A. E., "Ingan/gan distributed feedback laser diodes with deeply etched sidewall gratings," *IEEE Photonics Technology Letters* **28**, 2886–2888 (Dec 2016).

[10] Neumann, A., Wierer, J., Davis, W., Ohno, Y., Brueck, S., and Tsao, J., "Four-color laser white illuminant demonstrating high color-rendering quality," *Optics express* **19**(104), A982–A990 (2011).

[11] Denault, K. A., Cantore, M., Nakamura, S., DenBaars, S. P., and Seshadri, R., "Efficient and stable laser-driven white lighting," *AIP Advances* **3**(7), 072107 (2013).

[12] Islim, M. S. and Haas, H., "Modulation Techniques for Li-Fi," *ZTE Communications* **14**, 29–40 (April 2016).

[13] Levin, H. E., "A complete and optimal data allocation method for practical discrete multitone systems," in [*Global Telecommunications Conference, 2001. GLOBECOM'01. IEEE*], **1**, 369–374, IEEE (2001).

[14] Shannon, C. E., "A mathematical theory of communication," *ACM SIGMOBILE Mobile Computing and Communications Review* **5**(1), 3–55 (2001).

An Investigation of the Solar Irradiance Effect on Visible Light Communications

Mohamed Sufyan Islim and Harald Haas

LiFi Research and Development Centre, Institute for Digital Communications
University of Edinburgh, King's Buildings, Mayfield Road, Edinburgh, EH9 3JL, UK
Email: {m.islim, h.haas}@ed.ac.uk

Abstract—**This work aims to debunk the myth that visible light communication (VLC) systems cannot work under the presence of sunlight. It provides an investigation of an outdoor VLC system model in the presence of solar irradiance. Worst-case scenarios are considered in terms of location, link orientation and choice of photodiode. The effect of solar irradiance is investigated in terms of data rate and bit error rate (BER) degradation. An optical bandpass blue filter is shown to compensate for 53% of the reduced data rate in the presence of sunlight. Reliable communications above 1 Gb/s can be achieved using simple optical filtering under the effect of solar irradiance.**

I. INTRODUCTION

Traffic from wireless and mobile devices will account for two-thirds of the total internet traffic by 2020 [1]. The radio frequency (RF) bandwidth is a scarce resource, costing above £1m ($1.28m) per 1 MHz in the 2.4 GHz frequency band in the UK [2]. Visible light communication (VLC) offers a much larger frequency bandwidth that is unlicensed and safe to use. The VLC has the potential to reuse the existing lightning infrastructure for communications purposes [3]. Light fidelity (LiFi) is the network solution for VLC that is proposed to work seamlessly beside other RF access technologies [3]. A record data rate of 7.91 Gb/s was reported for orthogonal frequency division multiplexing (OFDM)-based VLCs using single violet micro-scale GaN light emitting diode (LED) (m-LED) [4]. Data rates above 100 Gb/s can be achieved if the complete visible spectrum is utilized [5].

The effect of solar irradiance on VLC is considered to be one of the main misconceptions surrounding VLC [6]. It is generally assumed that it could halt the operation of the communication system entirely due to the interference. However, the effect of solar irradiance is more apparent as a strong shot noise source rather than an interferernce source as the sunlight intensity does not vary tremendously over short periods of time. This allows multicarrier schemes such as OFDM to allocate the symbols over the usable frequency subcarriers of the deployed bandwidth [7].

The effect of solar irradiance on the performance of optical wireless communications (OWC) and VLC has been invistigated in the published research [8]–[10]. The use of optical filters with a special layer of microlouver to mitigate the effect of sunlight was suggested in [8]. However, the microlouver layer restricts the field of view (FOV) of the photodetector, which limits the overall system to narrow FOV communications. The performance of VLC systems in the presence of solar irradiance was studied using computer simulations in [9]. The solar irradiance was assumed to be incident from a window and reflected on multiple walls before it is collected by the photodiode. The performance degradation was estimated using the theoretical model for the incident solar irradiance in two geographic locations. However, the performance of an outdoor VLC system was not considered. The impact of solar irradiance on the performance of underwater OWC links was investigated for positive-intrinsic-negative (PIN) and avalanche photodiode (APD) in [10], where it was shown that sunlight affects the system performance at relatively low depths.

In this paper, we investigate the performance of outdoor VLC systems under solar irradiance. Worst-case scenarios are considered in terms of time and location. The investigation compares the use of a bandpass optical blue filter to the case where a filter is not considered in front of the photodetector. The performance is compared to a benchmark scenario of a dark room where background light does not reach the photodetector. The performance comparison is based on the predicted solar irradiance. The results show the solar irradiance to be affecting, but not significantly degrading, the performance of VLC. In addition, it is shown that at least 53% of the losses in data rate performance can be recovered using an inexpensive commercially available bandpass blue filter.

The rest of this paper is organized as follows. In Section II, we review an algorithm to calculate the position and irradiance of the Sun at any given location and time. The assumptions of this investigation are specified in Section III-A. The signal-to-noise ratio (SNR), maximum achievable data rate and bit error rate (BER) of the system are derived and the system modelling is discussed in Section III-B. The system performance is analyzed and the results are shown in Section IV.
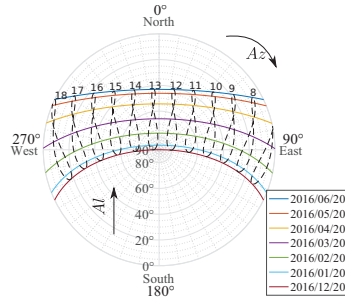
Fig. 1. Solar position described by altitude and azimuth for Antofagasta, Chile on the 20th of each considered month. The time of the day is listed above the elliptical shapes which represents the analemma diagrams.

Section V concludes the paper.

II. SOLAR IRRADIANCE AND POSITION

The solar constant flux density P_{SC} is given as 1366.1 w/m² outside the Earth's atmosphere by the American society for testing and materials (ASTM) standard (ASTM E-490) [11]. The solar irradiance is not limited to the visible spectrum as it spans the wavelengths from 250 nm to 2500 nm. The solar irradiance at different wavelengths is non-equally attenuated as it travels through the atmosphere due to the different absorption and scattering effects of the air molecules and aerosols of the atmosphere. The shortest path for the sunlight exists when the Sun is located at the zenith point (imaginary point above the head of the observer). The optical air mass (AM) is approximated as the ratio of the actual sunlight path to the minimum path at zenith point. It is given as AM0 for the extraterrestrial irradiance. When the Sun is at angle θ_Z relative to the zenith, the optical AM is approximated as:

$$\text{AM} \simeq \frac{1}{\cos\theta_Z}. \qquad (1)$$

The solar irradiance at $\theta_Z = 48.2°$ is given at an AM1.5 by the standard (ASTM E-490) [12] as a reference to help the solar energy community in testing and comparing the performance of various solar cells. However, the solar irradiance varies based on the geographical location; seasonal and diurnal variations arising from the rotation of the Earth around the Sun; and the rotation of earth around its own axis. The effect of solar irradiance on VLC varies based on the time and location. Therefore, it is essential to calculate the position of the Sun in the sky in order for the solar irradiance at a particular time and location to be estimated. Various algorithms with different complexities and accuracies for calculating the solar position exist in the astrophysics literature [13]. In this section, we review a simple algorithm based on the ecliptic coordinates with an

accuracy of $(1/60)°$ presented in [14] and proposed by the astronomical applications department of the U.S. naval observatory [15].

The horizontal coordinate system is usually used for solar energy applications where the horizon of the observer is considered to be the fundamental plane. The solar position can be described using two angles: altitude Al, and azimuth Az. The solar altitude $Al \in [0°, 90°]$ is given as the elevation of the Sun above the horizon. A solar altitude of $Al = 90°$ means that the Sun is at the zenith point. The solar altitude can also be given as $Al = 90° - \theta_Z$. The solar azimuth $Az \in [0°, 360°]$ is given as the angle between the north and the horizontal projection of the line-of-sight (LoS) between the Sun and the observer. Both angles are illustrated in Fig. 1 for Antofagasta, Chile on the 20th of each considered month. The solar altitude is shown to reach the zenith $Al = 90°$ around 13:00 on the 20th of December 2016. The time of the day is shown above the analemma diagrams, which depict the Sun motion throughout the year when observed at the same time and location. The solar position can be calculated using [14]:

$$\sin Al = \cos\phi_0 \cos\theta_L \cos\lambda_S +$$
$$(\cos\phi_0 \sin\theta_L \cos\epsilon + \sin\phi_0 \sin\epsilon)\sin\lambda_S \quad (2)$$

$$\tan Az = \frac{\Gamma_1}{\Gamma_2 - \Gamma_3}, \qquad (3)$$

where:

$$\Gamma_1 = -\sin\theta_L \cos\lambda_S + \cos\theta_L \cos\epsilon \sin\lambda_S, \qquad (4)$$
$$\Gamma_2 = -\sin\phi_0 \cos\theta_L \cos\lambda_S, \qquad (5)$$
$$\Gamma_3 = \sin\lambda_S(\sin\phi_0 \sin\theta_L \cos\epsilon - \cos\phi_0 \sin\epsilon), \qquad (6)$$

where ϕ_0 is the local latitude of the observer. The axial tilt between the equatorial plane and the ecliptic plane ϵ is given as [14]:

$$\epsilon = 23.429° - 0.00000036°D. \qquad (7)$$

where D is the time elapsed since the Greenwich noon of the 1st of January 2000. The axial tilt is zero valued in March/September equinox (20th March/September 2016) and takes a maximum value of around $\pm 23.429°$ in June/December solstice (20th June/December 2016). The local mean sidereal time (LMST) θ_L is the angle between March equinox and the meridian (an imaginary circle given at longitude of $0°$ and passing through the north and south poles and the zenith of an observer). A sidereal day is the time required for the Earth to complete a $360°$ rotation on its own axis. It is slightly shorter than the solar day mainly due to the rotation of the Earth around the Sun. The LMST can be given as:

$$\theta_L = \text{GMST}\frac{15°}{\text{hour}} + \lambda_0, \qquad (8)$$

where λ_0 is the longitude of the observer, and GMST is the Greenwich mean sidereal time (GMST), which can

Location	Antofagasta, Ch 23° 27'16.1"S 70°26'21.4"W
Dates	20th June/December 2016
APD model	Hamamatsu S8664-50K
APD detection area, A	19.6 mm^2
Bandwidth, B	60 MHZ
APD gain, M'	100
Dark current, I_d	3 nA
Blue filter FWHM	50 nm
Received optical power, P_R^L	2.51 mW

be defined as the hour angle between the March equinox and the meridian at Greenwich. GMST is calculated as [15]:

$$\text{GMST} = 18.697374558\text{h} + 24.06570982441908\text{h}.D, \tag{9}$$

where it is scaled to values $\text{GMST} \in [0, 24]$. The ecliptic longitude λ_S is given as [14]:

$$\lambda_S = q + 1.915° \sin g + 0.020° \sin 2g, \tag{10}$$

where q is the mean longitude given as [15]:

$$q = 280.459° + 0.98564736°D, \tag{11}$$

and g is the mean anomaly of the Sun which accounts for the varying speeds of the Earth motion throughout the year. This is given as [15]:

$$g = 357.529° + 0.98560028°D, \tag{12}$$

Direct solar irradiance is the sunlight that is directly reaching the surface of the Earth. Global solar irradiance is the combination of the direct and diffused solar irradiance. The simple model of the atmospheric radiative transfer of sunshine (SMARTS) is a transmittance model to evaluate the direct solar irradiance at any particular time and location [16], [17]. The model is used in generating the ASTM standard (ASTM E-490) with a resolution of 0.5-1 nm [11].

III. THEORETICAL STUDY

A. Assumptions

An OFDM-based VLC system is assumed due to its robustness against background illumination flickering. A real-valued OFDM waveform with a direct current (DC) bias is used to modulated the intensity of the LED in what is known as DC-biased optical OFDM (DCO-OFDM). Binary inputs are encoded into multiple M-ary quadrature amplitude modulation (M-QAM) symbols which are allocated into N_{FFT} subcarriers over a single-sided bandwidth of B. Three scenarios are considered:

- *Dark room (Scenario I)*: assumes an optimal case where no background illumination is reaching the photoreceiver.

- *with blue filter (Scenario II)*: assumes that the solar irradiance is collected with a bandpass blue filter in front of the photoreceiver.
- *w/o blue filter (Scenario III)*: assumes that the solar irradiance is collected without any optical filtering in front of the photoreceiver.

The system assumes a blue m-LED with a pixel size of 100 μm × 100 μm and a maximum optical power of 8 mW, and a focusing aspheric condenser optical lens (Thorlabs, ACL4532U-A). An optical bandpass blue filter from Edmund Optics is assumed in Scenario II with a centre wavelength of 450 nm, a transmittance higher than 90%, and a full width at half maximum (FWHM) of 50 nm. The photoreceiver is an APD (Hamamatsu, S8664-50K) where it is always assumed to be aligned with the m-LED. A choice of other types of photoreceivers is possible. However, APDs are used as a worst case choice in this investigation as they are shot-noise limited [18]. The APD will not always be collecting the solar irradiance due to the orientation of the communications link in practical situations. However, the APD is always assumed to be collecting the sunlight in this investigation.

The location considered is 23° 27' 16.1" S 70° 26' 21.4" W in Antofagasta, Chile which is claimed to have the highest solar radiation on Earth [19]. The model considers two dates: summer solstice and winter solstice where the solar position is calculated and used in SMARTS [16], [17] to estimate the hourly solar irradiance data. The model assumes a clear sky scenario due to the irregular variations in the local weather conditions which influence the solar irradiance. This allows us to consider the maximum possible solar irradiance.

B. System modelling

The photocurrent generated at the APD due to the optical power received from sunlight is given as:

$$I_b = A_d \int_{350}^{750} P_D^S(\lambda)R(\lambda)T_{bf}(\lambda)d\lambda, \tag{13}$$

where A_d is the APD detection area, $P_D^S(\lambda)$ is the direct solar irradiance given in W/m^2/nm, $R(\lambda)$ is the responsivity of the APD given in A/W, $T_{bf}(\lambda)$ is the transmittance of the bandpass optical blue filter, and λ is the wavelength considered for the visible light spectrum mainly from 350 nm to 750 nm.

Similarly the photocurrent generated at the APD due to the optical power received from the m-LED is given as:

$$I_s = A_d \int_{350}^{750} P_R^L(\lambda)R(\lambda)T_{bf}(\lambda)d\lambda, \tag{14}$$

where $P_R^L(\lambda)$ is the received optical power of the m-LED given in W/m^2/nm, which was measured for 100 μm × 100 μm sized m-LED using a Labsphere spectral irradiance head (E1000).

The random arrival of incident photons results in shot noise which can be modelled by a Poisson distribution. However, when the number of incident photons increases, the shot noise is approximated by a Gaussian distribution. The shot noise variance is given by [20]:

$$\sigma_s^2 = 2qM'^2F(I_b + I_s)B, \qquad (15)$$

where M' is the gain of the APD, q is the electron charge, B is the bandwidth of the APD, and F is the excess noise given as [21]:

$$F = \kappa M' + (2 - 1/M')(1 - \kappa), \qquad (16)$$

where κ is the holes/electrons ionization rate. The SNR at the receiver can be given by:

$$\text{SNR} = \frac{M'^2 I_s^2}{\sigma_n^2}, \qquad (17)$$

where $\sigma_n^2 = \sigma_s^2 + \sigma_t^2 + \sigma_d^2$ and σ_d^2 is the variance of the dark noise which is given as [20]:

$$\sigma_d^2 = 2qM'^2 F I_{dg} B + 2q I_{ds}, \qquad (18)$$

where I_{ds} is the surface dark current and I_{dg} is the bulk dark current that experience the avalanche effect of the APD, and where $I_d = I_{ds} + M' I_{dg}$. The variance of the thermal noise σ_T^2 is given by [22]:

$$\sigma_T^2 = 4\left(\frac{K_B T}{R_L}\right) F_n B, \qquad (19)$$

where K_B is Boltzmann constant, T is the temperature in Kelvin, R_L is the load resistance given as 50 Ω, and F_n is the photodiode noise figure.

The maximum achievable data rate is calculated using the channel capacity limit defined by Shannon as [23]:

$$R_{\text{Max}} = B \log_2(1 + \text{SNR}). \qquad (20)$$

The system performance in terms of BER can be calculated using the the theoretical BER of real-valued M-QAM OFDM given for additive white Gaussian noise (AWGN) channels as [24]:

$$\text{BER}(M, \gamma) \cong \frac{4}{\log_2(M)}\left(1 - \frac{1}{\sqrt{M}}\right) \times$$
$$\sum_{l=1}^{R} Q\left((2l-1)\sqrt{\frac{3\log_2(M)\gamma}{2(M-1)}}\right), \qquad (21)$$

where $Q(.)$ is the complementary cumulative distribution function (CCDF) for the standard normal distribution, γ is the SNR per bit, and $R = \min(2, \sqrt{M})$.

IV. RESULTS AND DISCUSSIONS

The spectral irradiance of the modelled m-LED, and the responsivity of the modelled APD with and without considering the optical bandpass blue filter are shown in Fig. 2. In addition, the predicted spectral irradiance of the sunlight is shown at three different times of the
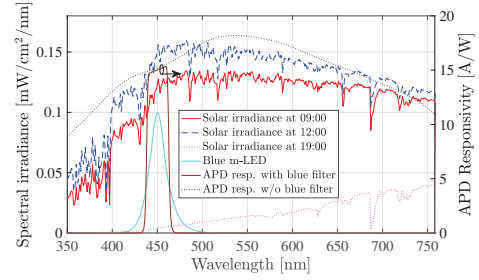
Fig. 2. The predicted solar irradiance in Antofagasta at 09:00, 12:00 and 19:00 on the 20th of December 2016 (left), alongside the spectral irradiance of the modelled m-LED centred at 450 nm (left), and response of the APD with and without considering the transmittance of the blue filter (right).
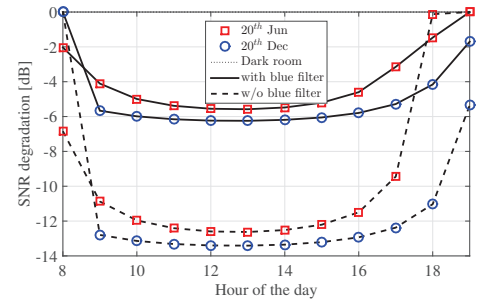
Fig. 3. SNR degradation given in dB versus the time of the day on the 20th of December 2016 at Antofagasta for the three considered scenarios.

summer solstice. It is shown that the solar irradiance is high at the ultra-violet (UV) and blue spectrum at sunrise. At sunset it becomes higher at the red and infra-red (IR) spectrum. The blue filter captures 70% of the m-LED irradiance.

The system performance is presented at Fig. 3 as a function of the SNR degradation against the time of the day for both summer and winter solstice. The degradation is calculated with reference to the benchmark case of the dark room in Scenario I. It is shown that the SNR degrades by a maximum of -13.4 dB at the noon of the summer solstice in Scenario III. However, when a blue filter is used in font of the APD, this degradation is reduced to -6.23 dB in Scenario II. Similar results are shown for the winter solstice with less than 0.8 dB lower SNR degradation. The system performance as a function of the BER against the time of the day is shown in Fig.4 for 128-QAM OFDM. The results show the SNR degradation effect on the BER performance for the OFDM-based VLC system. Both scenario II and scenario III are shown to allow the use of forward error correction (FEC) in both winter and

Fig. 4. BER of 128-QAM OFDM versus time of the day on the 20th of June 2016 at Antofagasta for the three considered scenarios.

Fig. 5. Maximum achieved data rate given in Gb/s versus the time of the day on the 20th of December 2016 at Antofagasta for the three considered scenarios.

summer solstice, although a significant improvement is shown to be achieved when the blue filter is used.
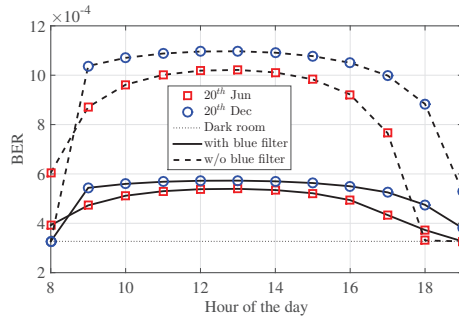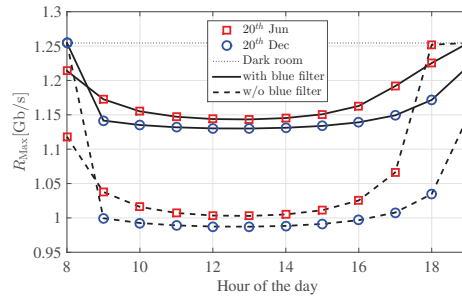
The system performance is investigated for the summer and winter solstice as a function of the maximum achievable data rate versus the time of the day in Fig. 5. The performance of Scenario II (after blue filter) and the performance of Scenario III (w/o blue filter) are compared to the benchmark performance recorded at 1.25 Gb/s of Scenario I (dark room) when solar irradiance is not reaching the APD. It is shown that the data rate degrades by 21.35% at noon during the winter solstice when the blue filter is not used. However, this degradation is reduced to 10% when the blue filter is introduced in front of the APD. A maximum achievable rate for the winter solstice under the solar irradiance is estimated at 1.03 Gb/s for Scenario III, and at 1.14 Gb/s for Scenario II. Similar trends are shown for the summer solstice with less than 15 Mb/s difference compared to the winter solstice at noon.

Optical filtering is beneficial for other objectives in VLC. White illumination is generally achieved by coating the blue LED with a yellow phosphor which introduces a slow component into the frequency response of the LED. Blue filters are required to eliminate the slow response component of the yellow phosphor. Monochromatic light sources with narrowband spectral distributions can guarantee a robust VLC system against solar irradiance with the potential of achieving data rates in the orders of multiple Gb/s. Contrary to the popular belief that LiFi does not work under sunlight, sunlight is essential to solar cell based LiFi systems which can act as high speed LiFi receivers, while at the same time it can harvest energy from sunlight [25].

V. CONCLUSION

An outdoor VLC system is feasible in the presence of solar irradiance. Worst-case scenarios are considered in this study to prove the concept of outdoor VLC systems. Shot noise caused by sunlight reduces the data rate of

VLC systems. However, optical bandpass blue filters can limit the degradation caused by solar irradiance. An improvement of at least 53% can be achieved for the data rates using off-the-shelf blue filters. Data rates in the order of multiple Gb/s can be achieved in the presence of solar irradiance using light amplification by stimulated emission of radiations (LASERs) with narrowband optical filters. Future work should consider the effect of automatic gain controller when saturation of the APD is considered.

REFERENCES

[1] Cisco Visual Networking Index, "Global Mobile Data Traffic Forecast Update, 2015-2020," CISCO, White Paper, Feb. 2016. [Online]. Available: http://www.cisco.com/c/en/us/solutions/collateral/service-provider/visual-networking-index-vni/mobile-white-paper-c11-520862.pdf

[2] OFCOM report, "Award of the 2.3 and 3.4 GHz Spectrum Bands: Competition Issues and Auction Regulations," OFCOM, Consultation , Jan. 2017. [Online]. Available: https://www.ofcom.org.uk/__data/assets/pdf_file/0026/93545/award-of-the-spectrum-bands-consultation.pdf

[3] S. Dimitrov and H. Haas, *Principles of LED Light Communications: Towards Networked Li-Fi*. Cambridge University Press, 2015.

[4] M. S. Islim, R. X. Ferreira, X. He, E. Xie, S. Videv, S. Viola, S. Watson, N. Bamiedakis, R. V. Penty, I. H. White, A. E. Kelly, E. Gu, H. Haas, and M. D. Dawson, "Towards 10 Gb/s Orthogonal Frequency Division Multiplexing-based Visible Light Communication Using a GaN Violet Micro-LED," *Photon. Res.*, vol. 5, no. 2, pp. A35–A43, Apr 2017. [Online]. Available: http://www.osapublishing.org/prj/abstract.cfm?URI=prj-5-2-A35

[5] D. Tsonev, S. Videv, and H. Haas, "Towards a 100 Gb/s Visible Light Wireless Access Network," *Opt. Express*, vol. 23, no. 2, pp. 1627–1637, Jan 2015. [Online]. Available: http://www.opticsexpress.org/abstract.cfm?URI=oe-23-2-1627

[6] G. Povey, "Top 10 Li-Fi Myths," June 2012. [Online]. Available: http://visiblelightcomm.com/top-10-li-fi-myths/

[7] M. S. Islim and H. Haas, "Modulation Techniques for Li-Fi," *ZTE Communications*, vol. 14, no. 2, pp. 29–40, April 2016.

[8] Y. H. Chung and S. B. Oh, "Efficient Optical Filtering for Out-door Visible Light Communications in the Presence of Sunlight or Articifical Light," in *Intelligent Signal Processing and Communications Systems (ISPACS), 2013 International Symposium on*, Nov 2013, pp. 749–752.

[9] M. Beshr, C. Michie, and I. Andonovic, "Evaluation of Visible Light Communication system performance in the presence of sunlight irradiance," in *2015 17th International Conference on Transparent Optical Networks (ICTON)*, July 2015, pp. 1–4.

[10] T. Hamza, M.-A. Khalighi, S. Bourennane, P. Léon, and J. Opderbecke, "Investigation of Solar Noise Impact on the Performance of Underwater Wireless Optical Communication Links," *Opt. Express*, vol. 24, no. 22, pp. 25 832–25 845, Oct 2016. [Online]. Available: http://www.opticsexpress.org/abstract.cfm?URI=oe-24-22-25832

[11] ASTM, *Standard Solar Constant and Zero Air Mass Solar Spectral Irradiance Tables*, ASTM-E490-00a Std., 2014. [Online]. Available: https://doi.org/10.1520/E0490

[12] ——, *Standard Tables for Reference Solar Spectral Irradiances: Direct Normal and Hemispherical on 37 Tilted Surface*, ASTM G173-03 Std., 2014. [Online]. Available: https://doi.org/10.1520/G0173-03R12

[13] W. B. Stine and M. Geyer, *Power from the Sun*, 2001. [Online]. Available: http://Powerfromthesun.net

[14] A. Smets, K. Jäger, O. Isabella, M. Zeman, and R. van Swaaij, *Solar Energy: The Physics and Engineering of Photovoltaic Conversion, Technologies and Systems*. UIT Cambridge, 2016. [Online]. Available: https://books.google.co.uk/books?id=vTkdjgEACAAJ

[15] I. Reda and A. Andreas, "Solar Position Algorithm for Solar Radiation Applications," *Solar energy*, vol. 76, no. 5, pp. 577–589, 2004.

[16] C. A. Gueymard, "Parameterized Transmittance Model for Direct Beam and Circumsolar Spectral Irradiance," *Solar Energy*, vol. 71, no. 5, pp. 325–346, 2001.

[17] C. Gueymard, *SMARTS2: a Simple Model of the Atmospheric Radiative Transfer of Sunshine: Algorithms and Performance Assessment*. Florida Solar Energy Center Cocoa, FL, 1995.

[18] F. Xu, M. A. Khalighi, and S. Bourennane, "Impact of Different Noise Sources on the Performance of PIN- and APD-based FSO Receivers," in *Proceedings of the 11th International Conference on Telecommunications*, June 2011, pp. 211–218.

[19] R. Rondanelli, A. Molina, and M. Falvey, "The Atacama Surface Solar Maximum," *Bulletin of the American Meteorological Society*, vol. 96, no. 3, pp. 405–418, 2015. [Online]. Available: https://doi.org/10.1175/BAMS-D-13-00175.1

[20] Hamamatsu Photonics K.K, "Characteristics and Use of SI-APD (avalanche photodiode)," May 2004. [Online]. Available: http://neutron.physics.ucsb.edu/docs/Characteristics_and_use_of_SI_APD.pdf

[21] G. Keiser, *Optical Communications Essentials*. McGraw-Hill, 2003.

[22] J. M. Kahn and J. R. Barry, "Wireless Infrared Communications," *Proc. IEEE*, vol. 85, no. 2, pp. 265–298, Feb. 1997.

[23] C. Shannon, "A Mathematical Theory of Communication," *Bell System Technical Journal*, vol. 27, pp. 379–423 & 623–656, Jul. & Oct. 1948.

[24] F. Xiong, *Digital Modulation Techniques*, 2nd ed. Artech House Publishers, 2006.

[25] Z. Wang, D. Tsonev, S. Videv, and H. Haas, "On the Design of a Solar-Panel Receiver for Optical Wireless Communications with Simultaneous Energy Harvesting," *IEEE J. Sel. Areas Commun.*, vol. 33, no. 8, pp. 1612–1623, Aug. 2015.

265

An Experimental Demonstration of an Energy Efficient DMT Technique for LiFi Systems

Mohamed Sufyan Islim and Harald Haas

School of Engineering, Institute for Digital Communications, LiFi R&D Centre, the University of Edinburgh,
King's Buildings, Mayfield Road, Edinburgh, EH9 3JL, UK
Email: {m.islim, h.haas}@ed.ac.uk

Abstract—**A direct current (DC) bias is required in DC-biased optical orthogonal frequency division multiplexing (DCO-OFDM) to enable visible light communication (VLC). However, the addition of the DC-bias leads to electrical and optical power inefficiency. An experimental demonstration of an energy efficient superposition modulation technique is presented based on augmented spectral efficiency discrete multitone (ASE-DMT). Significant energy savings with up to 14.27 dB gain in SNR are achieved in comparison with DCO-OFDM at low DC bias. The results highlight the potential of ASE-DMT in spectrum and energy efficient light fidelity (LiFi) systems.**

I. INTRODUCTION

The limited availability of the radio frequency (RF) spectrum is becoming an ever more important challenge as the demand for wireless broadband access increases [1]. Visible light communication (VLC) offers a low-cost solution to the looming spectrum crunch due to the availability of inexpensive front-end devices. The ubiquitous availability of light sources enables the opportunity of creating a dense network of access points. VLC is a unique option in scenarios where the RF propagation is considered to be hazardous, such as hospital theaters and petrochemical plants. Data rates in the excess of 100 Gb/s are predicted to be achievable when the complete visible spectrum is utilized [2]. Light fidelity (LiFi) is the high speed bidirectional light-based networking solution that is proposed to work seamlessly with other RF access technologies [3], [4]. LiFi can support multiuser access and handover between light-based access points.

Incoherent optical sources are widely used in LiFi transmitters due to their low cost and simple system design. The adoption of these transmitters limit the signaling to intensity modulation and direct detection (IM/DD). Orthogonal frequency division multiplexing (OFDM) is a promising candidate for both wired and wireless IM/DD-based systems due to its resilience to the frequency selective fading [3]. However, the power penalty of direct current (DC) biased optical OFDM (DCO-OFDM) increases at high spectral efficiency values due to the DC bias requirements [5]. Pulse-amplitude modulation discrete multitone modulation (PAM-DMT) is introduced to provide an energy efficient optical OFDM alternative to DCO-OFDM [6]. However, its energy efficiency degrades at high modulation orders due to the restrictions imposed on

the frame structures [7]. PAM-DMT uses pulse-amplitude modulation (PAM) on the imaginary part of the subcarriers. Therefore, the bit error ratio (BER) performance of M_{PAM} is equivalent to the performance of M_{DCO}^2-quadrature amplitude modulation (QAM). The BER performance gain of PAM-DMT degrades as the constellation size of M_{PAM} increases in comparison with DCO-OFDM at the same spectral efficiency.

The energy efficiency is a desired feature in communication systems. It is essentially required at the mobile user-end to reduce the power consumption. Dimming is recently becoming an indispensable feature for general lighting systems. Moreover, the dimming support of the cabin illumination system is a compulsory feature for airplanes. Low DC bias is required to enable the dimming of the light source. Therefore, DCO-OFDM is unable to support dimming. A novel computational and energy efficient superposition modulation technique is proposed in our previous work [7]. The selective loading algorithm in augmented spectral efficiency discrete multitone (ASE-DMT) allows multiple streams of PAM-DMT to be superimposed without affecting the demodulation of each individual stream. ASE-DMT avoids the spectral efficiency losses of PAM-DMT and provides energy efficiency gains over DCO-OFDM and PAM-DMT. A successful demonstration of 4-PAM ASE-DMT using a novel single inverse fast Fourier transform (IFFT) transmitter was achieved recently at a data rate of 18.4 Gb/s over a 10 km single mode fiber [8].

An experimental study on the performance of ASE-DMT is presented in this paper at unprecedented high spectral efficiency values up to 32-PAM. The performance of ASE-DMT is compared with DCO-OFDM and PAM-DMT using a blue light emitting diode (LED) (Vishay VLMB1500) and an infra-red (IR) vertical-cavity surface-emitting laser (VCSEL) (OPV300). Blue LEDs are widely used in light sources for general illumination purposes. Therefore, the choice of the blue LED is particularly interesting to demonstrate the performance of ASE-DMT for the dimming applications in VLC. Whereas, the IR VCSEL is suitable for the up-link of LiFi systems. The current-voltage (I-V) and luminance-voltage (L-V) characteristic functions for both the blue LED and the IR VCSEL are shown in Fig. 1(a & b), respectively. The L-V characteristic function of the blue LED in Fig. 1(a) is
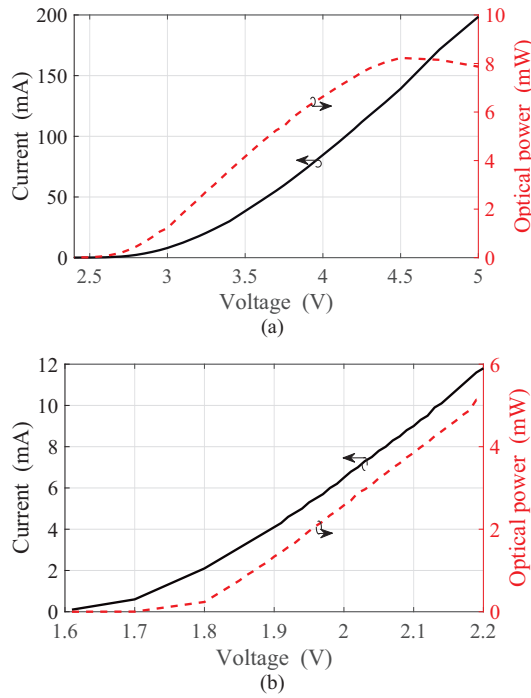
266

Fig. 1. (a) current-voltage and luminescence-voltage characteristics for: (a) the blue LED and (b) IR VCSEL.

shown to exhibit higher nonlinearity in comparison with the L-V characteristic function of the IR VCSEL in Fig. 1(b). Therefore, the sensitivity of ASE-DMT to the nonlinearity of the optical source can be investigated by comparing the results of the blue LED and the IR VCSEL.

The implementation of DCO-OFDM in this paper is similar to the demonstration presented in [9], while the implementations of PAM-DMT and ASE-DMT are presented in Section II. The experimental setup is detailed in Section III. The results are discussed in Section IV and the conclusions are summarized in Section V.

II. AN IMPLEMENTATION OF ASE-DMT

The waveform in ASE-DMT is generated by the selective loading of imaginary and real components of the subcarriers using MATLAB®. A pseudo-random series of bits is encoded into PAM symbols. The ASE-DMT stream at the first modulation depth $d = 1$ is exactly equivalent to a PAM-DMT stream [6]. Therefore, the implementation of ASE-DMT with one modulation depth $D = 1$ is identical to a PAM-DMT implementation. The modulated PAM symbols are loaded on the imaginary component of the subcarriers at the first modulation depth of an ASE-DMT modulator. A further $D-1$
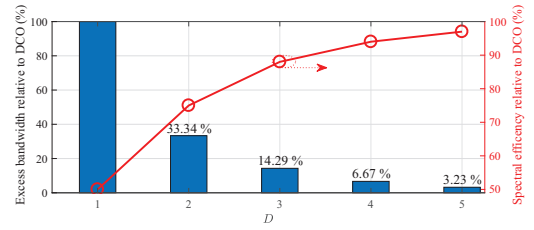

Fig. 2. The excess bandwidth required in ASE-DMT relative to DCO-OFDM as a function of the total number of modulation depths D.

streams can be superimposed on the first modulation depth without creating any distortion to the preceding modulation depths. This is achieved by loading the PAM symbols on the real-valued component of the subcarriers. Further details on the modulation concept and the theoretical analysis of ASE-DMT can be found in [7].

The spectral efficiency at a modulation depth d is given as follows:

$$\eta_{\text{ASE}}(d) = \frac{\log_2(M_{\text{PAM}})N_{\text{FFT},d}}{2^d(N_{\text{FFT}} + N_{\text{CP}})} \quad \text{bits/s/Hz}, \quad (1)$$

where $N_{\text{FFT},d} = N_{\text{FFT}} - 2$ for $d = 1$ and $N_{\text{FFT},d} = N_{\text{FFT}}$ for $d > 1$; M_{PAM} is the constellation size of PAM-DMT and ASE-DMT, N_{FFT} is the length of the OFDM frame and N_{CP} is the length of the cyclic prefix.

The performance of M_{PAM} in PAM-DMT and ASE-DMT is compared with the performance of M^2-QAM in DCO-OFDM. The spectral efficiency of ASE-DMT approaches twice the spectral efficiency of DCO-OFDM as the total number of depths increases. However, the energy efficiency comparison of both modulation techniques should be considered at an equivalent spectral efficiency. Therefore, the superimposed waveforms in ASE-DMT use smaller constellation sizes, $M_{\text{PAM}} = \sqrt{M_{\text{DCO}}}$, which can lead to an overall spectral efficiency that is equivalent to DCO-OFDM. The spectral efficiency of the first depth in ASE-DMT is equivalent to the spectral efficiency of a PAM-DMT modulation $\eta_{\text{PAM}} = \eta_{\text{ASE}}(1)$. The spectral efficiency of ASE-DMT can then be calculated as follows:

$$\eta_{\text{ASE,T}}(D) = \sum_{d=1}^{D} \eta_{\text{ASE}}(d) \quad \text{bits/s/Hz}. \quad (2)$$

The spectral efficiency of DCO-OFDM can be given by (1) when substituting $d = 1$ and $M_{\text{DCO}} = M_{\text{PAM}}^2$. The performance of ASE-DMT is investigated in this paper for up to $D = 5$ modulation depths. The spectral efficiency of ASE-DMT increases as the total number of modulation depths D increases as shown in Fig. 2. For example, the spectral efficiency of ASE-DMT is 87.5% of the spectral efficiency of DCO-OFDM when $D = 3$. Therefore, an excess bandwidth is allocated for PAM-DMT and ASE-DMT techniques to allow the performance comparison with DCO-OFDM to be
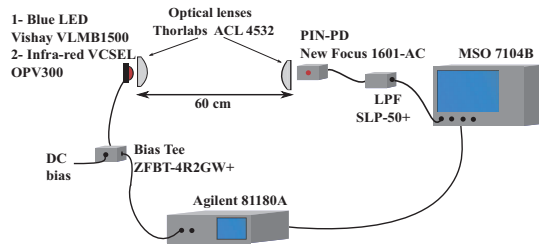
Fig. 3. The schematic setup of the experiment showing the optical system, AWG, oscilloscope, electrical filter and Bias-tee.

Fig. 4. The BER as a function of the average electrical power $P_{\text{elec}}^{\text{avg}}$ for each of the five superimposed modulation depths of a 4-PAM ASE-DMT waveform with $D = 5$. This is obtained for the blue LED.

performed at the same data rate. The relative excess bandwidth as a function of the total number of modulation depths is shown in Fig. 2. ASE-DMT can additionally be realized by employing arbitrary constellation sizes to close any remaining spectral efficiency gap with a maximum of three modulation depths [7]. This solution is particularly useful for the cases where the excess bandwidth is not practically available due to the frequency profile constraints of the considered VLC system. However, the excess bandwidth required for $D > 3$ is marginal as shown in Fig. 2.

The modulated signals of DCO-OFDM, PAM-DMT and ASE-DMT are clipped to fit within the dynamic range of the used digital-to-analog converter (DAC) and the considered transmitter device. The clipping results in a limited distortion that is controlled by the upper and lower clipping points [10]. The DCO-OFDM modulation signal is clipped to both an upper and a lower clipping points given at $\pm 3.2\sigma_x$, where σ_x is the standard deviation of the modulation signal. These values were experimentally found to achieve the best BER performance after exhaustive experiments. The PAM-DMT and ASE-DMT modulation signals are both unipolar. Therefore, the lower clipping is set to zero and the upper clipping is set to $6.4\sigma_x$ to allow for a fair comparison at an equivalent quantization noise with DCO-OFDM. The OFDM frame length is set to $N_{\text{FFT}} = 1024$ and the cyclic prefix length is set to $N_{\text{CP}} = 5$ for all the considered modulation techniques. These values were also selected based on the BER performance after extensive experiments.

An estimation of the channel and the achievable signal-to-noise ratio (SNR) over the utilized bandwidth is obtained using a conventional mean estimator [9]. A zero-forcing equalizer is used to maintain a relatively constant SNR over all of the considered subcarriers.

III. EXPERIMENTAL SETUP

The digital modulation signals are generated in MATLAB® and converted into analogue signals using the arbitrary waveform generator (AWG) (Agilent 81180A) with a $V_{\text{PP}} = 2$ V for the blue LED and a $V_{\text{PP}} = 125$ mV for the IR VCSEL. The ASE-DMT modulation signal is inherently unipolar. However, it is mapped to a bipolar signal at the DAC as the AWG
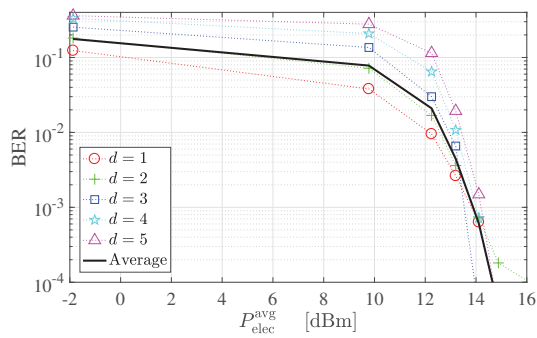
is unable to generate unipolar outputs. The AWG generates bipolar outputs with a DAC range between $-V_{\text{PP}}/2$ and $V_{\text{PP}}/2$. The DC bias is added to the modulation signals using a bias-tee (Mini-Circuits ZFBT-4R2GW+). The DC bias is required for the unipolar ASE-DMT signal due to the bipolarity of the AWG and the turn-on voltage of the used light source.

Two identical aspheric lenses (Thorlabs ACL 4532) are used at the photoreceiver and the transmitter ends as shown in Fig. 3. The communications link distance is 60 cm and the photoreceiver is a high speed positive-intrinsic-negative photodiodes (PIN-PD) (New Focus 1601-AC). An electrical low pass filter (SLP-50+) is used at the receiver with a pass-band between DC and 48 MHz to block any high RF interference. The received signal is captured at the oscilloscope (Agilent MSO7104B) and processed afterwards using MATLAB®.

IV. RESULTS AND DISCUSSION

The performance of ASE-DMT is measured for a total number of depths $D = \{1, 3\}$ when using the IR VCSEL and for $1 \leq D \leq 5$ when using the blue LED. Note that D refers to the total number of modulation depths of the ASE-DMT waveform whereas d refers to the index of the superimposed stream at the modulation depth d, given that $1 \leq d \leq D$.

The BER and average SNR are measured for DCO-OFDM, PAM-DMT and ASE-DMT against the DC bias voltage V_{DC}, average electrical power $P_{\text{elec}}^{\text{avg}}$ and average optical power $P_{\text{opt}}^{\text{avg}}$. The voltage signal applied on the considered transmitter device by the AWG is captured by the oscilloscope during the transmission period. The corresponding I-V curve is used to estimate the corresponding current values. These allow for the average electrical power to be estimated for each of the used modulation signals using both the blue LED and the IR VCSEL. The average optical power is measured using the spectral irradiance head (Labsphere E1000) and the monochromatic optical power meter (Thorlabs S121C).
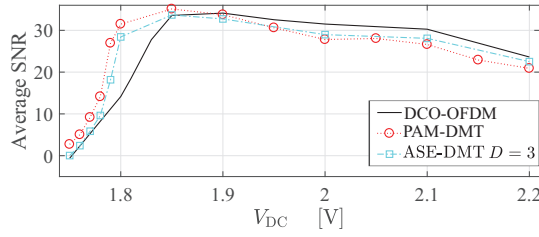
Fig. 5. The average SNR versus bias voltage V_{DC} for DCO-OFDM, PAM-DMT and ASE-DMT when $D = 3$.

The BER performance for each of the superimposed streams of a 4-PAM ASE-DMT modulation with $D = 5$ is presented as a function of the average electrical power of the blue LED in Fig. 4. The average BER is calculated based on the relative spectral efficiency contribution of each of the modulation depths. The BER performance is shown to degrade as the modulation depth order d increases. However, the BER performance for all of the modulation depths converges to a similar BER value as the average electrical power increases. At high electrical average power, the error propagation becomes insignificant to affect the BER performance at the higher modulation depth orders. This is due to the decrease in the number of wrongly decoded bits at the lower modulation depth orders. The average BER performance is shown to be heavily affected by the BER performance of the lower order modulation depths due to their higher spectral efficiency contribution. The number of transmitted PAM symbols at high modulation depth orders is small due to the selective loading algorithm as well as the limited memory size of the AWG. This affects the statistical significance of the results at low BER values. In addition, it explains the small deviation of the BER values below 1×10^{-3}.

The average SNR values are measured against V_{DC} in Fig. 5 for DCO-OFDM, PAM-DMT and ASE-DMT. The average SNR of ASE-DMT is presented for $D = 3$. It is shown that PAM-DMT and ASE-DMT achieve higher SNR levels at low DC bias levels. The SNR gain increases as the DC bias increases to reach a peak of 17.33 dB for PAM-DMT and 14.27 dB for ASE-DMT at $V_{DC} = 1.8$ V. The SNR gain of PAM-DMT is higher in comparison with ASE-DMT. However, this comes at the price of using 85.71% extra excess bandwidth as shown in Fig. 2. The SNR gain of ASE-DMT drops due to the clipping distortion and diminishes at 1.9 V. The SNR degradation at high DC bias values of PAM-DMT and ASE-DMT is in agreement with the SNR degradation of DCO-OFDM due to clipping distortion. However, the SNR degradation of PAM-DMT and ASE-DMT is shown to be higher due to their unipolar distributions.

The minimum required optical power levels to achieve a BER at the forward error correction (FEC) threshold are presented in Fig. 6(a & b) as a function of the spectral efficiency
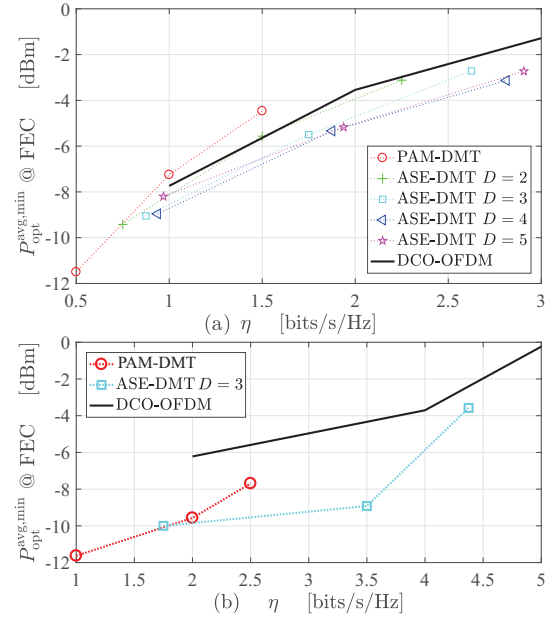
Fig. 6. The minimum average optical power $P_{opt}^{avg,min}$ required at a BER equals to the FEC threshold 3.8×10^{-3} versus the spectral efficiency of DCO-OFDM and ASE-DMT with a total number of depths $D = 1$ and $D = 3$ using (a) the blue LED and (b) the IR VCSEL.

when using the blue LED and the IR VCSEL, respectively. The results of ASE-DMT are presented for $1 \leq D \leq 5$ when using the blue LED and for $D = 1$ and $D = 3$ when using the IR VCSEL. The results for the IR VCSEL are presented for two representative cases to allow for a comparison with the trends obtained using the blue LED.

The comparison in Fig. 5 is performed at the same data rate. Therefore, a considerable excess bandwidth equal to the whole utilized bandwidth in DCO-OFDM is required for PAM-DMT. The results in Fig. 6(a & b) are presented at a normalized bandwidth to allow for a fair comparison between PAM-DMT and the different values of D in ASE-DMT.

The required optical average power $P_{opt}^{avg,min}$ is shown in Fig. 6(a) for the blue LED. The improvement in the optical average power of ASE-DMT with $D = 4$ at $\eta = 1$ bits/s/Hz approaches 1 dB when compared with DCO-OFDM. However, the optical power savings increases as the spectral efficiency increases. The reduction in the required optical power reaches 1.5 dB at $\eta = 2$ bits/s/Hz and 1.45 dB at $\eta = 2.5$ bits/s/Hz when $D = 4$. The improvements in the optical power requirements are higher for the case of the IR VCSEL as shown in Fig. 6(b). The optical power gain is estimated at 3.63 dB for ASE-DMT when $D = 3$. This is mainly due to the improved linearity of the L-V characteristic of the IR VCSEL. The differences in the optical power requirements for

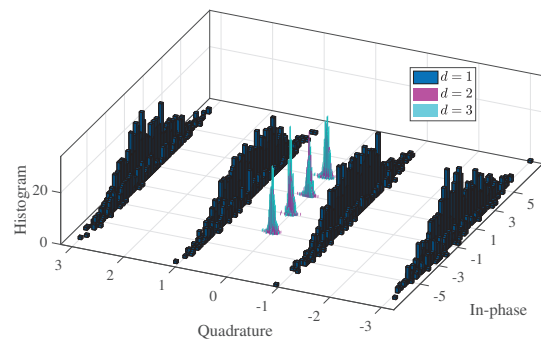Fig. 7. The histogram of the demodulated symbols constellations of 4-PAM ASE-DMT with a total number of depths $D = 3$. The constellations are shown for the superimposed modulation depths $d = \{1, 2, 3\}$. The demodulated symbols are obtained when using the IR VCSEL with a bias voltage $V_{DC} = 1.85$V.

the same modulation technique between the blue LED and the IR VCSEL are also attributed to the higher responsivity of the photoreceiver at the IR band. This allows the optical power levels of the IR VCSEL shown in Fig. 6(b) to be lower than the optical power levels of the blue LED shown in Fig. 6(a). ASE-DMT needs less optical power than DCO-OFDM to operate at the same data rate and the same BER. Therefore, ASE-DMT can support longer distance VLC links with more relaxed alignment/orientation constraints at the receiver.

The demodulated constellation diagram for 4-PAM ASE-DMT is presented in Fig. 7. The constellation diagram is obtained at a bias voltage $V_{DC} = 1.85$ V for the IR VCSEL. The demodulated symbols are shown in the constellation diagrams with a total number of modulation depths $D = 3$. The constellation points are given for the superimposed modulation depths $d = \{1, 2, 3\}$. The histogram reveals the distribution of the constellation points against the number of demodulated symbols. The information bits are conveyed in the imaginary component of the symbols at the first modulation depth when $d = 1$. The rest of the superimposed modulation depths are conveyed in the real component of the symbols. The bias levels represent the optimal bias point for ASE-DMT with the used transmitter devices. That explains the good representation of the constellation points which allows for ASE-DMT performance to reach the BER floor.

V. CONCLUSIONS

The proposed ASE-DMT is demonstrated as a promising choice for energy efficient LiFi systems. The SNR performance gain of ASE-DMT at low DC bias results in reduced electrical and optical power requirements in comparison with DCO-OFDM and PAM-DMT. ASE-DMT is a promising choice for any IM/DD system where the reduction of the energy consumption is required. An example of a potential application is the IR-based uplink of a LiFi system where ASE-DMT is shown to be a favorable solution for long

distance IM/DD systems. ASE-DMT is also a better choice than DCO-OFDM at low DC bias where the dimming of the light source is required.

The degradation of ASE-DMT at high optical power restricts the capability of the system to satisfy high illumination requirements. In addition, the inability to derive the transmitter device at a high DC bias results in a reduced 3-dB bandwidth of the considered transmitter. Therefore, it can be concluded that ASE-DMT is a less favorable choice when compared with DCO-OFDM at high DC bias points where the energy efficiency of the system is not the main concern. A possible solution for using ASE-DMT at high DC bias levels can be investigated by inverting the polarity of the ASE-DMT waveform. The details of this investigation will be the subject of our future research.

REFERENCES

[1] Cisco Visual Networking Index, "The Zettabyte Era: Trends and Analysis," Retrieved from https://www.cisco.com/c/en/us/solutions/collateral/service-provider/visual-networking-index-vni/vni-hyperconnectivity-wp.html, Jun. 2017.

[2] D. Tsonev, S. Videv, and H. Haas, "Towards a 100 Gb/s Visible Light Wireless Access Network," *OSA Opt. Express*, vol. 23, no. 2, pp. 1627–1637, Jan 2015. [Online]. Available: http://www.opticsexpress.org/abstract.cfm?URI=oe-23-2-1627

[3] S. Dimitrov and H. Haas, *Principles of LED Light Communications: Towards Networked Li-Fi*. Cambridge University Press, 2015.

[4] H. Haas, L. Yin, Y. Wang, and C. Chen, "What is LiFi?" *IEEE/OSA J. Lightw. Technol.*, vol. 34, no. 6, pp. 1533–1544, Mar. 2016.

[5] M. Islim, D. Tsonev, and H. Haas, "A Generalized Solution to the Spectral Efficiency Loss in Unipolar Optical OFDM-based Systems," in *Proc. of the International Conference on Communications (ICC)*. London, UK: IEEE, Jun., 8–12 2015.

[6] S. C. J. Lee, S. Randel, F. Breyer, and A. M. J. Koonen, "PAM-DMT for Intensity-Modulated and Direct-Detection Optical Communication Systems," *IEEE Photon. Technol. Lett.*, vol. 21, no. 23, pp. 1749–1751, Dec. 2009.

[7] M. S. Islim and H. Haas, "Augmenting the Spectral Efficiency of Enhanced PAM-DMT-based Optical Wireless Communications," *OSA Opt. Express*, vol. 24, no. 11, pp. 11932–11949, May 2016. [Online]. Available: http://www.opticsexpress.org/abstract.cfm?URI=oe-24-11-11932

[8] Q. Wang, B. Song, B. Corcoran, L. Zhuang, and A. J. Lowery, "Real-Time Demonstration of Augmented-Spectral-Efficiency DMT Transmitter Using a Single IFFT," *IEEE/OSA J. Lightwave Technol.*, vol. 35, no. 21, pp. 4796–4803, Nov 2017.

[9] D. Tsonev, S. Videv, and H. Haas, "Unlocking Spectral Efficiency in Intensity Modulation and Direct Detection Systems," *IEEE J. Sel. Areas Commun.*, vol. 33, no. 99, pp. 1758–1770, 2015.

[10] S. Dimitrov, S. Sinanovic, and H. Haas, "Clipping Noise in OFDM-Based Optical Wireless Communication Systems," *IEEE Trans. on Commun.*, vol. 60, no. 4, pp. 1072–1081, April 2012.

References

[1] Cisco Visual Networking Index, "The Zettabyte Era: Trends and Analysis." Retrieved from `https://www.cisco.com/c/en/us/solutions/collateral/service-provider/visual-networking-index-vni/vni-hyperconnectivity-wp.html`, June 2017.

[2] Cisco Visual Networking Index, "Global Mobile Data Traffic Forecast Update, 2016-2021." Retrieved from `https://www.cisco.com/c/en/us/solutions/collateral/service-provider/visual-networking-index-vni/complete-white-paper-c11-481360.html`, Sept. 2017.

[3] Ofcom, "Award of 2.3 and 3.4 GHz spectrum bands - Publication under regulation 111 of the Wireless Telegraphy (Licence Award) Regulations 2018 of results of auction." Retrieved from `https://www.ofcom.org.uk/__data/assets/pdf_file/0018/112932/Regulation-111-Final-outcome-of-award.pdf`, Apr. 2018.

[4] V. Chandrasekhar, J. Andrews, and A. Gatherer, "Femtocell Networks: A Survey," *IEEE Commun. Mag.*, vol. 46, no. 9, pp. 59–67, 2008.

[5] P. J. Winzer and D. T. Neilson, "From Scaling Disparities to Integrated Parallelism: a Secathlon for a Decade," *IEEE/OSA J. Lightw. Technol.*, vol. 35, pp. 1099–1115, March 2017.

[6] T. Cogalan and H. Haas, "Why Would 5G Need Optical Wireless Communications?," in *2017 IEEE 28th Annual International Symposium on Personal, Indoor, and Mobile Radio Communications (PIMRC)*, (Montreal, Canada), pp. 1–6, Oct., 8–13 2017.

[7] J. Andrews, S. Buzzi, W. Choi, S. Hanly, A. Lozano, A. Soong, and J. Zhang, "What Will 5G Be?," *IEEE J. Sel. Areas Commun.*, vol. 32, pp. 1065–1082, June 2014.

[8] F. R. Gfeller and U. Bapst, "Wireless In-House Data Communication Via Diffuse Infrared Radiation," *Proc. IEEE*, vol. 67, pp. 1474–1486, Nov. 1979.

[9] Y. Tanaka, T. Komine, S. Haruyama, and M. Nakagawa, "Indoor Visible Communication Utilizing Plural White LEDs as Lighting," in *Proc. of the 12th IEEE International Symposium on Personal, Indoor and Mobile Radio Communications*, vol. 2, (San Diego, CA, USA), pp. 81–85, Sept. 30–Oct. 3, 2001.

[10] T. Komine and M. Nakagawa, "Fundamental Analysis for Visible–Light Communication System using LED Lights," *IEEE Trans. Consum. Electron.*, vol. 50, pp. 100–107, Feb. 2004.

[11] D. Tsonev, S. Videv, and H. Haas, "Towards a 100 Gb/s Visible Light Wireless Access Network," *OSA Opt. Express*, vol. 23, pp. 1627–1637, Jan 2015.

[12] C. Lee, C. Shen, C. Cozzan, R. M. Farrell, S. Nakamura, A. Y. Alyamani, B. S. Ooi, J. E. Bowers, S. P. DenBaars, and J. Speck, "Semipolar GaN-based Laser Diodes for Gbit/s White Lighting Communication: Devices to Systems," in *Proc. SPIE*, vol. 10532, (San Francisco, CA, USA), pp. 10532 –10532, Feb., 23 2018.

[13] J. Brodrick, "Suggested Research Topics Supplement: Technology and Market Context." Retrieved from `https://www.energy.gov/sites/prod/files/2017/09/f37/ssl_supplement_suggested-topics_sep2017_0.pdf`, 2017.

[14] I. Navigant Consulting, "Adoption of Light-Emitting Diodes in Common Lighting Applications." Retrieved from `https://energy.gov/sites/prod/files/2017/08/f35/led-adoption-jul2017_0.pdf`, Aug. 2017.

[15] S. Dimitrov and H. Haas, *Principles of LED Light Communications: Towards Networked Li-Fi*. Cambridge University Press, 2015.

[16] H. Haas, L. Yin, Y. Wang, and C. Chen, "What is LiFi?," *IEEE/OSA J. Lightw. Technol.*, vol. 34, pp. 1533–1544, Mar. 2016.

[17] C. Chen, D. A. Basnayaka, and H. Haas, "Downlink Performance of Optical Attocell Networks," *IEEE/OSA J. Lightw. Technol.*, vol. 34, pp. 137–156, Jan. 2016.

[18] N. Serafimovski, R. Lacroix, M. Perrufel, S. Leroux, S. Clement, N. Kundu, D. Chiaroni, G. Patwardhan, A. Myles, C. Jurczak, M. Fleschen, M. Ragusky, V. Jungnickel, D. Ktenas, and H. Haas, "Light Communications for Wireless Local Area Networking ," *IEEE 5G Tech Focus*, vol. 2, May 2018.

[19] J. M. Kahn and J. R. Barry, "Wireless Infrared Communications," *Proc. IEEE*, vol. 85, pp. 265–298, Feb. 1997.

[20] J. B. Carruthers and J. M. Kahn, "Multiple-subcarrier Modulation for Nondirected Wireless Infrared Communication," *IEEE J. Sel. Areas Commun.*, vol. 14, pp. 538–546, Apr. 1996.

[21] J. Armstrong and A. Lowery, "Power Efficient Optical OFDM," *IET Electronics Letters*, vol. 42, pp. 370–372, Mar. 16, 2006.

[22] N. Fernando, Y. Hong, and E. Viterbo, "Flip-OFDM for Unipolar Communication Systems," *IEEE Trans. on Commun.*, vol. 60, pp. 3726–3733, Dec. 2012.

[23] D. Tsonev, S. Sinanović, and H. Haas, "Novel Unipolar Orthogonal Frequency Division Multiplexing (U-OFDM) for Optical Wireless," in *Proc. of the Vehicular Technology Conference (VTC Spring)*, (Yokohama, Japan), IEEE, May 6–9 2012.

[24] S. C. J. Lee, S. Randel, F. Breyer, and A. M. J. Koonen, "PAM-DMT for Intensity-Modulated and Direct-Detection Optical Communication Systems," *IEEE Photon. Technol. Lett.*, vol. 21, pp. 1749–1751, Dec. 2009.

[25] D. Tsonev and H. Haas, "Avoiding Spectral Efficiency Loss in Unipolar OFDM for Optical Wireless Communication," in *Proc. of the International Conference on Communications (ICC)*, (Sydney, Australia), IEEE, June, 10–14 2014.

[26] D. Tsonev, S. Videv, and H. Haas, "Unlocking Spectral Efficiency in Intensity Modulation and Direct Detection Systems," *IEEE J. Sel. Areas Commun.*, vol. 33, no. 99, pp. 1758–1770, 2015.

[27] Y. Zhou, J. Zhao, M. Zhang, J. Shi, and N. Chi, "2.32 Gbit/s Phosphorescent White LED Visible Light Communication Aided by Two-staged Linear Software Equalizer," in *2016 10th International Symposium on Communication Systems, Networks and Digital Signal Processing (CSNDSP)*, (Prague, Czech Republic), pp. 1–4, July, 20–22 2016.

[28] J. J. D. McKendry, R. P. Green, A. E. Kelly, Z. Gong, B. Guilhabert, D. Massoubre, E. Gu and M. D. Dawson, "High-Speed Visible Light Communications Using Individual Pixels in a Micro Light-Emitting Diode Array," *IEEE Photon. Technol. Lett.*, vol. 22, pp. 1346–1348, Sept. 2010.

[29] G. Povey, "Top 10 Li-Fi Myths." Retrieved from `http://visiblelightcomm.com/top-10-li-fi-myths/`, June 2012.

[30] M. Islim, D. Tsonev, and H. Haas, "Spectrally Enhanced PAM-DMT for IM/DD Optical Wireless Communications," in *Proc. of the 25th Int. Symp. Pers. Indoor and Mobile Radio Commun. (PIMRC)*, (Hong Kong, China), pp. 927–932, IEEE, Aug. 30–Sept. 2 2015.

[31] M. Islim, D. Tsonev, and H. Haas, "On the Superposition Modulation for OFDM-based Optical Wireless Communication," in *Signal and Information Processing (GlobalSIP), 2015 IEEE Global Conference on*, (Orlando, USA), IEEE, Dec., 14–16 2015.

[32] M. S. Islim and H. Haas, "Augmenting the Spectral Efficiency of Enhanced PAM-DMT-based Optical Wireless Communications," *OSA Opt. Express*, vol. 24, pp. 11932–11949, May 2016.

[33] R. X. G. Ferreira, E. Xie, J. J. D. McKendry, S. Rajbhandari, H. Chun, G. Faulkner, S. Watson, A. E. Kelly, E. Gu, R. V. Penty, I. H. White, D. C. O'Brien, and M. D. Dawson, "High Bandwidth GaN-Based Micro-LEDs for Multi-Gb/s Visible Light Communications," *IEEE Photon. Technol. Lett.*, vol. 28, pp. 2023–2026, Oct 2016.

[34] M. S. Islim, R. X. Ferreira, X. He, E. Xie, S. Videv, S. Viola, S. Watson, N. Bamiedakis, R. V. Penty, I. H. White, A. E. Kelly, E. Gu, H. Haas, and M. D. Dawson, "Towards 10 Gb/s Orthogonal Frequency Division Multiplexing-based Visible Light Communication Using a GaN Violet Micro-LED," *OSA Photon. Res.*, vol. 5, pp. A35–A43, Apr 2017.

[35] S. Viola, M. S. Islim, S. Watson, S. Videv, H. Haas, and A. E. Kelly, "15 Gb/s OFDM-based VLC Using Direct Modulation of 450 GaN Laser Diode," in *Proc. SPIE*, vol. 10437, (Warsaw, Poland), pp. 10437 – 10437 – 7, 2017.

[36] M. S. Islim and H. Haas, "An Investigation of the Sunlight Irradiance Effect on Visible Light Communications," in *2017 IEEE 28th Annual International Sympo-*

273

sium on Personal, Indoor, and Mobile Radio Communications (PIMRC), (Montreal, Canada), pp. 1–6, Oct., 8–13 2017.

[37] M. S. Islim, S. Videv, M. Safari, E. Xie, J. J. D. McKendry, E. Gu, M. D. Dawson, and H. Haas, "The Impact of Solar Irradiance on Visible Light Communications," *IEEE/OSA J. Lightw. Technol.*, vol. 36, pp. 2376–2386, Jun 2018.

[38] A. G. Bell, "Selenium and the Photophone," *Nature*, vol. 22, no. 569, pp. 500–503, 1880.

[39] M. Afgani, H. Haas, H. Elgala, and D. Knipp, "Visible Light Communication using OFDM," in *2nd International Conference on Testbeds and Research Infrastructures for the Development of Networks and Communities. TRIDENTCOM*, (Barcelona, Spain), pp. 6–134, Mar., 1–3 2006.

[40] M. Guarnieri, "The Rise of Light – Discovering Its Secrets," *Proc. IEEE*, vol. 104, pp. 467–473, Feb 2016.

[41] K. Uluc, G. C. Kujoth, and M. K. Baskaya, "Operating Microscopes: Past, Present, and Future," *Neurosurgical Focus*, vol. 27, no. 3, p. E4, 2009. PMID: 19722819.

[42] M. Guarnieri, "Two Millennia of Light: The Long Path to Maxwell's Waves," *IEEE Ind. Electron. Mag.*, vol. 9, pp. 54–60, June 2015.

[43] P. M. Neumann, "Reflections on Reflection in a Spherical Mirror," *The American Mathematical Monthly*, vol. 105, no. 6, pp. 523–528, 1998.

[44] W. G. Adams and R. E. Day, "V. The Action of Light on Selenium," *Proceedings of the Royal Society of London*, vol. 25, no. 171-178, pp. 113–117, 1877.

[45] V. W. S. Chan, "Free-Space Optical Communications," *IEEE/OSA J. Lightw. Technol.*, vol. 24, pp. 4750–4762, Dec. 2006.

[46] I. Akasaki, H. Amano, and S. Nakamura, "Blue LEDs–Filling the World with New Light," *Nobel Prize*, 2014.

[47] P. Banelli and S. Cacopardi, "Theoretical Analysis and Performance of OFDM Signals in Nonlinear AWGN Channels," *IEEE Trans. on Commun.*, vol. 48, pp. 430–441, March 2000.

[48] S. Dimitrov and H. Haas, "Information Rate of OFDM-Based Optical Wireless Communication Systems With Nonlinear Distortion," *IEEE/OSA J. Lightw. Technol.*, vol. 31, pp. 918–929, Mar. 2013.

[49] G. Stepniak, J. Siuzdak, and P. Zwierko, "Compensation of a VLC Phosphorescent White LED Nonlinearity by Means of Volterra DFE," *IEEE Photon. Technol. Lett.*, vol. 25, pp. 1597–1600, Aug 2013.

[50] W. Zhao, Q. Guo, J. Tong, J. Xi, Y. Yu, P. Niu, and X. Sun, "Orthogonal Polynomial-Based Nonlinearity Modeling and Mitigation for LED Communications," *IEEE Photon. J.*, vol. 8, pp. 1–12, Aug 2016.

[51] B. Inan, S.C.J. Lee, S. Randel, I. Neokosmidis, A.M.J. Koonen and J.W. Walewski, "Impact of LED Nonlinearity on Discrete Multitone Modulation," *IEEE/OSA J. Opt. Commun. Netw.*, vol. 1, pp. 439 –451, oct 2009.

[52] H. Elgala, R. Mesleh, and H. Haas, "Non-linearity Effects and Predistortion in Optical OFDM Wireless Transmission Using LEDs," *Inderscience International Journal of Ultra Wideband Communications and Systems (IJUWBCS)*, vol. 1, no. 2, pp. 143–150, 2009.

[53] D. Tsonev, S. Sinanovic, and H. Haas, "Complete Modeling of Nonlinear Distortion in OFDM-based Optical Wireless Communication," *IEEE/OSA J. Lightw. Technol.*, vol. 31, pp. 3064–3076, Sept. 15 2013.

[54] A. M. Khalid, G. Cossu, R. Corsini, P. Choudhury, and E. Ciaramella, "1-Gb/s Transmission Over a Phosphorescent White LED by using Rate-adaptive Discrete Multitone Modulation," *IEEE Photon. J.*, vol. 4, pp. 1465–1473, Oct. 2012.

[55] Y. Guo, O. Alkhazragi, C. H. Kang, C. Shen, Y. Mao, X. Sun, T. K. Ng, and B. S. Ooi, "A Tutorial on Laser-based Lighting and Visible Light Communications: Device and Technology

Invited

," *Chin. Opt. Lett.*, vol. 17, p. 040601, Apr 2019.

[56] H. Chun, A. Gomez, G. Faulkner, and D. O'Brien, "A Spectrally Efficient Equalization Technique for Optical Sources with Direct Modulation," *OSA Opt. Lett.*, vol. 43, pp. 2708–2711, Jun 2018.

[57] C. Foucher, M. I. Sufyan, B. J. E. Guilhabert, S. Videv, S. Rajbhandari, A. G. Diaz, H. Chun, D. A. Vithanage, G. A. Turnbull, I. D. W. Samuel, G. Faulkner, D. C. O'Brien, H. Haas, N. Laurand, and M. D. Dawson, "Flexible Glass Hybridized Colloidal Quantum Dots for Gb/s Visible Light Communications," *IEEE Photon. J.*, vol. 10, pp. 1–11, Feb 2018.

[58] M. F. Leitão, J. M. M. Santos, B. Guilhabert, S. Watson, A. E. Kelly, M. S. Islim, H. Haas, M. D. Dawson, and N. Laurand, "Gb/s Visible Light Communications With Colloidal Quantum Dot Color Converters," *IEEE J. Sel. Topics. Quantum Electron.*, vol. 23, pp. 1–10, Sept 2017.

[59] A. Neumann, J. Wierer, Jr., W. Davis, Y. Ohno, R. Brueck, and J. Tsao, "Four-color Laser White Illuminant Demonstrating High Color-rendering Quality," *OSA Opt. Express*, vol. 19, pp. A982–A990, July 2011.

[60] L.-Y. Wei, C.-W. Hsu, C.-W. Chow, and C.-H. Yeh, "20.231 Gbit/s Tricolor Red/Green/Blue Laser Diode Based Bidirectional Signal Remodulation Visible-Light Communication System," *OSA Photon. Res.*, vol. 6, pp. 422–426, May 2018.

[61] Y.-C. Chi, D.-H. Hsieh, C.-Y. Lin, H.-Y. Chen, C.-Y. Huang, J.-H. He, B. Ooi, S. P. DenBaars, S. Nakamura, H.-C. Kuo, *et al.*, "Phosphorous Diffuser Diverged Blue Laser Diode for Indoor Lighting and Communication," *Sci. Rep.*, vol. 5, p. 18690, 2015.

[62] I. Dursun, C. Shen, M. R. Parida, J. Pan, S. P. Sarmah, D. Priante, N. Alyami, J. Liu, M. I. Saidaminov, M. S. Alias, A. L. Abdelhady, T. K. Ng, O. F. Mohammed, B. S. Ooi, and O. M. Bakr, "Perovskite Nanocrystals as a Color Converter for Visible Light Communication," *ACS Photon.*, vol. 3, no. 7, pp. 1150–1156, 2016.

[63] C. Lee, C. Shen, C. Cozzan, R. M. Farrell, J. S. Speck, S. Nakamura, B. S. Ooi, and S. P. DenBaars, "Gigabit-per-second White Light-based Visible Light Communication Using Near-Ultraviolet Laser Diode and Red-, Green-, and Blue-emitting Phosphors," *OSA Opt. Express*, vol. 25, pp. 17480–17487, Jul 2017.

[64] P. A. Haigh, Z. Ghassemlooy, S. Rajbhandari, and I. Papakonstantinou, "Visible Light Communications Using Organic Light Emitting Diodes," *IEEE Commun. Mag.*, vol. 51, pp. 148–154, August 2013.

[65] T. Fukuda, T. Okada, B. Wei, M. Ichikawa, and Y. Taniguchi, "Influence of Carrier-injection Efficiency on Modulation Rate of Organic Light Source," *OSA Opt. Lett.*, vol. 32, pp. 1905–1907, Jul 2007.

[66] E. Sarbazi, M. Safari, and H. Haas, "Statistical Modeling of Single-Photon Avalanche Diode Receivers for Optical Wireless Communications," *IEEE Trans. on Commun.*, pp. 1–1, 2018.

[67] Z. Wang, D. Tsonev, S. Videv, and H. Haas, "On the Design of a Solar-Panel Receiver for Optical Wireless Communications with Simultaneous Energy Harvesting," *IEEE J. Sel. Areas Commun.*, vol. 33, pp. 1612–1623, Aug. 2015.

[68] Z. Chen, N. Serafimovski, and H. Haas, "Angle Diversity for an Indoor Cellular Visible Light Communication System," in *Proc. IEEE Veh. Technol. Conf.*, (Seoul, South Korea), pp. 1–5, May 18–21, 2014.

[69] J. B. Carruthers and J. M. Kahn, "Angle Diversity for Nondirected Wireless Infrared Communication," *IEEE Trans. on Commun.*, vol. 48, pp. 960–969, June 2000.

[70] P. P. Manousiadis, S. Rajbhandari, R. Mulyawan, D. A. Vithanage, H. Chun, G. Faulkner, D. O. Brien, G. A. Turnbull, S. Collins, and I. D. Samuel, "Wide field-of-view fluorescent antenna for visible light communications beyond the etendue limit," *OSA Optica*, vol. 3, no. 7, pp. 702–706, 2016.

[71] T. Peyronel, K. J. Quirk, S. C. Wang, and T. G. Tiecke, "Luminescent Detector for Free-space Optical Communication," *OSA Optica*, vol. 3, pp. 787–792, Jul 2016.

[72] S. Cova, M. Ghioni, A. Lacaita, C. Samori, and F. Zappa, "Avalanche Photodiode and Quenching Circuits for Single-photon Detection," *OSA Applied Optics*, vol. 35, pp. 1956–1976, Apr. 20 1996.

[73] Y. Li, S. Videv, M. Abdallah, K. Qaraqe, M. Uysal, and H. Haas, "Single Photon Avalanche Diode (SPAD) VLC System and Application to Downhole Monitoring," in *Proc. IEEE Global Communications Conference*, pp. 2108–2113, Dec. 2014.

[74] D. Chitnis, L. Zhang, H. Chun, S. Rajbhandari, G. Faulkner, D. O'Brien, and S. Collins, "A 200 Mb/s VLC Demonstration with a SPAD Based Receiver," in *2015 IEEE Summer Topicals Meeting Series (SUM)*, (Nassau, Bahamas), pp. 226–227, July 2015.

[75] S.-M. Kim and J.-S. Won, "Simultaneous Reception of Visible Light Communication and Optical Energy Using a Solar Cell Receiver," in *Proc. IEEE Int. Conf. Converg.*, (Jeju Island, South Korea), pp. 896–897, Oct. 14–16 2013.

[76] J. Fakidis, S. Videv, H. Helmers, and H. Haas, "0.5-Gb/s OFDM-Based Laser Data and Power Transfer Using a GaAs Photovoltaic Cell," *IEEE Photon. Technol. Lett.*, vol. 30, pp. 841–844, May 2018.

[77] S. Zhang, D. Tsonev, S. Videv, S. Ghosh, G. A. Turnbull, I. D. W. Samuel, and H. Haas, "Organic Solar Cells as High-speed Data Detectors for Visible Light Communication," *OSA Optica*, vol. 2, pp. 607–610, Jul 2015.

[78] R. Zhang and C. K. Ho, "MIMO Broadcasting for Simultaneous Wireless Information and Power Transfer," *IEEE Trans. on Wireless Commun.*, vol. 12, pp. 1989–2001, May 2013.

[79] F. M. Davidson and X. Sun, "Gaussian Approximation Versus Nearly Exact Performance Analysis of Optical Communication Systems with PPM Signaling and APD Receivers," *IEEE Trans. on Commun.*, vol. 36, pp. 1185–1192, Nov 1988.

[80] J. Barry, J. Kahn, W. Krause, E. Lee, and D. Messerschmitt, "Simulation of Multipath Impulse Response for Indoor Wireless Optical Channels," *IEEE J. Select. Areas Commun.*, vol. 11, pp. 367–379, Apr. 1993.

[81] S. Rajbhandari, J. J. D. McKendry, J. Herrnsdorf, H. Chun, G. Faulkner, H. Haas, I. M. Watson, D. O'Brien, and M. D. Dawson, "A Review of Gallium Nitride LEDs for Multi-Gigabit-per-second Visible Light Data Communications," *IOP Semiconductor Science and Technology*, vol. 32, no. 2, p. 023001, 2017.

[82] D. Tsonev, H. Chun, S. Rajbhandari, J. J. D. McKendry, S. Videv, E. Gu, M. Haji, S. Watson, A. E. Kelly, G. Faulkner, M. D. Dawson, H. Haas and D. O'Brien, "A 3-Gb/s Single-LED OFDM-based Wireless VLC Link Using a Gallium Nitride μLED," *IEEE Photon. Technol. Lett.*, vol. 26, pp. 637–640, Apr. 2014.

[83] S. Randel, F. Breyer, S. C. J. Lee, and J. W. Walewski, "Advanced Modulation Schemes for Short-Range Optical Communications," *IEEE Journal of Selected Topics in Quantum Electronics*, vol. PP, no. 99, pp. 1 –10, 2010.

[84] IEEE Std. 802.15.7-2011, "IEEE Standard for Local and Metropolitan Area Networks, Part 15.7: Short-Range Wireless Optical Communication Using Visible Light," 2011.

[85] S. H. Lee, S.-Y. Jung, and J. K. Kwon, "Modulation and coding for dimmable visible light communication," *IEEE Commun. Mag.*, vol. 53, pp. 136–143, Feb 2015.

[86] S. Dimitrov, S. Sinanovic, and H. Haas, "Clipping Noise in OFDM-Based Optical Wireless Communication Systems," *IEEE Trans. on Commun.*, vol. 60, pp. 1072–1081, April 2012.

[87] M. Mossaad, S. Hranilovic, and L. Lampe, "Visible Light Communications Using OFDM and Multiple LEDs," *IEEE Trans. Commun.*, vol. 63, pp. 4304–4313, Nov 2015.

[88] H. Dong, H. Zhang, K. Lang, B. Yu, and M. Yao, "OFDM Visible Light Communication Transmitter Based on LED Array," *Chin. Opt. Lett.*, vol. 12, p. 052301, May 2014.

[89] H. Elgala and T. D. C. Little, "Reverse Polarity Optical-OFDM (RPO-OFDM): Dimming Compatible OFDM for Gigabit VLC links," *OSA Opt. Express*, vol. 21, pp. 24288–24299, Oct 2013.

[90] H. Elgala and T. Little, "P-OFDM: Spectrally Efficient Unipolar OFDM," in *Optical Fiber Communications Conference and Exhibition (OFC), 2014*, (San Francisco, CA, USA), pp. 1–3, March 2014.

[91] H. Elgala and T. D. C. Little, "Polar-Based OFDM and SC-FDE Links Toward Energy-Efficient Gbps Transmission Under IM-DD Optical System Constraints," *IEEE/OSA J. Opt. Commun. Netw.*, vol. 7, pp. A277–A284, Feb 2015.

[92] K. Asadzadeh, A. Farid, and S. Hranilovic, "Spectrally Factorized Optical OFDM," in *12th Canadian Workshop on Information Theory (CWIT 2011)*, (Kelowna, BC, Canada), pp. 102–105, IEEE, May 17–20 2011.

[93] T. Mao, C. Qian, Q. Wang, J. Quan, and Z. Wang, "PM-DCO-OFDM for PAPR Reduction in Visible Light Communications," in *Opto-Electronics and Communications Conference (OECC), 2015*, (Shanghai, China), pp. 1–3, June 2015.

[94] M. S. Moreolo, R. M. noz, and G. Junyent, "Novel Power Efficient Optical OFDM Based on Hartley Transform for Intensity-Modulated Direct-Detection Systems," *IEEE/OSA J. Lightwave Technol.*, vol. 28, pp. 798–805, Mar 2010.

[95] W. Huang, C. Gong, and Z. Xu, "System and Waveform Design for Wavelet Packet Division Multiplexing-Based Visible Light Communications," *IEEE/OSA J. Lightwave Technol.*, vol. 33, pp. 3041–3051, July 2015.

[96] M. Noshad and M. Brandt-Pearce, "Hadamard Coded Modulation for Visible Light Communications," *IEEE Trans. Commun.*, vol. PP, no. 99, pp. 1–1, 2016.

[97] The International Commission on Illumination (CIE), "CIE 1931 Standard Colorimetric Observer." Retrieved from `http://www.cie.co.at`, Aug. 2008.

[98] F. Xiong, *Digital Modulation Techniques*. Artech House Publishers, 2nd edition ed., 2006.

[99] L. Chen, B. Krongold, and J. Evans, "Diversity Combining for Asymmetrically Clipped Optical OFDM in IM/DD Channels," in *Global Telecommunications Conference, 2009. GLOBECOM 2009. IEEE*, (Honolulu, HI, USA), pp. 1–6, Nov. 30–4 Dec. 2009.

[100] J. Dang, Z. Zhang, and L. Wu, "A Novel Receiver for ACO-OFDM in Visible Light Communication," *IEEE Commun. Lett.*, vol. 17, pp. 2320–2323, December 2013.

[101] N. Huang, J.-B. Wang, C. Pan, J.-Y. Wang, Y. Pan, and M. Chen, "Iterative Receiver for Flip-OFDM in Optical Wireless Communication," *IEEE Photon. Technol. Lett.*, vol. 27, pp. 1729–1732, Aug 2015.

[102] Y. Zheng, Z. Zhang, J. Dang, and L. Wu, "A Novel Receiver for Filp-OFDM in Optical Wireless Communication," in *Communication Technology (ICCT), 2015 IEEE 16th International Conference on*, (Hangzhou, China), pp. 620–625, Oct 2015.

[103] J. Dang, Z. Zhang, and L. Wu, "Frequency-Domain Diversity Combining Receiver for ACO-OFDM System," *IEEE Photon. J*, vol. 7, pp. 1–10, Dec 2015.

[104] J. Xu, W. Xu, H. Zhang, and X. You, "Asymmetrically Reconstructed Optical OFDM for Visible Light Communications," *IEEE Photon. J*, vol. 8, pp. 1–18, Feb 2016.

[105] N. Huang, J.-B. Wang, J. Wang, C. Pan, H. Wang, and M. Chen, "Receiver Design for PAM-DMT in Indoor Optical Wireless Links," *IEEE Photon. Technol. Lett.*, vol. 27, pp. 161–164, Jan 2015.

[106] N. Xiang, Z. Zhang, J. Dang, and L. Wu, "A Novel Receiver Design for PAM-DMT in Optical Wireless Communication Systems," *IEEE Photon. Technol. Lett.*, vol. 27, pp. 1919–1922, Sept 2015.

[107] S. Dissanayake, K. Panta, and J. Armstrong, "A Novel Technique to Simultaneously Transmit ACO-OFDM and DCO-OFDM in IM/DD Systems," in *IEEE GLOBECOM Workshops (GC Wkshps)*, (Houston, TX, USA), pp. 782–786, IEEE, Dec. 5–9 2011.

[108] B. Ranjha and M. Kavehrad, "Hybrid Asymmetrically Clipped OFDM-based IM/DD Optical Wireless System," *IEEE/OSA J. Opt. Commun. Netw.*, vol. 6, pp. 387–396, April 2014.

[109] N. Wu and Y. Bar-Ness, "A Novel Power-efficient Scheme Asymmetrically and Symmetrically Clipping Optical (ASCO)-OFDM for IM/DD Optical Systems," *EURASIP Journal on Advances in Signal Processing*, vol. 2015, no. 1, pp. 1–10, 2015.

[110] M. Islim, D. Tsonev, and H. Haas, "A Generalized Solution to the Spectral Efficiency Loss in Unipolar Optical OFDM-based Systems," in *Proc. of the International Conference on Communications (ICC)*, (London, UK), IEEE, June, 8–12 2015.

[111] H. Elgala and T. Little, "SEE-OFDM: Spectral and energy efficient OFDM for optical IM/DD systems," in *Personal, Indoor, and Mobile Radio Communication (PIMRC), 2014 IEEE 25th Annual International Symposium on*, (Washington DC, USA), pp. 851–855, 2–5 2014.

[112] Q. Wang, C. Qian, X. Guo, Z. Wang, D. G. Cunningham, and I. H. White, "Layered ACO-OFDM for Intensity-Modulated Direct-Detection Optical Wireless Transmission," *OSA Opt. Express*, vol. 23, pp. 12382–12393, May 2015.

[113] A. J. Lowery, "Comparisons of Spectrally-enhanced Asymmetrically-clipped Optical OFDM Systems," *OSA Opt. Express*, vol. 24, pp. 3950–3966, Feb 2016.

[114] J. Armstrong and B. J. C. Schmidt, "Comparison of Asymmetrically Clipped Optical OFDM and DC-Biased Optical OFDM in AWGN," *IEEE Commun. Lett.*, vol. 12, pp. 343–345, May 2008.

[115] ITU-T, "Forward Error Correction for High Bit-rate DWDM Submarine Systems," Tech. Rep. ITU-T G.975.1, ITU, Retrieved Nov. 19, 2013 from `http://www.itu.int/rec/T-REC-G.975.1-200402-I/en`, 2004.

[116] S. Long, M. Khalighi, M. Wolf, S. Bourennane, and Z. Ghassemlooy, "Channel Characterization for Indoor Visible Light Communications," in *2014 3rd International Workshop in Optical Wireless Communications (IWOW)*, (Funchal, Portugal), pp. 75–79, Sept 2014.

[117] F. Lopez-Hernandez, R. Perez-Jimenez, and A. Santamaria, "Ray-tracing Algorithms for Fast Calculation of the Impulse Response on Diffuse IR-wireless Indoor Channels," *SPIE Optical Engineering*, vol. 39, pp. 2775–2780, Oct. 2000.

[118] J. G. Proakis and D. K. Manolakis, *Digital Signal Processing: Principles, Algorithms and Application*. Prentice Hall, 4 ed., Apr. 2006.

[119] H. Hassanieh, P. Indyk, D. Katabi, and E. Price, "Simple and Practical Algorithm for Sparse Fourier Transform," in *Proceedings of the Twenty-third Annual ACM-SIAM Symposium on Discrete Algorithms*, SODA '12, (Philadelphia, PA, USA), pp. 1183–1194, Society for Industrial and Applied Mathematics, 2012.

[120] Q. Wang, B. Song, B. Corcoran, L. Zhuang, and A. J. Lowery, "Real-Time Demonstration of Augmented-Spectral-Efficiency DMT Transmitter Using a Single IFFT," *IEEE/OSA J. Lightwave Technol.*, vol. 35, pp. 4796–4803, Nov 2017.

[121] D. Tsonev, H. Chun, S. Rajbhandari, J. McKendry, S. Videv, E. Gu, M. Haji, S. Watson, A. Kelly, G. Faulkner, M. Dawson, H. Haas, and D. O'Brien, "A 3-Gb/s Single-LED OFDM-Based Wireless VLC Link Using a Gallium Nitride µLED," *IEEE Photon. Technol. Lett.*, vol. 26, pp. 637–640, Apr. 2014.

[122] J. Herrnsdorf, J. McKendry, E. Xie, M. Strain, E. Gu, I. Watson, and M. Dawson, "Gallium Nitride Structured Illumination Light Sources," in *Light, Energy and the Environment*, (Leipzig Germany), p. SSM2C.1, Optical Society of America, 11 2016.

[123] T.-C. Wu, Y.-C. Chi, H.-Y. Wang, C.-T. Tsai, and L. G-R, "Blue Laser Diode Enables Underwater Communication at 12.4 Gbps," *Sci. Rep.*, vol. 7, no. 40480, 2017.

[124] J. J. D. McKendry, D. Tsonev, R. Ferreira, S. Videv, A. D. Griffiths, S. Watson, E. Gu, A. E. Kelly, H. Haas, and M. D. Dawson, "Gb/s Single-LED OFDM-based VLC Using Violet and UV Gallium Nitride µLEDs," in *2015 IEEE Summer Topicals Meeting Series (SUM)*, (Nassau, Bahamas), pp. 175–176, July 2015.

[125] S. Pimputkar, J. S. Speck, S. P. DenBaars, and S. Nakamura, "Prospects for LED Lighting," *Nature photonics*, vol. 3, no. 4, p. 180, 2009.

[126] T. Sakano, T. Matsumoto, and K. Noguchi, "Three-Dimensional Board-to-Board Free-Space Optical Interconnects and Their Application to the Prototype Multi-processor System: COSINE-III," *Appl. Opt.*, vol. 34, pp. 1815–1822, Apr 1995.

[127] T. Kurner, "Towards Future THz Communications Systems," *International Journal of Terahertz Science and Technology*, vol. 5, pp. 11–17, Mar. 2012.

[128] B. Song, C. Zhu, B. Corcoran, Q. Wang, L. Zhuang, and A. J. Lowery, "Experimental Layered/Enhanced ACO-OFDM Short-Haul Optical Fiber Link," *IEEE Photon. Technol. Lett.*, vol. 28, pp. 2815–2818, Dec 2016.

[129] Q. Wang, B. Song, B. Corcoran, D. Boland, C. Zhu, L. Zhuang, and A. J. Lowery, "Hardware-Efficient Signal Generation of Layered/Enhanced ACO-OFDM for Short-Haul Fiber-Optic Links," *OSA Opt. Express*, vol. 25, pp. 13359–13371, Jun 2017.

[130] B. Song, B. Corcoran, Q. Wang, and A. J. Lowery, "Field-Trial of Layered/Enhanced ACO-OFDM," in *2017 European Conference on Optical Communication (ECOC)*, (Gothenburg, Sweden), pp. 1–3, Sept. 17–21 2017.

[131] H. E. Levin, "A Complete and Optimal Data Allocation Method for Practical Discrete Multitone Systems," in *Proc. IEEE Global Telecommun. Conf.*, vol. 1, (San Antonio, TX , USA), pp. 369–374, 25–29 Nov. 2001.

[132] C. Shannon, "A Mathematical Theory of Communication," *Bell System Technical Journal*, vol. 27, pp. 379–423 & 623–656, July & Oct. 1948.

[133] L. Peng, S. Haese, and M. Hélard, "Optimized Discrete Multitone Communication over Polymer Optical Fiber," *IEEE/OSA J. Opt. Commun. Netw.*, vol. 5, pp. 1313–1327, Nov 2013.

[134] J. Jiang, Y. Huo, F. Jin, P. Zhang, Z. Wang, Z. Xu, H. Haas, and L. Hanzo, "Video Streaming in the Multiuser Indoor Visible Light Downlink," *IEEE Access*, vol. 3, pp. 2959–2986, 2015.

[135] J. Fakidis, M. Ijaz, S. Kucera, H. Claussen, and H. Haas, "On the Design of an Optical Wireless Link for Small Cell Backhaul Communication and Energy Harvesting," in *Proc. IEEE 25th Annu. Int. Symp. Pers. Indoor Mobile Radio Commun.*, (Washington, DC USA), pp. 58–62, 9 2014.

[136] E. Diaz and M. Knobl, "Prototyping Illumination Systems with Stock Optical Components." Photonik International, 2012.

[137] OSRAM Opto Semiconductors GmbH, "Datasheet: Blue Laser Diode in TO38 ICut Package," Aug. 2018.

[138] D. Tsonev, S. Videv, and H. Haas, "Light Fidelity (Li-Fi): Towards All-Optical Networking," in *Proc. SPIE, Broadband Access Commun. Technol. VIII*, vol. 9007, (San Francisco, CA, USA), Dec. 18 2013.

[139] Y. H. Chung and S. B. Oh, "Efficient Optical Filtering for Outdoor Visible Light Communications in the Presence of Sunlight or Articifical Light," in *Intelligent Signal Processing and Communications Systems (ISPACS), 2013 International Symposium on*, (Naha, Japan), pp. 749–752, Nov., 12–15 2013.

[140] T. Hamza, M.-A. Khalighi, S. Bourennane, P. Léon, and J. Opderbecke, "Investigation of Solar Noise Impact on the Performance of Underwater Wireless Optical Communication Links," *OSA Opt. Express*, vol. 24, pp. 25832–25845, Oct 2016.

[141] M. Beshr, C. Michie, and I. Andonovic, "Evaluation of Visible Light Communication system performance in the presence of sunlight irradiance," in *2015 17th International Conference on Transparent Optical Networks (ICTON)*, (Budapest, Hungary), pp. 1–4, July, 5–9 2015.

[142] Y.-h. C. Yong-hyeon Kim, "Experimental Outdoor Visible Light Data Communication System using Differential Decision Threshold with Optical and Color Filters," *SPIE Optical Engineering*, vol. 54, pp. 54 – 54 – 3, 2015.

[143] D. R. Kim, S. H. Yang, H. S. Kim, Y. H. Son, and S. K. Han, "Outdoor Visible Light Communication for inter-vehicle Communication using Controller Area Network," in *2012 Fourth International Conference on Communications and Electronics (ICCE)*, (Hue, Vietnam), pp. 31–34, Aug., 1–3 2012.

[144] ASTM, "Standard Tables for Reference Solar Spectral Irradiances: Direct Normal and Hemispherical on 37° Tilted Surface," 2014.

[145] G. Cossu, R. Corsini, A. M. Khalid, S. Balestrino, A. Coppelli, A. Caiti, and E. Ciaramella, "Experimental Demonstration of High Speed Underwater Visible Light Communications," in *2013 2nd International Workshop on Optical Wireless Communications (IWOW)*, (Newcastle upon Tyne, UK), pp. 11–15, Oct., 21 2013.

[146] R. Rondanelli, A. Molina, and M. Falvey, "The Atacama Surface Solar Maximum," *Bulletin of the American Meteorological Society*, vol. 96, no. 3, pp. 405–418, 2015.

[147] ASTM, "Standard Solar Constant and Zero Air Mass Solar Spectral Irradiance Tables," 2014.

[148] W. B. Stine and M. Geyer, "Power from the Sun." Retrieved from `http://Powerfromthesun.net`, 2001.

[149] I. Reda and A. Andreas, "Solar Position Algorithm for Solar Radiation Applications," *Solar energy*, vol. 76, no. 5, pp. 577–589, 2004.

[150] A. Smets, K. Jäger, O. Isabella, M. Zeman, and R. van Swaaij, *Solar Energy: The Physics and Engineering of Photovoltaic Conversion, Technologies and Systems.* UIT Cambridge, 2016.

[151] C. A. Gueymard, "Parameterized Transmittance Model for Direct Beam and Circumsolar Spectral Irradiance," *Solar Energy*, vol. 71, no. 5, pp. 325–346, 2001.

[152] C. Gueymard, *SMARTS2: a Simple Model of the Atmospheric Radiative Transfer of Sunshine: Algorithms and Performance Assessment.* Florida Solar Energy Center Cocoa, FL, 1995.

[153] F. Xu, M. A. Khalighi, and S. Bourennane, "Impact of Different Noise Sources on the Performance of PIN- and APD-based FSO Receivers," in *Proceedings of the 11th International Conference on Telecommunications*, (Graz, Austria), pp. 211–218, June, 15–17 2011.

[154] S. Dimitrov, S. Sinanovic, and H. Haas, "Signal Shaping and Modulation for Optical Wireless Communication," *IEEE/OSA J. Lightwave Technol.*, vol. 30, pp. 1319–1328, May 2012.

[155] Hamamatsu Photonics K.K, "Characteristics and Use of SI-APD (avalanche photodiode)," May 2004.

[156] G. Keiser, *Optical Communications Essentials.* McGraw-Hill, 2003.

[157] C. M. Lampert, "Heat Mirror Coatings for Energy Conserving Windows," *Solar Energy Materials*, vol. 6, no. 1, pp. 1 – 41, 1981.

[158] Q. Wang, Z. Wang, X. Guo, and L. Dai, "Improved Receiver Design for Layered ACO-OFDM in Optical Wireless Communications," *IEEE Photon. Technol. Lett.*, vol. 28, pp. 319–322, Feb 2016.

[159] A. D. Griffiths, M. S. Islim, J. Herrnsdorf, J. J. D. McKendry, R. Henderson, H. Haas, E. Gu, and M. D. Dawson, "CMOS-integrated GaN LED Array for Discrete Power Level Stepping in Visible Light Communications," *OSA Opt. Express*, vol. 25, pp. A338–A345, Apr 2017.

[160] S. Lloyd, "Least Squares Quantization in PCM," *IEEE Trans. Inf. Theory*, vol. 28, pp. 129–137, March 1982.

[161] A. J. Lowery and L. B. Du, "Optical orthogonal division multiplexing for long haul optical communications: A review of the first five years," *Optical Fiber Technology*, vol. 17, no. 5, pp. 421 – 438, 2011. 100G and Beyond.

[162] A. Lowery and B. Corcoran, "Nanosecond-Latency IM/DD/DSB to Coherent/SSB Converter," in *2018 European Conference on Optical Communication (ECOC)*, (Rome, Italy), pp. 1–3, Sept. 23–27 2018.

[163] B. J. C. Schmidt, A. J. Lowery, and L. B. Du, "Low Sample Rate Transmitter for Direct-detection Optical OFDM," in *Optical Fiber Communications Conference and Exhibition (OFC), 2009*, (San Diego, CA, United States), pp. 1–3, Mar. 22–26, 2009.

[164] L. Zhang, T. Zuo, Y. Mao, Q. Zhang, E. Zhou, G. N. Liu, and X. Xu, "Beyond 100-Gb/s Transmission Over 80-km SMF Using Direct-Detection SSB-DMT at C-Band," *IEEE/OSA J. Lightwave Technol.*, vol. 34, pp. 723–729, Jan 2016.